NEW CHALLENGES FOR SEISMIC RISK MITIGATION IN URBAN AREAS

EDITED BY: Simone Barani, Aybige Akinci, Karin Sesetyan, Dario Albarello, Philippe Gueguen, Stefano Parolai, Roberto Paolucci and Dimitris Pitilakis

PUBLISHED IN: Frontiers in Earth Science

frontiers Research Topics

frontiers

ISSN 1664-8714
ISBN 978-2-83250-790-2
DOI 10.3389/978-2-83250-790-2

About Frontiers

Frontiers is more than just an open-access publisher of scholarly articles: it is a pioneering approach to the world of academia, radically improving the way scholarly research is managed. The grand vision of Frontiers is a world where all people have an equal opportunity to seek, share and generate knowledge. Frontiers provides immediate and permanent online open access to all its publications, but this alone is not enough to realize our grand goals.

Frontiers Journal Series

The Frontiers Journal Series is a multi-tier and interdisciplinary set of open-access, online journals, promising a paradigm shift from the current review, selection and dissemination processes in academic publishing. All Frontiers journals are driven by researchers for researchers; therefore, they constitute a service to the scholarly community. At the same time, the Frontiers Journal Series operates on a revolutionary invention, the tiered publishing system, initially addressing specific communities of scholars, and gradually climbing up to broader public understanding, thus serving the interests of the lay society, too.

Dedication to Quality

Each Frontiers article is a landmark of the highest quality, thanks to genuinely collaborative interactions between authors and review editors, who include some of the world's best academicians. Research must be certified by peers before entering a stream of knowledge that may eventually reach the public - and shape society; therefore, Frontiers only applies the most rigorous and unbiased reviews.
Frontiers revolutionizes research publishing by freely delivering the most outstanding research, evaluated with no bias from both the academic and social point of view. By applying the most advanced information technologies, Frontiers is catapulting scholarly publishing into a new generation.

What are Frontiers Research Topics?

Frontiers Research Topics are very popular trademarks of the Frontiers Journals Series: they are collections of at least ten articles, all centered on a particular subject. With their unique mix of varied contributions from Original Research to Review Articles, Frontiers Research Topics unify the most influential researchers, the latest key findings and historical advances in a hot research area! Find out more on how to host your own Frontiers Research Topic or contribute to one as an author by contacting the Frontiers Editorial Office: frontiersin.org/about/contact

NEW CHALLENGES FOR SEISMIC RISK MITIGATION IN URBAN AREAS

Topic Editors:
Simone Barani, University of Genoa, Italy
Aybige Akinci, Istituto Nazionale di Geofisica e Vulcanologia (INGV), Italy
Karin Sesetyan, Boğaziçi University, Turkey
Dario Albarello, University of Siena, Italy
Philippe Gueguen, UMR5275 Institut des Sciences de la Terre (ISTERRE), France
Stefano Parolai, Istituto Nazionale di Oceanografia e di Geofisica Sperimentale (Italy), Italy
Roberto Paolucci, Politecnico di Milano, Italy
Dimitris Pitilakis, Aristotle University of Thessaloniki, Greece

Citation: Barani, S., Akinci, A., Sesetyan, K., Albarello, D., Gueguen, P., Parolai, S., Paolucci, R., Pitilakis, D., eds. (2022). New Challenges for Seismic Risk Mitigation in Urban Areas. Lausanne: Frontiers Media SA. doi: 10.3389/978-2-83250-790-2

Table of Contents

frontiers in Earth Science

ORIGINAL RESEARCH
published: 31 March 2022
doi: 10.3389/feart.2022.812658

Amplification Behaviour of Compressional Waves in Unconsolidated Sediments

Janneke van Ginkel[1,2]*, *Elmer Ruigrok*[2,3], *Rick Wentinck*[4] and *Rien Herber*[1]

[1]Energy and Sustainability Research Institute Groningen, University of Groningen, Groningen, Netherlands, [2]R&D Seismology and Acoustics, Royal Netherlands Meteorological Institute, De Bilt, Netherlands, [3]Department of Earth Sciences, Utrecht University, Utrecht, Netherlands, [4]Independent Researcher, Haarlem, Netherlands

Similar to horizontal earthquake motions, vertical motions are amplified depedent on the local site conditions which can be critical for the safety of certain structures. Production of natural gas in Groningen, the Netherlands, results in reservoir compaction causing low magnitude, shallow earthquakes which are recorded with a borehole seismic network. These recordings form an excellent data set to understand how shallow unconsolidated subsurface geology influences the amplification behaviour of compressional waves (P-waves). First, we present borehole and single-station techniques (amplification factors, empirical transfer functions (ETF) and V/H spectral ratio implementations) to quantify vertical amplification. We show that vertical-wave incidence is a reasonable assumption. All techniques are capable of emphasising the sites with strong amplification of vertical ground motion during an earthquake. Subsequently, we compare ETF with single-station methods with the aim to develop proxies for vertical site-response using spectral ratios. In a second step, we link vertical site-response with shallow subsurface conditions, like the P-wave velocity and peat content. To better understand the amplification mechanisms, we analytically simulate P-wave propagation. In the simulations, we compute synthetic transfer functions using realistic subsurface conditions and make a comparison with the ETF. The simulations support the hypothesis that thin layers of shallow gas, originating from the Holocene peat, result in wave amplification. We observe strong vertical site-response in particular in the eastern part of Groningen, with industrial facilities and pipeline infrastructure in the region. Here, if high vertical amplifications are persistent at large earthquake magnitudes, appreciable levels of vertical loading may be expected. This study demonstrates that vertical motions should be assessed separately from horizontal motions, given that the amplification behaviour of P-waves is affected by distinctive mechanisms.

Keywords: Earthquakes, vertical ground motion amplification, unconsolidated sediments, 2D wave propagation modeling, transfer functions, V/H spectral ratios

OPEN ACCESS

Edited by:
Simone Barani,
University of Genoa, Italy

Reviewed by:
Mikhail Rodkin,
Institute of Earthquake Prediction Theory and Mathematical Geophysics (RAS), Russia
Hamid Zafarani,
International Institute of Earthquake Engineering and Seismology, Iran

***Correspondence:**
Janneke van Ginkel
j.a.vanginkel@gmail.com

Specialty section:
This article was submitted to Solid Earth Geophysics, a section of the journal Frontiers in Earth Science

Received: *10 November 2021*
Accepted: *09 March 2022*
Published: *31 March 2022*

Citation:
van Ginkel J, Ruigrok E, Wentinck R and Herber R (2022) Amplification Behaviour of Compressional Waves in Unconsolidated Sediments. Front. Earth Sci. 10:812658. doi: 10.3389/feart.2022.812658

1 INTRODUCTION

Although the subsurface is subjected to earthquake shaking simultaneously in the horizontal and vertical directions, vertical motions have received less attention in ground motion studies than the horizontal counterpart. Primarily because it is generally assumed that the margins against gravity-induced static forces provide adequate resistance to dynamic forces induced by vertical ground motion. As a result, studies on the characteristics of vertical ground motion are limited in number, particularly at sites where the earthquake intensity is low. Many seismic design codes do not consider the vertical component of motion at all, or use a single scalar multiplication factor on the horizontal component of motion.

Newmark et al. (1973) suggest that the effect of the vertical response amplitude spectrum is typically represented as two-thirds of the horizontal spectrum. Subsequently, Eurocode 8 (CEN, 2004), propose a maximum vertical acceleration factor of 0.45, normalised over horizontal acceleration. In Eurocode 8 it is emphasised that vertical ground motion is not very much affected by the underlying ground conditions and hence no correction is made for possible amplification in shallow soils. However, analyses on multiple strong earthquakes ($M \geq 5$) have proven that vertical ground accelerations can exceed values of 2/3 of horizontal, especially at short periods and in near-source distance range. Hence, vertical motion should be treated separately from the horizontal component in ground-motion studies (Ambraseys and Simpson, 1996; Bommer et al., 2011; Bozorgnia and Campbell, 2016a,b; Elnashai and Papazoglou, 1997; Yang and Sato, 2000; Yang and Lee, 2007; Yang and Yan, 2009). In addition, Elgamal and He (2004) analysed borehole arrays across the world and observed amplification characteristics for compressional waves as for the shear-waves. Amplification mostly occurs in the top 20 m of the unconsolidated sediments but compressional waves have a different site-dependence. This means that vertical ground motion cannot be treated as a single-value fraction of horizontal ground motion but should be assessed independently.

Previously mentioned studies focus on high intensity earthquakes with a tectonic origin and relatively deep hypocentres. This paper investigates vertical ground motion for shallow (3 km), low magnitude (M_{max} = 3.6 thus far) earthquakes in Groningen, in the northeast of the Netherlands. Over the past decades, the extraction of natural gas from the Groningen gas field has triggered induced seismicity. Although the maximum magnitude of the local earthquakes is relatively low, the ground motions form a risk since the existing buildings and infrastructures are not built to withstand earthquake shaking. The Groningen shallow subsurface consists of low-velocity, unconsolidated sediments with strong site amplification which has been studied in detail for motions in the horizontal direction (Bommer J. J. et al., 2017; Rodriguez-Marek et al., 2017; van Ginkel et al., 2019, 2021). So far, it has been assumed that for these low-magnitude earthquakes, vertical ground motion is not of enough importance to incorporate into the ground motion model and in seismic design for buildings (Bommer J. et al., 2017). Neither have shake table tests (Kallioras et al., 2020) and building response modeling (Malomo et al., 2019; Korswagen et al., 2019), applied on Dutch structures, included vertical motions into their tests. However, in the Groningen area, the implosive component and the shallow nucleation depth of the induced seismicity results in relatively strong compressional waves (P-waves) (Dost et al., 2020). Moreover, specific near-surface geology could result in strong, and locally varying, P-wave amplification. Consequently, structures with large horizontal extent, such as bridges, pipelines or industrial facilities might suffer from a lateral difference in vertical motion from one end to the other. This can lead to stress within the structure and subsequently in failure (Saadeghvariri and Foutch, 1991).

The objective of this study is to qualify, and where possible quantify, vertical site-response based on local induced earthquake recordings in 69 borehole sites of the Groningen seismic network. For this network, we show that the amplification measured on the vertical component corresponds primarily to P-wave amplification. Site-effect related to the local geology is evaluated through an analysis of the spectral characteristics of both earthquake and ambient noise records. Subsequently, by comparing several seismic methods, we are able to develop single-station proxies for vertical site-response. Additionally, we perform 2D wave propagation simulations, in order to understand the effect of (sub-wavelength) subsurface conditions and angle of incidence of the earthquake waves.

2 GEOLOGICAL SETTING

The province of Groningen, in the north-east of the Netherlands (**Figure 2**), is experiencing induced earthquakes due to the exploitation of a large onshore gas field. The Rotliegend sandstone reservoir is located at 3 km depth and is faulted during the Jurassic to Cretaceous rifting period. Here, reservoir compaction due to pressure depletion by the extraction of has reactivated the existing normal fault system that traverses the reservoir layer throughout the whole field Buijze et al. (2017).

The Groningen region has a flat topography and the groundwater table reaches almost up to the surface. The sedimentary cover is formed by the Cenozoic soft sediments, named the North Sea Group (NSG). In this study, we focus on the shallow subsurface, which is composed of unconsolidated Pleistocene sands and clays, overlain by a very heterogeneous Holocene formation (**Figure 1**). The Holocene formation is subdivided into several members. In Groningen, the Wormer and Walcheren Members mainly consist of marine clays, silt and fine sand. Two peat layers subdivide these two members. In the northern part, the Naaldwijk Formation mainly consists of sandy channel systems (MeijlesWong et al., 2007, 2015).

3 DATA SET

In order to monitor seismicity in the Groningen gas field, the Royal Netherlands Meteorological Institute (KNMI) deploys the

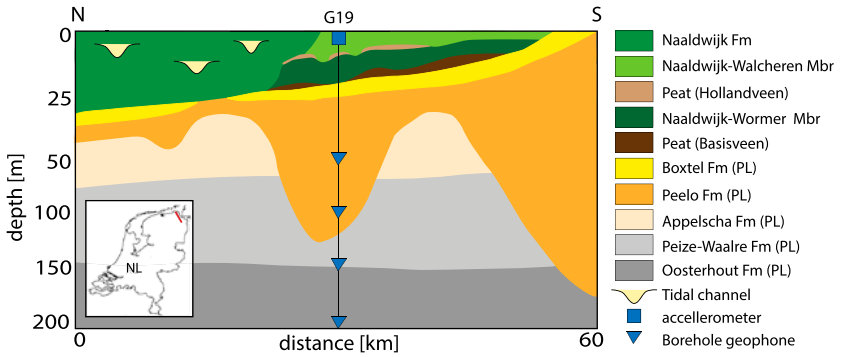

FIGURE 1 | Schematic geological cross section of the upper 200 m of the soft sedimentary cover in the northeastern Groningen region (red line in inset). Note that the vertical scale is inflated for the top 50 m to highlight the stratigraphy of the Holocene formations on top of the Pleistocene (PL) formations. Borehole station G19 is featured because this site is used for wave-propagation modeling. The G-network vertical arrays consists 5 seismometers (accellerometer (blue square) at the surface and geophones (blue triangles) at depth) with a 50 m depth interval. This cross section is based on GeoTOP (www.dinoloket.nl).

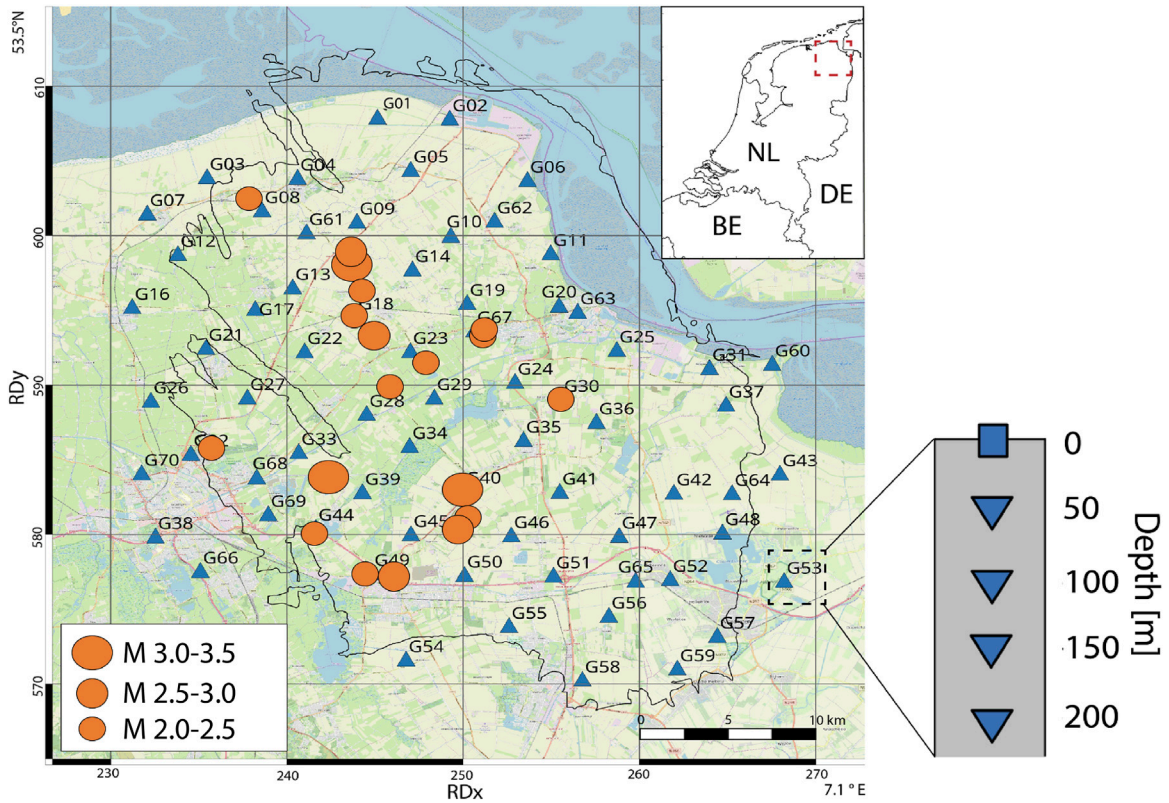

FIGURE 2 | Map view of the Groningen borehole network in the northeast of the Netherlands. The triangles represent the surface location of each borehole site in the network. Each borehole contains an accelerometer at the surface and four 4.5 Hz geophones at depth with a 50 m depth spacing. The orange circles represent the local earthquakes with magnitude 2 or higher, recorded in the G-network between 05–2015 and 05–2019. Coordinates are shown within the Dutch National Triangulation Grid (Rijksdriehoekstelsel or RD) and lat/lon coordinates in the corners for international referencing. Background map: OpenStreetMap contributors, CC-BY-SA, www.openstreetmap.org.

Groningen shallow borehole network (**Figure 2**). This so called G-network spreads out over some 850 km^2 and consists of 69 stations (Dost et al., 2017), each station is equipped with three-component, 4.5 Hz geophones at 50 m depth intervals (50, 100, 150, 200 m) and an accelerometer at the surface. The stations are continuously recording since 2015 and the data is available via the data portal of Royal Netherlands Meteorological Institute (KNMI, 1993). In this paper we refer to "station" for the

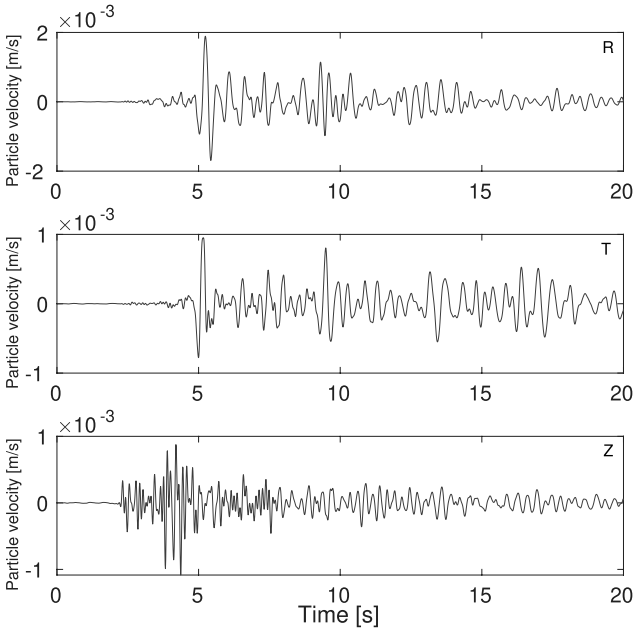

FIGURE 3 | 3-component seismogram recorded at the surface station of borehole G62 for the 08–01–2018 M3.4 Zeerijp earthquake. R = radial/east component, T = transverse/north component, Z = vertical component.

entire string with an accelerometer at the surface and four geophones at depth, and refer to "seismometer" for a single sensor measurement at a certain depth. Stations G15, G43, G53, and G68 are discarded from analysis due to malfunctioning of seismometers during a number of high magnitude earthquakes, hence not sufficient data is available.

The induced earthquakes recorded with the G-network have a magnitude of completeness of 0.5 (Dost et al., 2017). A maximum magnitude of 3.6 occurred during the Huizinge earthquake in 2012. Most earthquakes in Groningen have a normal faulting mechanism (Buijze et al., 2017; Dost et al., 2020).

4 BACKGROUND

This chapter presents details on wave propagation to illustrate the assumption of near-vertical earthquake wave incidence in Groningen. Secondly, we present our definition of amplification based on reference conditions at depth.

4.1 Wave Propagation and Incidence

In this study we assess P-wave amplification behaviour by using local earthquake recordings of the vertical component of the Groningen borehole seismometers. For a straightforward analysis, we assume that the vertical component measures primarily P-waves. In this sections we show that this simplifying assumption largely holds.

Figure 3 shows a typical 3-component recording at the Earth's surface in Groningen. P-waves are primarily recorded on the vertical component (Z), S-waves map primarily to the radial (R) and transverse (T) components. The well separation in wave types is largely due to the low near-surface velocities and hence small angles of incidence. In the top 200°m, P-wave velocities range, for most sites, between 1 and 2 km/s (Hofman et al., 2017). At close range to the epicenter, angles of incidence are close to zero. At larger range, P-waves have apparent horizontal propagation velocities of approximately 5.1 km/s (Jagt et al., 2017) resulting in angles of incidence varying between 11 and 23° in the top 200 m. Similar values are empirically found by Hofman et al. (2017). These angles of incidence results in 86–96% of the P-wave mapping to the vertical component. For S-waves, angles of incidence are even smaller in the near-surface due to very low velocities, down to about 35 m/s (Zwanenburg et al., 2020). And hence, not much S-wave energy can be recorded on the vertical component, as can be seen in **Figure 3**.

Further details of the near-surface propagation can be seen at **Figure 4**. In panel 1) the amplification can be noted when comparing the signal recorded at 200 m depth and at the surface. It can be seen that most of this amplification occurs in the top 50°m. The particle motion on the radial-vertical plane is presented in **Figures 4B,C**. The time window (0–4 s) around the first P-arrival shows that this arrival primarily oscillates in the vertical direction. The time window (5–9 s) around the first S-wave arrival, on the other hand, shows it has a near-horizontal polarization. P-S and S-P conversions do occur in the near-surface, but are small in size, again due to the small angles of incidence. In 4) and 5) the difference in Fourier Amplitude Spectra (FAS) are shown for the 200 m and surface levels. The FAS illustrate that the largest amplitudes reside between 2 and 10 Hz.

Therefore, also from an engineering point of view, processing of the raw earthquake records was performed in the frequency band of 1–10 Hz. This study uses the three-component data set of 19 earthquake recordings from local events with magnitude two or higher. Earthquakes in this magnitude range have sufficient energy to be recorded in the entire network and are therefore usable for assessing site-response. The FAS includes source, path and site-effect. Site-effects are extracted by taking spectral ratio's and or averaging over earthquakes with different hypocentres (and thus different source and path effects).

Further details on propagation from source to surface can be deduced from finite-difference simulations. The supplementary material contains the details of the model setup and input data for this simulation. **Figure 5** shows the seismic wave field in the subsurface originating moderate-size earthquakes at reservoir depth (3 km), mimicing a limited shear rupture in a fault plane. The figure shows three snapshots of the vertical (Z-component) and horizontal (R-component) particle velocities after the start of the event. The shape of seismic wave fronts deforms to almost horizontal when they reach the shallow subsurface. Hence, a borehole geophone near the epicentre measures mainly P-waves on the sensor for the vertical particle velocity. The waveform simulations support the observations from the earthquake recordings as presented in **Figure 4** and the assumption of almost vertical P-waves.

The following analyses of earthquake wave propagation includes time windows of 20°s after earthquake rupture, and comprises not just the first P-wave arrival time window as

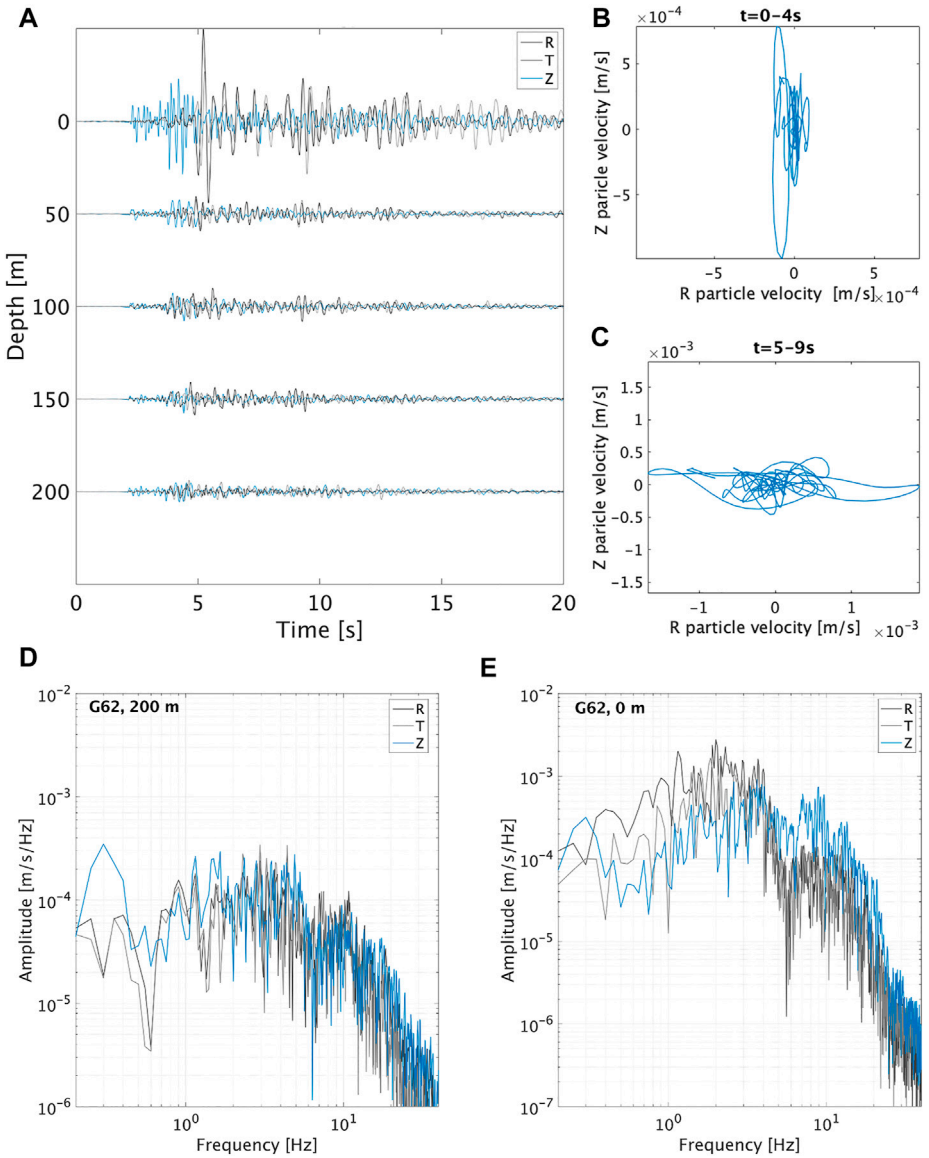

FIGURE 4 | Earthquake record in particle velocity for station G62 for the Zeerijp earthquake on January 2018 with magnitude 3.4 for a 20 s window after earthquake origin time. With in panel **(A)** 3-component borehole seismogram. **(B)** Particle motion in the R-Z plane for the direct P-wave arrival for a time window of 0–4 s for G62 surface seismometer. **(C)** Particle motion in the R-Z plane for the direct S-wave arrival for a time window of 5–9 s for G62 surface seismometer. **(D)** Fourier Amplitude Spectra of the 200 m seismometer. **(E)** Fourier Amplitude Spectra of the surface seismometer.

presented in **Figure 4B**. We deliberately choose this extended time window because in the frequency domain, the signal becomes more stable by including complex body-wave reverberations of the earthquake coda wave window. These complex arrivals experience similar amplification between 200°m depth and the surface.

4.2 Ground Motion Amplification in Groningen

In the Groningen region, S-wave ground motion amplification is mainly governed by two factors; firstly the reduction in seismic velocities with decreasing depth and secondly, the presence of a velocity contrast at a certain depth causing resonance in the near-surface layer (van Ginkel et al., 2019). If this resonance of this near-surface layer has a similar resonance frequency as the structures at the surface, hazardous shaking can develop. In addition, shaking will not only occur at a single fundamental frequency but also at overtones. Amplification of P-waves follows the same physics as for S-waves, but has a different susceptibility to the near-surface lithology. Firstly, as P-waves have longer wavelengths, a deeper portion of the near-surface zone is relevant for resonance. Secondly, different impedance

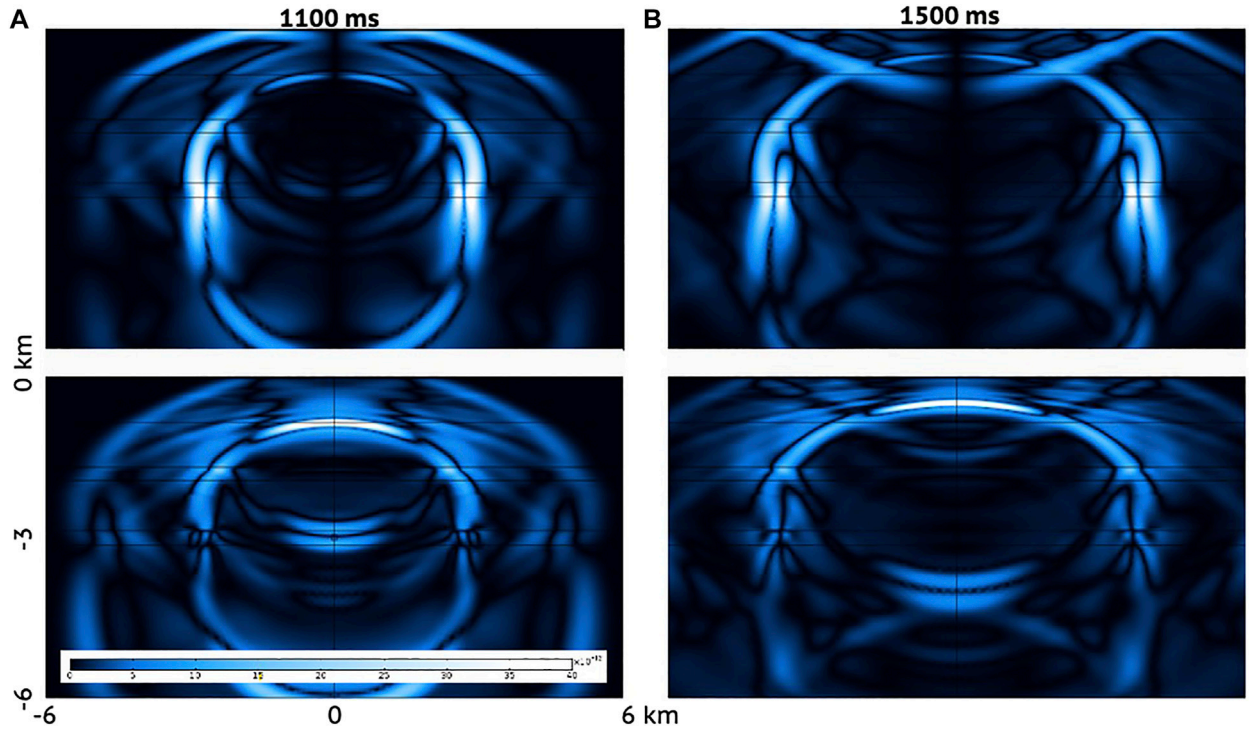

FIGURE 5 | 2D full wave form finite difference model snapshots of absolute vertical (top) and horizontal (bottom) particle velocity for **(A)** 1100 ms after start of the earthquake, **(B)** 1500 ms. All panels have the same distance and particle velocity scale as the panel in the bottom left. The used velocity model is shown in **Supplementary Figure S1**.

contrasts might be important, e.g., the interface between a water-saturated clay and sand has a high S-wave, but a low P-wave impedance contrast.

The example borehole seismograms and the FAS (**Figure 4**) show a major increase in amplitudes between the vertical component of the 200 m depth and the surface seismometer. Here, local site amplification occurs, on top of the free-surface effect. This amplification in the top 200 m is observed in multiple seismograms across the Groningen network.

Generally, amplification is quantified with respect to a hard rock outcrop over a full spectrum, however, these measurements are lacking in Groningen due to the 800–1,000 m thick sediment cover over the entire area. Alternatively, we define a reference site as a hypothetical outcrop with P-wave velocity of 1,900 m/s and a density of 2040 kg/m^3. These are the values that are found, on average, in Groningen at 200 m depth (Romijn, 2017; Hofman et al., 2017).

5 METHODOLOGY

Amplification defined in the frequency-domain uses the Fourier Amplitude Spectra (FAS) of the earthquake records. The FAS ($U_{ij}(f)$), for the ith event and jth station, can be written as a convolution (i.e., multiplication in the frequency domain) of a source, path, site-effect and instrument term:

$$U_{ij}(f) = S_i(f)G_{ij}(f)L_j(f)I_j(f), \tag{1}$$

where S_i is the source term, G_{ij} is the path term (between the ith event and the jth station), L_j is the site term, and I_j is the instrument-response term. I_j is known and removed before further processing the data. This leaves the source, path and site terms. Different approaches are used to extract from this the site term.

5.1 Empirical Transfer Functions

Quantification of site-effects across a frequency range of 1–10 Hz is performed by calculating borehole empirical transfer functions from local earthquake recordings. As shown in the previous section, we assume that vertical component is comprised of mainly P-waves in the 20 s time window used for the earthquake data processing. Therefore, the empirical transfer functions ($T_{m,n}$) represent P-wave amplification and are defined as a division of the Fourier amplitude spectra at two different depth levels

$$T_{m,n}(f) = \frac{U_m}{U_n}, \tag{2}$$

where m is the depth level of interest and n the reference horizon (Liu and Tsai, 2018; Rong et al., 2019). In U_m and U_n the source and path terms (**Eq. 1**) are (nearly) identical and hence the transfer function is only a description of the local propagation effects. When U_m is chosen at the Earth's surface, $T_{m,n}$ describes

site-effects and $|T_{m,n}|$ describes the frequency-dependent amplification with respect to the reference horizon.

In order to further improve estimation of the site-effect, we average the deconvolution (**Equation 2**) over 19 events with magnitudes > 2.0. This can be seen as an implementation of seismic interferometry by deconvolution (Wapenaar et al., 2010). We use 20 s long time windows for particle velocity recordings on the vertical component of the borehole stations. In this implementation, for each event the deconvolution is applied as in **Equation 2**. Subsequently, the deconvolution results are stacked to enhance stationary contributions. With a reference horizon at 200 m depth and the level of interest at the Earth's surface, the transfer function has both a causal and acausal part. The causal part maps upward-propagating waves, from the reference level to the surface. The acausal part maps downward-propagating waves back to the free surface (Nakata et al., 2013). To describe amplification, we are only interested in the causal part. We select this causal part of the estimated transfer function and compute its Fourier amplitude spectrum to obtain a measure of frequency-dependent amplification. The resulting amplitude spectrum we call the empirical transfer function (ETF). In order to get an estimate of uncertainty in the results, the above processing sequence is applied per earthquake and the standard deviation is computed from the resulting distribution.

5.2 V/H Spectral Ratios

Instead of the frequently used Horizontal-to-Vertical Spectral Ratio (HVSR) to estimate site-effects, we explore the option of using the inverse of the HVSR, the vertical-to-horizontal spectral ratio (VHSR). The HVSR-method (Nakamura, 1989, 2019) is based on the assumption that the vertical component spectrum is quite flat, hence a peak in the spectral ratios is generated by a peak in the horizontal component spectrum, which would be related to S-wave resonance. However, the spectrum of the vertical component is not flat, as demonstrated in the previous sections and supported by the findings of Sarmadi et al. (2021). By taking the inverse of HVSR, we can also not assume that the horizontal component spectrum is flat. However, peaks and troughs related to P-wave resonance and S-wave resonance are generally well separated in frequency. Comparing the spatial distribution between amplification established by the ETF and the one obtained with the VHSR, makes it possible to assess whether the VHSR can be used as tool to act as a proxy for P-wave amplification. Also, Lermo and Chavez-Garcia (1993) uses the VHSR to estimate resonance frequencies and peak amplitudes for the vertical component of ground motion from local earthquake recordings.

From earthquake recordings, generally time windows are picked containing direct arrivals of seismic waves to calculate the HVSR for site-response estimations (Chin and Aki, 1991; Mayeda et al., 1991; Kato et al., 1995; Su et al., 1996; Bonilla et al., 1997; Sánchez-Sesma et al., 2011). However, given that the local earthquakes are shallow and at short range, the window of the direct arrivals is very short, hence this implementation of VHSR is unstable. As alternative we use the coda window, which includes reverberations of the P-and S arrivals and reveals information on the local structure. Perron et al. (2018) evaluate the standard spectral ratio curves of the direct S and P-arrivals and the coda wave window and show that both parts of the waveform provide similar results. The signal must be of long enough duration to include sufficient reverberations to produce any resonance peak. The longer the picked window, the more back-scattered waves coming from many azimuths (illustrated in **Figure 5**) are included in the signal, resulting in a directionally averaged site-effect. By taking the ratio of the vertical and horizontal components, the propagation effects included in the signal largely vanish. Data processing for obtaining the VHSR from local event recordings is carried out in the following steps:

- Application of bandpass filter on earthquake recordings of 1–10 Hz
- Selection of a 15 s coda window, starting at (hypocentral distance/mean Vs.) + 5 s after earthquake origin time.
- Check whether the local earthquakes have a sufficient signal-to-noise ratio for the selected coda wave time window
- From the coda wave window, calculation of VHSR from power spectral densities (PSDs). Following (the reciprocal of) the procedure described in van Ginkel et al. (2020), the VHSR is computed from the vertical component (Z) and horizontal components (E and N) as:

$$VHSR = \frac{\sqrt{PSD_Z}}{\sqrt{PSD_E + PSD_N}}, \tag{3}$$

where the horizontal components are averaged by vector summation.

- Per site, averaging of the VHSR curves (by stacking in the frequency domain) over all local events. **Figures 9A–F** shows examples.
- Picking the peak amplitude for each averaged VHSR curve

6 RESULTS AND INTERPRETATION

6.1 Amplification Factors

We calculate an overall amplification factor in the range of 1–10 Hz over the borehole vertical array, following the procedure described in van Ginkel et al. (2019, 2021). The AF is computed for each borehole site by taking the ratio of the maximum amplitudes recorded within 20 s after rupture time at the vertical component of the surface and the 200 m deep seismometer. The amplitude at the surface was divided by a factor of 2 in order to remove the effect of free surface amplification. Next, the AF per borehole is obtained by repeating the above procedure for all available M > 2.0 events and subsequently averaging the values. A signal-to-noise threshold is applied on the events.

Throughout the borehole network, a maximum AF of 2.7 is reached at the eastern edge of the network, while other locations do not experience P-wave amplification at all (**Figure 6**). Hence, this AF-plot presents a first indication of the spatial variability across the G-network of vertical ground-motion amplification.

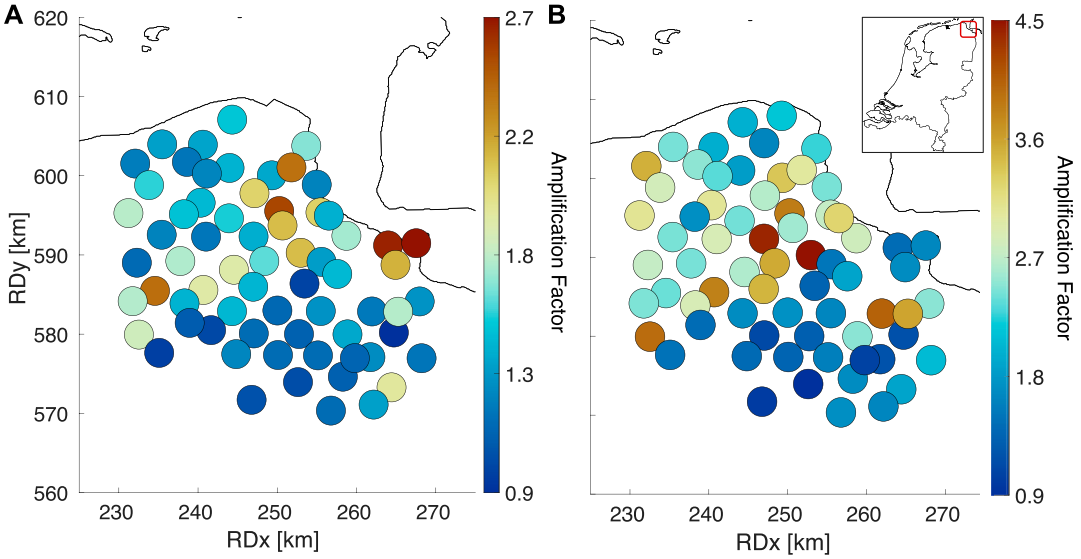

FIGURE 6 | (A) Spatial distribution of the amplification factors computed based on earthquake records on the vertical component of the borehole seismometer at 200 m and at the surface. **(B)** Spatial distribution of the amplification factors computed based on earthquake records on the horizontal components of the borehole seismometer at 200 m and at the surface, modified from van Ginkel et al. (2019).

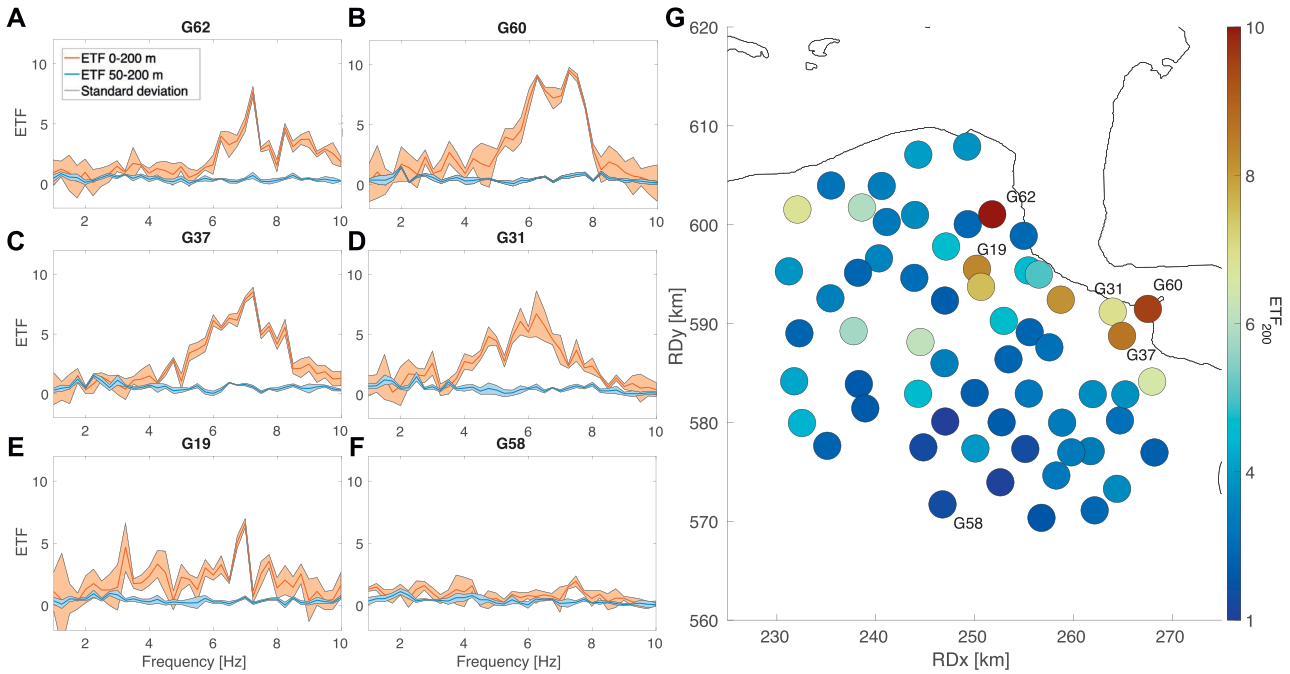

FIGURE 7 | (A) Each panel depicts the empirical transfer functions (ETFs) between the seismometer at 200 m depth and the surface (red) and standard deviation (pale red area) for sites G19, G31, G37, G60, and G62, displaying the frequency-dependent amplification. The blue lines illustrate the ETFs between the seismometers at 200 m and 50 m. Borehole G62 additionally depicts the ETF between the surface and 50 m seismometer (gray). Borehole G58 is added as example of a borehole site with no amplification measured. **(B)** Spatial distribution of the peak amplitudes from the ETF for 60 borehole station sites.

Amplification factors from records on the horizontal components are calculated by van Ginkel et al. (**Figure 4**; 2019) and display a different spatial pattern than the vertical AFs, which is further investigated in the following sections.

6.2 Empirical Transfer Functions

In order to get an estimate of uncertainty, the above processing sequence is applied per event and from the resulting distribution, the standard deviation is computed and examples are plotted in

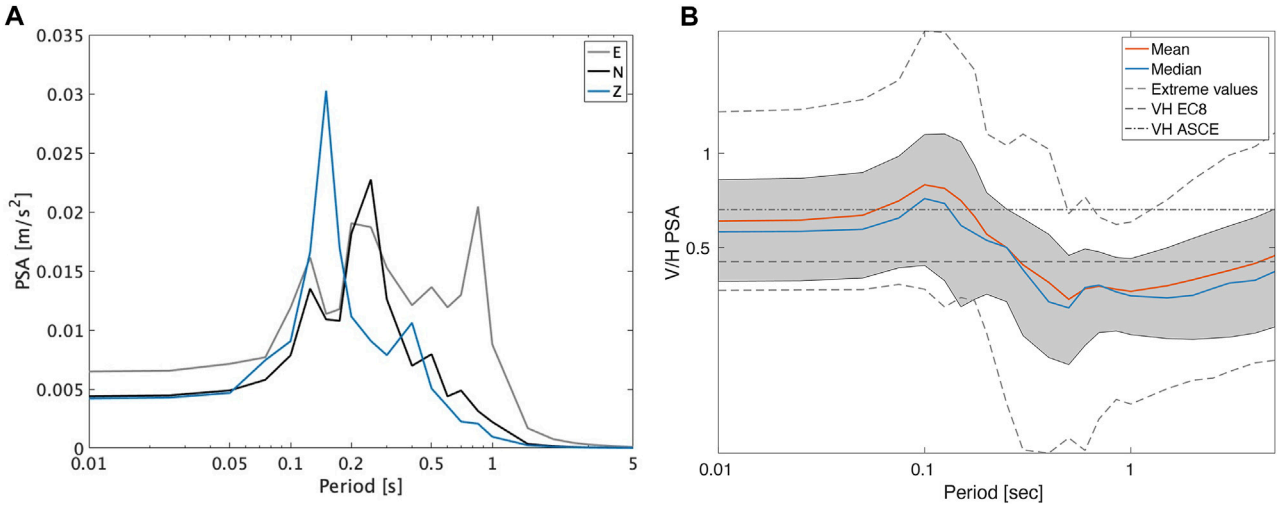

FIGURE 8 | (A) Example of acceleration response spectrum for the surface seismometer at station G60 from the Westerwijtwerd earthquake of M = 3.4, where the blue line represents the PSA at the vertical component, the gray line the eastern horizontal component and in black the northern horizontal component. **(B)** Averaged V/H from response spectra for each surface seismometer, processing 20 earthquake recordings, at each defined period plotted together with the mean (red) and median (blue) and extreme values (dashed gray) per period. The shaded area depicts the mean plus-minus one standard deviation, the black dashed line illustrates the 0.45 value as proposed by Eurocode 8 and the dot-dash the 2/3 value proposed by the ASCE.

Figure 7A–F. For these examples, also the ETF between 200 and 50 m depth is shown. It can be seen that most of the amplification occurs in the top 50 m.

Some ETFs show multiple side peaks, but the peak with largest amplitude value is identified as resonance peak, following the recommendation by Zhu et al. (2020). At some sites, this resonance peak has a large contribution to the overall amplification. Applying smoothing on the FAS and ETF can lead to suppression and shifting of peaks. We apply no smoothing and pick the largest amplitude and corresponding frequency. G58 has been added to **Figure 7F** to illustrate an ETF for a site with no amplification of P-waves. For 60 borehole stations, the ETF is computed. Subsequently, for each site, the corresponding peak amplitude for the 200 m -interval ETF is identified. **Figure 7G** depicts the spatial distribution of these peak amplitudes. Here, the distribution of amplitudes shows highest values in the eastern section of the region.

6.3 V/H From Spectral Acceleration

The previous section describes maximum amplification across a frequency range using the Fourier amplitude spectra of earthquake recordings of the borehole seismometers. However, Kramer. (1996) and Eurocode 8 (CEN, 2004) suggest using spectral ordinates at a varying range of periods in the acceleration response spectrum as ground-motion parameter.

As input, earthquake recordings (20 s after earthquake origin time) at the surface are taken to calculate the pseudo spectral acceleration (PSA). Subsequently response spectra (**Figure 8A**) for all three components, for each surface seismometer site, are calculated for pre-defined spectral periods (0.01–5.0 s), and taking the standard critical damping factor of 5% (Kramer, 1996; CEN et al., 2004). Per a defined period and per event, a V/H ratio is calculated from the PSA by dividing the vertical PSA with the geometric mean of the horizontal components. Subsequently, for each pre-defined period, an average V/H is calculated over all events and plotted in **Figure 8B**. As shown in 8b, in Groningen the V/H PSA value for certain locations at short periods is exceeding the standard values of 0.45 and 2/3 by Eurocode 8 and ASCE. Moreover, it is shown that for each period, there is a vast range of site-specific V/H PSA values. At long periods ($T > 0.3$ s) the average value becomes closer to the single values proposed in literature. At short periods ($T < 0.3$ s) the average is considerably higher (0.81 for $T = 0.1$ s).

6.4 V/H Spectral Ratios

In this section we assess an additional single-station method for characterizing the spatial distribution of P-wave amplification. In Groningen, the induced events do not include surface waves at the short ranges within the G-network. The coda-based VSHR is therefore primarily a spectral ratio of P- and S-wave reverberations in the unconsolidated sediments. At many sites in Groningen, VSHR curves reach levels above 1 for distinct frequencies (**Figure 9A**). Location G58 is added as reference illustrating a VHSR below 1; here the horizontal component is dominating over the vertical for all presented frequencies. **Figure 9A** is illustrating the spatial distribution of VHSR peak amplitudes across the Groningen area.

6.4.1 VHSR From the Ambient Seismic Field

Site-effects are commonly assessed by using the ambient seismic noise field, (e.g., Bonnefoy-Claudet et al. (2006)). In Groningen, the noise level is sufficiently high in order to exceed the sensitivity of the surface accelerometers (Koymans et al., 2021). In addition to coda VHSR, the VHSR is also estimated from 1 month of ambient noise field measurements ($VHSR_{ASF}$), using the approach presented in van Ginkel et al. (2020, 2019).

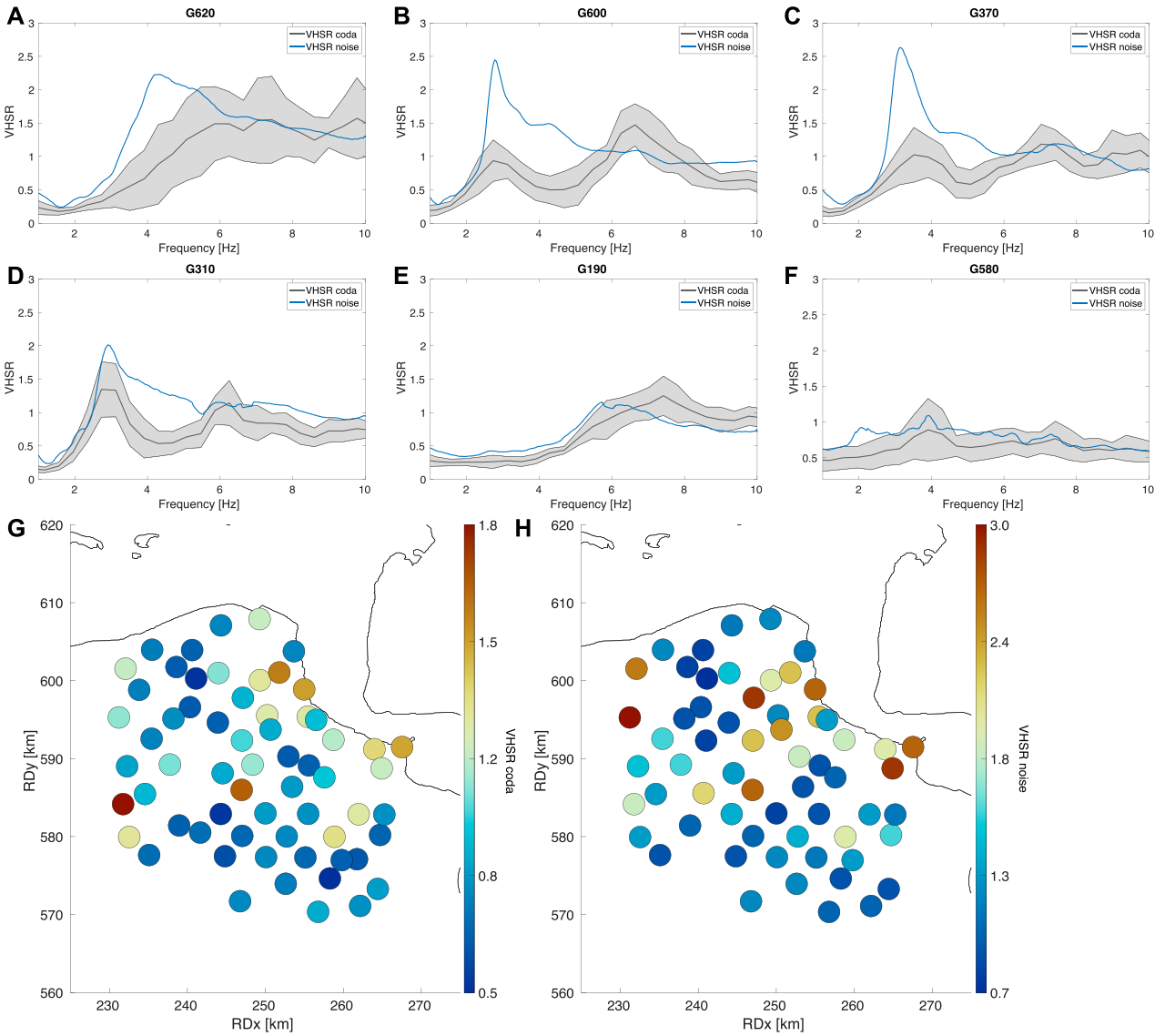

FIGURE 9 | (A–F) Each panel depicts the mean VHSR (black line) and standard deviation (dashed line) for the surface seismometer for the stations G19, G31, G37, G60, G62, where high VHSR amplitudes are calculated. Station G58 is added as reference to show a VHSR for a location with no amplification of P-waves. The blue line indicates the VHSR from the ambient noise field. **(G)** Spatial distribution of coda-based VHSR peak amplitudes for each surface seismometer in the Groningen network. **(H)** Spatial distribution of noise-based VHSR peak amplitudes for each surface seismometer in the Groningen network.

In **Figures 9A–F**, the mean $VHSR_{ASF}$ curves are added in blue for comparison with the $VHSR_{coda}$ curve characteristics in order to investigate whether noise can be used as a proxy for site amplification. From the VHSR curves, the corresponding peak amplitudes are determined for each surface seismometer in the Groningen network. In general, the noise-based VHSR peak amplitudes are larger than the coda-based VHSR peak amplitudes. This is a common observation, and is most likely caused by the strong presence of surface waves in the noise. The surface-wave ellipticity has notches which inflate the amplitude levels of VHSR (Bonnefoy-Claudet et al., 2006; Konno and Ohmachi, 1998). **Figures 9G,H** presents the peak amplitudes from coda-based and noise-based VHSR, for each surface seismometers in the Groningen network. The spatial distribution of amplitudes exhibits a comparable pattern for both types of VHSR.

6.5 Relationship With Subsurface Conditions

The AF, ETF and V/H ratio peak amplitude distribution demonstrate a consistent pattern of increased peak amplitudes measured in the eastern part of the Groningen region (**Figures 6**, **7**, **9**). In order to understand this large variation in amplification, this section elaborates on the effect of shallow subsurface conditions on amplification behaviour of P-waves.

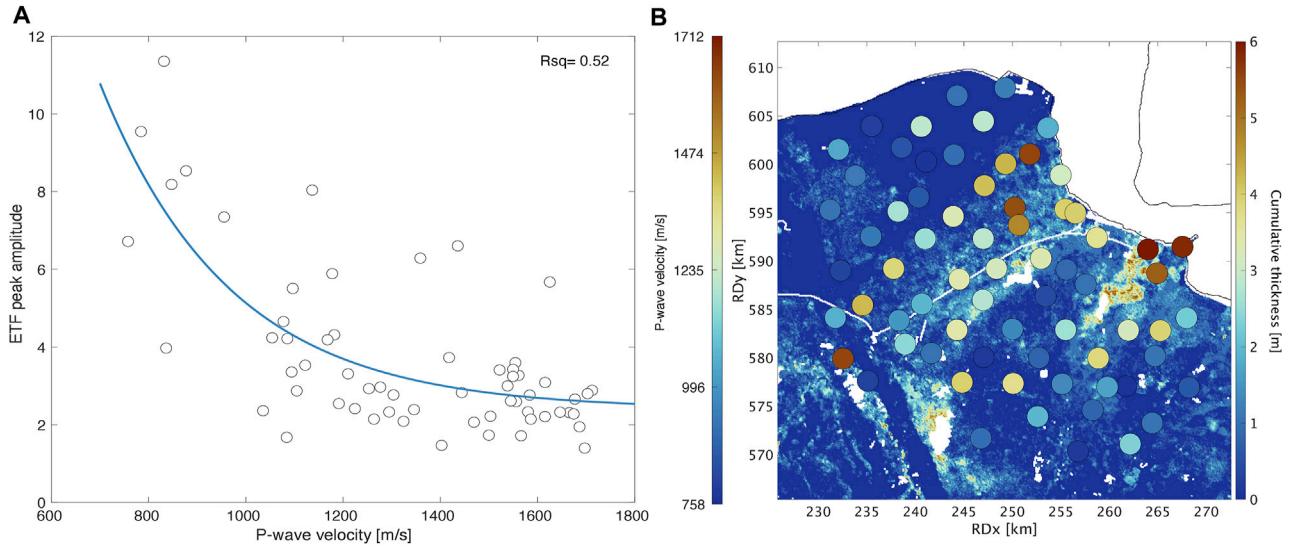

FIGURE 10 | (A) Correlation between P-wave velocities for the top 50 m and ETF peak amplitudes, fitted with an exponential decaying function (**Eq. 4**). **(B)** Spatial distribution of the P-wave velocity values (Hofman et al., 2017) for the top 50 m for each borehole location (circles) plotted on top of the cumulative thickness map of Holocene peat.

6.5.1 Seismic Velocities

Wave amplification is largely determined by local variations in seismic velocities. For each borehole location, P-wave interval velocities are known for the upper 200 m, with a 50 m interval resolution (Hofman et al., 2017). These velocities were computed by applying seismic interferometry to events recorded within the borehole stations. Since the majority of the peak amplitude increase arises in the top 50 m, the ETF peak amplitudes (**Section 6.2**) are plotted against the average P-wave velocities *Vp* for the top 50 m (**Figure 10A**). All strong amplifications (high ETF peak amplitudes) occur at velocities below 1,400 m/s. The relation between the near-surface P-wave velocity and the maximum amplification from the ETF is fitted (Rsq = 0.52) by an exponentially decaying function (**Eq. 4**). This empirical relation can be used to estimate the maximum amplification A in the vertical direction at other sites with unconsolidated sediments, when the average velocity Vp over the top 50 m is known:

$$A = 2.4 + 114e^{-0.004Vp} \tag{4}$$

Next, the interval P-wave velocity distribution is compared to the shallow lithostratigraphy throughout Groningen. For this purpose, cumulative thickness maps for different lithologies are extracted from the digital geological model GeoTOP (Stafleu et al. (2011; 2021), www.dinoloket.nl). The P-wave velocity distribution satisfactorily corresponds to areas with accumulations of peat in the shallow subsurface (10b). Thus, peat accumulations correlate with relatively low interval P-wave velocities. As a consequence, high ETF peak amplification develops during an earthquake where peat accumulates.

6.5.2 Effect of Gas on P-Wave Velocity

Since peat originates from organic material, methane can be generated, stored or migrated upwards and subsequently being trapped in the overlying sediments during burial. Although the peat layers are relatively thin in the Groningen field (less than 1 and up to 6 m throughout the top 50 m), their presence and resulting gas content can significantly reduce the P-wave velocity V_p [m/s]. The effect of gas on V_p can be understood from the Biot-Gassmann equations for wave propagation in poro-elastic media, such as soil Biot (1962) or Fjaer et al. (2008). Take that for seismic frequencies the so-called undrained condition holds and that the relative fluid displacement with respect to the rock can be neglected. In this case, $V_p = \sqrt{K''/\rho}$ where ρ [kg/m^3] is the bulk density and $K'' = K + \alpha^2 M + 4G/3$ [Pa] where K and G [Pa] are the bulk and shear moduli of the drained rock and $\alpha = 1 - K/K_s$ [-] is the so-called Biot constant. K_s [Pa] is the bulk modulus of the grains in the rock. M [Pa] is a poro-elastic constant which can be expressed as:

$$M = \frac{K}{(1-\alpha)\alpha - \phi\left(1 - \alpha - K\middle/K_f\right)} \tag{5}$$

Where ϕ [m^3/m^3] is the pore volume fraction and K_f [Pa] is the effective bulk modulus of the fluid. For a fluid containing both gas and water at equal pressure, $1/K_f = S_w/K_{fw} + (1 - S_w)/K_{fn}$. S_w [m^3/m^3] is the volume fraction of pore water or the water saturation. K_{fw} and K_{fn}[Pa] are the bulk moduli of water and gas. In the shallow subsurface, $K_{fn} \ll K_{fw}$. Even for very low gas saturations, $K_f \approx S_n/K_{fn}$. Further, $K \ll K_s$ at least for clay and sand. So this implies, $\alpha \approx 1$ and $M \approx K_f/\phi \approx S_n/(\phi K_{fn})$. Since unconsolidated soil has a reasonable porosity, $K'' \approx K + 4G/3$. So, the fluid stiffness hardly contributes to the stiffness of the rock and K'' approximates the so-called drained bulk modulus of soil. A direct consequence is that V_p values for peat at shallow depth

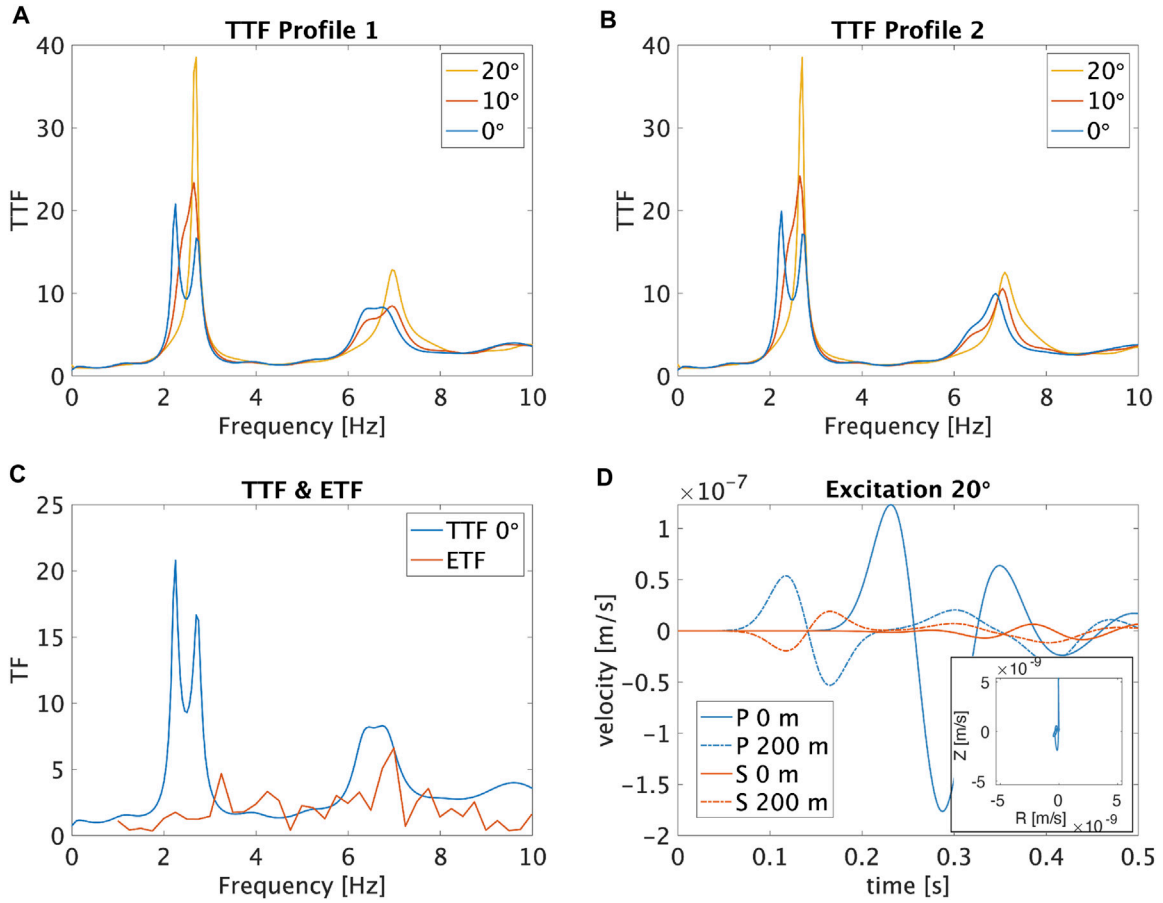

FIGURE 11 | (A) Theoretical transfer functions (TTF) for P-wave velocity Profile 1 for various angles of incidence. **(B)** TTF for P-wave velocity Profile 2 for various angles of incidence. **(C)** Theoretical (blue) and empirical (red) transfer function for borehole G19. **(D)** Excitation (in velocity) for the P-waves on the vertical plane (blue) and S-waves on the horizontal plane (red) at 200 m (dashed) and at the surface (solid) with θ of 20°. The inset depicts the related particle motion at surface for the P-wave arrival time window.

can be become quite low. Values in the range 0.2–0.5 km/s are possible as has been measured by Mad Said et al. (2015); Zimmer et al. (2007). In the following we show the effect of low V_p-layers in the shallow subsurface on P-wave amplification by computing theoretical transfer functions (TTFs) from 2D wave propagation simulations. As has been shown in **Section 4.1**, at the near surface, the incoming waves have a maximum angle of incidence of 23°. Hence, simulations have been done for 0, 10 and 20° angles of incidence.

6.6 Shallow 2D Wave Propagation Simulations

From 2D wave propagation simulations in the shallow subsurface, we calculate the impact of subsurface lithology on P-wave amplification. Details on the simulations like the velocity and damping profiles, and the model setup are presented in the **Supplementary Material**. The effect of gas saturated layers in the shallow subsurface is implicitly included in the choice of the V_p profiles. In particular, we have selected the lithology around borehole location G19 in the Groningen field where the ETF displays high peak amplitudes for frequencies around 6, 7 Hz. Instead of 1D simulations, we deliberately performed 2D simulations to understand also the effect of the angle of incidence on wave amplification and on P-to-S wave conversion. Moreover, we compared the empirically-derived ETFs with the synthetic or theoretical ones (TTFs) from the simulations. The supplementary material presents the simulation details, the input data and model set up (**Supplementary Section 1.2**).

6.6.1 Theoretical Transfer Functions

The theoretical transfer functions (TTF) are calculated from P-wave displacement velocities recorded at the vertical component of probe 1 at the surface and probe 2 at 200 m depth (**Supplementary Figure S3**). Since the shallow P-wave velocity profile is hypothetical (**Supplementary Section 1.2**) first a sensitivity analysis of the TTF on the P-wave velocity profile in performed (**Figures 11A,B**). For both profiles, the TTFs for various angles of incidence (θ = 0, 10 and 20°) exhibit similar characteristics in terms of peak frequencies and amplitudes. Furthermore, **Figure 11A** shows that the effect of the wave

front incidence angle is minor on the TTF curve characteristics. Higher angles of incidence shift the TTF peak frequency from 6.6 to 6.9 Hz as the travel time of the wave between the probe locations reduces.

Figure 11C compares the ETF with the TTF for velocity Profile 1 for zero angle of incidence (θ = 0°). Both transfer functions have a peak between 6 and 8 Hz, which peak is related to near-surface amplification. Between 2 and 3 Hz, the character of the transfer functions is quite different. The TTF peak around 2.5 Hz develops due to a notch at the 200 m recording. This notch is caused by the interference of up- and down-going waves. In the simulations, the subsurface is assumed laterally uniform. In reality, the subsurface is laterally quite heterogeneous, suppressing or disrupting such a notch. As a result, the ETF has no strong peak around 2.5 Hz. Moreover, the TTF is based on the propagation of a single wavelet while the ETF is an average from multiple earthquakes with various angles of incidence and azimuths. With this simulated transfer functions, we show that a varying angle of incidence is not of major influence on the amplification behaviour of P-waves.

6.6.2 P-To-S Wave Conversion

For non-zero angles of incidence on a layer interface, P-to-S wave conversion occurs. This conversion is of practical importance since prior to the direct S-wave arrival, P-waves might convert to S-waves and extend the period of exposure of buildings to horizontal ground motions during an earthquake. For the simulated small angles of incidence a limited P-to-S wave conversion can be seen in **Figure 11D**. It shows the simulated vertical P-wave and horizontal S-wave displacement velocities at 200 m and at the surface for a wave front with an angle of incidence of 20°. At around 0.23 s, when the high amplitude P-wave arrives at the surface, only minor S-wave excitation develops. Additionally, the particle motion plot (inset) for this time window comprises mainly a motion in the vertical (Z) plane. Since the generated S-wave amplitudes remain only a fraction of the P-wave amplitudes (less than 20%), this P-to-S wave conversion is deemed unimportant for the amplification and duration of the ground motion.

7 DISCUSSION

This paper presents various empirical methods for the qualification of site-effects on vertical ground motion amplification of signals originating from induced earthquakes for the Groningen gas field. In characterising amplification in the vertical direction, we used 1) amplification factors, 2) borehole transfer functions, 3) V/H from spectral accelerations, and 4) V/H spectral ratio's from earthquake coda-waves and the ambient seismic field. All four approaches exhibit a similar distribution of the degree of amplification in the vertical direction for each borehole site. In a second step, we explain this site-dependent amplification distribution depending upon the shallow subsurface composition and perform simulations in order to model the effect of low-velocity peat layers on P-wave propagation. In the following paragraphs we discuss the validity, uncertainties and the approaches presented, as well as the limitations.

Throughout this study we assume P-wave dominated vertical motions due to nearly vertical incidence of the seismic waves, hence the absence of direct wave type conversions. The following arguments show the validity of the previous hypothesis: 1) the range of angles of incidence (0–20°) is small and 2) empirical as well as theoretical particle motion plots mainly show motion in the vertical plane within the P-wave arrival time window. These criteria lead to an expectation we measure predominantly P-waves.

To test the influence of non-zero incidence, we varied the angle of incidence in the synthetic 2D wave propagation simulations. As shown in **Figure 11D**, varying the angle of incidence of the wave front does not lead to major P-to-S-wave conversions. Therefore, we consider the assumption that the vertical component represents the amplification of the P-waves as valid.

Previous studies (Kruiver et al., 2017; van Ginkel et al., 2019) have shown that horizontal ground motion amplification mostly occurs in the near-surface (top 50 m). Also the seismograms for the vertical component display most of the amplitude increase in this top 50 m, see **Figure 4**. Due to the free surface effect, constructive interference of the down going wave might influence the recordings on the seismometer at 50 m. At 200 m this interference can be excluded, hence we decided to compute transfer functions over the 200 m interval following the approach by van Ginkel et al. (2021) (**Figure 7**).

Because of the data richness in Groningen, we are able to test, compare and evaluate borehole and single-seismometer techniques. The purpose of this comparison is to evaluate which single-station method (V/H PSA and VHSR) yields the best proxy to identify sites with the potential of vertical ground-motion amplification. **Figure 12** compares the peak amplitudes of the various techniques. We are aware that the techniques include amplification computed from response spectra, FAS, as well as particle velocity in the time-domain. Hence the peak amplitudes are treated qualitatively in order to investigate whether all techniques identify sites with high amplitudes. Panel 12a is added to display the correlation between the AF and ETF peak amplitudes. It shows that the relatively simple approach of computing AFs enables us to identify locations with high P-wave amplification.

Figures 12B–E illustrate the correlation between maximum amplification (ETF peak amplitudes) and three possible single-station proxies for amplification: peak amplitudes from V/H pseudo-spectral accelerations for a period of 0.01 s, coda-based VHSR and noise-based VHSR. These data points are fitted, using $A_0 = a^{\star}e^{b\star P}$ as a functional form, where A_0 represents the peak amplitude and P the input proxy. a and b are the two unknown parameters that are found through the fitting exercise. The correlation coefficient (Rsq) is calculated to qualify the fit. The spatial distributions of peak amplitudes for respectively the ETF (**Figure 7**) and VHSR (**Figures 9G,H**) display a similar pattern, but discrepancy still remains between the absolute amplitudes. This is expressed in the relatively low Rsq-values in **Figures 12B–D**. Still each of the three presented methods makes it

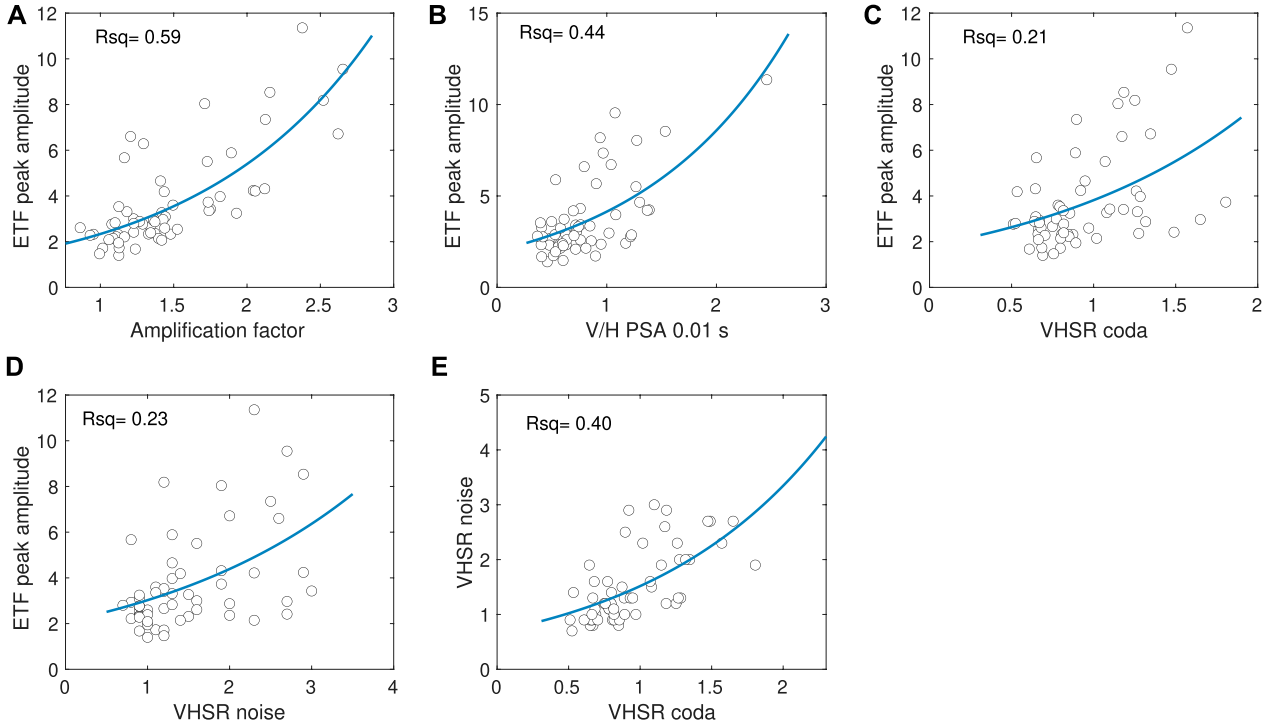

FIGURE 12 | Each panel depicts the correlation between the ETF and **(A)** Amplification factor from maximum amplitudes of earthquake records, **(B)** the V/H from pseudo-spectral accelerations at 0.01 s, **(C)** the coda-based peak amplitudes of the VHSR and **(D)** the noise-based peak amplitudes of the VHSR, and **(E)** the correlation between the VHSR coda and noise. Each blue line illustrates the fitting function between the two parameters.

possible to identify the borehole sites with potentially high vertical ground motion amplification during an earthquake.

For this study we use mainly local earthquake signals to estimate seismic site-effect in the vertical direction, following for example, Perron et al. (2018); Bommer et al. (2011). These approaches have the disadvantage that they require the occurrence of earthquakes in the first place. For that reason, a comparison between the VHSR of the earthquake signal and from the ambient noise field is made. The noise VHSR reasonably resembles the earthquake VHSR in terms of curve characteristics and peak amplitudes (**Figure 12D**), hence the noise VHSR can act as first proxy for increased P-wave amplification at certain locations, in case of absence of earthquakes. In general, measurements of noise microtremors have proven to be very informative for site-response estimation and remain a valuable input for seismic site-response zonation (Bonnefoy-Claudet et al., 2006; Molnar et al., 2018). However, the VHSR coda and noise absolute amplitudes have some discrepancies, mainly because the noise is composed of a mixture of surface and body waves. Further discussion about this discrepancy is beyond the scope of this paper.

The 2D full waveform simulations (**Figure 5**) show that the angle of incidence of the wavefront at the surface near the earthquake epicentre is relatively small ($< 20°$). For the expected range of angles of incidence, the TTFs appear to be quite similar and amplification not influenced by inclining earthquake waves. This also holds for the TTFs of two comparable but different synthetic V_p profiles, showing that the TTFs are not very sensitive to uncertainties in V_p in gas containing shallow subsurface layers, such as peat. Also, the simulations indicate that P-to-S conversion in the shallow subsurface is minor.

The wide range of V/H and ETF peak amplitude distributions found in the Groningen borehole network are consistent with the observations from Ambraseys and Simpson (1996); Bozorgnia et al. (2000); Liu and Tsai (2018); Elgamal and He (2004); Yang and Sato (2000). Empirically we show that vertical ground motion amplification is very site dependent and comprises a different spatial pattern than it is horizontal counterpart. We show that peat content plays an important role in P-wave ground motion amplification. while S-wave amplification is largely controlled by the stiffness of the Holocene sediments (van Ginkel et al., 2019, 2021). These insights are relevant for the Groningen region and as a consequence, it is not recommended to use the standard practise for assigning a single-value fraction of horizontal ground motion in order to assess motion in the vertical direction as suggested by CEN. (2004); Newmark et al. (1973); Loads (2017) is not recommended.

Furthermore, we show that in absence of a borehole network, the methods using a single surface seismometers are a reliable first proxy to highlight locations with likely elevated amplification in the vertical direction. The borehole earthquake transfer functions indicate that mainly the eastern part of Groningen (borehole locations G19, G62, G60, G31, and G37) is experiencing vertical

ground motion amplification (**Figure 10**). These borehole sites are in the vicinity of large industrial facilities and pipeline infrastructure nearby the city of Delfzijl. If high vertical amplifications are persistent at large magnitudes, appreciable levels of vertical loading may be expected.

8 CONCLUSIONS

An interdisciplinary approach based on detailed geological and geophysical analyses is performed to asses the potential for local P-wave amplification in an unconsolidated shallow sediment setting. Near-surface P-wave amplification is in the Groningen setting primarily recorded on the vertical component of the borehole seismometers. This study demonstrated empirically and analytically that vertical ground motion amplification occurs especially at sites with low P-wave velocities. Regarding the influence of shallow local geology, it could be shown that peat-generated gas impacts the P-wave velocities. The data richness in Groningen allowed the analysis of borehole earthquake amplification factors and transfer functions as well as a comparison with the analysis of single-station techniques, using local earthquake records and noise data. Qualitatively, there is a good agreement between the earthquake ground motion amplification, as determined with the various approaches. To this extent we showed that surface seismometer recordings can be used as first proxy to indicate the site-effect of ground motion amplification by P-waves to an earthquake. Furthermore, the theoretical transfer functions appear to be quite similar for various angles of incidence, hence the level of amplification is not influenced by inclining earthquake waves.

The P-wave amplifications (up to a factor of 2.7) observed especially at the eastern part of the Groningen study area, illustrate the significance of a detailed study of amplification in the vertical direction. Given that this amplitude distribution shows a different pattern than for the amplification of the horizontal ground motion, we conclude that vertical ground motion amplification by low magnitude earthquakes at shallow depth cannot be treated as an average percentage of horizontal ground motion. In Groningen, unconsolidated sediments with low V_p lead to significant P-wave amplification, and should be considered to be included in predictive ground motion equations. P-to-S wave conversion in the shallow subsurface is found to be unimportant.

Although the gas production in Groningen will be ceased in the coming years, knowledge on vertical ground motion amplification by shallow and low magnitude earthquakes in a soft sedimentary setting is also key in other areas with seismic hazard, either in the Netherlands or at any site across the globe with similar conditions.

DATA AVAILABILITY STATEMENT

Publicly available datasets were analyzed in this study. This data can be found here: http://rdsa.knmi.nl/dataportal/.

AUTHOR CONTRIBUTIONS

JvG: method development, data analysis, provided input for the 2D simulations, writing of manuscript with input from all co-authors. ER: daily advisor, input on data analysis method and results, performed text input. RW: performed the 2D wave propagation simulations and performed text input. RH: promotor, initiator of this research project, advisor, final text editor.

FUNDING

This work is funded by EPI Kenniscentrum.

ACKNOWLEDGMENTS

Figures are produced in Matlab, except **Figure 1** is produced in QGIS. The authors like to thank Jan Stafleu from TNO for compiling the cumulative thickness maps based on GeoTOP. The authors like to thank the reviewers Mikhail Rodkin and Hamid Zafarani for their valuable input.

SUPPLEMENTARY MATERIAL

The Supplementary Material for this article can be found online at: https://www.frontiersin.org/articles/10.3389/feart.2022.812658/full#supplementary-material

REFERENCES

Ambraseys, N. N., and Simpson, K. A. (1996). Prediction of Vertical Response Spectra in Europe. *Earthquake Engng. Struct. Dyn.* 25, 401–412. doi:10.1002/(sici)1096-9845(199604)25:4<401::aid-eqe551>3.0.co;2-b

Biot, M. A. (1962). Mechanics of Deformation and Acoustic Propagation in Porous media. *J. Appl. Phys.* 33, 1482–1498. doi:10.1063/1.1728759

Bommer, J., Dost, B., Edwards, B., Kruiver, P., Meijers, P., Rodriguez-Marek, A., et al. (2017a). V4 Ground-Motion Model (GMM) for Response Spectral Accelerations, Peak Ground Velocity, and Significant Durations in the Groningen Field. A report prepared for NAM. Available from: https://www.nam.nl/feiten-en-cijfers/onderzoeksrapporten.html.

Bommer, J. J., Akkar, S., and Kale, O. (2011). A Model for Vertical-To-Horizontal Response Spectral Ratios for Europe and the Middle East. *Bull. Seismological Soc. America* 101, 1783–1806. doi:10.1785/0120100285

Bommer, J. J., Stafford, P. J., Edwards, B., Dost, B., van Dedem, E., Rodriguez-Marek, A., et al. (2017b). Framework for a Ground-Motion Model for Induced Seismic hazard and Risk Analysis in the Groningen Gas Field, the Netherlands. *Earthquake Spectra* 33, 481–498. doi:10.1193/082916eqs138m

Bonilla, L. F., Steidl, J. H., Lindley, G. T., Tumarkin, A. G., and Archuleta, R. J. (1997). Site Amplification in the San Fernando valley, California: Variability of Site-Effect Estimation Using the S-Wave, Coda, and H/V Methods. *Bull. Seismological Soc. America* 87, 710–730. doi:10.1785/bssa0870030710

Bonnefoy-Claudet, S., Cotton, F., and Bard, P.-Y. (2006). The Nature of Noise Wavefield and its Applications for Site Effects Studies. *Earth-Science Rev.* 79, 205–227. doi:10.1016/j.earscirev.2006.07.004

Bozorgnia, Y., and Campbell, K. W. (2016a). Ground Motion Model for the Vertical-To-Horizontal (V/H) Ratios of PGA, PGV, and Response Spectra. *Earthquake Spectra* 32, 951–978. doi:10.1193/100614eqs151m

Bozorgnia, Y., Campbell, K. W., and Niazi, M. (2000). "Observed Spectral Characteristics of Vertical Ground Motion Recorded during Worldwide Earthquakes from 1957 to 1995," in *Proceedings of the 12th World Conference on Earthquake Engineering* (Auckland: New Zealand), 2671.

Bozorgnia, Y., and Campbell, K. W. (2016b). Vertical Ground Motion Model for PGA, PGV, and Linear Response Spectra Using the NGA-West2 Database. *Earthquake Spectra* 32, 979–1004. doi:10.1193/072814eqs121m

Buijze, L., Van Den Bogert, P. A. J., Wassing, B. B. T., Orlic, B., and Ten Veen, J. (2017). Fault Reactivation Mechanisms and Dynamic Rupture Modelling of Depletion-Induced Seismic Events in a Rotliegend Gas Reservoir. *Neth. J. Geosciences* 96, s131–s148. doi:10.1017/njg.2017.27

Cen, E. (2004). *1 Design of Structures for Earthquake Resistance–Part 1: General Rules Seismic Actions and Rules for Buildings*. European Committee for Standardization.

Chin, B.-H., and Aki, K. (1991). Simultaneous Study of the Source, Path, and Site Effects on strong Ground Motion during the 1989 Loma Prieta Earthquake: a Preliminary Result on Pervasive Nonlinear Site Effects. *Bull. Seismological Soc. America* 81, 1859–1884.

[Dataset] Knmi (1993). *Netherlands Seismic and Acoustic Network*. De Bilt: Royal Netherlands Meteorological Institute. Other/Seismic Network. 10.21944/e970fd34-23b9-3411-b366-e4f72877d2c5.

Dost, B., Ruigrok, E., and Spetzler, J. (2017). Development of Seismicity and Probabilistic hazard Assessment for the Groningen Gas Field. *Neth. J. Geosciences* 96, s235–s245. doi:10.1017/njg.2017.20

Dost, B., van Stiphout, A., Kühn, D., Kortekaas, M., Ruigrok, E., and Heimann, S. (2020). *Probabilistic Moment Tensor Inversion for Hydrocarbon-Induced Seismicity in the Groningen Gas Field, the Netherlands, Part 2: Application*. Washington: Bulletin of the Seismological Society of America.

Elgamal, A., and He, L. (2004). Vertical Earthquake Ground Motion Records: an Overview. *J. Earthquake Eng.* 8, 663–697. doi:10.1080/13632460409350505

Elnashai, A. S., and Papazoglou, A. J. (1997). Procedure and Spectra for Analysis of Rc Structures Subjected to strong Vertical Earthquake Loads. *J. Earthquake Eng.* 1, 121–155. doi:10.1080/13632469708962364

Fjaer, E., Holt, R. M., Horsrud, P., Raaen, A. M., and Risnes, R. (2008). *Petroleum Related Rock Mechanics in Developments in Petroleum Science*. 2nd edition 53. Amsterdam: Elsevier.

Hofman, L. J., Ruigrok, E., Dost, B., and Paulssen, H. (2017). A Shallow Seismic Velocity Model for the Groningen Area in the Netherlands. *J. Geophys. Res. Solid Earth* 122, 8035–8050. doi:10.1002/2017jb014419

Jagt, L., Ruigrok, E., and Paulssen, H. (2017). Relocation of Clustered Earthquakes in the Groningen Gas Field. *Neth. J. Geosciences* 96, s163–s173. doi:10.1017/njg.2017.12

Kallioras, S., Correia, A. A., Graziotti, F., Penna, A., and Magenes, G. (2020). Collapse Shake-Table Testing of a clay-URM Building with Chimneys. *Bull. Earthquake Eng.* 18, 1009–1048. doi:10.1007/s10518-019-00730-0

Kato, K., Aki, K., and Takemura, M. (1995). Site Amplification from Coda Waves: Validation and Application to S-Wave Site Response. *Bull. Seismological Soc. America* 85, 467–477.

Konno, K., and Ohmachi, T. (1998). Ground-motion Characteristics Estimated from Spectral Ratio between Horizontal and Vertical Components of Microtremor. *Bull. Seismological Soc. America* 88, 228–241. doi:10.1785/bssa0880010228

Korswagen, P. A., Longo, M., Meulman, E., and Rots, J. G. (2019). Crack Initiation and Propagation in Unreinforced Masonry Specimens Subjected to Repeated In-Plane Loading during Light Damage. *Bull. Earthquake Eng.* 17, 4651–4687. doi:10.1007/s10518-018-00553-5

Koymans, M., Ballesta, J. D., Ruigrok, E., Sleeman, R., Trani, L., and Evers, L. (2021). Performance Assessment of Geophysical Instrumentation through the Automated Analysis of Power Spectral Density Estimates. *Earth Space Sci.*, e2021EA001675. doi:10.1029/2021ea001675

Kramer, S. L. (1996). *Geotechnical Earthquake Engineering*. London, United Kingdom: Pearson Education India.

Kruiver, P. P., Wiersma, A., Kloosterman, F. H., de Lange, G., Korff, M., Stafleu, J., et al. (2017). Characterisation of the Groningen Subsurface for Seismic hazard and Risk Modelling. *Neth. J. Geosciences* 96, s215–s233. doi:10.1017/njg.2017.11

Lermo, J., and Chávez-García, F. J. (1993). Site Effect Evaluation Using Spectral Ratios with Only One Station. *Bull. seismological Soc. America* 83, 1574–1594. doi:10.1785/bssa0830051574

Liu, H.-W., and Tsai, C.-C. (2018). Site Effect of Vertical Motion-Amplification Behavior Observed from Downhole Arrays. *J. GeoEngineering* 13, 39–48.

Loads, M. D. (2017). *Associated Criteria for Buildings and Other Structures: Asce/sei 7-16*. Reston, VA: American Society of Civil Engineers.

Mad Said, M. J., Zainorabidin, A., and Madun, A. (2015). "Soil Velocity Profile on Soft Soil Using Seismic Refraction," in *Amm (Trans Tech Publications Ltd)* (Applied Mechanics and Materials), 773-774, 1549–1554. doi:10.4028/www.scientific.net/amm.773-774.1549

Malomo, D., Pinho, R., and Penna, A. (2019). Applied Element Modelling of the Dynamic Response of a Full-Scale clay brick Masonry Building Specimen with Flexible Diaphragms. *Int. J. Architectural Heritage*, 1–18. doi:10.1080/15583058.2019.1616004

Mayeda, K., Koyanagi, S., and Aki, K. (1991). Site Amplification from S-Wave Coda in the Long Valley Caldera Region, California. *Bull. Seismological Soc. America* 81, 2194–2213. doi:10.1785/bssa0810062194

Meijles, E. (2015). *De Ondergrond Van Groningen: Een Geologische Geschiedenis*. Assen: NAM.

Molnar, S., Cassidy, J. F., Castellaro, S., Cornou, C., Crow, H., Hunter, J. A., et al. (2018). Application of Microtremor Horizontal-To-Vertical Spectral Ratio (Mhvsr) Analysis for Site Characterization: State of the Art. *Surv. Geophys.* 39, 613–631. doi:10.1007/s10712-018-9464-4

Nakamura, Y. (1989). *A Method for Dynamic Characteristics Estimation of Subsurface Using Microtremor on the Ground Surface*. Washington: Railway Technical Research Institute. Quarterly Reports 30.

Nakamura, Y. (2019). What Is the Nakamura Method? *Seismological Res. Lett.* 90, 1437–1443. doi:10.1785/0220180376

Nakata, N., Snieder, R., Kuroda, S., Ito, S., Aizawa, T., and Kunimi, T. (2013). Monitoring a Building Using Deconvolution Interferometry. I: Earthquake-Data Analysis. *Bull. Seismological Soc. America* 103, 1662–1678. doi:10.1785/0120120291

Newmark, N. M., Blume, J. A., and Kapur, K. K. (1973). in *Seismic Design Spectra for Nuclear Power plantsTech. Rep.* (Urbana, IL: Consulting Engineering Services).

Perron, V., Gélis, C., Froment, B., Hollender, F., Bard, P.-Y., Cultrera, G., et al. (2018). Can Broad-Band Earthquake Site Responses Be Predicted by the Ambient Noise Spectral Ratio? Insight from Observations at Two Sedimentary Basins. *Geophys. J. Int.* 215, 1442–1454. doi:10.1093/gji/ggy355

Rodriguez-Marek, A., Kruiver, P. P., Meijers, P., Bommer, J. J., Dost, B., van Elk, J., et al. (2017). A Regional Site-Response Model for the Groningen Gas Field. *Bull. Seismological Soc. America* 107, 2067–2077.

Romijn, R. (2017). *Groningen Velocity Model 2017. Tech. rep., NAM)*. Assen: Nederlands Aardolie Maatschappij.

Rong, M., Li, H., and Yu, Y. (2019). The Difference between Horizontal-To-Vertical Spectra Ratio and Empirical Transfer Function as Revealed by Vertical Arrays. *PloS one* 14, e0210852. doi:10.1371/journal.pone.0210852

Saadeghvariri, M. A., and Foutch, D. A. (1991). Dynamic Behaviour of R/C Highway Bridges under the Combined Effect of Vertical and Horizontal Earthquake Motions. *Earthquake Engng. Struct. Dyn.* 20, 535–549. doi:10.1002/eqe.4290200604

Sánchez-Sesma, F. J., Rodríguez, M., Iturrarán-Viveros, U., Luzón, F., Campillo, M., Margerin, L., et al. (2011). A Theory for Microtremor H/V Spectral Ratio: Application for a Layered Medium. *Geophys. J. Int.* 186, 221–225. doi:10.1111/j.1365-246x.2011.05064.x

Sarmadi, M. A., Heidari, R., Mirzaei, N., and Siahkoohi, H. R. (2021). The Improvement of the Earthquake and Microseismic Horizontal-To-Vertical Spectral Ratio (Hvsr) in Estimating Site Effects. *Acta Geophysica*, 1–12. doi:10.1007/s11600-021-00619-0

Stafleu, J., Maljers, D., Busschers, F. S., Schokker, J., Gunnink, J. L., and Dambrink, R. M. (2021). Models Created as 3-D Cellular Voxel Arrays. *Appl. Multidimensional Geol. Model. Informing Sustain. Hum. interactions shallow subsurface*, 247–271. doi:10.1002/9781119163091.ch11

Stafleu, J., Maljers, D., Gunnink, J. L., Menkovic, A., and Busschers, F. S. (2011). 3D Modelling of the Shallow Subsurface of Zeeland, the Netherlands. *Neth. J. Geosciences* 90, 293–310. doi:10.1017/s0016774600000597

Su, F., Anderson, J. G., Brune, J. N., and Zeng, Y. (1996). A Comparison of Direct S-Wave and Coda-Wave Site Amplification Determined from Aftershocks of the Little Skull Mountain Earthquake. *Bull. Seismological Soc. America* 86, 1006–1018.

van Ginkel, J., Ruigrok, E., and Herber, R. (2019). Assessing Soil Amplifications in Groningen, the Netherlands. *First Break* 37, 33–38. doi:10.3997/1365-2397.2019026

van Ginkel, J., Ruigrok, E., and Herber, R. (2020). Using Horizontal-To-Vertical Spectral Ratios to Construct Shear-Wave Velocity Profiles. *Solid Earth* 11, 2015–2030. doi:10.5194/se-11-2015-2020

van Ginkel, J., Ruigrok, E., Stafleu, J., and Herber, R. (2021). Development of a Country-wide Seismic Site-Response Zonation Map for the Netherlands. *Nat. Hazards Earth Syst. Sci. Discuss.*, 1–34.

Wapenaar, K., Slob, E., Snieder, R., and Curtis, A. (2010). Tutorial on Seismic Interferometry: Part 2 - Underlying Theory and New Advances. *Geophysics* 75, 75A211–75A227. doi:10.1190/1.3463440

Wong, T. E., Batjes, D. A., and de Jager, J. (2007). *Geology of the Netherlands*. Amsterdam: The Publishing House of the Royal Netherlands Academy of Arts and Sciences.

Yang, J., and Lee, C. M. (2007). Characteristics of Vertical and Horizontal Ground Motions Recorded during the Niigata-Ken Chuetsu, Japan Earthquake of 23 October 2004. *Eng. Geology.* 94, 50–64. doi:10.1016/j.enggeo.2007.06.003

Yang, J., and Sato, T. (2000). Interpretation of Seismic Vertical Amplification Observed at an Array Site. *Bull. Seismological Soc. America* 90, 275–285. doi:10.1785/0119990068

Yang, J., and Yan, X. R. (2009). Factors Affecting Site Response to Multi-Directional Earthquake Loading. *Eng. Geology*. 107, 77–87. doi:10.1016/j.enggeo.2009.04.002

Zhu, C., Cotton, F., and Pilz, M. (2020). *Detecting Site Resonant Frequency Using HVSR: Fourier versus Response Spectrum and the First versus the Highest Peak Frequency*. Washington: Bulletin of the Seismological Society of America.

Zimmer, M. A., Prasad, M., Mavko, G., and Nur, A. (2007). Seismic Velocities of Unconsolidated Sands: Part 1 - Pressure Trends from 0.1 to 20 MPa. *Geophysics* 72, E1–E13. doi:10.1190/1.2399459

Zwanenburg, C., Konstadinou, M., Meijers, P., Goudarzy, M., König, D., Dyvik, R., et al. (2020). Assessment of the Dynamic Properties of Holocene Peat. *J. Geotech. Geoenviron. Eng.* 146, 04020049. doi:10.1061/(asce)gt.1943-5606.0002259

Conflict of Interest: The authors declare that the research was conducted in the absence of any commercial or financial relationships that could be construed as a potential conflict of interest.

Publisher's Note: All claims expressed in this article are solely those of the authors and do not necessarily represent those of their affiliated organizations, or those of the publisher, the editors, and the reviewers. Any product that may be evaluated in this article, or claim that may be made by its manufacturer, is not guaranteed or endorsed by the publisher.

frontiers | Frontiers in Earth Science

MINI REVIEW
published: 07 April 2022
doi: 10.3389/feart.2022.819153

Evolution, Recent Progress and Perspectives of the Seismic Monitoring of Building Structures in Romania

Alexandru Tiganescu[1,2]*, *Iolanda-Gabriela Craifaleanu*[2,3], *Alexandru Aldea*[2], *Bogdan Grecu*[1], *Radu Vacareanu*[2], *Dragos Toma-Danila*[1], *Stefan-Florin Balan*[1] and *Claudiu-Sorin Dragomir*[3,4]

[1]National Institute for Earth Physics (INFP), Magurele, Romania, [2]Department of Reinforced Concrete Structures, Technical University of Civil Engineering Bucharest (UTCB), Bucharest, Romania, [3]National Institute for Research and Development in Construction, Urban Planning and Sustainable Spatial Development, URBAN-INCERC, Bucharest, Romania, [4]Department of Environment and Land Reclamation, University of Agronomic Sciences and Veterinary Medicine of Bucharest, Bucharest, Romania

The seismic instrumentation of structures in order to assess their condition and to track it over long periods or after representative events has proven to be a topic of large interest, under continuous development at international level. The seismic hazard of Romania poses one of the most dangerous threats for the country, in terms of potential physical and socio-economic losses. In recent years, taking advantage of the new scientific and technological advances, among which the exponential growth in computational resources, significant improvements have been made in extending the seismic networks for structural monitoring and using the data as input for products and services addressed not only to the research community but also to stakeholders. The paper covers focused aspects of the topic for Romania, referring to past developments of the most important institutions and seismic networks in the country and the current status, including the research and regulatory gaps. Currently, three main research and academic institutions perform structural health monitoring of twenty-two buildings in Romania. As the number of monitored buildings grows and new actors in the private sector start to get involved in the process, the need for data standardization and a regulatory framework increases. Ongoing national and international projects (PREVENT, SETTING, TURNkey) address these issues and outline the roadmap for future actions of the main institutions responsible for seismic risk reduction, including authorities, research and academia.

Keywords: seismic monitoring, structural health monitoring, building structures, seismic instrumentation, Vrancea earthquakes

OPEN ACCESS

Edited by:
Dimitris Pitilakis, Aristotle University of Thessaloniki, Greece

Reviewed by:
Sotirios Argyroudis, Brunel University London, United Kingdom
Kosmas Dragos, Hamburg University of Technology, Germany

***Correspondence:**
Alexandru Tiganescu
alexandru.tiganescu@infp.ro

Specialty section:
This article was submitted to Geohazards and Georisks, a section of the journal Frontiers in Earth Science

Received: *20 November 2021*
Accepted: *04 March 2022*
Published: *07 April 2022*

Citation:
Tiganescu A, Craifaleanu I-G, Aldea A, Grecu B, Vacareanu R, Toma-Danila D, Balan S-F and Dragomir C-S (2022) Evolution, Recent Progress and Perspectives of the Seismic Monitoring of Building Structures in Romania. Front. Earth Sci. 10:819153. doi: 10.3389/feart.2022.819153

INTRODUCTION

An essential activity for seismic countries is the monitoring and tracking of the condition of the building stock, aiming to ensure the safety of the population and quick recovery after extreme events. This endeavor has proved important not only for preparedness, mitigation and decision-making in emergency situations, but also for opening and supporting a wide range of multi-disciplinary research approaches. The condition assessment of aging structures and infrastructures is becoming a

more and more critical issue, especially when developing life extension and replacement strategies. A cost-effective maintenance strategy should aim for minimizing the total life-cycle cost of a structure, considering the costs for preventive maintenance, inspection, monitoring, repair, and failure losses (Bergmeister et al., 2003). The importance and the benefits were analyzed, by assessing the Value of Information (VoI) for structural health monitoring (SHM) systems, by Pozzi and Der Kiureghian (2011) and Kamariotis et al. (2022).

The main objectives of SHM are to assess the structural condition and to rapidly detect the changes that could reveal damage occurrence, based on vibration recordings. The research in the field of SHM was initiated with a special focus on the aerospace, nuclear power and gas exploration industries (Doebling et al., 1996; Sohn et al., 2004). The following decades witnessed a large and diversified development of SHM approaches and methods, supported by the progress of sensing technology, computer hardware and software and leveraged by the need of integration of SHM in earthquake early-warning (EEW) systems (Cosenza et al., 2010; Wu and Beck, 2012; Su et al., 2020; Iaccarino et al., 2021; Sivasuriyan et al., 2021).

In Romania, a country affected by recurring earthquakes originating from various shallow and intermediate-depth sources (Radulian et al., 2000), a large percentage of the building stock dates from before 1963 (Lungu et al., 2008; Pavel et al., 2016), the year of the enforcement of the first mandatory seismic design code, with many of them being highly vulnerable. According to data from the latest National Census (2011), more than 40% of the residential building stock in the whole country and more than 44% in the capital city Bucharest were erected before 1963. The significant losses generated by the 1977 Vrancea earthquake (when almost 33,000 buildings were partially or completely damaged), highlighted the need for an improved seismic design of buildings and for extending seismic instrumentation.

The extensive implementation of SHM systems and rapid damage assessment tools is nowadays essential for assisting decision-makers to set up strategies for the retrofit of the vulnerable building stock. Several countries have already elaborated specific guidelines and standards for the seismic instrumentation of buildings (Çelebi, 2000) and SHM (ISIS Canada, 2001; Mufti, 2002—Canada; Teshigawara et al., 2004—Japan; Moreu et al., 2018; Yang et al., 2017—China; Porter et al., 2004; Rücker et al., 2006). At present, no detailed regulations for SHM exist in Romania, even though several buildings and infrastructures are monitored and several research projects in the field have been completed or are in progress.

The article presents an overview of the evolution and current status of the seismic instrumentation of building structures in Romania, with reference to the international research and regulatory framework and to the national implementation. It covers a broad perspective, from long-term SHM under operational conditions to seismic monitoring of structures under weak-to-moderate Vrancea earthquakes. The current research gaps regarding the seismic instrumentation of structures in Romania are discussed, as well as potential future actions to overcome these issues, including the improvement of the national legislation in the field.

EVOLUTION OF THE SEISMIC INSTRUMENTATION OF BUILDING STRUCTURES IN ROMANIA

In Romania, seismic monitoring of buildings started in the 1960's, when buildings in several cities were instrumented, mainly for scientific purposes, by the National Institute for Building Research, INCERC[1] (Georgescu et al., 2010). By the time the M_W 7.4, 4 March 1977, Vrancea earthquake occurred, four accelerographs were installed at the top and in the basement of two reinforced concrete (RC) buildings, located in the cities of Bucharest (RC shear walls, 11 stories) and Galati (RC frames, 12-story) (Berg et al., 1980; Balan et al., 1982). The first reference also mentions partially instrumented multistory buildings, with accelerographs installed, at that time, either in the basement or near the top, located in Bucharest (RC frames, 13 stories), Bacau (RC shear walls) and Focsani (masonry, 3 stories). In addition, in the years before the 1977 earthquake, an extensive campaign was conducted to determine the dynamic characteristics of various buildings, by ambient vibrations measurements. The database compiled from these measurements was used, after the earthquake, as a reference to assess modifications of natural periods for 47 residential buildings in Bucharest, with various structural systems and numbers of stories ranging from 8 to 18 (Balan et al., 1982). The availability of the reference values was crucial for later seismic vulnerability assessments, given that a large part of the mentioned buildings was based on standardized designs. It was shown that an increase of the natural period of vibration of the buildings with less than 20–25% was associated with low damage, percentages of 25–50% corresponded to light damage, while multiple, systematic or local and significant damage was observed for percentages higher than 50%.

The seismic network of INCERC evolved significantly after the 1977 earthquake, when new strong motion accelerographs were used for the instrumentation of multistory residential buildings, hotels, public and administrative buildings (Craifaleanu et al., 2011). The height of the monitored buildings ranged between 4 and 11 stories, with the recording equipment typically placed in the basement and at the top floor. In 2010, the seismic network of URBAN-INCERC consisted of over 100 stations, with 11 instrumented buildings (Georgescu et al., 2010). A database of seismic records obtained on buildings instrumented by INCERC during strong earthquakes (M_W 7.1, 30 August 1986; M_W 6.9, 30 May 1990, and M_W 6.4, 31 May 1990), was compiled (Borcia et al., 2013, 2014, 2015; Craifaleanu and Borcia, 2015). The seismic data recorded in buildings were analyzed by Popescu

[1]Today a branch of the National Institute for Research and Development in Constructions, Urban Planning and Sustainable Spatial Development, URBAN-INCERC

and Demetriu (1994, 1994b, 1996) and by Demetriu and Borcia (Demetriu and Borcia, 2001; Demetriu, 2002). For the data recorded on a RC building during the 1986 earthquake, Popescu and Demetriu (1994) identified five vibration modes on each direction by running a system identification algorithm based on fitting of multivariate autoregressive model (MAR), assuming a multi-input single-output system. Popescu and Demetriu (1994) reported the initial (35–40 s) nonlinear behavior of a 12-story RC building during the 1986 earthquake, based on recorded acceleration components.

Two buildings in the Bucharest area and an experimental building at INCERC were instrumented in 1996–1998 in the framework of the Collaborative Research Center "Strong Earthquakes: A Challenge for Geosciences and Civil Engineering" project SFB 461 (Wenzel, 1997), with the National Institute for Earth Physics (INFP), the Technical University of Civil Engineering Bucharest (UTCB) and INCERC as partners (Aldea et al., 2004b). In 2003, for 3 months, one pair of strong motion instruments was deployed in a 11-story RC building, headquarters of the Institute of Atomic Physics (TURN), to study the influence of the building structure on the seismic waveforms. The monitoring was conducted within the framework of the Urban Seismology (URS) project (Ritter et al., 2005), having as partners the University of Karlsruhe and INFP.

Another structure of interest, instrumented by National Centre for Seismic Risk Reduction (NCSRR[2]), was the Faculty of Civil, Industrial and Agricultural Buildings (FCCIA) of UTCB, a RC frame, low-code building. The experimental data recorded during ambient vibration monitoring campaigns were used to validate its numerical model. In addition, the soil-structure interaction (SSI) analysis revealed slight interaction effects, however with no significant numerical impact (Demetriu et al., 2012).

The progress in the seismic instrumentation of buildings occurred in the broader context of the general development of the seismic networks in Romania. In addition, it should be mentioned that distinct monitoring is performed, by other organizations, for dams, bridges or for the subway lines in Bucharest. These construction categories are, however, beyond the scope of this paper.

CURRENT STATUS OF STRUCTURAL HEALTH MONITORING FOR BUILDINGS IN ROMANIA. RECENT PROJECTS

With the enforcement of the 2006 and 2013 editions of the Romanian seismic design codes, P100-1/2006 (UTCB, 2006) and P100-1/2013 (UTCB, 2013), both drafted by UTCB, the seismic monitoring of structures has gained additional momentum. The in force code state mandatory instrumentation for importance-exposure class I buildings, as well as for buildings higher than 45 m above ground level, located in areas with peak ground design acceleration values equal or greater than 0.25 g. In addition, since 2005, a Ministerial Order (OMTCT/OMAI No. 1995/1160 from 2005/2006) requires all the public and private buildings to be instrumented, if they have more than 16 stories (or are more than 50 m-high) or have a developed area larger than 7,500 m^2. At present, INFP, URBAN-INCERC and UTCB monitor twenty-two buildings in Romania (**Figure 1** and **Table 1**). Information on instrument types and representative photos are provided in the **Supplementary Material**.

At URBAN-INCERC, the National Network for the Seismic Monitoring and Protection of Building Stock is the department in charge of the operation of the seismic network, including the instrumented buildings (Dragomir et al., 2015a; Dragomir et al., 2015b; Dragomir et al., 2016; Dragomir et al., 2021). Currently, URBAN-INCERC monitors, mainly for research purposes, eight buildings with various functions and occupancies, located in Bucharest (7) and Iasi (1); six of these are connected online to the Data Center of the Institute. The instrumentation of these buildings consists of at least two sensors (ground floor/basement and top); two of them also have sensors close to the building, in free-field conditions. Other buildings have at present only ground-level sensors installed, complete instrumentation being envisaged in the future. In addition, short-term building vibration monitoring is being conducted, generally focused on actions induced by industrial or transportation activities. In a study conducted by Dragomir et al. (2017b), the fundamental period (0.18 s) of the Biotechnology Faculty building (BTH) was experimentally determined based on the Fourier Spectra (FS) of several recordings and validated with the values from the design code (0.15 s) and by using the Operational Modal Analysis tool of the ARTeMIS Modal Pro software[3] (0.19 s). Dragomir et al. (2017a) estimated the fundamental frequency for two other buildings, a 10-story RC shear walls apartment block (BLA) and a 15-story RC shear walls office building (APL), using noise and earthquake data. Applying the FS, they found fundamental frequencies of f_x = 1.73 Hz and f_y = 2.05 Hz for the first building, and f_x = 1.5 Hz and f_y = 1.3 Hz for the second building, respectively. Moreover, there is an ongoing experimental project for real-time damage detection in buildings (Dragomir et al., 2019; Dragomir et al., 2020) using ARTeMIS and an extensive campaign, in the framework of the ECOSMARTCONS project, for the seismic instrumentation of the premises of national research institutes all over the country. Starting with 2022, the Data Center of URBAN-INCERC has implemented SeisComP[4].

Significant progress in seismic instrumentation was made within the Japan International Cooperation Agency (JICA) Technical Cooperation Project "Reduction of Seismic Risk for Buildings and Structures", in which the NCSRR instrumented four representative buildings in Bucharest (Aldea et al., 2004a; Aldea et al., 2007a; Aldea et al., 2007b): the Romanian National

[2]NCRRS functioned between 2003 and 2010. The seismic instrumentation installed by NCRRS continued to be operated by URBAN-INCERC and at present by UTCB

[3]https://svibs.com

[4]https://www.seiscomp.de

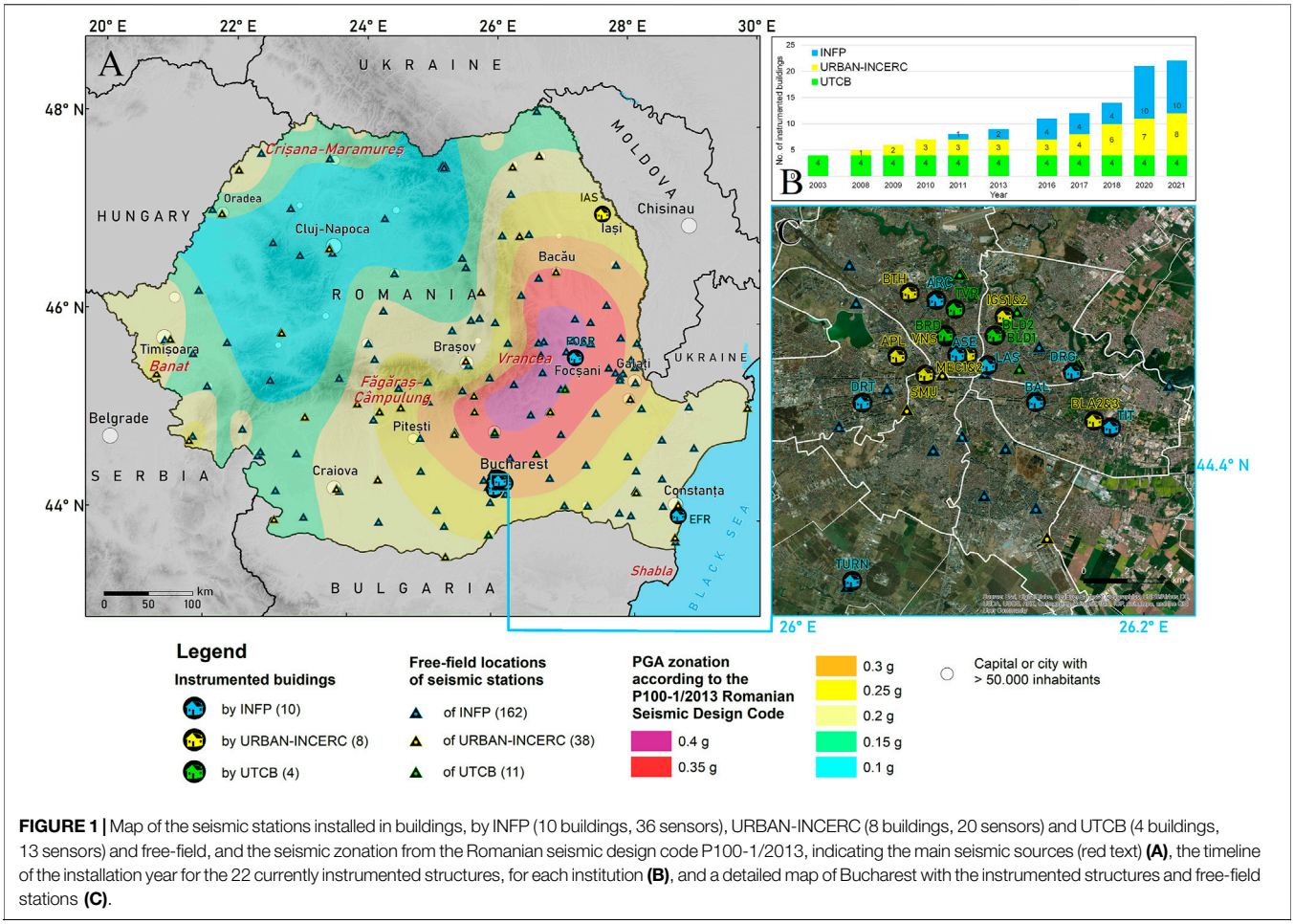

FIGURE 1 | Map of the seismic stations installed in buildings, by INFP (10 buildings, 36 sensors), URBAN-INCERC (8 buildings, 20 sensors) and UTCB (4 buildings, 13 sensors) and free-field, and the seismic zonation from the Romanian seismic design code P100-1/2013, indicating the main seismic sources (red text) **(A)**, the timeline of the installation year for the 22 currently instrumented structures, for each institution **(B)**, and a detailed map of Bucharest with the instrumented structures and free-field stations **(C)**.

Television (TVR), the BRD-SG Tower (BRD), and two residential multistory buildings (BLD1 and BLD2). Several detailed analyses of the modal frequencies, based on ambient vibration and earthquake data, were performed on the BRD-SG Tower, a newly constructed RC office building (Demetriu and Aldea, 2006). The SSI effect was investigated based on free-field and borehole data by Aldea et al. (2007c). For the same building, Perrault et al. (2013) proposed a methodology to reduce the uncertainty of the single-building fragility curve using experimental data. First, a linear MDOF model was adjusted for experimental modal analysis using a Timoshenko beam model (Boutin et al., 2005) and based on Anderson's criteria (Anderson, 2004). Then, the structure's response to a large set of accelerograms simulated by the SIMQKE software (Gasparini and Vanmarcke, 1976) was computed and, for the final step, the fragility curves were constructed by comparing numerical inter-story drift with the threshold criteria provided by the Hazus methodology (FEMA, 2003) for the slight damage state. Recent research on SHM, performed by UTCB, widened the scope of previous studies, approaching heritage buildings, such as the minaret of the Royal Mosque in Constanta (Aldea et al., 2018), and traditional Romanian timber framed masonry houses (Aldea et al., 2020).

In 2011, a heritage building of the University of Economic Studies (ASE), located in Bucharest, was retrofitted using seismic isolators and viscous dampers, the first action of this kind in Romania. INFP was in charge of SHM and of the efficiency assessment of this innovative solution, by placing accelerometers under and above the seismic isolators. Data recorded during two seismic events (M_W 5.5, 28 October 2018 and M_W 4.8, 31 January 2020) revealed a reduction of the acceleration amplitude by a factor ranging from 2.0 to 3.8, for the two horizontal components. The same promising results were reported for the same earthquakes on another heritage structure equipped with earthquake-protection system in Bucharest, the Arch of Triumph (ARC), with reductions of acceleration amplitude by a factor up to 4.5 (Balan et al., 2020).

INFP is currently monitoring 10 buildings, with 36 sensors (**Table 1**). The instrumentation setup consists of strong motion sensors located mainly at the ground (or basement) level, at an intermediate floor and at the roof level. New low-cost sensors (Raspberry Shake[5] RS3D and RS4D) are tested to extend the building monitoring network in the framework of the TURNkey[6]

[5]https://raspberryshake.org
[6]https://earthquake-turnkey.eu

TABLE 1 | Characteristics of the instrumented structures.

Institution	Station code	Construction year/period	Structure type	Number of stories[a]	No. of sensors	Location of sensors	Instrument code[b]
URBAN-INCERC	APL	2008	RC Shear walls	2B + GF + 14S	3	B, 4th S, 14th S	GRN + EPI
	SMU	1978/retrofitted in 1996	RC Shear walls	B + GF + 13S	3	GF, 6th S, 14th S	K2 + EPI
	IGS1&2	1968	RC Frames	B + GF + 7S + partial story	2	GF, partial story	ETNA2
	MEC1&2	1969	RC Frames	B + GF + 6S + mechanical floor	2	B, mechanical floor	ETNA2
	BLA2&3	1971	RC Shear walls	B + GF + 10S	2	B, 10th S	GRN; ETNA
	BTH	2016	RC Frames and shear walls	B + GF + 2S	3	B, partial story + free-field	GRN + EPI
	VNS	2000s	RC Shear walls	3B + GF + 14S + mechanical floor	2	3rd B, roof	ETNA
	IAS7	1985	RC Frames	GF + 3S	3	GF, 3rd S + free-field	GRN + EPI
UTCB	BLD1	1980s	RC frames	B + GF + 10S	4	1st S, 5th S, 11th S, 12th S	K2 + EPI
	BLD2	1960s	RC frames	B + GF + 6S	4	B, 4th S, 7th S + free-field	K2 + EPI
	TVR	1960s	RC frames	B + GF + 13S	3	B, 14th S, 15th S	K2 + EPI
	BRD	2003	RC dual	3B + GF + 18S	2	3rd B, 19th S	K2 + EPI
INFP	ARC	1922/retrofitted in 2016	RC	27 m	3	GF, top + free-field	TSA-SMA; K2 + EPI
	ASE	1905/retrofitted in 2011	Masonry	B + GF + 2S + attic	2	GF	K2 + EPI
	TURN	1973/retrofitted in the 1990s	RC shear walls	B + GF + 9S	10	B, 1st S, 3rd S, 6th S, 7th S, 10th S	IDAS + TSA-100S; RS4D; RS3D
	FOCR	1971	RC frame	GF + 8S	3	B, 4th S, 8th S	TSA-SMA
	EFR	2008	RC frame	B + GF + 2S	3	B, GF, 3rd S	RS4D
	DRG	1982	Large panel structure (precast shear walls structure)	B + GF + 8S	3	B, 5th S, 8th S	RS4D
	BAL	before 1963 (<1940)	Unreinforced Masonry	B + GF + Attic	2	B, attic	RS4D
	DRT	before 1963	Large panel structure (precast shear walls structure)	GF + 8S	3	GF, 5th S, 9th S	RS4D
	TIT	1963–1977	Large panel structure (precast shear walls structure)	B + GF + 10S	3	GF, 5th S, 10th S	RS4D
	LAS	2008	RC frame	3B + GF + 11S	4	3rd B, GF, 5th S, 11th S	RS4D

[a]*B—basement story; GF—ground floor; S—story/stories.*

[b]*The instrument type and representative photos are presented in* ***Supplementary Table S1****—Supplementary Material.*

and PREVENT[7] projects. Low-cost sensors (Micro-electromechanical systems - MEMS accelerometers) have proven useful and provided promising results when used for early-warning systems (Nof et al., 2019), small local earthquake detection (Cascone et al., 2021) or even initial ground-motion assessment (Holmgren and Werner, 2021). However, their usability and reliability for SHM has not yet been extensively studied. The very high level of digital noise is masking any type of low-amplitude ambient vibrations. This type of sensors should be of paramount importance in case of earthquakes with $M_W > 6.0$, given the amount of data they can provide from a larger number of instrumented structures, when compared to professional equipment, within the same monitoring expenses.

The data from all stations are transmitted in real-time to the Romanian National Data Center (RONDC) of INFP. For data acquisition, quality control and recording, real-time data processing and exchange, network status monitoring, automatic and interactive event detection and location, waveform archiving and distribution, INFP has run, since 2008, SeisComP, in parallel with Kinemetrics Antelope[8] (Marmureanu et al., 2021).

[7]https://prevent.infp.ro

[8]The Boulder Real-Time Technologies, Inc. (BRTT) https://brtt.com

Recently, Tiganescu et al. (2020) analyzed the dynamic characteristics (fundamental period and damping ratio) of the three representative high-rise buildings from Bucharest, based on ambient vibration data recorded during a two-day measurement campaign. The fundamental periods obtained using FS analysis, Random Decrement Technique (Cole, 1973) and Transfer Function were validated against results computed using empirical formulas from the design code corresponding to each building. The values were consistent for both the fundamental period and the damping ratio of the buildings, regardless of the method and of the measurement day. However, small diurnal and weekly variations were reported for the two parameters, due to small differences in atmospheric conditions and building occupancy at different moments of data acquisition.

Preliminary analysis of earthquake data recorded on structures during the latest moderate magnitude Vrancea seismic event (M_W 5.5, 28 October 2018) highlighted different behaviors and trends, depending on the structural characteristics and of the existence of earthquake-protection system. Amplification and reduction of motion on different frequency ranges were revealed, with clear peaks corresponding to the dynamic characteristics of the buildings (Tiganescu et al., 2019).

The Bighorn module, an extension of the Antelope package, is also used at INFP to perform seismic monitoring of structures. The system computes near real-time response spectra and issues alarms, depending of the level of exceedance of a preset limit spectra. This procedure was tested for Bucharest using the 28 October 2018 earthquake data (Balan et al., 2019). The reporting service is currently performed in an offline environment, on request. The permanent seismic stations installed in buildings were used in a recent study conducted by Grecu et al. (2021) to assess the effect of the COVID-19 related restrictions on the level of high-frequency content of the ambient vibrations generated by human activity. Significant noise reductions (40–80%) on the 15–40 Hz frequency range for stations in and near buildings were associated to the mobility restrictions of people working inside the office buildings and with the shift to online classes for educational units.

In the context of other studies highlighting the influence of atmospheric conditions on the dynamic parameters of structures (Clinton et al., 2006; Herak and Herak, 2009; Mikael et al., 2013; Guéguen and Tiganescu, 2018), a case-study building (TURN) was instrumented with both seismic sensors and a meteorological station (Tiganescu et al., 2021a), in the framework of the PREVENT project. A fundamental frequency variation analysis was conducted on a 72-h dataset of ambient vibration and earthquake data, using the Frequency Domain Decomposition method (Brincker et al., 2001). Small variations of the fundamental frequency were observed in the ambient vibration regime, while for the forced vibrations (earthquake) the variation was larger (drop of 10%) and followed by a recovery. Moreover, correlation of the atmospheric and environmental conditions (mainly air temperature, relative humidity and wind speed) with the building's natural frequency was tested, but with no sharp conclusions due to limited timespan.

DISCUSSION

A large number of buildings, representing different typologies (construction period, structural system, material, height, exposure to earthquakes, vulnerability) were previously and are currently instrumented in Romania, as a need for acquiring pre-, during and post-event vibration data. From the point of view of the coverage of areas of interest considering seismic hazard levels and building exposure, there is still a need to instrument and monitor structures that could be affected by crustal earthquakes (**Figure 1A**), in seismic zones such as Banat, Fagaras-Campulung, Crisana-Maramures or nearby Shabla, Bulgaria.

The effort is ongoing by means of national and international projects involving seismic instrumentation of structures and the development of web platforms for data and metadata inventory (SETTING[9] or TURNkey) and waveform acquisition, processing and visualization (PREVENT). Data standardization for easy integration in international infrastructures such as European Plate Observing System - EPOS (Luzi et al., 2016; Astorga et al., 2020) and for use in international research projects is another objective that the Romanian research and engineering community working on SHM is envisaging.

In addition, the low and narrow-band frequency content of the ground motion, observed in Bucharest for large-magnitude Vrancea earthquakes (Lungu and Cornea, 1988; Lungu et al., 1992; Craifaleanu, 2011), and its effect on different building typologies (Ambraseys 1977), needs further investigations. Outcomes of the seismic monitoring of structures can also significantly help as input for refined rapid seismic loss estimates, using already available systems such as SeisDaRo (Toma-Danila and Armas, 2017).

There is also a crucial need to continuously develop and upgrade the national guidelines regarding SHM, including clear requirements for modern digital sensors, standard installation procedures, data acquisition and processing. Currently, there are no specific procedures for the elaboration, checking and approval of the seismic instrumentation plan. A better definition of the technical specifications of the digital accelerometers is needed, regarding their minimum sensitivity, the maximum amplitude that can be recorded, the frequency sampling, the storage, and the time precision. Moreover, online access should be mandatory ensured for easy maintenance and periodical checks on the system operational status. The data processing and results interpretation should be performed by specialists, using well-established routines and algorithms, to obtain reliable results and to avoid any artefact errors or uncertainties that can arise and propagate during the signal processing stage.

In the recent years, the collaboration between Romanian institutions involved in the health monitoring of structures (URBAN-INCERC, UTCB and INFP) has been enforced by joint research projects and publications (Tiganescu et al., 2021a; Tiganescu et al., 2021b; Tiganescu et al., 2021c; Marmureanu et al., 2021). A system integrating URBAN-INCERC's SHM system and INFP's

[9]https://setting.epos-ro.eu

EEW was proposed by Dragomir et al. (2016). The SETTING project, as well as the Romanian consortium[10] contributing in the EPOS research infrastructure[11] aim to provide a national research platform consisting of a standardized inventory of organizations which could provide data, products, and services relevant for the field of Earth Sciences—including SHM relevant categories. The platform will be designed to meet the needs of various user communities (research, academia, industry and general public). The effort to strengthen the collaboration with local and central authorities has gained momentum, as well, as several researchers from the three institutions are participating in the elaboration of a national strategy for the seismic risk reduction of the building stock, and in the development of a national emergency procedure in case of a strong earthquake. A special SHM section will be held at the third European Conference on Earthquake Engineering and Seismology (Bucharest, 2022), as a step towards bringing together the significant actors in the field and bridging the gap between research, academia and industry.

AUTHOR CONTRIBUTIONS

AT and I-GC designed the paper, and all the authors contributed to the manuscript. AA and RV contributed to the part referring to UTCB network, I-GC and C-SD contributed to the part referring to the URBAN-INCERC network, AT, BG, DT-D, and S-FB contributed to the part referring to the INFP network. DT-D designed Figure 1. All the authors contributed to the Discussion section.

FUNDING

Part of the developments received support through the following INFP Projects PREVENT (Open system for integrated civil structures monitoring; no. PN-III-P2-2.1-PED-2019-0832) and Pre-Quake (Preparing for the next major earthquake: exploring new scientific opportunities; No. PN-III-P1-1.1-PD-2019-0969) supported grants from the Romanian Ministry of Research, Innovation and Digitalization, CNCS–UEFISCDI within PNCDI III, as well as the SETTING Project (Integrated thematic services in the field of Earth observation: a national platform for innovation; No. 108206) cofinanced from the Regional Development European Fund (FEDR) through the Operational Competitivity Programme 2014–2020; TURNkey (Towards more earthquake-resilient urban societies through a multisensor-based information systemenabling earthquake forecasting, early warning and rapid response actions, available at https://earthquake-turnkey.eu/, GA 821046), funded by the European Commission (EC); The paper refers also some of the results obtained at INCD URBAN-INCERC within the projects PN 18-35 01 01, "Research for the development of an instrumental detection system for structural damage caused by seismic or non-seismic sources", and PN 19-33 01 01, "Research on the implementation of an integrated system for ensuring the security of the constructed space, with semi-automatic generation of PGA maps provided by seismic actions or other vibratory sources and quick evaluation of vulnerability of instrumented buildings", funded in the framework of the "Nucleu" Programmes CONCRET and ECOSMARTCONS by the Romanian Ministry of Research, Innovation and Digitalization.

ACKNOWLEDGMENTS

Japan International Cooperation Agency (JICA) is gratefully acknowledged for the donation of equipment for seismic instrumentation in the frame of the Technical Cooperation Project "Reduction of Seismic Risk for Buildings and Structures" Ref.#7241011E0, equipment operated at present by UTCB. The authors also thank to Editor DP and two independent reviewers for their helpful and constructive reviews, which lead to an improvement of the manuscript.

SUPPLEMENTARY MATERIAL

The Supplementary Material for this article can be found online at: https://www.frontiersin.org/articles/10.3389/feart.2022.819153/full#supplementary-material

REFERENCES

Aldea, A., Albota, E., Demetriu, S., and Kashima, T. (2007a). "Seismic Response of a Low-Code High-Rise RC Building in Bucharest," in Proc. of the International Symposium on Strong Vrancea Earthquakes and Risk Mitigation, Bucharest, Romania.

Aldea, A., Demetriu, S., Albota, E., and Kashima, T. (2007b). "Instrumental Response of Buildings. Studies within JICA Project in Romania," in Proc. of the International Symposium on Seismic Risk Reduction. The JICA Technical Cooperation Project in Romania, Vacareanu. Editor R. Hiroto and, 157–170.

Aldea, A., Dutu, A., Demetriu, S., and Dima, D. I. (2020). Dynamic Properties Identification for a Timber Framed Masonry House. *Constructii* 21 (1), 3–12.

Aldea, A., Iiba, M., Demetriu, S., and Kashima, T. (2007c). "Evidence of Soil-Structure Interaction from Earthquake Records at a High-Rise Building Site in Bucharest," in Proc. of the 4th International Conference on Earthquake Geotechnical Engineering, Thessaloniki, Greece, 1523.

Aldea, A., Kashima, T., Lungu, D., Vacareanu, R., Koyama, S., and Arion, C. (2004a). "Modern Urban Seismic Network in Bucharest, Romania," in Proc. of the First International Conference on Urban Earthquake Engineering, Tokyo, Japan.

Aldea, A., Lungu, D., Vacareanu, R., and Arion, C. (2004b1800). "Development of Strong Ground Motion Network in Romania and Bucharest Instrumentation for Site Effects Assessment," in Proc. of the 13th World Conference on Earthquake Engineering, Vancouver (Canada).

[10]https://epos-ro.eu

[11]https://www.epos-eu.org

Aldea, A., Neagu, C., Lozinca, E., Demetriu, S., El-Amine Bourdim, S. M., and Turano, F. (2018). "Toward the Seismic Evaluation of "Carol I" Royal Mosque in Constanța," in *Seismic Hazard and Risk Assessment*. Editors R. Vacareanu and C. Ionescu (Springer), 345–359. doi:10.1007/978-3-319-74724-8_23

Ambraseys, N. N. (1977). Long-period Effects in the Romanian Earthquake of March 1977. *Nature* 268, 324–325. doi:10.1038/268324a0

Anderson, J. G. (2004). "Quantitative Measure of the Goodness-Of-Fit of Synthetic Seismograms," in Proc. of the 13th World Conference on Earthquake Engineering, Vancouver (Canada), 243.

Astorga, A., Guéguen, P., Ghimire, S., and Kashima, T. (2020). NDE1.0: a New Database of Earthquake Data Recordings from Buildings for Engineering Applications. *Bull. Earthquake Eng.* 18 (4), 1321–1344. doi:10.1007/s10518-019-00746-6

Balan, S., Capatina, D., Cornea, I., Cristescu, V., Dumitrescu, D., Enescu, D., et al. (1982). *Cutremurul de pamint din Romania de la 4 martie 1977 (The 1977 March 4, Earthquake in Romania)*. Bucharest: The Publishing House of the Romanian Academy. (in Romanian).

Balan, S. F., Tiganescu, A., Apostol, B. F., and Danet, A. (2019). Post-earthquake Warning for Vrancea Seismic Source Based on Code Spectral Acceleration Exceedance. *Earthq. Struct.* 17 (4), 365–372. doi:10.12989/eas.2019.17.4.365

Balan, S. F., Tiganescu, A., and Apostol, B. F. (2020). Structure Response Analysis of the Seismic Isolated Buildings in Bucharest City. *IOP Conf. Ser. Earth Environ. Sci.* 609, 012080. doi:10.1088/1755-1315/609/1/012080

Berg, G. V., Bolt, B. A., Sozen, M. A., and Rojahn, C. (1980). *Earthquake in Romania, March 4, 1977. An Engineering Report*. Washington, DC: The National Academies Press. doi:10.17226/19783

Bergmeister, K., Aktan, A. E., Bucher, C., Dorfmann, L., Fehling, E., Frey, R. P., et al. (2003). *Monitoring and Safety Evaluation of Existing concrete Structures: State-Of-Art Report*. Lausannef:ib Bulletin 22. doi:10.35789/fib.BULL.0022

Borcia, I. S., Craifaleanu, I. G., Calarasu, E. A., Tanase, N. F., and Praun, I. C. (2015). SM-ROM-GL (Strong Motion ROMania Ground Level) Database. *Constructii* 16 (1), 3–10.

Borcia, I. S., Craifaleanu, I. G., Georgescu, E. S., and Praun, I. C. (2014). "The National strong-motion Network of URBAN-INCERC: Recent Developments," in Proc. of the 2nd European Conference on Earthquake Engineering and Seismology, Turkey (Istanbul), 3354.

Borcia, I. S., Craifaleanu, I. G., Praun, I. C., and Tanase, N. F. (2013). Banca de date SP VRANCEA NT - Prelucrari ale inregistrarilor cutremurelor vrancene (The SP VRANCEA NT Databank - Processing of Vrancea earthquakes records). *Urbanism. Arhitectura. Constructii.* 4 (1), 71–78. (in Romanian).

Boutin, C., Hans, S., Ibraim, E., and Roussillon, P. (2005). *In Situ* experiments and Seismic Analysis of Existing Buildings. Part II: Seismic Integrity Threshold. *Earthquake Engng Struct. Dyn.* 34 (12), 1531–1546. doi:10.1002/eqe.503

Brincker, R., Zhang, L., and Andersen, P. (2001). Modal Identification of Output-Only Systems Using Frequency Domain Decomposition. *Smart Mater. Struct.* 10 (3), 441–445. doi:10.1088/0964-1726/10/3/303

Cascone, V., Boaga, J., and Cassiani, G. (2021). Small Local Earthquake Detection Using Low-Cost MEMS Accelerometers: Examples in Northern and Central Italy. *Seismic Rec.* 1 (1), 20–26. doi:10.1785/0320210007

Çelebi, M. (2000). *Seismic Instrumentation of Buildings. Open-File Report 2000-157*. Menlo Park, CA: US Geological Survey. doi:10.3133/ofr00157

Clinton, J. F., Bradford, S. C., Heaton, T. H., and Favela, J. (2006). The Observed Wander of the Natural Frequencies in a Structure. *Bull. Seismological Soc. America* 96 (1), 237–257. doi:10.1785/0120050052

Cole, H. A., Jr. (1973). *On-line Failure Detection and Damping Measurement of Aerospace Structures by Random Decrement signatures Report NASA CR-2205*. Washington, DC: National Aeronautics and Space Administration.

Cosenza, E., Galasso, C., and Iervolino, I. (2010). "Ongoing Applications of EEW and SHM at the University of Naples Federico II," in Proc. of the 5th European Workshop on Structural Health Monitoring. Editors F. Casciati and M. Giordano (DEStech Publications), 25–31.

Craifaleanu, I. G., Borcia, I. S., and Praun, I. C. (2011). "Strong-motion Networks in Romania and Their Efficient Use in the Structural Engineering Applications," in *Earthquake Data in Engineering Seismology: Predictive Models, Data Management and Networks*. Editors S. Akkar, P. Gülkan, and T. van Eck (Springer), 247–259. doi:10.1007/978-94-007-0152-6_17

Craifaleanu, I. G., and Borcia, I. S. (2015). Reconsideration of Ground-Level Seismic Records Obtained in Instrumented Buildings: a Preliminary Study for strong Vrancea Earthquakes. *Constructii* 16 (2), 35–44.

Craifaleanu, I. G. (2011). "Investigation of the Frequency Content of Ground Motions Recorded during strong Vrancea Earthquakes, Based on Deterministic and Stochastic Indices," in Proc. of the 8th International Conference on Structural Dynamics EURODYN. Editors G. De Roeck, G. Degrande, G. Lombaert, and G. Muller, 2893–2898.

Demetriu, S., and Aldea, A. (2006). "Recorded Seismic Response of an Instrumented High-Rise Reinforced-concrete Building in Bucharest," in Proc. of the First European Conf. on Earthquake Engineering and Seismology, Geneva, Switzerland, 777.

Demetriu, S., Aldea, A., and Udrea, A. (2012). "Modal Parameters of RC Frame Structure Identified from Ambient Vibration Measurements," in Proc. of the 15th World Conference on Earthquake Engineering, Lisbon, Portugal.

Demetriu, S., and Borcia, I. S. (2001). *Seismic Response of Instrumented Buildings during Vrancea Earthquakes*, 2. Bulletin of the Technical University of Civil Engineering, Structural Mechanics and Structural Engineering, 1–12.

Demetriu, S. (2002). *Modal Identification of Instrumented Buildings from Vrancea Earthquake Records*, 2. Bulletin of the Technical University of Civil Engineering, Structural Mechanics and Structural Engineering, 13–21.

Doebling, S. W., Farrar, C. R., Prime, M. B., and Shevitz, D. W. (1996). *Damage Identification and Health Monitoring of Structural and Mechanical Systems from Changes in Their Vibration Characteristics: A Literature Review*. Los Alamos National Laboratory Report LA-13070-MS. doi:10.2172/249299

Dragomir, C.-S., Craifaleanu, I.-G., Dobre, D., and Georgescu, E.-S. (2019). Prospective Studies for the Implementation of a Remote Access Earthquake Damage Detection System for High-Rise Buildings in Romania. *IOP Conf. Ser. Earth Environ. Sci.* 221, 012036. doi:10.1088/1755-1315/221/1/012036

Dragomir, C.-S., Meita, V., Dobre, D., Georgescu, E.-S., and Borcia, I.-S. (2015b). A Holistic and Integrative Concept for strong-motion Records on Constructions of the URBAN-INCERC National Seismic Network. *Present Environ. Sustain. Dev.* 9 (2), 113–124. doi:10.1515/pesd-2015-0029

Dragomir, C. S., Craifaleanu, I.-G., Dobre, D., and Georgescu, E. S. (2016). "An Experimental Investigation on the Health Monitoring of the new City Hall Building in Bucharest Based on Real-Time Data Transmission," in *Life-Cycle of Engineering Systems: Emphasis on Sustainable Civil Infrastructure*. Editors J. Bakker, D. M. Frangopol, and K. Van Breugel (CRC Press), 239–244. doi:10.1201/9781315375175-24

Dragomir, C. S., Craifaleanu, I. G., Meiță, V., Georgescu, E. S., Dobre, D., Sandu, M., et al. (2021). Insights from the Management of a Large Research Infrastructure in Romania: National Network for the Seismic Monitoring and Protection of Building Stock at NIRD URBAN-INCERC. *IOP Conf. Ser. Mater. Sci. Eng.* 1138, 012021. doi:10.1088/1757-899X/1138/1/012021

Dragomir, C. S., Dobre, D., Craifaleanu, I., and Georgescu, E.-S. (2017a). On-line Data Transmission, as Part of the Seismic Evaluation Process in the Buildings Field. *IOP Conf. Ser. Earth Environ. Sci.* 95, 022004. doi:10.1088/1755-1315/95/2/022004

Dragomir, C. S., Dobre, D., Craifaleanu, I. G., and Georgescu, E. S. (2020). An Integrated National System for Assuring the Quick Evaluation of the Vulnerability of All Instrumented Buildings after an Earthquake. Recent Developments. *Scientific Papers-Series E-Land Reclamation Earth Observation Surv. Environ. Eng.* 9, 94–97.

Dragomir, C. S., Dobre, D., Craifaleanu, I. G., and Georgescu, E. S. (2017b). Ex-ante and Ex-post Instrumental Diagnosis of Buildings Structural Health. An Approach at the Level of the National Seismic Network, URBAN-INCERC. *Scientific Papers-Series E-Land Reclamation Earth Observation Surv. Environ. Eng.* 6, 77–80.

Dragomir, C. S., Dobre, D., and Georgescu, E. S. (2015a). "Seismic Instrumentation on Vibrations to Determine the Dynamic Characteristics of Buildings," in Proc. of the 15th International Multidisciplinary Scientific GeoConference SGEM, Albena, Bulgaria, 957–964.

FEMA (2003). *HAZUS-MH MR3 Technical Manual*. Washington, D.C.: Federal Emergency Management Agency.

Gasparini, D. A., and Vanmarcke, E. H. (1976). *Simulated Earthquake Motions Compatible with Prescribed Response Spectra. Research Report*, R76-4. Cambridge, MA: MIT Department of Civil Engineering, Massachusetts Institute of Technology.

Georgescu, E. S., Borcia, I. S., Praun, I. C., and Dragomir, C. S. (2010). "State of the Art of Structural Health Monitoring in Seismic Zones of Romania," in *Proc. Of the MEMSCON Workshop* (Bucharest, Romania, 89–93.

Grecu, B., Borleanu, F., Tiganescu, A., Poiata, N., Dinescu, R., and Tataru, D. (2021). The Effect of 2020 COVID-19 Lockdown Measures on Seismic Noise Recorded in Romania. *Solid Earth* 12, 2351–2368. doi:10.5194/se-12-2351-2021

Guéguen, P., and Tiganescu, A. (2018). Consideration of the Effects of Air Temperature on Structural Health Monitoring through Traffic Light-Based Decision-Making Tools. *Shock and Vibration* 2018, 1–12. doi:10.1155/2018/9258675

Hefford, R. T., Tyler, R. G., and Skinner, R. I. (1980). The M02A Strong-Motion Accelerograph. *Bnzsee* 13 (4), 374–379. doi:10.5459/bnzsee.13.4.374-379

Herak, M., and Herak, D. (2009). Continuous Monitoring of Dynamic Parameters of the DGFSM Building (Zagreb, Croatia). *Bull. Earthquake Eng.* 8 (3), 657–669. doi:10.1007/s10518-009-9112-y

Holmgren, J. M., and Werner, M. J. (2021). Raspberry Shake Instruments Provide Initial Ground-Motion Assessment of the Induced Seismicity at the United Downs Deep Geothermal Power Project in Cornwall, United Kingdom. *Seismic Rec.* 1 (1), 27–34. doi:10.1785/0320210010

Iaccarino, A. G., Gueguen, P., Picozzi, M., and Ghimire, S. (2021). Earthquake Early Warning System for Structural Drift Prediction Using Machine Learning and Linear Regressors. *Front. Earth Sci.* 9, 666444. doi:10.3389/feart.2021.666444

ISIS Canada (2001). *Guidelines for Structural Health Monitoring – Design Manual No. 2. Winnipeg: Intelligent Sensing for Innovative Structures (ISIS) Canada*.

Kamariotis, A., Chatzi, E., and Straub, D. (2022). Value of Information from Vibration-Based Structural Health Monitoring Extracted via Bayesian Model Updating. *Mech. Syst. Signal Process.* 166, 108465. doi:10.1016/j.ymssp.2021.108465

Lungu, D., Aldea, A., and Arion, C. (2008). "Romania'S Seismicity and Seismic Hazard: From Historical Records to Design Codes," in *Harmonization of Seismic Hazard in Vrancea Zone*. Editors A. Zaicenco, I. G. Craifaleanu, and I. Paskaleva (Dordrecht): Springer, 1–16. doi:10.1007/978-1-4020-9242-8_1

Lungu, D., Cornea, T., and Demetriu, S. (1992). "Frequency Bandwidth of Vrancea Earthquakes and the 1991 Edition of Seismic Code in Romania," in Proc. of the 10th Conf. on Earthquake Engineering, Madrid, Spain, 5633–5638.10

Lungu, D., and Cornea, T. (1988). "Power Spectra in Bucharest for Vrancea Earthquakes," in Proc. of the Symposium on reliability-based design in civil engineering, Lausanne, Switzerland, 17–24.

Luzi, L., Puglia, R., Russo, E., D'Amico, M., Felicetta, C., Pacor, F., et al. (2016). The Engineering Strong-Motion Database: A Platform to Access Pan-European Accelerometric Data. *Seismological Res. Lett.* 87 (4), 987–997. doi:10.1785/0220150278

Mărmureanu, A., Ionescu, C., Grecu, B., Toma-Danila, D., Tiganescu, A., Neagoe, C., et al. (2021). From National to Transnational Seismic Monitoring Products and Services in the Republic of Bulgaria, Republic of Moldova, Romania, and Ukraine. *Seismol. Res. Lett.* 92 (3), 1685–1703. doi:10.1785/0220200393

Mikael, A., Gueguen, P., Bard, P. Y., Roux, P., and Langlais, M. (2013). The Analysis of Long-Term Frequency and Damping Wandering in Buildings Using the Random Decrement Technique. *Bull. Seismological Soc. America* 103 (1), 236–246. doi:10.1785/0120120048

Moreu, F., Li, X., Li, S., and Zhang, D. (2018). Technical Specifications of Structural Health Monitoring for Highway Bridges: New Chinese Structural Health Monitoring Code. *Front. Built Environ.* 4, 10. doi:10.3389/fbuil.2018.00010

Mufti, A. A. (2002). Structural Health Monitoring of Innovative Canadian Civil Engineering Structures. *Struct. Health Monit.* 1 (1), 89–103. doi:10.1177/147592170200100106

Nof, R. N., Chung, A. I., Rademacher, H., Dengler, L., and Allen, R. M. (2019). MEMS Accelerometer Mini-Array (MAMA): A Low-Cost Implementation for Earthquake Early Warning Enhancement. *Earthquake Spectra* 35 (1), 21–38. doi:10.1193/021218EQS036M

Pavel, F., Vacareanu, R., Douglas, J., Radulian, M., Cioflan, C., and Barbat, A. (2016). An Updated Probabilistic Seismic hazard Assessment for Romania and Comparison with the Approach and Outcomes of the SHARE Project. *Pure Appl. Geophys.* 173 (6), 1881–1905. doi:10.1007/s00024-015-1223-6

Perrault, M., Gueguen, P., Aldea, A., and Demetriu, S. (2013). Using Experimental Data to Reduce the Single-Building Sigma of Fragility Curves: Case Study of the BRD tower in Bucharest, Romania. *Earthq. Eng. Eng. Vib.* 12 (4), 643–658. doi:10.1007/s11803-013-0203-z

Popescu, T. D., and Demetriu, S. (1994a). Change Detection in Dynamic Characteristics of a Structural System. *Proc. 1994 Am. Control. Conf. - ACC* 941, 937–941. doi:10.1109/ACC.1994.751881

Popescu, T. D., and Demetriu, S. (1996). Dynamic Characteristics Identification of a Structural System from Earthquake Records. *Syst. Anal. Model. Sim.* 23 (3), 223–236.

Popescu, T. H. D., and Demetriu, S. (1994b). Identification of a Multi-story Structure from Earthquake Records. *IFAC Proc. Volumes* 27 (8), 707–712. doi:10.1016/S1474-6670(17)47792-5

Porter, K. A., Beck, J. L., Ching, J. Y., Mitrani-Reiser, J., Miyamura, M., Kusaka, A., et al. (2004). *Real-time Loss Estimation for Instrumented BuildingsReport No. EERL 2004-08*. Pasadena, CA: Earthquake Engineering Research Laboratory, California Institute of Technology.

Pozzi, M., and Der Kiureghian, A. (2011). "Assessing the Value of Information for Long-Term Structural Health Monitoring," in *Proc. Of SPIE, Health Monitoring of Structural and Biological Systems*. Editor T. Kundu, 7984. 79842W. doi:10.1117/12.881918

Radulian, M., Vaccari, F., Mândrescu, N., Panza, G. F., and Moldoveanu, C. L. (2000). Seismic Hazard of Romania: Deterministic Approach. *Pure Appl. Geophys.* 157, 221–247. doi:10.1007/PL00001096

Ritter, J. R. R., Balan, S. F., Bonjer, K.-P., Diehl, T., Forbriger, T., Marmureanu, G., et al. (2005). Broadband Urban Seismology in the Bucharest Metropolitan Area. *Seismological Res. Lett.* 76 (5), 574–580. doi:10.1785/gssrl.76.5.574

Rücker, W., Hille, F., and Rohrmann, R. (2006). *Guideline for Structural Health Monitoring*. European Association on Structural Assessment Monitoring and Control SAMCO.

Sivasuriyan, A., Vijayan, D. S., Górski, W., Wodzyński, Ł., Vaverková, M. D., and Koda, E. (2021). Practical Implementation of Structural Health Monitoring in Multi-Story Buildings. *Buildings* 11 (6), 263. doi:10.3390/buildings11060263

Sohn, H., Farrar, C. R., Hemez, F. M., Shunk, D. D., Stinemates, D. W., Nadler, B. R., et al. (2004). *A Review of Structural Health Monitoring Literature: 1996-2001*. Los Alamos National Laboratory Report LA-13976-MS.

Su, J., Xia, Y., and Weng, S. (2020). Review on Field Monitoring of High-rise Structures. *Struct. Control Health Monit.* 27, e2629. doi:10.1002/stc.2629

Teshigawara, M., Isoda, H., Morita, K., Kitagawa, Y., Mita, A., Nakai, S., et al. (2004). "Technology Utilization Guidelines of Structural Health Monitoring for Buildings and its Application," in Proc. of the 13th World Conference on Earthquake Engineering, Vancouver (Canada), 2221.

Tiganescu, A., Balan, S. F., Toma-Danila, D., and Apostol, B. F. (2019). "Preliminary Analysis of Data Recorded on Instrumented Buildings from Bucharest Area during the 28Th October 2018 Vrancea Earthquake," in Proc. of the 19th International Multidisciplinary Scientific GeoConference SGEM, Albena, Bulgaria, 897–904. doi:10.5593/sgem2019/1.1/S05.111

Tiganescu, A., Craifaleanu, I. G., and Balan, S. F. (2021b). Dynamic Parameters of a RC Building Extracted from Earthquake Data Using the Random Decrement Technique. *IOP Conf. Ser. Earth Environ. Sci.* 664, 012088. doi:10.1088/1755-1315/664/1/012088

Tiganescu, A., Craifaleanu, I. G., and Balan, S. F. (2021a). Short-term Evolution of Dynamic Characteristics of a RC Building under Seismic

and Ambient Vibrations. *IOP Conf. Ser. Earth Environ. Sci.* 664, 012105. doi:10.1088/1755-1315/664/1/012105

Tiganescu, A., Grecu, B., and Craifaleanu, I. G. (2020). Dynamic Identification for Representative Building Typologies: Three Case Studies from Bucharest Area. *Civ Eng. J.* 6 (3), 418–430. doi:10.28991/cej-2020-03091480

Tiganescu, A., Toma-Danila, D., Grecu, B., Craifaleanu, I.-G., Florin Balan, S., and Sorin Dragomir, C. (2021c). "Current Status and Perspectives on Seismic Monitoring of Structures and Rapid Seismic Loss Estimation in Romania," in Proc. of the 1st Croatian Conference on Earthquake Engineering, 1CroCEE, Zagreb, Croatia. Editors S. Lakušić and J. Atalić, 81–91. doi:10.5592/CO/1CroCEE.2021.120

Toma-Danila, D., and Armaş, I. (2017). Insights into the Possible Seismic Damage of Residential Buildings in Bucharest, Romania, at Neighborhood Resolution. *Bull. Earthquake Eng.* 15 (3), 1161–1184. doi:10.1007/s10518-016-9997-1

UTCB (2006). *Cod de proiectare seismica – partea I –Prevederi de proiectare pentru cladiri P 100-1/2006 (Seismic design code - part I: Design prescriptions for buildings P 100-1/ 2006).* Bucharest: Monitorul Oficial. Part I, No. 803bis of 25.09 (In Romanian).

UTCB (2013). *Cod de proiectare seismica – partea I –Prevederi de proiectare pentru cladiri P 100-1/2013 (Seismic design code - part I: Design prescriptions for buildings P 100-1/2013).* Bucharest: Monitorul Oficial. Part I, No. 558bis of 03.09.2013 (In Romanian).

Wenzel, F. (1997). Strong Earthquakes: A Challenge for Geosciences and Civil Engineering--A New Collaborative Research Center in Germany. *Seismological Res. Lett.* 68 (3), 438–443. doi:10.1785/gssrl.68.3.438

Wu, S., and Beck, J. L. (2012). Synergistic Combination of Systems for Structural Health Monitoring and Earthquake Early Warning for Structural Health Prognosis and Diagnosis. *ProcSPIE* 8348, 83481Z. doi:10.1117/12.914996

Yang, Y., Li, Q., and Yan, B. (2017). Specifications and Applications of the Technical Code for Monitoring of Building and Bridge Structures in China. *Adv. Mech. Eng.* 9 (1), 168781401668427. doi:10.1177/1687814016684272

Conflict of Interest: The authors declare that the research was conducted in the absence of any commercial or financial relationships that could be construed as a potential conflict of interest.

frontiers | Frontiers in Earth Science

ORIGINAL RESEARCH
published: 09 May 2022
doi: 10.3389/feart.2022.885724

Combining Earthquake Ground Motion and Ambient Vibration Recordings to Evaluate a Local High-Resolution Amplification Model—Insight From the Lucerne Area, Switzerland

Paulina Janusz[1]*, *Vincent Perron*[1], *Christoph Knellwolf*[2] and *Donat Fäh*[1]

[1]Swiss Seismological Service, ETH Zürich, Zürich, Switzerland, [2]Verkehr und Infrastruktur, Abteilung Naturgefahren, Kanton Luzern, Kriens, Switzerland

OPEN ACCESS

Edited by:
Dimitris Pitilakis,
Aristotle University of Thessaloniki, Greece

Reviewed by:
Iolanda-Gabriela Craifaleanu,
Technical University of Civil Engineering of Bucharest, Romania
Maria Manakou,
Aristotle University of Thessaloniki, Greece

***Correspondence:**
Paulina Janusz
paulina.janusz@sed.ethz.ch

Specialty section:
This article was submitted to Geohazards and Georisks, a section of the journal Frontiers in Earth Science

Received: 28 February 2022
Accepted: 22 March 2022
Published: 09 May 2022

Citation:
Janusz P, Perron V, Knellwolf C and Fäh D (2022) Combining Earthquake Ground Motion and Ambient Vibration Recordings to Evaluate a Local High-Resolution Amplification Model—Insight From the Lucerne Area, Switzerland. Front. Earth Sci. 10:885724. doi: 10.3389/feart.2022.885724

Amplification factors are often estimated using empirical methods based on earthquake ground motion; however, especially in low-seismicity urban areas, recording a statistically representative number of high-quality signals may take years. Hence, the attempts to use ambient vibration instead have progressed. This includes the development of the hybrid site-to-reference spectral ratio (SSRh) method that combines earthquake and ambient vibration recordings. We applied the method in the Lucerne area in central Switzerland that is characterized by low-to-moderate seismicity but was struck by several strong earthquakes in historical times (i.e., Mw 5.9 in 1,601) and is located in a glacial basin filled with unconsolidated deposits prone to significant amplification. To develop the high-resolution local site amplification model for the city of Lucerne using the SSRh method, we took advantage of a small seismic monitoring network installed in the Lucerne area in total for about a year and the stations of the Swiss Strong Motion Network (SSMNet). In addition, we performed two extensive surveys to record ambient vibrations and used dozens of measurements performed in the area since 2001. The resulting amplification model referring to the Swiss reference bedrock conditions indicates high-amplification factors (up to 10-fold) for a broad range of frequencies. The model is consistent with geological data and site response proxies such as f_0 values. The direct comparison of our results with the SSR amplification functions for several sites shows good agreement. However, the model is characterized by high uncertainty and influenced by daily variation of the noise wavefield, as well as the spatial distribution of the stations of the seismic network. We also discussed the extent of the applicability of the method, concluding that the main factor influencing its performance is not the distance but the similarity of the site condition between the stations.

Keywords: seismic site effects, seismic hazard, urban areas, microzonation, ambient vibration, earthquake ground motion

INTRODUCTION

Estimation of site effects plays a crucial role in local seismic hazard and risk assessment. Indeed, the local soil condition can modify seismic ground motions' amplitude and duration and impose significant spatial variability. In particular, the thick and soft sedimentary basins can considerably amplify the seismic waves. Events in 1985 in Mexico City and 1906 in the San Francisco area are examples, where earthquake-induced damage was significantly increased due to local site effects (e.g., Bard, 1997). Urban areas are especially vulnerable to earthquakes because of high-population density and the accumulation of exposed infrastructure. Due to recent rapid urban development, seismic risks in the cities cannot be neglected, even in countries characterized by moderate seismic hazards such as Switzerland.

The empirical site response can be evaluated from ground motion observations using the standard spectral ratio technique (SSR—Borcherdt, 1970) referenced to the local outcropping rock or methods based on the generalized inversion scheme (e.g., Andrews et al., 1986; Bindi et al., 2009) such as empirical spectral modeling (ESM) by Edwards et al. (2013). This method is used to obtain the empirical amplification functions with respect to the Swiss reference rock profile (Poggi et al., 2011). Nevertheless, the empirical approaches require a good statistical number of recordings with a high signal-to-noise ratio. In low-to-moderate seismicity urban areas that are characterized by the high background noise level, instruments often need to operate for years before recording a significant number of earthquakes. The associated cost of such deployment together with the lack of free-field space impedes using earthquake observations to assess the site response at high spatial resolution in urban environments. On the contrary, ambient vibration measurements can be performed easily and quickly even in densely populated cities. The ambient noise horizontal-to-vertical spectral ratio (HVSR) method first introduced by Nogoshi and Igarashi, (1971) and then revised and promoted by Nakamura, (1989) is commonly applied to determine the fundamental resonance frequency f0 of the site (e.g., Bonnefoy-Claudet et al., 2006; Fäh et al., 2001). However, the HVSR amplitude cannot be interpreted as a measure of amplification factors (e.g., Bonilla et al., 1997; Perron et al., 2018a; Poggi and Fäh, 2016). Therefore, the attempts to use ambient vibration to estimate directly the amplification factors were made by calculating spectral ratios from ambient noise recordings (SSRn—Kagami et al., 1982). As in the SSR method, the source and path components are assumed similar for both stations, and the spectral ratio expresses only the site effect term. It is, however, a strong statement regarding ambient noise, and many authors demonstrated that the SSRn approach overestimates the rock-relative amplification factors (e.g., Field et al., 1990; Perron et al., 2018a). Some other authors showed that it enables only to estimate the shape of the amplification curve (e.g., Lermo and Chavez-Garcia, 1994; Yamanaka et al., 1993), while several authors observed merely the similarity of the

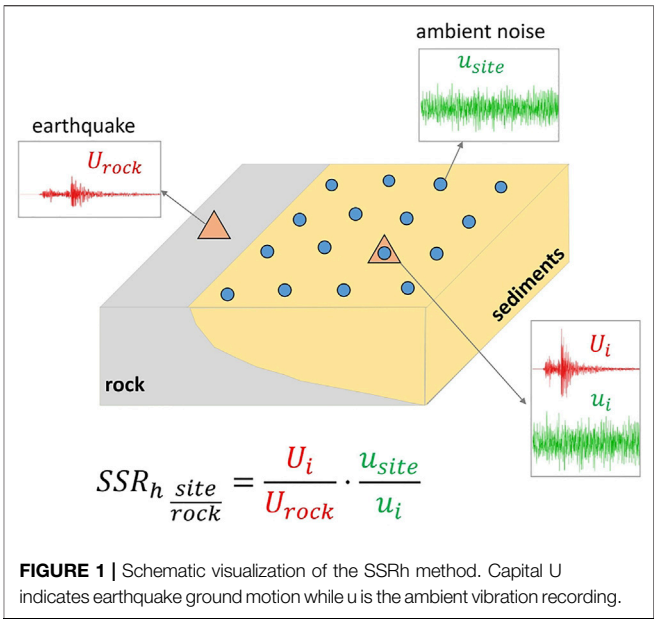

FIGURE 1 | Schematic visualization of the SSRh method. Capital U indicates earthquake ground motion while u is the ambient vibration recording.

frequency of the SSRn main peak and fundamental frequency of resonance f0 (e.g., Field et al., 1990). No correlation was observed in other studies (e.g., Field, 1996). Perron et al. (2018a) provided detailed literature reports on this topic. The strong influence of close transient noise sources and effects of the impedance contrast between sediments and rock on the ambient noise wavefield may be the main reasons for the failure of the SSRn approach (Perron et al., 2018a). Hence, Perron et al. (2018a) introduced the hybrid approach (SSRh) combining the SSR and SSRn methods (**Figure 1**). The main idea of the SSRh method is to perform the SSRn approach only between sites located inside the sedimentary basin to map the spatial variation of the site response. Then, the SSRn curves are corrected using the rock-relative SSR at a few stations (at least one) inside the basin where earthquake recordings are available. The SSRh approach has shown comparable results to the direct SSR based on earthquake recordings (Perron et al., 2018a; Perron et al., 2022). In addition, the SSRh method allows for much higher spatial resolution because ambient noise can be fast recorded across wide areas, and it requires only a limited number of permanent seismic stations to be present in the region.

In this study, we will focus on Lucerne that is middle-sized but a densely populated town in central Switzerland (**Figure 2A**). The city is located on a soft sedimentary basin that is prone to site effects. During the last 50 years, the seismicity in central Switzerland has been low (Gisler et al., 2004); however, several strong historical earthquakes are evidenced, including an event in 1,601 with a moment magnitude Mw of 5.9 (Fäh et al., 2011). It was the strongest historical event in central Switzerland in the past millennium and one of the strongest events in the whole of Switzerland (Schwarz-Zanetti et al., 2003) and was followed by a 4–5 m-high tsunami (Schnellmann et al., 2004).

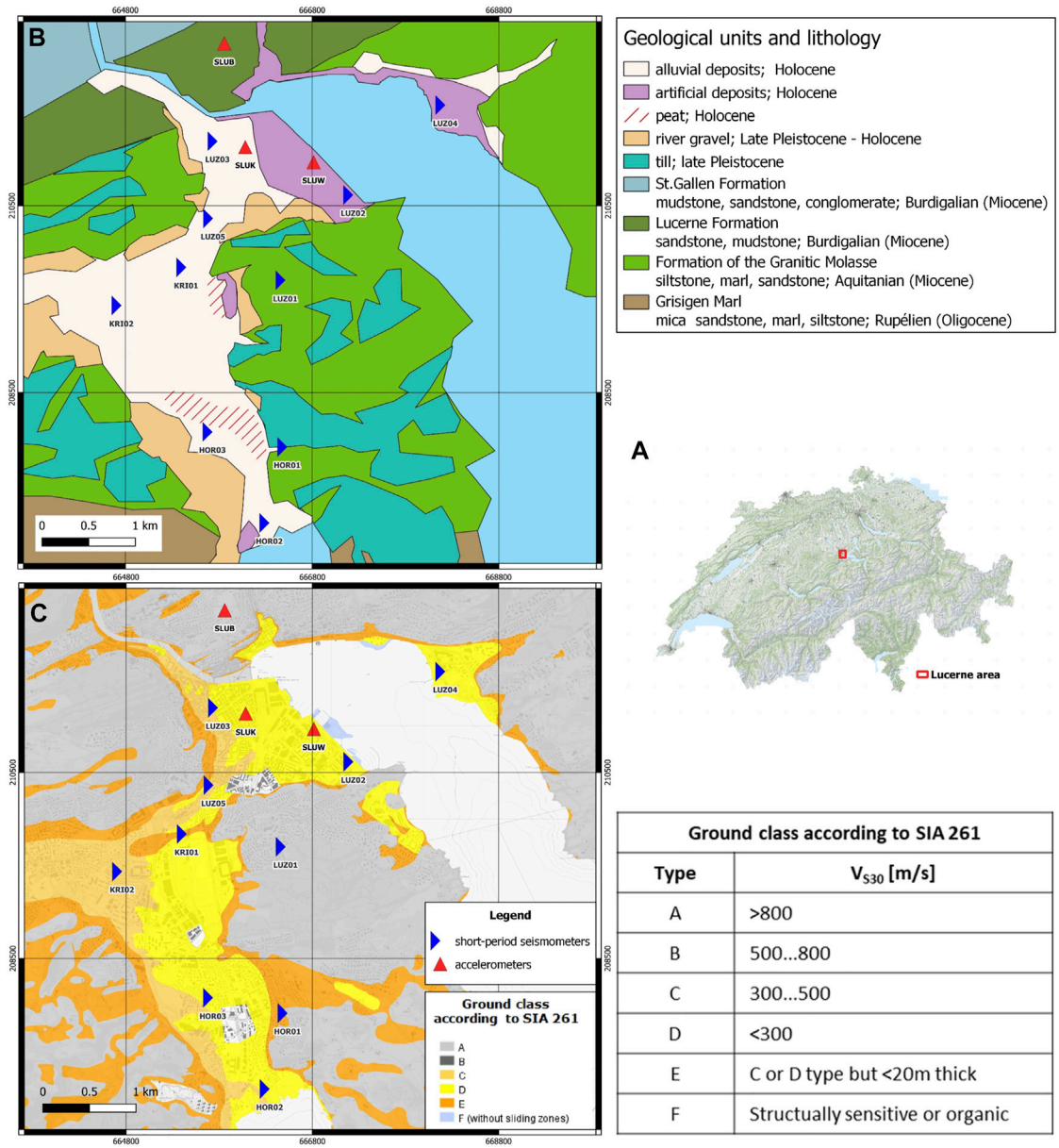

Ground class according to SIA 261	
Type	V_{S30} [m/s]
A	>800
B	500...800
C	300...500
D	<300
E	C or D type but <20m thick
F	Structually sensitive or organic

FIGURE 2 | (A) Red rectangle on the map of Switzerland shows the location of the investigated area. **(B)** Simplified geological map based on Geological Vector Datasets GeoCover (s.geo.admin.ch/95a803e945) **(C)** Ground classes in the Lucerne area according to SIA 261 (SIA, 2020) (s.geo.admin.ch/96572c02d9). Stations of local seismic monitoring networks are shown.

Our study focuses on the application and optimization of the SSRh approach for the Lucerne area. We developed an amplification model at high spatial resolution and in a broad frequency range using the SSRh method. We verified the results by comparing them to the earthquake-based amplification functions. In addition, we tested several parameters that may influence the results. Moreover, we compared our results to geological data and to the fundamental resonance frequency that we mapped across the area. The aim of this article is not only to show an example of the SSRh method application but also to offer practical guidelines and advice to future users.

GEOLOGICAL SETTING AND INSTRUMENTATION

The study area is a relatively small basin filled with unconsolidated Quaternary fluvio-lacustrine deposits (**Figure 2B**), mainly consisting of interspersed layers of sand, gravel, clay, and silt (Keller + Lorenz, 2010; Poggi et al., 2012). Such predominantly soft sediments are classified as soil classes D, C, and E (**Figure 2C**), according to the Swiss building code classification (SIA, 2020), which is defined in terms of V_{s30} ranges and is similar to EC8 classification (EC8, 2004). The basin was

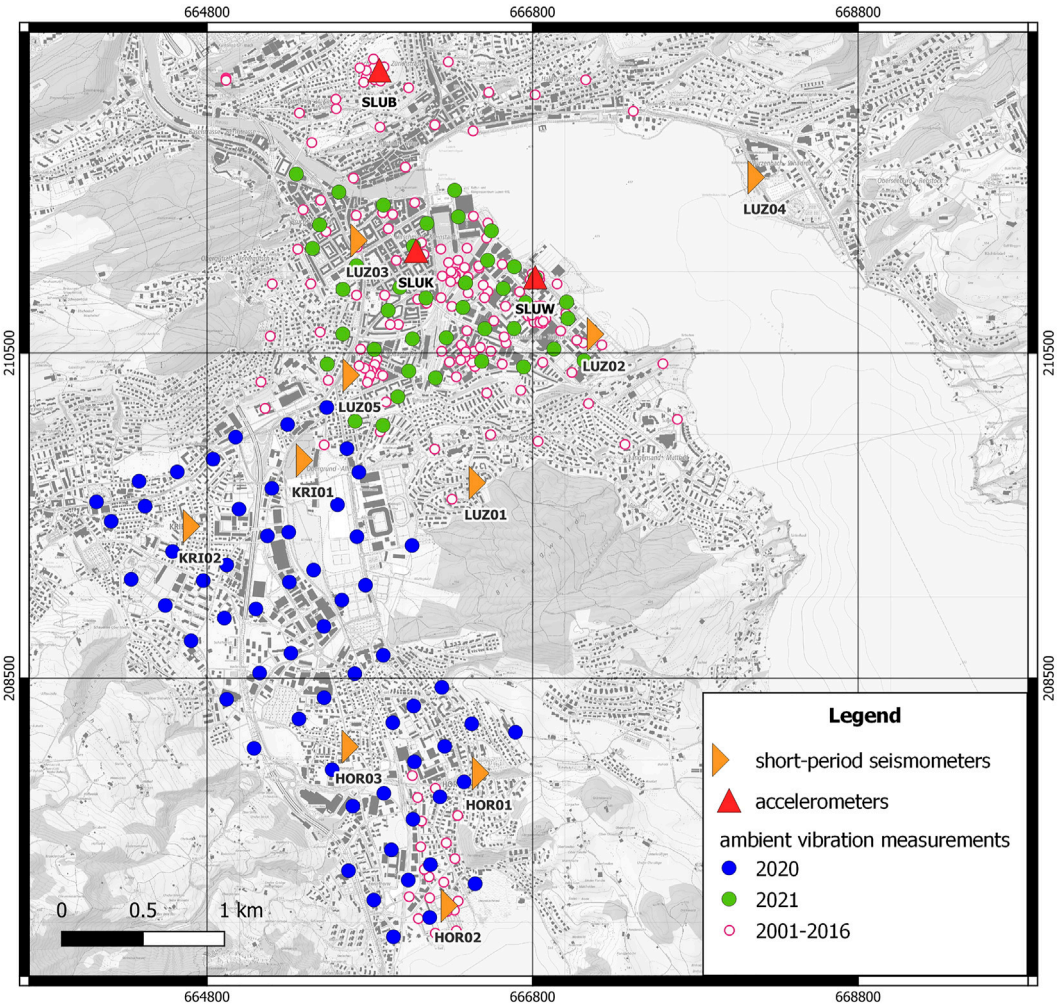

FIGURE 3 | Stations of seismic monitoring networks located in the Lucerne area and single-station ambient noise measurements. Short-period seismometers are part of the temporary local network, while accelerometers belong to SSMNet (Michel et al., 2014; Hobiger et al., 2021).

formed by the inter- and intraglacial processes in clastic sedimentary rocks, such as hard sandstones, siltstones, and mudstones deposited in the Subalpine Molasse basin. Hence, the bedrock interface geometry is complex; the southern part of the study area is a long (about 4 km), very narrow basin (about 700 m in the narrowest part) with sediment thickness reaching 150 m. In the northern part of the basin, where the historical Lucerne's old town and train station are located, the basin shape is more asymmetrical with the thick sedimentary layers by the lakefront (50–100 m thick) extending southwest into a shallower terrace with gradually decreasing sediment thickness.

In November 2019, nine temporary seismic stations and then again in December 2020, ten temporary seismic stations were deployed in the Lucerne area for 5–6 months to record local and teleseismic earthquakes (**Figure 3**, **Figure 4A**). It consisted of 3-component short-period seismometers Lennartz 5 s (LE-3D 5-s) associated with Centaur digitizers. In total, most of the stations were recording for about one year. All sensors were buried 0.4 m below the ground, except for one (LUZ03) which was situated in the underground parking; the instrument was laid directly on the concrete floor. In addition, our dataset was supplemented by three permanent accelerometers of the Swiss Strong Motion Network (SSMNet—Hobiger et al., 2021; Michel et al., 2014). Some details concerning the deployment and geological and geotechnical characteristics of the sites can be found in **Supplementary Table 1A** (in Appendix).

Two ambient vibration measurement campaigns were performed in June 2020 and in April 2021, (**Figure 3**, **Figure 4B**) respectively, while the temporary seismic stations were still operating. In total, we recorded at least 1–2 h of ambient noise at 100 sites using the same sensor-digitizer configuration as for the earthquake monitoring (LE-3D 5-s—Centaur). During short-time measurements, sensors were not buried but installed on tripods directly on the ground. In addition to the temporary seismic stations, longer ambient noise recordings were performed at four sites with a buried sensor to capture the 24 h variations of the ambient noise seismic wavefield inside the basin. During both campaigns, the ambient vibration measuring points were

FIGURE 4 | (A) LUZ02—example of the station of the temporary network. **(B)** Example of measurement of ambient noise during the survey in June 2020. The setup consists of a Lennartz 5-s sensor and Centaur digitizer.

recording simultaneously with earthquake monitoring stations, and the instruments deployed for 24 h. In addition, there were short overlaps (from a few minutes to one hour) between some short-term measuring points, but only a maximum of six of them were recording at the same time. Moreover, we supplemented our dataset with a few hundred short ambient vibration recordings (**Figure 3**) performed in the Lucerne area during the last 20 years (e.g., Poggi et al., 2012). These old recordings were used to map the fundamental resonance frequency in detail across the area but not to develop the amplification model since the SSRh cannot be applied without the simultaneous presence of the earthquake monitoring stations.

METHODOLOGY AND PROCESSING

All earthquake and ambient vibration recordings that we used are first pre-processed using the ObsPy library (Beyreuther et al., 2010); in other words, instrumental correction and bandpass filter (a cosine taper with corner frequencies: 0.01, 0.05, 95, and 100 Hz) are applied.

As for the SSR method, a number of local and teleseismic earthquakes are extracted and processed for each site of the local temporary network and permanent SSMNet stations. In total, 44 events (**Supplementary Table 2A** in Appendix) are analyzed considering a part of the signal from P-wave arrival until coda (Perron et al., 2018b), requiring that the signal-to-noise ratio (SNR) is at least 3 for frequency bands longer than half an octave. To ensure that the earthquake source and path components are approximately the same for both considered stations, the SSR is computed for a given event if the distance between two stations was much shorter than the approximated epicentral distance; the factor of 5 was chosen. The SSR curve is then smoothed using the Konno and Ohmachi, (1998) algorithm with a b-value of 40.

The final amplification function for each pair is a geometric mean of several realizations of the SSR. The horizontal component is defined here as the geometric mean of the eastern and northern components. ESM amplification functions (Edwards et al., 2013) are automatically computed for all stations of the Swiss network including temporary deployment but only for local earthquakes and if SNR is more than three in a broad frequency range (at least an order of magnitude).

As for the SSRn technique, we randomly selected one week (10-16.03.2021) of continuous noise recording for temporary stations; for short-term ambient vibration measurements, the whole recordings (often 1–2 h long) are used. All recordings are divided into shorter windows before applying a short-time Fourier transform, where the window length and overlap value are dependent on the signal length to optimize the computing time; typically, the length of the window is 40 s with 50% overlapping. Noise-based spectral ratios for each short window are averaged using a geometric mean after excluding outliers and smoothed with the Konno and Ohmachi (1998) algorithm with a b-value of 40.

As for the SSRh technique, the SSR and SSRn computed in previous steps are used. For SSR functions, only frequency bands where at least two earthquakes contribute are considered because several stations of our local monitoring network might serve as a potential intermediate station; hence, to avoid subjectivity, we calculated a weighted geometrical mean of several SSRh realizations computed using different intermediate stations with the squared inverse of the difference of f_0 values between the site (f_0^s) and the intermediate station (f_0^i) as a weight (w). However, usage of other weights is also tested (e.g., inverse of the squared distance between stations) and is discussed later in the present article.

$$w = \frac{1}{\left(f_0^i - f_0^s\right)^2}$$

While mapping the amplification variability for the Lucerne area using ambient vibration data, we have a limited choice of

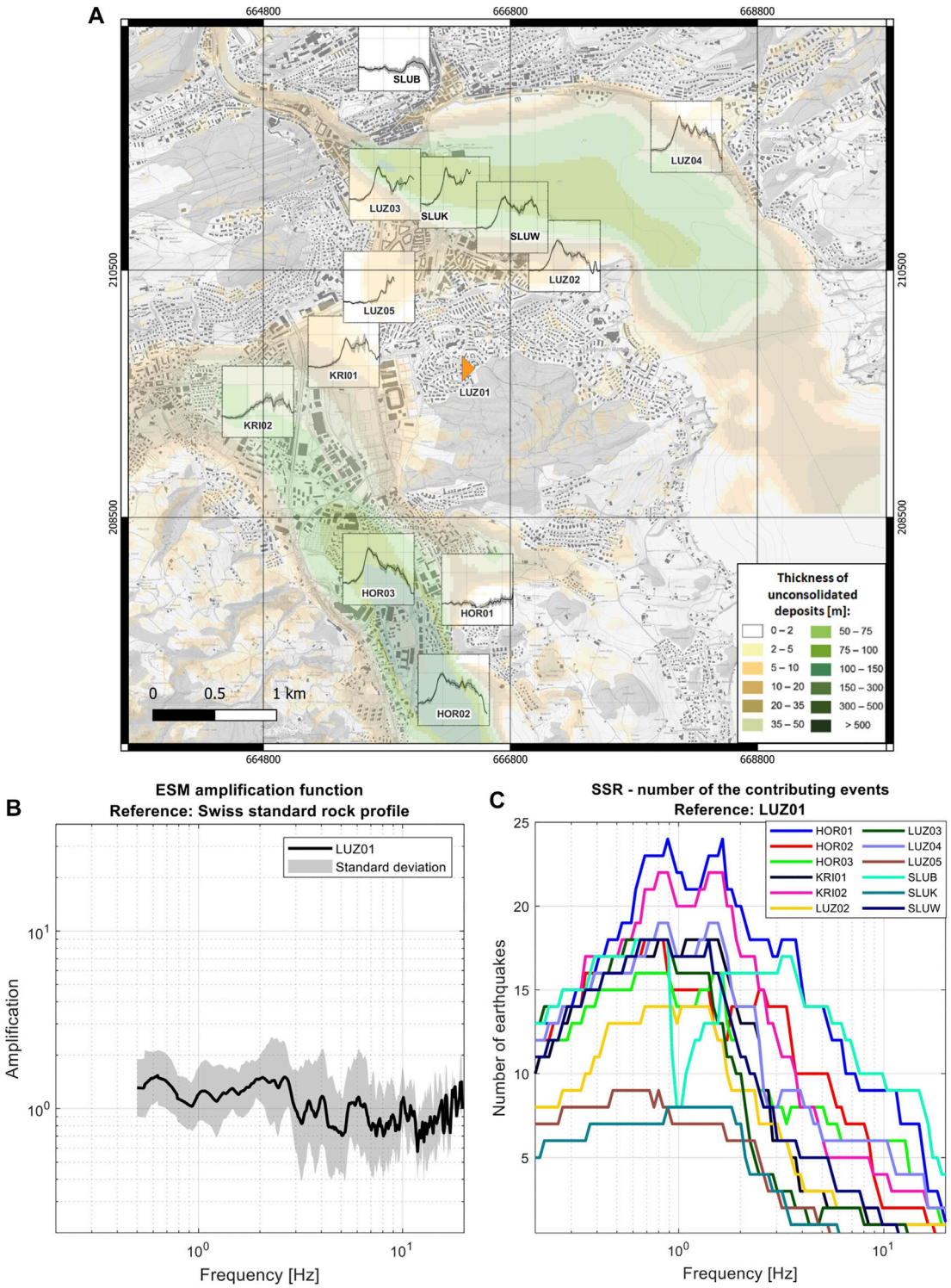

FIGURE 5 | (A) Amplification functions (horizontal component) for stations located in the Lucerne area using the SSR method referenced to the rock station LUZ01. The center of each plot corresponds to the station location. All plots have the same scale as the plot in **(B)**. In the background, the thickness of the unconsolidated deposits map is shown. **(B)** ESM amplification function (Edwards et al., 2013) for rock station LUZ01. **(C)** Number of contributing events for each frequency for all sites for the SSR method.

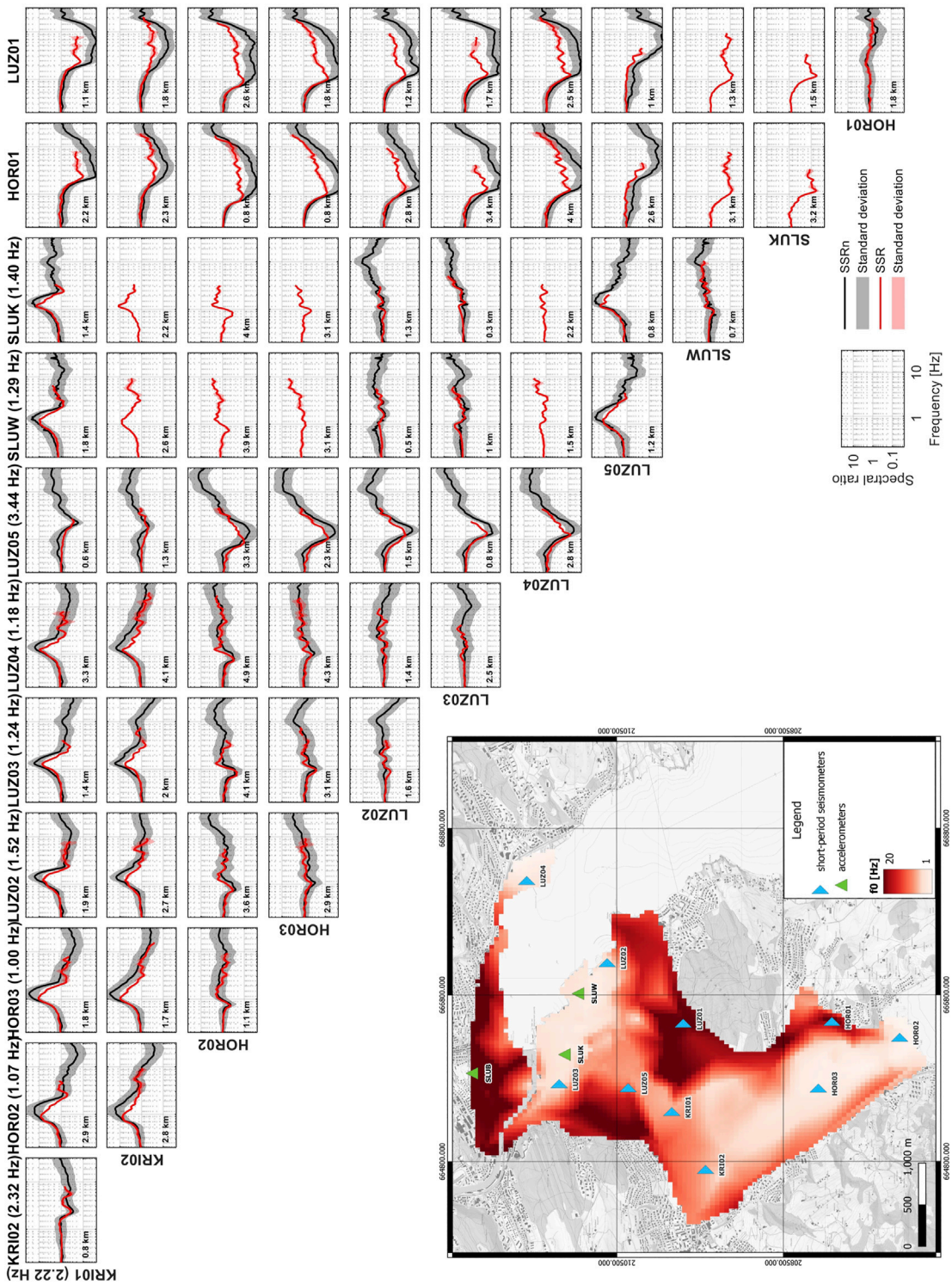

FIGURE 6 | Comparison between SSRn and SSR for all combinations of short-period seismometers. Each column corresponds to one site and each row to one reference station. The distances between sites and f0 values are indicated. In the case of SLUK and SLUW, the short-period seismometers deployed close to the permanent accelerometer were not operating simultaneously with all stations. The map shows the interpolated map of f0; for the rock sites where a peak was indiscernible, the value of 20 Hz was allocated for visualization purposes.

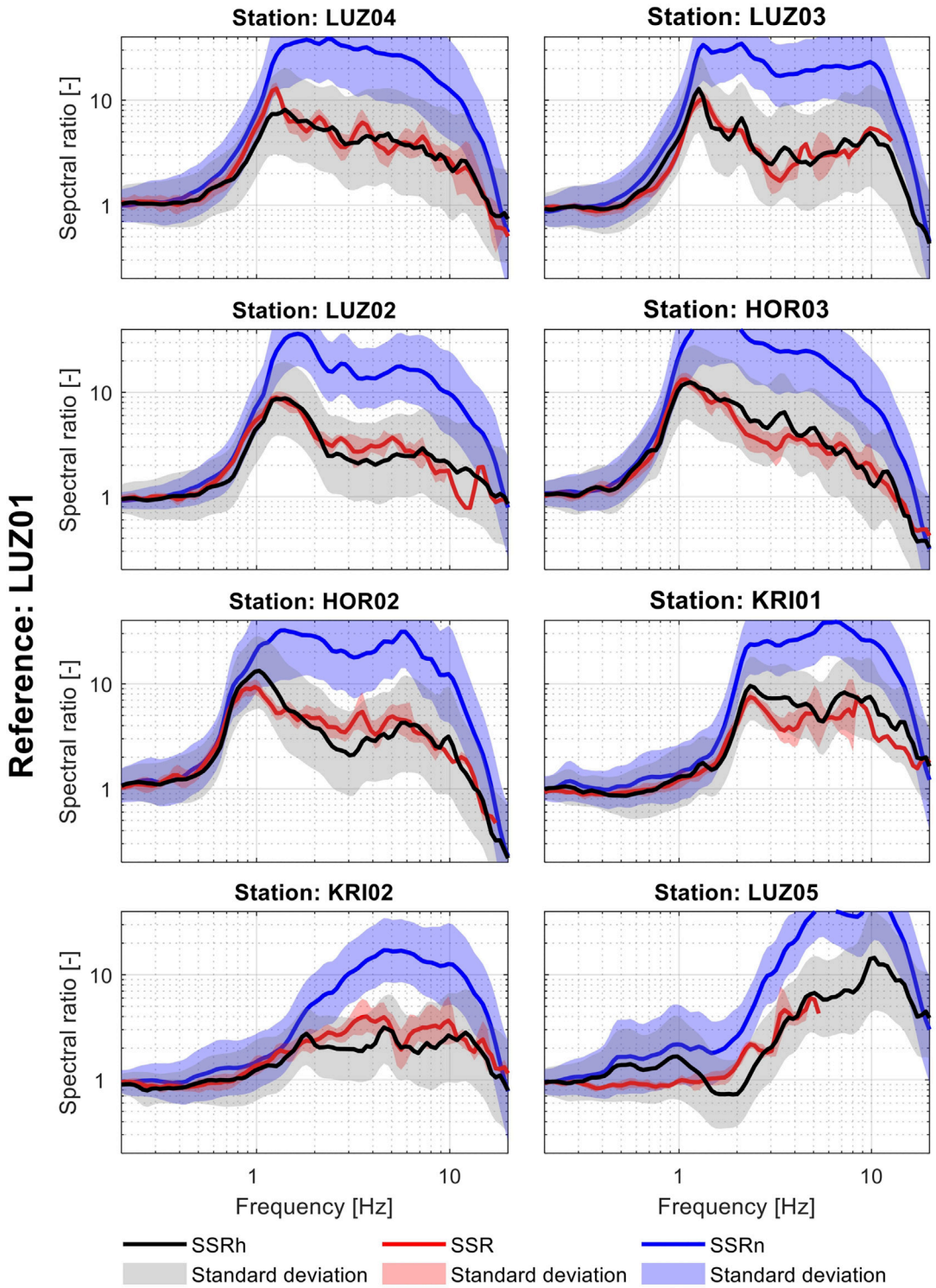

FIGURE 7 | Comparison of the relative amplification functions for sedimentary sites using the SSR, SSRn, and SSRh methods with standard deviation (reference—rock station LUZ01).

intermediate stations because we needed to remove part of our temporary network earlier. For the dataset collected in June 2020, only stations HOR02, HOR03, KRI01, and KRI02 were available; during the campaign in April 2021, we had our disposal stations LUZ02, LUZ03, and LUZ05, as well as SLUK and SLUW. Because the last two are accelerometers, we decided not to directly

compare ambient vibration recorded by accelerometers to short-period seismometers; instead, we deployed short-period seismometers very close for about 24 h to record ambient noise.

Finally, we developed a detailed interpolated amplification map for the Lucerne basin at several frequencies. The model is referenced to either a local rock outcrop reference station or a Swiss reference rock profile (Poggi et al., 2011) by multiplying the values by the ESM amplification function (Edwards et al., 2013) for a local rock station. For measurement points where only ambient vibration data are available, the SSRh functions are used to estimate amplification, while for stations of the temporary and permanent monitoring networks, the SSR used is supplemented by SSRh at higher frequencies if there are not enough earthquake recordings.

The uncertainty of the final amplification model is a combined geometric standard deviation of SSRn and SSR, and ESM amplification functions are as follows:

$$std\,(SSRh) = \exp\left(\sqrt{\log(std\,(SSR))^2 + \log(std\,(SSRn))^2 + \log(std\,(ESM))^2}\right).$$

In the case of using several intermediate stations, the weighted geometric standard deviation of such several realizations is also included.

In addition, for mapping the fundamental frequency of resonance f_0 across the area, we used the HVSR calculated with the RayDec method (Hobiger et al., 2009), which emphasizes the influence of Rayleigh and suppresses the body and Love wave impact, allowing to retrieve the Rayleigh wave ellipticity curve. We utilized all available ambient vibration recordings since 2001, including data from the temporary and permanent stations, for which we chose 4 h randomly from continuous noise records considering only night to decrease the influence of cultural noise. The f_0 values are picked manually at each ambient noise recording point separately using the HVSR curve, but the consistency of the f_0 for neighboring points is verified. Finally, we interpolated the detailed f_0 model for the Lucerne area.

RESULTS AND DISCUSSION

The Rock-Relative Amplification Functions Using Earthquake Data

The SSR and ESM amplification functions are used in this study to adjust the SSRn to the rock condition and to verify that these noise-based amplification functions give similar results as earthquake-based ones. In **Figure 5A**, the SSR amplification functions with respect to the rock station LUZ01 for each station of the temporary and permanent seismic monitoring networks are shown. In the background, the map of the thickness of unconsolidated deposits derived from the bedrock elevation model and provided by the Federal Office of Topography (Swisstopo) is displayed. The comparison indicates a good agreement between the thickness of sediments and the SSR amplification functions, at least regarding the first peak at low frequency. In addition, for LUZ01, the ESM amplification function is plotted (**Figure 5B**). For stations located on thick sedimentary layers (above 50 m thick), the peak amplification is observed at about 0.8–1.2 Hz, and amplification exceeds a factor of 10 (i.e., HOR02, HOR03, LUZ02, LUZ03, LUZ04, SLUK, and SLUW). The high amplification values present a plateau over a broad range of frequencies. Even for stations located closer to the basin edges such as KRI01, KRI02, and LUZ05, site effects are not negligible; above about 2 Hz, the amplification factors reach even 6-fold in the case of KRI01. In addition, we observed two peaks on the amplification functions for stations in the city center (i.e., LUZ03, SLUK, SLUW, and LUZ02) and a broad response with no clear peak for the stations closer to the basin edge (i.e., KRI02, etc.), and this may be due to the complexity of the basin and possible 2D site effects. For the stations located on the rock (SLUB and HOR01), the relative amplification function is close to unity; similarly, the ESM amplification function for LUZ01 shows negligible amplification in the frequency range of 0.5–3 Hz compared to the Swiss reference rock profile.

The standard deviation for the SSR represented by the gray band is relatively small; however, the number of events exceeding the required signal-to-noise ratio (SNR) is low mainly due to the high background noise level and relatively short recording time of the stations (~1 year). The frequency band where many high-quality earthquakes are recorded is very narrow; on average, about 15 earthquakes contribute between 0.6 and 2 Hz. For higher frequencies, the number of events with sufficient SNR decreases rapidly (**Figure 5C**), and so far for some stations (e.g., LUZ05), we have recorded no earthquakes with high enough SNR at higher frequencies. Nevertheless, the frequency of the first and highest peak amplification often coincides with the frequency band with the highest number of contributing events; hence, the highest amplification values can be treated with relatively high confidence. However, to resolve the amplification function better at higher frequencies and to create a more reliable amplification model, more high-quality events are needed; therefore, a longer recording time is required.

The ESM adopts higher standards accepting only very good recordings (SNR>3 on a 10-Hz frequency band minimum) from local earthquakes solely; hence, in low-seismicity areas such as Lucerne, the station should be deployed even longer to reach a good statistical significance. Therefore, we used the ESM amplification functions only for local rock sites in order to refer the amplification model for the Lucerne area to the Swiss reference rock profile. It allows comparing the results between different methods and between different areas in Switzerland. In addition, it enables the calculation of site-specific hazard spectral acceleration maps. However, a high standard deviation of the ESM amplification functions compared to the SSR increases the uncertainty of the final model.

Validity and Performance of the Method

Figure 6 shows a comparison between SSR (in red) and SSRn (in black) for all combinations of short-period seismometers in the Lucerne area. An average SSRn over one week of recording is plotted and in the case of the SLUK and SLUW stations, it is plotted for about 24 h. In the last two columns, at least one of the station pairs is located under rock conditions. The rock-relative SSRn overestimates the amplification as was also observed by other authors (e.g., Field et al., 1990). However, when considering spectral ratios between pairs of stations located on the soil, the

TABLE 1 | RMS between SSR and SSRh calculated using different strategies of weighting intermediate stations. More explanations in the text.

Weight	LUZ04	LUZ03	LUZ02	HOR03	HOR02	KRI01	KRI02	LUZ05
f_0	0.1896	0.1891	0.1869	0.2196	0.2668	0.2132	0.2528	0.3407
Distance	0.2290	0.4065	0.2318	0.3473	0.2531	0.2175	0.2930	0.3487
Distance + selection	0.1844	0.2180	0.2146	0.2204	0.2565	0.2406	0.2128	0.3321

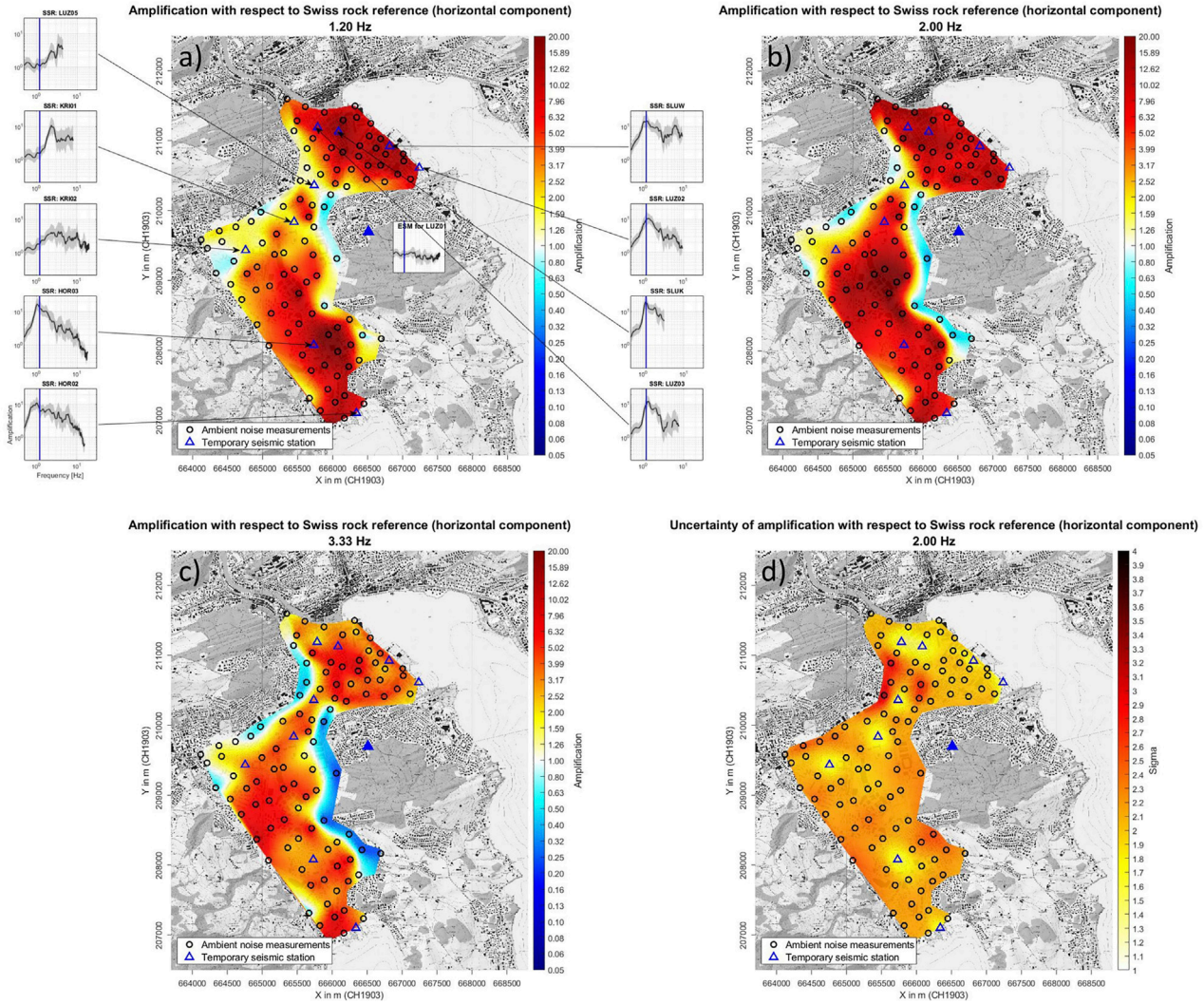

FIGURE 8 | Amplification factors with respect to the Swiss reference rock profile for the Lucerne area for **(A)** 1.2 Hz, **(B)** 2 Hz, and **(C)** 3.33 Hz. Blue triangles are the stations of the seismic monitoring network, and black circles represent ambient vibration measurements. The amplification functions referenced to the Swiss reference rock profile for the stations are shown outside the map **(A)**; blue lines show the value for 1.2 Hz. **(D)** Standard deviation for the amplification map for 2 Hz.

SSRn and SSR fit quite well, and most of the discrepancies are within the SSRn mean ± standard deviation. These observations are also confirmed in **Figure 7**, where the SSR, SSRn, and SSRh are compared for all stations located in the sedimentary basin with respect to the rock station LUZ01; the SSRh curves are calculated as a weighted mean of all intermediate stations with f_0 difference as a weight. As expected, the rock-relative SSRn overestimates the amplification factors for frequencies higher than the frequency of the peak amplitude, while the mean SSRh curves are consistent with the SSR; the discrepancies are observed at higher frequencies and are often within one SSRh standard deviation. Nevertheless, the uncertainty of the SSRh and SSRn methods is much higher than in the case of the earthquake-based approach because of the high variability of the ambient vibration wavefield in time.

The direct comparison between SSR and SSRn for stations inside the sedimentary basin is a straightforward way to assess the

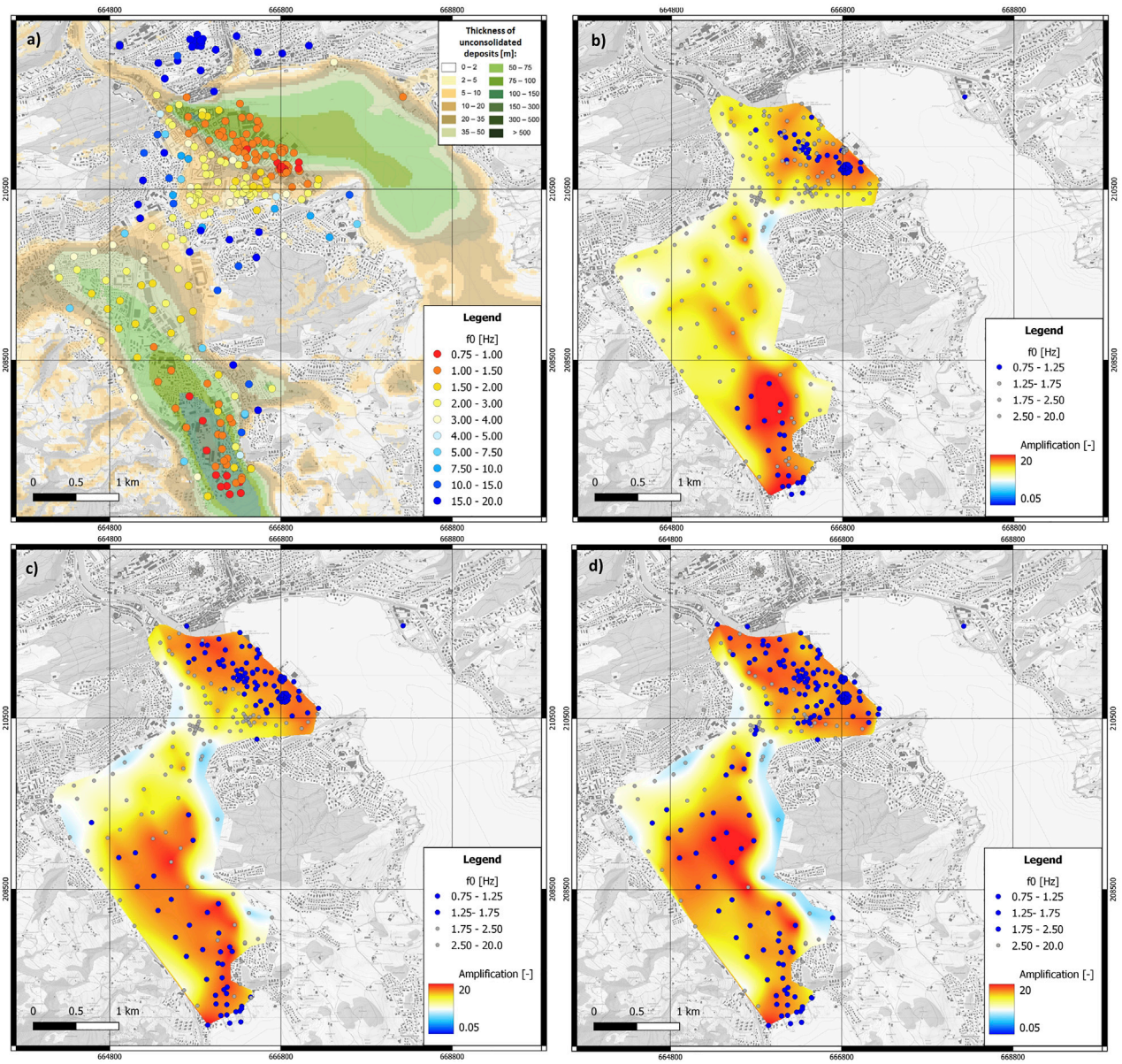

FIGURE 9 | Fundamental resonance frequency f0 for more than 300 points in the Lucerne area compared to **(A)** the map of the thickness of the unconsolidated deposits, **(B–D)** amplification map derived using the SSRh method for 1, 1.5, and 2 Hz, respectively. The reference for amplification maps is the Swiss reference rock profile.

applicability of the SSRh method in a given area. The similarity between curves verifies experimentally that the basin site response can be estimated using a soil-to-soil spectral ratio of ambient vibration. While the noise-based spectral ratios between the sedimentary site and the rock cannot be employed to obtain reliable amplification factors, the SSRn between stations inside the sedimentary basin gives a good estimation of the basin response and can be corrected using SSR to obtain rock-relative amplification. A detailed discussion of the potential reasons for these observations can be found in Perron et al. (2018a). In case the SSR–SSRn comparisons show weak or no correlation for most of the stations, the SSRh method cannot be used in the basin, at least using that specific configuration of intermediate stations. The reasons may be among others, namely, very great distance, very different site conditions, or very much variable ambient vibration wavefields. Nevertheless, experimental evidence of the SSRh reliability was observed in other sites (Perron et al., 2018a; Perron et al., 2022).

In **Figure 6**, we can observe that the agreement between SSRn and SSR varies from one pair of stations to another. Based on the map of the thickness of unconsolidated deposits (**Figure 5A**) and fundamental resonance frequency map (**Figure 6**), the Lucerne basin can be divided into three parts: the northern and southern deep basins characterized by low f_0 and the middle basin with

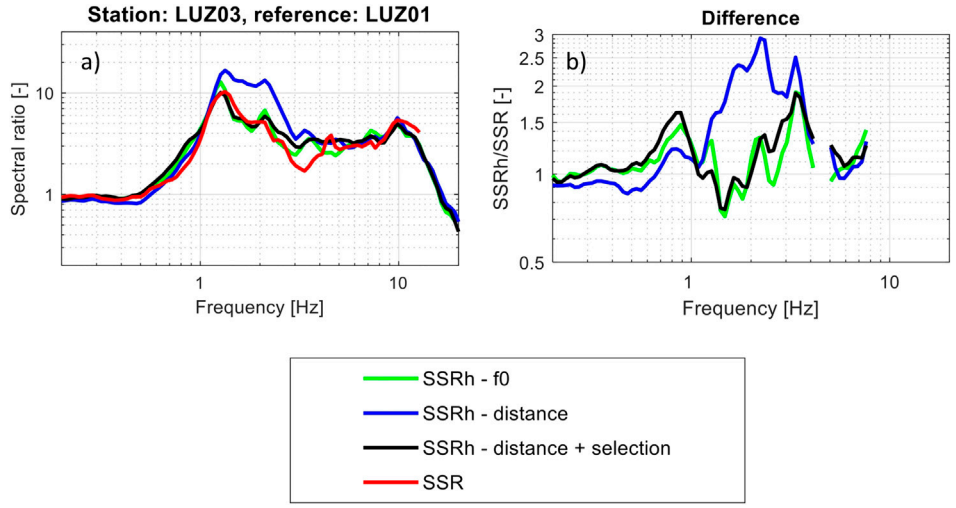

FIGURE 10 | (A) Direct comparison of SSR and SSRh for the station LUZ03 calculated using different strategies considering the intermediate stations. **(B)** Relative difference between SSR and SSRh calculated using different strategies. More explanations in the text.

shallower sediments and higher f_0. The best fit is obtained for nearby stations located in the same part of the basin, for example, the spectral ratio between HOR02 and HOR03 located in the deep southern part or between KRI01 and KRI02 in the shallower basin gives similar SSRn and SSR amplification functions. We observed the flat spectral ratios without significant peaks between these stations indicate that the site response is similar for both of them. All other combinations (e.g., KRI02 and HOR03) where we see an apparent peak show some discrepancy between SSRn and SRR, especially misestimating the amplitude of peak amplification. It may indicate that the sources controlling the noise wavefield are much different in those parts of the basin; hence, the assumptions required to retrieve site effects using SSRn are not valid. Similarly, the SSRn calculated for any pair of the close by group of LUZ02, LUZ03, SLUK, SLUW, and LUZ04 provides a curve that is almost identical to the corresponding SSR function. All are located in the northern part of the Lucerne basin characterized by high sediment thickness and low f_0. However, the stations located in northern and southern deep basins also give good results when combined, even though the distances between them are relatively high. We also observed a flat SSR and SSRn for those pairs. These examples indicate the higher importance of closeness of the site condition and lower significance of the spatial proximity between stations to the maximal extent of our experimental area. A simple indicator of similarity of the site condition is the f_0 value. Nevertheless, in Sion (Perron et al., 2022), no significant difference in the goodness of the fit between different station pairs was noticed; however, the difference of f_0 between most of the stations was also insignificant. Therefore, this effect needs to be investigated for several other case studies to study what is the decisive factor affecting the goodness of the fit between noise- and earthquake-based spectral ratios.

We suspected that with increasing distance, the fit would become worse, even if the site condition remains the same. However, because of the lack of short-period seismometers nearby that are located inside the sedimentary basin, we were not able to investigate the applicability of the method with the increasing distance for the Lucerne area. At this moment, the furthest pair in Lucerne for which good compatibility between SSRn and SSR is observed is 4.9 km apart. In Argostoli (Perron et al., 2018a), the maximum distance was about 1.2 km, while in Sion (Perron et al., 2022) it was more than 13 km.

In addition, when SSRh functions are considered, the best fit is observed (**Figure 7**; **Table 1**) for stations located in the deep northern part of the basin (LUZ02, LUZ03, and LUZ04), while worse for the stations situated in the shallower part of the basin, especially LUZ05 which is characterized by the highest f_0 value. More investigation needs to be carried out; however, these results may indicate that the method performance is the best for sites located on the thick sedimentary layers, decreasing toward the basin margins. In Perron et al. (2022), it was noticed that for stations located at the edges of the Rhône valley, the SSRh method gives poor results, especially at low frequencies. We have recently deployed two new temporary stations in the Lucerne area close to the basin margin in order to test that behavior; however, not enough earthquakes have been recorded so far to derive the empirical amplification functions.

Amplification Map for the Lucerne Area

Because of the promising results using the stations of the seismic monitoring network, we applied the SSRh method for 100 single-station ambient noise measurements that we performed in 2020 and 2021. **Figures 8A–C** show the maps of the amplification factors for three frequencies with respect to the Swiss reference rock profile. Based on the model, we can expect amplification factors of more than 10 at the fundamental frequency (between 0.8 and 1.5 Hz) in the deep parts of the basin (>50 m of sediments). Significant amplifications are also expected for these sites at higher frequencies (up to 5 Hz). Due to the lower number of recorded earthquakes at frequencies higher than 5 Hz, the reliability of the

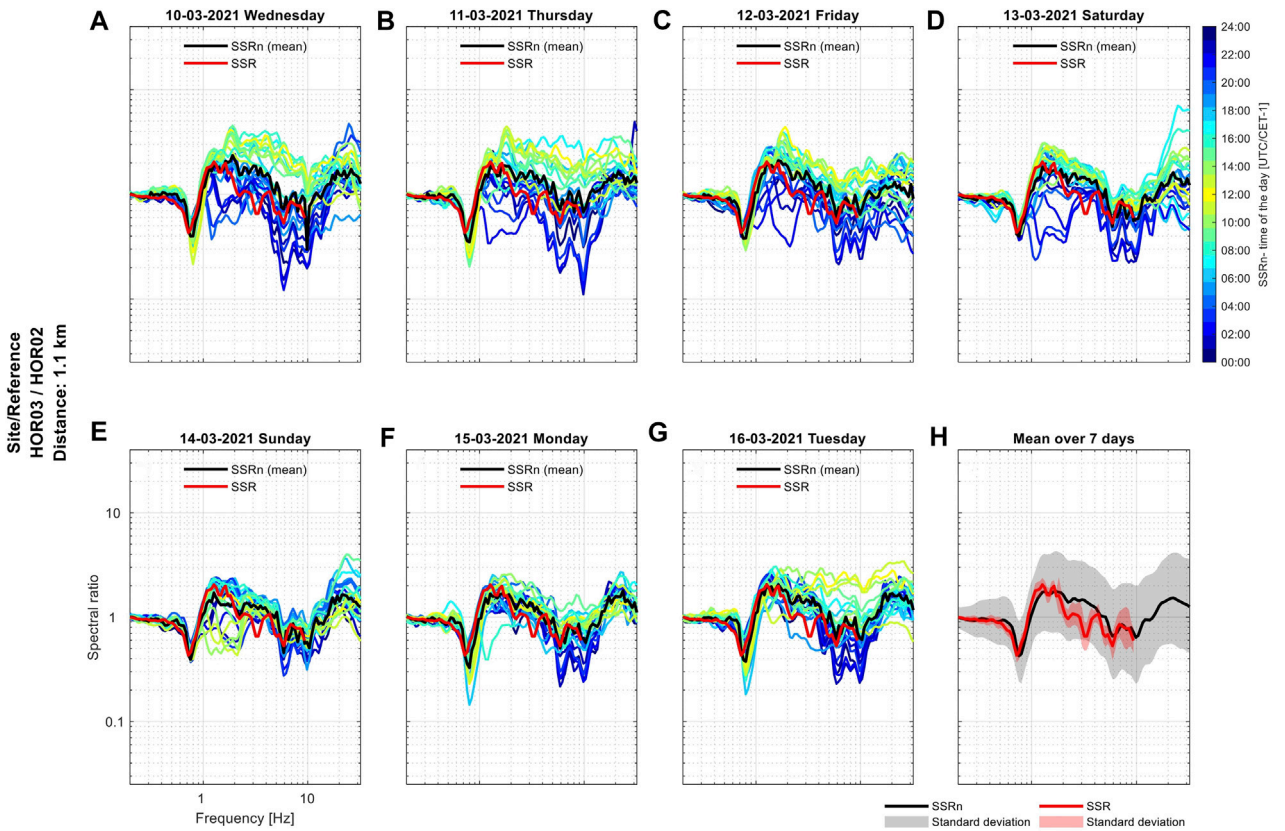

FIGURE 11 | Example of the influence of ambient noise daily variations on SSRn. Each of the plots **(A–G)** corresponds to one day and each line to one hour of recording. The colors indicate the time of the day when noise was recorded. The black line is a mean over 24 h, and the red line is SSR. Plot **(H)** shows the mean SSRn over 7 days with standard deviation compared to the SSR.

model above that frequency is limited. Some amplification is also evident closer to the basin edges where the sediment thickness is lower. The uncertainty of the model that varies depending on the frequency (**Figure 8D**) is relatively high, especially due to the variability of the ambient vibration wavefield and high standard deviation for the ESM amplification functions (**Figure 5B**). The animations showing the amplification and the uncertainty for frequencies between 0.2 and 20 Hz for local reference (LUZ01) and the Swiss reference rock profile can be found in the **Supplementary Materials**. Generally, in the Lucerne area, the lowest uncertainty values are characteristic for frequencies between 1 and 2 Hz that coincide with the range where the highest amplification values are often observed. However, for most of the points, the standard deviation often exceeds 2. For frequencies lower than 1 Hz and higher than 2 Hz, the values are even higher. In a noisy city such as Lucerne, high uncertainty values cannot be significantly reduced because of the variable nature of the recorded noise.

To verify if the obtained model predicts the reliable amplification factors and their spatial variability, a very dense network of stations deployed for several months would be needed. A cost-effective but a less solid approach is to use a few test sites for validation and to compare the model with site response proxies such as f_0 values and other geological information. Although the amplitude of the HVSR curve cannot be used to predict amplification factors directly (e.g., Bonilla et al., 1997; Perron et al., 2018a), the high amplification values are expected at the frequency of the HVSR peak and above (Poggi and Fäh, 2016). We mapped the frequency of the peak of the Rayleigh wave ellipticity function for the Lucerne basin using more than 300 points (**Figure 9A**). In **Figures 9B–D**, the amplification maps from the SSRh method for 1, 1.5, and 2 Hz are shown together with the points, where the f_0 value is similar or lower than the respective frequency. To account for the uncertainty, the broader ranges are adopted, for example, for an amplification map for 1 Hz; the points where f_0 is between 0.75 and 1.25 are highlighted. We can observe a good correlation for all shown frequencies, especially in the southern part of the basin, indicating that our model is consistent with f_0, which is one of the important site response proxies. The f_0 values as shown in **Figure 9A** are in good agreement with the thickness of unconsolidated deposits derived from gravity measurements. This indicates that f_0 is mainly controlled by that parameter, confirming that our amplification model is also consistent with the thickness of sediments. In the northern part of the basin, the observed agreement between the SSRh amplification, f_0, and the sediment thickness is still clearly visible but less distinctly. The reason is probably the dominance of the artificial fillings (**Figure 2B**) that increases the variability of the site response and due to higher density of the infrastructure in the city center affecting the ambient noise wavefield. In the future, we would

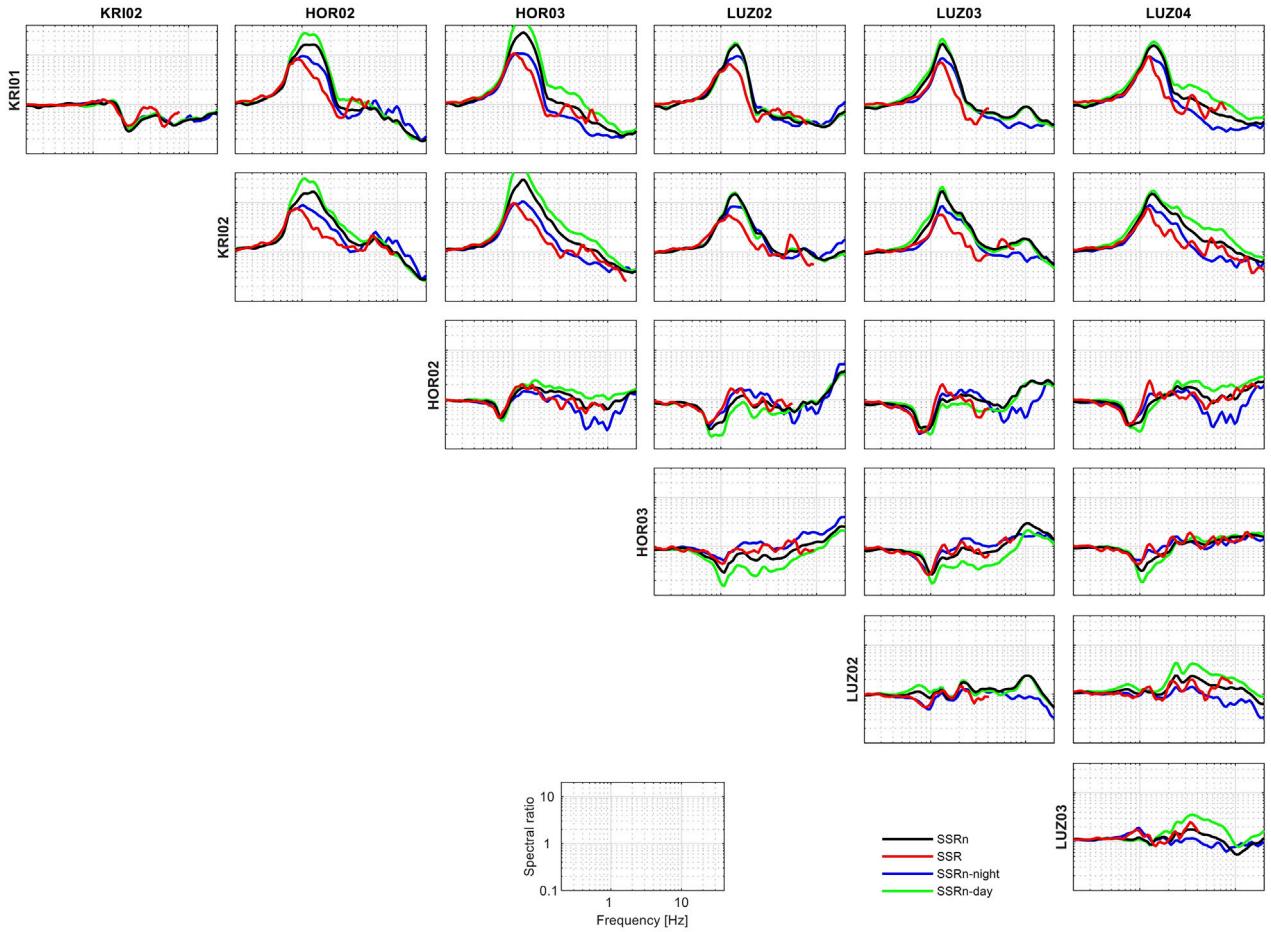

FIGURE 12 | Comparison between SSR and SSRn for all combinations of stations located inside the sedimentary basin. The SSRn is a mean over 7 days, respectively, considering the whole day (black), the night between 00:00–3:00 UTC (blue), and the day between 08:00–11:00 UTC (green).

also apply other methods such as canonical correlations (Panzera et al., 2021) or simulations of wave propagation using numerical modeling that may help us to validate the model.

On the Choice of the Intermediate Stations and the Weighting Process

In the SSRh method, the intermediate stations located in the basin are used in order to estimate the rock-relative amplification function for each site. In case more than one station can serve as an intermediate station, adequate decisions should be made. Generally, two main scenarios exist, either one intermediate station can be chosen for each site or an average of several realizations using different intermediate stations can be calculated. In both approaches, a subjective decision needs to be made concerning the spatial extent where usage of a specific intermediate station is justifiable. In our study, we decided to calculate the weighted mean of many realizations in order to avoid too many subjective decisions. Analyzing the comparison between SSR and SSRn (**Figure 6**) can provide some hints if the area has to be divided into zones according to the usability of the intermediate stations.

First, we tested the inverse of square distance weight that emphasizes the influence of nearby stations. On the one hand, the basis of the SSRn is an assumption that is similar to the earthquake data, and we can retrieve the site effect component by assuming that source and path terms for both stations are the same. Hence, the emphasis on proximity and yet similarity of the wavefield seems to be a valid choice. However, as we showed, good results are obtained by also using stations located further away but similar in terms of the site condition. Therefore, another tested option was the inverse of squared difference of f_0 values to indicate the similarity of the site condition. The RMS between SSR and SSRh for different approaches is shown for each station (**Table 1**). For many stations, the approach based on f_0 seems to give better results (**Figure 10**); for some stations, no significant difference between both methods was noticed (**Table 1**). However, often, the highest differences are concentrated in the frequency band with the highest amplification values (**Figure 10**), indicating that this effect should not be neglected. However, if we divide intermediate stations into two regions (i.e., the deep basin and the shallow basin) and use the distance as a weight, the results for many stations improve significantly, giving similar results as

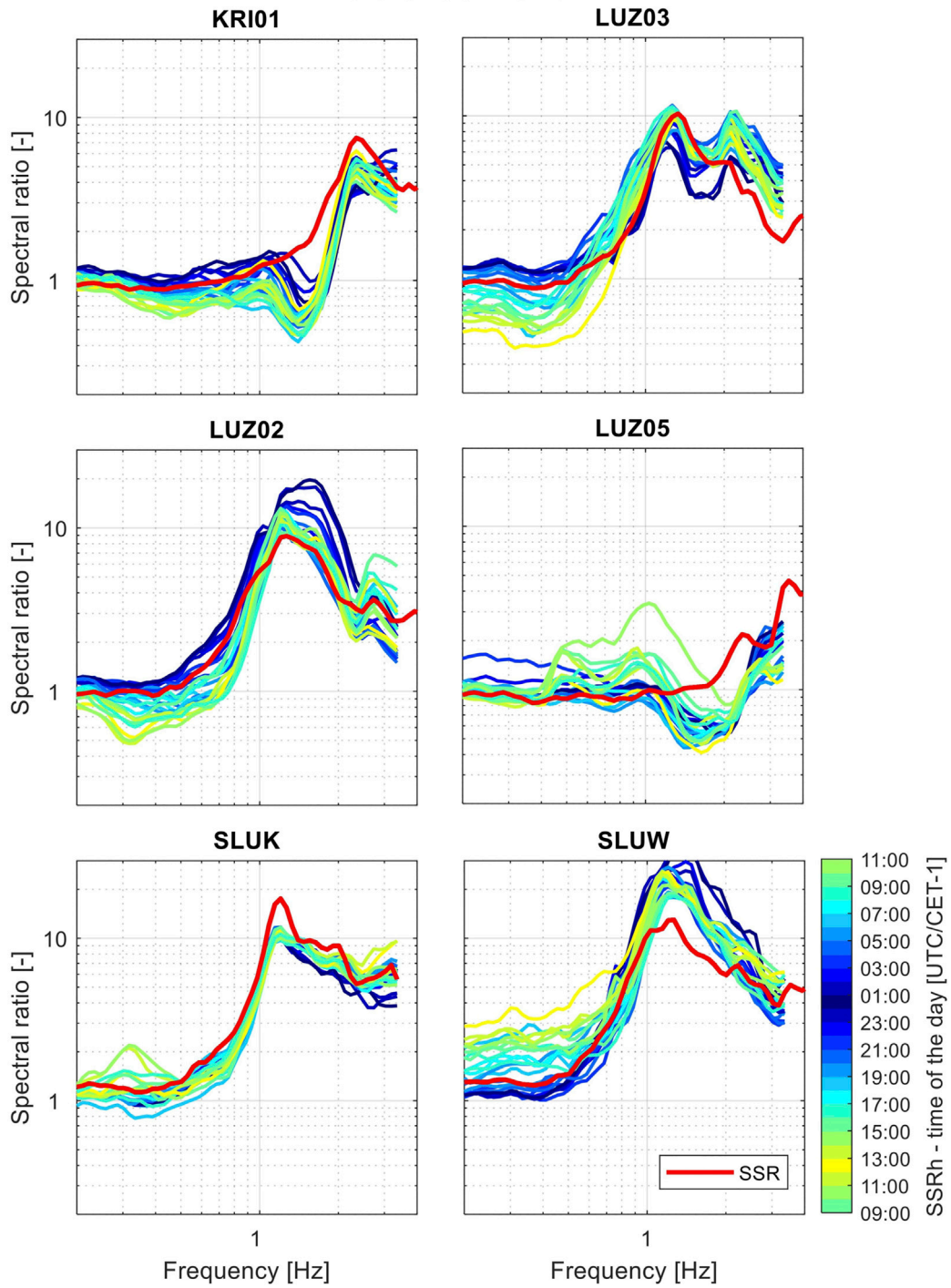

FIGURE 13 | Variability of the SSRh results between all stations that recorded for at least 24 h in the period 8-9.04.2021.

using f_0 weighting (**Table 1**). We also compared several other possible weights (e.g., logarithmic difference of f_0, inverse vs. inversed square of distance); however, no significant improvements were noticed.

In the case of Lucerne, the weighting using f_0 difference and careful selection of stations and then usage of distance as a weight give similar results. However, we assumed that the former is a more objective scheme allowing to use all possible stations as

intermediate stations as long as the HVSRs are similar, indicating the similarity of profiles. However, an initial test including several stations with earthquake-derived amplification function is strongly recommended to verify the validity of the results. The validity of the SSRh approach should therefore be tested in areas of interest before being applied. For instance, in the area of Sion (Perron et al., 2022), calculating the median value of different intermediate stations appeared to be the optimal choice. Nevertheless, based on our findings, we recommend planning the deployment of a temporary network having in mind the influence of both the distance and site conditions and trying to cover different sites to sample the basin's site response variability.

Influence of Ambient Vibration Daily Variation

The amplitude of ambient vibration recordings shows systematic cyclic variations due to the changing intensity of human activities (Bonnefoy-Claudet et al., 2006). We investigated the influence of that variability on the performance of the SSRh method. In **Figures 11A–G**, the SSRn function for seven consecutive days is compared to SSR, where each line corresponds to one hour of the noise recording with colors indicating the time. The mean SSRn over 7 days (**Figure 11H**) is comparable to the SSR, while if we consider short 1-h recordings, large variability is observed, especially during weekdays where the clear separation between daily and nightly recordings is visible. In addition, **Figure 12** shows the comparison between SSRn calculated using only nightly and daily recordings for all station combinations. The main reason is a changing intensity of the noise wavefield, which is not proportional for all the stations. The observed variability differs between different station pairs and usually increases with distance but not necessarily, the presented example is a pair situated close to each other; however, the variability is still relatively high. One of the conclusions is that 1-h recordings are too short to sample the variability of the ambient noise wavefield; the mean over a longer period is needed to obtain reliable results. For the majority of the pairs, the 24 h average is quite stable (as in **Figures 11A–G**) with slightly better results obtained during weekends or during nights (**Figure 12**) because of the lower influence of close human-generated transient noise sources. However, if we consider station pairs located under similar geological conditions, the difference between night and day recordings is slight (**Figure 12**), and in many cases, it is the mean over the whole day that has the best fit, while for other combinations (e.g., HOR/KRI) using night recordings improve significantly the correlation with the SSR curve.

While for permanent or semi-permanent stations that are recording continuously, daily variations are not a significant issue because a mean over a long time can always be computed or only night hours can be considered, the ambient vibration measurements are often performed during busy weekday hours. In addition, when a limited number of stations are available, a compromise between the recording time and a number of points needs to be made. Of course, the best strategy is to use hundreds of stations and to measure for at least 24 h at each site, which allows calculating the relatively stable mean. Such dense measurement campaigns become more and more feasible with the development of low-cost and portable instruments such as the seismic nodes. An alternative approach is to use a temporary network first to assess the significance of the variability due to the daily changes of noise intensity and to plan the measurement campaign accordingly, for instance, by avoiding recording during specific days or hours at given sites. Another option is to limit the usage of some intermediate stations to small, restricted areas assuming the noise wavefield intensity changes similarly in the proximity.

In the case of the data that we collected during measurement campaigns in June 2020 and April 2021, we could not verify how strong the influence of the ambient vibration's daily variation is; however, most of the data were collected during weekdays and day hours. The recordings are often only 1–2 h long because of the time constraints and a small number of available instruments. **Figure 13** shows the variability of the SSRh functions during the measurements in 2021 for sites where we have at least 24 h of recordings. We observed some dispersion of the results, mostly at low frequencies; however, the variability is not very significant compared to the ambient vibration observations which were made using the temporary network on different days (e.g., **Figure 11**). It allows us to assume that single 1–2 h of recordings that we collected are enough to create a relatively reliable amplification model. However, we identified some points for which the amplification using the SSRh method seems specifically suspicious (e.g., too high compared to the neighboring points or characterized by a strange shape at low frequencies), which may be due to the disturbances by strong artificial noise sources.

CONCLUSIONS AND OUTLOOK

Empirical site-to-reference methods using earthquake observations are commonly used to estimate the site response. However, in low-seismicity urban areas, the effective application of such methods is limited due to the scarcity of earthquake recordings. Seismic stations have to be deployed for a considerable time in order to record a significant number of high-quality earthquake ground motions. On the other hand, ambient noise measurements are easy to perform and are cheaper than the deployment of the monitoring network. They allow achieving higher spatial resolution; however, it was shown by many authors that the amplification factors derived using ambient noise are overestimated when referred to rock sites. In this study, we tested the SSRh method that combines earthquakes and ambient noise recordings in order to estimate the variability of amplification factors with high spatial resolution. The SSRh technique allows avoiding the limitations of the sole earthquake or noise-based approaches. First of all, the amplification factors estimated using the SSRh approach show good agreement with the classical SSR at the tested sites. In addition, the detailed amplification maps produced for the Lucerne area show consistency with tested site response proxies (i.e., f_0 and thickness of the unconsolidated deposits). Second, a dense long-term monitoring network is not necessary to map the amplification with high spatial resolution and for a broad range of frequencies. The minimum strategy is to deploy only two stations—one on the rock and one in the basin; however, installation of more instruments is strongly recommended,

especially for the initial testing phase in particular when soil characteristics in the area show strong variability. On the other hand, one of the disadvantages has relatively high uncertainty compared to the SSR due to the daily variability of the ambient vibration wavefield.

The validity of the SSRh approach is probably very site-specific. Therefore, we recommend before applying the technique to test its performance by comparing it with the SSR and verifying the influence of different factors on a small seismic monitoring network, which is deployed in a way to sample different site conditions and regions characterized by different ambient noise intensities. Nevertheless, based on our observation in the Lucerne area, we conclude that concerning the performance of the SSRh method, the distance between stations is not as important as the similarity of the site condition, at least to the maximum extent of the seismic stations in the Lucerne area. In addition, in case the SSRh function for a given site can be derived using different intermediate stations, the most optimal approach for the Lucerne area was to calculate a weighted mean of many realizations with weights indicating the similarity of the site condition (e.g., using f_0 value). Last but not least, while the amplification functions estimated using 24 h of ambient noise recording seem to be robust, the results using shorter recordings may show some variability. Generally, more reliable outcomes are obtained during times of lower human activity; however, the improvement is significant only in some cases. Our recommendation is to use longer ambient noise recordings, preferably 24 h, and/or to plan the measurement campaign accordingly to minimize the influence of changing the intensity of the ambient noise wavefield.

We showed experimentally that the SSRh method provides comparable results as the empirical approaches based on analyzing earthquakes' ground motion at several sites. Nevertheless, a better theoretical understanding needs to be provided, preferably confirmed by numerical simulations. Even though the derived amplification maps are consistent with geological data and some site response proxies (i.e., f_0), it has to be verified if the method allows to correctly estimate the variability of the basin response either experimentally or by using other indirect methods. We installed two new seismic monitoring stations in the Lucerne area to check if the SSRh techniques correctly predict the amplification close to the basin margins. Moreover, in November 2021, we repeated the installation of the seismic monitoring network in order to assess more reliable earthquake-base amplification factors in the area; hence, the presented model will be consequently updated.

The results for the Lucerne area indicate high amplification factors reaching or exceeding 10 for the peak frequency (1–1.5 Hz) in some parts of the basin; significant amplification is also predicted for higher frequencies and in shallower parts. Such results indicate the seismic hazard is considerably increased in the Lucerne area. Hence, we will further investigate the city of Lucerne and its surroundings using other empirical and numerical methods and perform a detailed site response analysis considering the non-linear soil behavior in order to assess the seismic hazard and risk in the area more specifically.

DATA AVAILABILITY STATEMENT

The datasets presented in this article are not readily available because the data of the stations of the temporary network (doi.org/10.12686/sed/networks/xy) will be made publicly available at the end of the project. The data of short-term ambient vibration measurements are available on request after the end of the project (doi.org/10.12686/sed-stationcharacterizationdb). Requests to access the datasets should be directed to paulina.janusz@sed.ethz.ch.

AUTHOR CONTRIBUTIONS

PJ—first authorship, the main contributor. VP—co-supervisor of the project and contributor in the field and for data processing. CK—local government representative and contributor in the field. DF—main supervisor of the project, funding provider and project manager.

FUNDING

This PhD project is performed in the framework of the URBASIS-EU project–New challenges for Urban Engineering Seismology (grant agreement no 813137) funded by the European Union's Horizon 2020 ITN program, which focuses on the seismic hazard and risk in urban areas.

ACKNOWLEDGMENTS

The study is also a part of the "Earthquake Risk Model for Switzerland" (ERM-CH) project conducted at the Swiss Seismological Service (SED). We would not be able to install our temporary monitoring network and perform measurements if not for the permission and support of local authorities (Kanton Luzern, Stadt Luzern, Gemeinde Horw) and several institutions in Lucerne (Verkehrshaus der Schweiz, Pfarrei St. Paul, Kantonsschule Alpenquai, and Armee-Ausbildungszentrum Luzern), Horw (Schulhaus Biregg, Friedhof Horw, and Seefeld Horw), and Kriens (Pfarrei Bruder Klaus). We would also like to acknowledge and Zimmermann, and Faesi, Franziska Vercueil, Rafał Lupa, Erich Wigger, Paul Studhalter, Philippe Ehrler, Toni Amstutz, and Hans Kauffmann for their cooperation and help with planning, installations, and maintenance of the network. We also acknowledge Pascal Graf, Dario Chieppa, Miroslav Hallo, Agostiny Lontsi, Carla Schöb, Nora Schweizer, and Manuel Studer for their help during the fieldwork. We would like also to thank the reviewers and editors for their help in improving this article.

SUPPLEMENTARY MATERIAL

The Supplementary Material for this article can be found online at: https://www.frontiersin.org/articles/10.3389/feart.2022.885724/full#supplementary-material

Supplementary Video S1 | Amplification factors with respect to the rock station LUZ01 derived using the SSRh method for the Lucerne area for the frequency range between 0.2 and 20 Hz. The amplification functions for stations of the temporary network are shown outside the map.

Supplementary Video S2 | Amplification factors with respect to the Swiss reference rock profile derived using the SSRh method for the Lucerne area for the frequency range between 0.5 and 20 Hz. The amplification functions for stations of the temporary network are shown outside the map.

Supplementary Video S3 | Standard deviation for the amplification factors with respect to the rock station LUZ01.

Supplementary Video S4 | Standard deviation for the amplification factors with respect to the Swiss reference rock profile.

REFERENCES

Andrews, D. J. (1986). "Objective Determination of Source Parameters and Similarity of Earthquakes of Different Size," in *Earthquake Source Mechanics*. Editors S. Das, J. Boatwright, and C. H. Scholz (American Geophysical Union AGU), 37, 259–267. doi:10.1029/GM037p0259

Bard, P.-Y. (1997). "Local Effects of strong Ground Motion: Basic Physical Phenomena and Estimation Methods for Microzoning Studies," in *SERINA—Seismic Risk: An Integrated Seismological, Geotechnical and Structural Approach* (Thessaloniki, Greece: Thessaloniki, Greece, publisher - Institute of Engineering Seismology and Earthquake Engineering (ITSAK), Ministry of Environment and Public Works), 229–299.

Beyreuther, M., Barsch, R., Krischer, L., Megies, T., Behr, Y., and Wassermann, J. (2010). ObsPy: A Python Toolbox for Seismology. *Seismological Res. Lett.* 81 (3), 530–533. doi:10.1785/gssrl.81.3.530

Bindi, D., Parolai, S., Cara, F., Di Giulio, G., Ferretti, G., Luzi, L., et al. (2009). Site Amplifications Observed in the Gubbio Basin, Central Italy: Hints for Lateral Propagation Effects. *Bull. Seismological Soc. America* 99 (2A), 741–760. doi:10.1785/0120080238

Bonilla, L. F., Steidl, J. H., Lindley, G. T., Tumarkin, A. G., and Archuleta, R. J. (1997). Site Amplification in the San Fernando Valley, California: Variability of Site-Effect Estimation Using the S-Wave, Coda, and H/V Methods. *Bull. Seismological Soc. America* 87 (3), 710–730. doi:10.1785/bssa0870030710

Bonnefoy-Claudet, S., Cotton, F., and Bard, P.-Y. (2006). The Nature of Noise Wavefield and its Applications for Site Effects Studies. *Earth-Science Rev.* 79 (3), 205–227. doi:10.1016/j.earscirev.2006.07.004

Borcherdt, R. D. (1970). Effects of Local Geology on Ground Motion Near San Francisco Bay. *Bull. Seismological Soc. America* 60 (1), 29–61.

EC8 (2004). *Design of Structures for Earthquake Resistance*. Brussels, Belgium: European Committee for Standardization CEN.

Edwards, B., Michel, C., Poggi, V., and Fäh, D. (2013). Determination of Site Amplification from Regional Seismicity: Application to the Swiss National Seismic Networks. *Seismological Res. Lett.* 84, 611–621. doi:10.1785/0220120176

Fäh, D., Giardini, D., Kästli, P., Deichmann, N., Gisler, M., Schwarz-Zanetti, G., et al. (2011). *ECOS-09 Earthquake Catalogue of Switzerland Release*. Zürich, Switzerland: Swiss Seismological Service ETH Zürich.

Fäh, D., Kind, F., and Giardini, D. (2001). A Theoretical Investigation of averageH/Vratios. *Geophys. J. Int.* 145 (2), 535–549. doi:10.1046/j.0956-540x.2001.01406.x

Field, E. H. (1996). Spectral Amplification in a Sediment-Filled Valley Exhibiting clear basin-edge-induced Waves. *Bull. Seismological Soc. America* 86 (4), 991–1005. doi:10.1785/BSSA0860040991

Field, E. H., Hough, S., and Jacob, K. H. (1990). Using Microtremors to Assess Potential Earthquake Site Response: A Case Study in Flushing Meadows, New York City. *Bull. - Seismological Soc. America* 80, 1456–1480. doi:10.1785/BSSA08006A1456

Gisler, M., Fäh, D., and Kästli, P. (2004). Historical Seismicity in Central Switzerland. *Eclogae Geol. Helv.* 97 (2), 221–236. doi:10.1007/s00015-004-1128-3

Hobiger, M., Bard, P.-Y., Cornou, C., and Le Bihan, N. (2009). Single Station Determination of Rayleigh Wave Ellipticity by Using the Random Decrement Technique (RayDec). *Geophys. Res. Lett.* 36, L14303. doi:10.1029/2009GL038863

Hobiger, M., Bergamo, P., Imperatori, W., Panzera, F., Marrios Lontsi, A., Perron, V., et al. (2021). Site Characterization of Swiss Strong-Motion Stations: The Benefit of Advanced Processing Algorithms. *Bull. Seismological Soc. America* 111 (4), 1713–1739. doi:10.1785/0120200316

Kagami, H., Duke, C. M., Liang, G. C., and Ohta, Y. (1982). Observation of 1- to 5-second Microtremors and Their Application to Earthquake Engineering. Part II. Evaluation of Site Effect upon Seismic Wave Amplification Due to Extremely Deep Soil Deposits. *Bull. Seismological Soc. America* 72 (3), 987–998. doi:10.1785/BSSA0720030987

Keller + Lorenz, A. G. (2010). *Baugrund-Hinweiskarte, Blatt 1150 Luzern*. Lucerne, Switzerland: Keller + Lorenz AG.

Konno, K., and Ohmachi, T. (1998). Ground-motion Characteristics Estimated from Spectral Ratio between Horizontal and Vertical Components of Microtremor. *Bull. Seismological Soc. America* 88 (1), 228–241. doi:10.1785/BSSA0880010228

Lermo, J., and Chavez-Garcia, J. (1994). Are Microtremors Useful in Site Response Evaluation? *Bull. Seismological Soc. America* 84, 1350–1364. doi:10.1785/BSSA0840051350

Michel, C., Edwards, B., Poggi, V., Burjánek, J., Roten, D., Cauzzi, C., et al. (2014). Assessment of Site Effects in Alpine Regions through Systematic Site Characterization of Seismic Stations. *Bull. Seismological Soc. America* 104 (6), 2809–2826. doi:10.1785/0120140097

Nakamura, Y. (1989). A Method for Dynamic Characteristics Estimation of Subsurface Using Microtremor on the Ground Surface. *Railway Tech. Res. Inst. Q. Rep.* 30 (1), 25–33.

Nogoshi, M., and Igarashi, T. (1971). On the Amplitude Characteristics of Microtremor (Part 2). *Jssj* 24 (1), 26–40. doi:10.4294/zisin1948.24.1_26

Panzera, F., Bergamo, P., and Fäh, D. (2021). Canonical Correlation Analysis Based on Site-Response Proxies to Predict Site-specific Amplification Functions in Switzerland. *Bull. Seismological Soc. America.* 111, 1905–1920. doi:10.1785/0120200326

Perron, V., Bergamo, P., and Fäh, D. (2022). Site Amplification at High Spatial Resolution from Combined Ambient Noise and Earthquake Recordings in Sion, Switzerland. *Seism. Res. Let.*

Perron, V., Gélis, C., Froment, B., Hollender, F., Bard, P.-Y., Cultrera, G., et al. (2018a). Can Broad-Band Earthquake Site Responses Be Predicted by the Ambient Noise Spectral Ratio? Insight from Observations at Two Sedimentary Basins. *Geophys. J. Int.* 215 (2), 1442–1454. doi:10.1093/gji/ggy355

Perron, V., Laurendeau, A., Hollender, F., Bard, P.-Y., Gélis, C., Traversa, P., et al. (2018b). Selecting Time Windows of Seismic Phases and Noise for Engineering Seismology Applications: A Versatile Methodology and Algorithm. *Bull. Earthquake Eng.* 16 (6), 2211–2225. doi:10.1007/s10518-017-0131-9

Poggi, V., Edwards, B., and Fäh, D. (2011). Derivation of a Reference Shear-Wave Velocity Model from Empirical Site Amplification. *Bull. Seismological Soc. America* 101 (1), 258–274. doi:10.1785/0120100060

Poggi, V., Fäh, D., Burjanek, J., and Giardini, D. (2012). The Use of Rayleigh-Wave Ellipticity for Site-specific hazard Assessment and Microzonation: Application to the City of Lucerne, Switzerland. *Geophys. J. Int.* 188 (3), 1154–1172. doi:10.1111/j.1365-246X.2011.05305.x

Poggi, V., and Fäh, D. (2016). Guidelines and Strategies for Seismic Microzonation in Switzerland [Report]. *SED/ETH Zurich*. doi:10.3929/ethz-a-010735479

Schnellmann, M., Anselmetti, F., Giardini, D., McKenzie, J., and Ward, S. (2004). Ancient Earthquakes at Lake Lucerne. *Amer. Scientist* 92, 46. doi:10.1511/2004.1.46

Schwarz-Zanetti, G., Deichmann, N., Fäh, D., Giardini, D., Jiménez, M., Masciadri, V., et al. (2003). The Earthquake in Unterwalden on September 18, 1601: A Historico-Critical Macroseismic Evaluation. *Eclogae Geol. Helv.* 96, 3. doi:10.5169/seals-169031

SIA (2020). *Actions on Structures, SIA 261. Swiss Standards*. Zürich, Switzerland: Swiss Society of Engineers and Architects.

Yamanaka, H., Dravinski, M., and Kagami, H. (1993). Continuous Measurements of Microtremors on Sediments and Basement in Los Angeles, California. *Bull. Seismological Soc. America* 83 (5), 1595–1609. doi:10.1785/BSSA0830051595

Conflict of Interest: The authors declare that the research was conducted in the absence of any commercial or financial relationships that could be construed as a potential conflict of interest.

Publisher's Note: All claims expressed in this article are solely those of the authors and do not necessarily represent those of their affiliated organizations, or those of the publisher, the editors, and the reviewers. Any product that may be evaluated in this article, or claim that may be made by its manufacturer, is not guaranteed or endorsed by the publisher.

frontiers | Frontiers in Earth Science

ORIGINAL RESEARCH
published: 13 June 2022
doi: 10.3389/feart.2022.886606

Testing Site Amplification Curves in Hybrid Broadband Ground Motion Simulations of M6.0, 24 August 2016 Amatrice Earthquake, Italy

Marta Pischiutta[1], Aybige Akinci[1], Chiara Felicetta[2], Francesca Pacor[2] and Paola Morasca[2]*

[1]Istituto Nazionale di Geofisica e Vulcanologia, Rome, Italy, [2]Istituto Nazionale di Geofisica e Vulcanologia, Milano, Italy

This research focuses on predicting and assessing earthquake impact due to future scenarios regarding the ground motion seismic hazard by accounting mainly for site effect in the Central Apennines. To this end, we produced synthetic broadband seismograms by adopting a hybrid simulation technique for the M_w6.0 Amatrice earthquake, Central Italy, on 24 August 2016, accounting for site conditions by means of amplification curves, computed with different approaches. Simulations were validated by comparing with data recorded at 57 strong-motion stations, the majority installed in urban areas. This station sample was selected among stations recording the Amatrice earthquake within an epicentral distance of 150 km and potentially prone to experience site amplification effects because of lying in particular site conditions (sedimentary basins, topographic irregularities, and fault zones). The evaluation of amplification curves best suited to describe local effects is of great importance because many towns and villages in central Italy are built in very different geomorphological conditions, from valleys and sedimentary basins to topographies. In order to well reproduce observed ground motions, we accounted for the site amplification effect by testing various generic and empirical amplification curves such as horizontal-to-vertical spectral ratios (calculated from Fourier spectra using both earthquake, HVSR, and ambient noise, HVNSR, recordings) and those derived from the generalized inversion technique (GIT). The site amplifications emanated from GIT improve the match between observed and simulated data, especially in the case of stations installed in sedimentary basins, where the empirical amplification curve effectively reproduces spectral peaks. On the contrary, the worst performances are for the spectral ratios between components, even compared to the generic site amplification, although the latter ignores the strong bedrock/soil seismic impedance contrasts. At sites on topography, we did not observe any systematic behavior, the use of empirical curves ameliorating the fit only in a small percentage of cases. These results may provide a valuable framework for developing ground motion models for earthquake seismic hazard assessment and risk mitigation, especially in urban areas located in the seismically active central Italy region.

Keywords: site amplification effects, Amatrice earthquake, central Italy, ground motion simulations, horizontal-to-vertical spectral ratio (HVSR), generalized inversion technique (GIT)

OPEN ACCESS

Edited by:
Nicola Alessandro Pino, National Institute of Geophysics and Volcanology (INGV), Italy

Reviewed by:
Chuanbin Zhu, GFZ German Research Centre for Geosciences, Germany
Yefei Ren, China Earthquake Administration, China

****Correspondence:***
Marta Pischiutta
marta.pischiutta@ingv.it

Specialty section:
This article was submitted to Solid Earth Geophysics, a section of the journal Frontiers in Earth Science

Received: *28 February 2022*
Accepted: *26 April 2022*
Published: *13 June 2022*

Citation:
Pischiutta M, Akinci A, Felicetta C, Pacor F and Morasca P (2022) Testing Site Amplification Curves in Hybrid Broadband Ground Motion Simulations of M6.0, 24 August 2016 Amatrice Earthquake, Italy. Front. Earth Sci. 10:886606. doi: 10.3389/feart.2022.886606

1 INTRODUCTION

On 24 August 2016, at 03:36 local time, an Mw 6.0 earthquake with a shallow focal depth (8.0 km) occurred close to the Accumoli village and Amarice town in Central Apennines. This event triggered an extended sequence with five Mw ≥ 5 earthquakes, including a strong shock Mw6.5 on 30 October 2016. The first shock caused heavy damage in several villages, mainly in Accumoli, Amatrice, and Arquata del Tronto, with X to XI MCS intensity values (Galli et al., 2016a; Galli et al., 2016b; Quest, 2016; Zanini et al., 2016), and several ancient building collapsed due to the vicinity of the causative fault and the high vulnerability. During the 2016 Central Italy seismic sequence in various municipalities and hamlets, the damage patterns indicated strong evidence of local site effects (Sextos et al., 2018), mainly related to stratigraphic and topographic effects.

It is fundamental to know the features of the ground shaking during an earthquake to support the interventions and actions both in the emergency and the reconstruction phases. For example, shake maps (Wald et al., 1999; Michelini et al., 2008; Licia Faenza et al., 2016), generated in a quasi-real-time, interpolating observed and predicted data represent the distribution of ground-motion parameters following an earthquake. Generating these maps for future events from a given seismic source's selected locations, magnitudes, and rupture mechanisms has important implications for land use planning and seismic risk mitigation of a given area.

There exist a variety of empirical and numerical methods for generating shaking maps from empirical ground motion models to physics-based approaches (Douglas and Aochi, 2008; Goulet et al., 2015) that implement different strategies to include the local site effects. In empirical models, the site-local effects are introduced through site proxies, among which the S-wave velocity in the first 30 m, V_{s30}, is the most common. 1D and 3D site effects may directly be introduced in the numerical physics-based approach, but they need detailed knowledge of the site-local geological and geomorphology setting, including geophysical and geotechnical properties. An alternative strategy is to simulate ground motion at rock and then add the amplification curves, empirically or numerically estimated, using 1D simplified models overlaying rigid substrate. The aim of the work is the inclusion of the site response in shaking scenarios calculations using broadband ground motion hybrid modeling for the 24 August 2016 earthquake, to make available a tool useful to reduce seismic hazards and improve risk mitigations in urban areas. The evaluation of amplification curves best suited to describe local effects is of great importance because many towns and villages in Central Italy are built in very different geomorphological conditions, from valleys and sedimentary basins to topographies.

In sedimentary basins, the presence of superficial soft sediments and strong shear-wave velocity and impedance contrasts led to strong amplification of seismic waves, even produced by earthquakes originating at relevant distances (hundreds of meters). First observations date back to the 80s and 90s of the last century all over the world, firstly involving soft soil deposits: in Mexico city during Michoacàn earthquakes (1985, M = 8.1 and 7.5, e.g., Sánchez-Sesma et al., 1988); in Los Angeles basin during M_w 6.7, 1994 Northridge earthquake (e.g., Graves, 1995); in Osaka basin after M 7.2 1995 Kobe earthquake (e.g., Iwata et al., 1996). The physical mechanism at the basis of the phenomenon involves refraction of seismic waves by a velocity contrast between superficial soft sediments and an underlying stiff bedrock and subsequent phase constructive interference causing a resonance effect. Stratigraphic resonance effects are considered in seismic design codes of many countries for seismic risk mitigation (e.g., Eurocode8 in EU, NTC18 in Italy, NEHRP in the United States, NZS1170.5), through the use of scaling factors defined on the basis of the shear-wave velocity profile and the V_{s30} parameter. The Italian seismic design prescribes five classes: A (average V_{s30} over 800 m/s); B (V_{s30} between 360 and 800 m/s); C (V_{s30} between 180 and 360 m/s); D (V_{s30} lower than 180 m/s); E (particular cases). The former represents rock sites that are considered to be unaffected by site amplification, apart from high-frequency effects due to superficial weathering. Nevertheless, many recent studies have highlighted that even at frequencies of engineering interest (0.5–20 Hz) at rock sites, seismic waves can be amplified due to the local properties of the rock (i.e., the presence of pervasive fractures and/or large open cracks in different domains — fault zones, landslides, volcanoes, for example, Pischiutta et al., 2012, 2017; Panzera et al., 2014; Falsaperla et al., 2010; Ben-Zion and Sammis 2003; Lewis and Ben-Zion, 2010, Felicetta et al., 2018; Lanzano et al., 2020 (to cite a few among many). Maximum amplification (with an increase of over 100%) occurs along a site-dependent azimuth at a high angle to the fault strike; this is the reason for calling such effect "directional amplification" (using a term coined by Bonamassa and Vidale, 1991).

Finally, even sites on topography can be affected by seismic amplification. Therefore, design codes account for topographic irregularities considering scaling factors depending on the topographic slope surrounding the studied site. This is particularly important in the framework of seismic hazards and for cultural heritage maintenance and prevention since many historical and ancient settlements in Italy were built on the top of hills, for defense reasons. The topic is complex and has been under debate for the last 5 decades. Seminal papers explained the effect in terms of constructive interference of seismic waves diffracted by the convex shape of topography ("topo-resonant model", e.g., Géli et al., 1988). However, recent studies underlined that when considering a large number of sites (e.g., Burjánek et al., 2014a; Burjanek et al., 2014b; Pischiutta et al., 2018; Kaiser et al., 2022), this model is often not satisfied because a significant role is played by local velocity distribution and geological setting, as 1) large-scale open cracks (Moore et al., 2011; Burjanek et al., 2012); 2) microcracks in fractured rocks associated to fault activity (Martino et al., 2006; Marzorati et al., 2011; Pischiutta et al., 2012, 2015, 2017); 3) rock instabilities (e.g., Del Gaudio et al., 2019).

In this study, we investigated how to insert in hybrid simulations such amplification effects, observed in different geological and morphological conditions. The modeling was obtained by merging the low-frequency contribution from the kinematic rupture model proposed by Tinti et al. (2016), and the

high-frequency contribution achieved by stochastic simulation performed through the EXSIM code (e.g., Boore, 2009), both at bedrock and the site. In stochastic simulations, we exploit the model parameters validated in previous work (Pischiutta et al., 2021), including regional-specific source scaling, attenuation parameters, and the source complexity. They demonstrated that such a model can adequately explain spectral amplitudes, temporal characteristics of observed seismograms, and detect near-source effects related to the distribution of asperities on the fault plane. However, Pischiutta et al. (2021) also proved that, despite the general good consistency, in some cases simulations were not able to reproduce particular features of the observed acceleration spectrum. They ascribed such discrepancies to the occurrence of site amplification effects that are not accounted for by the use of generic amplification curves obtained through the quarter wavelength technique, due to improper consideration of the site contribution in ground-motion amplification. Also, Boore (2013) has revealed their constraints inferred by the method, which smooths, underestimating the primary resonant peaks provoked by the strong bedrock/soil seismic impedance contrasts. Moreover, several investigations have also suggested the significance of the soil/bedrock impedance contrast, the thickness of soil, and soil belongings in representing the site response in terms of amplitude and frequency content (e.g., Akinci et al., 2021).

Therefore, in this work, we have adopted different amplification curves to include the site contribution, such as the generic site curve; the horizontal-to-vertical spectral ratio (HVSR); the site functions from spectral inversion techniques (GIT). Then, we evaluated their performance by comparing observed and simulated ground motion, calculating the residual and the bias as a function of frequency.

2 METHODS

Broadband synthetic motion was generated following a hybrid approach exploited in Akinci et al. (2017), Ojeda et al. (2021), and Pischiutta et al. (2021). Here, the low-frequency (LF) portion of the synthetics (below 1 Hz) was obtained from the rupture model published by Tinti et al. (2016). Conversely, the high-frequency (HF) portion of synthetics (over 1 Hz) was attained by using a stochastic finite-fault simulation model, based on dynamic corner frequency, explained in the following section (Motazedian and Atkinson 2005; Boore 2009). These two frequency portions were merged in the frequency domain at each station following Mai and Beroza (2003). First, the LF component was selected to merge with the HF part using the consistency of the plateau level of acceleration in the Fourier space. Two frequency values are considered, **f1** and **f2**: below **f1** the signal is 100% LF, over **f2** the signal is 100% HF, and between **f1** and **f2** the LF and HF spectra should be identical. Considering that LF simulations are reliable up to 1 Hz, we adopted 0.3 and 0.8 Hz for **f1** and **f2**, respectively. However, at stations in deep sedimentary basins where site effects are expected below 1 Hz, we tailored the choice of f1 and f2 values, adopting values of 0.2 and 0.6 Hz, respectively (ex. CLF, GBP, SULA, etc). In this, way we ensure that at these stations, hybrid synthetics include site amplification effects that are accounted for only by the HF signals.

The HF and LF signals were synchronized using a long- and short-time average (LTA/STA) automatic picking algorithm. To avoid a mismatch in the plateau levels between the HF and LF spectrum, we rotated the two horizontal low-frequency components by increments of 1°. The application of this procedure resulted in hybrid broadband signals related to the horizontal components of ground motion. More details can be found in Akinci et al. (2017).

2.1 High-Frequency Stochastic Ground Motion Simulations

In order to simulate the strong ground motion of the Amatrice earthquake we applied the stochastic finite-fault method, and later examined the residual of the ground motions between observed and simulated ground motion parameters both in the time and frequency domain. We follow the approach and parameters already exploited in Pischiutta et al. (2021). The finite-fault simulation employed the EXSIM code, produced by Motazedian and Atkinson (2005) and revised by Boore (2009), which requires as input model parameters a region-specific source model, path, and site contributions.

The total spectrum of the ground motion in this approach consists of earthquake sources, paths, sites, and instruments. These terms can be included in a comprehensive equation in the frequency domain, as follows:

$$A(M_0, r, f) = E(M_0, f) \cdot P(R, f) \cdot G(f) \cdot I(f) \qquad (1)$$

where $A(M_0, r, f)$, is the Fourier spectra acceleration, M_0, f and R are the seismic moment, the corner frequency, and the hypocentral distance from the observation point, respectively. The term $E(M_0, f)$ is the earthquake source spectrum,and the term *P(R,f)* is the path that models the geometric spreading and the anelastic attenuation effects as a function of R and f. The term $G(f)$ is the site effect and $I(f)$ is the instrumental transfer function. The exploited parameters required by the method for the source, the path, and the site terms, are derived from those several current models published in Central Italy. Their adequateness was confirmed in Pischiutta et al. (2021), where the general good consistency found between synthetic and observed ground motion (both in the time and frequency domains) demonstrated that this model can adequately explain spectral amplitudes, temporal characteristics of observed seismograms, and to detect near-source effects related to the distribution of asperities on the fault plane. In order to show the performance of the adopted parameters in reproducing ground-motion estimates for the Amatrice earthquake, in **Supplementary Figure S1** we plot the simulated hybrid broadband PGAs, PGVs up to 150 km as a function of R_{JB} for the seismic stations in the "A" site class (blue reverse triangles), and for 961 virtual stations (turquoise dots) distributed in a 4-km grid space (see Pischiutta et al., 2021). Three Italian GMPE models are plotted as well, together with their ±σ standard deviations: Bindi et al., 2011 (cyan); Malagnini et al., 2011 (green); Sgobba et al., 2020 (violet). Simulated PGAs and PGVs lie within the standard deviation of

the three considered GMPEs, suggesting the adequateness of the adopted regional-specific source scaling and attenuation parameters in hybrid simulations in satisfactory reproducing ground-motion estimates.

2.1.1 Source

We adopt the same spectral parameters describing the earthquake source, employed and validated in Pischiutta et al. (2021). They are tabulated in **Supplementary Table S1**. The stress drop parameter σ, which rules the levels of the acceleration spectrum at high frequencies, was calculated at about 150 bars by Malagnini and Munafò, 2018, and Akinci et al. (2021). We also adopted the kinematic rupture model proposed by Tinti et al. (2016), divided into 0.5 km × 0.5 km sub faults along the strike and dip. According to earlier studies, source parameters, such as geometry (strike 156°, dip 50°), density (2.8 km/m^3), and rupture propagation velocity (3.1 km/s), are employed among ordinarily referred values (**Supplementary Table S1**).

2.1.2 Propagation and Attenuation

Seismic wave propagation and seismic attenuation are essential topics, and they are required for the earthquake ground motion estimations in seismic hazard analysis. In our study, we decided to use the most recently described seismic attenuation parameters presented in Malagnini et al. (2011) model. It was obtained from several regressions of 170 weak-motion records belonging to foreshocks and aftershocks of the 2009 L'Aquila seismic sequence and realized through regression analyses of velocity time-series and Fourier spectra from 0.1 to 10 Hz, recorded at distances between 40 and 350 km. It provides the average features of three contributions in the wave propagation: geometrical attenuation, anelastic attenuation, and ground motion duration.

The chosen spectral parameters for seismic wave propagation are reported in **Supplementary Table S2**. The path spectrum, $P(R, f)$, depends on geometrical spreading, $Z(R, f)$, and quality factor (Q_s).

$$P(R, f) = Z(R) \cdot exp\left(- \frac{\pi f R_{ij}}{Q_S} \right) \tag{2}$$

Concerning the geometrical spreading coefficient$Z(R, f)$, we adopted a conventional piecewise function as represented by $r^{-1.1}$ at distances smaller than 10 km as a body-wave-like function; within 10 and 40 km, it is defined as r^{-1}; within 40 and 100 km, it is defined as $r^{-0.7}$; beyond 100 km distance, it is characterized by $r^{-0.5}$, that is compatible with the surface waves attenuation characteristics in a half-space.

A power-law pattern of Q_s gives the anelastic attenuation:

$$Q_S = Q_0 f^{\eta} \tag{3}$$

where Q_0 is the value of Q_s at a frequency of 1 Hz, and η is the frequency parameter proposed by Aki and Chouet (1975). For the Central Italy region, the quality factor at frequencies > 0.6 Hz is given by

$$Q_s(f) = 140 f^{0.25} \tag{4}$$

Values adopted for frequency < 0.6 Hz are given in **Supplementary Table S2**. However, at such low frequency ranges the hybrid motion is dominated by the LF contribution due to the merging procedure previously explained.

2.1.3 Site Amplification

In the code EXSIM, site amplification is accounted for through the combination of the amplification $A(f)$ and attenuation $D(f)$ contributions as follows:

$$G(f) = A(f) \cdot D(f) \tag{5}$$

$D(f)$ is a diminution operator accounting for deamplification effects from the near-surface:

$$D(f) = exp(-\pi \kappa_0 f) \tag{6}$$

where an exponential decay marks the kappa parameter (κ_0), representing the slope of the high-frequency declines of spectra in the stochastic finite-fault method (Anderson and Hough, 1984).

2.2 Including the Site Effects

Here, we aimed to involve the site amplifications determined from different approaches to testing the performance and using such generic, empirical, and "specific" site amplification curves at stations selected in conditions potentially prone to experiencing site effects (ex. basin, topography). We used the following site amplification curves, determined throughout commonly affirmed techniques:

1. Generic site curves employed in Pischiutta et al. (2021), and representative of NTC-18 classes A, B, C, and D. According to **Eq. 5**, they are composed of the product of the wave amplification term A(f) and the diminution term D(f), this latter accounting for high-frequency attenuation.

Many studies in the literature have provided generic amplification curves for the term A(f), in the framework of the National Earthquake Hazard Reduction Program, NEHRP which is the seismic code adopted in the United States (e.g., Boore and Joyner, 1997; Boore, 2003; Boore 2016; Campbell and Boore, 2016). However, considering that the class thresholds for Italian and United States seismic design codes are different (see Table 4 in Pischiutta et al., 2021), in this study we choose to exploit such curves only for NTC-18 classes -B and -C (corresponding to NEHRP -C and -D, respectively). In particular, we adopted two A(f) curves proposed in Boore and Joyner, 1997 without particular frequency peaks and with associated Vs_{30} parameter lying in the middle of the ranges allowed in each class (520 and 255, respectively, for representative curves chosen for -B and -C classes). They are reported in **Supplementary Table S3** and graphed in **Supplementary Figure S2** (green and red continuous lines). Considering the differences between Vs_{30} thresholds in the Italian NTC-18 and United States seismic codes, for NTC-18 class-A we adopted an A(f) curve generated in Pischiutta et al. (2021) using the quarter wavelength approach (Boore, 2003; Boore, 2005) considering a typical velocity profile for Italian soft rocks (limestones, marls, and flysch), without strong impedance contrasts. It is reported in **Supplementary Table S4** and shown

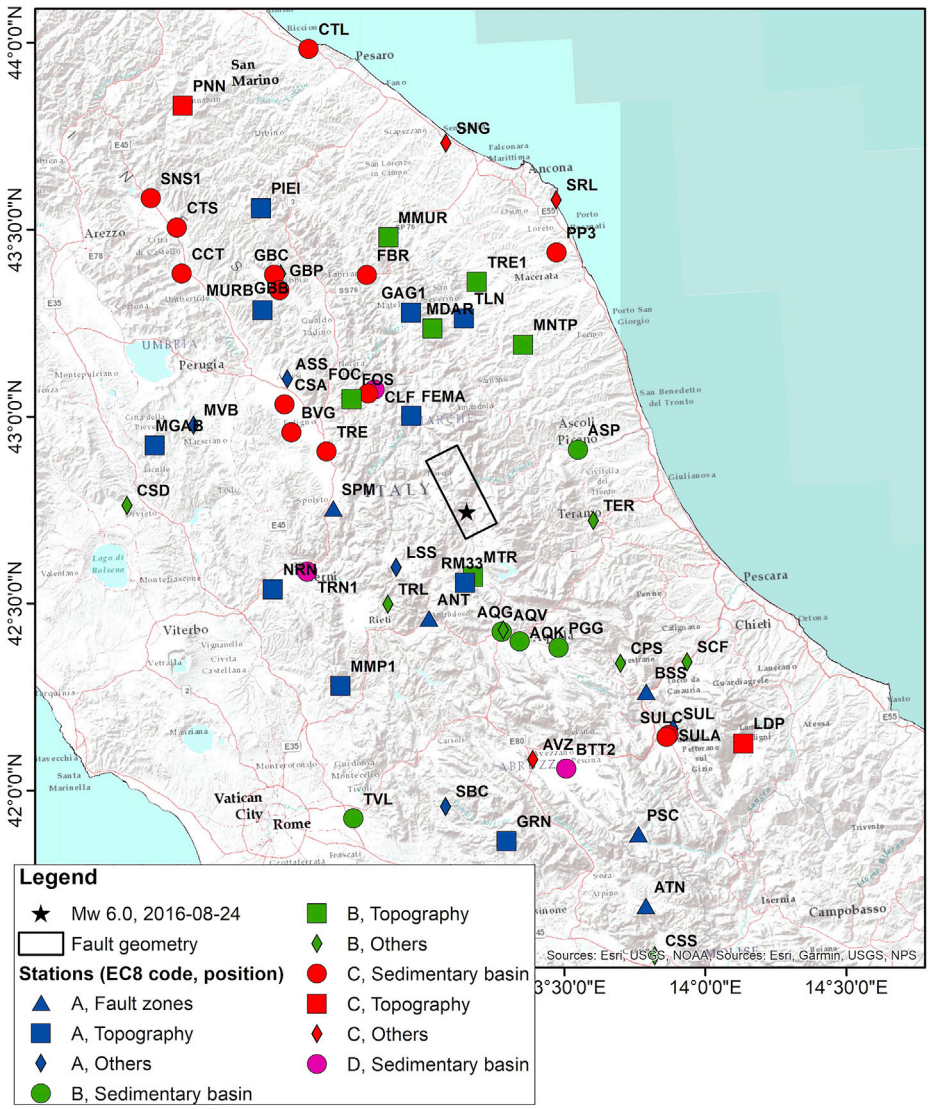

FIGURE 1 | Map showing stations considered in this study up to a distance of 150 km to the epicenter of the M_w6.0 Amatrice earthquake (black star), and lying in particular site conditions, such as sedimentary basins (circle), topographic irregularities (square), fault zones (triangles). They belong to RAN ("IT") and RSN ("IV") networks (**Table 1**). We also add the fault surface projection of the causative fault proposed in Tinti et al. (2016). Symbol color is related to site classification according to NTC18 based on the V_{s30} parameter (blue = class A, green = class B, red = classes C, and pink = D).

in **Supplementary Figure S2** (blue continuous line). Similarly, for the NTC18 class-D (corresponding to NEHRP class-E), we exploited another A(f) curve generated by Pischiutta et al. (2021) considering a velocity profile with Vs_{30} in the ranges prescribed by NTC18 (<180 m/s) and without significant impedance and velocity contrasts (see also **Supplementary Table S4** and the orange continuous line in **Supplementary Figure S2**). We remark that generic site amplification curves determined throughout the quarter wavelength procedure are represented by velocity gradients being insensitive to impedance variances connecting the layers (Joyner and Fumal, 1984; Boore and Joyne, 1997; Boore et al., 1994, 2011).

To calculate the diminution term D(f) representing high-frequency attenuation, we used the following values for the kappa parameter (κ_0):

$$\kappa_0 = \begin{cases} 0.02\,s & for\ class-A \\ 0.03\,s & for\ class-B \\ 0.04\,s & for\ class-C \\ 0.045\,s & for\ class-D \end{cases} \quad (7)$$

The G(f) curves obtained following **Eq. 5** are reported in **Supplementary Figure S2** through dotted lines.

2. Generalized inversion technique (GIT, Andrews 1986; Castro et al., 1990). This approach is a reference site

TABLE 1 | Station sample considered in this study.

Net code	Station code	Station name	Latitude [°]	Longitude [°]	Position	EC8 code
IT	ANT	ANTRODOCO	42,4182	13,0786	Fault zones	A
IT	AQG	L AQUILA V. ATERNO COLLE GRILLI	42,373474	13,337026	Sedimentary basin	B
IT	AQK	L AQUILA V. ATERNO AQUIL PARK ING.	42,344967	13,400949	Sedimentary basin	B
IT	AQV	L AQUILA V. ATERNO CENTRO VALLE	42,377222	13,343888	Others	B
IT	ASP	ASCOLI PICENO	42,848	13,6479	Sedimentary basin	B
IT	ASS	ASSISI	43,074982	12,604141	Others	A
IT	ATN	ATINA	41,620319	13,801154	Fault zones	A
IT	AVZ	AVEZZANO	42,0274	13,4259	Others	C
IT	BSS	BUSSI	42,191732	13,845266	Fault zones	A
IT	BTT2	BORGO OTTOMILA - 2 (CELANO)	41,998333	13,543056	Sedimentary basin	D
IT	BVG	BEVAGNA	42,932367	12,611065	Sedimentary basin	C
IT	CCT	CITTA DI CASTELLO (TRESTINA)	43,3683	12,2346	Sedimentary basin	C
IT	CLF	COLFIORITO	43,036714	12,920428	Sedimentary basin	D
IT	CSA	CASTELNUOVO ASSISI	43,008015	12,590602	Sedimentary basin	C
IT	CTL	CATTOLICA	43,955116	12,735809	Sedimentary basin	C
IT	CTS	CITTA DI CASTELLO REGNANO	43,491987	12,223396	Sedimentary basin	C
IT	FBR	FABRIANO	43,343601	12,9119	Sedimentary basin	C
IV	FEMA	Monte Fema	42,9621	13,04976	Topography	A
IT	FOC	FOLIGNO	43,0263	12,896506	Sedimentary basin	C
IT	FOS	FOLIGNO SEGGIO	43,01459	12,83513	Topography	B
IV	GAG1	Gagliole	43,238063	13,067434	Topography	A
IT	GBB	GUBBIO	43,356972	12,597252	Others	B
IT	GBC	Gubbio	43,355301	12,5726	Sedimentary basin	C
IT	GBP	GUBBIO PIANA	43,31381	12,58949	Sedimentary basin	C
IT	GRN	GUARCINO	41,8134	13,3169	Topography	A
IT	LDP	LAMA DEI PELIGNI	42,0392	14,1826	Topography	C
IT	LSS	LEONESSA NUOVA	42,558243	12,968894	Others	A
IV	MDAR	Monte Daria	43,1927	13,1427	Topography	B
IV	MGAB	Montegabbione	42,91263	12,11214	Topography	A
IT	MMP1	MOMPEO 1	42,249229	12,748319	Topography	A
IV	MMUR	Monte Murano	43,44183	12,9973	Topography	B
IV	MNTP	Montappone	43,137378	13,469252	Topography	B
IT	MTR	MONTEREALE	42,524	13,2448	Topography	B
IV	MURB	MONTE URBINO	43,263	12,5246	Topography	A
IT	MVB	MARSCIANO MONTE VIBIANO	42,9619	12,257	Others	A
IT	NRN	NARNI	42,51556	12,51944	Topography	A
IT	PGG	POGGIO PICENZE	42,322872	13,539446	Sedimentary basin	B
IV	PIEI	PIEIA	43,53567	12,535	Topography	A
IT	PNN	PENNABILLI	43,818159	12,262846	Topography	C
IV	PP3	PP3	43,37783	13,6095	Sedimentary basin	C
IT	PSC	PESCASSEROLI	41,812042	13,789196	Fault zones	A
IV	RM33	PELLESCRITTA	42,50898	13,21452	Topography	A
IT	SBC	SUBIACO	41,9132	13,1055	Others	A
IT	SCF	SCAFA	42,265117	13,998489	Others	B
IT	SNG	SENIGALLIA	43,68558	13,226162	Others	C
IT	SNS1	SANSEPOLCRO 2	43,573502	12,1312	Sedimentary basin	C
IT	SPM	SPOLETO MONTELUCO	42,72324	12,751268	Fault zones	A
IT	SRL	SIROLO	43,517905	13,619388	Others	C
IT	SUL	SULMONA	42,089	13,934	Others	A
IT	SULA	SULMONA AUTOPARCO	42,0734	13,9166	Sedimentary basin	C
IT	SULC	SULMONA CONSORZIO	42,068	13,909	Sedimentary basin	C
IT	TLN	TOLENTINO	43,215904	13,25838	Topography	A
IT	TRE	TREVI	42,876499	12,7358	Sedimentary basin	C
IV	TRE1	Treia	43,311198	13,312848	Topography	B
IT	TRL	TERMINILLO	42,461314	12,932308	Others	B
IT	TRN1	TERNI 2	42,558201	12,6461	Sedimentary basin	D
IT	TVL	Tivoli	41,893015	12,773221	Sedimentary basin	B

method such as the standard spectral ratio method (SSR) but, in contrast with the SSR, the GIT curves are the result of a nonparametric inversion scheme applied to a dataset composed of multiple events and stations. In this study, we used the GIT amplification functions obtained from a dataset of 283 stations and 455 events that occurred in Central Italy (Morasca et al., 2022). The GIT analysis was performed on a frequency range of

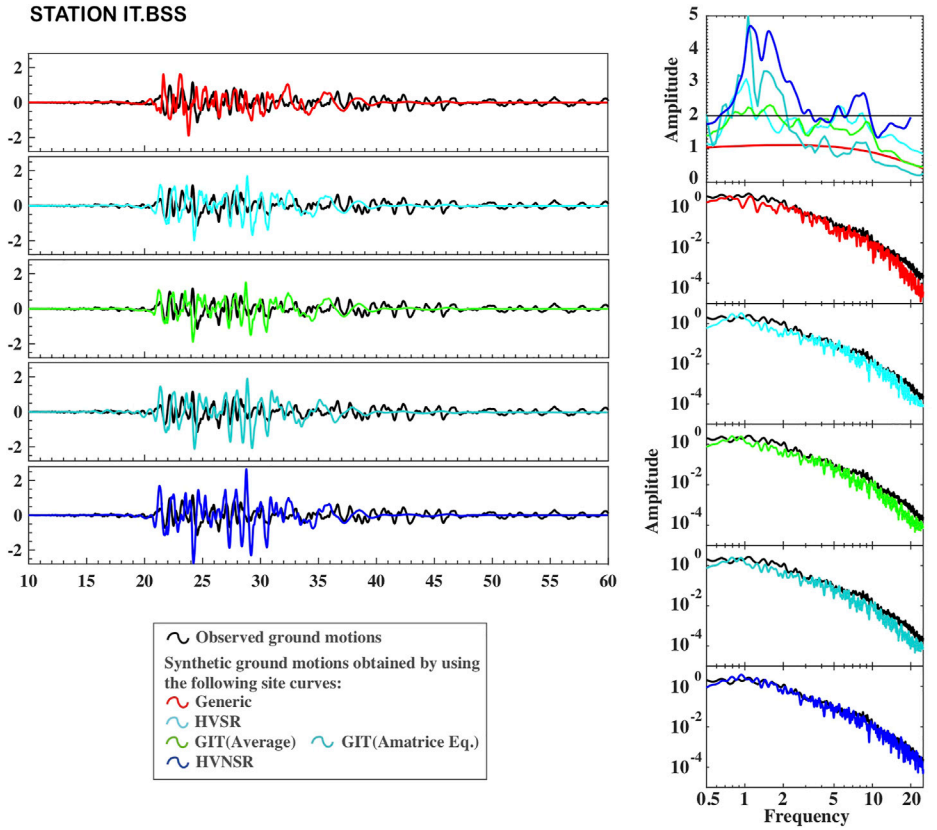

FIGURE 2 | Exemplification simulation results at station BSS (Bussi), belonging to the IT network. The left-top panel shows amplification curves applied as the term G(f) in the EXSIM code used for stochastic simulations (**Eq. 5**). The red curve is the generic one that we used for all class B sites defined in NTC-18 based on the V_{s30} value (see also **Supplementary Figure S3**). The other tested site-empirical specific curves are: the cyan curve is the HVSR calculated using earthquake weak motion (S waves); the green and turquoise curves are the GIT-derived amplification function by using 455 earthquakes and only the Amatrice earthquake, respectively (Morasca et al., 2022); the blue curve is the HVNSR calculated using ambient noise or earthquake coda waves. Synthetic hybrid broadband horizontal component velocity time histories (left panel) and Fourier velocity amplitude spectra (top-right panel) are compared with the recorded ground motions (black lines). For the latter, we calculated the geometric mean, and mean of the two horizontal components of ground motion, respectively, for time histories and Fourier spectra.

0.5–25 Hz and considered a hypocentral distance range of 10–120 km. The solution of the linear system composed of three terms (source, attenuation, and site contributions) required two prior constraints to remove unresolved degrees of freedom. A first assumption is that for all frequencies the attenuation term is set to unity at the reference distance of 10 km (the smallest in the dataset). The second one is a reference site condition. Considering six reference sites (LSS, MNF, NRN, SNO, SDM, and SLO) located on the rock and carefully selected on the base of Lanzano et al., 2021 analysis, their average amplification is fixed to 1, removing the linear dependence between source and site terms. We also exploit the GIT amplification function obtained only from the Amatrice earthquake (when available). In **Supplementary Figure S3** we provide such GIT curves at the eleven stations that are thoroughly investigated in this paper. At some of them (CLF, FOC, TRE, FEMA, BSS, SULA, GBB) the two GIT curves show differences both in terms of amplified frequency band and amplitude level. This prompted us to test both of them in stochastic simulations, in a way to better reproduce observed motions.

3. Horizontal-to-vertical (HV) spectral ratio computed on the Fourier Amplitude Spectra (FAS) of strong-motion recordings (HVSR) and ambient noise (HVNSR). Although these methods are usually adopted to estimate the resonance frequencies of the site, we test if they can be also adopted to evaluate the site amplification in specific geomorphological conditions (Molnar et al., 2018; Kawase teal., 2019; Zhu et al., 2020). The HV method may estimate the site amplification function if the vertical amplification is negligible (Lachet and Bard, 1994; Field and Jacob, 1995). The HV curves are available in the Italian Accelerometric Archive v 3.2 (ITACA, Russo, et al., 2022). If the HVNSR curve is missing, we select the HV computed on the coda waves since many studies demonstrated that the curves obtained from noise and coda waves are comparable. Instead, if the HVSR curve is not available in ITACA we use the HV curves

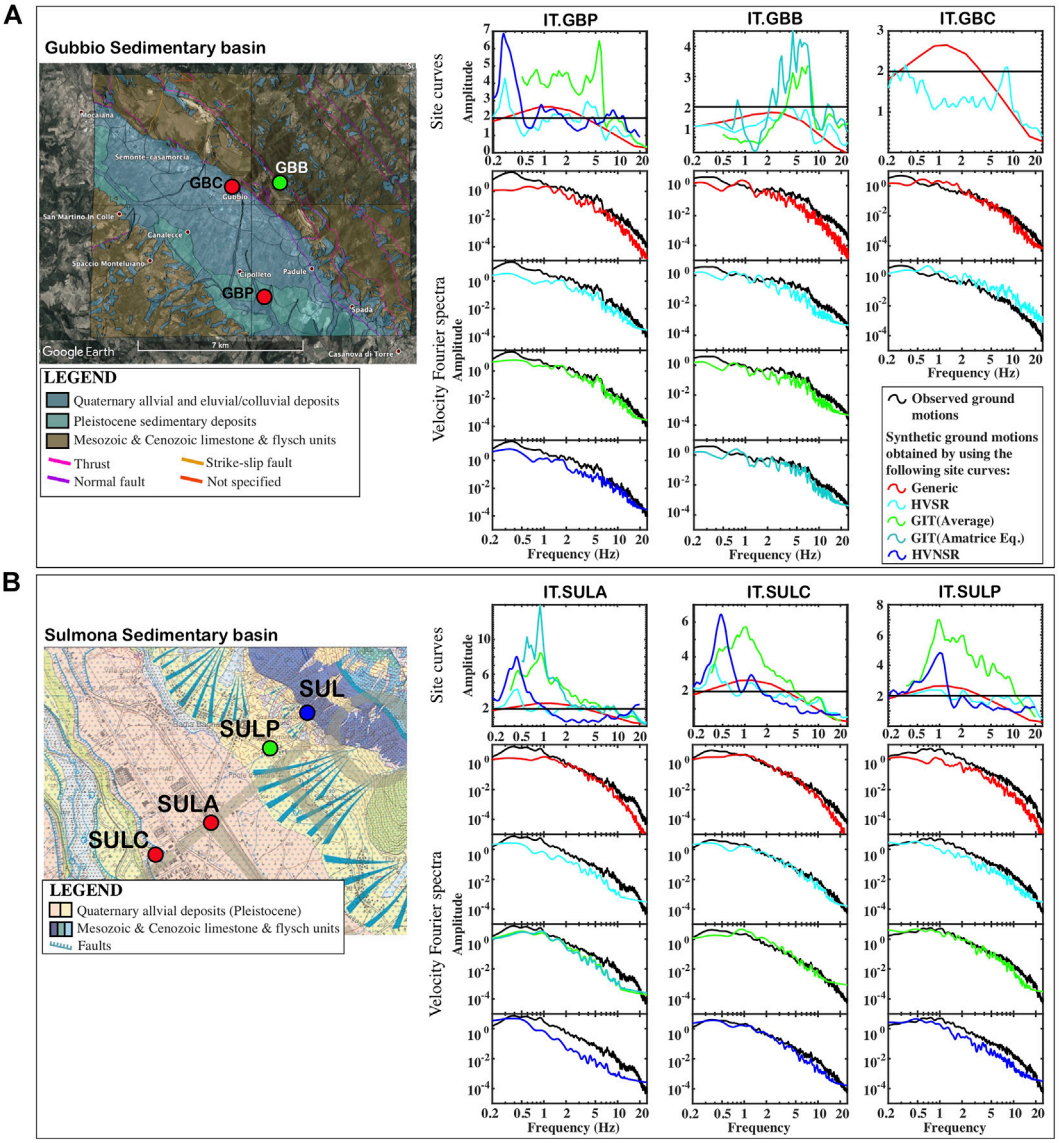

FIGURE 3 | Simulation results and records of Amatrice earthquake at Gubbio [panel **(A)**] and Sulmona sedimentary basins [panel **(B)**]. For each site, we add: a rough geological map of the area (provided in the ITACA database); the applied generic and empirical site curves at each station (consistently with **Figure 2**); Synthetic velocity Fourier spectra were obtained using the different site curves and recorded velocity Fourier spectra (geometric mean of the two horizontal components).

from an independent study (Priolo et al., 2019) estimated using records of small events (magnitude < 4.5).

Adopted site amplification curves were not concurrently available at all stations. The kappa coefficient κ_0 was not applied for the simulations for the GIT, HVRS, and HVNSR experimental curves, since implicitly cconsiders the total attenuation effects.

2.3 Dataset and Recording Stations

Among stations recording the Amatrice 24 August 2016 earthquake at 150 km from the epicenter, we selected a subset of 57, installed in different site conditions potentially prone to experience site amplification effects (**Figure 1**) (**Table 1**), as

1. Twenty-two (22) stations in sedimentary basins (circles in **Figure 1**) mostly related to site classes C and D, with only a minor percentage (five stations) in class B. An inspection of the HVSRs and HVNSRs published on the ITACA database resulted in relevant amplification (exceeding a factor of three).
2. Eighteen (18) stations are located on topographic irregularities (squares in **Figure 1**). Most parts of them lie in site class A (10) and B (6).

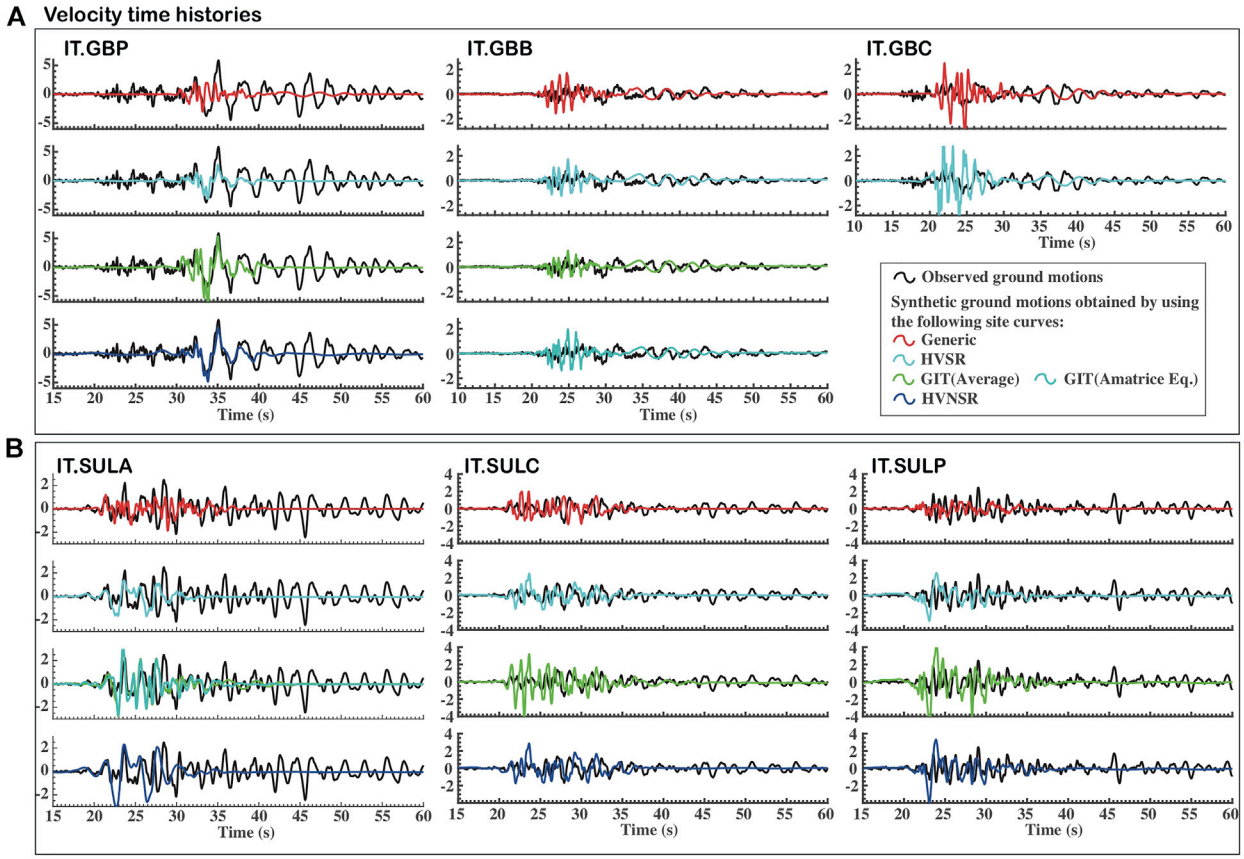

FIGURE 4 | Velocity time series at Gubbio [panel **(A)**] and Sulmona [panel **(B)**] sites. In black, we plot recorded seismograms (arithmetic mean of the two horizontal components). Colored lines depict synthetic hybrid seismograms obtained from the HF and LF contributions (see **Section 2.3**), obtained through the EXSIM code seismic source inversion by Tinti et al. (2016). They were obtained by using empirical site curves in the EXSIM code: GIT (green), HVSR (cyan), and HVNSR (blue).

3. Six (6) stations on class A rock sites and close to fault zones (as identified by a visual inspection of geological maps and information archived in the ITACA database).
4. Eleven (11) and other stations belong to A, B, and C sites (no faults/topography/sedimentary basins) as a further constraint.

Such a station sample is a portion of the one used in Pischiutta et al. (2021) work, where 133 stations at 150 km from the epicenter were selected to validate stochastic simulations through comparison with recorded data in this work.

3 RESULTS

A comparison between observed and simulated ground motion was led to get insight into simulation reliability and the performance of the different adopted site amplification curves. **Figure 2**, reports exemplificative simulation results at station BSS (Bussi) of the IT network, related to site class A and located close to a tectonized zone. The left-top panel shows amplification curves used for stochastic simulations (**Eq. 5**). The red curve is the generic one that we used for all class B sites defined in NTC-18 based on the V_{s30} value (see also **Supplementary Figure S2**). According to **Eqs 5**, and **6**, it is obtained by the product of $A(f)$ and $D(f)$. For $A(f)$, we adopted as representative of NTC-18 class-B an amplification curve proposed in Joyner and Boore (1997) and related to V_{s30} of 520 m/s. $D(f)$ was calculated using **Eq. 6** considering κ_0 a value of 0.03 s. The other tested site-empirical specific curves were applied as $G(f)$, considering that attenuation contribution should be implicitly included:

1) The cyan curve is the HVSR calculated using S-waves of seismic recordings
2) The green and turquoise curves are the GIT-derived amplification for the station by using, respectively, 455 events (Morasca et al., 2022), the empirical function resulting from average overall events for robustness reasons, and only the Amatrice 24 August 2015 earthquake
3) The blue curve is the HVNSR calculated using ambient noise or earthquake coda waves

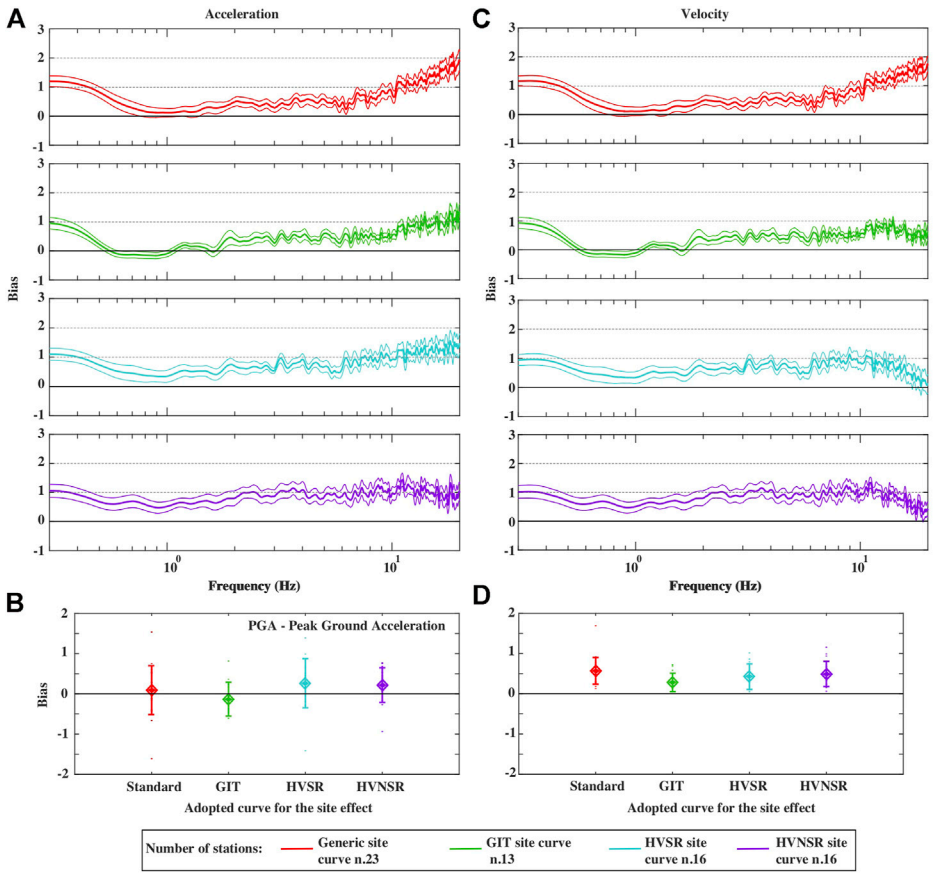

FIGURE 5 | Bias calculated following **Eq. 10**, to get an insight into the performance of the generic and empirical site amplification curves exploited in the EXSIM code all over the station sample in sedimentary basins. The top panels show bias versus frequency for both acceleration **(A)** and velocity **(B)** spectra. Black curves represent the bias obtained by applying the generic site curve, while color curves are related to the use of GIT (green), HVSR (cyan), and HVNSR (violet) site curves. The standard deviation is plotted as well. The bottom panels show the bias calculated for peak ground acceleration [PGA, panel **(B)**] and peak ground velocity [PGV, panel **(C)**].

To validate the effectiveness of our simulations to reproduce observations and test the different site curves, we compared the synthetic velocity time histories (right panel) to recorded horizontal ground motion (arithmetic mean). Velocity Fourier amplitude spectra (left-bottom panel) were also compared with recorded ones (geometric and mean of the two horizontal components of ground motion).

The HVNSR curve and the GIT curve obtained from the Amatrice earthquake consistently show a peculiar characteristic concerning other amplification curves presenting two prominent peaks between 1 and 2 Hz at station BSS. These peaks are easily observed in the simulated time histories, as shown in the left-bottom panel of **Figure 2**.

As a second step, to quantitatively assess simulations' overall performance we calculated residuals $RF_j(f)$ between observed F_j and simulated $\underline{F_j}$ spectra considering the different generic and empirical curves, related to station j as

$$RF_j(f) = \left(\frac{F_j}{\underline{F_j}}\right) \tag{8}$$

Similarly, we calculated the residual R_j between observed Y_j and simulated $\underline{Y_j}$ ground-motion parameters (PGA and PGV) at each station j as

$$R_j = \frac{Y_j}{\underline{Y_j}} \tag{9}$$

We finally computed the bias averaging over the total station sample N:

$$BIAS\,RF(f) = \frac{1}{N}\sum_{j=1}^{N}\ln\left(R_j(f)\right)$$
$$BIAS\,R = \frac{1}{N}\sum_{j=1}^{N}\ln\left(R_j\right) \tag{10}$$

.

A perfect match between the empirical model and the broadband simulation would have null BIAS values, whereas positive/negative residual shows an underprediction/overprediction of the simulations concerning observed ground motion.

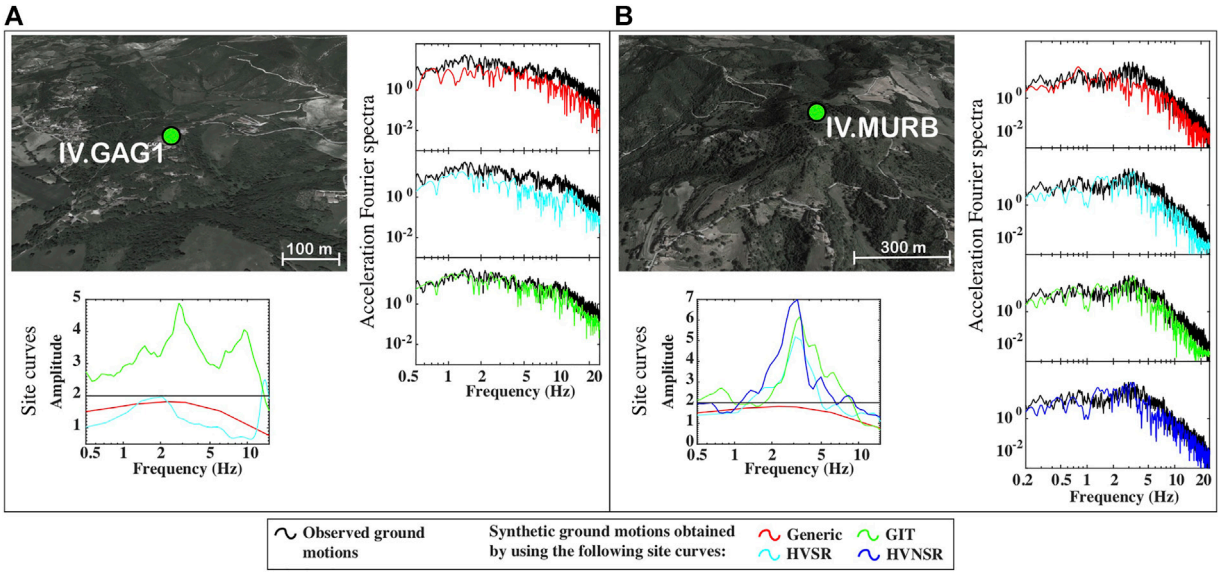

FIGURE 6 | Simulation results and records of the Amatrice earthquake at stations GAG1 [panel **(A)**] and MURB [panel **(B)**], located on topographic irregularities. For each one, we show a digital elevation model to evince topography shape; the applied generic and empirical site curves at each station (consistently with **Figure 2**); Synthetic velocity Fourier spectra were obtained using the different site curves and recorded velocity Fourier spectra (geometric mean of the two horizontal components).

3.1 Stations in Sedimentary Basins

In order to thoroughly investigate how many stratigraphic effects are accounted for/unaccounted for in the earthquake-induced ground motions, we selected twenty-two stations in sedimentary basins.

Figure 3 details results at two sedimentary basins where Gubbio (panel A) and Sulmona (panel B) towns are settled. Gubbio is a historical town in the Umbria region, central Italy, with more than 30,000 inhabitants and a rich artistic and cultural heritage dating to the Middle-Age. The historical part was built at the lower slope of Ingino hill, but the modern portion expanded towards the alluvial plain. In this area, three stations of the Italian seismic network IT are installed: GBP in the middle of the alluvial basin (site class C); GBC on the basin border, inside Gubbio settlement (site class C); GBB outside the alluvial basin (site class B). Bindi et al. (2009) observed that time series of local earthquakes recorded in the Gubbio plain are characterized by locally generated surface waves, which increase in duration and amplitude with respect to the nearby reference station on a rock (GBB), the spectral energy is distributed over the range 0.4–2 Hz. In particular, they found that the peak ground velocity is amplified by a factor of 5, and the duration is increased by a factor of about 2 where the sedimentary cover is thickest (ca 600 m).

In the top panel A of **Figure 3**, we report a basic geological map of the area. We also add the site curves for each station, consistently with **Figure 2**. While the generic curve (red) which does not account for the specific basin structure, does not show any significant peaks, the GIT curves (green and turquoise) show a relevant amplitude peak at about 5 Hz and between 2 and 10 Hz at stations GBB and GBP, respectively. The use of GIT curves led to better reproduction of the general spectral trend and velocity recorded signals (**Figure 4A**). At station GBP, in the middle of the basin, the HVSR and HVNSR curves show a peak at about 0.35 Hz, up to a factor of 4 and 7, respectively. In **Figure 4**, we include synthetic velocity time series for Gubbio (panel A) and Sulmona (panel B) cases. Especially by using the HVNSR and GIT curves, we obtained synthetic time histories with amplitudes and spectral content more consistent with recorded signals. At station GBC we applied only the empirical HVSR curve together with the generic one. Bindi et al. (2009) highlighted that in the Gubbio basin the HVSR are strongly affected by amplification on the vertical component, and this is particularly evident close to the basin border. In this study, we found that at station GBC the use of the HVSR curve did not lead to obtaining synthetic signals consistent with observed data.

The sedimentary basin hosting the Sulmona town in the Abruzzi region hosts more than 20,000 inhabitants (**Figure 3B**). Sulmona was founded in Roman times and holds a rich artistic and cultural heritage dating from the Middle-Age. Sulmona rises in the center of the Peligna Valley, which in prehistoric times was occupied by a vast lake. It is located between the Vella torrent and the Gizio rivers, to the west of the Maiella and Morrone mountains, which overlook the city.

In this study, we consider four stations of the Italian seismic network IT: SULA, in the middle of the alluvial basin (site class C); SULC and SULP, on the basin borders (site class C and B, respectively); SUL, outside the alluvial basin (site class A). In **Figure 3**, we also show the geological map of the area, as well as the adopted site curves at each station. While the generic (red) and HVSR (cyan) site curves do not show any significant peaks, the GIT curves at stations SULA, SULC, and SULP show a peak at about 1 Hz, with amplitudes varying from 5 close to the basin borders (SULP and SULP) to over 8 in the middle of the basin

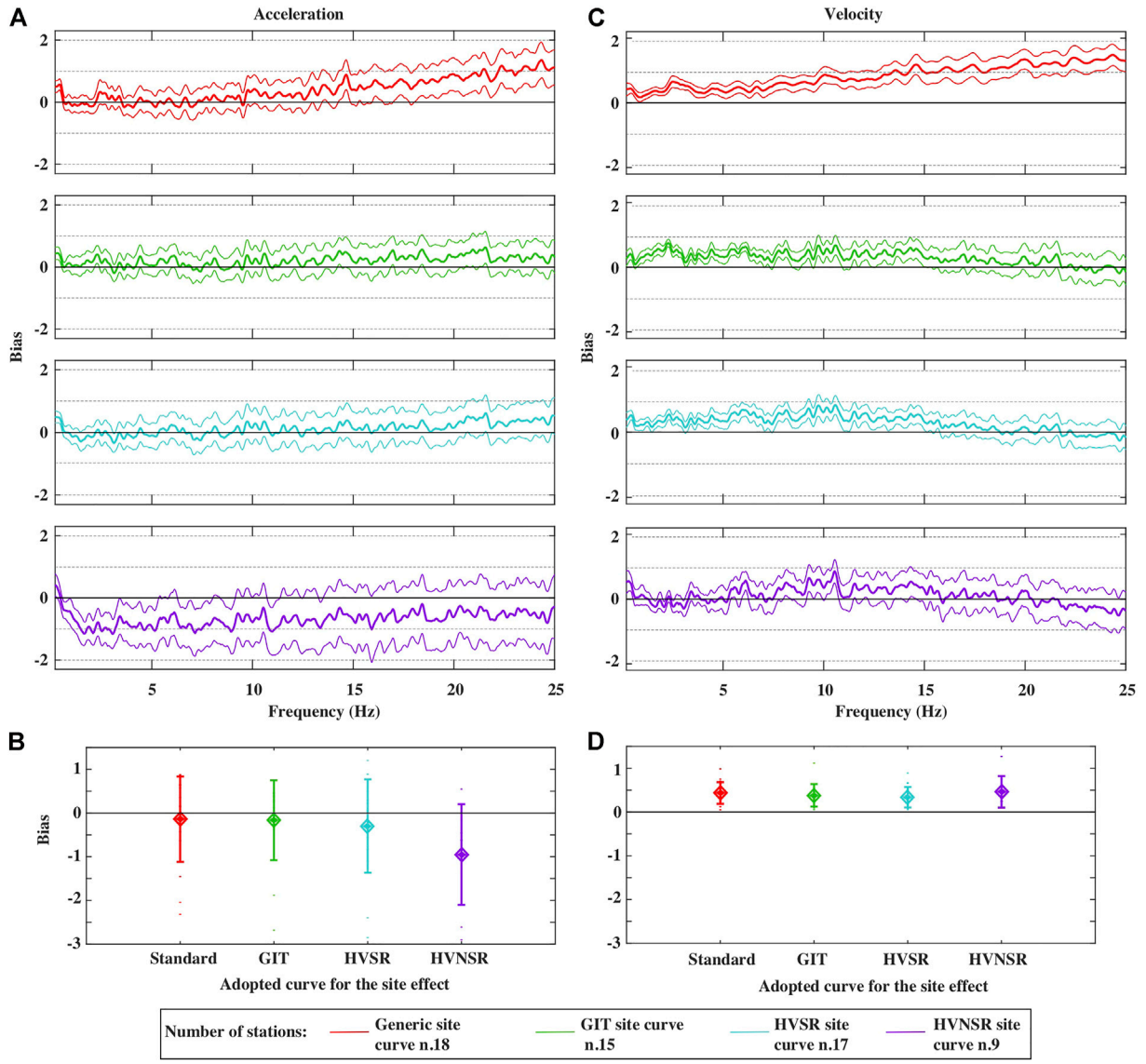

FIGURE 7 | Bias calculated following **Eq. 10**, to get an insight into the performance of the generic and empirical site amplification curves exploited in the EXSIM code all over the station sample on topography. The top panels show bias versus frequency for both acceleration **(A)** and velocity **(C)** spectra. Black curves represent the bias obtained by applying the generic site curve, while color curves are related to the use of GIT (green), HVSR (cyan), and HVNSR (violet) site curves. The standard deviation is plotted as well. The bottom panels show the bias calculated for peak ground acceleration [PGA, panel **(B)**] and peak ground velocity [PGV, panel **(D)**].

(SULA). The HVNSR curves show another peak at about 0.45 Hz at SULA and SULC, with amplitudes decreasing from 8 to 6. It is also evident on the HVSR curve even if with lower amplitude levels (ranging from 3 to 4). By applying the GIT site curves we obtained synthetic velocity spectra reproducing the observed spectral trend on data at stations SULA, SULP, and SULC. At this latter station, a better performance was achieved by adopting the HVSR and HVNSR. Finally, at station SUL there are no differences in synthetic spectra obtained by adopting the different site curves (velocity time histories are given in the **Supplementary Figure S4**.

We finally highlight that at stations in the middle of the two investigated sedimentary basins (GBP and SULA), recorded seismograms show the presence of low-frequency phases, mainly in the coda, due to 3D amplification caused by the impedance contrast between soft sediments and underlying rock formations and by wave reverberation across the sedimentary body in the basin (e.g., Cornou and Bard, 2003). Such empirical 3D effects cannot be thoroughly simulated by employing the stochastic finite-fault technique implemented in this study. However, these effects are not observed at stations installed near the sedimentary basin borders (GBC, SULC, SULP). Finally, stations outside sedimentary basins (GBB and SUL) do not significantly improve by using different amplification curves in fitting the observed time histories. In

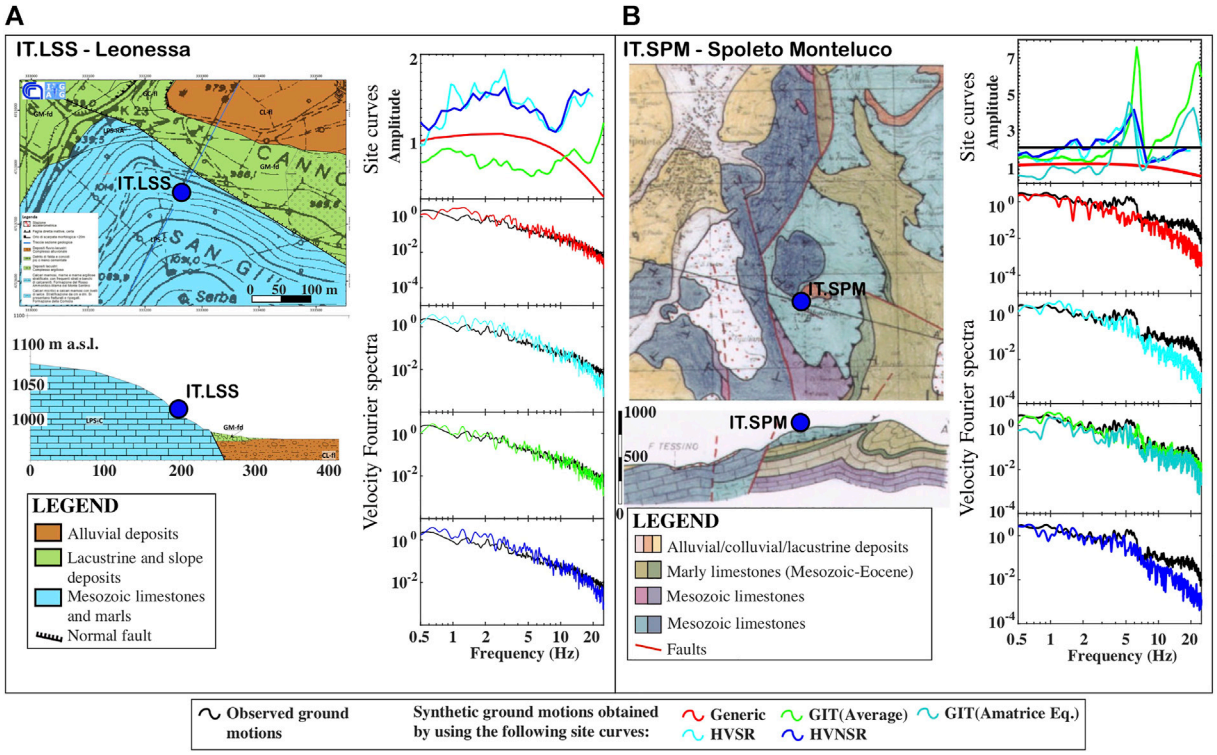

FIGURE 8 | Simulation results and records of Amatrice earthquake at stations LSS [panel **(A)**] and SPM [panel **(B)**], installed on rock and related to site class A. For each one, we show: the geological map and profile furnished in the ITACA database; the applied generic and empirical site curves at each station (consistently with **Figure 2**); Synthetic velocity Fourier spectra were obtained using the different site curves, and recorded velocity Fourier spectra (geometric mean of the two horizontal components).

fact, since they are installed outside the sedimentary basin, they are not affected by any significant site amplification effects.

In **Supplementary Figure S5**, we also provide results from two other study cases in sedimentary basins: Colfiorito and Foligno. They are both located in the Umbria region (central Italy) and experienced an MCS damage intensity of VII during the 1997 seismic sequence (e.g., Camassi et al., 2008), where over six shocks with magnitude larger than 5.0 were produced. In the Colfiorito basin, two stations of the Italian seismic network "IT" are installed: FOC (close to the basin border) and CLF (in the middle of the basin). The former station is inside the small village of Colfiorito, hosting about 5,000 inhabitants and some interesting monuments (i.e., a Church dating back to the fifth century). In **Supplementary Figure S5A**, we report several geological information included in the ITACA database: a geological map and section passing through station FOC and a velocity profile above station CLF. The latter highlights a strong velocity contrast at about 50 m depth, probably responsible for the about 1.0 Hz peak observed on both the GIT and HVNSR curves. However, at this station, empirical site-specific curves in stochastic simulations did not generally result in better reproducing observed data. Conversely, at station FOC the use of the GIT curves (in particular the ones derived by using only the Amatrice earthquake) led to obtaining synthetic spectra similar to the observed trend on recorded spectra at frequencies over 5 Hz.

Foligno municipality has more than 50,000 inhabitants and is located close to Colfiorito (20 km far), in the center of the Umbrian Valley that is crossed by the Topino river. Foligno possesses an important cultural heritage, with many civil and religious edifices dated since the Middle-Ages. The two stations installed in this area (BVG and TRE) show a relevant amplitude peak between 1 and 3 Hz, most prominent on the GIT curves (**Supplementary Figure S5B**). The use of the latter (in particular the ones derived by using only the Amatrice earthquake at station TRE) led to achieving the best consistency between synthetic and recorded spectra.

In order to get an insight into the performance of the generic and empirical site amplification curves exploited in the EXSIM code all over the station sample in sedimentary basins, we calculated the bias of the model as the logarithm (base n) of the ratio of the observed to the simulated following **Eq. 10**: it is an indication of the difference in the frequency domain between simulated and observed ground motion. In the top panels in **Figure 5**, we plot the bias versus frequency for both acceleration (panel A) and velocity (panel C) spectra. Colored curves represent the bias obtained between observed and simulated spectra by applying the generic site (red), GIT (green), HVSR (cyan), and HVNSR (violet) site curves. The standard deviation is plotted as well. An overall bias reduction is achieved using the GIT site curve, whose performance is better than the generic one at low (0.5–1.5 Hz) and high frequencies (>10 Hz). This is quite evident

in the bias related to velocity spectra (**Figure 5B**) and to the peak ground velocity (PGV, **Figure 5D**), where it is lower than 0.5. Moreover, at high frequencies (>10 Hz) there is a tendency in all empirical curves for the bias reduction, that can be ascribed to the implicit inclusion of the attenuation effect in empirical curves. Conversely, in generic curves attenuation was not derived but only hypothesized through the application of the κ_0 parameter, arbitrarily assigned on the basis of the site class (**Section 2**).

3.2 Stations on Topography

To investigate the topographic effects on the earthquake-induced ground motions, we have considered 18 stations located on topographic irregularities (middle slope or top), mainly belonging to class A (V_{s30} > 800 m/s) and class B (360 < V_{s30} > 800 m/s), as prescribed by the Italian NTC18 seismic design code.

Figure 6 shows two examples, both stations belonging to seismic network IV. The former (panel A) is station GAG1 (B site class), installed in Gagliole (Marche region), a village built in the Middle-Age on the top of a 1,000 m high hill. The historic center retains the original urban structure with the ancient medieval castle, the walls dating back to the 14th century, some ancient churches, and a monastic complex dated back to the 12th century. The GIT site amplification curves show overall higher amplitudes than both the HVSR and generic ones, with a peak at about 3.5 Hz. Its use led to achieving synthetic spectra more consistent with observed ones.

The second example (**Figure 6B**) is station MURB, installed on the top of Monte Urbino, an 800 m-high uninhabited hill in the Umbria region. While the generic site curve (related to B class) attains amplitude levels lower than 2 (see also **Supplementary Figure S2**, green-dotted curve), the three-empirical site curves (GIT, HVSR, and HVNSR) show a similar trend, with an amplitude up to eight peaks between 3 and 4 Hz. We, therefore, got synthetic spectra more consistent with observed ones between 2 and 5 Hz. Finally, through the use of the HVNSR curve, synthetic signals better reproduce the observed spectral trend even at high frequencies (>10 Hz).

In the **Supplementary Material**, we show four other study cases. While station FEMA is located on an uninhabited prominent ridge (over 1,500 m high), stations MMP1, PIEI, and TLN are close to small towns and have less prominent topography. All stations site curves show peaks at site-specific frequencies (about 10 Hz at FEMA; 1.5–3 Hz at MMP1; about 3 and 10 Hz at PIEI; about 2 Hz at TLN). This led to generally obtaining synthetic spectra more similar to observations in these frequency bands. Moreover, as for stations in sedimentary basins, at high frequencies (>10 Hz) the use of empirical site curves led to achieving a spectral trend more consistent with observed data. This is particularly evident at station FEMA, where the use of the GIT curve derived from the Amatrice earthquake (turquoise) led to a better fit of the velocity Fourier spectra at 2 Hz, where a prominent peak is observed. Finally, at station MMP1, empirical curves led to overestimating observation, so the generic site curves became more appropriate.

In **Figure 7**, similar to **Figure 5**, we plot the bias following **Eq. 10** to get an indication of the difference in the frequency domain between simulated and observed ground motion. At high frequencies (>10 Hz) empirical site curves (HVSR and GIT) are more performant in producing a better fit with data. In fact, while they led to bias values lower than 0.5, the use of the generic curve is associated with bias values increasing from 0.5 to 1 from 10 to 25 Hz. Conversely, at low frequencies, no improvements are observed in the use of empirical site curves. Finally, observed PGA and PGV values are slightly but systematically underestimated and overestimated by the simulations.

3.3 Stations on the Rock Site

To study the site amplification effect of the rocks we utilized five stations installed on rock and related to site class A. However the HVSR and HVNSR amplification curves, published on the ITACA database, unexpectedly highlight the presence of peaks over a factor of three at intermediate frequencies (between 1 and 10 Hz), where we consider no amplification.

In **Figure 8A**, we show station LSS as an example of a reference rock site (i.e., no site amplification) installed on Mesozoic limestone lithotypes. All site curves (both generic and empirical) show amplitudes lower than a factor of 1.5, the difference between them being small without sharp peak/s at certain frequencies. Therefore, no differences are observed on synthetic velocity Fourier spectra when using the different site curves. Conversely, SPM is an exemplificative station for site amplification on rock sites (**Figure 8B**). It is installed on Mesozoic limestone, in an intensely tectonized zone, and at the middle slope of a hill. Empirical site curves show an amplitude exceeding three peaks at about 5 Hz. However, visually speaking, we may say that the GIT curves lead to better reproduction of observed Fourier spectra, particularly at frequencies higher than 5 Hz.

In **Supplementary Figure S7**, we furnish two other examples. The former (panel A) is represented by station ANT, installed in the town of Antrodoco (Latium region) on dolomite lithotypes and in an intensely tectonized area. Using empirical site curves HVSR and HVNSR (showing the amplitude of three peaks at about 2 Hz) led to overestimating observed velocity Fourier spectra, while by using the GIT curve simulated Fourier spectra they are consistent with observed data, especially at high frequencies. Moreover, the use of the GIT curve derived only using the Amatrice earthquake led to better reproduction of observed ground-motion levels. The same findings are shown at station PSC (**Figure 8B**) installed in Pescasseroli village (Abruzzi region) on calcarenites.

4 CONCLUSION

We produced synthetic broadband seismograms using a hybrid simulation technique for the M_w6.0 Amatrice earthquake, Central Italy, on 24 August 2016, following the previous work of Pischiutta et al. (2021). In the present study, we focused on the site amplification parameters and tried to understand their

impact on ground motions with the aim to improve the hazard assessment for seismic risk reductions, particularly in urban areas in the central Apennines. To do so, the 57 stations selected, mainly located in urban areas, are potentially prone to experience site amplification effects because of lying in particular site conditions (sedimentary basins, topographic irregularities, and fault zones).

In this work, we tested the use of different empirical amplification curves, such as horizontal-to-vertical spectral ratios (calculated using both earthquakes, HVSR, and ambient noise recordings, HVNSR), and site curves derived from the generalized inversion technique (GIT) to improve our simulations. The latter were derived by using 455 earthquakes that occurred in Central Italy (Morasca et al., 2022). We also tested the use of the GIT curve derived only by the Amatrice earthquake. Their performance was linked to the generic curves by comparing the goodness of fit with recorded data. In general, we observed the following:

- In sedimentary basins, the presence of superficial soft sediments and strong shear-wave velocity and impedance contrasts leads to strong amplification due to refraction of seismic waves by an underlying stiff bedrock and subsequent phase constructive interference causing a resonance effect. We found that at the 22 stations in sedimentary basins selected in this study, empirical site curves led to a better fit with the data. They include amplitude peaks at site-characteristic frequencies, which depend on the superficial mean shear-wave velocities and the depth of the velocity contrast. In particular, the GIT site curve was most performant among the empirical adopted curves, achieving the best fit between observed and simulated velocity Fourier spectra. The GIT curve derived only by the Amatrice earthquake is more performant than the one derived as an average among considered earthquake data set in Morasca et al., 2022, suggesting that site correction may be scenario-dependent.
- An overall bias reduction is achieved using the GIT site curve, whose performance is better than the generic one. This behavior is quite evident on velocity spectra both at (i) low frequencies (0.5–1.5 Hz), where amplification effects are generally realized in deep sedimentary basins (hundreds of meters); (ii) high frequencies (>10 Hz), since all empirical curves implicitly include the attenuation effect in empirical curves that is hypothesized on generic curves through the application of k_0 parameter, arbitrarily assigned on the basis of the site class. However, due to the limitation intrinsic to the 1D stochastic finite-fault approach implemented in this study, our simulations could not reproduce wave reverberation across the sedimentary body, visible at stations installed in the middle of the basins on time histories as low-frequency coda phases.
- Amplification effects occur on the top of reliefs, due to the constructive interference of seismic waves diffracted by the convex topography. Almost certainly, a significant role is played by the local velocity distribution and subsoil structure. This study selects 18 stations installed on topography at which empirical site curves show peaks at different frequencies which depend on site specificities. As for stations in sedimentary basins, even at these sites, the use of empirical curves led to achieving a spectral trend more consistent with observed data at high frequencies (>10 Hz). Conversely, at low frequencies, no general improvements are observed in the use of empirical site curves. In fact, each site shows its own peculiar behavior, and a preferential empirical/generic curve leading to achieving synthetic motion more consistent with observed data.
- Rock sites are considered to be unaffected by site amplification. Nevertheless, many recent studies have highlighted that seismic waves can be amplified due to the local properties of the rock (i.e., the presence of pervasive fractures and/or large open cracks). We investigate five stations installed on rock and related to site class A, where empirical site curves highlight the occurrence of amplification effects at intermediate frequencies (between 1 and 10 Hz). Again, we found that the GIT empirical site curves led to obtaining synthetic spectra more consistent with observed ones. This is particularly evident when using the GIT site curve derived only from the Amatrice earthquake suggesting that site correction may be scenario-dependent.

Similar efforts have been shown in different parts of the world. For example, recently Zhu et al. (2022a) have tested and compared the effectiveness of different estimation techniques using a unique benchmark dataset at 1725 K-NET and KiK-net sites, in Japan. Evaluated prediction approaches included: 1) the empirical correction to the horizontal-to-vertical spectral ratio of earthquakes (c-HVSR, see also Kawase et al., 2019 and Zhu et al., 2020); 2) one-dimensional ground response analysis (GRA); 3) the square-root-impedance (SRI) method (also called the quarter wavelength approach). They found that, at the majority of analyzed sites, the empirical correction to HVSR was highly effective in achieving a "good match" in both spectral shape and amplitude. Since this technique has great potential in seismic hazard assessments, even considering that it does not require a velocity model, its use could be evaluated in similar further tests involving hybrid simulations.

We finally stress that, due to the 1D stochastic finite-fault approach implemented in this study, our simulations could not reproduce several scattering and resonance effects. 3D deterministic approaches may rather enhance the ground motion simulations in the sedimentary basins and the presence of topography (Pitarka et al., 2022). Moreover, many studies present clear evidence of rupture directivity in the M_w6.0 2016 Amatrice earthquake, Central Italy (e.g., Calderoni et al., 2017; Ren et al., 2017). However, the method used in this study, the stochastic model through the EXSIM code (Motazedian and Atkinson, 2005; Boore, 2009), is a simplistic model and dismisses the effect of rupture directivity on the azimuth dependent variability of ground motions. Although our simulations at low frequencies capture the directivity effect (Tinti et al., 2016; Pischiutta et al., 2021), the goodness of fit between simulated and observed ground motions might be biased for some of the stations only at higher frequencies.

DATA AVAILABILITY STATEMENT

Publicly available datasets were analyzed in this study. This data can be found at: https://itaca.mi.ingv.it/ItacaNet_32/#/home.

AUTHOR CONTRIBUTIONS

MP, AA, and FP contributed to the conception and design of the study. MP and CF organized the database. CF and PM furnished the site amplification curves adopted in this study. MP and AA wrote the first draft of the manuscript. FP wrote sections of the manuscript. All authors contributed to manuscript revision and read and approved the submitted version.

SUPPLEMENTARY MATERIAL

The Supplementary Material for this article can be found online at: https://www.frontiersin.org/articles/10.3389/feart.2022.886606/full#supplementary-material

REFERENCES

Aki, K., and Chouet, B. (1975). Origin of Coda Waves: Source, Attenuation, and Scattering Effects. *J. Geophys. Res.* 80, 3322–3342. doi:10.1029/jb080i023p03322

Akinci, A., Aochi, H., Herrero, A., Pischiutta, M., and Karanikas, D. (2017). Physics-Based Broadband Ground-Motion Simulations for ProbableMw≥7.0 Earthquakes in the Marmara Sea Region (Turkey). *Bull. Seismol. Soc. Am.* 107 (3), 1307–1323. doi:10.1785/0120160096

Akinci, A., Cheloni, D., and Dindar, A. A. (2021). The 30 October 2020, M7.0 Samos Island (Eastern Aegean Sea) Earthquake: Effects of Source Rupture, Path and Local-Site Conditions on the Observed and Simulated Ground Motions. *Bull. Earthq. Eng.* 19, 4745–4771. doi:10.1007/s10518-021-01146-5

Anderson, J. G., and Hough, S. E. (1984). A Model for the Shape of the Fourier Amplitude Spectrum of Acceleration at High Frequencies. *Bull. Seismol. Soc. Am.* 74 (5), 1969–1993. doi:10.1785/BSSA0740051969

Andrews, D. J. (1986). Objective Determination of Source Parameters and Similarity of Earthquakes of Different Size. *Earthq. Source Mech.* 37, 259–267. doi:10.1029/GM037p0259

Ben-Zion, Y., and Sammis, C. G. (2003). Characterization of Fault Zones. *Pure Appl. Geophys.* 160, 677–715. doi:10.1007/pl00012554

Bindi, D., Pacor, F., Luzi, L., Puglia, R., Massa, M., Ameri, G., et al. (2011). Ground Motion Prediction Equations Derived from the Italian Strong Motion Database. *Bull. Earthq. Eng.* 9 (6), 1899–1920. doi:10.1007/s10518-011-9313-z

Bindi, D., Parolai, S., Cara, F., Di Giulio, G., Ferretti, G., Luzi, L., et al. (2009). Site Amplifications Observed in the Gubbio Basin, Central Italy: Hints for Lateral Propagation Effects. *Bull. Seismol. Soc. Am.* 99 (2A), 741–760. doi:10.1785/0120080238

Bonamassa, O., and Vidale, J. E. (1991). Directional Site Resonances Observed from Aftershocks of the 18 October Loma Prieta Earthquake. *Bull. Seism. Soc. Am.* 81 (5), 1945–1957. doi:10.1785/BSSA0810051945

Boore, D. M. (2005). SMSIM—Fortran Programs for Simulating Ground Mo- tions from earthquakes: Version 2.3—A Revision of OFR 96-80-A. Available at: http://www.daveboore.com/smsim.

Boore, D. M. (2009). Comparing Stochastic Point-Source and Finite-Source Ground-Motion Simulations: SMSIM and EXSIM. *Bull. Seismol. Soc. Am.* 99, 3202–3216. doi:10.1785/0120090056

Boore, D. M. (2016). Determining Generic Velocity and Density Models for Crustal Amplification Calculations, with an Update of the Boore and Joyner (1997) Generic Site Amplification for VS(30) = 760 M/s. *Bull. Seismol. Soc. Am.* 106, 316–320. doi:10.1785/0120150229

Boore, D. M., Joyner, W. B., and Fumal, T. E. (1994). Estimation of Response Spectra and Peak Accelerations from Western North American Earthquakes: an Interim Report, Part 2. *U.S. Geol. Surv. Open-File rept.* 94–127, 40. doi:10.3133/ofr94127

Boore, D. M., and Joyner, W. B. (1997). Site Amplifications for Generic Rock Sites. *Bull. Seismol. Soc. Am.* 87, 327–341. doi:10.1785/bssa0870020327

Boore, D. M. (2003). Simulation of Ground Motion Using the Stochastic Method. *Pure Appl. Geophys.* 160, 635–676. doi:10.1007/pl00012553

Boore, D. M. (2013). The Uses and Limitations of the Square-Root-Impedance Method for Computing Site Amplification. *Bull. Seismol. Soc. Am.* 103, 2356–2368. doi:10.1785/0120120283

Boore, D. M., Thompson, E. M., and Cadet, H. (2011). Regional Correlations of VS30 and Velocities Averaged over Depths Less Than and Greater Than 30 Meters. *Bull. Seismol. Soc. Am.* 101, 3046–3059. doi:10.1785/0120110071

Burjánek, J., Edwards, B., and Fäh, D. (2014a). Empirical Evidence of Local Seismic Effects At Sites With Pronounced Topography: A Systematic Approach *Geophys. J. Intern.* 197 (1), 608–619. doi:10.1093/gji/ggu014

Burjanek, J., Fäh, D., Pischiutta, M., Rovelli, A., Calderoni, G., and Bard, P.-Y. (2014b). "NERA-JRA1 Working Group," in *Site Effects at Sites with Pronounced Topography: Overview & Recommendations* (Research report for EU project NERA), 64.

Burjánek, J., Moore, J. R., Yugsi Molina, F. X., and Fäh, D. (2012). Instrumental Evidence of Normal Mode Rock Slope Vibration. *Geophys. J. Int.* 188 (2), 559–569. doi:10.1111/j.1365-246x.2011.05272.x

Calderoni, G., Rovelli, A., and Di Giovambattista, R. (2017). Rupture Directivity of the Strongest 2016-2017 Central Italy Earthquakes. *J. Geophys. Res. Solid Earth* 122, 9118–9131. doi:10.1002/2017jb014118

Camassi, R., Azzaro, R., and Tertulliani, A. (2008). Macroseismology: the Lessons Learnt from the 1997/1998 Colfiorito Seismic Sequence. *Ann. Geophys.* 51 (2/3). doi:10.4401/ag-4453

Campbell, K. W., and Boore, D. M. (2016). Evaluation of Six NEHRP B/C Crustal Amplification Models Proposed for Use in Western North America. *Bull. Seismol. Soc. Am.* 106, 673–686. doi:10.1785/0120150242

Castro, R. R., Anderson, J. G., and Singh, S. K. (1990). Site Response, Attenuation and Source Spectra of S Waves along the Guerrero, Mexico, Subduction Zone. *Bull. Seismol. Soc. Am.* 80, 1481–1503. doi:10.1785/BSSA08006A1481

Chiara, F., Giovanni, L., Maria, D. A., Rodolfo, P., Lucia, L., and Francesca, P. (2018). Ground Motion Model for Reference Rock Sites in Italy. *Soil Dyn. Earthq. Eng.* 110, 276–283. doi:10.1016/j.soildyn.2018.01.024

Cornou, C., and Bard, P. Y. (2003). Site-to-bedrock over 1D Transfer Function Ratio: An Indicator of the Proportion of Edge-Generated Surface Waves? *Geophys. Res. Lett.* 30, 1453–1457. doi:10.1029/2002gl016593

Del Gaudio, C., De Risi, M. T., Ricci, P., and Verderame, G. M. (2019). Empirical Drift-Fragility Functions and Loss Estimation for Infills in Reinforced Concrete Frames under Seismic Loading. *Bull. Earthq. Eng.* 17, 1285–1330. doi:10.1007/s10518-018-0501-y

Douglas, J., and Aochi, H. (2008). A Survey of Techniques for Predicting Earthquake Ground Motions for Engineering Purposes. *Surv. Geophys* 29, 187–220. doi:10.1007/s10712-008-9046-y

Falsaperla, S., Cara, F., Rovelli, A., Neri, M., Behncke, B., and Acocella, V. (2010). Effects of the 1989 Fracture System in the Dynamics of the Upper SE Flank of Etna Revealed by Volcanic Tremor Data: the Missing Link? *J. Geophys. Res.* 115 (B11306). doi:10.1029/2010JB007529

Field, E., and Jacob, K. (1995). A Comparison and Test of Various Site-Response Estimation Techniques, Including Three that Are Not Reference-Site Dependent. *Bull. Seismol. Soc. Am.* 85 (4), 1127–1143. doi:10.1785/BSSA0850041127

Galli, P., Peronace, E., Bramerini, F., Castenetto, S., Naso, G., Cassone, F., et al. (2016b). The MCS Intensity Distribution of the Devastating 24 August

2016 Earthquake in Central Italy (MW 6.2). *Ann. Geophys* 59. doi:10.4401/ag-7287

Galli, P., Peronace, E., and Tertulliani, A. (2016a). Rapporto sugli effetti macrosismici del terremoto del 24 agosto 2016 di Amatrice in scala MCS, Roma, Rapporto congiunto DPC, CNRIGAG, 15. doi:10.5281/zenodo.161323

Géli, L., Bard, P.-Y., and Jullien, B. (1988). The Effect of Topography on Earthquake Ground Motion: a Review and New Results. *Bull. Seism. Soc. Am.* 78 (1), 42–63. doi:10.1785/BSSA0780010042

Goulet, C. A., Abrahamson, N. A., Somerville, P. G., and Wooddell, K. E. (2015). The SCEC Broadband Platform Validation Exercise: Methodology for Code Validation in the Context of Seismic-Hazard Analyses. *Seismol. Res. Lett.* 86 (1), 17–26. doi:10.1785/0220140104

Graves, R. W. (1995). Preliminary Analysis of Long-Period Basin Response in the Los Angeles Region from the 1994 Northridge Earthquake. *Geophys. Res. Lett.* 22 (2), 101–104. doi:10.1029/94gl02894

Iwata, T., Hatayama, K., Kawase, H., and Irikura, K. (1996). Site Amplification of Ground Motions during Aftershocks of the 1995 Hyogo-Ken Nanbu Earthquake in Severely Damaged Zone. *J. Phys. Earth* 44 (5), 553–561. doi:10.4294/jpe1952.44.553

Joyner, W., and Fumal, T. (1984). Use of Measured Shear-Wave Velocity for Predicting Geologic Site Effects on Strong Ground Motion. *Proc. 8th world conf. Earthq. Eng.* 2, 777–783.

Kaiser, A., Massey, C., Pischiutta, M., Fry, B., and Nicol, A. (2022). *Quantifying Seismic Amplification on Topography in New Zealand and its Relationship to Landslide Occurrence: First Steps under New Zealand's Resilience Challenge Programme*. Bellevue, Washington: Sesmological Society America Annual Meeting.

Kawase, H., Nagashima, F., Nakano, K., and Mori, Y. (2019). Direct Evaluation of S-Wave Amplification Factors from Microtremor H/V Ratios: Double Empirical Corrections to "Nakamura" Method. *Soil Dyn. Earthq. Eng.* 126, 105067. doi:10.1016/j.soildyn.2018.01.049

Lachetl, C., and Bard, P.-Y. (1994). Numerical and Theoretical Investigations on the Possibilities and Limitations of Nakamura's Technique. *J. Phys. Earth* 42 (5), 377–397. doi:10.4294/jpe1952.42.377

Lanzano, G., Felicetta, C., Pacor, F., Spallarossa, D., and Traversa, P. (2022). Generic-to-reference Rocks Scaling Factors for the Seismic Ground Motion in Italy. *Bull. Seismol. Soc. Am.*. (accepted), 1–24. doi:10.1785/0120210063

Lanzano, G., Felicetta, C., Pacor, F., Spallarossa, D., and Traversa, P. (2020). Methodology to Identify the Reference Rock Sites in Regions of Medium-To-High Seismicity: an Application in Central Italy. *Geophys. J. Int.* 222 (3), 2053–2067. doi:10.1093/gji/ggaa261

Lewis, M. A., and Ben-Zion, Y. (2010). Diversity of Fault Zone Damage and Trapping Structures in the Parkfield Section of the San Andreas Fault from Comprehensive Analysis of Near Fault Seismograms. *Geophys. J. Int.* 183, 1579–1595. doi:10.1111/j.1365-246x.2010.04816.x

Licia Faenza, L., Valentino Lauciani, V., and Alberto Michelini, A. (2016). The ShakeMaps of the Amatrice, M6, Earthquake. *Ann. Geophys.* 59. FAST TRACK 5. doi:10.4401/ag-7238

Mai, P. M., and Beroza, G. C. (2003). A Hybrid Method For Calculating Near Source, Broadband Seismograms: Application To Strong Motion Prediction *Phys. Earth Planet. Inter.* 137 (1/4), 183–199. doi:10.1016/S0031-9201(03)00014-1

Malagnini, L., Akinci, A., Mayeda, K., Munafo', I., Herrmann, R. B., and Mercuri, A. (2011). Characterization of Earthquake-Induced Ground Motion from the L'Aquila Seismic Sequence of 2009, Italy. *Geophys J. Int.* 184 (1), 325–337. doi:10.1111/j.1365-246x.2010.04837.x

Malagnini, L., and Munafò, I. (2018). On the Relationship between M_L and M_W in a Broad Range: An Example from the Apennines, Italy. *Bull. Seism. Soc. Am.* 108 (2), 1018–1024. doi:10.1785/0120170303

Zanini, M. A., Lorenzo Hofer, L., Flora Faleschini, F., Paolo Zampieri, P., Nicola Fabris, N., and Carlo Pellegrino, C. (2016). Preliminary Macroseismic Survey of the 2016 Amatrice Seismic Sequence. *Ann. Geophys.* 59. Fast Track 5. doi:10.4401/ag-7172

Martino, S., Minutolo, A., Paciello, A., Rovelli, A., Mugnozza, G. S., and Verrubbi, V. (2006). Evidence of Amplification Effects in Fault Zone Related to Rock Mass Jointing. *Nat. Hazards* 39, 419–449. doi:10.1007/s11069-006-0001-2

Marzorati, S., Ladina, C., Falcucci, E., Gori, S., Saroli, M., Ameri, G., et al. (2011). Site Effects "on the Rock": the Case of Castelvecchio Subequo (L'Aquila, Central Italy). *Bull. Earthq. Eng.* 9, 841–868. doi:10.1007/s10518-011-9263-5

Michelini, A., Faenza, L., Lauciani, V., and Malagnini, L. (2008). Shakemap Implementation in Italy. *Seismol. Res. Lett.* 79, 688–697. doi:10.1785/gssrl.79.5.688

Moore, J. R., Gischig, V., Burjanek, J., Loew, S., and Fah, D. (2011). Site Effects in Unstable Rock Slopes: Dynamic Behavior of the Randa Instability (Switzerland). *Bull. Seismol. Soc. Am.* 101 (6), 3110–3116. doi:10.1785/0120110127

Molnar, S., Cassidy, J. F., Castellaro, S., Cornou, H., Crow, J. A., Hunter, S., et al. (2018). Application of Microtremor Horizontal-to-Vertical Spectral Ratio (MHVSR) Analysis for Site Characterization: State of the Art *Surv. Geophys.* 39, 613–631. doi:10.1007/s10712-018-9464-4

Morasca, P., D'Amico, M., Lanzano, G., Sgobba, S., Colavitti, L., Pacor, F., et al. (2022). Empirical Correlations between a FAS Non-ergodic Ground Motion Model and a GIT Derived Model for Central Italy. *Geophys. J. Int.*. (in prep.).

Motazedian, D., and Atkinson, G. M. (2005). Stochastic Finite-Fault Modeling Based on a Dynamic Corner Frequency. *Bull. Seismol. Soc. Am.* 95, 995–1010. doi:10.1785/0120030207

NEHRP Building Seismic Safety Council (2015). "NEHRP Recommended Seismic Provisions for New Buildings and Other Structures," in *Part 1 Provisions, Part 2 Commentary, FEMA Rept*. 2015 Edition (Washington, D.C: National Institute of Building Sciences), 1, P-1050-1051.

NTC18 (2018). Italian building code 'Norme Tecniche per le Costruzioni – Ministero delle Instrutture e dei Trasporti. Available at: https://www.gazzettaufficiale.it/eli/gu/2018/02/20/42/so/8/sg/pdf. (Accessed December 2020).

NZS (2004). *Standards New Zealand 2004. Structural Design Actions—Part 5 Earthquake Actions—New Zealand*. Standards New Zealand. Private Bag 2439, Wellington 6020. ISBN 1-86975-018-7 (incorporating Amendment 1 (following Canterbury Earthquake Sequence). Available at: https://www.standards.govt.nz/shop/nzs-1170-52004/.

Ojeda, J., Akinci, A., Tinti, E., Arriola, S., and Ruiz, S. (2021). Hybrid Broadband Strong-Motion Simulation to Investigate the Near-Source Characteristics of the M6.5, 30 October 2016 Norcia, Italy Earthquake. *Soil Dyn. Earthq. Eng.* 149, 106866. doi:10.1016/j.soildyn.2021.106866

Panzera, F., Pischiutta, M., Lombardo, G., Monaco, C., and Rovelli, A. (2014). Wavefield Polarization in Fault Zones of the Western Flank of Mt. Etna: Observations and Fracture Orientation Modelling. *Pure Appl. Geophys.* 171, 3083–3097. doi:10.1007/s00024-014-0831-x

Pischiutta, M., Akinci, A., Tinti, E., and Herrero, A. (2020). Broad-band Ground-Motion Simulation of 2016 Amatrice Earthquake, Central Italy. *Cent. Italy. Geophys. J. Int.* 224, 1753–1779. doi:10.1093/gji/ggaa412

Pischiutta, M., Cianfarra, P., Salvini, F., Cara, F., and Vannoli, P. (2018). A Systematic Analysis of Directional Site Effects at Stations of the Italian Seismic Network to Test the Role of Local Topography. *Geophys. J. Int.* 214 (1), 635–650. doi:10.1093/gji/ggy133

Pischiutta, M., Fondriest, M., Demurtas, M., Magnoni, F., Di Toro, G., and Rovelli, A. (2017). Structural Control on the Directional Amplification of Seismic Noise (Campo Imperatore, Central Italy). *Earth Planet. Sci. Lett.* 471, 10–18. doi:10.1016/j.epsl.2017.04.017

Pischiutta, M., Salvini, F., Fletcher, J., Rovelli, A., and Ben-Zion, Y. (2012). Horizontal Polarization of Ground Motion in the Hayward Fault Zone at Fremont, California: Dominant Fault-High-Angle Polarization and Fault-Induced Cracks. *Geophys. J. Int.* 188 (3), 1255–1272. doi:10.1111/j.1365-246x.2011.05319.x

Pischiutta, M., Savage, M. K., Holt, R. A., and Salvini, F. (2015). Fracture-related Wavefield Polarization and Seismic Anisotropy across the Greendale Fault. *J. Geophys. Res. Solid Earth* 120, 7048–7067. doi:10.1002/2014jb011560

Pitarka, A., Akinci, A., De Gori, P., and Buttinelli, M. (2022). Deterministic 3D Ground-Motion Simulations (0-5 Hz) and Surface Topography Effects of the 30 October 2016 Mw 6.5 Norcia, Italy, Earthquake. *Bull. Seismol. Soc. Am.* 112 (1), 262–286. doi:10.1785/0120210133

Priolo, E., Pacor, F., Spallarossa, D., Milana, G., Laurenzano, G., Romano, M. A., et al. (2019). Seismological Analyses of the Seismic Microzonation of

138 Municipalities Damaged by the 2016–2017 Seismic Sequence in Central Italy. *Bull. Earthq. Eng.* 18 (12), 1–41. doi:10.1007/s10518-019-00652-x

Quest, W. G., Raffaele, A., Andrea, T., Filippo, B., Romano, C., Sergio Del, M., et al. (2016). The 24 August 2016 Amatrice Earthquake: Macroseismic Survey in the Damage Area and EMS Intensity Assessment. *Ann. Geophys.* 59. fast track 5. doi:10.4401/ag-7203

Ren, Y., Wang, H., and Wen, R. (2017). Imprint of Rupture Directivity from Ground Motions of the 24 August 2016 M W 6.2 Central Italy Earthquake. *Tectonics* 36, 3178–3191. doi:10.1002/2017tc004673

Russo, E., Felicetta, C., D' Amico, M., Sgobba, S., Lanzano, G., Mascandola, C., et al. (2022). "Italian Accelerometric Archive v3.2 - Istituto Nazionale di Geofisica e Vulcanologia," in *Dipartimento Della Protezione Civile Nazionale*. doi:10.13127/itaca.3.2

Sánchez-Sesma, F., Chávez-Pérez, S., Suàrez, M., Bravo, M. A., and Pérez-Rocha, L. E. (1988). The Mexico Earthquake of September 19, 1985—On the Seismic Response of the Valley of Mexico. *Earthq. Spectra* 4 (3), 569–589. doi:10.1193/1.1585491

Sextos, A., De Risi, R., Pagliaroli, A., Foti, S., Passeri, F., Ausilio, E., et al. (2018). Local Site Effects and Incremental Damage of Buildings during the 2016 Central Italy Earthquake Sequence. *Earthq. Spectra* 34 (4), 1639–1669. doi:10.1193/100317eqs194m

Sgobba, S., Lanzano, G., and Pacor, F. (2020). Empirical Nonergodic Shaking Scenarios Based on Spatial Correlation Models: An Application to Central Italy. *Earthq. Engng Struct. Dyn.* 50, 60–80. doi:10.1002/eqe.3362

Tinti, E., Scognamiglio, L., Michelini, A., and Cocco, M. (2016). Slip Heterogeneity and Directivity of the ML 6.0, 2016, Amatrice Earthquake Estimated with Rapid Finite-Fault Inversion. *Geophys. Res. Lett.* 43, 10745–10752. doi:10.1002/2016gl071263

Wald, D. J., Quitoriano, V., Heaton, T. H., and Kanamori, H. (1999). Relationships between Peak Ground Acceleration, Peak Ground Velocity, and Modified Mercalli Intensity in California. *Earthq. Spectra* 15 (3), 557–564. doi:10.1193/1.1586058

Zhu, C., Cotton, F., Kawase, H., Haendel, A., and Nakano, K. (2022b). How Well Can We Predict Earthquake Site Response So Far? Machine Learning vs. *Physics-Based Modeling*. doi:10.13140/RG.2.2.34933.91365

Zhu, C., Cotton, F., Kawase, H., Haendel, A., Pilz, M., and Nakano, K. (2022a). How Well Can We Predict Earthquake Site Response So Far? Site-specific Approaches. *Earthq. Spectra* 38 (2), 1047–1075. doi:10.1177/87552930211060859

Zhu, C., Pilz, M., and Cotton, F. (2020). Which Is a Better Proxy, Site Period or Depth to Bedrock, in Modelling Linear Site Response in Addition to the Average Shear-Wave Velocity? *Bull. Earthq. Eng.* 18 (3), 797–820. doi:10.1007/s10518-019-00738-6

Conflict of Interest: The authors declare that the research was conducted in the absence of any commercial or financial relationships that could be construed as a potential conflict of interest.

Publisher's Note: All claims expressed in this article are solely those of the authors and do not necessarily represent those of their affiliated organizations, or those of the publisher, the editors, and the reviewers. Any product that may be evaluated in this article, or claim that may be made by its manufacturer, is not guaranteed or endorsed by the publisher.

frontiers | Frontiers in Earth Science

ORIGINAL RESEARCH
published: 14 June 2022
doi: 10.3389/feart.2022.915083

Seismo-Stratigraphic Model for the Urban Area of Milan (Italy) by Ambient-Vibration Monitoring and Implications for Seismic Site Effects Assessment

M. Massa, S. Lovati, R. Puglia, G. Brunelli, A. Lorenzetti, C. Mascandola, C. Felicetta, F. Pacor and L. Luzi*[1]

[1]National Institute of Geophysics and Volcanology (INGV), Milano, Italy

OPEN ACCESS

Edited by:
Roberto Paolucci,
Politecnico di Milano, Italy

Reviewed by:
Alessandro Vuan,
Istituto Nazionale di Oceanografia e di Geofisica Sperimentale, Italy
Maria Rosaria Gallipoli,
Institute of Methodologies for Environmental Analysis (IMAA), Italy

***Correspondence:**
M. Massa
marco.massa@ingv.it

Specialty section:
This article was submitted to Geohazards and Georisks, a section of the journal Frontiers in Earth Science

Received: 07 April 2022
Accepted: 19 May 2022
Published: 14 June 2022

Citation:
Massa M, Lovati S, Puglia R, Brunelli G, Lorenzetti A, Mascandola C, Felicetta C, Pacor F and Luzi L (2022) Seismo-Stratigraphic Model for the Urban Area of Milan (Italy) by Ambient-Vibration Monitoring and Implications for Seismic Site Effects Assessment. Front. Earth Sci. 10:915083. doi: 10.3389/feart.2022.915083

In this paper, we present the work carried out to characterize the spatial variability of seismic site response related to local soil conditions in the city of Milan and its surroundings, an area with ~3 million inhabitants and a high density of industrial facilities. The area is located at the northwestern end of the Po Plain, a large and deep sedimentary basin in northern Italy. An urban-scale seismo-stratigraphic model is developed based on new passive and active seismic data, supported by the available geological data and stratigraphic information from shallow and deep vertical wells. In particular, 33 single-station and 4 ambient-vibration array measurements are acquired, together with 4 active multichannel analyses of surface waves (*MAWS*). To estimate the resonant frequencies of the sediments, the horizontal to vertical spectral ratio technique (*HVSR*) is applied to the ambient-vibration recordings, whereas to determine the Rayleigh-wave dispersion curves from the passive array, the data are analysed using the conventional frequency-wavenumber, the modified spatial autocorrelation and the extended spatial autocorrelation (*ESAC*) techniques. The array data are used to determine the local shear wave velocity profiles, $V_{S,}$ via joint inversion of the Rayleigh-wave dispersion and ellipticity curves deduced from the *HVSR*. The results from *HVSR* show three main bands of amplified frequencies, the first in the range 0.17–0.23 Hz, the second from 0.45 to 0.65 Hz and the third from 3 to 8 Hz. A decreasing trend of the main peaks is observed from the northern to the southern part of the city, allowing us to hypothesize a progressive deepening of the relative regional chrono-stratigraphic unconformities. The passive ambient noise array and *MASW* highlight the dispersion of the fundamental mode of the Rayleigh-wave in the range 0.4–30 Hz, enabling to obtain detailed Vs. profiles with depth down to about 1.8 km. The seismo-stratigraphic model is used as input for 1D numerical modelling assuming linear soil conditions. The theoretical 1D transfer functions are compared to the *HVSR* curves evaluated from both ambient noise signals and earthquake waveforms recorded by the IV. MILN station in the last 10 years.

Keywords: milan (Italy), seismic site characterisation, seismostratigrahic model, vs. velocity profile, seismic array, MASW, HVSR (horizontal to vertical spectral ratio), 1D numerical modeling

INTRODUCTION

It is widely recognized that a significant proportion of the variability of earthquake ground motion is related to local geological conditions, which can modify the ground-motion amplitude, duration, and frequency. In alluvial basins (or valleys), layers can cause resonance of vertically propagating shear waves at specific frequencies and/or trap surface waves generated locally at the edges of the basin (e.g., Hanks, 1975; Hisada et al., 1993; Bielak et al., 1999; Sato et al., 1999; Joyner, 2000; Kagawa et al., 2004; Somerville et al., 2004; D'Amico et al., 2006; D'Amico et al., 2008; De Ferrari et al., 2010; Ronald Abraham et al., 2015).

In this framework and in particular for urban planning (e.g. Ansal et al., 2009; Ansal et al., 2010, Crespellani 2014, Celikbilek and Sapmaz 2016, Aversa and Crespellani 2016, etc.), the seismic site effect estimation plays a crucial role in earthquake risk reduction.

The importance of site characterization of urban or metropolitan areas is recognized worldwide, with several studies performed in New York (Stephenson et al., 2009), Taipei (Wang, 2008), Perth (Liang et al., 2009), Seoul (Sun et al., 2014; Kim et al., 2017), Beijing (Liu et al., 2014), Vancouver (Molnar et al., 2020), San Josè, Costa Rica (Moya et al., 2000), Istanbul (Picozzi et al., 2009; Ansal et al., 2010), Memphis (Schneider et al., 2001), Bucharest (Ritter et al., 2005), among others.

Similar studies in Italy are performed for other cities like Matera (Tragni et al., 2021), Rome (Marcucci et al., 2019), and Firenze (D'Amico et al., 2008), as well as small villages like Mirandola (Tarabusi and Caputo, 2017) and Cavezzo (Lai et al., 2020), both located in the Po plain and strongly struck

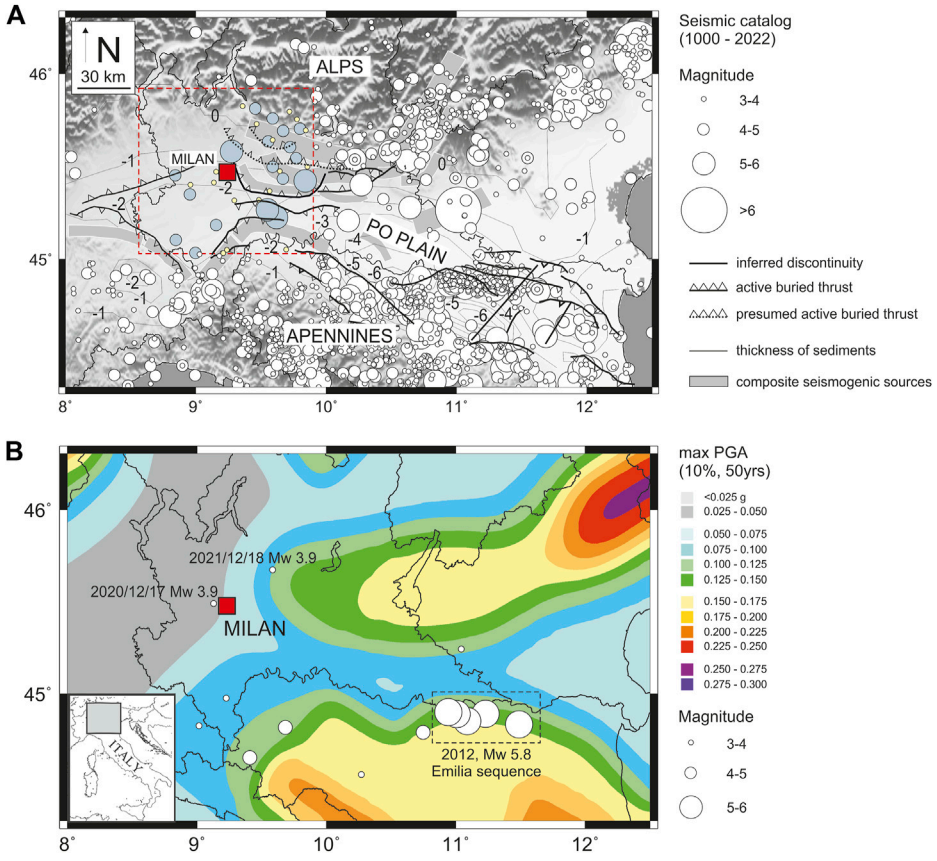

FIGURE 1 | Panel **(A)** simplified structural sketch of the Po plain (from Pieri and Groppi, 1981; Bigi et al., 1990). The red square indicates the urban area of Milan. White circles indicate the seismicity from yrs. 1000 to 2022. Dark gray and yellow circles drawn in the red inset indicate the recent (after 1 January 1985, http://terremoti.ingv.it/) and the historical seismicity (yrs. 1000–1985, https://emidius.mi.ingv.it/CPTI15-DBMI15/; Rovida et al., 2020), respectively, occurred in an area of 100 km^2 around the MMA. The composite seismogenic sources are derived from DISS (Database of Individual Seismogenis Sources, http://diss.ingv.it). Panel **(B)** Seismic hazard maps of Italy (MPS Working Group, 2004; Stucchi et al., 2011), in terms of peak ground acceleration (PGA) with 10% possibility of exceedance in 50 years (i.e., a return period of 475 years), referred to the rigid soils (i.e., *Vs*. > 800 m/s; NTC 2018). White circles indicate the epicenters of the earthquakes used for the *HVSR* analyses (see also **Table 1**).

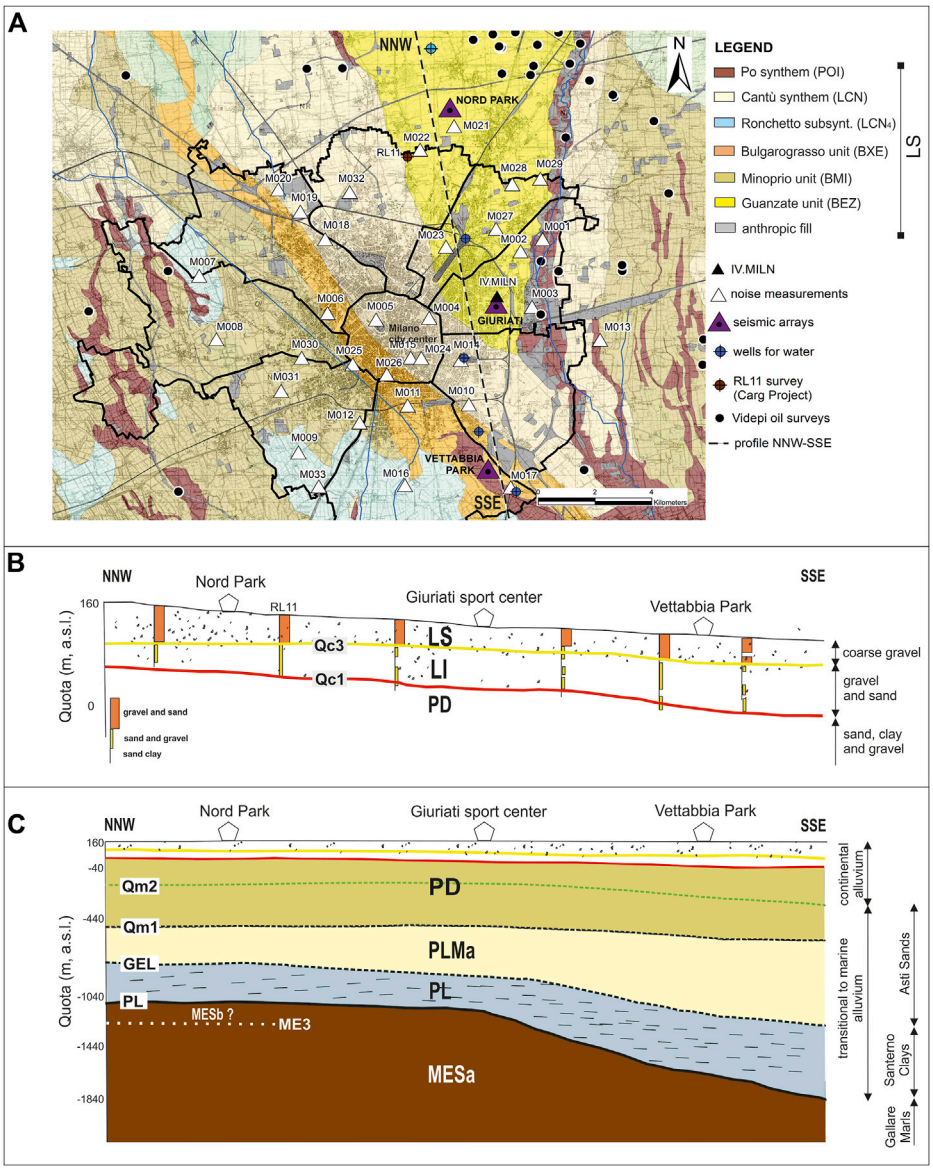

FIGURE 2 | Panel **(A)** 1:10000 Geological map from the 118 Milan sheet (ISPRA et al., 2016). Po synthem (POI, Upper Pleistocene-Holocene), Cantù synthem (LCN, Upper Pleistocene), Ronchetto delle Rane subsynthem (LCN_4, Upper Pleistocene), Bulgarograsso unit (BXE, Middle-Upper Pleistocene), Minoprio Unit (BMI, Middle-Upper Pleistocene) and Guanzate unit (BEZ, Middle-Upper Pleistocene) are the stratigraphic units characterizing the MMA (ISPRA et al., 2016). The dotted black line indicates the NNW-SSE geological section showed in panel **(B)**. Panel **(B)** geological section from North Park (NNW) to Vettabbia park (SSE), with thickness of about 200 m. Yellow line represents the Qc3 Unconformity from GeoMol Team, 2015 (or Y-Surface from Scardia et al., 2012), while red line represents the Qc1 Unconformity from GeoMol Team, 2015 (or R-Surface from Muttoni et al., 2003). LS and LI indicate the upper and lower Padano supersynthem, while PD indicates the Padano supersynthem (ISPRA et al., 2016). Panel **(C)** geological section from North Park (NNW) to Vettabbia park (SSE), with thickness of about 1800 m. MESa (Burdigalian-Tortonian), MESb (Messinian), PL (early-middle Pliocene) and PLMa (Middle lower Pleistocene) indicate the stratigraphic units as recognized by GeoMol project (2015), while PL (base of Pliocene, 5,3 Myrs), GEL (base of Pleistocene, 2,6 Myrs), Qm1 (1,5 Myrs) and Qm2 (1,25 Myrs) represent the related unconformities. Dotted lines indicate the deduced depths on the basis of the ViDEPI project (2009) deep wells.

by the 2012 Emilia seismic sequence (Luzi et al., 2013). Worth mentioning is the intensive studies that have been performed after the 2016–2017 Central Italy seismic sequence (Michele et al., 2016) to obtain detailed microzonation maps in the 138 most damaged municipalities (Hailemikael et al., 2020).

In this paper, we focus on the city of Milan, with an area of about 1.570 km^2 and a population of more than 3 million (http://www.istat.it). Milan and its hinterlands represent the area with the highest density of industrial plants, service industries, skyscrapers and high-speed railways in Italy (http://www.istat.it). In particular, Milan is the Italian city that has grown more vertically through the construction of skyscrapers, at present with maximum height of ~230 m and 50 stories (https://en.wikipedia.org/wiki/List_of_tallest_buildings_in_Milan). Recently, a couple

of 5s seismometers, with reserved data, is installed at the floors −3 (i.e., −15 m from surface) and 37 (height ~140 m), respectively, of the skyscraper *Lombardia-building* (https://en.wikipedia.org/wiki/Palazzo_Lombardia), allowing us to preliminary recognize a natural periods of vibration of ~3.2 s.

The MMA (northern Italy, **Figure 1**, panel A) is located in the northwestern part of the Po Plain, one of the largest alluvial basins worldwide. The Po alluvial basin covers an area of about 50.000 km^2, with alluvial deposits that can reach a depth of several kilometers and that directly overlie the deep Miocene geological bedrock (Pieri and Groppi, 1981; Regione Lombardia, Eni Divisione Agip, 2002).

The bottom panel of **Figure 1** (panel B) shows the reference Italian seismic hazard map of Italy in terms of peak ground acceleration for rock-site conditions with 10% probability of exceedance in 50 years (MPS Working Group, 2004; Stucchi et al., 2011): despite the low-to-medium seismic hazard of the area, the exposure level of the city, the local geological condition (**Figure 2**) and the proximity with active buried seismogenic structure (**Figure 1**, panel A) make the MMA a medium to high seismic risk zone.

The studied area is, in general, characterized by a low rate of annual seismicity (**Figure 1**, panel A). In particular, in the last 40 years no local earthquakes with magnitude >4.5 have occurred. However, the area has often undergone ground motion over the long-period, namely in the case of distant earthquakes with higher magnitude, such as the 2012 Emilia, Mw 5.8, seismic sequence (Luzi et al., 2013).

The importance of the long-period (>1 s) component of seismic ground motion has been recognized worldwide during some strong earthquakes (e.g., 1985, Mw 8.1, Michoacán, Furumura and Kennett, 1998; Furumura and Kennett, 1999, Mw 7.1, Hector Mine, Grazier et al., 2002, Mw 7.9, Denali, Ratchkovski et al., 2003, Mw 8.0, Tokachi-Oki, Miyazaki et al., 2004). Significant damage to long-period structures at large hypocentral distances, as well as prolonged duration of seismic ground motion, has prompted seismologists to focus in understanding the seismic wave propagation and amplification effects in deep sedimentary basins. The Mexico City records of the 1985 Michoacan earthquake lead to far source long-period ground motions being known around the world, with long-period components between 2 and 4 s (Beck and Hall, 1986). Before the 1985 Michoacan earthquake, Japanese seismologists observed far-source long-period ground motion in the Niigata basin, during the 1964 Niigata, 1968 Tokachi-oki, and 1983 Japan Sea earthquakes (Koketsu and Miyake, 2008). Subsequently, the 2003 Tokachi-oki earthquake provided the southern coast of Hokkaido in Japan, with one of the most significant examples (Koketsu et al., 2005; Hatayama, 2008) of far-source long-period ground motion, with dominant amplitudes in the range 7–8 s and displacements of a few meters (Koketsu and Miyake, 2008).

Long-period ground motion amplification is a significant issue in the Po Plain. In this area, long-period resonance phenomena have been well-documented by many studies (e.g., Priolo et al., 2012; Luzi et al., 2013; Martelli and Romani, 2013; Massa and Augliera, 2013; Milana et al., 2013; Paolucci et al., 2015; Laurenzano et al., 2017; Mascandola et al., 2017; Tarabusi and Caputo, 2017). However, most of these are performed in the epicentral area of the 2012 Emilia seismic sequence (e.g., Luzi et al., 2013), during which significant ground-motion amplifications and increased duration are observed. A recent study by Mascandola et al. (2019) widely mapped 1–3 s long-period resonance phenomena in the Po Plain, through extensive ambient-vibration measurements performed in the basin.

This study attempts to investigate the influence of the shallow to deep (down ~1.8 km) alluvial deposits for the metropolitan area of Milan, where amplification effects in the frequency range 0.2–8 Hz are observed. Milan has the disadvantage of having few earthquake recordings due to the relatively low seismicity and distant reference sites in the Alps or in the Apennine Mountains (**Figure 1**, panel A). These features prevent applying the standard spectral ratio approach (SSR, Bocherdt, 1970) to compute the empirical soil amplification functions and lead to adopting techniques based on numerical modelling, which are more accurate the more detailed the seismo-stratigraphic model is.

Therefore, in this study a detailed seismo-stratigraphic model obtained from the analysis of existing geological and stratigraphic data (e.g., Regione Lombardia, Eni Divisione Agip, 2002; Muttoni et al., 2003; De Franco et al., 2009; ViDEPI project, 2009; Scardia et al., 2012; GeoMol Team, 2015; ISPRA et al., 2016) and newly acquired geophysical data is proposed.

Different active and passive seismic measurements are carried out to characterize the subsoil. The passive analyses represent the main part of the study, consisting of 33 single-station and 4 array measurements of ambient noise (**Figure 2**, panel A). The single-station measurements allowed defining the resonance frequency of the site through the Nakamura (1989) horizontal-to-vertical spectral ratio (*HVSR*) method. The microtremor arrays, performed in correspondence of three selected sites (i.e., North Park, Giuriati sports center, Vettabbia park) located along the alignment reported in **Figure 2** (panel A), enabled assessing vs. profiles down to depths of about ~1.8 km.

The active measurements consisted of 4 Multichannel Analyses of Surface Waves (*MASW*, Park et al., 1999) at North and Vettabbia public parks (**Figure 2**, panel A) which are useful to define the soil categories, according to the Italian (Nuove Norme Tecniche per le Costruzioni, NTC, 2018) and the European (Eurocode 8, CEN 2004) seismic codes for buildings. Soil categories are defined according to the values of the average seismic shear-wave velocity from the surface to a depth of 30 m ($V_{S,30}$).

The results obtained from ambient noise *HVSR* are compared to the HVSR curves considering 17 earthquakes with magnitude from 3.7 to 5.8 recorded by the IV. MILN station (**Figure 2**, panel B) in the last 10 years (**Table 1**).

The Vs profiles are finally validated through 1D numerical models performed assuming a linear elastic behaviour of the soil using the SHAKE91 code (Idriss and Sun, 1993).

Seismicity of the Area and Recorded Ground Motion

In the last 30 years, thousands of small-energy seismic events (~200/year, **Figure 1**, panel A, http://terremoti.ingv.it/) have

TABLE 1 | Earthquakes with magnitude ≥3.7 recorded at station IV.MILN in the last 10 years and used for the *HVSR* analyses. The epicentres are depicted in panel B) of **Figure 1**. In bold are indicated magnitude values > 5.

YYYY/MM/DD hh:mm:ss (UTC)	Lon (°)	Lat (°)	Depth (km)	Mw (ML)	Stat	REPI (km)
2012/02/29 15:34:57	9.0170	44.8240	6.50	3.7	IV.MILN	74
2012/05/20 02:03:50	11.2300	44.8900	6.30	5.8	IV.MILN	169
2012/05/20 13:18:02	11.4900	44.8310	4.70	5.1	IV.MILN	191
2012/05/29 07:00:02	11.0900	44.8500	10.20	5.6	IV.MILN	161
2012/05/29 10:55:57	11.0080	44.8880	6.80	5.3	IV.MILN	153
2012/06/03 19:20:43	10.9430	44.8990	9.20	5.1	IV.MILN	148
2018/05/19 16:41:21	9,684	44.8160	28.30	4.3	IV.MILN	81
2020/04/16 09:42:51	9.4087	44.6488	3.40	4.2	IV.MILN	93
2020/04/19 09:53:40	9.2257	44.9760	31.80	3.7	IV.MILN	56
2020/12/17 15:59:22	9.1282	45.4918	56.20	3.9	IV.MILN	8
2020/12/29 14:36:57	11.0425	45.2442	9.40	3.9	IV.MILN	143
2021/07/01 11:11:49	8.3508	46.6062	5.00	3.7	IV.MILN	142
2021/12/18 10:34:47	9.5860	45.6752	26.30	3.9	IV.MILN	35
2022/02/01 22:43:07	10.2703	44.5547	47.40	3.7	IV.MILN	131
2022/02/09 20:00:57	10.7470	44.7887	6.40	4.3	IV.MILN	141

occurred in the Po Plain. Except of the 20 May 2012, Mw 5.8, Emilia seismic sequence (Luzi et al., 2013), with epicenters located 170 km southeast of Milan, the western part of the Po Plain area underwent a few moderate events, with magnitude between 4.5 and 5.5, such as the 14th August 2000, Mw 4.8, Asti the 3rd April 2003, Mw 4.8, Novi Ligure, the 14th September 2003, Mw 5.2, Monghidoro, the 24th November 2004, Mw 5.2, Salò and the 23rd December 2008, Mw 5.4, Parma events (http://terremoti.ingv.it). These moderate earthquakes did not cause losses of human life, but had negative economic consequences amounting to hundreds of millions of Euros (e.g., damage to buildings, schools, churches, industrial facilities etc.) highlighting the high degree of exposure of the region.

Focusing on MMA, the most powerful events recorded in the last decades occurred on 17th December 2020 (Mw 3.9 at epicentral distance of 5 km, http://terremoti.ingv.it) and on 18th December 2021 (Mw 3.9 at epicentral distance of 35 km, http://terremoti.ingv.it). In particular, in the past 10 years, the station IV. MILN (http://terremoti.ingv.it/instruments/station/MILN), now installed at INGV Milan department, recorded 17 seismic events in the magnitude (Mw) range 3.7–5.8, with epicentral distances up to 200 km (**Table 1**). Considering the historical seismicity (Rovida et al., 2020; https://emidius.mi.ingv.it/CPTI15-DBMI15/), the more significant earthquakes that struck the MMA occurred along the buried thrust systems reported in **Figure 1** (panel A). The main seismogenic sources of the area (**Figure 1**, panel A) are derived from the Database of Individual Seismogenis Sources (DISS, http://diss.ingv.it). Considering 100 km^2 around MMA, (**Figure 1**, panel A), the main historical events occurred on 26th November 1369 (Monza, Mw 5.33), on 12th May 1802 (Valle dell'Oglio, Mw 5.60), on 7th April 1786 (Po Plain, Mw 5.22) and on 15th May 1951 (Lodigiano, Mw 5.17). The highest macroseismic intensity (I = 7, https://emidius.mi.ingv.it/CPTI15-DBMI15/) for the area is associated to the 3rd January 1117, Mw 6.52, Verona earthquake, occurred ~140 km, South-East of MMA.

Figure 3 shows the ground motion values recorded by the IV.MILN station in terms of peak ground acceleration (*PGA*), peak ground velocity (*PGV*) and response spectral (*Sa*) ordinates at period (T) of 3.0 s. The highest values of shaking in terms of acceleration is recorded on the 18th December 2021, Mw 3.9, Dalmine event (2021/12/18 10:34:47 UTC, http://terremoti.ingv.it) with maxima horizontal and vertical *PGAs* of 36 *gal* and 13 *gal*, respectively. PGAs between 5 *gal* and 10 *gal*, are recorded during the 17th December 2020, Mw 3.9, Pero event (2020/12/17 15:59:22 UTC, http://terremoti.ingv.it) and the 20th and 29th May 2012 Emilia main events (2012/05/20 02:03:52 UTC, Mw 5.8 and 2012/05/29 07:00:03 UTC, Mw 5.6, http://terremoti.ingv.it). This sequence produced seismic motion characterized by the dominance of surface waves (Love and Rayleigh waves) with amplitude higher than S-phases and by the arrival of a quasi-monochromatic wave train centered at 0.2 Hz. This phenomenon, described in Luzi et al. (2013) is more evident in the central and eastern sectors of the Po Plain, even if it is also observed at IV. MILN station in the case of the 20 May 2012, Mw 5.8, Emilia mainshock.

Geological Setting and Model

The municipality of Milan (**Figure 1**, panel A) is located in the north-western sector of the Po Plain, a large and deep sedimentary basin between the south-verging thrust system of the Alps and the north-verging thrust system of the Apennines (Pieri and Groppi, 1981; Bigi et al., 1990); **Figure 1** (panel A) also shows the expected maximum thickness of the Po plain sediments, represented by light grey contour lines. The Plio-Quaternary deposits of the Po Plain, overlie, in discordance, the geologic bedrock composed of deep-sea turbiditic deposits, which are deformed by compressive tectonic phases that lasted until the Upper Miocene along the piedmont edge of the Southern Alps. Since the Messinian, the tectonic phases of alpine structures stopped and the northern Apennines migrated towards NE. Since that time, the deposition and the geometries of the Po plain have been constrained by rapid uplift and forward

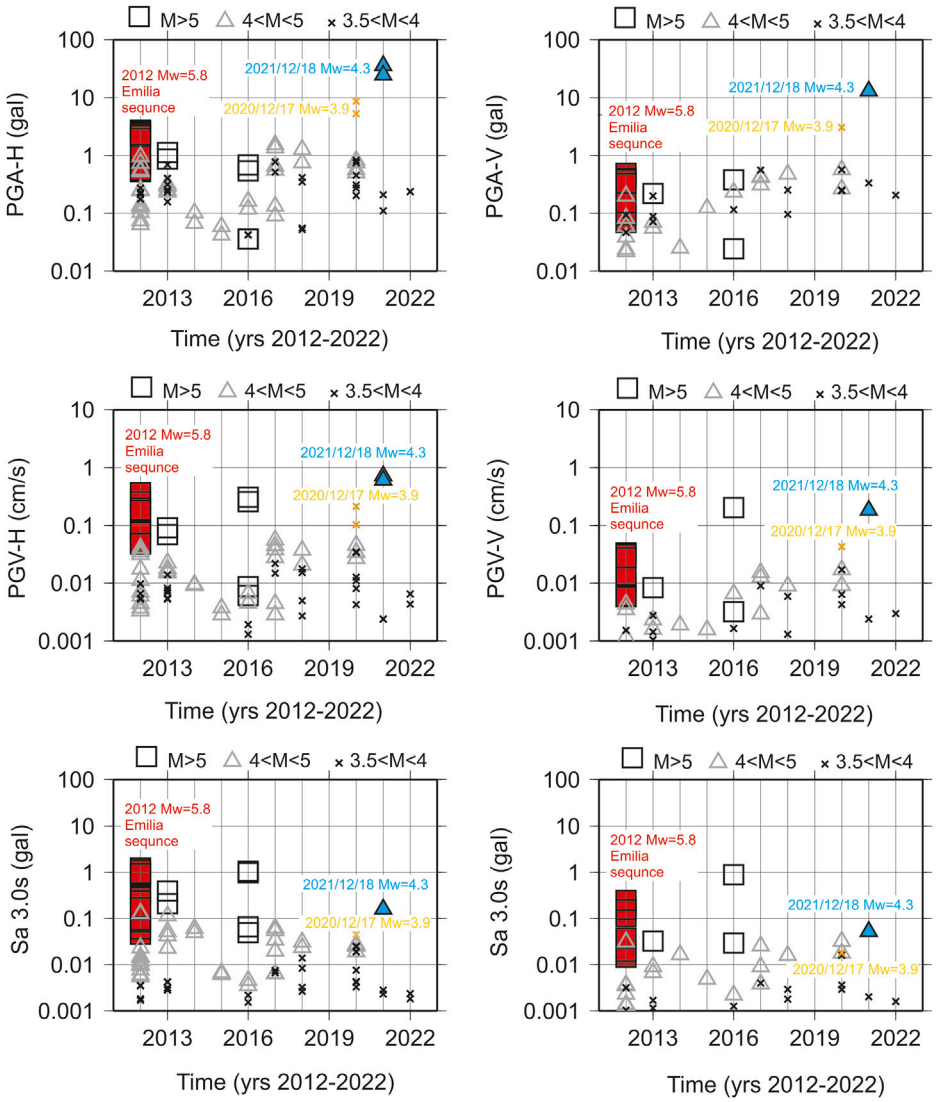

FIGURE 3 | Peak Ground Acceleration (PGA), Velocity (PGV) and response spectral ordinates at period of 3.0 s for all events of magnitude ≥3.5 recorded at IV. MILN station from 1st January 2012. Left and right side indicate the horizontal and the vertical ground motion values, respectively.

movements of Apennine system, and to very long periods of isostatic subsidence of the basin.

From the available geological and geophysical information, a subsoil model with depth down to ~1.8 km is built up along a NNW-SSE section, that crosses the three sites selected for the geophysical surveys (i.e., North Park, Giuriati sports center and Vettabbia park, see **Figure 2**, panel A).

In particular, we made use of:

- the 1:10.000 sheet 118 geological map (ISPRA et al., 2016);
- 5 selected water wells down to 120 m in depth (blue circles, **Figure 2**, panel A) available at https://www.geoportale.regione.lombardia.it/;
- one core drilling down to 100 m in depth (brown circle, **Figure 2**, panel A) performed in the framework of the Carg Project (ISPRA et al., 2016);
- the deep wells of ViDEPI project (2009) surrounding the metropolitan area of Milan (black circles in **Figure 2**, panel A);
- the stratigraphic units from Carg (ISPRA et al., 2016) and GeoMol Team (2015) projects;
- the isobaths published by ISPRA et al. (2016), in the framework of the Carg project (https://www.isprambiente.gov.it/Media/carg/118_MILANO_SOTTO/Foglio.html);
- the North South high-resolution reflection seismic profile acquired in the western area of Milan by De Franco et al. (2009).

The geological map reported in **Figure 2** (panel A) show with different colours all the outcropping units of the 118-Milano geological sheet that belong to the Upper Pleistocene-Holocene continental succession. From a lithological point of view, these

TABLE 2 | Subsoil models at North park, Giuriati sports center and Vettabbia park.

Period	Epoch	Lithology	Facies	Stratigraphic units	Unconformity	Hydrogeological units	North Park (Depth, m)	Giuriati (Depth, m)	Vettabbia (Depth, m)
Quaternary	Upper Pleistocene-Holocene	Coarse gravel	Continental	LS	QC3 (0,45My)	Aquifer A	50	40	45
Quaternary	Upper Pleistocene	Fine gravel with sand and clay	Continental	LI	QC1 (0,87My)	Aquifer B	100	100	120
Quaternary	Upper Pleistocene	Mixture of fine gravel, sand, clay	Continental	PD	QM2 (1,25My)	Aquifer C	300	300	400
Quaternary	Middle lower Pleistocene	Sand (*Sabbie di Asti*) with % of clay	Transitional marine	PD	QM1 (1,5My)	Aquifer D	600	620	700
Quaternary	Middle lower Pleistocene	Fine sand (*Sabbie di Asti*)	Transitional marine	PLMa	GEL (2,6My)	-	900	1000	1300
Neogene	Middle upper Pliocene	Clays (*Argille del Santerno*)	Marine	PL	PL (5,3 My)	-	1200	1320	1800
Neogene	Miocene	Chaotic layer (*Sergnano*)	-	MESb	ME3	-	-	-	-
Neogene	Miocene	Marls (*Marne di Gallare*)	-	MESa	-	-	-	-	-

Dark grey cells indicate the stratigraphic units proposed by the Carg project (ISPRA et al., 2016) locally developed in the framework of the 1:10.000 sheet 118 geological map. In correspondence of the studied area they are described down to the base of group aquifer D *(Regione Lombardia, Eni Divisione Agip (2002); for deeper deposits, the stratigraphic units proposed by Geomol project (2015), are considered (dark cells). The main chrono stratigraphic unconformities refer to the GeoMol project (2015). The hydrogeological units are described following Regione Lombardia, Eni Divisione Agip (2002). Depths of the chrono-stratigraphic unconformities (GeoMol Team, 2015) reported in the last three columns are referred to the countryside level.*

surface units are characterized by coarse and medium gravels, with subordinate levels of medium and coarse sands, and belong to the Supersintema Lombardo Superiore (LS).

The stratigraphy units from the top to the bottom are (**Figure 2**, panels B,C):

(1) *LS* unit (Supersintema Lombardo Superiore, Upper Pleistocene-Holocene; ISPRA et al., 2016, **Figure 2**, panel B) or group or aquifer-A (Regione Lombardia, Eni Divisione Agip, 2002) is made of clast-supported gravel, medium-coarse gravel and sparse pebbles (Scardia et al., 2012). LS is marked at the base by the Qc3 (**Figure 2**, panel B) regional chronostratigraphic Unconformity (0,45 My, GeoMol Team, 2015) or Y-surface (Scardia et al., 2012) that defines a regional change in fluvial depositional style (i.e., proximal braidplain according to Scardia et al., 2012), suggesting the occurrence of important erosional processes. All the outcropping units of the 118-Milano geological sheet (**Figure 2**, panel A) are sub-units of LS. LS unit has an average thickness of 50 m (**Figure 2**, panel b and **Table 2**);

(2) *LI* unit (Supersintema Lombardo Inferiore, Upper Pleistocene; ISPRA et al., 2016, **Figure 2**, panel B) or group acquifer-B (Regione Lombardia, Eni Divisione Agip, 2002) is an alternation of medium to coarse grained sand, gravel and subordinate silt, interpreted as a distal braidplain with wandering fluvial channels (Scardia et al., 2012). At the bottom, LI is marked by Qc1 (**Figure 2**, panel B), a regional chronostratigraphic Unconformity (0,87 My, GeoMol Team, 2015) or R-surface (Muttoni et al., 2003), correlated to the onset of major Pleistocene glaciations in the Alps. The average thickness of LI unit ranges from about 50 to 75 m moving NNW-SSE (**Figure 2**, panel B and **Table 2**);

(3) *PD* unit (Padano Supersynthem, Middle lower Pleistocene; ISPRA et al., 2016, **Figure 2**, panel C) is made of marine coastal and platform deposits (sand, with some clay layers) at the base, that evolve upwards to delta, delta-conoid and lagoon sediments (fine and very fine sand, mud, clay with some organic material, locally gravel) and to completely continental deposits (meandering river depositional system in alluvial plain, Scardia et al., 2012).

In between, the transition from marine to continental environment is defined by the regional 1,25 My unconformity called Qm2 (GeoMol Team, 2015, **Figure 2**, panel C), corresponding to the bottom of group acquifer-C (Regione Lombardia, Eni Divisione Agip, 2002); at the base, PD is marked by the 1,5 My unconformity called Qm1 (GeoMol Team, 2015) that corresponds to the base of group acquifer-D (Regione Lombardia, Eni Divisione Agip, 2002). The average thickness of the PD unit ranges from about 500 to 600 m moving NNW-SSE (**Figure 2**, panel c and **table 2**);

(4) *PLMa* unit (Middle lower Pleistocene, Geomol Team, 2015, **Figure 2**, panel C) is made of sand deposits with some clay levels and thin gravel layers saturated with salty water (i.e., "*Sabbie di Asti*" formation, Regione Lombardia, ENI Divisione Agip 2002). At the bottom, PLMa unit is marked by the 2,6 My *GEL*asian Unconformity (GeoMol Team, 2015). The average thickness of the PLMa unit range from about 300 to 600 m moving NNW-SSE (**Figure 2**, panel C and **Table 2**);

(5) *PL* unit (early-middle Pliocene, Geomol Team, 2015, **Figure 2**, panel C) is made of mud and clay deposits (i.e., "*Argille del Santerno*" formation, Dondi et al., 1982). At the base, the PL unit is marked by the 5,3 My intra Zanclean Unconformity called *PL* ("base of Pliocene", GeoMol Team, 2015). The average thickness of the PL unit ranges from about 300 to 500 m moving NNW-SSE (**Figure 2**, panel C and **Table 2**);

(6) *MESa* unit (Burdigalian-Tortonian, GeoMol Team, 2015, **Figure 2**, panel C) is characterized by the "Marne di Gallare" formation (Rizzini and Dondi, 1978), that represents the geological bedrock of the area. In between, the formation is broken off at the top by the ME3 intra Messinian Unconformity (GeoMol Team, 2015, **Figure 2**, panel C), that marks the transition to the Messinian "Ghiaie del Sergnano" formation (chaotic gravel and sand, cemented levels, marls and sandstone, ViDEPI project 2009), that represents the potential reservoir between the Miocenic marls and the caprock of "Argille del Santerno," a target of oil exploration.

The subsoil schemes describing the geological cross section of **Figure 2** (panels B, C) are presented in **Table 2**. In particular, the depths of the *Qc3*, *Qc1* and *PL* unconformities (Geomol project, 2015) are well-constrained by the isobaths published in the framework of the Carg project (https://www.isprambiente.gov.it/Media/carg/118_MILANO_SOTTO/Foglio.html, ISPRA et al., 2016), while the depths of the *QM2*, *QM1*, *GEL* unconformities (Geomol project, 2015) are deduced on the basis of the stratigraphy of ViDEPI project (2009).

Noise Horizontal-To-Vertical Spectral Ratio

From March to June 2021, 33 single-station ambient noise measurements are performed in the MMA (**Figure 2**, panel A). The sites selected for the measurements cover an area of about 15 km^2 and are characterized by minimum and maximum inter distances between each measure of ~1 and 4 km, respectively. Although it is not possible to plan a regular grid, the measurements are devised to avoid significant sources of anthropic noise such as industrial facilities, railways etc. Additional data are available from the continuous data stream recorded by the IV. MILN permanent station (**Figure 2**, panel A), equipped with a broadband Nanometrics Trillium 40s seismometer (https://www.nanometrics.ca/) and a Kinemetrics Episensor-FBA accelerometer (https://kinemetrics.com/).

The measurements are performed using a 6-channel Reftek-130 24-bits datalogger (https://reftek.com/) coupled with two Lennartz 5s seismometers (https://www.lennartz.de/en/) with sampling frequency of 100 Hz. Each measurement has a duration spanning from at least 30 min to about 1 h. All measures are performed during working days and in absence of wind. In any case, the couple of seismometers are always covered by a cap and, if possible, partially buried, in order to avoid any disturbances that may adversely affect the results. (e.g., Mucciarelli et al., 2005). The measures are performed in all cases by expert operators and each single point is a priori checked in order to avoid the proximity of underground services or important skyscrapers. In this regard, a comprehensive description of the good practices for the acquisition and the analysis of ambient noise vibrations are provided by Molnar et al., 2022.

Considering, moreover, the SESAME (SESAME, 2004; Bard, 2008) recommendations *for reliable HVSR curves*, the first two criteria, based on the availability of adequate data windows length and number of cycles, are always satisfied. Concerning the third criterion, based on the standard deviation of the *HVSR* amplitude in dependence of the frequency, few measuring points for *pk1* (see black cells in **Supplementary Table S1**) exceed the limit of 3 at frequency <0.5 Hz; at higher frequencies, solely for the measurement 19, the third criterion is not satisfied in case of *pk2* (see black cell in **Supplementary Table S1**).

The data processing removes the mean and the linear trend partitioning the signal in time sub-windows with increasing duration, from 60 to 240 s. A cosine taper function (5%) is applied to better highlight possible low frequency peaks (<0.5 Hz).

As shown in **Figure 4** (panel A), in order to avoid low resolution or aliasing phenomena at low frequency, a minimum window of analyses of 60 s is necessary. After removing possible transient signals identified through visual inspection, the fast Fourier transform (FFT) is calculated for each time window, which is smoothed using the Konno and Ohmachi (1998) algorithm with the b coefficient set to 40 (**Figure 4**, panel B), allowing to distinguish better the single peaks observed in the *HVSR* curves. Independent of the processing, a further important peculiarity for the evidence of low-frequency peaks in the Po Plain is the atmospheric pressure condition where the measurements are performed. The ambient noise level in the area undergo significant daily and seasonal variations with evident consequences on HVSR results at frequencies <0.5 Hz (e.g., Marzorati and Bindi, 2006). An example is reported in **Figure 4** (panel C) by comparing the FFTs of ambient noise windows recorded in October 2021 at IV. MILN station, during sunny and stormy days, respectively.

To calculate the *HVSRs,* for each single sub-window the spectral ratio between the root-mean-square average spectra of the horizontal components over the vertical components is calculated (Nakamura, 1989). Finally, the mean and standard deviation are computed.

For completeness, the results obtained for the 33 ambient noise measurements are illustrated in the **Supplementary Material**, in figures from **Supplementary Figure S1–S6**, while **Supplementary Table S1** indicates all frequency peaks (i.e., *pk*) and related uncertainties recognized at urban scale by multiple measurements.

Figure 5 (panel A) shows the results in terms of mean ± standard deviations (black solid and dotted lines, respectively) of the 33 ambient noise measurements, together with the mean *HVSR* curves obtained from independent sets of measurements performed in the northern (i.e., North of M002, **Figure 2**, panel A), central and southern (i.e., South of M026, **Figure 2**, panel A) parts of the urban area, respectively, and the mean *HVSR* curves representative of the seismic passive arrays performed at North Park, Giuriati sports center and Vettabbia park (**Figure 2**, panel A).

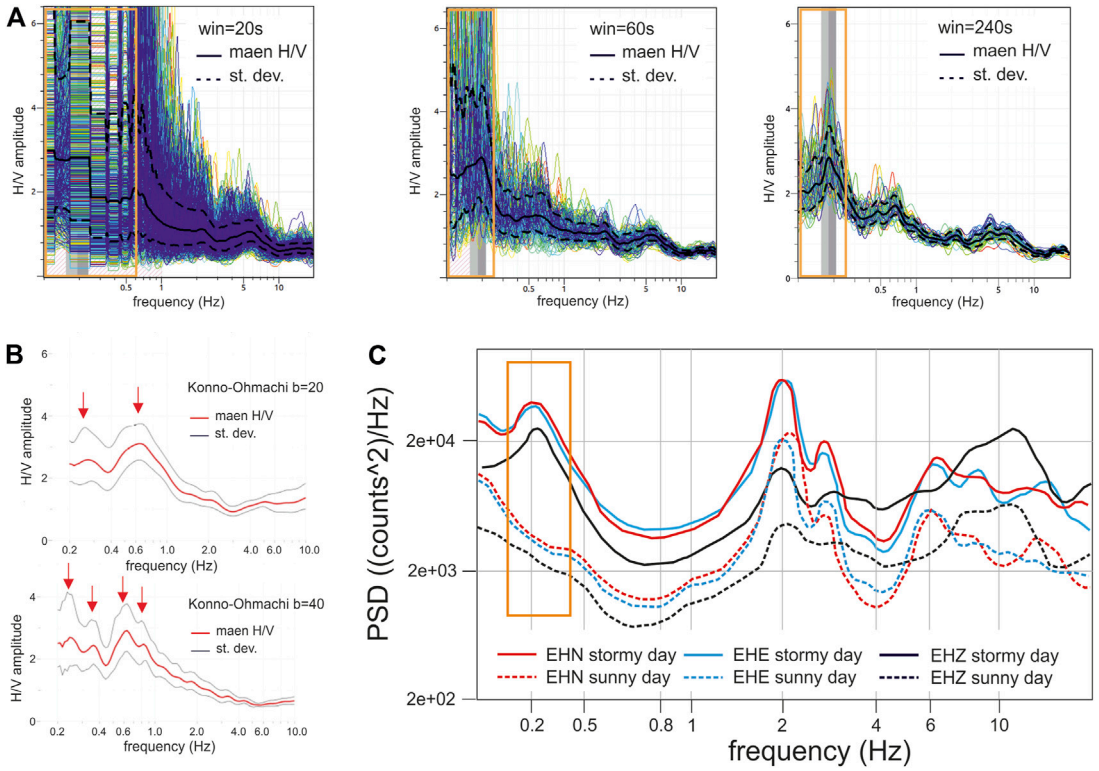

FIGURE 4 | Panel **(A)** example of ambient noise *HVSR*s (Nakamura, 1989) calculated at IV. MILN station during a non-working day (i.e., 8th December 2021) using time sub-windows of increasing length of 20, 60 and 240 s, respectively; Panel **(B)** example of ambient noise *HVSR*s (Nakamura, 1989) calculated at IV. MILN station considering FFTs obtained by the Konno-Ohmachi smoothing windows, with *b* equal to 20 and 40; Panel **(C)** example of Power Spectral Density (PSD) calculated at IV. MILN station from ambient noise recorded at the end of October 2021 during a sunny and a stormy day, respectively.

In general, the *HVSR* curves (**Figure 5**, panel A) show a high degree of coherence, which showed 3 main amplified bands of frequency that are from 0.17 to 0.23 Hz (*pk1*, **Supplementary Table S1**), from 0.48 to 0.66 Hz (*pk2*, **Supplementary Table S1**) and from 3.2 to 7.6 Hz (*pk3*, **Supplementary Table S1**). In general, the *HVSR* curves show a slight decrease in frequency of the three main peaks moving from the Northern to the Southern part of the area.

Considering, the SESAME (2004) criteria *for clear HVSR peaks*, *pk1* is the resonance frequency that shows a more reliable peak, with 2–4 satisfied criteria for about 70% of the measuring points (**Supplementary Table S1**). *Pk3*, instead, is the resonance peak that shows the highest number of satisfied criteria for a *clear HVSR peak* (5 satisfied criteria, **Supplementary Table S1**), even if for a lower percentage of measuring points (from 3 to 5 of satisfied criteria for about 40% of measuring points, **Supplementary Table S1**). *Pk2* is the resonance frequency having more uncertainties concerning *clear HVSR peaks*. In particular, concerning the HVSR amplitude, except *pk1*, which shows values > 2 for the 80% of the measuring points (i.e., the lower bound for significant peaks), at higher frequency more variability is observable. All frequency peaks showing amplitude >2 are indicated in bold in **Supplementary Table S1**.

In general, the *HVSR*s variability in terms of both resonant peaks and amplitude at high frequency (>1 Hz) could be associated with very local factors (i.e., local soil conditions, anthropic ambient noise levels etc.). For example, **Figure 5** (panel B) shows a comparison between the *HVSR* calculated for the new 33 ambient noise measurements and the *HVSR* calculated from ambient noise recorded by the Trillium 40s installed at IV. MILN station, both during a non-working day (i.e. 8th December 2021) and during the lockdown against the Covid-19 pandemic (i.e. April 2020, Sunday 6th and April 2020, Monday 7th). This example shows the strong influence in an urban area of the anthropic noise on the vertical component of motion and, consequently, on the final results in terms of *HVSR*. The relative Power Spectral Density (PSD) is shown in the **Supplementary Material** (**Supplementary Figure S7**).

At low frequency (<1 Hz), the noise level could be affected by variations due to differences in the environmental conditions during the period when the measurement is performed (e.g., Marzorati and Bindi, 2006).

Finally, to detect possible polarization effects of the horizontal components, Fourier spectra are computed by rotating the north–south (N-S) and east-west (E-W) noise components clockwise from the North, from 0° to 180° with step of 10°. For each direction, the *HVSR* is computed considering the ratio between the Fourier spectrum of each rotated horizontal component and the Fourier spectrum of the vertical component. **Figure 5** (panel C) shows the rotated *HVSR* obtained at North

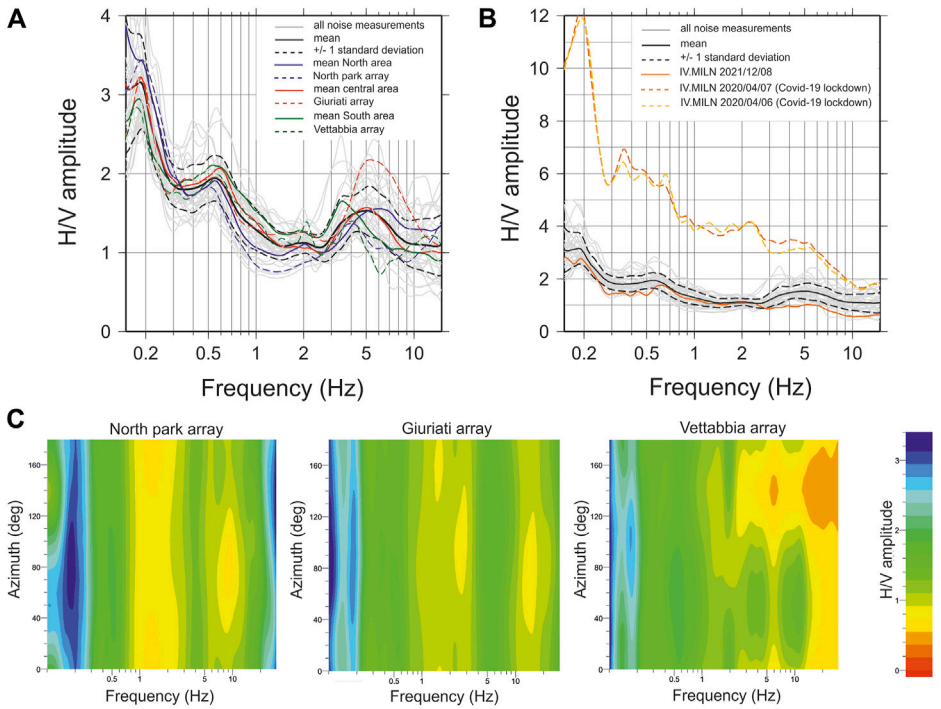

FIGURE 5 | Panel **(A)** *HVSR*s relative to the 33 new ambient noise measurements (light grey) performed in the Milan urban area from March to June 2021 (in black mean amplification and ±1 standard deviation). Blue, red and green solid lines indicate the mean amplification functions for the north, central and south parts of the target area. Blue, red and green dotted lines indicate the amplification functions for the three target sites of North Park (north of the area), Giuriati (center part) and Vettabbia park (south of the area); Panel **(B)** comparison in terms of *HVSR*s between the new ambient noise measurements (light grey; in black mean amplification and ±1 standard deviation) and the results obtained at IV. MILN station using time windows selected both recently (i.e., December 2021) and during the Covid-19 lockdown (i.e., April 2020). Panel **(C)** directional ambient noise *HVSR*s obtained for North Park (left), Giuriati (center) and Vettabbia park (right).

park, Giuriati sports center and Vettabbia park, where in all cases just negligible polarization in directions ranging from 40°N to 120°N is detected around 0.2 Hz.

Figure 6 shows, in the map, the variability of the more relevant frequency peaks detected at high (*pk3*, panel A) and low (*pk1*, panel B) frequency, highlighting decreasing values moving from the northern to the southern part of the studied area.

Earthquake Horizontal-To-Vertical Spectral Ratio

The results obtained from ambient noise *HVSR*s are compared with those from earthquake *HVSR*s (e.g., Lermo and Chavez-Garcìa, 1993), calculated considering the set of seismic events reported in **Table 1**. The selected earthquakes, with magnitude (Mw) ranging from 3.7 to 5.8, are recorded by the IV. MILN station and occurred in the Po Plain area and surroundings from the 1st January 2012 until today. The velocimetric data selected for the analyses are downloaded from the EIDA web site (http://www.orfeus-eu.org/data/eida/).

The simple data processing involved the application of a baseline operator to the entire record to obtain the zero-mean signal and subsequently to remove any linear trends, a tapering cosine function (0.05%) applied at the beginning and the end of each selected window and a 4th order Butterworth band-pass acausal (Boore and Akkar, 2003) filter to remove the high and low-frequency noises; for each analysed event the filter cut-off thresholds are selected by a visual inspection.

Given the long-period effects due to the low frequencies propagation in the Po plain basin during the 2012 Emilia seismic sequence (e.g., Luzi et al., 2013), the earthquakes *HVSR*s are computed on both the S-waves train and the coda. Time windows from 10 to 20 s are selected for the S-waves starting from their onset after a visual inspection. Time lengths for the surface train waves are determined through a time-frequency analysis on each single earthquake. Finally, coda windows ranging from 15 to 60 s are selected at the end of the S-phase depending on each earthquake's magnitude, distance and ray-path.

An example of propagation effects on train waves crossing along the Po plain alluvial deposits is shown in **Figure 7** (bottom panels), where the EW velocimetric waveforms recorded at IV. MILN station during the 20th May 2012, Mw 5.8, Emilia mainshock (Repi 169 km) and during the 18th December 2021, Dalmine, Mw 3.9, event (Repi 35 km, see **Table 1**) are shown; in the first case, the example shows the generation of surface waves with the consequence of long earthquake ground motion duration and *PGV* recorded on coda. In the second case, the hypocentre is located at a depth of 31 km and the source to site distance is 35 km, so no surface waves are generated and the *PGV* is found on the S-phase.

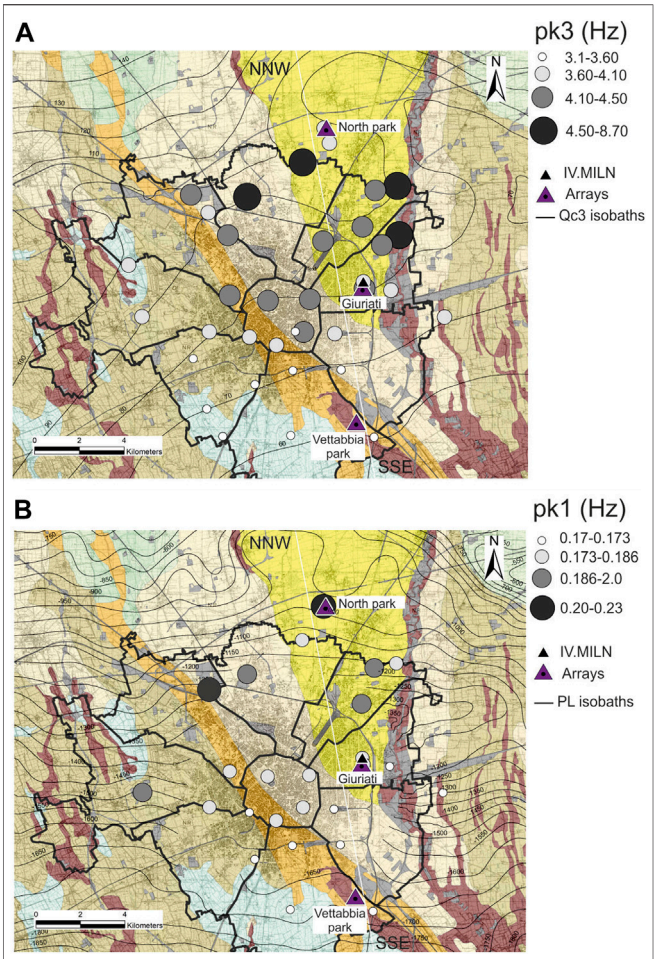

FIGURE 6 | Resonance frequency intervals for *pk3* (panel A) and *pk1* (panel B) *HVSR* ambient noise peaks (see **Supplementary Table S1**) superimposed on the geological map of the area (**Figure 2**, panel A). Measuring points that not satisfied the SESAME (2004) criteria for *clear HVSR peaks* (see black and dark grey cells in **Supplementary Table S1**) are not considered. Top and bottom panels also indicate the isobaths of Qc3 (base of the upper Padano Supersynthem, see **Figure 2B** and **Table 2**) and PL (base of Pliocene, **Figure 2C** and **Table 2**) unconformities as recognized by the Geomol project (2015).

In detail, the *HVSR*s are calculated by splitting the earthquakes in two different sets of data, the first including the 2012 Emilia earthquakes with Mw > 5, epicentral distances ranging from 148 to 191 km (**Table 1**) and homogeneous azimuth of ~290°N (**Figure 1**, panel B); the second including earthquakes occurring mainly at the edge of the basin, with Mw < 4.5, maximum epicentral distance of 142 km (**Table 1**) and sparse azimuths in the range 2°–352°N (**Figure 1**, panel B).

The earthquakes HVSRs are shown in **Figure 7**, where panels A, B show the curves for the higher and lower magnitude set of events, respectively. In particular, top and central panels show the results in terms of mean amplitude calculated from S-phase and coda, respectively. The results obtained considering the ambient noise and the set of earthquakes with magnitude >5 show that the two *HVSR* curves agree at frequencies <0.5 Hz, particularly considering the coda waves for the higher magnitude set of events.

In case of the available local earthquakes, characterized by short distances and low magnitude, the windows lengths do not always assure the calculation of stable HVSR curves for frequencies lower than ~0.5 Hz (**Figure 7**, right panels). This issue is even more relevant in case of high levels of ambient noise, such as at the IV. MILN station during working days (i.e., −110 < dB < −90 in the range 1–20 Hz).

The most relevant result comparing of earthquake and ambient noise *HVSR*s is that, at frequencies between 1 and 2 Hz, the ambient noise *HVSR*s do not show any amplification peak. In contrast, S-phase and coda depict clear amplification peaks for both set of events. Concerning the amplitude values, earthquakes *HVSR*s calculated both from S-phase and coda show in general higher amplitudes with respect to ambient noise, in particular for frequencies >0.5 Hz.

Concerning the possible influence of the different azimuths of the local earthquakes reported in **Table 1**, just in case of the two events of Mw = 3.9, recorded at IV. MILN station on 2021/12/18 10:34:47 (epicentral distance 35 km, depth 26 km and azimuth 293°N) and on 2020/12/17 15:59:22 (epicentral distance 8 km, depth 56 km, azimuth 83°N) higher amplitudes along the related ray-paths are detected on S-phase in the frequency range 1–8 Hz.

As in the case of ambient noise *HVSR*s, no polarization phenomena due to the recording site are observable from earthquake signals.

Geophysical Surveys

To characterize the shear wave velocity with depth, active and passive geophysical tests are carried out.

Two Multichannel Analyses of Surface Waves (MASW, Park et al., 1999) are performed at North public park and at Vettabbia public park using in both cases 24 vertical geophones with eigen natural frequency of 4.5 Hz and a vertical impact source (6.8 kg hammer). In both sites, the geophones are set out in a linear array varying the inter geophonic distance from 2.5 to 5 m (total length of 60 and 120 m respectively) and using a minimum offset moving from 5 to 10 m. The linear arrays allow investigating depths ranging from 30 to 35 m. The Rayleigh wave dispersion of the acquired data set is obtained from the stacking of 7 shots. For each shot, a sampling frequency of 2000 Hz and a time of acquisition of 2 s are chosen. To generate the phase velocity spectrum of Rayleigh waves, the phase shift algorithm (Park et al., 1998) is used.

In general, as expected, in the configuration with the greater geophonic inter distance (5 m) an improvement in signal correlation is observed in the low frequency phase velocity spectrum. In particular, at Vettabbia Park, in the configuration with the smaller geophonic inter distance (2.5 m) an improvement in signal correlation is also observed in the high frequency phase velocity spectrum (20–30 Hz). The cause of this observation is probably due to the attenuation properties of the more superficial soil layers that resulted, from local geognostic investigations (https://www.geoportale.regione.lombardia.it/), to be mostly incoherent fine deposits. From the phase velocity spectra obtained with the two configurations (5–2.5 m), the

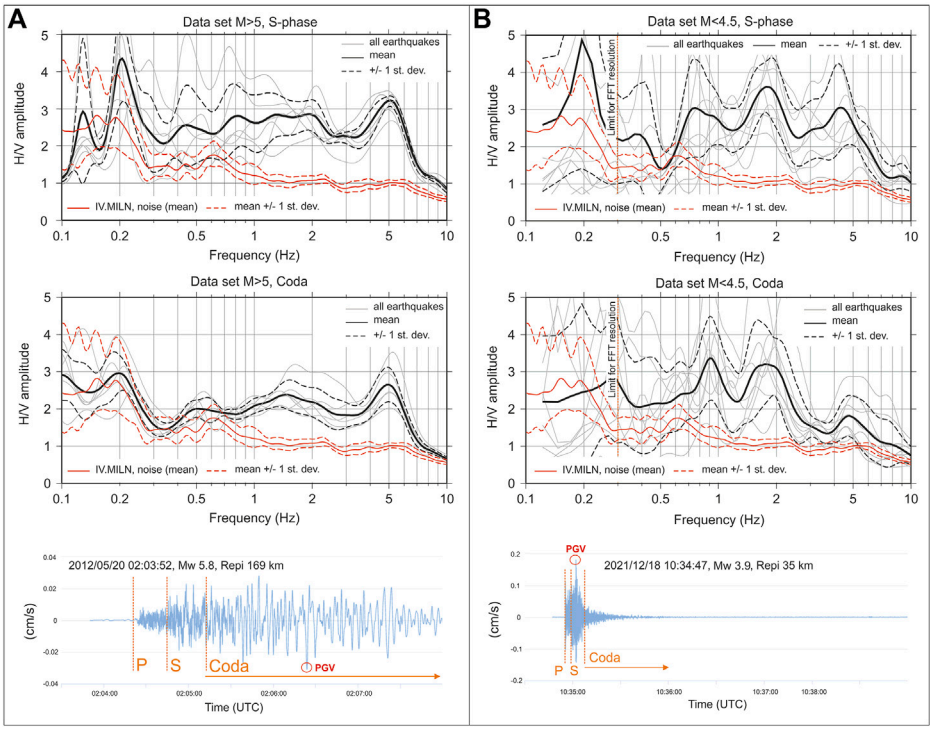

FIGURE 7 | Earthquake *HVSR*s calculated on the events listed in **Table 1**. Panel **(A)** shows the results obtained on a sub set of events with magnitude >5 and epicentral distances from 127 to 191 km, while panel **(B)** indicates the results obtained considering events with magnitude <4.5 and epicentral distances from 8 to 143 km; the vertical orange dotted lines indicate the lower limit for stable HVSR curves obtained by using the available local earthquakes. The epicentres of the considered events are reported in the panel **(B)** of **Figure 1**. Bottom panels show two examples of near and far field waveforms recorded at IV. MILN station for the 2012/12/18 Dalmine M_w 3.9 event (right) and for the 2012/05/20 Emilia M_w 5.8 mainshock (left).

fundamental mode picking covered the frequency range 6–30 Hz at Vettabbia park and the frequency range 5.5–30 Hz at North park (**Supplementary Figures S8 and S9** respectively). The Vs.30 calculated from MASW at North and Vettabbia park results equal to 345 m/s and to 265 m/s respectively, allowing classifying the analysed sites in C class (i.e. Vs.30 < 360 m/s) of Italian (NTC, 2018) and European (CEN, 2004) seismic codes.

To define S-wave velocity profiles for larger depths, 4 different microtremor arrays, with increasing apertures and different layouts are installed at North public park (**Figure 8**, panel A), Giuriati sports center, very close to the IV. MILN station (**Figure 8**, panel B), and Vettabbia public park (**Figure 8**, panel C). At Giuriati sports center, two microtremor arrays are carried out using a circular geometry with radii of 12 and 50 m, respectively (**Figure 8**, panel B). The layout of the two arrays consisted of a central receiver surrounded by 8 stations deployed with an angular distance of 45°. The instrumentation comprised Lennartz-5s high-sensitivity (400 V/m/s) velocimeters coupled with a 24-bit Reftek 130 three-channel digitizer. The sampling frequency is set at 100 Hz, with the recording period for each array of 3 h.

For both North and Vettabbia public parks, one microtremor array is set up using the layouts reported in **Figure 8** (panel A, C) and 14 Lennartz-5s high-sensitivity (400 V/m/s) velocimeters coupled with a 24-bit Reftek 130 three-channel digitizer. The sampling frequency and recording period are the same as that used at Giuriati. In this case, the two types of geometry enable work with inter distances among sensors in the range 5–600 m.

For each array, the first step of the analysis consists of a visual inspection of the recordings at each station. In particular, in order to identify malfunctioning and to select suitable signal windows for the surface wave analysis, the quality of the recording is evaluated by analysing the signal stationarity in the time domain, the relevant unfiltered Fourier spectra and the *HVSR* variation over time. During surface wave investigation, it is common practice to verify the reliability of the one-dimensional site structure assumption (Aki, 1957; Okada, 2003). For this reason, we estimated the *HVSR* at each station of the array and the stability of *HVSR* throughout the array stations is in the range of frequency (0.2–30 Hz). The analyses use synchronized signal windows, with lengths ranging from 60 to 120 s, extracted from the available recordings, avoiding time windows affected by local disturbances.

The Rayleigh wave dispersion curve relative to the fundamental mode is calculated for each seismic array, taking account of the vertical ground-motion components, using the modified spatial autocorrelation (*mSPAC*) method (Bettig et al., 2001), the *f-k* (frequency-wavenumber) beamforming method (Capon 1969; Lacoss et al., 1969) and the ESAC (Extended Spatial Auto Correlation) method (Ohori et al., 2002; Okada 2003).

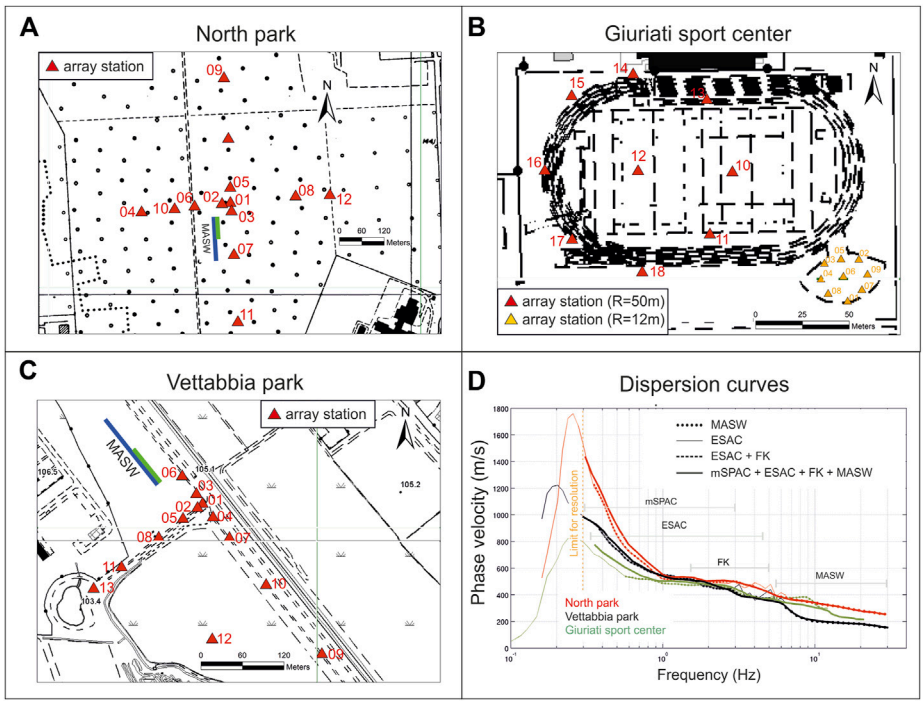

FIGURE 8 | Panel **(A)** location of the MASW active surveys and of the 2D passive array performed at North Park; Panel **(B)** location of the two 2D passive microtremor arrays performed at Giuriati sports center; Panel **(C)** the same as in panel **(A)**, but for Vettabbia public park; Panel **(D)** Rayleigh-wave dispersion curves from 2D passive microtremor array and MASW surveys.

Although the *f-k* methods are considered stable and robust algorithms, the *mSPAC* and *ESAC* methods give reliable estimates of the dispersion characteristics within a larger frequency band. In any case, the use of various combinations is always advisable (Bard 2005; Parolai et al., 2006; Puglia et al., 2011; SESAME, 2004).

It is worth mentioning that in this case no higher modes of vibration are detected. It is well known that by recognizing just the fundamental mode of ellipticity, it is generally difficult to correct for the energy of *SH* and Love waves present in the horizontal components of the ambient vibration wavefield (e.g., Poggi and Fäh, 2010). In this way, the quality of results also depends on the number of the available receivers, on the quality of the sensors installation, on the selected array geometry and, in particular, from the available levels of background ambient noise (**Supplementary Figure S7**). Moreover, in our case, also the application of the high-resolution frequency-wavenumber analysis and the use of the three-component of motion (e.g., Lai et al., 2020) does not allow to improve the results obtained by using the vertical component.

At Giuriati sports center, the experimental dispersion curve is obtained by using the *f-k* and *mSPAC* methods; in particular, the microtremor arrays with radii equal to 12 and 50 m, allow the definition of the dispersion curve in the intervals ~2.5–18 Hz and ~0.4–3.5 Hz, respectively (**Figure 8**, panel D).

At North and Vettabbia public parks, the experimental dispersion curves are obtained by using the *f-k, mSPAC* and *ESAC* methods; in these cases, the analyses on microtremor arrays allow defining the dispersion curves in the intervals ~0.3–3.0 Hz and ~0.3–3.5 Hz, respectively; at higher frequencies, the dispersion curves are obtained by the interpretation of the MASW surveys in the intervals ~5.5–30 Hz and ~6.0–30 Hz, respectively (**Figure 8**, panel D).

The inversion procedure to obtain the 1D velocity profile is performed using the nearest neighborhood algorithm, as implemented in the Dinver software (Wathelet et al., 2008). To obtain the best results from the available data, at each target site a joint inversion of the experimental dispersion and the ellipticity curves is carried out, since the single station *HVSR* contains information on the mean S-wave velocity and the thickness of the sedimentary cover (Parolai et al., 2005). The ellipticity curves are evaluated by using the single station analysis (*HVSR*), selecting of the main peaks or the associated flanks, dividing the amplitude by $\sqrt{2}$ to reduce the Love-wave and body wave contributions (Fäh et al., 2001; Fäh et al., 2003). At Vettabbia park and Giuriati sports center, the inversion procedure to obtain the Vs. profiles is constrained by using the resonance peaks around 0.17 and 0.19 Hz respectively, while at North park a portion of *HVSR* curve in the range 0.2–0.8 Hz is used.

Shear Waves Velocity (V_s) Profile

The Vs. profiles obtained for the three sites are shown in **Figures 9**, **10**, **11** (panels A). **Supplementary Figure S8** shows a detail of the Vs. profiles in the first 400 m of depth. The profiles are calculated using the dispersion curves obtained both from the passive arrays (**Figures 9–11**, panels B) and the active

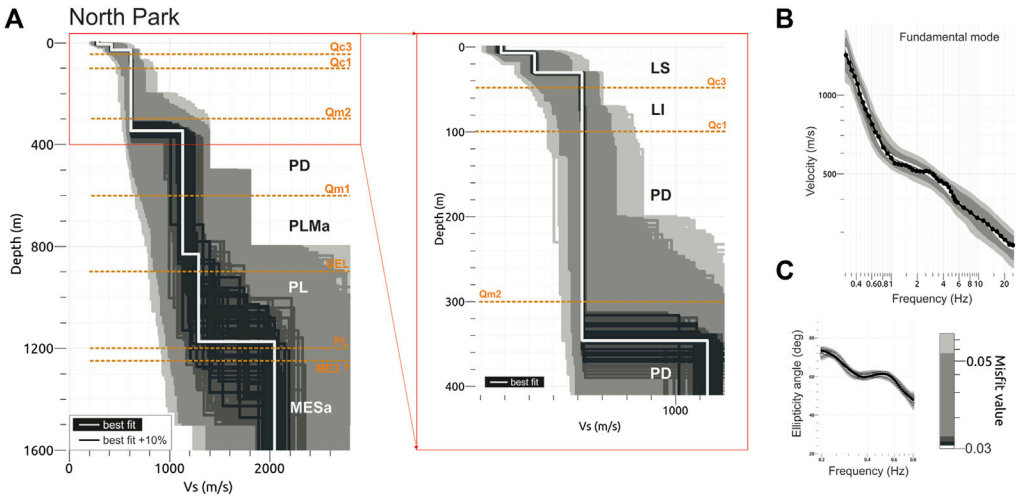

FIGURE 9 | Panel **(A)** Vs. shear wave velocity profile obtained from the joint inversion (Rayleigh-wave dispersion curve and ellipticity curve) at North park. The main chrono stratigraphic units and the related unconformities (GeoMol Team, 2015), as reported in **Figure 2** (Panels B, C) and **Table 2**, are also indicated. The central panel shows a detail of the Vs. shear wave velocity profile in the first 400 m of depth. Panel **(B)** experimental Rayleigh-wave dispersion (black dotted line) relative to the fundamental mode of vibration compared to the theoretical models (grey scale lines). The white line indicates the best-fit. Panel **(C)** experimental ellipticity curve (black line) obtained from a portion of ambient noise *HVSR* in the frequency range 0.2–0.8 Hz. Grey scale lines indicate the theoretical models. White line indicates the best fit.

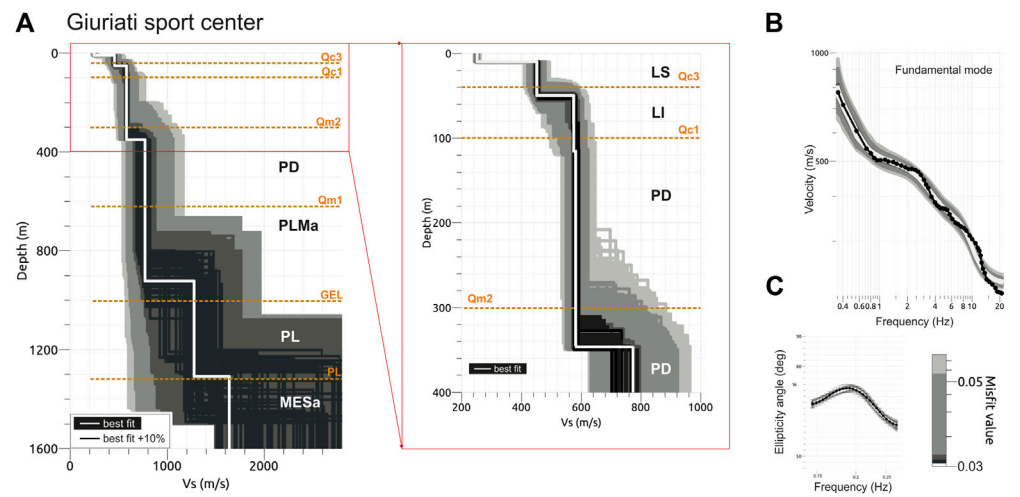

FIGURE 10 | The same as for **Figure 9**, but considering the same analyses performed at Giuriati sports center.

multichannel analysis of the surface waves, while the ellipticity contribution is estimated from a selected portion of the ambient noise *HVSR* curves (**Figures 9–11**, panels C).

The Vs. profile shows, in general, a similar trend of Vs. with depth and an increasing depth of the main contrasts of impedance towards South.

In particular, all Vs. profiles show a superficial layer with Vs. lower than 250 m/s and a first significant increase of Vs. to ~420 m/s (Vettabbia park), ~440 m/s (Giuriati sports center) and ~500 m/s (North park) at depths ranging from ~10 m (North park) to ~20 m (Vettabbia park).

A second slight increase of Vs. is observable at depth of ~35 m (North park), ~45 m (Giuriati sports center) and ~80 m (Vettabbia park), respectively, where the Vs. approaches the value of ~600 m/s at all investigated sites.

The Vs. values keep constant before a third interface located at depths ranging from ~300 m (North Park and Giuriati sports center) to ~400 m (Vettabbia park); at all sites, the Vs. values reach or exceed 800 m/s, that correspond to the engineering bedrock (i.e., site class A, Vs.30 > 800 m/s) according to the European (CEN, 2004) and the Italian (NTC, 2018) seismic codes.

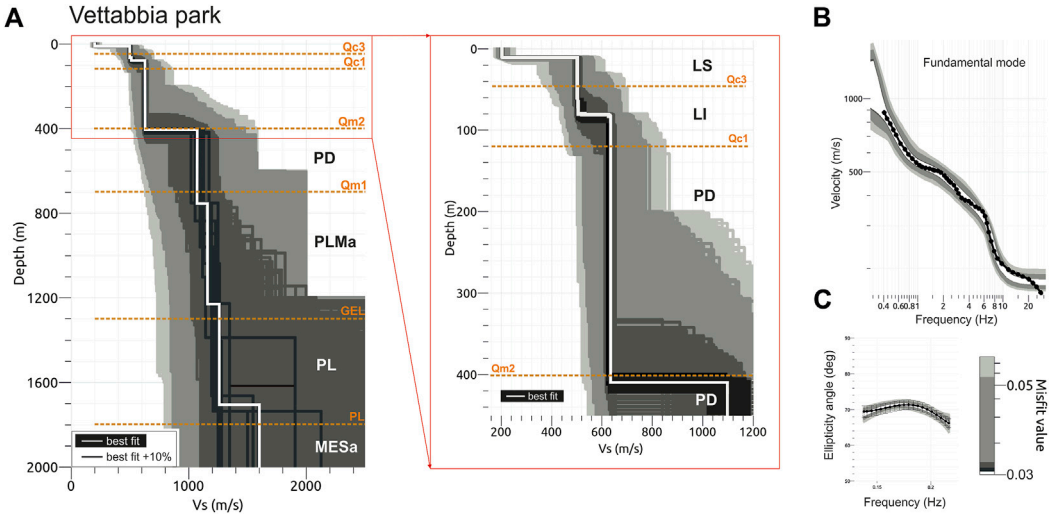

FIGURE 11 | The same as for **Figure 9**, but considering the same analyses performed at Vettabbia public park.

TABLE 3 | Shear-wave velocities (V_S) and layer thickness (H) used for 1D modelling at North Park, Giuriati sports center and Vettabbia park, together with the relative theoretical fundamental modes ($f_{0(ID)}$). The $f_{0(ID)}$ values evidenced in bold indicate seismic impedance-contrasts between subsequent layers greater than 1.5. Values for unit weight (ρ), mean effective stress (σ'_0) and damping at low-strains (D_0), at each layer (ID) are also reported.

	Vettabbia Park				North Park			Giuriati Sport Center			All Sites		
	ID	VS. [m/s]	H [M]	f0,ID	VS. [m/s]	H [M]	f 0,ID	VS. [m/s]	H [M]	f0,ID	ρ [t/m3]	σ′0 [Atm]	D0 [%]
Best-fit	1	199	11	4.54	287	8	8.96	249	9	6.91	1.45	0.2	1.3
	2	501	71	1.27	422	24	2.95	455	42	1.95	1.50	0.8	0.9
	3	620	323	0.35	612	41	1.66	576	59	1.08	1.60	1.4	0.7
	4	1080	346	0.24	620	272	0.42	580	239	0.39	1.65	2.7	0.6
	5	1169	481	0.17	1126	489	0.25	773	572	0.18	1.70	11	0.4
	6	1240	475	0.14	1292	342	0.20	1276	388	0.15	2.10	41	0.3
	7	1604	-	-	2051	-	-	1645	-	-	2.50	56	0.3
min	1–3	Same as above			Same as above			Same as above					
	4	1000	425	0.22									
	5	1070	550	0.15	950	575	0.22	700	651	0.16			
	6	1170	420	0.12	1060	430	0.17	1050	400	0.14			
	7	1360	-	-	1700	-	-	1500	-	-			
max	1–3	Same as above			Same as above			Same as above					
	4	1160	285	0.26									
	5	1250	465	0.19	1300	425	0.27	900	451	0.23			
	6	1350	465	0.15	1450	280	0.23	1500	400	0.18			
	7	1890	-	-	2300	-	-	1850	-	-			

At larger depths, ranging from ~850 m (North park) to ~1250 m (Vettabbia park), the Vs. values reach ~1150 m/s to ~1250 m/s at all investigated sites. The deepest and observable Vs. interface is located at depths varying from ~1200 m (North park) to ~1700 m (Vettabbia park), although associated with large uncertainties. At these depths, the Vs. profile of the Giuriati sports center (**Figure 10**, panel A) follows an intermediate trend with respect to the results obtained at North (**Figure 9**, panel A) and Vettabbia (**Figure 11**, panel A) parks.

For all investigated sites, both the Vs. values and the depths of the main interfaces appear better constrained down to ~400 m. In particular, in the uppermost 30 m the Vs. values are constrained by the dispersion curves obtained by both active and passive measurements, while the available stratigraphy from the shallow (https://www.geoportale.regione.lombardia.it/) and deep wells (Carg project, ISPRA et al., 2016; ViDEPI project, 2009), and the available literature (e.g., De Franco et al., 2009; Scardia et al., 2012) allow us to constrain the geological model. In general, the uncertainties of the Vs. models increase with increasing depths, in particular in the southern part of the city (i.e., Vettabbia park), where a limited amount of information is available. The Vs. values and the corresponding thickness of the model showing the

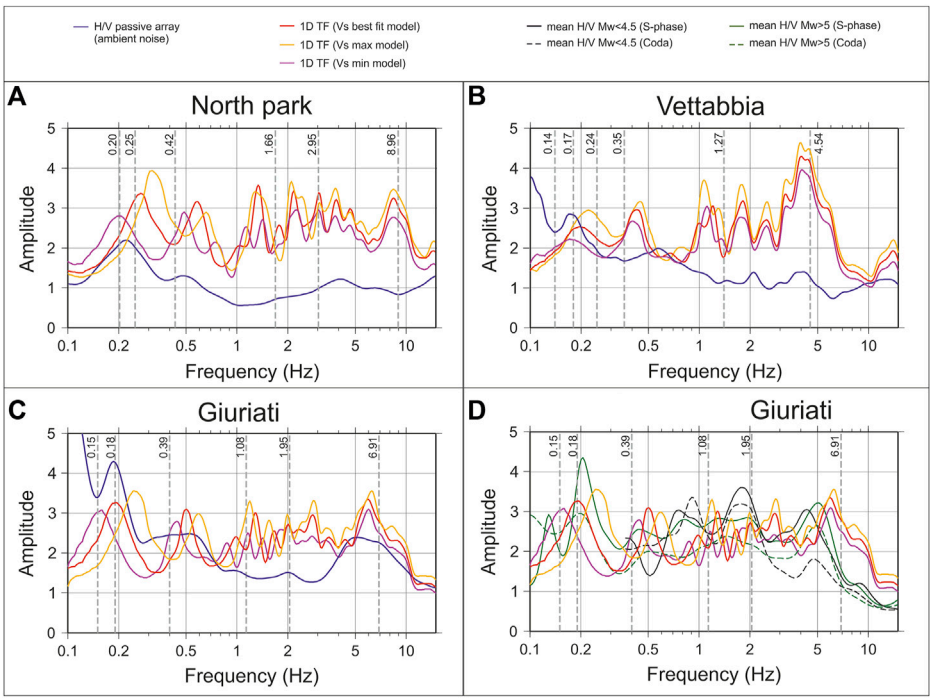

FIGURE 12 | Theoretical transfer functions (TFs) obtained through 1D numerical modelling based on the linear field assumption at North Park **(A)**, Vettabbia park **(B)** and Giuriati **(C,D)**. Red, yellow and violet lines indicate the TFs obtained considering the best Vs-model and two Vs. profiles (i.e. *min*, *max*) that envelop the Vs. values with uncertainties of 10% with respect to the best fit. The vertical grey bars indicate for each site and layer (*ID*) the values of the theoretical resonance frequencies associated to the fundamental-modes $f_{0,ID}$, obtained by **eq. 1** (see also **Table 3**). All panels show the comparison with the amplitude functions obtained from ambient noise *HVSR* (blue lines). At Giuriati also earthquakes *HVSR*s are reported **(D)**.

best fit (white lines in **Figures 9–11**, panels A) are reported in **Table 3**.

1D Numerical Modeling

Given the available ground-motion recordings (i.e., maximum PGA = 36 gal), a linear site response model (i.e., within the low-strain field) is preferred to validate the proposed shear wave velocity models (**Figures 9–11**, panels A), by comparing the theoretical transfer functions (TFs) and the fundamental modes with the resonance peaks highlighted by ambient noise and earthquake *HVSR*s. The 1D linear site response is done by means of the software SHAKE91 (Schnabel, 1972; Idriss and Sun, 1993; Schnabel et al., 1993). In **Table 3**, for each layer (ID) and site, are also reported the values of the theoretical resonance frequencies associated to the fundamental-modes $f_{0,ID}$, obtained by the equation:

$$f_{0,ID} = V_{ST,ID} / (4 * H_{T,ID}) \quad (1)$$

where $H_{T,ID}$ is the sum of the layer thicknesses (H_{ID}), starting from the topmost layer and moving towards, and $V_{ST,ID}$ is the weighted average of shear-wave velocities over $H_{T,ID}$, obtained by the equation:

$$V_{ST,ID} = H_{T,ID} / \sum (H_{ID} / V_{S,ID}) \quad (2)$$

where H_{ID} and $V_{S,ID}$ are the thickness and the shear-wave velocity, respectively.

Table 3 also indicates the values for unit weight (ρ), useful for the impedance-contrast calculation, together with an estimation of the mean effective stress (σ'_0) at each layer (ID), to be used in the equation by Darendeli (2001) for the low-strain damping (D_0) calculation. In particular, the parameters of the Darendeli equations are fixed to: plasticity index: 0.0%; over-consolidation ratio: 1.0; cycles of loading: 10; characteristic frequency: 1 Hz. The mean effective stress (σ'_0) is estimated from unit weight (ρ) considering a coefficient of lateral earth pressure equal to 0.50.

It is well known that the choice of the seismic input for a low-deformation field is theoretically not relevant. Then, as the seismic input for modeling, a generic strong-motion waveform is selected, just characterized by enough energy to overcome the numerical limits of the software in the frequency band of interest (i.e., 0.1–10 Hz). In fact, the fundamental modes estimated by **eq. (1)** are within the same frequency band of about 0.1–10 Hz, for the numerical models in question.

Finally, in order to also account for the variations of both V_S and H in the modeling, **Table 3** reports the two further V_S models *min* and *max*. These models represent the minimum and maximum limit of the envelope that includes all V_S profiles (i.e., black lines in panels *a* of **Figures 9–11**) obtained with

uncertainties of 10% with respect to the best-fit model (i.e., white line in panels A of **Figures 9–11**).

The theoretical transfer functions are computed using the *best* model, together with the min and max models and are plotted in **Figure 12**, applying the Konno-Ohmachi smoothing (1998) operator with $b = 40$. The TFs are compared with the ambient noise *HVSR*s; except in the case of Giurati sports centre, which is sited very close to IV. MILN (~300 m), where the *HVSR* from earthquakes is considered (**Figure 12D**).

For all the analysed sites, the numerical model matches the resonance frequencies recognized by the experimental results, in particular for *pk1* and *pk3*. On the contrary, more uncertainties are present in the range 0.5–3 Hz, where many peaks and valleys are present at different periods, as a consequence of the one-dimensional modeling adopted, which is composed by 7 homogeneous layers (**Table 3**). For all cases, a significant discrepancy in terms of peak amplitudes is evident by comparing the obtained TFs and the ambient noise *HVSR* curves.

In particular, both at North and Vettabbia parks the resonance frequencies obtained from the noise *HVSR*s at ~ 0.2 Hz better match the resonant frequency of the TFs derived from the min model (**Table 3**). At Giuriati site, the mean earthquake *HVSR* agrees with TFs in terms of frequency and amplitudes, with except of the peak at ~ 0.2 Hz, where the TFs slightly underestimate the experimental *HVSR*s obtained both from ambient noise and earthquakes.

DISCUSSIONS AND CONCLUSION

In this paper, we present the work carried out to characterize the spatial variability of local soil conditions in the city of Milan and its surroundings and propose a seismo-stratigraphic model oriented to seismic site amplification. The model is derived from a combination of passive and active geophysical tests supported by a dense grid of geological and stratigraphic information from shallow and deep vertical wells and it is cross-checked with 1D numerical modeling.

The work consists of performing different geophysical tests; both active (i.e., MASW) and passive measurements are carried out to investigate both shallow and deep deposits. The passive analyses comprise 33 single-station ambient noise measurements and 4 microtremor arrays at 3 sites (i.e., North Park, Giuriati, Vettabbia) selected along a NNW-SSE alignment. The passive arrays are performed using different geometries and increasing aperture to explore the frequency range from 0.35 to 30 Hz. The geophysical analysis is supported by a subsoil model built along the NNW-SSE section after the collection and re-interpretation of all available geological and stratigraphic information and the documentation related to surficial and deep wells for exploration. Therefore, the resulting Vs. profiles, down to ~1.8 km in depth, can be associated with the geophysical interfaces and stratigraphic discontinuities.

The transfer functions obtained from numerical models and cross-checked by experimental curves (*HVSR* from ambient noise and earthquakes) identify a first resonant frequency at about 0.2 Hz, namely the expression of a deep contrast of impedance, that we associate with the PL transition (**Figures 10–12**) between the Miocene sedimentary rocks (i.e., Gallare marls) and the overlying Pliocene deposits (i.e., Santerno clays).

The second contrast of impedance, relevant for site effects, is found at a depth between 300 and 400 m (**Figures 10–12**), at the transition between marine and continental sedimentation. In this case, a chronostratigraphic unconformity, Qm2 (**Figures 10–12**), is functional to geophysics, although the corresponding frequency is not evident from ambient noise *HVSR*s.

Shallower layers with low shear wave velocity (<250 m/s, **Figures 10–12**) result in high frequency peaks (between 3 and 8 Hz) that are evident in the ambient noise *HVSR*s.

A general trend, from all measurements, is the decrease in the frequency of the three main identified peaks, interpreted as the increase in depth of the deposits towards the centre of the Po plain, to the south.

Our hypotheses on the Vs. model should be verified due to the uncertainties and trade-off typical of the passive techniques (e.g., Lai et al., 2020). As an example, De Franco et al. (2009) interpret the subsoil of Milan by analysing a very deep active reflection profile, performed in the western part of the city and, in that case, except for superficial impedance contrast, the Vs. gradually increase down to ~900 m without marked changes.

Another source of uncertainty can be the amplification peak around 0.2 Hz, which is interpreted as the coincidence with the microseismic long-period double-frequency peak by Marzorati and Bindi (2006) or Ferretti et al. (2013). Other authors, e.g., Paolucci et al. (2015), highlight a correlation between the amplitude values of the low-frequency peak and the sea-wave height, not observed for the high-frequency peaks. This issue could be resolved performing a generalised inversion of seismic data (e.g., Parolai et al., 2000; Ameri et al., 2011).

Moreover, the 1D approach which, in our opinion, is acceptable for the target area because surface stratigraphy is typically characterized by horizontal layers of alluvial deposits, does not account for the generation of surface waves, and the response of soil deposits is assumed to be predominantly related to *SH* waves propagating vertically from the underlying bedrock. Numerical modelling performed in the Po Plain highlighted that 2D and 3D effects can be significant because of the complex buried morphology of the basin (e.g., Vuan et al., 2011; Paolucci et al., 2015; Klin et al., 2019; Mascandola et al., 2021). In particular, due to the very large dimensions of the Po basin few attempts are available in the literature to objectively quantify 2D or 3D morphological effects on wave field propagation, in particular at low frequency, which makes this still an open issue.

This study will be useful for future site response assessments, numerical modelling of seismic-wave propagation, dynamic ground response analyses, and site-specific seismic hazard evaluation, contributing to future urban planning and risk mitigation (Eurocode 8, CEN, 2004; NTC, 2018).

DATA AVAILABILITY STATEMENT

The raw data supporting the conclusions of this article will be made available by the authors, without undue reservation.

AUTHOR CONTRIBUTIONS

This study started from an original idea of LL, MM and SL. MM, SL, GB, AL and CF contributed to the data acquisition of the passive seismic arrays and MAWS. All the Authors participated to the ambient noise single measurements performed in the urban area of Milan. MM analysed ambient noise and earthquakes data throught the HVSR method. MM, SL and RP worked on the ambient noise arrays to estimate the surface wave dispersion curves. MM and RP worked on the shear wave velocity profiles. RP performed the 1D numerical modeling. SL interpreted the geological and stratigraphic data and worked about the subsoil model.

FUNDING

National Institute of Geophysics and Volcanology (INGV).

ACKNOWLEDGMENTS

The authors thank the colleagues of INGV-Milano for the cooperation during the geophysical surveys, in particular Antonucci A., Manganello P., Mirenna S., Pessina V., Rizzo A. and Rovida A. Particular thanks to the Associate Editor, Roberto Paolucci, and to the reviewers who provided helpful reviews that improved this paper.

SUPPLEMENTARY MATERIAL

The Supplementary Material for this article can be found online at: https://www.frontiersin.org/articles/10.3389/feart.2022.915083/full#supplementary-material

REFERENCES

Aki, K. (1957). Space and Time Spectra of Stationary Stochastic Waves, with Special Reference to Microtremors. *Bull. Earthq. Res. Inst.* 35, 415–457.

Ameri, G., Oth, A., Pilz, M., Bindi, D., Parolai, S., luzi, L., et al. (2011). Separation of Source and Site Effects by Generalized Inversion Technique Using the Aftershock Recordings of the 2009 L'Aquila Earthquake. *Bull. Earthq. Eng.* 9, 717–739. doi:10.1007/s10518-011-9248-4

Ansal, A., Tönük, G., and Kurtulucs, A. (2009). "Microzonation for Urban Planning,". *Earthquakes and Tsunamis, Geotechnical, Geological, and Earthquake Engineering*. Editor A. T. Tankut (Dordrecht: Springer), Vol 11, 133–152. doi:10.1007/978-90-481-2399-5_9

Ansal, A., Kurtuluş, A., and Tönük, G. (2010). Seismic Microzonation and Earthquake Damage Scenarios for Urban Areas. *Soil Dyn. Earthq. Eng.* 30, 1319–1328. doi:10.1016/j.soildyn.2010.06.004

Aversa, S., and Crespellani, T. (2016). Seismic Microzonation: an Essential Tool for Urban Planning in Seismic Areas. *Upl. J. Urban Plann Landsc. Environ. Des.* 1 (1), 121–152. doi:10.6092/2531-9906/5035

Bard, P.-Y. (2008). Foreword. *Bull. Earthq. Eng.* 6 (1), 1–2. doi:10.1007/s10518-008-9059-4

Bard, P. Y. (2005). *Site Effects Assessment Using Ambient Excitations (SESAME). WP 6: Derivation of Dispersion Curves*. Grenoble: Technical report.

Beck, J. L., and Hall, J. F. (1986). Factors Contributing to the Catastrophe in Mexico City during the Earthquake of September 19, 1985. *Geophys. Res. Lett.* 13, 593–596. doi:10.1029/gl013i006p00593

Bettig, B., Bard, P. Y., Scherbaum, F., Riepl, J., Cotton, F., Cornou, C., et al. (2001). Analysis of Dense Array Measurements Using the Modified Spatial Auto-Correlation Method (SPAC). Application to Grenoble Area. *Bol. Geofis. Teor. Appl.* 42 (3-4), 281–304.

Bielak, J., Xu, J., and Ghattas, O. (1999). Earthquake Ground Motion and Structural Response in Alluvial Valleys. *J. Geotechnical Geoenvironmental Eng.* 125 (5), 413–423. doi:10.1061/(asce)1090-0241(1999)125:5(413)

Bigi, G., Costantino, D., Parotto, M., Sartori, R., and Scandone, P. (1990). – *Structural Model of Italy. Firenze, Società Elaborazioni Cartografiche (S.EL.CA.), Consiglio Nazionale Delle Ricerche Progetto Finalizzato Geodinamica, Scala 1:500.000, 9 Fogli*.

Bocherdt, R. D. (1970). Effects of Local Geology on Ground Motion Near San Francisco Bay. *Bull. Seismol. Soc. Am.* 60, 29–61. doi:10.1785/BSSA0600010029

Boore, D. M., and Akkar, S. (2003). Effect of Causal and Acausal Filters on Elastic and Inelastic Response Spectra. *Earthq. Engng. Struct. Dyn.* 32, 1729–1748. doi:10.1002/eqe.299

Capon, J. (1969). High-resolution Frequency-Wavenumber Spectrum Analysis. *Proc. IEEE* 57, 1408–1418. doi:10.1109/proc.1969.7278

Celikbilek, A., and Sapmaz, G. (2016). Risk Management and Microzonation in Urban Planning: an Analysis for Istanbul. *Disaster Sci. Eng.* 2 (2), 59–66.

Crespellani, T. (2014). Seismic Microzoning in Italy: a Brief History and Recent Experiences. *Ing. Sism* 31 (2), 3–31.

D'Amico, V., Picozzi, M., Baliva, F., Albarello, D., Menichetti, M., Bozzano, F., et al. (2006). "Test Sites in Europe for the Evaluation of Ground Motion Amplification: Site Response of the Gubbio Basin (Central Italy) Using Geological Data and Seismic Noise Measurements," in Proceeding of the 1st European Conference on Earthquake Engineering and Seismology, Geneva, Switzerland (Geneva: Abstract Book), 301.

D'Amico, V., Picozzi, M., Baliva, F., and Albarello, D. (2008). Ambient Noise Measurements for Preliminary Site-Effects Characterization in the Urban Area of Florence, Italy. *Bull. Seismol. Soc. Am.* 98 (3), 1373–1388. doi:10.1785/0120070231

Darendeli, M. B. (2001). *Development of a New Family of Normalized Modulus Reduction and Material Damping Curves*. (PhD thesis). Austin, Texas: University of Texas. Available at: https://repositories.lib.utexas.edu/bitstream/handle/2152/10396/darendelimb016.pdf March, accessed 2022).

De Ferrari, R., Ferretti, G., Barani, S., and Spallarossa, D. (2010). Investigating on the 1920 Garfagnana Earthquake (Mw=6.5): Evidences of Site Effects in Villa Collemandina (Tuscany, Italy). *Soil Dyn. Earthq. Eng.* 30, 1417–1429. doi:10.1016/j.soildyn.2010.07.004

De Franco, R., Biella, G., Caielli, G., Berra, F., Guglielmin, M., Lozej, A., et al. (2009). Overview of High Resolution Seismic Prospecting in Pre-Alpine and Alpine Basins. *Quat. Int.* 204 (1-2), 65–75. doi:10.1016/j.quaint.2009.02.011

Dondi, L., Mostardini, F., and Rizzini, A. (1982). "Evoluzione sedimentaria e paleogeografia nella pianura padana," in *Guida alla geologia del margine appenninico-padano, Guida Geol. Reg. S.G.I.* Editors G. Cremonini and F. Ricci Lucchi (Bologna (Italy), 47–58.

Eurocode 8, CEN (2004). Eurocode 8: Design of Structures for Earthquake Resistance. P1: General Rules, Seismic Actions and Rules for Buildings. *Draft* 6, 522. Doc CEN/TC250/SC8/N335.

Fäh, D., Kind, F., and Giardini, D. (2001). A Theoretical Investigation of Average H/V Ratios. *Geophys. J. Int.* 145 (2), 535–549. doi:10.1046/j.0956-540x.2001.01406.x

Fäh, D., Kind, F., and Giardini, D. (2003). Inversion of Local S-Wave Velocity Structures from Average H/V Ratios, and Their Use for the Estimation of Site-Effects. *J. Seismol.* 7 (4), 449–467. doi:10.1023/b:jose.0000005712.86058.42

Ferretti, G., Zunino, A., Scafidi, D., Barani, S., and Spallarossa, D. (2013). On Microseisms Recorded Near the Ligurian Coast (Italy) and Their Relationship with Sea Wave Height. *Geophys. J. Int.* 194, 524–533. doi:10.1093/gji/ggt114

Furumura, T., and Kennett, B. L. N. (1998). On the Nature of Regional Seismic Phases-III. The Influence of Crustal Heterogeneity on the Wavefield for Subduction Earthquakes: the 1985 Michoacan and 1995 Copala, Guerrero, Mexico Earthquakes. *Geophys. J. Int.* 135 (3), 1060–1084. doi:10.1046/j.1365-246x.1998.00698.x

GeoMol Team(2015). in *GeoMol – Assessing Subsurface Potentials of the Alpine Foreland Basins for Sustainable Planning and Use of Natural Resources – Project Report*. Lf. U. Augsburg, 188.

Grazier, V., Shakal, A., Scrivner, C., Hauksson, E., Polet, J., and Jones, L. (2002). TriNet Strong-Motion Data from the M 7.1 Hector Mine, California, Earthquake of 16 October 1999. *Bull. Seismol. Soc. Am.* 92, 1525–1542. doi:10.1785/0120000925

Hailemikael, S., Amoroso, S., and Gaudiosi, I. (2020). Guest editorial: Seismic Microzonation of Central Italy Following the 2016-2017 Seismic Sequence. *Bull. Earth. Eng.* 18, 5415–5422. doi:10.1007/s10518-020-00929-6

Hanks, T. C. (1975). Strong Ground Motion of the San Fernando, California, Earthquake: Ground Displacements. *Bull. Seismol. Soc. Am.* 65 (1), 193–225. doi:10.1785/bssa0650010193

Hatayama, K. (2008). Lessons from the 2003 Tokachi-Oki, Japan, Earthquake for Prediction of Long-Period Strong Ground Motions and Sloshing Damage to Oil Storage Tanks. *Journal.of Seismol* 12, 255–263. doi:10.1007/s10950-007-9066-y

Hisada, Y., Aki, K., and Teng, T. L. (1993). 3-D Simulations of Surface Wave Propagation in the Kanto Sedimentary Basin, Japan Part 2: Application of the Surface Wave BEM. *Bull. Seismol. Soc. Am.* 83 (6), 1700–1720. doi:10.1785/BSSA0830061700

Idriss, I. M., and Sun, J. I. (1993). *User's Manual for SHAKE91: A Computer Program for Conducting Equivalent Linear Seismic Response Analyses of Horizontally Layered Soil Deposits*. Davis, CA, USA: Center for Geotechnical Modeling, Department of Civil and Environmental Engineering, University of California.

ISPRAGeologico d'Italia, S., and Lombardia, R. (2016). in *Carta Geologica d'italia alla scala 1:50.000, Foglio 118 Milano (con note illustrative)*. Editors V. A cura di Francani, A. Piccin, M. Credali, F. Berra, D. Battaglia, P. Gattinoni, et al.

Joyner, W. B. (2000). Strong Motion from Surface Waves in Deep Sedimentary Basins. *Bull. Seismol. Soc. Am.* 90 (6B), S95–S112. doi:10.1785/0120000505

Kagawa, T., Zhao, B., Miyakoshi, K., and Irikura, K. (2004). Modeling of 3D Basin Structures for Seismic Wave Simulations Based on Available Information on the Target Area: Case Study of the Osaka Basin, Japan. *Bull. Seismol. Soc. Am.* 94 (4), 1353–1368. doi:10.1785/012003165

Kim, H.-S., Sun, C.-G., and Cho, H.-I. (2017). Geospatial Big Data-Based Geostatistical Zonation of Seismic Site Effects in Seoul Metropolitan Area. *Int. J. Geo-Information* 6 (6), 174. doi:10.3390/ijgi6060174

Klin, P., Laurenzano, G., Romano, M. A., Priolo, E., and Martelli, L. (2019). ER3D: a Structural and Geophysical 3-D Model of Central Emilia-Romagna (Northern Italy) for Numerical Simulation of Earthquake Ground Motion. *Solid earth*. 10 (3), 931–949. doi:10.5194/se-10-931-2019

Koketsu, K., Hatayama, K., Furumura, T., Ikegami, Y., and Akiyama, S. (2005). Damaging Long-Period Ground Motions from the 2003 Mw 8.3 Tokachi-Oki, Japan Earthquake. *Seismol. Res. Lett.* 76, 67–73. doi:10.1785/gssrl.76.1.67

Koketsu, K., and Miyake, H. (2008). A Seismological Overview of Long-Period Ground Motion. *J. Seismol.* 12 (2), 133–143. doi:10.1007/s10950-007-9080-0

Konno, K., and Ohmachi, T. (1998). Ground-motion Characteristics Estimated from Spectral Ratio between Horizontal and Vertical Components of Microtremor. *Bull. Seismol. Soc. Am.* 88, 228–241. doi:10.1785/bssa0880010228

Lacoss, R. T., Kelly, E. J., and Toksöz, M. N. (1969). Estimation of Seismic Noise Structure Using Arrays. *Geophysics* 34, 21–38. doi:10.1190/1.1439995

Lai, C. G., Poggi, V., Famà, A., Zuccolo, E., Bozzoni, F., Meisina, C., et al. (2020). An Inter-disciplinary and Multi-Scale Approach to Assess the Spatial Variability of Ground Motion for Seismic Microzonation: the Case Study of Cavezzo Municipality in Northern Italy. *Eng. Geol.* 274, 105722. doi:10.1016/j.enggeo.2020.105722

Laurenzano, G., Priolo, E., Mucciarelli, M., Martelli, L., and Romanelli, M. (2017). Site Response Estimation at Mirandola by Virtual Reference Station. *Bull. Earthq. Eng.* 15 (6), 2393–2409. doi:10.1007/s10518-016-0037-y

Lermo, J., and Chávez-García, F. J. (1993). Site Effect Evaluation Using Spectral Ratios with Only One Station. *Bull. Seism. Soc. Am.* 83 (5), 1574–1594. doi:10.1785/bssa0830051574

Liang, J. Z., Hao, H., Wang, Y., and Bi, K. M. (2009). Design Earthquake Ground Motion Prediction for Perth Metropolitan Area with Microtremor Measurements for Site Characterization. *J. Earthq. Eng.* 13 (7), 997–1028. doi:10.1080/13632460802687710

Liu, L., Chen, Q.-f., Wang, W., and Rohrbach, E. (2014). Ambient Noise as the New Source for Urban Engineering Seismology and Earthquake Engineering: a Case Study from Beijing Metropolitan Area. *Earthq. Sci.* 27 (1), 89–100. doi:10.1007/s11589-013-0052-x

Luzi, L., Pacor, F., Ameri, G., Puglia, R., Burrato, P., Massa, M., et al. (2013). Overview on the Strong-Motion Data Recorded during the May-June 2012 Emilia Seismic Sequence. *Seismol. Res. Lett.* 84 (4), 629–644. doi:10.1785/0220120154

Maddalena Michele, M., Raffaele Di Stefano, R., Lauro Chiaraluce, L., Marco Cattaneo, M., Pasquale De Gori, P., Giancarlo Monachesi, G., et al. (2016). The Amatrice 2016 Seismic Sequence: a Preliminary Look at the Mainshock and Aftershocks Distribution. *Ann. Geophys. Fast track* 59, 59. doi:10.4401/ag-7227

Marcucci, S., Milana, G., Hailemikael, S., Carlucci, G., Cara, F., Di Giulio, G., et al. (2019). The Deep Bedrock in Rome, Italy: a New Constraint Based on Passive Seismic Data Analysis. *Pure Appl. Geophys.* 176 (6), 2395–2410. doi:10.1007/s00024-019-02130-6

Martelli, L., and Romani, M. (2013). *Microzonazione Sismica e analisi della condizione limite per l'emergenza delle aree epicentrali dei terremoti della pianura emiliana di maggio-giugno 2012, relazione illustrativa, Servizio geologico, sismico e dei suoli Regione Emilia Romagna (in Italian)*.

Marzorati, S., and Bindi, D. (2006). Ambient Noise Levels in North Central Italy. *G-Cube* 7 (9), 1–14. doi:10.1029/2006gc001256

Mascandola, C., Massa, M., Barani, S., Lovati, S., and Santulin, M. (2017). Long-Period Amplification in Deep Alluvial Basins and Consequences for Site-Specific Probabilistic Seismic-Hazard Analysis: An Example from the Po Plain (Northern Italy). *Bull. Seismol. Soc. Am.* 107 (2), 770–786. doi:10.1785/0120160166

Mascandola, C., Massa, M., Barani, S., Albarello, D., Lovati, S., Martelli, L., et al. (2019). Mapping the Seismic Bedrock of the Po Plain (Italy) through Ambient-Vibration Monitoring. *Bull. Seismol. Soc. Am.* 109 (1), 164–177. doi:10.1785/0120180193

Mascandola, C., Barani, S., Massa, M., and Albarello, D. (2021). New Insights on Long-Period (>1s) Seismic Amplification Effects in Deep Sedimentary Basins: the Case of the Po Plain (Northern Italy). *Bull. Seism. Soc. Am.* 111 (4), 2071–2086. doi:10.1785/0120200315

Massa, M., and Augliera, P. (2013). Teleseisms as Estimators of Experimental Long-Period Site Amplification: Application to the Po Plain (Italy) for the 2011 Mw 9.0 Tohoku-Oki (Japan) Earthquake. *Bull. Seismol. Soc. Am.* 103 (5), 2541–2556. doi:10.1785/0120120164

Milana, G., Bordoni, P., Cara, F., Di Giulio, G., Hailemikael, S., and Rovelli, A. (2013). 1D Velocity Structure of the Po River Plain (Northern Italy) Assessed by Combining Strong Motion and Ambient Noise Data. *Bull. Earthq. Eng.* 12 (5), 2195–2209. doi:10.1007/s10518-013-9483-y

NTC (2018). *Aggiornamento delle Norme Tecniche per le Costruzioni. Part 3.2.2: Categorie di sottosuolo e condizioni topografiche*, 42. Rome: Gazzetta Ufficiale n. del 20 febbraio 2018 (in Italian).

Miyazaki, S. I., Segall, P., Fukuda, J., and Kato, T. (2004). Space Time Distribution of Afterslip Following the 2003 Tokachi-oki Earthquake: Implications for Variations in Fault Zone Frictional Properties. *Geophys. Res. Lett.* 31 (6), 410. doi:10.1029/2003gl019410

Molnar, S., Assaf, J., Sirohey, A., and Adhikari, S. R. (2020). Overview of Local Site Effects and Seismic Microzonation Mapping in Metropolitan Vancouver, British Columbia, Canada. *Eng. Geol.* 270, 105568. doi:10.1016/j.enggeo.2020.105568

Molnar, S., Sirohey, A., Assaf, J., Bard, P. Y., Castellaro, S., Cornou, C., et al. (2022). A Review of the Microtremor Horizontal-To-Vertical Spectral Ratio (MHVSR) Method. *J. Seismol* 16, 1–33. doi:10.1007/s10950-021-10062-9

Moya, A., Schmidt, V., Segura, C., Boschini, I., and Atakan, K. (2000). Empirical Evaluation of Site Effects in the Metropolitan Area of San José, Costa Rica. *Soil Dyn. Earthq. Eng.* 20 (1-4), 177–185. doi:10.1016/s0267-7261(00)00049-x

MPS Working Group (2004). *Redazione della mappa di pericolosità sismica prevista dall'Ordinanza PCM del 20 marzo 2003Rapporto Conclusivo per il Dipartimento della Protezione Civile*.

Mucciarelli, M., Gallipoli, M. R., Di Giacomo, D., Di Nota, F., and Nino, E. (2005). The Influence of Wind on Measurements of Seismic Noise. *Geophys. J. Int.* 161 (2), 303–308. doi:10.1111/j.1365-246x.2004.02561.x

Muttoni, G., Carcano, C., Garzanti, E., Ghielmi, M., Piccin, A., Pini, R., et al. (2003). Onset of Major Pleistocene Glaciations in the Alps. *Geol* 31 (11), 989–992. doi:10.1130/g19445.1

Nakamura, Y. (1989). A Method for Dynamic Characteristics Estimation of Subsurface Using Microtremor or the Ground Surface. *QR Railw. Tech. Res. Inst.* 30 (1), 25–33.

Ohori, M., Nobata, A., and Wakamatsu, K. (2002). A Comparison of ESAC and FK Methods of Estimating Phase Velocity Using Arbitrarily Shaped Microtremor Arrays. *Bull. Seismol. Soc. Am.* 92, 2323–2332. doi:10.1785/0119980109

Okada, H. (2003). *The Microtremor Survey Method*. Houston, TX, United States: SEG library.

Paolucci, E., Albarello, D., D'Amico, S., Lunedei, E., Martelli, L., Mucciarelli, M., et al. (2015). A Large Scale Ambient Vibration Survey in the Area Damaged by May-June 2012 Seismic Sequence in Emilia Romagna, Italy. *Bull. Earthq. Eng.* 13 (11), 3187–3206. doi:10.1007/s10518-015-9767-5

Park, C. B., Miller, R. D., and Xia, J. (1998). "Imaging Dispersion Curves of Surface Waves on Multi-Channel Record," in *SEG Technical Program Expanded Abstracts 1998* (Houston, TX, United States: Society of Exploration Geophysicists), 1377–1380.

Park, C. B., Miller, R. D., and Xia, J. (1999). Multichannel Analysis of Surface Waves. *Geophysics* 64, 800–808. doi:10.1190/1.1444590

Parolai, S., Bindi, D., and Augliera, P. (2000). Application of the Generalized Inversion Technique (GIT) to a Microzonation Study: Numerical Simulations and Comparison with Different Site-Estimation Techniques. *Bull. Seismol. Soc. Am.* 90 (2), 286–297. doi:10.1785/0119990041

Parolai, S., Picozzi, M., Richwalski, S. M., and Milkereit, C. (2005). Joint Inversion of Phase Velocity Dispersion and H/V Ratio Curves from Seismic Noise Recordings Using a Genetic Algorithm, Considering Higher Modes. *Geophys. Res. Lett.* 32, L01303. doi:10.1029/2004GL021115

Parolai, S., Richwalski, S. M., Milkereit, C., and Fäh, D. (2006). S-wave Velocity Profiles for Earthquake Engineering Purposes for the Cologne Area (Germany). *Bull. Earthq. Eng.* 4, 65–94. doi:10.1007/s10518-005-5758-2

Picozzi, M., Strollo, A., Parolai, S., Durukal, E., Özel, O., Karabulut, S., et al. (2009). Site Characterization by Seismic Noise in Istanbul, Turkey. *Soil Dyn. Earthq. Eng.* 29 (3), 469–482. doi:10.1016/j.soildyn.2008.05.007

Pieri, M., and Groppi, G. (1981). "Subsurface Geological Structure of the Po Plain, Italy," in *Progetto Finalizzato Geodinamica/Sottoprogetto "Modello Strutturale"* (Rome: Consiglio Nazionale delle Ricerche Publ. N°), 414.

Poggi, V., and Fäh, D. (2010). Estimating Rayleigh Wave Particle Motion from Three-Component Array Analysis of Ambient Vibrations. *Geophys. J. Int.* 180 (Issue 1), 251–267. doi:10.1111/j.1365-246x.2009.04402.x

Puglia, R., Tokeshi, K., Picozzi, M., D'Alema, E., Parolai, S., and Foti, S. (2011). Interpretation of Microtremor 2D Array Data Using Rayleigh and Love Waves: the Case Study of Bevagna (Central Italy). *Near Surf. Geophys.* 9 (6), 529–540. doi:10.3997/1873-0604.2011031

Priolo, E., Romanelli, M., Barnaba, C., Mucciarelli, M., Laurenzano, G., Dall'Olio, L., et al. (2012). The Ferrara Thrust Earthquakes of May-June 2012: Preliminary Site Response Analysis at the Sites of the OGS Temporary Network. *Ann. Geophy.* 55 (4), 591–597. doi:10.4401/ag-6172

Ratchkovski, N. A., Hansen, R. A., Stachnik, J. C., Cox, T., Fox, O., Rao, L., et al. (2003). Aftershock Sequence of the Mw 7.9 Denali Fault, Alaska, Earthquake of 3 November 2002 from Regional Seismic Network Data. *Seismol. Res. Lett.* 74 (6), 743–752. doi:10.1785/gssrl.74.6.743

Regione Lombardia, Eni Divisione Agip (2002). *Geologia degli acquiferi Padani della Regione Lombardia, a cura di Cipriano Carcano e Andrea Piccin*. Firenze: S.EL.CA. (in Italian).

Ritter, J. R. R., Balan, S. F., Bonjer, K.-P., Diehl, T., Forbriger, T., Marmureanu, G., et al. (2005). Broadband Urban Seismology in the Bucharest Metropolitan Area. *Seismol. Res. Lett.* 76 (5), 574–580. doi:10.1785/gssrl.76.5.574

Rizzini, A., and Dondi, L. (1978). Erosional Surface of Messinian Age in the Subsurface of the Lombardian Plain (Italy). *Mar. Geol.* 27, 303–325. doi:10.1016/0025-3227(78)90037-3

Ronald Abraham, J., Lai, C. G., and Papageorgiou, A. (2015). Basin-effects Observed during the 2012 Emilia Earthquake Sequence in Northern Italy. *Soil Dyn. Earthq. Eng.* 78, 230–242. doi:10.1016/j.soildyn.2015.08.007

Rovida, A., Locati, M., Camassi, R., Lolli, B., and Gasperini, P. (2020). The Italian Earthquake Catalogue CPTI15. *Bull. Earthq. Eng.* 18 (7), 2953–2984. doi:10.1007/s10518-020-00818-y

Sambridge, M. (1999). Geophysical Inversion with a Neighbourhood Algorithm-I. Searching a Parameter Space. *Geophys. J. Int.* 138, 479–494. doi:10.1046/j.1365-246x.1999.00876.x

Sato, T., Graves, R. W., and Somerville, P. G. (1999). Three-dimensional Finite-Difference Simulations of Long-Period Strong Motions in the Tokyo Metropolitan Area during the 1990 Odawara Earthquake (MJ 5.1) and the Great 1923 Kanto Earthquake (MS 8.2) in Japan. *Bull. Seismol. Soc. Am.* 89 (3), 579–607. doi:10.1785/bssa0890030579

Scardia, G., De Franco, R., Muttoni, G., Rogledi, S., Caielli, G., Carcano, C., et al. (2012). Stratigraphic Evidence of a Middle Pleistocene Climate-driven Flexural Uplift in the Alps. *Tectonics* 31 (6), 3108. doi:10.1029/2012tc003108

Schnabel, P. B., Lysmer, J., and Seed, H. B. (1993). *SHAKE-91: Equivalent Linear Seismic Response Analysis of Horizontally Layered Soil Deposits*. Berkeley, CA, USA: The Earthquake Engineering Online Archive NISEE E-Library.

Schnabel, P. B. (1972). *SHAKE a Computer Program for Earthquake Response Analysis of Horizontally Layered Sites*. Berkeley, CA, USA: EERC Report; University of California.

Schneider, J. A., Mayne, P. W., and Rix, G. J. (2001). Geotechnical Site Characterization in the Greater Memphis Area Using Cone Penetration Tests. *Eng. Geol.* 62 (1-3), 169–184. doi:10.1016/s0013-7952(01)00060-6

SESAME (2004). Guidelines for the Implementation of H/V Spectral Ratio Technique on Ambient Vibration Measurements, Processing and Interpretation. Available at: http://sesame-fp5.obs.ujf-grenoble.fr/Delivrables/Del-D23-HV_User_Guidelines.pdf Last accessed March, 2022).

Somerville, P. G., Collins, N. F., Graves, R. W., and Pitarka, A. (2004). "An Engineering Ground Motion Model for Basin Generated Surface Waves," in Proc. 13th World Conference on Earthquake Engineering, Vancouver, B.C., Canada, August 2004.

Stephenson, W. J., Hartzell, S., Frankel, A. D., Asten, M., Carver, D. L., and Kim, W. Y. (2009). Site Characterization for Urban Seismic Hazards in Lower Manhattan, New York City, from Microtremor Array Analysis. *Geophys. Res. Lett.* 36 (3), 444. doi:10.1029/2008gl036444

Stucchi, M., Meletti, C., Montaldo, V., Crowley, H., Calvi, G. M., and Boschi, E. (2011). Seismic Hazard Assessment (2003-2009) for the Italian Building Code. *Bull. Seismol. Soc. Am.* 101, 1885–1911. doi:10.1785/0120100130

Sun, C.-G., Kim, H.-S., Chung, C.-K., and Chi, H.-C. (2014). Spatial Zonations for Regional Assessment of Seismic Site Effects in the Seoul Metropolitan Area. *Soil Dyn. Earthq. Eng.* 56, 44–56. doi:10.1016/j.soildyn.2013.10.003

Tarabusi, G., and Caputo, R. (2017). The Use of HVSR Measurements for Investigating Buried Tectonic Structures: the Mirandola Anticline, Northern Italy, as a Case Study. *Int. J. Earth Sci. Geol. Rundsch)* 106 (1), 341–353. doi:10.1007/s00531-016-1322-3

Tragni, N., Calamita, G., Lastilla, L., Belloni, V., Ravanelli, R., Lupo, M., Salvia, V., and Gallipoli, M. R. (2021). Sharing Soil and Building Geophysical Data for Seismic Characterization of Cities Using CLARA WebGIS: A Case Study of Matera (Southern Italy). *Appl. Sci.* 11 (9), 4254. doi:10.3390/app11094254

ViDEPI project (2009). *Visibilità dei dati afferenti all'attività di esplorazione petrolifera in Italia Ministero dello sviluppo economico DGRME - Società Geologica Italiana, Assomineraria*. Available at: https://www.videpi.com.

Vuan, A., Klin, P., Laurenzano, G., and Priolo, E. (2011). Far-Source Long-Period Displacement Response Spectra in the Po and Venetian Plains (Italy) from 3D Wavefield Simulations. *Bull. Seismol. Soc. Am.* 101 (3), 1055–1072. doi:10.1785/0120090371

Wang, J. H. (2008). Urban Seismology in the Taipei Metropolitan Area: Review and Prospective. *TAO Terr. Atmos. Ocean. Sci.* 19 (3), 2. doi:10.3319/tao.2008.19.3.213(t)

Wathelet, M., Chatelain, J.-L., Cornou, C., Giulio, G. D., Guillier, B., Ohrnberger, M., et al. (2020). Geopsy: A User-Friendly Open-Source Tool Set for Ambient Vibration Processing. *Seism. Soc. Lett.* 91 (3), 1878–1889. doi:10.1785/0220190360

Wathelet, M., Jongmans, D., Ohrnberger, M., and Bonnefoy-Claudet, S. (2008). Array Performances for Ambient Vibrations on a Shallow Structure and Consequences over V S Inversion. *J. Seismol.* 12, 1–19. doi:10.1007/s10950-007-9067-x

Wessel, P., and Smith, W. H. F. (1995). New Version of the Generic Mapping Tools. *EOS Trans. AGU* 76, 329. doi:10.1029/95eo00198

Conflict of Interest: The authors declare that the research was conducted in the absence of any commercial or financial relationships that could be construed as a potential conflict of interest.

Publisher's Note: All claims expressed in this article are solely those of the authors and do not necessarily represent those of their affiliated organizations, or those of the publisher, the editors and the reviewers. Any product that may be evaluated in this article, or claim that may be made by its manufacturer, is not guaranteed or endorsed by the publisher.

frontiers | Frontiers in Earth Science

ORIGINAL RESEARCH
published: 16 June 2022
doi: 10.3389/feart.2022.886145

Building Stock Classification Using Machine Learning: A Case Study for Oslo, Norway

Federica Ghione[1,2]*, *Steffen Mæland*[3], *Abdelghani Meslem*[1,4] and *Volker Oye*[1,2]

[1]Department of Applied Seismology, NORSAR, Kjeller, Norway, [2]Department of Geosciences, University of Oslo, Oslo, Norway, [3]Department of Holistic Systems, SimulaMet, Oslo, Norway, [4]Norwegian University of Life Sciences (NMBU), Ås, Norway

This paper describes a new concept to automatically characterize building types in urban areas based on publicly available image databases, making parts of seismic risk assessment more time and cost-effective, and improving the reliability of seismic risk assessment, especially in regions where building stock information is currently not documented. One of the main steps in evaluating potential human and economic losses in a seismic risk assessment, is the development of inventory databases for existing building stocks in terms of load-resisting structural systems and material characteristics (building typologies classification). The common approach for building stock model classification is to perform extensive fieldwork and walk-down surveys in representative areas of a city, and in some cases using random sample surveys of geounits. This procedure is time and cost consuming, and subject to personal interpretation: to mitigate these costs, we have introduced a machine learning methodology to automate this classification based on publicly available image databases. We here use a Convolutional Neural Network (CNN) to automatically identify the different building typologies in the city of Oslo, Norway, based on facade images taken from *in-situ* fieldwork and from Google Street View. We use transfer learning of state-of-the-art pretrained CNNs to predict the Model Building Typology. The present article attempts to categorize Oslo's building stock in five main building typologies: timber, unreinforced masonry, reinforced concrete, composite (steel-reinforced concrete) and steel. This method results in 89% accuracy score for timber buildings, though only 35% success score for steel-reinforced concrete buildings. We here classify and define for the first time a relevant set of five typologies for the Norwegian building typologies as observed in Oslo and applicable at national level. In addition, this study shows that CNNs can significantly contribute in terms of developing a cost-effective building stock model.

Keywords: building stock model, convolutional neural network, machine learning, seismic risk assessment, Oslo (Norway)

OPEN ACCESS

Edited by:
Roberto Paolucci,
Politecnico di Milano, Italy

Reviewed by:
Roberto Gentile,
University College London, United Kingdom
Dennis Wagenaar,
Nanyang Technological University, Singapore

***Correspondence:**
Federica Ghione
federica.ghione@norsar.no

Specialty section:
This article was submitted to Geohazards and Georisks, a section of the journal Frontiers in Earth Science

Received: *28 February 2022*
Accepted: *26 May 2022*
Published: *16 June 2022*

Citation:
Ghione F, Mæland S, Meslem A and Oye V (2022) Building Stock Classification Using Machine Learning: A Case Study for Oslo, Norway. Front. Earth Sci. 10:886145. doi: 10.3389/feart.2022.886145

1 INTRODUCTION

Within the last century, earthquakes, flooding and droughts have been the dominating phenomena responsible for causing fatalities and economic losses worldwide (see Data Availability Statement section). In the last few decades though, earthquakes are the dominating phenomena standing for most fatalities (Wallemacq and House, 2018), providing the motivation and requirement for more

detailed and effective seismic risk assessment studies. A seismic risk assessment estimates the probability of losses if an earthquake occurs, can assist through updated building regulations and to initiate other mitigation actions to avoid likelihood for casualties and economic losses. To do that, information regarding seismic hazard, vulnerability and exposure models of the area are needed (Silva et al., 2014). In particular, the exposure model contains information about all the buildings in a specific area, infrastructures, and population data. A seismic risk assessment for a building stock in a city needs a classification of the buildings in accordance with their structural typologies, an important parameter to define the building performance under seismic load.

The development of a building stock model is always challenging and time consuming, especially when the area of investigation is large. Until today it is a common practice to use both Google Earth and *in-situ* surveys to get information on building structural systems and material characteristics. However, machine learning methods to analyze visual imagery have recently been applied to classify building stocks, using online available façade images, obtained through Google Street View (GSV), as key information. To our knowledge, this automatic image analysis using Convolutional Neural Network (CNN) was previously only tested in two places to automatically detect building materials and types of lateral-load resistance: Gonzalez et al. (2020) for Medellin city, Colombia and Aravena Pelizari et al. (2021) for Santiago de Chile. Those two examples are similar to our study, in terms of applying CNNs to automatically detect and identify the different building typologies for the two cities using GSV images. In this study, however, we define for the first time a Model Building Typology (MBT) for Oslo, and we conduct a survey amongst experts within earthquake engineering. Based on the survey's results, the MBT identified in Oslo can further be applied at the national scale (Norway). Another example by GFDRR (2018) shows that using a combination of deep learning and GSV together with drone images may lead to remotely identify buildings that require further inspection and possible retrofitting/strengthening for Guatemala city, Guatemala.

This paper presents the building stock model for Oslo, capital of Norway. The general information of the buildings is obtained from the public cadastre from www.kartverket.no. This information contains the total number of buildings in Oslo with the corresponding coordinates, number of stories, number of housing units, usable area, and total area.

To perform seismic risk studies, the availability of detailed building stock typologies is a necessity. This is usually a very time-consuming process, and our innovative approach using transfer learning and CNNs for the classification may provide this required input in much shorter time and at lower cost. This could be a solution for most of the urbanized regions in the world to develop seismic risk assessments and incorporate earthquake preparedness actions.

The paper is organized as follow: in **Section 2** we describe the methodology followed and the CNN approach; **Section 3** describes the study area, the identified building typologies, and the data used for this work; **Section 4** introduces the results and **Section 5** presents the main conclusion.

2 METHODOLOGY

The methodology is based on the use of a CNN for automating the typology classification step. While the classification itself requires no manual involvement, the main workload goes into compiling a labelled image dataset (discussed in **Section 3**) and training the parameters of the CNN (described in this section). Once a CNN structure is selected and the CNN is suitably trained, classifying a set of unseen images is done quickly and at low computational cost. A diagram depicting the workflow is shown in **Figure 1**. First, a representative set of façade images must be collected and labelled, which entails the manual part of the process. Using these images to train a CNN, subsequent images of unknown typologies can be downloaded online and classified in bulk and used for seismic risk assessment. There are two challenges when using CNNs for this task: the need for a large set of labelled images, and the computational load of training them. We mitigate both by the use of *transfer learning*, which will be described in this section.

2.1 Image Recognition

Current state-of-the-art methods for recognizing objects in images are based on variants of CNNs, which are artificial neural networks that use sliding filters (or kernels) to process their inputs (LeCun et al., 2015). Unlike traditional image processing, these filters are learnt from examples during a training phase, and they are typically stacked so that the output from one convolutional layer is used as input to the next one. A benefit of the convolutional filters is that they are invariant under translations, meaning that the positioning of objects in an image does not matter (Goodfellow et al., 2016). Stacking convolutional layers allows for learning pattern hierarchies, where the first layers recognize simple shapes such as vertical or horizontal lines, while the last layers recognize compositions of these patterns, for instance the shape of a building. In most approaches, the convolutional layers are interspersed with pooling layers, which reduce the dimensions by downsampling. These reduce the required number of learnable parameters, and at the same time introduce invariance to rotation and scaling (Goodfellow et al., 2016). In addition, it is common to add special layers and mechanisms that facilitate the learning process, such as dropout (Srivastava et al., 2014) and residual (skip) connections (He et al., 2016a). The composition of layers is referred to as the *architecture* of the network, while we use *model* to indicate a network with a particular set of optimized parameters. For classification purposes, the output of the final convolution layer is input to one or several fully connected layers, which ultimately output a mutually exclusive prediction for which class an input image belongs to. The learnable parameters of a model include both the convolution filters and the weights of the classification layer.

2.2 Transfer Learning and Network Architectures

Modern CNNs typically have millions of free learnable parameters and optimizing them requires large corpora of

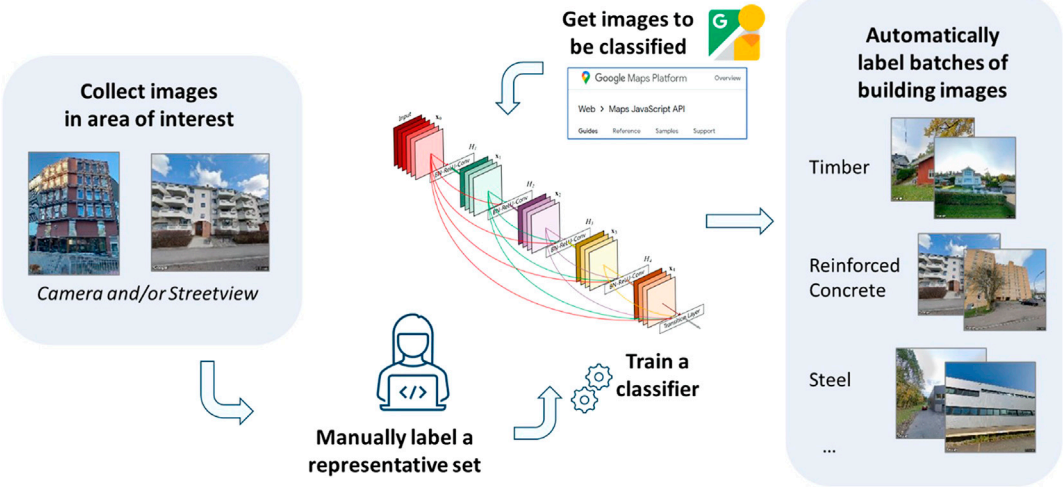

FIGURE 1 | Workflow diagram. Using manually annotated façade images from fieldwork, from GSV, or a combination of the two, a CNN is trained to classify building typologies. A large set of images is then downloaded from GSV, and automatically classified to obtain the building stock for the area of interest.

data. In image recognition, the standard dataset for training and performance evaluation is the *ImageNet (ILSVRC)* database (Russakovsky et al., 2015), which contains nearly 1.3 million labelled images of various common objects. When training a CNN on such a diverse dataset, the first layers will be sensitive to simple shapes like straight or curved lines, while the middle layers are sensitive to different compositions of these basic patterns. Since only the last layers are highly specific to the particular dataset the CNN is trained on, applications such as ours can benefit from *transfer learning*, where one first trains the CNN on a large, generic dataset such as ImageNet, and subsequently re-trains (or *fine-tunes*) the last layers on the application-specific data. This allows for re-using the knowledge contained in the first and middle layers and is particularly useful in cases like ours where the application-specific dataset is comparatively small.

To select the optimal CNN architecture for our case, we compute four performance metrics (described in next paragraph) for eleven candidates, all pre-trained on ImageNet data. These are available in the Keras framework (Chollet, 2015). For each candidate, we set all parameters to remain constant, but replace the final classification layer by a new layer with six output nodes, corresponding to the number of building typologies under consideration. As a measure against overfitting, we apply dropout (Srivastava et al., 2014) before the classification layer. This means temporarily removing nodes from the network during training, which improves robustness by reducing the nodes' reliance on each other. We randomly drop nodes at a 20% probability. We then train on our data, updating only the parameters of the classification layer. We perform 4-fold cross-validation, meaning we divide the training data into four equally sized parts, and use three parts for training and one for computing metrics. The parts are then rotated so that all parts are used for computing metrics. Since the weights of the final layer are randomly initialized for each training round, potentially affecting the final performance, we repeat the cross-validation process twice, and report the average results for the in total eight trained models per architecture. Training is done for up to 100 epochs, where an epoch is a single pass over all the training data, followed by a metric evaluation. If learning fails to improve over five consecutive epochs, the learning rate is reduced by half, thereby taking shorter steps toward the optimal solution. If learning fails to improve over ten consecutive epochs, the training is stopped.

The four computed metrics are: accuracy, precision, recall, and area under the receiver operating characteristic curve. Accuracy is defined as the fraction of samples where the predicted class exactly matches the true class; in our case of 6 distinct classes, a random classifier would have an accuracy of 1/6 = 0.17, assuming that the number of samples of each class are the same. Precision is defined as the number of true positives divided by the sum of true positives and false positives, indicating the quality of the positive predictions. Recall, on the other hand, is defined as the number of true positives divided by the sum of true positives and false negatives, indicating the completeness of the positive predictions. In addition, we compute the area under the receiver operating curve (ROC), which is obtained by plotting the true positive rate against the false positive rate. Since true and false predictions relate to a binary classification problem, we compute precision, recall and ROC individually for each class, in a one-vs-all fashion, and then report the average across all classes. The results are listed in **Table 1**. For all metrics, the best possible result is 1, while the worst possible result is 0.

2.3 Fine-Tuning

From **Table 1** we observe that most CNN architectures yield similar results, but the three members of the DenseNet (Huang et al., 2017) family stand out as the highest performers across all evaluation metrics. They are structurally similar but differ in the number of convolution layers, which is given by the number at the end of their names (121, 169 and 201, respectively). The DenseNet201 architecture excels on all metrics and is therefore

TABLE 1 | Metrics for different CNN architectures. Highlighted in bold are the best observed values. The last column indicates the total number of parameters for each architecture.

Architecture	Accuracy	Precision	Recall	ROC AUC	Parameters
Xception Chollet. (2017)	0.759	0.762	0.759	0.920	20,873,774
VGG16 Simonyan and Zisserman. (2015)	0.740	0.739	0.740	0.906	14,717,766
VGG19 Simonyan and Zisserman. (2015)	0.732	0.733	0.732	0.904	20,027,462
ResNet50V2 He et al. (2016b)	0.759	0.757	0.759	0.917	23,577,094
ResNet101V2 He et al. (2016b)	0.762	0.760	0.762	0.917	42,638,854
ResNet152V2 He et al. (2016b)	0.757	0.757	0.757	0.912	58,343,942
InceptionV3 Szegedy et al. (2016)	0.762	0.762	0.762	0.922	21,815,078
InceptionResNetV2 Szegedy et al. (2017)	0.750	0.752	0.750	0.912	54,345,958
DenseNet121 Huang et al. (2017)	0.764	0.764	0.764	0.922	7,043,654
DenseNet169 Huang et al. (2017)	0.770	0.772	0.770	0.926	12,652,870
DenseNet201 Huang et al. (2017)	**0.778**	**0.780**	**0.778**	**0.932**	18,333,510

selected for further optimization. While being largest in the DenseNet family, we note that this family of architectures is the smallest in terms of number of learnable parameters, compared to the other ones tested. This indicates that raw model size, as listed in the last column of **Table 1**, cannot be directly considered as a proxy for performance, and comparisons are required to find the best architecture for a given application. We find, however, that there is an approximately linear relationship between the model size and the training time. Compared to DenseNet201, the smallest architecture (DenseNet121) takes 12% shorter time to train a single epoch, while the largest architecture (ResNet151V2) takes 31% longer, when training on a Nvidia V100 (NVIDIA, 2020) graphics card.

Proceeding with the DenseNet201 architecture, we fine-tune it to our data in a two-step procedure. Using the full training dataset, apart from 20% of images that are set aside as validation data to monitor the training progress, we first train only the final classification layer of the model. Like before, we halve the learning rate if training has stagnated for five epochs, and end training if it has still not improved after ten epochs. In the second step, we now additionally unfreeze the parameters of the last 64 convolution layers. This allows for adapting a larger part of the model specifically to our data, while still retaining the low-level pattern recognition of the first convolution layers. The DenseNet201 architecture is organized into five blocks of multiple convolution layers, where each block has a complicated internal structure, but has a single connection to the next block. Therefore, we only consider it useful to free the parameters of entire blocks at the time; freeing the last 64 convolution layers equals the entire last block. Doing so means we now train 38% of all parameters in the model (approximately 7 million out of 18 million). Experiments with freeing a larger number of blocks resulted in overfitting, where the accuracy on the validation data diverges greatly from that of the training data. As for the first step, training is run until improvement has failed to improve for ten epochs.

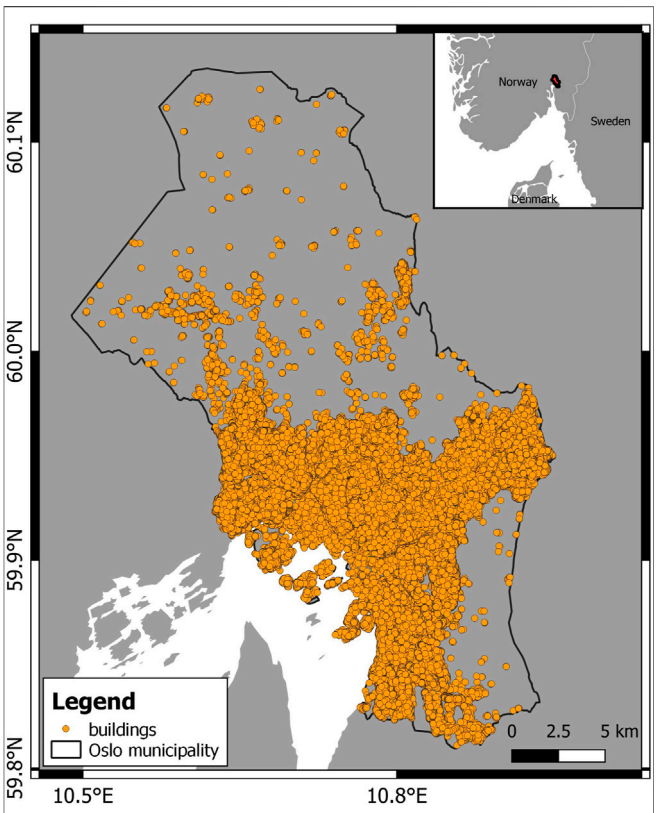

FIGURE 2 | Building distribution (shown with orange dots) in Oslo municipality (study area).

3 DATA

In order to conduct seismic risk assessment a building stock model needs to be available, and the key input data to develop such building stock models are the building typologies as extracted in the relevant region. Building typologies are related to the ability of a building to resist lateral loads that mainly affects the structural system and depends on material and height. The lateral load-resisting system and its material can be identified only from the blueprints (two-dimensional set of technical/engineering drawings that specify a building's dimensions, construction materials, and the exact placement of all its components) or by direct expert observations. Unfortunately, structural blueprints are not always available. Therefore, expert

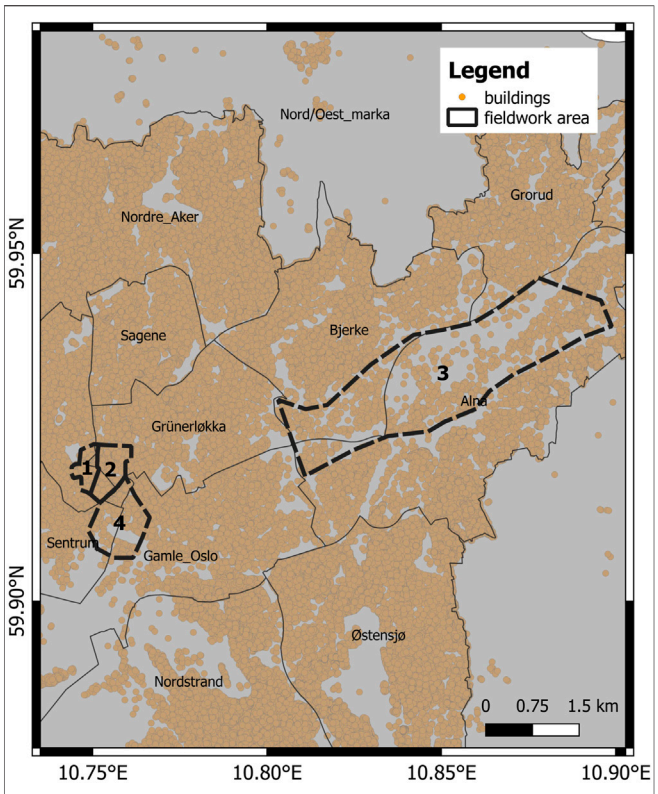

FIGURE 3 | In the figure, the fieldwork area is represented with dashed line.

opinions seem to be the best option to assemble building inventories and fundamental information. However, in most of the cases, it is timewise and economically not possible to survey each asset. For this reason, many assumptions need to be made to establish a building stock model and interpolate data from surveyed areas to not surveyed neighborhoods. Recently, using GSV (Google Street View) and Google Earth has become an alternative way to carry out fieldwork for visualizing façade and material information remotely (GFDRR, 2018; Kang et al., 2018; Gonzalez et al., 2020; Aravena Pelizari et al., 2021). However, uncertainties are remaining in the building typology classification. In this paper, we use the EMS-98 building taxonomy (Grünthal, 1998) with some extension related to specific typology that are not present in the original classification [e.g. composite (steel-reinforced concrete) typology].

3.1 Study Area

Our study area is the city of Oslo, the capital of Norway (**Figure 2**). The oldest settlements in the area are from around 11000 BC, but Oslo was only founded in 1000 AC. The oldest part of the city is the eastern part, called Bjørvika in Gamle Oslo (see **Figure 3**). In 1624, a disastrous fire destroyed most of the city, and built on the ashes, the new town was called Christiania. After that devastating fire, a ban on wooden houses was introduced allowing only solid brick, and half-timbered brick houses (Eriksson et al., 2016). In 1769 Christiania had about 7500 inhabitants. During the 1600s the demand for wood rose, and Christiania became an important harbour for trading wood. Outside the city centre, many small wooden houses were built, and some of those still exist today. During the industrial period of the 1840s, many factories were built along the river Akerselva and the population increased significantly to about 113.000 inhabitants. In the late 1880s, many multi-stories brick tenements were constructed to fulfil the request for more living space. In 1925 the city changed its name back to Oslo and the Ring Road was introduced; in 1948 another important step for the city was the development of the new subway system (Eriksson et al., 2016). In 2020 Oslo had a population count of 697,549 and by 2040 the expected number is around 926,000 (Eriksson et al., 2016). This prediction has a direct consequence for the city, i.e. it will need to accommodate the new residents with new buildings. Oslo municipality covers an area of 480 km^2 and it is subdivided in 17 boroughs or *bydel* in Norwegian.

One key element to consider during the planning of a city expansion with respect to new infrastructures is an accurate evaluation of the seismic risk, which is strongly depending on the local seismic hazard conditions, in turn influenced by soil amplification. Norway shows low to medium seismicity that leads to a lower level of seismic hazard compared to other Southern European countries (Danciu et al., 2021). Compared on a national scale, the city of Oslo falls within a zone of intermediate seismic hazard. Oslo was hit by a significant earthquake (5.4 Mw) on the 23rd of October 1904 (Bungum et al., 2009). Although the epicenter was located 115 km south of Oslo, the event (known as 1904 Oslofjord earthquake) generated ground motions that propagated on both sides of the Oslo fjord from the south of Fredrikstad/Tønsberg to the north of Oslo. The earthquake was felt over an area of 800.000 km^2 from Namsos in the north to Poland, and across southern Norway to Helsinki in the east (Bungum et al., 2009). The maximum intensity on the Mercalli scale in Oslo was reported to VI and major damages were reported, mainly for wooden and unreinforced masonry buildings in the Oslo area. Although the severe damages to the buildings, no relevant and significant mitigation measures were put in place after this event. The first seismic standard introduced in Norway was by the end of the 1980s, and it was mostly destinated for seismic design of offshore structures. Within the same period there was also another document destinated for buildings, but it was introduced and used only as recommendation. In 2004 a new standard on the design of structures considering loads from seismic influence was adopted (NS 3491-12). In 2008, Norway adopted the Eurocode and since then it has been the only standard for seismic design for all types of structures and infrastructures.

3.2 Model Building Typology

Building stocks usually vary from locality to locality and certainly even more between different countries due to different construction practices, material availability and construction period.

The following steps are followed to recognize the different building typologies for Oslo and to develop a Model Building Typology (MBT):

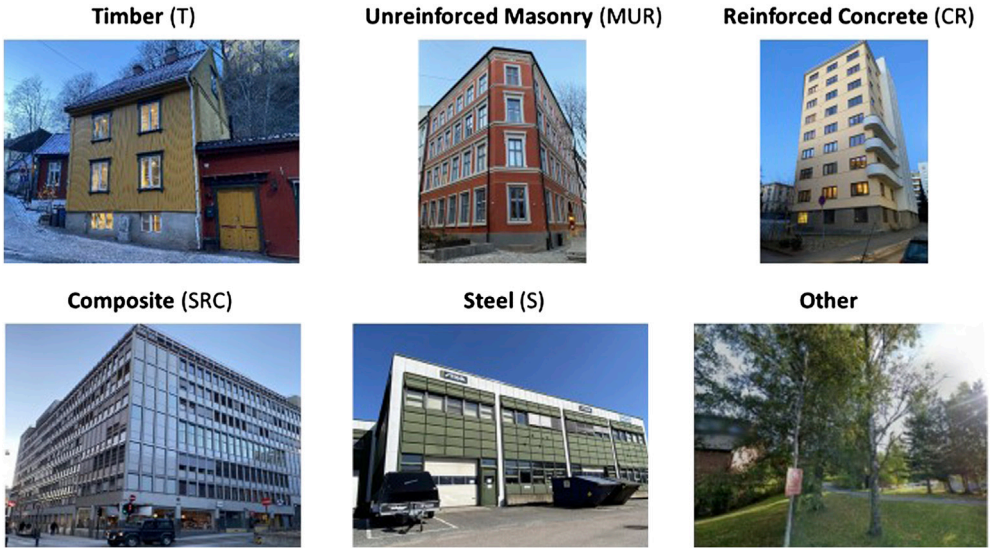

FIGURE 4 | Building typologies for the building stock in Oslo: timber (T), unreinforced masonry (MUR), reinforced concrete (CR), composite (SRC), steel (S) and other.

1) a first overview of the building typologies is obtained from Google Earth for the different neighborhoods in the city. The building stock is observed at different scales (from small to large):
   - the inbuilt 3D-building option allows us to identify the lateral load bearing systems, predominant work material for walls, façade decoration, flooring and roofing types and number of stories.
   - The Street View mode gives us a ground-level view of the different buildings and it helps us to identify similarity and heterogeneity in the same geounit.
2) - With the plan view, we understand the general distribution of the building stock in the city looking from the top. It allows us to identify different roof materials and characteristics that can be potentially linked to different building typologies. Through the first evaluation using Google Earth, some area of the city center (Grünerløkka, Oslo central station, Bjørvika) and Alna (see **Figure 3**) are chosen for detailed *in-situ* fieldwork. Those areas contain a good representation of all the typologies and are good candidates to test the machine learning methodology to automatically identify different building typologies.
3) During 5 days of fieldwork during the winter of 2021, about 350 pictures of the facade buildings are taken manually, and information related to structural system and material related data are collected (e.g. lateral loadbearing systems observed, material type, flooring/roofing system, number of stories, usage/type of activity). These form key information to define a MBT.
4) After steps 1 and 2, we define an initial building typology classification, and we divide the observations into five groups with the corresponding typology.
5) To confirm and validate the initial evaluation of the typologies, a survey questionnaire regarding seismic vulnerability assessment of the existing building stock in Oslo is sent out to experts (mainly engineers working in Norway) in order to validate the building typologies that they have been identified. The survey was divided into eleven different sections, with questions related to the structural system and material characteristics of the building stock in Oslo, date of practice of a given typology and general practices. The expert's opinion confirmed the initial evaluation and they agreed that the building typologies recognized in Oslo are applicable at national scale. The questionnaire shows results compatible to the preliminary assessment.
6) Combining results from both fieldwork and survey questionnaire, a final Model Building Typology (MBT) is defined, and it represents the existing building typologies in Oslo city and Norway.
7) Images from GSV are downloaded for all the districts of the city. A total of 5074 pictures are manually labelled using the MBT previously defined. The pictures are used to train the Convolutional Neural Network (CNN). As Gonzalez et al. (2020), Aravena Pelizari et al. (2021), also here the CNN methodology is applied to automatically detect the different building typologies in Oslo.

The results of the survey questionnaire combined with the field survey have shown that the existing building stock in Oslo can be divided into three main construction periods:

1) Buildings built before 1950, estimated to represent roughly 35% of the total existing building stock, and mostly made of timber and unreinforced masonry.
2) Buildings built between 1950 and 1998, estimated to represent 25% of the total number of buildings, and they are mainly made of reinforced concrete.

TABLE 2 | Confusion matrix computed on the test data set. Rows show the true class, and the columns the CNN-identified class. Correct predictions follow the diagonal, highlighted in bold. As an example, 73% of CR buildings are correctly identified, but 3% are classified as MUR, 3% are classified as S, 2% SRC, 9% as T and 10% as other. In parentheses are the actual number of images.

		Predicted					
		CR	**MUR**	**S**	**SRC**	**T**	**Other**
True	CR	**0.73 (86)**	0.03 (4)	0.03 (3)	0.02 (2)	0.09 (11)	0.10 (12)
	MUR	0.05 (5)	**0.71 (76)**	0.00 (0)	0.00 (0)	0.20 (21)	0.05 (5)
	S	0.18 (5)	0.00 (0)	**0.57 (16)**	0.00 (0)	0.11 (3)	0.14 (4)
	SRC	0.60 (12)	0.00 (0)	0.05 (1)	**0.35 (7)**	0.00 (0)	0.00 (0)
	T	0.01 (3)	0.01 (6)	0.00 (0)	0.00 (0)	**0.89 (424)**	0.09 (42)
	Other	0.02 (4)	0.00 (1)	0.01 (2)	0.00 (0)	0.12 (32)	**0.87 (232)**

3) Buildings built between 1998 and up to today, estimated to cover 40% and they are found as reinforced concrete, composite (steel-reinforced concrete) and steel.

The following typologies are identified in Oslo and can be applied at national scale (see **Figure 4**):

- Timber (T): the construction with timber has been in practice for many years (before 1950), and the timber buildings mostly are frame structures consisting of wooden frames with solid or plate timber members. This typology is mainly used for housing and typically can be one to two stories, but there are also some 3 to 4 story-high buildings that can also be found as residential apartments and public buildings for various activities, e.g., schools. The timber construction is still in practice and starting from 2000 there have been new modern timber buildings that can also be found as high-rise buildings with more than 8 stories. As per the situation today, timber buildings represent around 20% of the existing building stock in Oslo.
- Unreinforced masonry (MUR): unreinforced masonry constructions are load-bearing wall system structures made of material that vary depending on the construction's age, and which can be burnt clay bricks, stone masonry blocks, concrete blocks or mixtures of other materials. Most of the existing buildings of this type were constructed before 1950. The majority can be found as low/mid-rise structures with 2–5 stories, and very few with more than 6 stories. They are used for residential, commercial and other general activities. In terms of location, this type of construction mostly can be found in the center of the city, and as a rough estimate, they represent 30% of the current building stock in Oslo.
- Reinforced concrete (RC): the construction of reinforced concrete buildings has been in practice since 1950, and the construction procedure of this typology consists of reinforced concrete frames (columns and beams), cast-in-place. But starting from 2000, the pre-cast practice has become more frequent in the construction of this type of structures. The existing RC buildings can cover different ranges of height classes (low, mid and high-rise) and can be found in most of the districts and zones of the city. It is estimated that this type of buildings represents 35% of the total existing buildings in the city.
- Composite (steel-reinforced concrete) (SRC): the composite construction has been in practice since 2000s, and it is estimated that it represents almost 10% of the total existing building stock of Oslo. Typically, the number of stories for this type of building can range between 2 to more than 15 stories for a few of the most recent buildings. The construction procedure of this typology consists of steel frames and cast-in-place concrete frames (columns and beams) and/or concrete shear walls. Buildings of this typology are mostly used as residential apartments, offices, commercial activities, and they are found in most of the districts and zones of the city.
- Steel (S): the existing steel structures are load-bearing steel moment frame constructions, and mostly are found outside the city center. This type of structures is, in general, used for industrial activities, also as big grocery stores, supermarkets, malls, parking lots, and hangars. Due to the nature of the utilization, story heights can be up to 6 m, and the number of stories can be up to 2 stories. The construction in steel has recently increased with the urban development, and currently it is estimated that this type of construction covers about 5% of the existing buildings in the city of Oslo.

In addition to the above typologies, one extra category "other" is added to account for the case that the algorithm could not recognize the typology or that no building could be identified in the picture at all.

3.3 Image Dataset

The dataset of all buildings in Oslo is obtained from the public cadastre (downloaded in December 2020) and it contains the number and the coordinates of all free-standing buildings of more than 50 m^2. In addition to façade photographs collected manually, images for each building position are downloaded automatically using the Google *Street View* API (GSV). The Street View service provides near-continuous street level imagery of most of the world's cities, and the service's API allows for direct download of images for a given set of coordinates. In order to accept an image to be related to a building, we set a threshold that the image needs to be taken within 40 m from the requested building coordinate. For the

FIGURE 5 | Examples of correctly **(A)** and falsely **(B)** classified images.

TABLE 3 | Distribution in terms of numbers and percentages of the predicted building typologies.

Typologies	Number of buildings	%
T	56,305	56.7
MUR	7,979	8.0
CR	7,536	7.6
SRC	399	0.4
S	515	0.5
other	26,605	26.8

134,432 buildings in Oslo, 74% of them fulfil this requirement and it has façade imagery available. Coverage is better in the city center where images for 94% of the buildings are available but can be as low as 50% in distant suburbs.

We do not manually check the image quality, such as how many of the requested buildings are included in the image, or whether it is occluded by trees, passing vehicles, scaffolding or similar. Such cases, where the building typology cannot be identified from the image, are labeled as "other", and the occurrence in the fieldwork area is approximately 27%. An example of this category is shown in **Figure 4**. Labelling of these cases is often difficult and can be subjective, and is expected to be a considerable source of uncertainty for training the automatic labelling procedure.

A total of 5,074 images from fieldwork and from GSV are manually labelled, and they constitute the dataset used for training and validating the CNN model. We set aside 20% (1,019 images) as a test dataset for the final performance evaluation, leaving 4055 images to use for training. Of the latter, we will also set aside a fraction of them for monitoring the training progress that is described in **Section 2**.

For CNN training and prediction, all images are downsampled to 224 × 224 pixels, which is the input resolution of the CNN model. Images from GSV are downloaded in a square format, while rectangular images from fieldwork are center cropped before downsampling. In order to artificially increase the size of the training data, we augment the images by applying the following transformations: randomly zooming in by up to 20%, randomly rotating by up to 25°, and randomly mirroring along the vertical axis. This is done only during training, and it is a standard procedure to improve the model's ability to generalize.

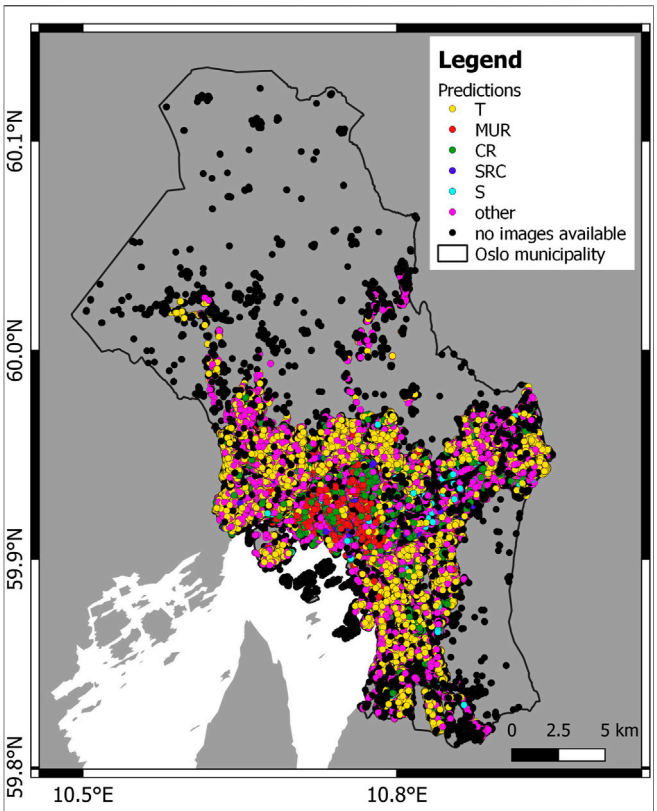

FIGURE 6 | Distribution of the predicted building typologies in Oslo, also including the categories "other" and "no images available".

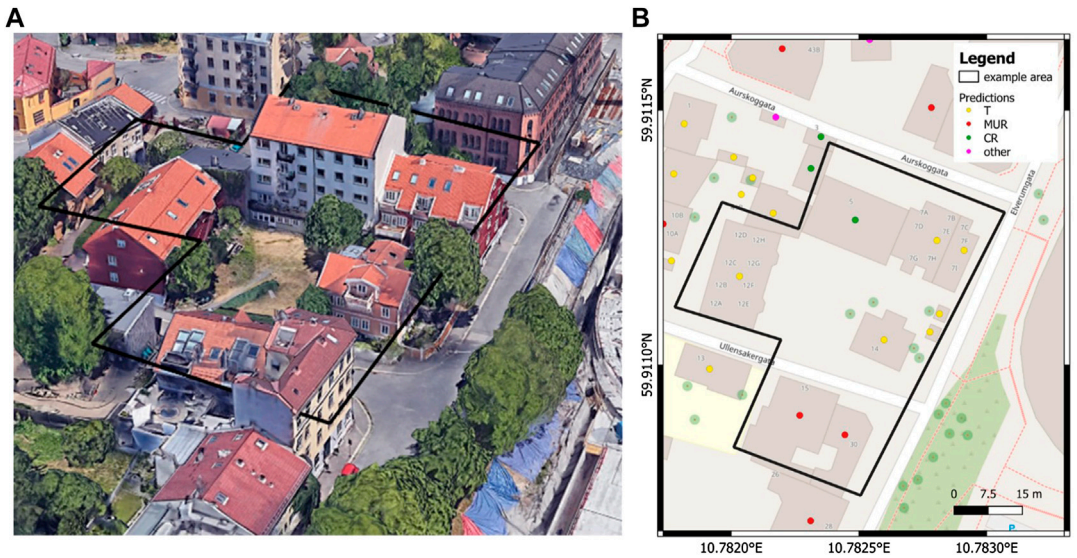

FIGURE 7 | (A): Google Earth 3D building's view of the example area in Oslo; **(B)**, the predicted MBT for the same example area. The observed and true MBT for the selected area coincides with the predicted one.

4 RESULTS

Having completed the fine-tuning, we compute the final performance metrics on the test dataset. The model achieves an accuracy of 0.825, a precision of 0.825, and a recall of 0.825. Without fine-tuning, we obtain an accuracy of 0.763, precision of 0.775 and recall of 0.769, showing that fine-tuning is greatly beneficial to performance. To investigate the classification performance per typology, we present a confusion matrix in **Table 2**. For each true typology (given by the rows), the confusion matrix shows the rate of test images that are assigned to each predicted label (given by the columns). The best performance is seen for timber (T), where 89% of images are classified correctly. This is expected, because timber is the most common typology in the training data, and therefore the category which the CNN has seen the largest variation of. It is also desirable, since we consider the training (and testing) data to be representative of the entire study area, and a high accuracy for the most common category will necessarily lead to a high overall accuracy.

The poorest performance is seen for steel-reinforced concrete (SRC), where 35% of the images are classified correctly, while 60% of them are classified as reinforced concrete (CR). These two typologies can be difficult to distinguish even for experts, as the façade characteristics may not unambiguously determine the typology. The classification of the "other" groups is in general quite successful with 87%. Within the 13% of misclassifications, almost all images in the "other" category are identified as timber buildings, which can be explained by the frequent presence of fences, rooftops and parked cars in these images, which are typical elements in residential areas common for timber buildings. Some examples of images and their predicted labels are shown in **Figure 5**. In **Figure 5** we can observe an example of a timber building correctly classified and a steel-reinforced concrete building misclassified as reinforced concrete.

Concerning the confusion matrix, we note that we did not apply class-specific weights to the images during training, i.e., all images were given equal priority. It is an option, however, to weight the images by the inverse of the class prevalence, so that rare classes are given higher priority than common ones. This would lead to a more equal classification accuracy across the typologies, instead of having a very high accuracy for the most prominent class (timber) and low accuracy for the least prominent one (steel-reinforced concrete). At the same time, it would also reduce the overall accuracy, and thereby the quality of the final result, which is why we decided against it.

The predicted building typologies are shown in **Table 3**, in terms of number of buildings and percentages, and in **Figure 6** in terms of spatial distribution. It is important to mention that the total number of buildings of Oslo (134,432) also includes buildings where no GSV images are available to perform the classification ("no images available" category includes 35,093 buildings, shown in **Figure 6**). This category is not shown in **Table 3** because we want to present the percentages of the classified buildings that used GSV images for the classification using machine learning. The "no image available" category represents 26.1% of the total number of buildings, and together with the "other" typology, the two categories sum to 45.9% of the total number of buildings. This means that we were able to automatically attribute a model building typology to 54.1% of the buildings in Oslo.

The predominant typology identified in Oslo is timber, that represents 56.7% of the classified buildings. In **Figure 6** we can observe the distribution of the predicted building typologies: most of the classified buildings are localized in the city center and in the urbanized area. GSV images are not available in remote areas (as forest) in Nordmarka and Østmarka: based on our local knowledge and through supervised learning in the area with Google Earth, the main typology identified is timber, represented by private cabins.

Figure 7 shows the predicted building typologies for an example area in Oslo. This area is chosen because we have a

good representation of different typologies in a small area. On the left side of the figure, the Google Earth 3D building's view is allowing to identify the MBT of the buildings under investigation. The right side of the figure shows the predicted MBT, that coincide with the observed MBT.

5 DISCUSSION AND CONCLUSION

This work shows the potential for combining machine learning and publicly available street-level imagery to automate the process of classifying Model Building Typologies for large-scale seismic risk assessment, using Oslo city (Norway) as a case study. Using a state-of-the-art Convolutional Neural Network (CNN) pre-trained on the ImageNet database, we developed a model that classifies typology in unseen images with 83% accuracy, using only data sources available online: the public cadastre and Google Street View. Supplemental high-quality images taken during field work were also used but are not required. Our workflow shows how seismic risk assessment can be highly automated and performed quickly without or limiting time-consuming and costly on-site surveys.

We observe that the classification accuracy varies with building typology: from 89% for timber and down to 35% for steel-reinforced concrete. The reason for this is twofold:

1. first, the distribution of the building mass in Oslo is heavily skewed towards timber buildings, with few steel or steel-reinforced concrete (SRC) buildings to use in the CNN training.
2. Secondly, SRC buildings are typically misclassified as reinforced concrete (CR), which is unfortunately also often the case in manual classification analysis. These misclassifications were verified by breaking down the separate typology predictions for an unseen test dataset by the true labels.

Misclassifications also occur between typologies that share the surrounding environment; in particular, we observe timber buildings surrounded by trees and fences being classified as "other", and vice versa. This indicates that the CNN to some extent incorporates the environment into the prediction and does not rely on the building properties alone. There exist several techniques (Simonyan et al., 2013; Samek et al., 2017; Selvaraju et al., 2017) to investigate this on a per-image basis, which should be considered in future studies.

The performance of the classifier can be improved by adding more labelled images, which is a matter of additional analyst time. Still, using a pre-trained model reduces the need for training data drastically (Yosinski et al., 2014), as well as lowering the computational cost compared to training a model from scratch. Our method is limited by the availability and good quality of GSV images, which do not offer complete geographical coverage and may be blocked by trees or vehicles. Hence, supplemental field work may be necessary for certain areas. Other online image providers can also complement GSV.

Given the success of this transfer learning approach, also demonstrated by Gonzalez et al. (2020), future work should investigate how well the CNN methodology generalizes and can hence be applied to other Nordic cities, both with and without additional re-training. We expect that this should be possible at least within Norway, likely also further to Sweden and Finland with generally similar building stocks.

Until recently, the identification of building typologies and the development of a building stock model for seismic risk assessment were limited regarding their spatial coverage as well as financial resources and the lack of representative *in-situ* information. With the data and methodology presented in this paper, these limitations can now be overcome for many areas of the world.

Future work within this topic could include a semi-automatic pre-classification of certain neighborhoods. For instance, we could feed the CNN with pre-conditioning data about the type of the current neighborhood, e.g. residential, commercial, industrial area, which will likely increase the success rate. In addition, one could think about merging information from google-maps roof aspect-ratio with the façade information as done in our current work.

DATA AVAILABILITY STATEMENT

The datasets presented in this study can be found in online repositories. The names of the repository/repositories and accession number(s) can be found below: https://github.com/NorwegianSeismicArray/ML-for-building-typologies.

AUTHOR CONTRIBUTIONS

FG is the main author of the article. She focused in the abstract, introduction, data, results, discussion and conclusion sections. She prepared all the pictures in the article. Her main contribution to the research work is represented by fieldwork in Oslo, taking manually and labelling all the pictures, to develop the different building typologies and to prepare and to analyse the results of the survey sent to the experts. SM, as second author, focused on the methodology, results, discussion and conclusion. He implemented and trained the CNN model, compared the different architectures, and prepared the classification results. AM helped to recognize and identify the different building typologies, to write the description of the typologies and to review the paper. VO helped in the writing and review processes. He discussed with the other authors regarding the best approach to develop the research and the article itself.

FUNDING

The results and the research showed in this article are connected to the GEObyIT project, funded by the Research Council of Norway (grant number 311596).

ACKNOWLEDGMENTS

The authors are grateful for the economic support provided by the Research Council of Norway.

REFERENCES

Aravena Pelizari, P., Geiß, C., Aguirre, P., Santa María, H., Merino Peña, Y., and Taubenböck, H. (2021). Automated Building Characterization for Seismic Risk Assessment Using Street-Level Imagery and Deep Learning. *ISPRS J. Photogrammetry Remote Sens.* 180, 370–386. doi:10.1016/j.isprsjprs.2021.07.004

Bungum, H., Pettenati, F., Schweitzer, J., Sirovich, L., and Faleide, J. I. (2009). The 23 October 1904 MS 5.4 Oslofjord Earthquake: Reanalysis Based on Macroseismic and Instrumental Data. *Bull. Seismol. Soc. Am.* 99, 2836–2854. doi:10.1785/0120080357

Chollet, F. (2015). Keras, GitHub. Available at: https://github.com/fchollet/keras.

Chollet, F. (2017). Xception: Deep Learning with Depthwise Separable Convolutions. in Proceedings - 30th IEEE Conference on Computer Vision and Pattern Recognition, CVPR 2017. doi:10.1109/CVPR.2017.195

Danciu, L., Nandan, S., Reyes, C., Basili, R., Weatherill, G., Beauval, C., et al. (2021). The 2020 Update of the European Seismic Hazard Model - ESHM20: Model Overview. *EFEHR Tech. Rep. 001 v1* 0.0, 1–121. doi:10.12686/a15

Eriksson, I., Borchgrevink, J., Sæther, M. M., Daviknes, H. K., Adamou, S., and Andresen, L. (2016). TU1206 COST Sub-urban WG1 Report. Available at: https://static1.squarespace.com/static/542bc753e4b0a87901dd6258/t/5707869ae707eb820b4118a5/1460111042910/TU1206-WG1-012+Oslo+City+Case+Study.pdf.

GFDRR (2018). Machine Learning for Disaster Risk Management. Available at: http://doi.wiley.com/.51, doi:10.1111/j.1468-0394.1988.tb00341.x

Gonzalez, D., Rueda-Plata, D., Acevedo, A. B., Duque, J. C., Ramos-Pollán, R., Betancourt, A., et al. (2020). Automatic Detection of Building Typology Using Deep Learning Methods on Street Level Images. *Build. Environ.* 177, 106805–106812. doi:10.1016/j.buildenv.2020.106805

Grünthal, G. (1998). *European Macroseismic Scale 1998*.

He, K., Zhang, X., Ren, S., and Sun, J. (2016a). Deep Residual Learning for Image Recognition. in Proceedings of the IEEE Computer Society Conference on Computer Vision and Pattern Recognition, Las Vegas, NV, USA, 27-30 June 2016 770–778. doi:10.1109/CVPR.2016.90

He, K., Zhang, X., Ren, S., and Sun, J. (2016b). "Identity Mappings in Deep Residual Networks," in *Lecture Notes in Computer Science (Including Subseries Lecture Notes in Artificial Intelligence and Lecture Notes in Bioinformatics)*, 630–645. doi:10.1007/978-3-319-46493-0_38

Heaton, J., Bengio, Y., and Courville, A. (2018). *Deep Learning*. MIT Press. Cambridge, Massachusetts, United States, doi:10.1007/s10710-017-9314-z

Huang, G., Liu, Z., Van Der Maaten, L., and Weinberger, K. Q. (2017). Densely Connected Convolutional Networks. in Proceedings - 30th IEEE Conference on Computer Vision and Pattern Recognition, CVPR 2017. doi:10.1109/CVPR.2017.243

Kang, J., Körner, M., Wang, Y., Taubenböck, H., and Zhu, X. X. (2018). Building Instance Classification Using Street View Images. *ISPRS J. Photogrammetry Remote Sens.* 145, 44–59. doi:10.1016/j.isprsjprs.2018.02.006

LeCun, Y., Bengio, Y., and Hinton, G. (2015). Deep Learning, Y. LeCun, Y. Bengio and G. Hinton. *Nature* 521, 436–444. doi:10.1038/nature14539

NVIDIA (2020). NVIDIA V100 TENSOR CORE GPU. Available at: https://images.nvidia.com/content/technologies/volta/pdf/volta-v100-datasheet-update-us-1165301-r5.pdf.

Russakovsky, O., Deng, J., Su, H., Krause, J., Satheesh, S., Ma, S., et al. (2015). ImageNet Large Scale Visual Recognition Challenge. *Int. J. Comput. Vis.* 115, 211–252. doi:10.1007/s11263-015-0816-y

Samek, W., Wiegand, T., and Müller, K.-R. (2017). Explainable Artificial Intelligence: Understanding, Visualizing and Interpreting Deep Learning Models. Available at: http://arxiv.org/abs/1708.08296.

Selvaraju, R. R., Cogswell, M., Das, A., Vedantam, R., Parikh, D., and Batra, D. (2017). Grad-CAM: Visual Explanations from Deep Networks via Gradient-Based Localization. in Proceedings of the IEEE International Conference on Computer Vision, Venice, Italy, 22-29 Oct. 2017 doi:10.1109/ICCV.2017.74

Silva, V., Crowley, H., Pagani, M., Monelli, D., and Pinho, R. (2014). Development of the OpenQuake Engine, the Global Earthquake Model's Open-Source Software for Seismic Risk Assessment. *Nat. Hazards* 72, 1409–1427. doi:10.1007/s11069-013-0618-x

Simonyan, K., Vedaldi, A., and Zisserman, A. (2013). Deep inside Convolutional Networks: Visualising Image Classification Models and Saliency Maps. Preprint at http://arxiv.org/abs/1312.6034.arXiv.org.

Simonyan, K., and Zisserman, A. (2015). Very Deep Convolutional Networks for Large-Scale Image Recognition. in 3rd International Conference on Learning Representations, ICLR 2015 - Conference Track Proceedings.

Srivastava, N., Hinton, G., Krizhevsky, A., Sutskever, I., and Salakhutdinov, R. (2014). Dropout: A Simple Way to Prevent Neural Networks from Overfitting. *J. Mach. Learn. Res.* 15, 1929–1958.

Szegedy, C., Ioffe, S., Vanhoucke, V., and Alemi, A. A. (2017). Inception-v4, Inception-ResNet and the Impact of Residual Connections on Learning. in 31st AAAI Conference on Artificial Intelligence, AAAI 2017.

Szegedy, C., Vanhoucke, V., Ioffe, S., Shlens, J., and Wojna, Z. (2016). Rethinking the Inception Architecture for Computer Vision. in Proceedings of the IEEE Computer Society Conference on Computer Vision and Pattern Recognition. doi:10.1109/CVPR.2016.308

Wallemacq, P., and House, R. (2018). Economic Losses, Poverty & Disasters: 1998-2017. *Nat. Resour.* Available at: https://www.researchgate.net/profile/Pascaline-Wallemacq-3/publication/331642958_Economic_Losses_Poverty_and_Disasters_1998-2017/links/5c859a6d92851c69506b1f0f/Economic-Losses-Poverty-and-Disasters-1998-2017.pdf?origin=publication_detail.

Yosinski, J., Clune, J., Bengio, Y., and Lipson, H. (2014). "How Transferable Are Features in Deep Neural Networks?" in *Advances in Neural Information Processing Systems*.

Conflict of Interest: The authors declare that the research was conducted in the absence of any commercial or financial relationships that could be construed as a potential conflict of interest.

frontiers | Frontiers in Earth Science

ORIGINAL RESEARCH
published: 13 July 2022
doi: 10.3389/feart.2022.917855

Evaluating the Minimum Number of Earthquakes in Empirical Site Response Assessment: Input for New Requirements for Microzonation in the Swiss Building Codes

Vincent Perron, Paolo Bergamo and Donat Fäh*

Swiss Seismological Service, Swiss Federal Institute of Technology of Zürich (ETHZ), Zürich, Switzerland

Site-specific hazard analyses and microzonation are important products for densely populated areas and facilities of special risk. The empirical amplification function is classically estimated using the standard spectral ratio (SSR) approach. The SSR simply consists in comparing earthquake recordings on soil sites with the recording of the same earthquake on a close-by rock reference. Recording a statistically significant number of earthquakes to apply the SSR can however be difficult, especially in low seismicity areas and noisy urban environments. On the contrary, computing the SSR from too few earthquakes can lead to an uncertain evaluation of the mean amplification function. Defining the minimum number of earthquake recordings in empirical site response assessment is thus important. We compute empirical amplification functions at 60 KiKnet sites in Japan from several hundred earthquakes and three Swiss sites from several tens of earthquakes. We performed statistical analysis on the amplification functions to estimate the geometric mean and standard deviation and more importantly to determine the distribution law of the amplification factors as a function of the number of recordings. Independent to the site and to the frequency, we find that the log-normal distribution is a very good approximation for the site response. Based on that, we develop a strategy to estimate the minimum number of earthquakes from the confidence interval definition. We find that 10 samples are the best compromise between minimizing the number of recordings and having a good statistical significance of the results. As a general rule, a minimum of 10 uncorrelated earthquakes should be considered, but the higher the number of earthquakes, the lower the uncertainty on the geometric mean of the site amplification function. Moreover, the linear site response is observed to be independent to the intensity of the ground motion level for the analyzed dataset.

Keywords: seismic hazard, site effects, microzonation, statistic, signal processing

OPEN ACCESS

Edited by:
Simone Barani,
University of Genoa, Italy

Reviewed by:
Giovanni Forte,
University of Naples Federico II, Italy
Enrico Paolucci,
University of Siena, Italy

****Correspondence:***
Vincent Perron
vincent.perron.mail@gmail.com

Specialty section:
This article was submitted to Geohazards and Georisks, a section of the journal Frontiers in Earth Science

Received: *11 April 2022*
Accepted: *01 June 2022*
Published: *13 July 2022*

Citation:
Perron V, Bergamo P and Fäh D (2022) Evaluating the Minimum Number of Earthquakes in Empirical Site Response Assessment: Input for New Requirements for Microzonation in the Swiss Building Codes. Front. Earth Sci. 10:917855. doi: 10.3389/feart.2022.917855

INTRODUCTION

Site effects can significantly increase the seismic hazard and risk locally. Unconsolidated deposits such as thick and soft sediments in sedimentary basins are prone to strongly amplify the ground motion. Site effects are caused, among others, by the seismic impedance between rock and sediments, the 1D, 2D and 3D resonances, and the edge-generated surface waves. In turn, the site response can vary significantly from one site to another (site-to-site variability, e.g., Bindi et al., 2009; Hollender et al., 2015; Bindi et al., 2017; Imtiaz et al., 2018; Perron et al., 2018) and from one earthquake to another (within-site variability, e.g., Thompson et al., 2012; Ktenidou et al., 2016; Ktenidou et al., 2017; Maufroy et al., 2017; Perron, 2017; Zhu et al., 2018; Zhu et al., 2022). At large ground motion levels, non-linear effects in specific soils will increase the site response uncertainty as well (Régnier et al., 2013; Régnier et al., 2016). Understanding and reducing the ground motion estimation uncertainty is important for Probabilistic Seismic Hazard Assessment, especially at a long return period (Bommer and Abrahamson, 2006). The site-to-site and within-site variabilities have practical implications for site-specific study and microzonation, for instance on the spatial resolution and required duration of the instrumentation.

The within-site variability is very small when estimated from 1D SH site response analysis because it is a strong simplification of the real phenomena. On the contrary, approaches based on direct observations from real earthquake recordings are appropriate for analyzing the variability of the site response. One of the most commonly used approaches to measure the empirical amplification function is the standard spectral ratio (SSR) introduced by Borcherdt (1970). It consists in performing the ratio in the Fourier domain between the signal recorded at one station on sediments and the signal obtained at another station located nearby on a stiffer site condition (i.e., a rock site) for the same earthquake. However, in noisy urban areas in regions of low-to-moderate seismicity, recording earthquakes with a good signal-to-noise ratio (SNR) can require several months, if not years. It is thus important to estimate the number of earthquakes that should be recorded at the sites to evaluate the empirical site amplification function based on the desired accuracy.

The main goal of this work is to define, for the specification in the Swiss building SIA 261/1 (SIA, 2020), the minimum number of earthquakes in empirical site effect assessment. We first evaluate the stability and validity of the mean amplification as a function of the number of earthquake recordings used to compute it. The variations of the mean amplification are expected to be directly related to the within-site variability at each site. To verify that, we estimate the SSR and surface-to-borehole spectral ratio (SBSR) amplification function for stations of the Swiss strong motion network and of the Japanese KiKnet network having recorded hundreds of earthquakes. We use this large amount of data to determine the statistical distribution of the site amplification. Based on the statistical distribution, we propose an analytic equation predicting the variation of the mean amplification according to the standard deviation and to the number of recorded events. We also determined the dependence on the mean amplification functions of the ground motion intensity, measured as the peak ground acceleration (PGA).

METHOD AND RESOURCES

In Switzerland, we developed a waveform database covering the time period from January 1998 to September 2019. Waveforms at each Swiss site were selected according to a magnitude–distance filter. In Japan, the database is covering the time period from October 1997 to March 2016. The SSR is computed for each component individually or the mean of the two horizontal components and can be noted as follows:

$$SSR_i(f) = \frac{FAS_{Si}(f)}{FAS_{Ri}(f)}, \quad (1)$$

where $SSR_i(f)$ is the SSR for the ith component as a function of frequency f and FAS_{Si} and FAS_{Ri} are respectively the Fourier amplitude spectra (FAS) at the site and at the reference computed over the ith component. The SSR approach is based on the assumption that the earthquake source and wave propagation along the path are the same between the site and the reference and thus canceled out when performing the spectral ratio between the two. This assumption is valid if the site-to-reference distance (R_{STA}) is much smaller than the hypocentral distance (Rh). In practice, adopting $Rh > 10R_{STA}$ is considered to be enough, even though a certain part of the SSR variability can probably be explained by a remaining influence of the source and of the path (Borcherdt, 1970; Perron, 2017). The ground motion amplification at the reference station is assumed to be negligible, that is to say, equal to one at every frequency. In practice, it is never the case (Hollender et al., 2017; Hollender et al., 2018; Hobiger et al., 2021), so the SSR-based amplification factors are not absolute but are always relative to the considered reference. One of the main limitations of the SSR is of having a rock outcropping susceptible to be used for the reference site located not too far from the considered site of interest. An alternative to the classical SSR is to deploy one station at the earth's surface on sediments and the second at the same location but in a borehole deep enough to reach the geophysical bedrock. This so-called SBSR approach has the advantage of solving the between-station distance limitation but introduces some new difficulties because of the seismic wave reflection at the earth's surface. The upgoing and downgoing waves are indeed fully constructive at the earth's surface, although they can be destructive at certain frequencies at depth (Cadet et al., 2012). However, in the context of analyzing only the variability of the site response, the downgoing wave interaction can reasonably be neglected (Cadet et al., 2012; Hollender et al., 2018). We followed the same procedure for every computation of the site response in Switzerland and Japan. This procedure is as follows:

1) Automatic quality checks of earthquake recordings and automatic picking of the P and S wave arrival (T_P, T_S) through a time–frequency analysis;

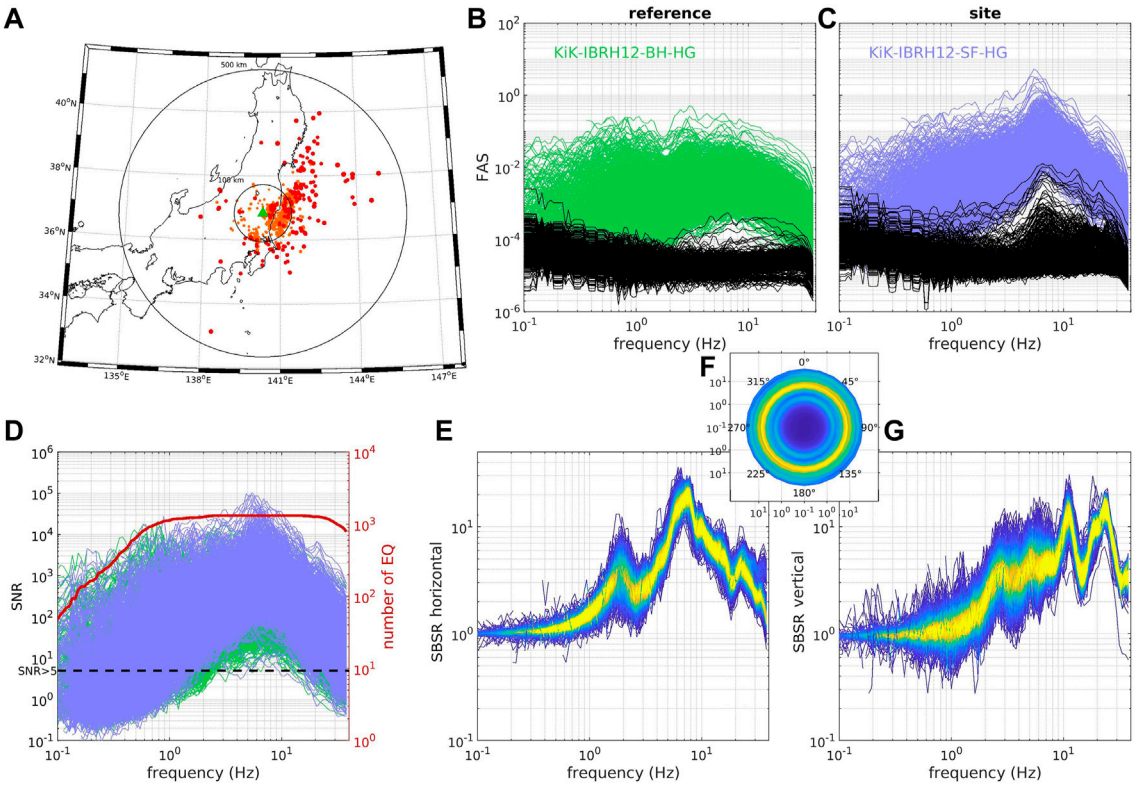

FIGURE 1 | Example of the surface-to-borehole spectral ratio (SBSR) computation at KiKnet station IBRH12 in Japan. **(A)** The map shows the location of the site (green triangle) and the epicenters of the selected earthquakes (yellow-to-red dot according to the earthquake magnitude). Panels **(B)** and **(C)** present the power spectral density (PSD) for the noise (black lines) and for the earthquake recording on the horizontal mean component at the site (blue lines) and at the reference (green lines). Panel **(D)** indicates the SNR at the site (blue lines) and at the reference (green lines), as well as the number of earthquakes spectrum with SNR > 5 (red line) as a function of frequency. The distribution of the SBSR as a function of frequency for the horizontal mean component **(E)**, for the horizontal as a function of the azimuth **(F),** and for the vertical **(G)** component. The color scale indicates the density of lines, each line corresponding to the SBSR of one single earthquake.

2) Selection of earthquakes with hypocentral distance at least five times the interstation distance (R_{STA});
3) Selection of the signal window between T_P and the coda defined by $3.3T_S$–$2.3T_P$ (Perron et al., 2017) and of the noise window before T_P and of the same duration as the signal window. Site and reference use the same time windows;
4) Computation of the FAS for the noise and the signal window;
5) Computation of the horizontal mean FAS using the quadratic mean: $\sqrt{\frac{N^2+E^2}{2}}$;
6) Smoothing and resampling of the horizontal mean FAS on a logarithmic scale using the Konno and Ohmachi (1998) approach with a b-value of 50;
7) Estimation of the SNR;
8) Selection of earthquakes with SNR > 5 over at least a two-octave frequency band window both at the site and at the reference;
9) Spectral ratio computation between the horizontal mean FAS at the site and at the reference for each earthquake;
10) Estimation of the within-site events geometric mean and standard deviation at each frequency;
11) Detection of outliers as a group of samples of probability <0.1% over a frequency band larger than one octave;
12) Outliers are discarded, and the geometric mean and standard deviation are recomputed

Figure 1 shows an example of the SBSR computation in Japan.

STANDARD SPECTRAL RATIO AND SURFACE-TO-BOREHOLE SPECTRAL RATIO RESULTS

In total, SSR is estimated from three pairs of stations where approximately 100 good-quality earthquakes have been recorded in Switzerland, and SBSR is computed from 60 pairs of surface-to-borehole stations with up to 2000 good-quality earthquakes in Japan. **Figure 2** and **Figure 3** respectively show the distribution of the SBSR for 60 pairs of surface-to-borehole stations in Japan and the SSR for the three pairs of surface stations in Switzerland. **Figure 4** provides a summary of the number of good-quality earthquake recordings, geometric mean, and geometric standard deviation as a function of frequency in Japan (gray curves) and Switzerland (red curves).

Figure 2, **Figure 3**, and **Figure 4** clearly show that the amplification functions are different from one site to another, both in terms of mean and standard deviation. It reflects the differences in the geological conditions of the sites, which determine, among others, the fundamental resonance

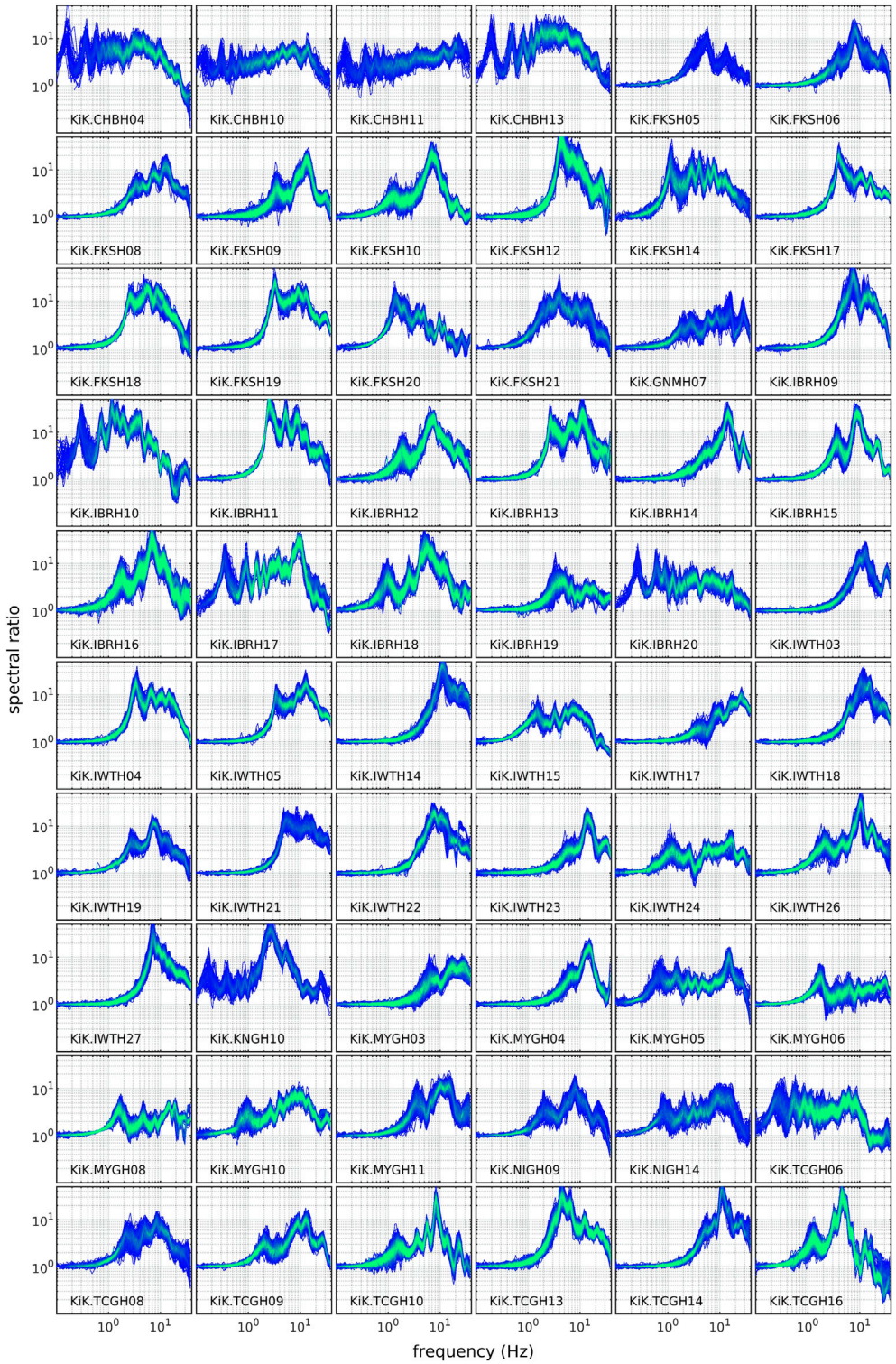

FIGURE 2 | Amplification function computed from the SBSR between 60 pairs of stations in Japan. The color from dark blue to light green indicates an increasing density of curves, each curve corresponding to one single earthquake.

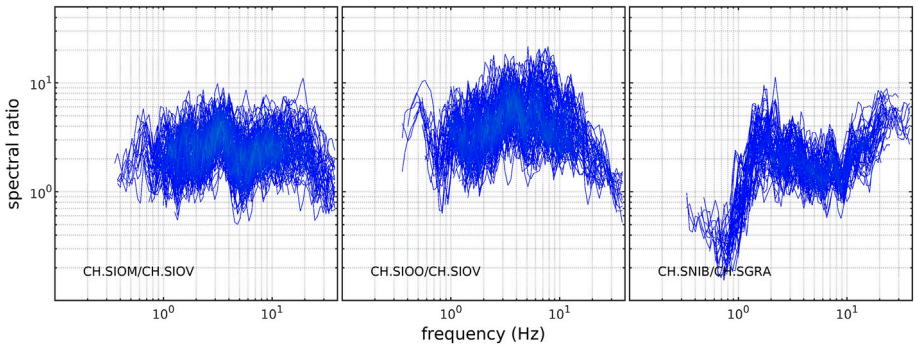

FIGURE 3 | Amplification function computed from the standard spectral ratio between 3 pairs of stations in Switzerland. The color from dark blue to light blue indicates an increasing density of curves, each curve corresponding to one single earthquake.

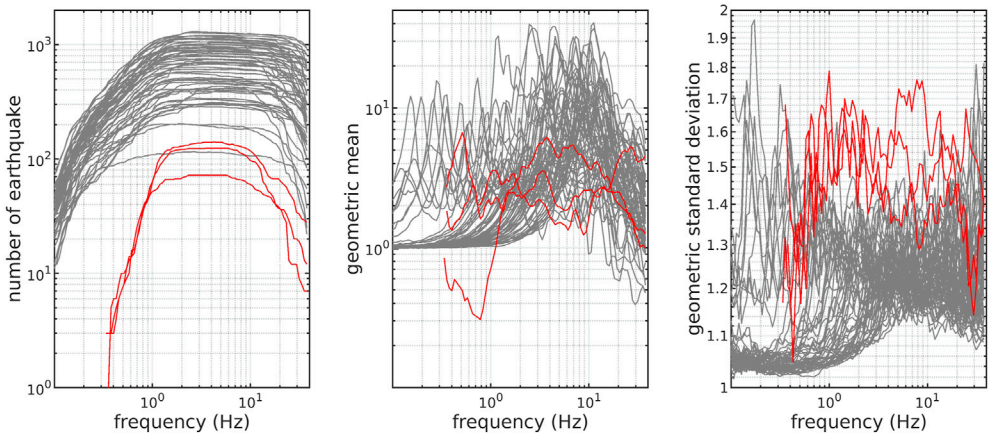

FIGURE 4 | Number of good-quality earthquakes (left panel), within-site geometric mean (central panel), and within-site geometric standard deviation (right panel) as a function of frequency for 60 surface-to-borehole spectral ratios in Japan (gray curves) and three standard spectral ratio in Switzerland (red curves).

frequency of the site (f_0), here corresponding to the first peak on the amplification function. The within-site standard deviation can also vary drastically from one site to another and depending on the frequency. In Japan, we can separate the amplification functions into two groups: the first group with $f_0 > 0.5$ Hz, with an amplification function equal to one and low standard deviation (close to 1.05) for frequency below f_0; a second group with f_0 below the minimum frequency of the analysis here (0.1 Hz), and having significant amplification (above one) and high variability at low frequency. It is also clear that the variability of the site response is on average higher in Switzerland than that in Japan. For the Swiss sites, this is probably because of the SSR method imposing relatively high site-to-reference distances and non-negligible site effects at the surface reference station. In Japan, we can observe some anomalies (eye shapes departing from the log-normal distribution) in the amplification function at high frequency (e.g., for stations: KiK-IBRH13; KiK-IBRH17; KiK-TCGH16). It is not possible to clearly determine its origin, but from our experience, this is very probably an artificial artifact because of coupling issues of the borehole instrumentation or because of a modification on the instrumentation at some point due to maintenance of the station for instance.

DISTRIBUTION OF THE WITHIN-SITE VARIABILITY

As we have seen in the previous section, both the mean and standard deviation of the amplification function as a function of frequency are dependent to the geological characteristics of the site itself. However, the nature of the site response distribution is the same independently to the site or to the frequency and has been shown to be well modeled by a log-normal distribution (Ktenidou et al., 2011). In other words, the distribution of the logarithm of the relative amplification of the ground motion between two sites is Gaussian. To qualitatively verify the log-normal distribution of the site response at every frequency, the quantile–quantile (Q–Q) plot and the histogram are represented at frequencies 0.5, 1.0, 2.5, 5.1, 9.9, and 20.6 Hz in **Figure 5**. The shape of the histograms of the logarithm of the amplification

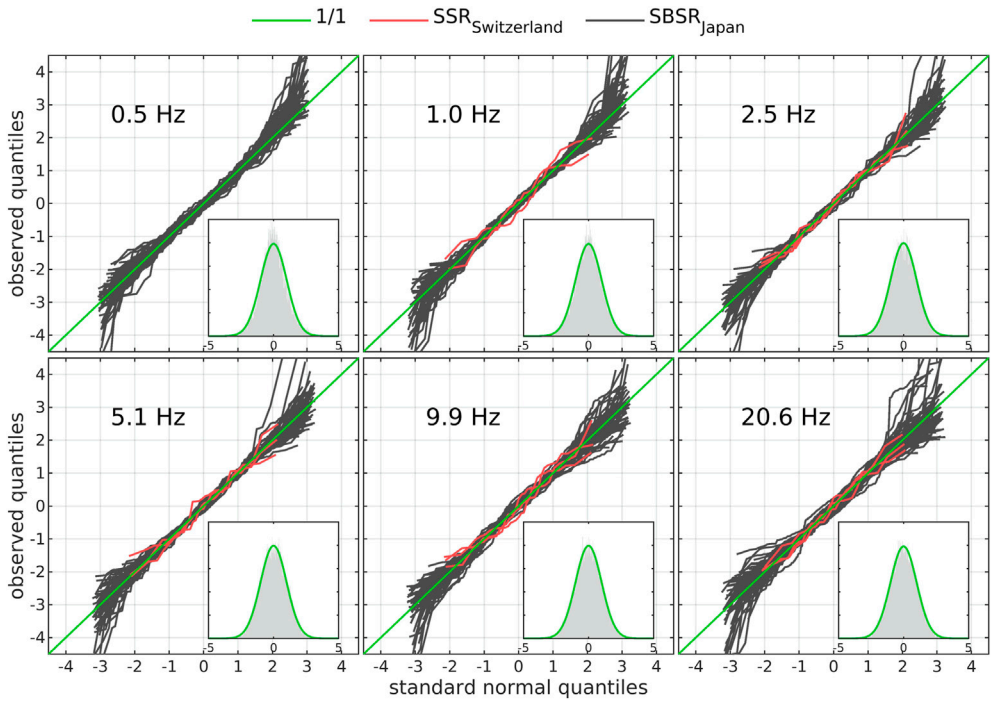

FIGURE 5 | Quantile–quantile plot of the logarithm of the amplification factors for 60 surface-to-borehole spectral ratios in Japan (gray curves) and three standard spectral ratios in Switzerland (red curves) at six different frequencies (one panel per frequency). On each panel, the histogram (gray area) of the standard normal distribution computed from the logarithm of the amplification factors at all sites at the corresponding frequency is compared with the best normal distribution fit (green curve).

factors represents a Gaussian and Q–Q curves of every site at every frequency are well aligned along the 1/1 line, in particular in the interval ± 2σ to the mean. These indicate that the site response is very well approximated by log-normal distribution at least up to ± 2σ. Beyond 2σ, the few non-natural outliers and the limited number of samples increase the scatter of the Q–Q curves, meaning that the log-normal distribution is still valid but interpretations made out of it are less reliable.

Proving the log-normal distribution of the amplification function is important because then peculiar statistical properties apply. For example, if a variable x is normally distributed then the distribution of sample means ($\overline{x_n}$) computed from subsets of n samples also are normally distributed. One major output of that is the confidence interval (Ic). Given that a sample mean ($\overline{x_n}$) and unbiased standard deviation (s_n) have been estimated from a finite number of samples (n), the confidence interval is the interval inside which the population mean (μ) for an infinite number of samples has a certain confidence level to be included in. It is defined as follows:

$$Ic_{1-\alpha\%} = \left[\overline{x_n} - Z_{\alpha/2}\frac{s_n}{\sqrt{n}};\ \overline{x_n} + Z_{\alpha/2}\frac{s_n}{\sqrt{n}}\right], \quad (2)$$

where $Z_{\alpha/2}$ is the critical value that defines the confidence level $(1 - \alpha)$. For a normal distribution and a confidence level of 95%, $Z_{0.025}$ is equal to 1.96. However, because the number of samples can be sometimes very limited (i.e., only a few earthquakes have been recorded), it is preferable to use the Student distribution, also called t-distribution. This distribution correctly accounts for a small number of samples and tends to be a normal distribution as the number of samples increases. For a Student distribution, the formulation of $Ic_{1-\alpha\%}$ is the same (**Eq. 2**), but the estimation of $Z_{\alpha/2}$ is different, as it now also depends on n. The evolution of $Z_{\alpha/2,n}$ as a function of n and for the confidence levels 68, 95, 99, and 99.9% is given in **Figure 6**, left panel. In the following, we will keep using the notation $\overline{x_n}$ and s_n for the measured sample geometric mean and standard deviation, whereas μ and σ represent the population geometric mean and standard deviation of the distribution. For an infinite number of samples, the two notations become equivalent: $\overline{x_\infty} = \mu$ and $s_\infty = \sigma$. Moreover, we will only focus on the confidence level of 95%, because the 95% confidence interval corresponds approximately to the interval comprised between $[-1.96\sigma\ 1.96\sigma]$, which in turn corresponds to the portion where the Q–Q plot best fit the 1/1 line (**Figure 5**). As the distribution is not normal but log-normal, we accordingly modified the confidence interval formulation. The 95% confidence interval for a log-Student distribution is finally:

$$Ic_{95\%} = \left[\overline{x_n} * \frac{1}{\exp\left(Z_{0.025,\,n}\frac{ln(s_n)}{\sqrt{n}}\right)};\ \overline{x_n} * \exp\left(Z_{0.025,\,n}\frac{ln(s_n)}{\sqrt{n}}\right)\right], \quad (3)$$

with $\overline{x_n}$ and s_n respectively the sample geometric mean and standard deviation computed as

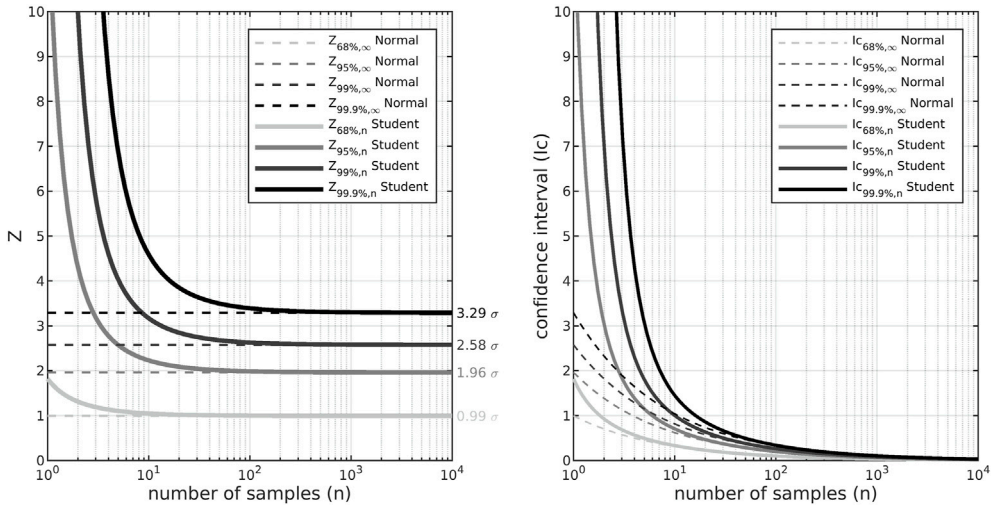

FIGURE 6 | Critical value Z (left panel) and confidence interval (right panel) as a function of the number of samples for the confidence levels 68%, 95%, 99%, and 99.9% for the standard normal distribution (dashed lines), and the standard Student distribution (solid lines).

$$\overline{x_n} = \exp\left(\frac{1}{n}\sum_{i=1}^{n}\ln(x_i)\right), \tag{4}$$

$$s_n = \exp\left(\sqrt{\frac{1}{(n-1)}\sum_{i=1}^{n}(\ln(x_i)-\ln(\bar{x}_n))^2}\right), \tag{5}$$

Figure 6 (right panel) shows the evolution of $Ic_{68\%}$, $Ic_{95\%}$, $Ic_{99\%}$, and $Ic_{99.9\%}$ for a standard normal and standard Student distribution ($\mu = 0$; $\sigma = 1$). It illustrates the very rapid reduction of the confidence interval as the number of samples increases, from more than 10 σ when $n < 10$ to less than 1 σ when $n > 10$.

VALIDITY OF THE CONFIDENCE INTERVAL PREDICTIONS

After demonstrating the validity of the log-normal assumption, we verified the validity of the prediction of $Ic_{95\%}$ for a Student distribution as a function of the number of earthquakes n by comparing $Ic_{95\%}$ with the observations in Switzerland and Japan. First, we defined two different confidence intervals:

$$Ic_{95N}(n) = \left[\overline{x_N}*\frac{1}{\exp\left(Z_{0.025,\,N}\frac{ln(s_N)}{\sqrt{n}}\right)};\ \overline{x_N}*\exp\left(Z_{0.025,\,N}\frac{ln(s_N)}{\sqrt{n}}\right)\right] \tag{6}$$

$$Ic_{95n}(n) = \left[\overline{x_n}*\frac{1}{\exp\left(Z_{0.025,\,n}\frac{ln(s_n)}{\sqrt{n}}\right)};\ \overline{x_n}*\exp\left(Z_{0.025,\,n}\frac{ln(s_n)}{\sqrt{n}}\right)\right] \tag{7}$$

where $\overline{x_N}$ and s_N are respectively the total geometric mean and standard deviation computed over the entire dataset of N events. $\overline{x_n}$ and s_n are respectively the local geometric mean and standard deviation computed over a subset of n randomly selected events. $Ic_{95N}(n)$ is the total 95% confidence interval used to predict the variation of any local mean $\overline{x_n}$ computed from n events. $Ic_{95n}(n)$ is the local 95% confidence interval used to predict the interval of variation of the total mean $\overline{x_N}$. This assumes that $\overline{x_N} = \mu$ and $s_N = \sigma$, which is reasonably correct here since N is most of the time much higher than 100 earthquakes.

To estimate the reliability of the confidence interval more quantitatively, we bootstrapped the amplification factors at each frequency over 1000 random selections of n events, with n = [2 3 4 6 8 10 14 18 24 32]. We evaluated the proportion of local means included inside the total confidence interval ($P_1 = \overline{x_n} \subset Ic_{95N}(n)$), and the proportion of total means included inside the local confidence interval ($P_2 = \overline{x_N} \subset Ic_{95n}(n)$). Following **Eq. 3**, P_1 and P_2 can be written:

$$P_1(f,n) = \frac{1}{1000}\sum_{k=1}^{1000}\left(\overline{x_N}(f)*\frac{1}{\exp\left(Z_{0.025,\,N}\frac{\ln(s_N(f))}{\sqrt{n}}\right)} \le \overline{x_{nk}}(f) \le \overline{x_N}(f)*\exp\left(Z_{0.025,N}\frac{\ln(s_N(f))}{\sqrt{n}}\right)\right) \tag{8}$$

$$P_2(f,n) = \frac{1}{1000}\sum_{k=1}^{1000}\left(\overline{x_{nk}}(f)*\frac{1}{\exp\left(Z_{0.025,n}\frac{\ln(s_{nk}(f))}{\sqrt{n}}\right)} \le \overline{x_N}(f) \le \overline{x_{nk}}(f)*\exp\left(Z_{0.025,n}\frac{\ln(s_{nk}(f))}{\sqrt{n}}\right)\right) \tag{9}$$

with the inequation equal to 1 when it is true and 0 otherwise. $\overline{x_{nk}}$ and s_{nk} are respectively the k^{th} local geometric mean and standard

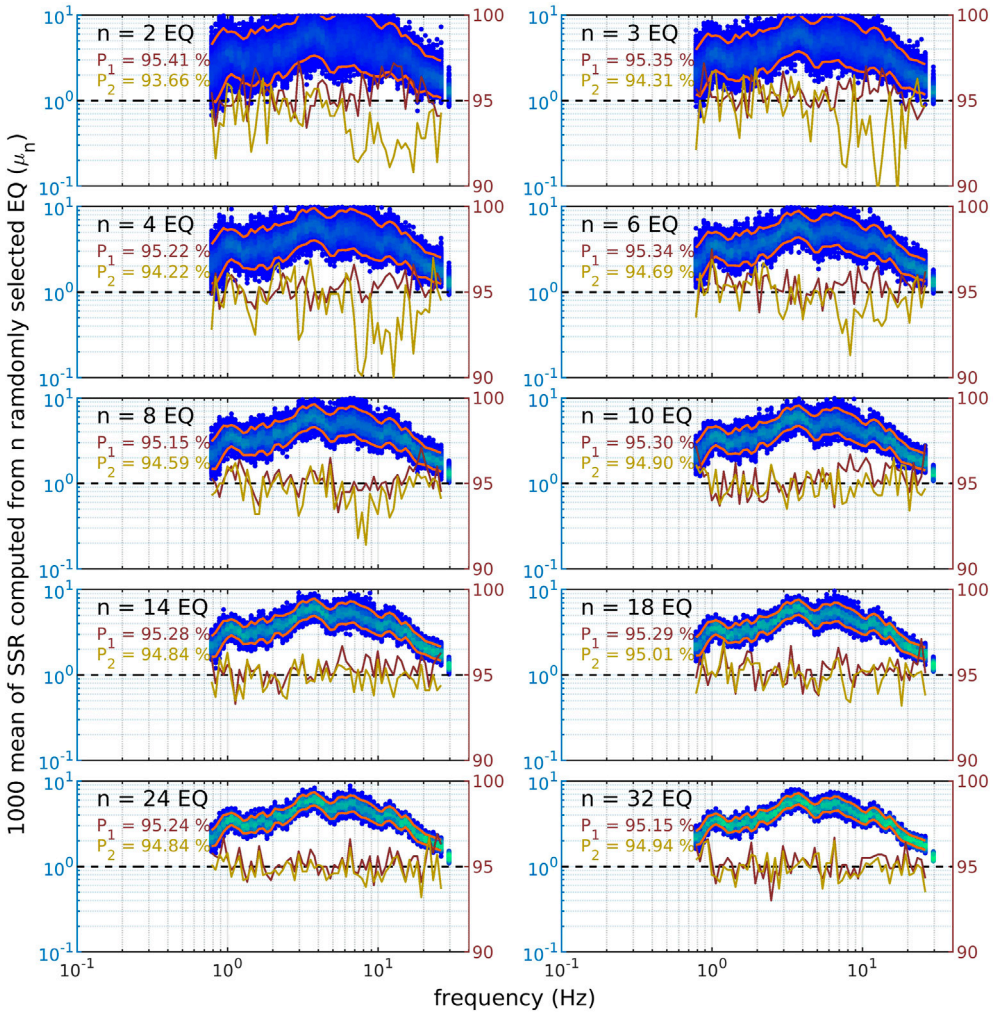

FIGURE 7 | Evaluation of P1 (dark brown line) and P2 (light brown line) on the standard spectral ratio computed at Swiss station SIOO/SIOV from 1000 randomly selected subsets of $\boldsymbol{n}$ = [2 3 4 6 8 10 14 18 24 32] earthquakes (top-left to bottom-right panel). On each panel, the left axis provides the amplification scale and the right axis indicates P1 and P2 proportion in percentages. The 1000 local means $\overline{\boldsymbol{x_n}}$ are represented according to their density of points from dark blue to light green. The total 95% confidence interval prediction for $\boldsymbol{n}$ events ($\boldsymbol{Ic_{95N}}$) is represented with orange lines. P1 can be easily visualized by looking at the proportion of $\overline{\boldsymbol{x_n}}$ points exceeding the $\boldsymbol{Ic_{95N}}$ (blue points outside the orange lines). There is no way to simply represent P2 here. The number of events, and the mean P1 and P2 over the frequency range are written on each panel.

deviation computed over a subset of n randomly selected events. If the distribution is perfectly normal, then both P_1 and P_2 are equal to 95%. However, we do not expect the site response distribution to be perfectly normal at every site and for all frequencies, so a certain convergence to 95% should be observed as the number of events n increases.

Figure 7 shows the bootstrap estimation of P_1 and P_2 from the amplification function of SIOO/SIOV in Switzerland. First, it is clear that the variability between the 1000 $\overline{x_{nk}}$ decreases (blue points) as n increases (from top-left to bottom-right panel). This decay seems well predicted by Ic_{95N} (orange lines). This observation is also supported by P_1 which is relatively close to the value of 95% at all frequency and for any $n > 2$. For $n = 2$ we can observe that P_1 is slightly higher than 95% between 10 and 20 Hz. In contrast, P_2 shows some significant low values for any $n < 10$. However, P_2 shows a better agreement with the 95% value as n increases. This observation confirms the good approximation of using the log-normal distribution to model the site amplification variability. $Ic_{95\%}$ makes a relatively good prediction of the observed variability of $\overline{x_n}$, even when the number of samples is low.

Now, we follow the same procedure for every three SSR in Switzerland and SBSR in Japan. The corresponding results are given in **Figure 8**. We can make a similar observation as in **Figure 7**, P_1 is the average equal to the 95% value at all frequency and for every number of events. For the Swiss SSR, we can, however, observe a stronger scatter when the numbers of events are minimum ($n < 4$). Again, we observe a stronger deviation of 95% in P_2 both in Switzerland and in Japan. In Switzerland, the discrepancy of P_2 is higher, especially close to 1 Hz and for $n < 6$.

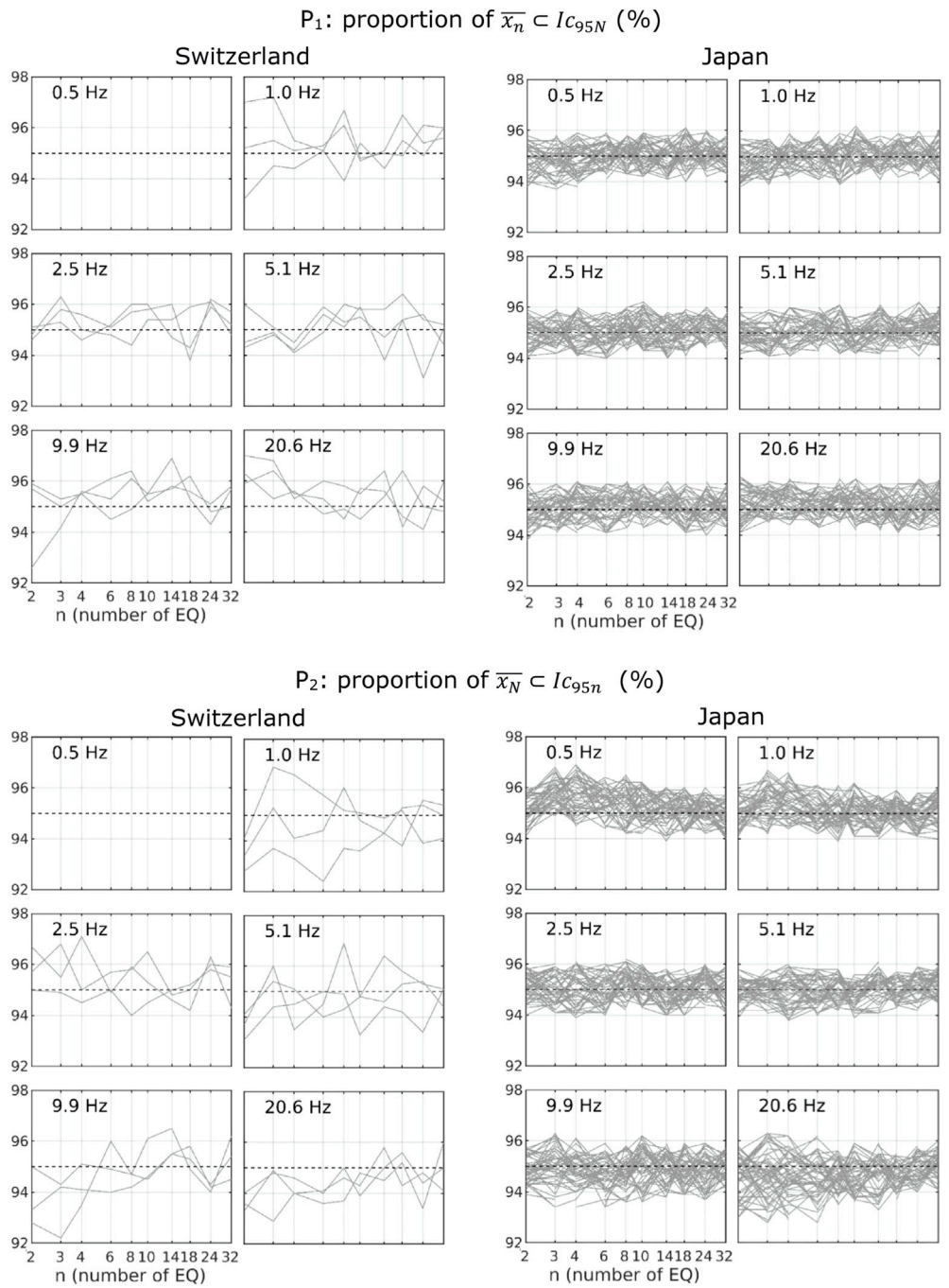

FIGURE 8 | Evaluation of P1 and P2 as a function of the number of events ***n*** at 6 frequencies (0.5, 1.0, 2.5, 5.1, 9.9, and 20.6 Hz) for three Swiss sites and 60 Japanese sites.

P_2 is an average lower than 95% but tends to it as n increases. A good agreement is found for $n > 6$ and a complete stabilization is observed above 14 events. In Japan, we observed a different behavior, with P_2 being too low when $n = 2$, and then too high when $2 < n < 8$ mainly at low frequency (f < 2 Hz). For $n > 8$, we observed a good stabilization of P_2 with mean values slightly below 95%.

The confidence interval computed from a large site response dataset is a good estimator of what is going to be the behavior of the mean computed from much smaller subsets of even only three earthquakes and for any frequency. However, it is clear that using 10 recordings of earthquakes or above greatly improves the quality of the prediction and the significance of the results. In conclusion, at least 10 events should be considered to have a good

statistical significance and to make good use of the confidence interval predicting power.

VARIABILITY OF THE MEAN AMPLIFICATION FUNCTION AS A FUNCTION OF THE NUMBER OF EVENTS

Some questions which arise when evaluating the amplification function at a specific site are as follows: Is the number of earthquake recordings sufficient to accurately estimate the amplification function? Which minimal number of earthquakes (n_{min}) should be used to evaluate the site response? Based on the confidence interval definition (**Eq. 3**), it is clear that the variability of $\overline{x_n}$ depends both on s_n and n. Because s_n is site- and frequency-dependent (**Figure 4**), n_{min} is by consequence also site- and frequency-dependent. In other words, there is no unique value of n_{min} which can be considered for every site response analysis in the world. On the other hand, the property of the site response to be log-normally distributed can be supposed as universal. It is then possible to determine n_{min} for any site response analysis, based on the log-normal distribution assumption and the use of the confidence interval definition.

Provided that the geometric mean $\overline{x_n}$ and standard deviation s_n of the site response has been measured at a particular site over a certain number of earthquakes n, it is possible to determine in which confidence interval the population mean for an infinite number of events μ has a certain confidence level (here 95%) to be included in. It is also possible to predict what will be the reduction of this interval if the number of earthquake observations increases. In the same way, it is possible to determine the number of earthquakes required to limit to a certain level the width of the interval where μ has a 95% probability to be found within. The width of the interval is independent to the $\overline{x_n}$ and can be defined from **Eq. 3** by

$$C_{95\%} = \exp\left(Z_{0.025,\,n}\frac{ln(s_n)}{\sqrt{n}}\right), \tag{10}$$

$C_{95\%}$ is the coefficient of variation between μ and $\overline{x_n}$ such as $\frac{\overline{x_n}}{C_{95\%}} \le \mu \le C_{95\%}\overline{x_n}$ with a 95% probability. It is now possible to estimate the minimum number of earthquakes required to limit the variation between μ and $\overline{x_n}$ below a certain coefficient $C_{95\%}$ as

$$n_{min} = \left(Z_{0.025,\,n}\frac{ln(s_n)}{ln(C_{95\%})}\right)^2 \tag{11}$$

For example, if the amplification at 1 Hz has been measured from $n = 10$ earthquakes with a geometric standard deviation of $s_{10} = 1.5$, we can estimate the minimum number of earthquake n_{min} to have $C_{95\%} = 1.2$ (20% of variation) with a probability of 95% as

$$n_{min} = \left(Z_{0.025,10}\frac{ln(s_{10})}{ln(C_{95\%})}\right)^2 = \left(2.26\frac{ln(1.50)}{ln(1.20)}\right)^2 = 25.31 \rightarrow 26\,earthquakes$$

It is important to note that for a Student distribution, $Z_{0.025,\,n}$ is the function of n. $Z_{0.025,\,n}$ will decrease very rapidly as the number of measured earthquakes increases (**Figure 6**). Using **Eq. 11** and measured s_n (**Figure 4**), n_{min} is computed for every site in Switzerland and Japan, and at every frequency. The results are reported in **Figure 9**. As already discussed, n_{min} is dependent on s_n, so it is variable for the different sites and frequency. Swiss SSRs have the highest uncertainty and logically required the highest number of earthquakes for a given coefficient of variation $C_{95\%}$. **Table 1** summarizes the minimum number of earthquakes which is valid for 99, 95, and 84% of our sites and frequencies as a function of $C_{95\%}$. For 10 earthquakes recorded, the estimation of the mean is only 40% accurate approximately ($C_{95\%} = 1.4$). It is possible to reduce this uncertainty to 25% by recording 20 events ($C_{95\%} = 1.25$). Depending on the desired limit for the coefficient of variation of the mean, one can make own estimations of the minimum number of earthquakes using **Eq. 7**.

It has to be highlighted that s_n is the key parameter for the estimation of n_{min}. If s_n is wrongly determined, so will be n_{min}. One difficulty to have a representative determination of s_n is how to deal with the outliers. Including erratic outliers will artificially increase s_n, while removing natural outliers from rare events will truncate the true distribution and reduce s_n. Another difficulty is that looking only at the value of n_{min} might not be enough for all sites. One could claim that because the site response has been measured from 30 earthquakes, the statistical significance of the result is good and the coefficient of variation of the mean is low. However, if all the events present the same characteristic and location because they belong to the same cluster of events, then the significance of the results is not good and the true variability of the site response might be strongly underestimated. For instance, Perron (2017) showed that approximately 50% of the within-site variability in 2D and 3D basins comes from the lighting effect, which strongly depends on the source location. This implies that both the number of events and their spatial distribution around the site should be considered in site response analysis.

DEPENDENCE OF THE SITE RESPONSE VARIABILITY ON THE INTENSITY OF THE GROUND MOTION

The dependence of the site response on the intensity of the ground motion is a complex research topic that interests the community for several decades (e.g., Sánchez-sesma, 1987; Aki, 1993). The non-linear behavior of unconsolidated soil to strong ground motion solicitations is of major interest in engineering seismology. Non-linearity tends to reduce the fundamental resonance frequency of the site, leading to an increase of the hazard at low frequency and a decrease at high frequency (Régnier et al., 2016). In extreme cases, it can also lead to liquefaction phenomena.

One question often arises when speaking about empirical site effects assessment which is: is the measured amplification function from weak ground motion representative of site

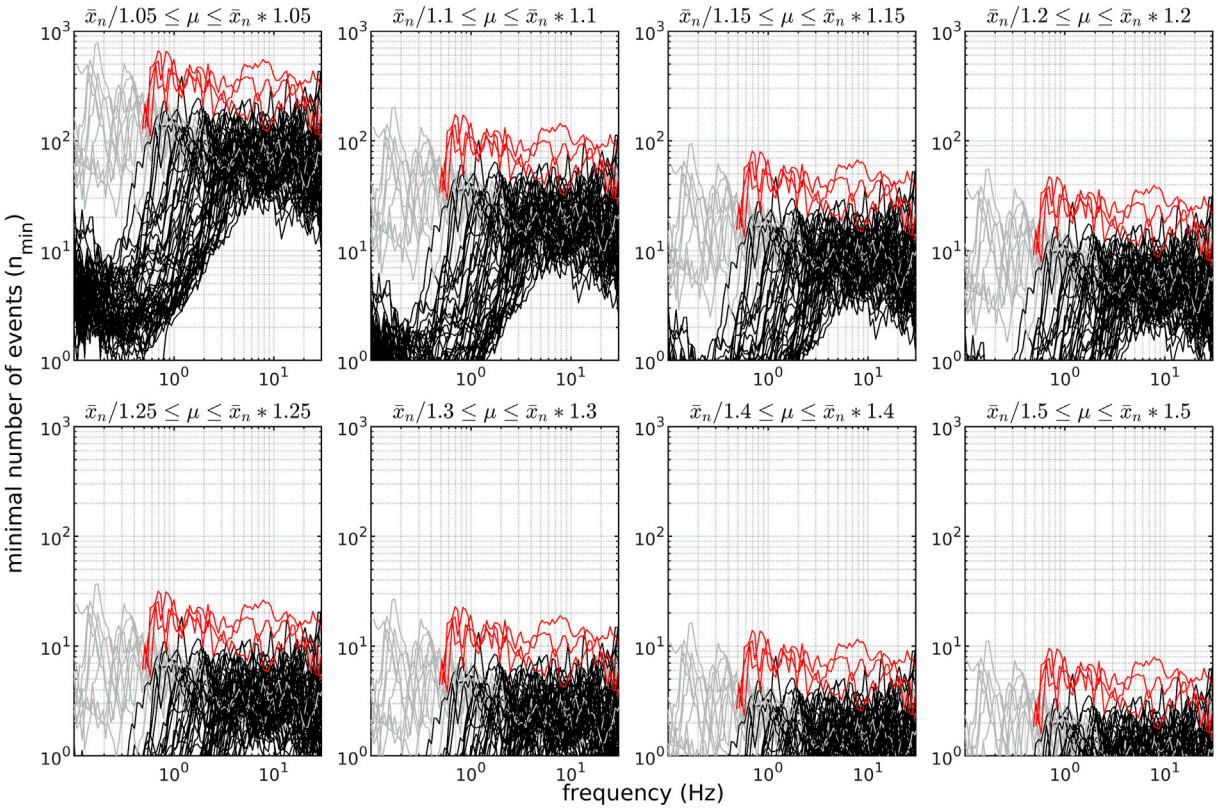

FIGURE 9 | Minimum number of earthquakes as a function of frequency for the coefficient of variation $C_{95\%}$ equal to 1.05, 1.10, 1.15, 1.20, 1.25, 1.30, 1.4, and 1.5 (panels). KiKnet stations with $f_0 > 0.5$ Hz are represented in black, KiKnet stations with $f_0 < 0.1$ Hz are represented in gray, and Swiss stations are represented in red.

TABLE 1 | Minimum number of earthquakes n_{min} as a function of the coefficient of variation $C_{95\%}$.

$C_{95\%}$	1.05 (5%)	1.10 (10%)	1.15 (15%)	1.20 (20%)	1.25 (25%)	1.30 (30%)	1.40 (40%)	1.50 (50%)
$n_{min\,99\%}$	403	106	50	29	20	14	9	6
$n_{min\,95\%}$	214	56	26	16	11	8	5	4
$n_{min\,84\%}$	109	29	14	8	6	4	3	2

response to strong ground motion? To address this question, we compute the equivalent of the standard normal distribution ($\mu = 0$, $\sigma = 1$) for every individual amplification function at all sites in Switzerland and Japan as

$$Zi = \frac{ln(xi) - ln\left(\overline{x_n}\right)}{ln(s_n)}, \tag{12}$$

This common standard normal distribution formulation allows using the site response of every site together. $Zi(f)$ represent the ith normalized amplification function normally distributed with $\overline{x_n} = 0$ and $s_n = 1$. Together, it represents about 28,000 normalized amplification functions obtained from thousands of earthquakes recorded at 63 pairs of stations (three Swiss sites and 60 Japanese sites). For each normalized amplification function, we computed on the corresponding waveforms the horizontal mean PGA.

Figure 10 shows the number of events per frequency, the distribution of the PGA and the normalized amplification function for four PGA bins [(0.001 0.01), (0.01 0.1), (0.1 1), and (1 10) m/s^2]. First, it should be mentioned that the number of events varies strongly from one PGA bin to another. This explains the apparent differences when looking at the normalized amplification function (black curves) of the different bin. We observe that the normalized amplification function for every PGA bin can be explained by the standard normal distribution, which indicates that no non-linear behavior is observed here. The mean is fairly equal to 0 and the standard deviation is equal to 1 for every frequency of every bin. That demonstrates, first, that the linear behavior characterizes the vast majority of the sites, and second, that the linear site response is independent to the ground motion intensity. Therefore, if we consider a specific site having a linear behavior, the amplification function observed from the weak motion of a small magnitude earthquake will be the same as the one for the strong motion of a large magnitude earthquake, all other things being the same. This highlights the importance and the validity of using the recording of low-to-moderate earthquakes to assess the anelastic amplification functions for larger earthquakes as long as there is no significant non-linear site response at the site of interest.

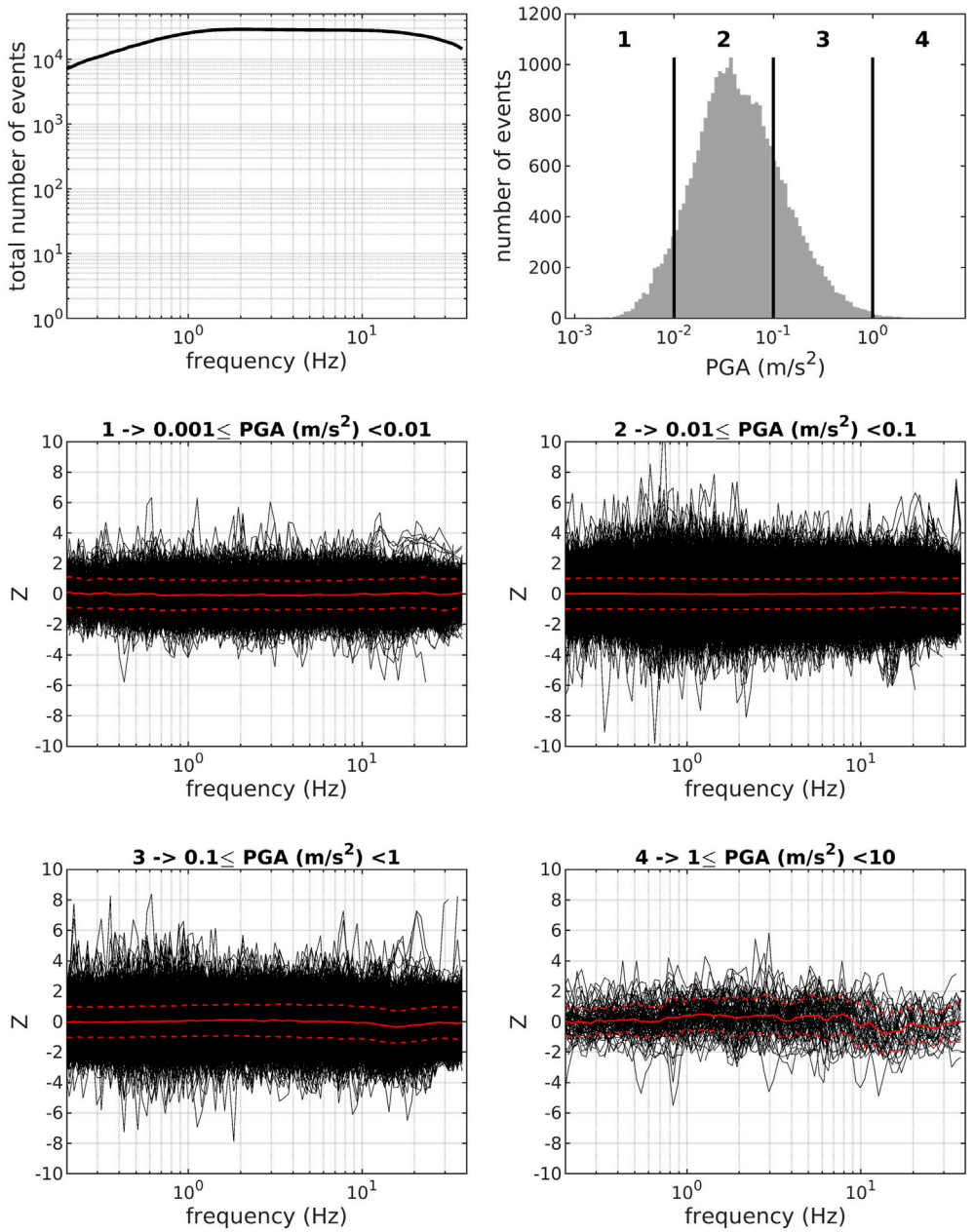

FIGURE 10 | Top-left panel: Total number of normalized amplification functions obtain from 3 Swiss SSR distribution and 60 SBSR Japanese distribution and as a function of frequency. Top right: Histogram of the peak ground acceleration (PGA) distribution. From middle left to bottom-right panel: normalized amplification function for four PGA bins and as a function of frequency. The mean and mean plus/minus standard deviation are represented with solid red lines and dotted red lines respectively.

CONCLUSION

Site effect is a major contributor to the seismic hazard, and its evaluation at specific sites of interest generally requires the recording of several earthquakes. We address here the question of the site response variability and of the minimum necessary number of earthquakes to be recorded.

To address this question, we carefully compute empirical amplification functions at 60 KiKnet sites from several hundred earthquakes and three Swiss sites from several tens of earthquakes. We performed statistical analysis on the amplification function to estimate the geometric mean and standard deviation, and more importantly to determine the distribution law of the amplification factor at each frequency.

Independent to the site and to the frequency, we found that the log-normal distribution is a very good approximation for the site response. Based on that we developed a strategy to estimate the minimum number of earthquakes from the confidence interval definition. We first demonstrate the validity of the use of the confidence interval to model the uncertainty of the geometric mean estimation. We found that between 8 and 14 earthquakes are necessary to have a good prediction by the confidence interval, that is to say, a good statistical significance. For most of the sites, 10 samples seem to be the best compromise between minimizing the number of recordings and having a good statistical significance of the results. Based on the confidence interval, we provide the analytic formula to estimate the minimum number of earthquakes to be recorded, as a function of the within-site standard deviation (**Eq. 11**). We used it on the Swiss and Japanese amplification function and determine, among others, that with a 95% probability: the mean varies by less than 40% for 10 earthquakes, and less than 25% for 20 events.

It is very important to point out that satisfying the minimal number of earthquakes by itself is not sufficient. The selected earthquakes should be uncorrelated and as much evenly distributed around the site as possible to cover the entire variability of the site response. Therefore, one should not use only earthquakes belonging to a single cluster of events. In our dataset, the linear site response is observed to be independent to the intensity of the ground motion. In other words, assessing the site response from the recording of low PGA and low magnitude earthquakes, provides the same amplification functions as from recording of high PGA and large magnitude earthquakes, as far as the soil behaves linearly.

As a general rule, a minimum of 10 uncorrelated earthquakes should be considered, but the higher the number of earthquakes, the lower the uncertainty on the geometric mean site response assessment. Based on our results, the specification in the Swiss building SIA 261/1 recommends taking a minimum of 10 uncorrelated earthquakes to perform site-specific studies.

DATA AVAILABILITY STATEMENT

Publicly available datasets were analyzed in this study. This data can be found here: The data of the Swiss stations (CH, https://doi.org/10.12686/sed/networks/ch) can be accessed following the instruction on the webpage http://www.seismo.ethz.ch/en/research-and-teaching/products-software/waveform-data/ (last accessed April 2022). The data of the station site characterization can be accessed at http://stations.seismo.ethz.ch (last accessed April 2022). The figures were produced using MATLAB which is available at www.mathworks.com/products/matlab (last accessed August 2021). Japaness KiKnet data are available at https://www.kyoshin.bosai.go.jp/ (last accessed June 2022).

AUTHOR CONTRIBUTIONS

VP did most of the work, as well as the writing of the article. PB helped with the statistic and reviewing work. DF is the main supervisor and fund provider.

FUNDING

This work received financial contributions from the Swiss Federal Office for the Environment (FOEN), the Swiss Federal Office for Civil Protection (FOCP), and the Swiss Federal Institute of Technology Zurich (ETHZ). Open access funding is provided by ETH Zurich.

ACKNOWLEDGMENTS

This work was made in the framework of the Earthquake Risk Model for Switzerland project financed by contributions from the Swiss Federal Office for the Environment (FOEN), Swiss Federal Office for Civil Protection (FOCP), and Swiss Federal Institute of Technology Zurich (ETHZ).

REFERENCES

Aki, K. (1993). Local Site Effects on Weak and Strong Ground Motion. *Tectonophysics* 218, 93–111. doi:10.1016/0040-1951(93)90262-i

Bindi, D., Luzi, L., and Pacor, F. (2009). Interevent and Interstation Variability Computed for the Italian Accelerometric Archive (ITACA). *Bull. Seismol. Soc. Am.* 99, 2471–2488. doi:10.1785/0120080209

Bindi, D., Spallarossa, D., and Pacor, F. (2017). Between-Event and Between-Station Variability Observed in the Fourier and Response Spectra Domains: Comparison with Seismological Models. *Geophys. J. Int.* 210, 1092–1104. doi:10.1093/gji/ggx217

Bommer, J. J., and Abrahamson, N. A. (2006). Why Do Modern Probabilistic Seismic-Hazard Analyses Often Lead to Increased Hazard Estimates? *Bull. Seismol. Soc. Am.* 96, 1967–1977. doi:10.1785/0120060043

Borcherdt, R. D. (1970). Effects of Local Geology on Ground Motion Near San Francisco Bay. *Bull. Seismol. Soc. Am.* 60, 29–61.

Cadet, H., Pierre-Yves, B., and Adrian, R.-M. (2012). Site Effect Assessment Using KiK-Net Data: Part 1. A Simple Correction Procedure for Surface/Downhole Spectral Ratios. *Bull. Earthq. Eng.* 10, 421–448. doi:10.1007/s10518-011-9283-1

Hobiger, M., Bergamo, P., Imperatori, W., Panzera, F., Marrios Lontsi, A., Perron, V., et al. (2021). Site Characterization of Swiss Strong-Motion Stations: The Benefit of Advanced Processing Algorithms. *Bull. Seismol. Soc. Am.* 111, 1713–1739. doi:10.1785/0120200316

Hollender, F., Cornou, C., Dechamp, A., Oghalaei, K., Renalier, F., Maufroy, E., et al. (2017). Characterization of Site Conditions (Soil Class, VS30, Velocity Profiles) for 33 Stations from the French Permanent Accelerometric Network (RAP) Using Surface-Wave Methods. *Bull. Earthq. Eng.* 16, 2337–2365. doi:10.1007/s10518-017-0135-5

Hollender, F., Perron, V., Imtiaz, A., Svay, A., Mariscal, A., Bard, P.-Y., et al. (2015). "Close to the Lair of Odysseus Cyclops: The SINAPS@ Post-seismic Campaign and Accelerometric Network Installation on Kefalonia Island," in 9ème Colloque National AFPS, Marne-la-Vallée, France, 30 Nov-2 Dec 2015.

Hollender, F., Roumelioti, Z., Regnier, J., Perron, V., and Bard, P.-Y. (2018). "Respective Advantages of Surface and Downhole Reference Stations for Site Effect Studies: Lessons Learnt from the Argonet (Cephalonia Island, Greece) and Cadarache (Provence, France) Vertical Arrays," in 16th European Conference on Earthquake Engineering (16ECEE), Thessaloniki, Greece, 18-21June 2018, 13.

Imtiaz, A., Perron, V., Hollender, F., Bard, P. Y., Cornou, C., Svay, A., et al. (2018). Wavefield Characteristics and Spatial Incoherency: A Comparative Study from Argostoli Rock- and Soil-Site Dense Seismic Arrays. *Bull. Seismol. Soc. Am.* 108, 2839–2853. doi:10.1785/0120180025

Konno, K., and Ohmachi, T. (1998). Ground-Motion Characteristics Estimated from Spectral Ratio between Horizontal and Vertical Components of Microtremor. *Bull. Seismol. Soc. Am.* 88, 228–241. doi:10.1785/bssa0880010228

Ktenidou, O.-J., Chávez-García, F.-J., Raptakis, D., and Pitilakis, K. D. (2016). Directional Dependence of Site Effects Observed Near a Basin Edge at Aegion, Greece. *Bull. Earthq. Eng.* 14, 623–645. doi:10.1007/s10518-015-9843-x

Ktenidou, O.-J., Chavez-Garcia, F. J., and Pitilakis, K. D. (2011). Variance Reduction and Signal-To-Noise Ratio: Reducing Uncertainty in Spectral Ratios. *Bull. Seismol. Soc. Am.* 101, 619–634. doi:10.1785/0120100036

Ktenidou, O.-J., Roumelioti, Z., Abrahamson, N., Cotton, F., Pitilakis, K., and Hollender, F. (2017). Understanding Single-Station Ground Motion Variability and Uncertainty (Sigma): Lessons Learnt from EUROSEISTEST. *Bull. Earthq. Eng.* 16, 2311–2336. doi:10.1007/s10518-017-0098-6

Maufroy, E., Chaljub, E., Theodoulidis, N. P., Roumelioti, Z., Hollender, F., Bard, P. Y., et al. (2017). Source-Related Variability of Site Response in the Mygdonian Basin (Greece) from Accelerometric Recordings and 3D Numerical Simulations. *Bull. Seismol. Soc. Am.* 107, 787–808. doi:10.1785/0120160107

Perron, V. (2017). Apport des enregistrements de séismes et de bruit de fond pour l'évaluation site-spécifique de l'aléa sismique en zone de sismicité faible à modérée. PhD thesis. Grenoble, France: Université Grenoble Alpes.

Perron, V., Gélis, C., Froment, B., Hollender, F., Bard, P.-Y., Cultrera, G., et al. (2018). Can Broad-Band Earthquake Site Responses Be Predicted by the Ambient Noise Spectral Ratio? Insight from Observations at Two Sedimentary Basins. *Geophys. J. Int.* 215, 1442–1454. doi:10.1093/gji/ggy355

Perron, V., Laurendeau, A., Hollender, F., Bard, P.-Y., Gélis, C., Traversa, P., et al. (2017). Selecting Time Windows of Seismic Phases and Noise for Engineering Seismology Applications: A Versatile Methodology and Algorithm. *Bull. Earthq. Eng.* 16, 2211–2225. doi:10.1007/s10518-017-0131-9

Régnier, J., Cadet, H., and Bard, P. Y. (2016). Empirical Quantification of the Impact of Nonlinear Soil Behavior on Site Response. *Bull. Seismol. Soc. Am.* 106, 1710–1719. doi:10.1785/0120150199

Régnier, J., Cadet, H., Bonilla, L. F., Bertrand, E., and Semblat, J.-F. (2013). Assessing Nonlinear Behavior of Soils in Seismic Site Response: Statistical Analysis on KiK-Net Strong-Motion Data. *Bull. Seismol. Soc. Am.* 103, 1750–1770. doi:10.1785/0120120240

Sánchez-sesma, F. J. (1987). Site Effects on Strong Ground Motion. *Soil Dyn. Earthq. Eng.* 6, 124–132. doi:10.1016/0267-7261(87)90022-4

SIA (2020). *SIA 261 Einwirkungen auf Tragwerke*. Zurich, Switzerland (in German): Schweizerischer Ingenieur- und Architekentverein, Swiss Society of Engineers and Architects. Available at: http://shop.sia.ch/normenwerk/ingenieur/sia%20261/d/2020/D/Product/(Accessed April 1, 2022).

Thompson, E. M., Baise, L. G., Tanaka, Y., and Kayen, R. E. (2012). A Taxonomy of Site Response Complexity. *Soil Dyn. Earthq. Eng.* 41, 32–43. doi:10.1016/j.soildyn.2012.04.005

Zhu, C., Chávez-García, F. J., Thambiratnam, D., and Gallage, C. (2018). Quantifying the Edge-Induced Seismic Aggravation in Shallow Basins Relative to the 1D SH Modelling. *Soil Dyn. Earthq. Eng.* 115, 402–412. doi:10.1016/j.soildyn.2018.08.025

Zhu, C., Cotton, F., Kwak, D.-Y., Ji, K., Kawase, H., and Pilz, M. (2022). Within-Site Variability in Earthquake Site Response. *Geophys. J. Int.* 229, 1268–1281. doi:10.1093/gji/ggab481

Conflict of Interest: The authors declare that the research was conducted in the absence of any commercial or financial relationships that could be construed as a potential conflict of interest.

Publisher's Note: All claims expressed in this article are solely those of the authors and do not necessarily represent those of their affiliated organizations, or those of the publisher, the editors, and the reviewers. Any product that may be evaluated in this article, or claim that may be made by its manufacturer, is not guaranteed or endorsed by the publisher.

frontiers | Frontiers in Earth Science

ORIGINAL RESEARCH
published: 04 August 2022
doi: 10.3389/feart.2022.910118

Seismic Risk Assessment of Multiple Cities: Biases in the Vulnerability Derivation Methods for Urban Areas With Different Hazard Levels

Maria Camila Hoyos[1]* *and Andres Felipe Hernandez*[2]

[1]Independent Seismic Risk Consultant, Bogota, Colombia, [2]Institut des Sciences de la Terre, Université Grenoble Alpes, Grenoble, France

Previously, it has been shown that probabilistic seismic risk assessments (PSRAs) at urban scale present important discrepancies when compared with analyses conducted using methodologies from regional or national PSRA. However, conducting site-specific urban-scale analyses for a considerable number of cities may not be feasible due to limitations in time, resources, and in some cases availability of information, and thus more general models or methodologies are used. This brings into the picture the importance of identifying and quantifying the possible biases, discrepancies, and uncertainties when using different methods, both in the hazard and vulnerability components. Regarding the latter, several sources of uncertainty and biases have been identified in 1) the selection of ground motion records, either by using a general pool of records such as the ones from FEMA P695 or by performing a site- or hazard-specific analysis that requires a significant effort, especially in areas with a poor history of seismic instrumentation and even more in regions with no evidence of previous PSRA at all; and 2) the fragility or vulnerability derivation nonlinear dynamic methods: incremental dynamic analysis [IDA], cloud analysis [CA], and multi-stripe Analysis [MSA], among others. Focusing on these sources of uncertainty and bias, and with the challenge to bring solutions for places with scarce information, in this study, we aim to explore the use of different vulnerability derivation assumptions for the three principal cities of Colombia: Bogota, Medellin, and Cali, where most of the economic growth is concentrated. This considers the different seismic hazard levels and tectonic environment contributions in each city. Afterward, a comparison between the results of the analysis without the hazard-specific record selection and the site-specific one for each city is performed to establish the cases in which the former is applicable without adding more biases or uncertainties in the process.

Keywords: seismic risk assessment, fragility function derivation, record selection, multi-site analysis, urban risk

OPEN ACCESS

Edited by:
Dimitris Pitilakis, Aristotle University of Thessaloniki, Greece

Reviewed by:
Anastasia Nekrasova, Institute of Earthquake Prediction Theory and Mathematical Geophysics (RAS), Russia
M. Amin Hariri-Ardebili, National Institute of Standards and Technology (NIST), United States

***Correspondence:**
Maria Camila Hoyos
mc.hoyos.ramirez@gmail.com

Specialty section:
This article was submitted to Geohazards and Georisks, a section of the journal Frontiers in Earth Science

Received: *31 March 2022*
Accepted: *17 June 2022*
Published: *04 August 2022*

Citation:
Hoyos MC and Hernandez AF (2022) Seismic Risk Assessment of Multiple Cities: Biases in the Vulnerability Derivation Methods for Urban Areas With Different Hazard Levels. Front. Earth Sci. 10:910118. doi: 10.3389/feart.2022.910118

1 INTRODUCTION

Probabilistic seismic risk assessment (PSRA) at the urban scale has become a critical tool for local governments, disaster risk reduction offices, and insurers in the definition of long-term actions for risk management in cities such as the response planning after an event, the definition of city-specific insurance plans, and the overall urban planning. This considering that cities concentrate 80% of the GDP generation

worldwide and 56% of the global population, with an estimation to increase to 68% by mid-century (United Nations, 2019).

In recent decades, earthquake disaster risks in cities have increased mainly due to the high rate of urbanization, lack of urban planning, and inadequate or uncontrolled construction practices, among others. Because of this, special attention has been given to the analysis of urban environments with the inclusion of specific targets, indicators, or goals for urban resilience in the sustainable development goals (Goal 11), the Sendai framework for disaster risk reduction (Indicator E2), and The New Urban Agenda (United Nations, 2015; United Nations Office for Disaster Risk Reduction, 2015; United Nations, 2016).

Considering this new demand for urban-specific models, many studies have downsized the methodologies followed for global, regional, or national PSRAs, without much consideration of the implications and biases generated in the process. From the three main inputs of a seismic risk model, hazard, exposure, and vulnerability, this is particularly true for the vulnerability component. As stated by Kohrangi et al. (2017b), when deriving vulnerability models for portfolios in multiple cities, even if they have different hazard characteristics, the common engineering practice is to use a pool of general records regardless of their consistency with the hazard at each site, which has been shown to lead to potentially biased risk estimates, even under a "sufficient" intensity measure (IM). For this reason, some studies have proposed methods to reduce this bias by improving the record selection (Jayaram et al., 2011; Lin et al., 2013b) by modifying the general pool of records to include in some way the expected spectral shape of the site (Haselton et al., 2011) or by using more "sufficient" and "efficient" IMs as the average spectral acceleration—AvgSa (De Biasio et al., 2014; Eads et al., 2015; Kohrangi et al., 2017a).

Among those studies, Kohrangi et al. (2017b) established that identical buildings should be characterized by different vulnerability functions at different sites because the magnitude of the earthquakes around the site and the distance to the nearby faults, among others, can modify the type of ground motions that could occur at each site. In this regard, there has been an ever-growing group of studies comparing the results in terms of fragility or vulnerability curves or even risk estimates between analyses considering general pools of records such as the FEMA P-695 far-field set (Federal Emergency Management Agency, 2009) with the ones using more detailed site-specific record selection methodologies (Lin et al., 2013a; Kohrangi et al., 2017a; Kohrangi et al., 2020). Overall, it has been shown that there is no general rule to follow and that the use of a general pool of records or a specific one should be based on more careful consideration of the characteristics of the hazard in the site, the expected ground motions, the structures to analyze, and the availability of resources.

Another important source of uncertainty comes from using different fragility derivation methodologies as each one considers different assumptions, follows different methodologies, and needs specific inputs that could add to the uncertainties of the fragility derivation process. Among the nonlinear dynamic models that use time-history analyses within the analytical fragility derivation methods, incremental dynamic analysis, multi-stripe analysis, and cloud analysis have been given much attention. As in the previous case, some studies have conducted comparisons between the different derivation methods, illustrating the variabilities that can be encountered in the process and giving recommendations on when each one should be considered based on the limitations and benefits of each method (Jalayer, 2003; Mackie and Stojadinovi, 2005; Baker, 2015; Jalayer et al., 2017). However, as with its ground motion selection counterpart, many studies are based on specific case studies and thus their considerations apply only in similar scenarios to those that have been studied. For this reason, there is a need to study in more regions and under different assumptions if the conditions to use one or the other are fulfilled or if there needs to be special care under some circumstances when using one procedure over the other.

Considering this and the small number of studies that have been presented analyzing nonengineered structures located in urban environments exposed to different hazard levels and with different tectonic regime contributions, we aim to provide a reference to establish if the methods currently used in the engineering practice are applicable under these conditions. For the case study, we will derive fragility functions for the three archetype buildings previously presented in Hoyos and Hernández (2021) for the three principal cities of Colombia, Bogota, Medellin, and Cali, where each one is exposed to a different hazard level and different tectonic regime contributions. In the following sections, we will present the methodologies that will be used and compared within the scope of this research, followed by the specifics of the case study included in a more detailed manner, the characteristics of the sites, and the structures to be analyzed. Later, the record selection process is described, and the fragility curves derived following the different record selection procedures and nonlinear dynamic fragility derivation methodologies are shown and compared, establishing the biases incurred in each case and giving some recommendations on when the analyses of some of the structures should be performed.

2 METHODOLOGY

2.1 Record Selection

A set of records must be used to perform the fragility analysis and for this, two different approaches were determined, using a hazard-specific selection through the conditioned spectrum (CS) as well as using the most common set of records from the FEMA P695 (Federal Emergency Management Agency, 2009).

2.1.1 Conditioned Spectrum

The CS method (Jayaram et al., 2011) was used to select the ground motion records by computing the mean scenario (i.e., mean magnitude, M, mean distance, R, and mean epsilon, ε) that best represents the site of analysis for the selected intensity measure level types (Harmsen, 2001) and tectonic regimes. There are several variations of this approach (Lin et al., 2013), but what we followed is the so-called "approximate" method where the CS is estimated using the mean values of magnitude and distance as well as the logic-tree weights of the ground motion prediction models. To perform this method, correlation models for the tectonic regimes of active shallow crust and subduction were considered (Jayaram and Baker, 2009; Jaimes and Candia, 2019).

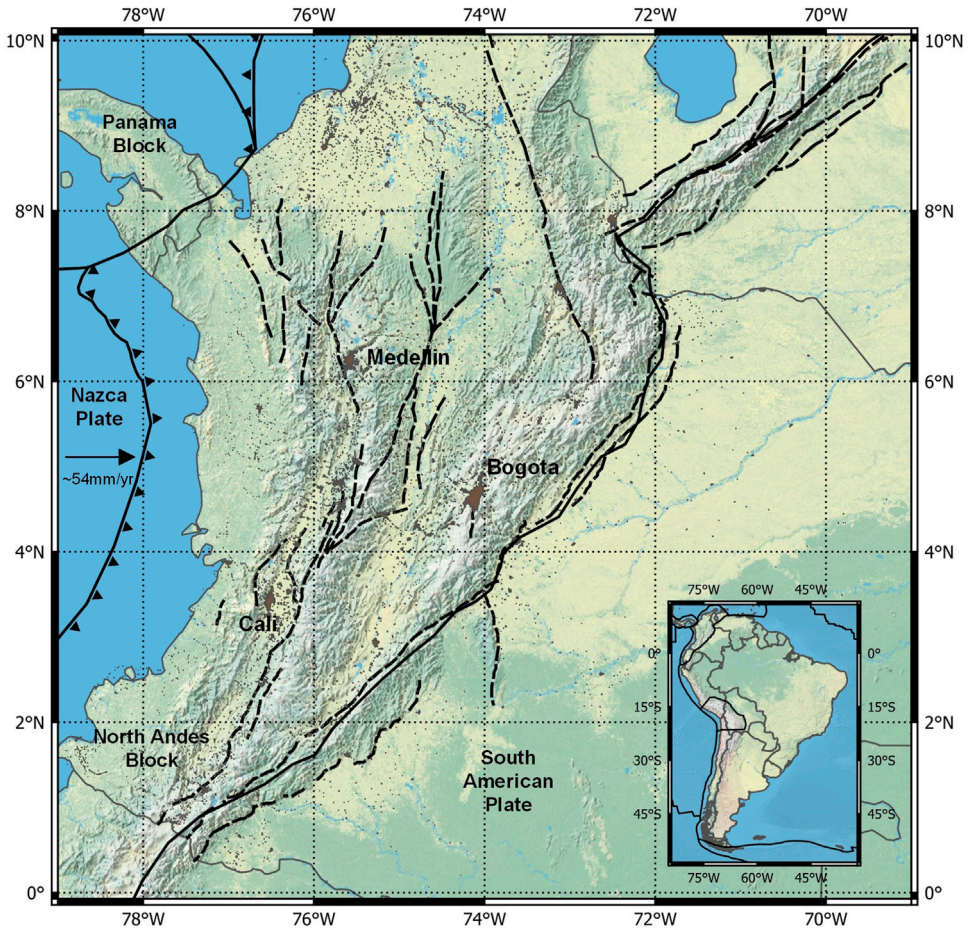

FIGURE 1 | Location of Bogota, Medellin, and Cali as well as some characteristics of the seismicity in the country. Dash-dotted lines: active faults traces. Continuous lines: boundary tectonic plates.

TABLE 1 | Main characteristics of the different typologies considered in the analysis.

Typology	Inter-storey height	Structural period [s]	Γ	Yield drift [%]	Ultimate drift [%]	References
MUR-H2	2.4	0.25	1.2	0.1	0.5	Acevedo et al. (2017)
CR-H4	2.95	0.5	1.3	0.15	0.8	Sinisterra (2017)
CR-H8	2.95	1.0	1.3	0.15	0.8	Sinisterra (2017)

Adapted from Table 4 from (Hoyos and Hernández, 2021).

The advantage of this method is the definition not only of the target intensities but also the spectral shape of all the records selected, which in comparison to other scaling methods provides a much more accurate and realistic spectral shape.

2.1.2 FEMA

The site-independent far-field set of 44 records from the FEMA P695 was used as a comparison method because it is a common practice to perform nonlinear dynamic analysis with them, but without the proper assessment of which cases, these scenarios are suitable to be used.

2.2 Nonlinear Dynamic Methods for Fragility Curve Derivation

Among the literature on the topic, there are three main nonlinear dynamic methods for the derivation of analytical fragility models: the incremental dynamic analysis—IDA (Vamvatsikos and

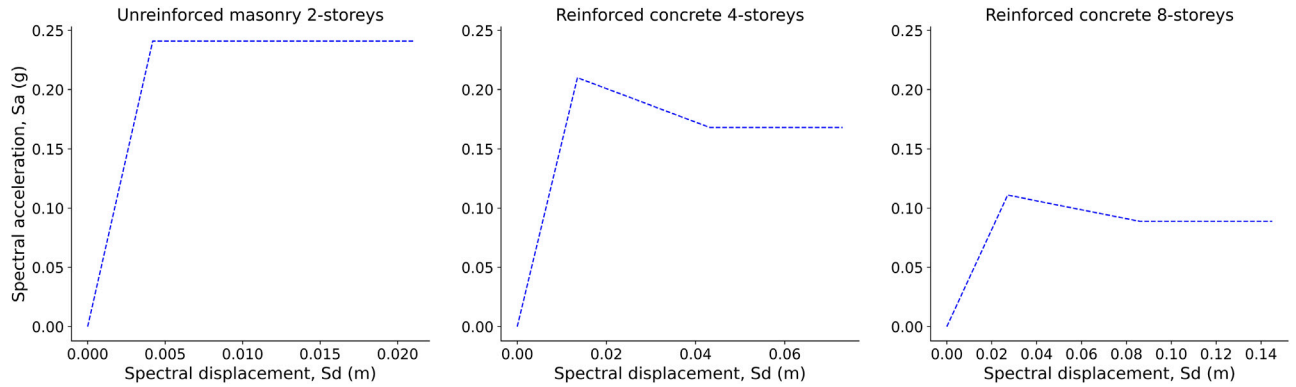

FIGURE 2 | Capacity curves for the three typologies considered. Left: unreinforced masonry two-storeys (MUR-H2). Center: reinforced concrete four-storeys (CR-H4). Right: reinforced concrete eight-storeys (CR-H8).

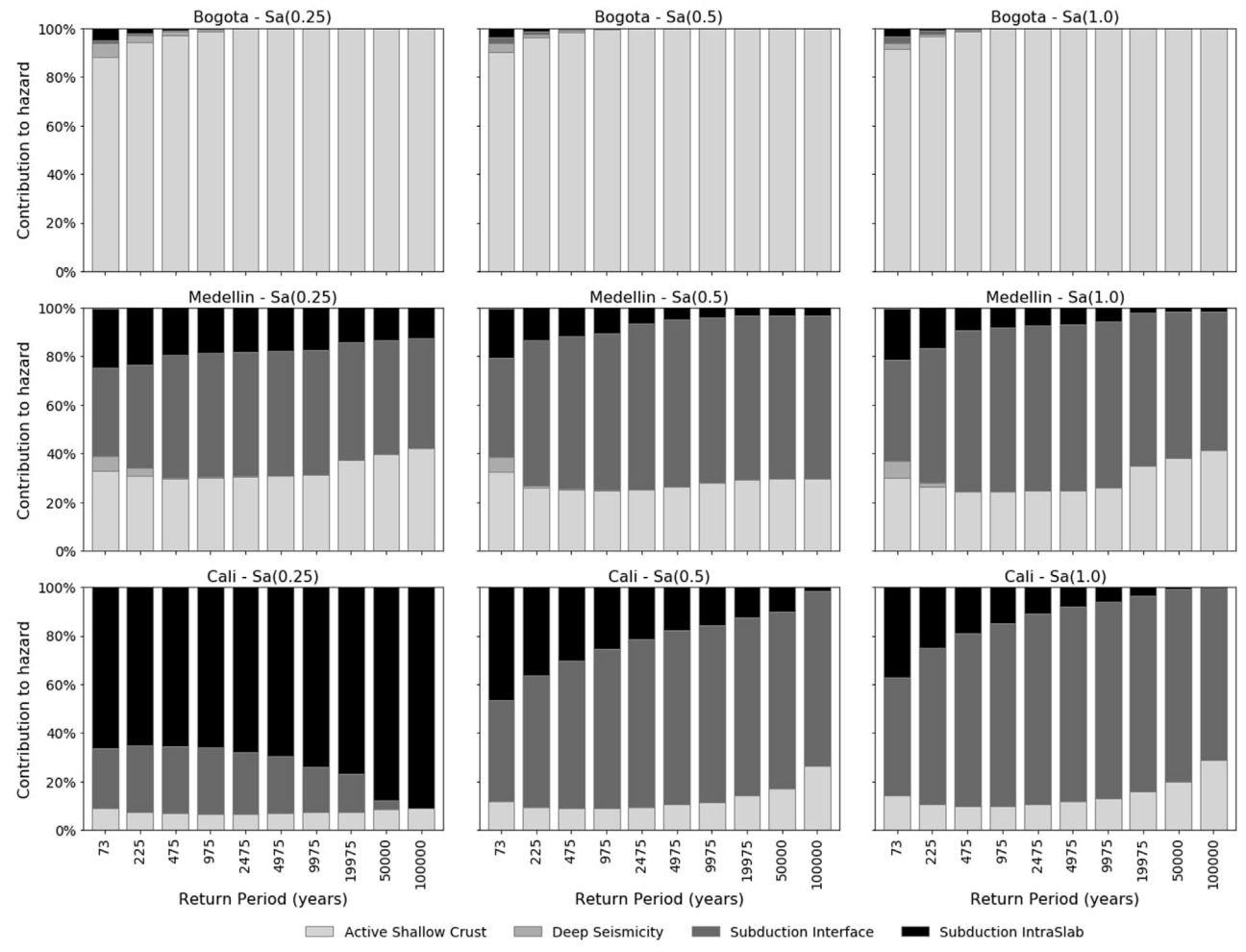

FIGURE 3 | Tectonic regime contribution in the three cities: Bogotá (top), Medellín (center), and Cali (bottom) for the three-building types: two-story unreinforced masonry (left), four-story reinforced concrete (center), and eight-story reinforced concrete (right), for different return periods.

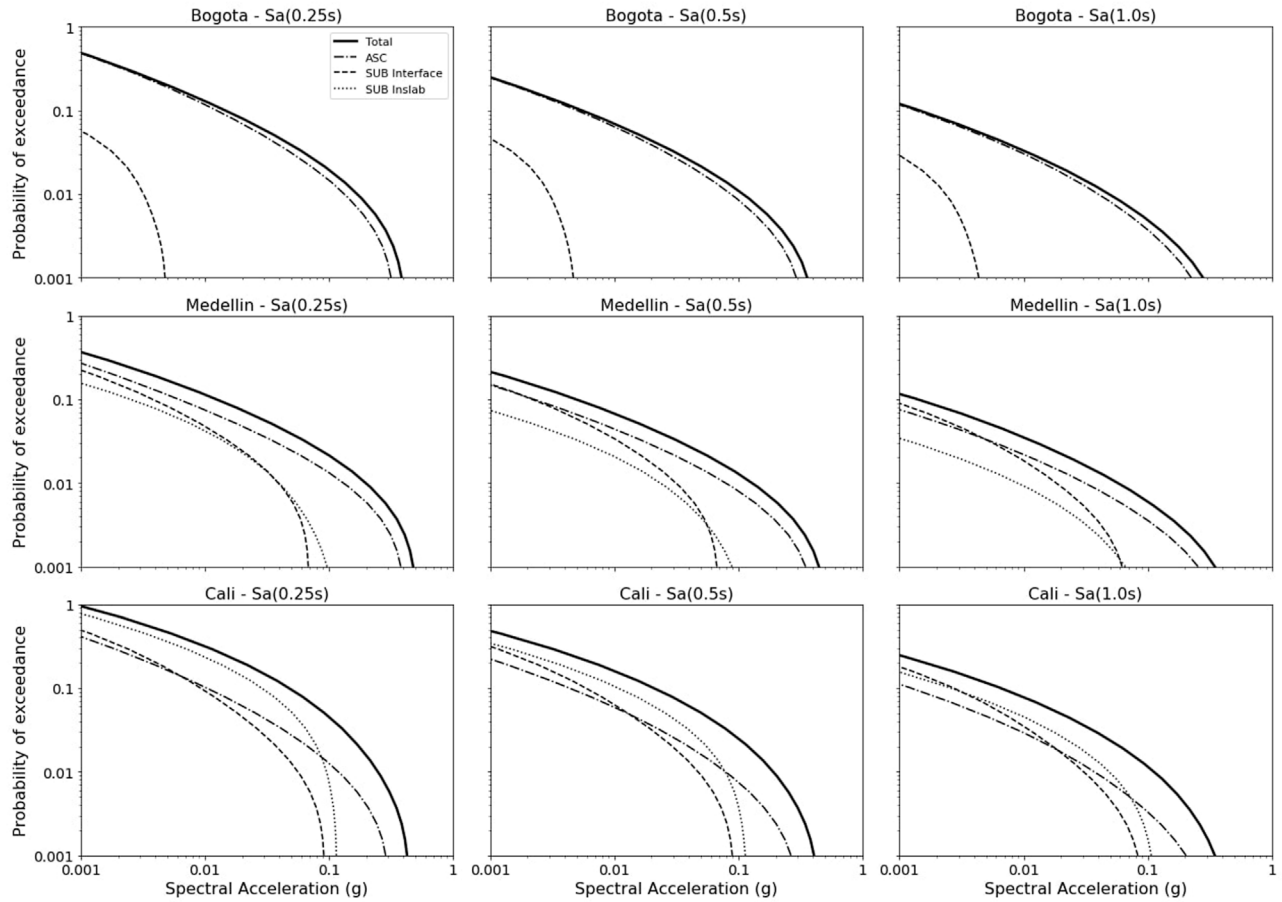

FIGURE 4 | Uniform hazard spectra for 10% probability of exceedance (poe) for Sa (0.25 s) left, Sa (0.5 s) center, and Sa (1.0 s) right for the three cities: Bogotá (top), Medellín (center), and Cali (bottom).

Cornell, 2002), the multi-stripe analysis—MSA (Jalayer, 2003; Jalayer and Cornell, 2009), and the cloud analysis—CA (Cornell et al., 2002) which are the ones considered in this study, clarifying that the adaptative IDA version—AIDA (Lin and Baker, 2013) was considered instead of the IDA when the CS selected set of records was used, and the Bayesian CA (Jalayer et al., 2015) following the procedure reported in Martins and Silva (2020) was used instead of the original CA. For the derivation of fragility curves, the IDA considers a fixed suite of records scaled successively to higher intensity levels, where each ground motion in the suite is scaled until it causes structural collapse. This method was the one followed when deriving the fragility curves using the FEMA P695 far-field record set. The AIDA follows a similar principle but considers different suites of records that are scaled to multiple IMs while they fulfill the hazard characteristics at said IM level, and thus not one but many curves are generated across the multiple bins selected by connecting the records that are repeated from one level to the other.

The MSA, on the other hand, establishes some discrete intensity levels and includes in each a different set of ground motions selected based on site-specific characteristics considering methods such as the CS. This is done since the representative ground motions (and thus their properties) change at each IM level and with the objective to avoid one of the criticisms of the IDA methodology, the over-scaling of the records. This consideration of the local hazard characteristics makes it the most accurate or reliable method if a significant number of records is available for each IM level. Finally, the CA considers performing a regression fitting between the IM and the engineering demand parameter—EDP—in the logarithmic space. Its updated Bayesian version goes one step ahead and includes a differentiation in the regression between the cases where the structure exceeds the collapse limit state and indeed collapses and where it does not.

3 CASE STUDY

Colombia is located in the northwestern part of South America where the interaction between the tectonic plates of Nazca, the Caribbean, and South American, as well as the Panama and North Andes blocks produces deformations that trigger events in the country of different characteristics, some of them with destructive

TABLE 2 | Percentages of the number of events selected for each city, structural period, and tectonic regime type.

Tectonic regime type	Bogota			Medellin			Cali		
	Sa (0.25)	Sa (0.5)	Sa (1.0)	Sa (0.25)	Sa (0.5)	Sa (1.0)	Sa (0.25)	Sa (0.5)	Sa (1.0)
Active shallow crust	100%	100%	100%	37.3%	34.6%	36.0%	7.5%	12.9%	14.5%
Subduction interface	0%	0%	0%	46.1%	58.8%	57.3%	19.5%	65.4%	72.9%
Subduction intraslab	0%	0%	0%	16.7%	6.6%	6.7%	73.0%	21.8%	12.6%

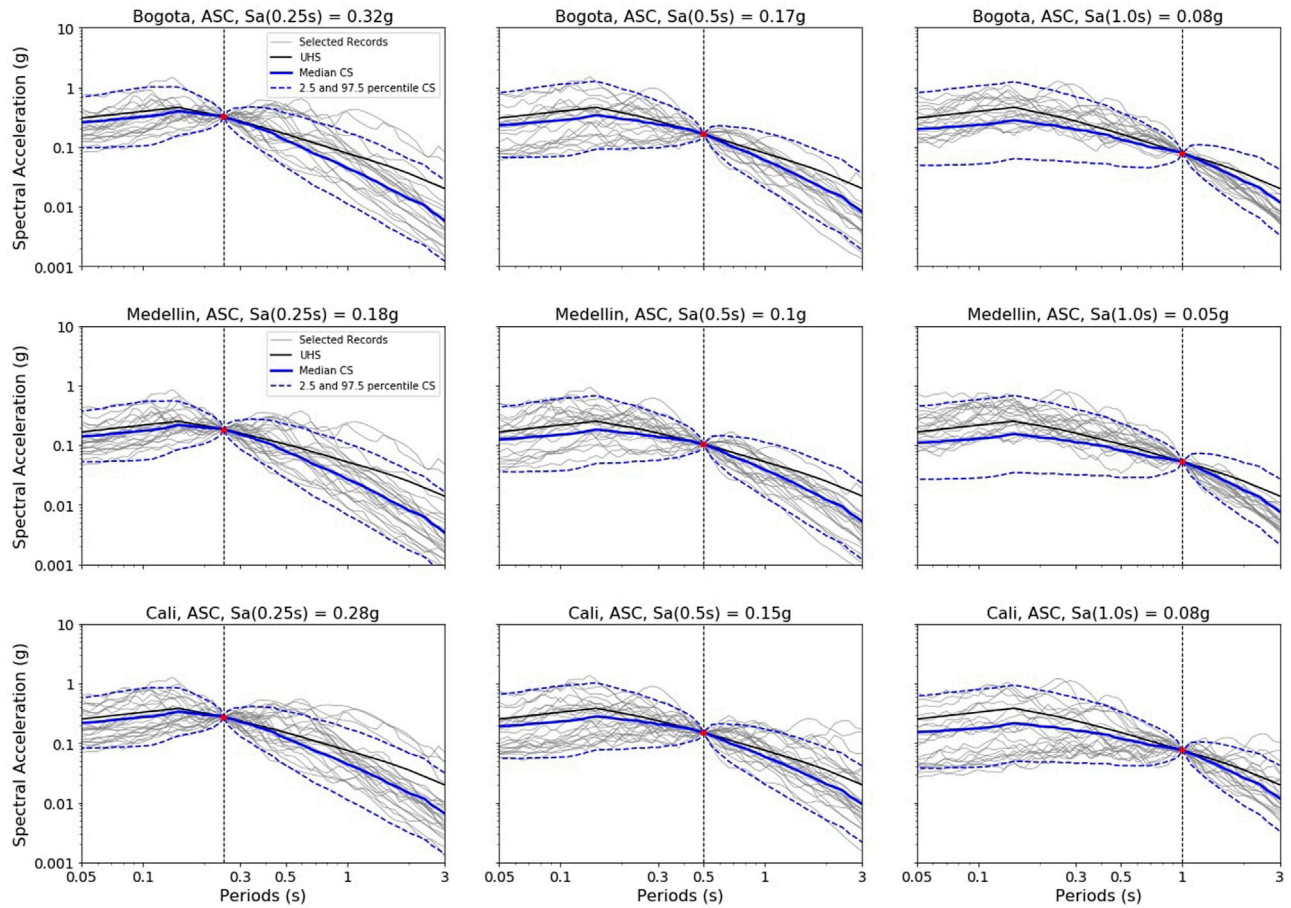

FIGURE 5 | Conditioned spectra (CS), response spectra from the records selected, and uniform hazard spectra (UHS) for active shallow crust at the intensity measure level of 10% probability of exceedance in 50 years for Sa (0.25 s) left, Sa (0.5 s) center, and Sa (1.0 s) right for the three cities: Bogotá (top), Medellín (center), and Cali (bottom). Continuous blue thick line: median CS. Dash-lines: 2.5 and 97.5 CS percentiles. Continuous grey thin lines: records selected.

consequences in the past. This complex tectonic environment generates several geologic faults along the three branches of the Andes Mountains from Ecuador to Venezuela.

Then, to study the effect of different hazard intensity levels and the contributions of different tectonic regimes and thus different hazard scenarios, the three main cities in Colombia, Bogotá, Medellín, and Cali, are included in the case study (**Figure 1**). These are the cities with the largest contribution to the GDP in the country and account for more than 20% of the total population of the country (DANE, 2018). All of them are located in the central part of the country; Bogota is in the eastern Cordillera, while Medellin and Cali are between the central and western branches. The proximity of these cities with some traces of active shallow faults as well as the subduction events generated on the Pacific coast, and the history of destructive events in the past such as the M_w 6.1 Armenia earthquake on 25 January 1999, is sufficient enough to develop and execute plans for the prevention and mitigation of seismic risk in the country.

The seismic hazard model (SHM) used is provided by the Colombian Geological Survey which was made in collaboration with the Global Earthquake Model Foundation and takes into account the seismological and geologic studies in the country as

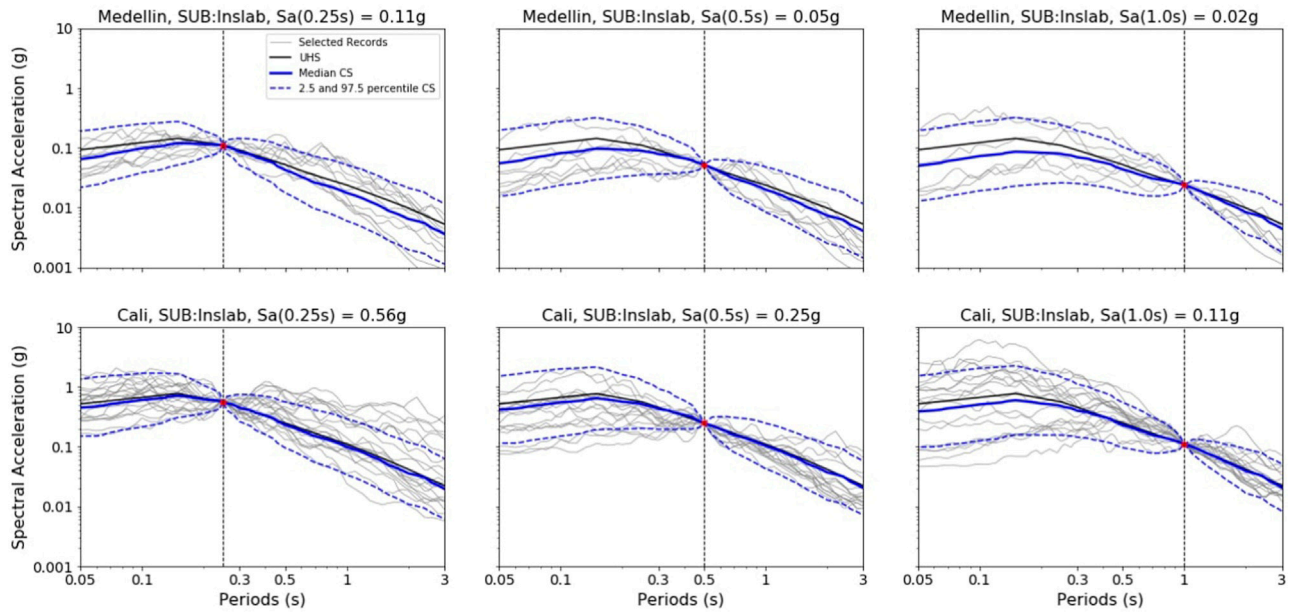

FIGURE 6 | Conditioned spectra (CS), response spectra from the records selected, and uniform hazard spectra (UHS) for subduction intraslab at the intensity measure level of 10% probability of exceedance in 50 years for Sa (0.25 s) left, Sa (0.5 s) center, and Sa (1.0 s) right for the cities: Medellín (top) and Cali (bottom). Continuous blue thick line: median CS. Dash-lines: 2.5 and 97.5 CS percentiles. Continuous gray thin lines: records selected.

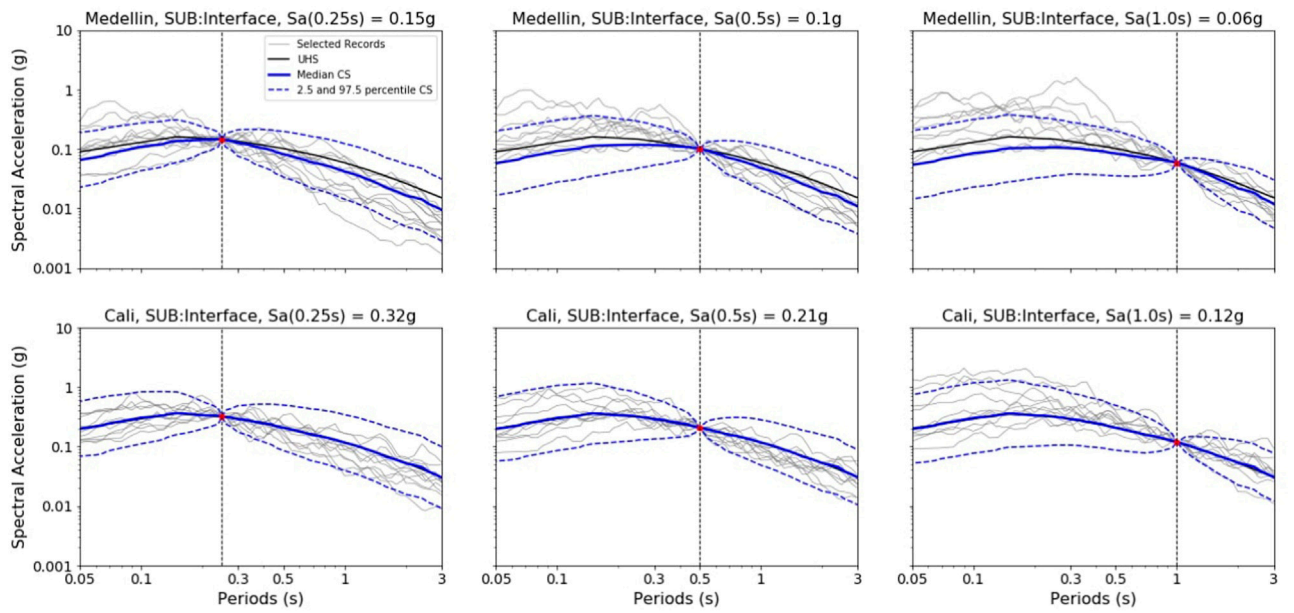

FIGURE 7 | Conditioned spectra (CS), response spectra from the records selected, and uniform hazard spectra (UHS) for subduction interface at the intensity measure level of 10% probability of exceedance in 50 years for Sa (0.25 s) left, Sa (0.5 s) center, and Sa (1.0 s) right for the cities: Medellín (top) and Cali (bottom). Continuous blue thick line: median CS. Dash-lines: 2.5 and 97.5 CS percentiles. Continuous grey thin lines: records selected.

well as a homogeneous earthquake catalog from the national seismological network updated until 2020. A detailed study of the intensity levels registered by the national accelerometric network allowed the authors of the SHM to establish a selection of ground motion prediction models that, using a logic tree, take into account the uncertainty in the intensity levels estimation. The SHM has four different tectonic regimes that contribute to the seismic hazard levels in the country: active shallow crust,

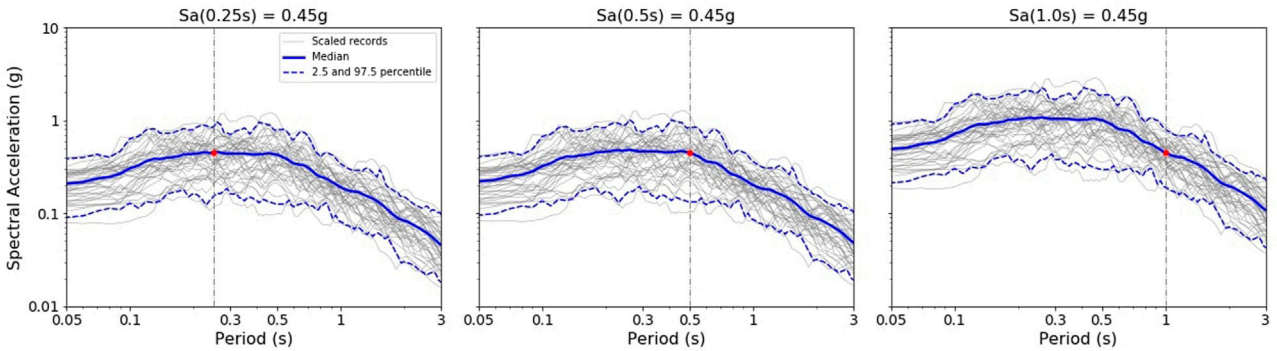

FIGURE 8 | Scaled records from FEMA to the intensity level of 0.45 g for the three different intensity measures of Sa (0.25 s) left, Sa (0.5 s) center, and Sa (1.0 s) right. Gray lines: scaled records. Continuous blue line: mean. Dashed blue lines: 2.5 and 9.7 percentiles.

TABLE 3 | Damage states used in the derivation of fragility curves.

DS1: Slight	DS2: Moderate	DS3: Extensive	DS4: Collapse
0.75Sdy	0.5Sdy + 0.33Sdu	0.25Sdy + 0.67Sdu	Sdu

subduction interface, subduction intraslab, and deep seismicity. However, for the cities of Bogota, Medellin, and Cali, the seismic sources of active shallow crust and subduction are the most relevant. For more details on the seismic hazard model, the reader could refer to (SGC, 2018; Arcila et al., 2020).

Three different structural types, representative of some of the most common vulnerable building classes in Colombia and ranging from the short to the medium structural period, are considered in the case study: the two-storey unreinforced masonry structures (MUR-H2) and the four-storey (CR-H4) and eight-storey (CR-H8) pre-code reinforced concrete buildings. The structural characteristics of the archetype buildings were taken considering the local 1 type of structures reported in Hoyos and Hernández (2021), which are presented in **Table 1**.

Taking the values of the characteristics reported in **Table 1** and using **Eqs 1**, **2** taken from Villar-Vega et al., (2017), the capacity curves of the equivalent single degree of freedom—SDOF—model in terms of Sa and Sd were derived. These curves are presented in **Figure 2**.

$$Sd = \frac{N_{storeys}\, x\, h_{storey}\, x\, \theta_{global}}{\Gamma}. \quad (1)$$

(Villar-Vega et al., 2017)

$$Sa_y = Sd_y \left(\frac{2\pi}{T_y}\right) \; and \; Sa_u = C{*}Sa_y, \quad (2)$$

(adapted Villar-Vega et al., 2017)where C = 1.0 for the two-story masonry structure and C = 0.8 for the concrete structures.

4 RECORD SELECTION

The seismic hazard levels or target levels used to scale the ground motion records were computed for the three cities using the seismic hazard model by Arcila et al. (2020), which is developed in OpenQuake software (Pagani et al., 2014; Silva et al., 2014). The contributions per tectonic environment were estimated for the sites of analysis at different return periods, and as a result, the dominant sources that contribute to the hazard of those cities come from the active shallow crust and subduction (interface and intraslab) tectonic environments. **Figure 3** presents the contribution to the hazard for each city and structural period studied at ten different intensity measure levels or return periods (from 73 to 100,000 years). As it can be seen, the contribution of deep seismicity sources is minimum for all cities; so from now on, it will not be taken into account in further analysis. Likewise, in Bogota, only sources of the active shallow crust will be considered because they represent almost all the contributions to the hazard. On the contrary, in Cali, the higher contribution comes from the subduction sources, but a small proportion of the active shallow crust is still present. Medellin, on the other hand, presents a balanced proportion between sources of active shallow crust and subduction.

Ten different intensity measure levels (IMLs) were established to obtain the target intensity values at the intensities measured close to the fundamental periods, T1, of the systems presented in **Table 1**, to increase the efficiency and ensure lower uncertainties in the response predictions (Luco and Cornell, 2007). **Figure 4** shows the hazard curves of the three cities for the intensity measures (IMs) considered, Sa(0.25s), Sa(0.5s), and Sa(1.0s). The figure depicts in each case the total hazard curve as well as the contribution of active shallow crust (ASC), subduction interface (SUB Interface), and subduction intraslab (SUB Inslab). As it can be seen, Cali is the city with the highest hazard levels for all the IMs due to the proximity to subduction sources on the Pacific coast, while Bogota as stated before only has an important contribution of active shallow sources.

It is worth mentioning that the target intensity levels were estimated per each case for the different tectonic environments and not for the total hazard, as well as considering a response on rock (soil type B). In the view of the authors, using target values much higher than that could occur according to the hazard model, leading to an overestimation of the intensity levels in the records selected. Therefore, the record selection was performed independently for active shallow crust and subduction (interface and intraslab).

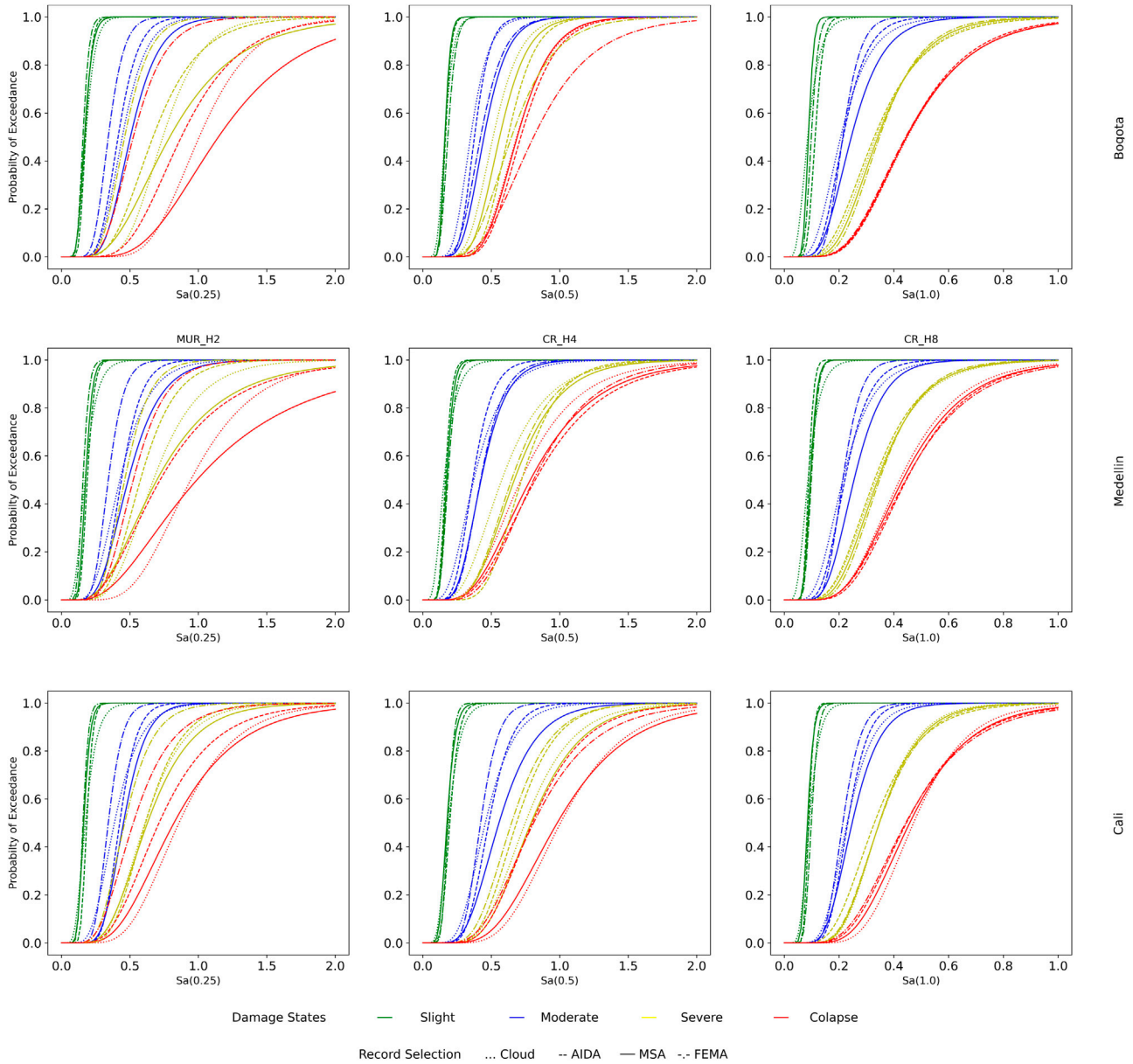

FIGURE 9 | Fragility curves derived using different methods: cloud (dotted), AIDA (dashed line), MSA (continuous line), and FEMA (dotted-dashed line); in the three cities: Bogotá (top), Medellín (center), and Cali (bottom); for the three-building types: two-story unreinforced masonry (left), four-story reinforced concrete (center), and eight-story reinforced concrete (right).

The accelerograms were collected from several ground motion databases worldwide that include events for the tectonic environments presented in the analysis, such as Pacific Earthquake Engineering Research (PEER) NGA-West2 (Ancheta et al., 2014), NGA-Sub (Bozorgnia, 2020), Colombian Geological Survey (SGC, 2022), K-NET and KiK-net networks (NIED, 2022), National Seismological Service of Mexico (SSN-UNAM, 2022), and the SIBER-RISK strong motion database of Chilean earthquakes (Castro et al., 2020). A set of about 200 records was found per each case (i.e., city and structural period), ensuring that when no records were available for a particular target intensity value, a maximum scaling factor of 5.0 was set as a threshold. Then, to unify all the records, we used the contributions of the hazard excluding the deep seismicity sources to create a set of about 1800 records in total for all the cases. **Table 2** presents the proportion of the number of events selected per case.

4.1 Conditioned Spectra

Figure 5 shows the response spectrum from the records selected and scaled for the intensity measure level of 10% probability of exceedance (i.e., 475 years return period) in Bogota, Medellin,

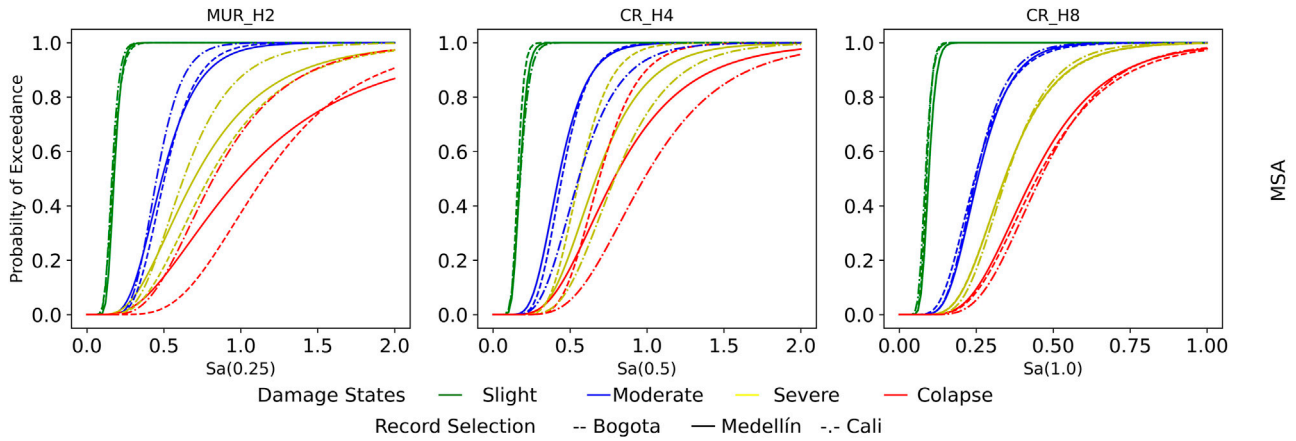

FIGURE 10 | Comparison of the MSA fragility curves between the three cities: Bogotá (dashed line), Medellín (continuous line), and Cali (dotted-dashed line) for the three-building types: two-story unreinforced masonry (left), four-story reinforced concrete (center), and eight-story reinforced concrete (right).

and Cali for the active shallow crust tectonic regime type, on each of the three intensity measures of interest, Sa (0.25 s), Sa (0.5 s), and Sa (1.0 s). As it can be seen from the figure, all the response spectra follow the shape of the conditioned spectrum (CS) and more or less are between the 2.5 to 97.5 percentiles of the CS. **Figures 6** and **7** present the same results as **Figure 5** but for the cases of subduction intraslab and subduction interface. In those cases, only records from Medellin and Cali were selected.

4.2 FEMA

The FEMA records were scaled by the mean of all the 44 ground motion records to different target intensity levels. **Figure 8** shows the response spectra of all the records scaled and the mean spectrum scaled to an intensity level of 0.45 g for the different intensity measures of Sa (0.25 s), Sa (0.5 s), and Sa (1.0 s). This procedure was repeated ten times from 0.15 to 1.5 g with increments of 0.15 g.

5 FRAGILITY DERIVATION

The SDOF models for each of the structural types whose capacity curves are presented in **Figure 2** were then subjected to two nonlinear time history analyses—NLTHA; the first used input ground motions those of the FEMA P695 far-field record set described in **Section 2.1.2** and the second one using the CS record set for each structural type and each city as described in **Section 2.1.1**. The maximum IM and EDP measures for each record were then recorded and later used to derive fragility functions using the methods explained in **Section 2.2**, considering the damage states reported in **Figure 6** by Martins and Silva (2020), which are presented in **Table 3**.

For each method, a different procedure was followed. For the cloud analysis, a linear regression is conducted between an IM and EDP values in the logarithmic space, differentiating the noncollapse and collapse cases by censoring the last ones. The median and standard deviation of each damage state can be calculated using the procedure described in Martins and Silva (2020), which is available in the Vulnerability Modelers Toolkit open code (Martins et al., 2021). On the other hand, the IDA procedure follows the derivation of IDA curves that also provide an IM–EDP relationship. For calculating the mean and standard deviation, following an IM-based procedure, **Eqs 3**, **4** can be used for each damage state

$$\theta = \frac{\sum_{i=1}^{n} ln\, Sa^{DCR=1}}{n}, \tag{3}$$

$$\beta_{Sa|DS=dsi} = \sqrt{\frac{\sum_{i=1}^{n} (ln\, Sa^{DCR=1} - \theta)^2}{n-1}}, \tag{4}$$

where DCR is the ratio between the recorded EDP over the DS. Finally, for the MSA procedure, considering the damage matrix, for each IM used as the target, it is possible to establish how many records can cause collapse (or for other damage states how many exceed the value) and using the maximum likelihood estimator, it is possible to fit lognormal parameters for each damage state. The comparison of the fragility curves obtained from each of the methods, for each structural type in each city, is presented in **Figure 9**. Additionally, the comparison of the MSA curves between the three cities is presented in **Figure 10**. The comparison of the fragility curves obtained from each of the methods, for each structural type in each city, is presented in **Figure 9**. Additionally, the comparison of the MSA curves between the three cities is presented in **Figure 10**.

6 ANALYSIS OF RESULTS

There is an important variability in the results obtained for the three studied building types shown in **Figures 9** and **10**. In the case of the eight-story reinforced concrete building (CR-H8), the derived fragilities seem to be unaffected by the record selection approach as can be observed in the right plot of **Figure 10**. In this case, the differences between the curves for the three cities compared with the one derived with the FEMA P695 records are insignificant, and also the differences between the fragility

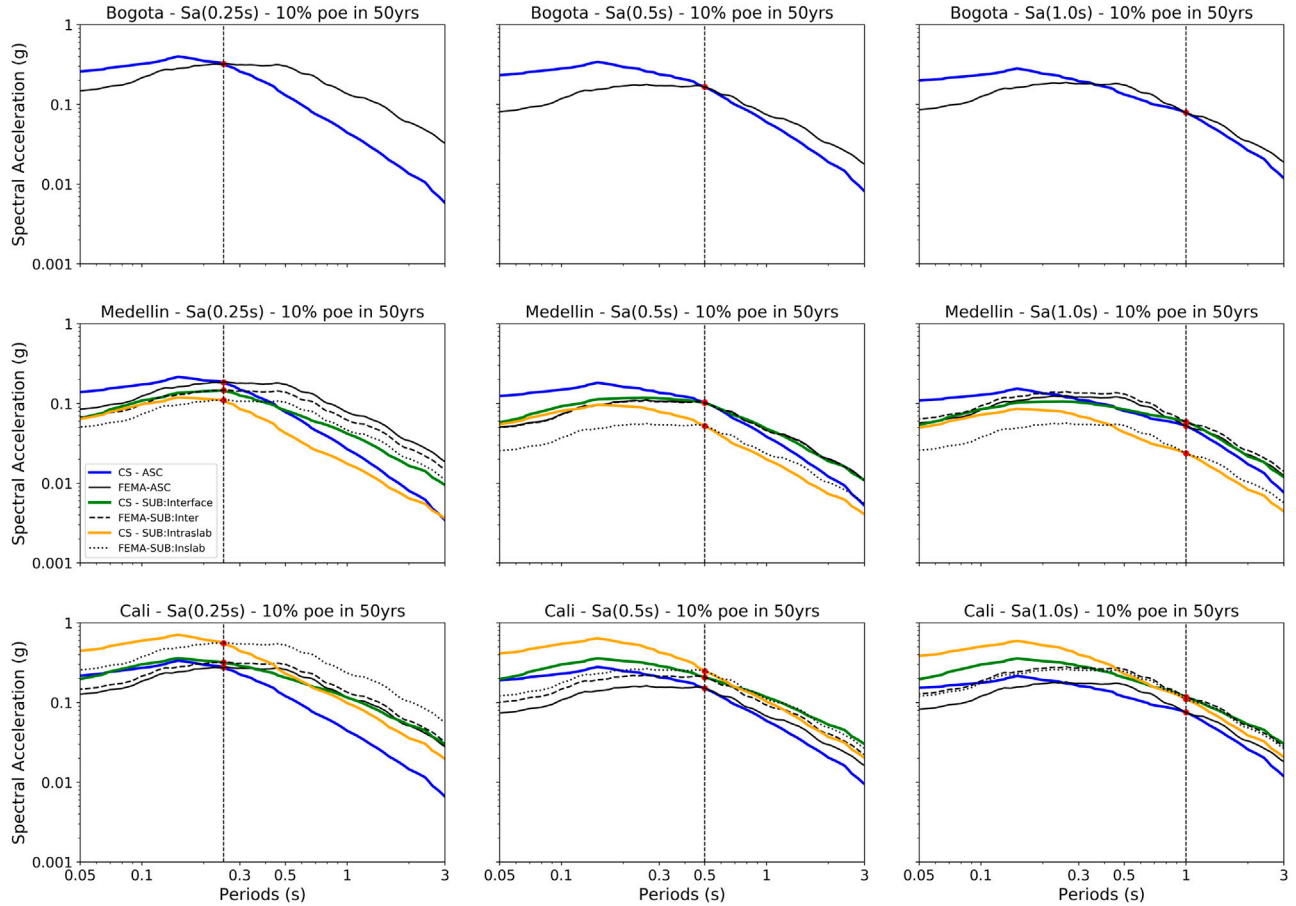

FIGURE 11 | Comparison of the CS and mean FEMA spectra for 10% probability of exceedance in 50 years for Sa (0.25 s) left, Sa (0.5 s) center, and Sa (1.0 s) right for the three cities: Bogotá (top), Medellín (center), and Cali (bottom).

derivation methods are minimal, as shown in the three plots on the right of **Figure 9**. Thus, for this particular building type, it could be said that the site-specific record selection, which can be more time-consuming, could be neglected as the general pool of records will give accurate results.

On the opposite side, however, the results for the two-story unreinforced masonry structure (MUR-H2) are shown to be extremely sensitive to both the record selection procedure and the fragility curve derivation methodology. Considering the former, for the three cities under study, the fragilities derived using the FEMA P695 record set largely underestimate the capacity of the structures and thus can cause extremely conservative risk results, as they are the most fragile curves in the left plots of **Figure 9**. On the other hand, regarding the fragility curve derivation method, there is a large dispersion in the results in particular for the severe and collapse damage states. For all cases, the MSA method gives the less conservative fragilities, while the AIDA method tends to give the most conservative ones, having the CA landing usually between both. It is interesting to see that even when the AIDA and not the original IDA is used, the results still tend to be more conservative when using this procedure than the other two methods. However, at this point, it is important to mention that given the large IMs at which the records needed to be scaled to reach collapse, there can be a considerable reduction in the number of available records that can be used for these high IMs without reaching the limit of 5 in the scale factors, and thus the results were expected to produce larger variabilities for the final damage states.

Regarding the four-story reinforced concrete structure CR-H4, there is considerable variability in the fragility curves derived using different methods for all damage states but the slight one, however, not as pronounced as in the MUR-H2 case. In this case, there is not an overall behavior present among all cities when comparing the site-specific curves with those derived from FEMA (as in the case of MUR-H2 and CR-H8). As it can be appreciated in the center plots of **Figure 9**, there is a similarity with the FEMA fragilities for the Medellin case; however, for Cali, the IDA using FEMA P695 far-field records tends to overestimate the capacity of the structures, while in Bogotá it underestimates it.

Considering this last point, an interesting result could be seen in the comparison between cities. As previously stated, both the MUR-H2 and the CR_H4 buildings present very different fragilities among cities (see **Figure 10**). In the CR-H4 case, this behavior seems to be counterintuitive when looking at the total hazard curves presented in **Figure 4**, as the total hazard in

Cali is shown to be higher than that of Bogotá and Medellín. At this point, it is important to mention that within the selection of records using the CS procedure, given that tectonic regime-specific records were searched for, the conditioning intensity from the spectrum was that of the specific tectonic regime spectrum and not the one from the total spectrum. This considering that within the hazard model that was used, the sources of each tectonic regime cannot experience or produce values above those specifically calculated from them, and thus using the total hazard spectrum instead of the tectonic regime specific one could cause an overestimation of the demand of the site when compared with its known hazard. In this way, based on the percentages of records by the contribution of the tectonic regime in each city, that were obtained considering the disaggregation in each site and that are presented in **Table 2** and looking at **Figure 4**, it can be seen that in some cases, the contribution of the modeled active shallow crust in Bogotá can be higher than any of the contributions of a specific regime type in Medellin and Cali. Considering this issue, further studies should be conducted to see the sensitivity and accuracy of fragility curves derived in regions with contributions of multiple sources to see if there is a considerable overestimation when assuming the total hazard spectra instead of that of each specific source.

Finally, to try to understand the overall behavior of the fragility curves, an analysis of the mean conditional spectra for the site-specific record sets and the FEMA recordset was conducted, looking into the spectral shapes of the mean response for each. **Figure 11** shows the mean conditional spectra representing 10% of exceedance in 50 years for all cases. It is very interesting to see that the spectral shape of the CS in all cities for the CR-H8 structure is very similar to that of the FEMA P695 far-field recordset. This agreement in the spectra can be the cause of the similarities of the fragility curves in this case and brings up a possible analysis that can be conducted to see if the FEMA P695 recordset can indeed be used in the derivation of fragility curves at a site.

Continuing with the analyses of **Figure 11**, for the MUR-H2 case, it can be seen that in all cases, the mean spectra from the FEMA dataset differ in spectral shape from that of any of the site-specific CS in the cities and tend to be higher after the structural period of analysis (0.25s). This is why for the larger damage states, when the structures start to present cracks and elongate their period, the FEMA fragilities are more fragile than the other ones. Finally considering the CR-H4 case, a very similar spectral shape can be seen for the Medellin case (the reason why the fragilities were also so similar in that case), while for Bogotá, the mean for the FEMA records after the structural period (0.5 s) tends to fall while the ones in Cali rise.

7 CONCLUSION

There is no general rule to follow to choose either a record selection approach or a fragility derivation method as it should be evaluated in every specific case based on a more careful consideration of the characteristics of the hazard at the site, the expected ground motions, the structures to analyze, and the availability of resources. However, it could be seen that the spectral shape does seem to be an important parameter in the record selection method and the set of records that should be included in the analysis. Likewise, the ground motion prediction model (GMPM) plays an important role in the spectral shape of the CS and should be given more attention; in particular in sites where there is no locally derived GMPM. In this way, the use of a general set of records such as the FEMA P-695 far-field set seems appropriate for the fragility analysis of structures with medium-to-high fundamental periods. On the contrary, for a short fundamental period of vulnerable building types, a more detailed record selection should be performed as the FEMA P-695 most likely underestimates the capacity of the structures.

The use of target values much higher than what could occur according to the hazard model leads to an overestimation of the intensity levels in the records selected. Based on the hazard model used, the sources of each tectonic regime cannot experience or produce values above those specifically calculated from them, and thus using the total hazard spectrum instead of the tectonic regime specific one could cause an overestimation of the demand of the site when compared with its known hazard.

With all of these in mind, further studies should be conducted to see the sensitivity and accuracy of 1) fragility curves derived in regions with contributions from multiple sources to see if there is a considerable overestimation when assuming the total hazard spectra instead of that of each specific source; 2) the use of different GMPM to compute the conditioned spectra and the impact on the spectral shape in the record selection; 3) the consideration of using different methods in the computation of the conditioned spectra, with one or multiple GMPMs, different logic tree weights, different disaggregation weights, and by including all the possible scenarios (magnitudes and distances).

DATA AVAILABILITY STATEMENT

The original contributions presented in the study are included in the article; further inquiries can be directed to the corresponding author.

AUTHOR CONTRIBUTIONS

AH CS, record selection 50% MH NLTHA, Derivation fragility curves 50%.

FUNDING

This work was funded by the EU Horizon 2020 program under Grant Agreement Number 813137, ITN-MSCA URBASIS project.

ACKNOWLEDGMENTS

The authors thank the Colombian Geological Survey for sharing the National Seismic Hazard Model of Colombia.

REFERENCES

Acevedo, A. B., Jaramillo, J. D., Yepes, C., Silva, V., Osorio, F. A., and Villar., M. (2017). Evaluation of the Seismic Risk of the Unreinforced Masonry Building Stock in Antioquia, Colombia. *Nat. Hazards* 86 (S1), 31–54. doi:10.1007/s11069-016-2647-8

Ancheta, T. D., Darragh, R. B., Stewart, J. P., Seyhan, E., Silva, W. J., Chiou, B. S.-J., et al. (2014). NGA-West2 Database. *Earthq. Spectra* 30 (3), 989–1005. doi:10.1193/070913EQS197M

Arcila, M., Garcia, J., Montejo, J., Eraso, J., Valcacer, J., Mora, M., et al. (2020). *Modelo Nacional De Amenaza Sísmica Para Colombia*. Servicio Geológico Colombiano. doi:10.32685/9789585279469

Baker, J. W. (2015). Efficient Analytical Fragility Function Fitting Using Dynamic Structural Analysis. *Earthq. Spectra* 31 (1), 579–599. doi:10.1193/021113EQS025M

Bozorgnia, Y. (2020). *Data Resources for NGA-Subduction Project*. NGA-Subduction Principal Investigator. Pacific Earthquake Engineering Research Center.

Castro, S., Benavente, R., Crempien, J. G., Candia, G., and de la Llera, J. C. (2020). A Consistently Processed Strong-Motion Database for Chilean Earthquakes. *Seismol. Res. Lett.*

Cornell, C. A., Jalayer, F., Hamburger, R. O., and FoutchFoutch, D. A. (2002). Probabilistic Basis for 2000 SAC Federal Emergency Management Agency Steel Moment Frame Guidelines. *J. Struct. Eng.* 128 (4), 526–533. doi:10.1061/(asce)0733-9445(2002)128:4(526)

DANE (2018). *Censo Nacional de Población y Vivienda – CNPV*. Base de Datos. Departamento Administrativo Nacional de Estadistica. Available at: https://www.datos.gov.co/Estad-sticas-Nacionales/Censo-Nacional-de-Poblaci-n-y-Vivienda-CNPV-2018/qzc6-q9qw (Accessed February 15, 2022).

De Biasio, M., Grange, S., Dufour, F., Allain, F., and Petre-Lazar, I. (2014). A Simple and Efficient Intensity Measure to Account for Nonlinear Structural Behavior. *Earthq. Spectra* 30 (4), 1403–1426. doi:10.1193/010614EQS006M

Eads, L., Miranda, E., and Lignos, D. G. (2015). Average Spectral Acceleration as an Intensity Measure for Collapse Risk Assessment. *Earthq. Eng. Struct. Dyn.* 44 (12), 2057–2073. doi:10.1002/eqe.2575

Federal Emergency Management Agency (2009). Quantification of Building Seismic Performance Factors. Available at: www.ATCouncil.org (Accessed January 31, 2022).

Harmsen, S. C. (2001). Mean and Modal in the Deaggregation of Probabilistic Ground Motion. *Bull. Seismol. Soc. Am.* 91 (6), 1537–1552. doi:10.1785/0120000289

Haselton, C. B., Baker, J. W., Liel, A. B., and Deierlein, G. G. (2011). Accounting for Ground-Motion Spectral Shape Characteristics in Structural Collapse Assessment through an Adjustment for Epsilon. *J. Struct. Eng.* 137 (3), 332–344. doi:10.1061/(asce)st.1943-541x.0000103

Hoyos, M. C., and Hernández, A. F. (2021). Impact of Vulnerability Assumptions and Input Parameters in Urban Seismic Risk Assessment. *Bull. Earthq. Eng.* 19 (11), 4407–4434. doi:10.1007/s10518-021-01140-x

Jaimes, M. A., and Candia, G. (2019). Interperiod Correlation Model for Mexican Interface Earthquakes. *Earthq. Spectra* 35 (3), 1351–1365. doi:10.1193/080918EQS200M

Jalayer, F., and Cornell, C. A. (2009). Alternative Non-linear Demand Estimation Methods for Probability-Based Seismic Assessments. *Earthq. Eng. Struct. Dyn.* 38 (8), 951–972. doi:10.1002/eqe.876

Jalayer, F., De Risi, R., and Manfredi, G. (2015). Bayesian Cloud Analysis: Efficient Structural Fragility Assessment Using Linear Regression. *Bull. Earthq. Eng.* 13 (4), 1183–1203. doi:10.1007/s10518-014-9692-z

Jalayer, F., Ebrahimian, H., Miano, A., Manfredi, G., and Sezen, H. (2017). Analytical Fragility Assessment Using Unscaled Ground Motion Records. *Earthq. Eng. Struct. Dyn.* 46 (15), 2639–2663. doi:10.1002/eqe.2922

Jalayer, F. (2003). *Direct Probability Seismic Analysis: Implementing Non-linear Dynamic Assessment*. Stanford University.

Jayaram, N., and Baker, J. W. (2009). Correlation Model for Spatially Distributed Ground-Motion Intensities. *Earthq. Eng. Struct. Dyn.* 38 (15), 1687–1708. doi:10.1002/eqe.922

Jayaram, N., Lin, T., and Baker, J. W. (2011). A Computationally Efficient Ground-Motion Selection Algorithm for Matching a Target Response Spectrum Mean and Variance. *Earthq. Spectra* 27 (3), 797–815. doi:10.1193/1.3608002

Kohrangi, M., Bazzurro, P., Vamvatsikos, D., and Spillatura, A. (2017a). Conditional Spectrum-Based Ground Motion Record Selection Using Average Spectral Acceleration. *Earthq. Eng. Struct. Dyn.* 46 (10), 1667–1685. doi:10.1002/eqe.2876

Kohrangi, M., Vamvatsikos, D., and Bazzurro, P. (2017b). Site Dependence and Record Selection Schemes for Building Fragility and Regional Loss Assessment. *Earthq. Eng. Struct. Dyn.* 46 (10), 1625–1643. doi:10.1002/eqe.2873

Kohrangi, M., Vamvatsikos, D., and Bazzurro, P. (2020). Multi-Level Conditional Spectrum-Based Record Selection for IDA. *Earthq. Spectra* 36 (4), 1976–1994. doi:10.1177/8755293020919425

Lin, T., and Baker, J. W. (2013). "Introducing Adaptive Incremental Dynamic Analysis: A New Tool for Linking Ground Motion Selection and Structural Response Assessment," in 11th International Conference on Structural Safety & Reliability, New York, NY, 805–811.

Lin, T., Harmsen, S. C., Baker, J. W., and Luco, N. (2013). Conditional Spectrum Computation Incorporating Multiple Causal Earthquakes and Ground-Motion Prediction Models. *Bull. Seismol. Soc. Am.* 103 (2A), 1103–1116. doi:10.1785/0120110293

Lin, T., Haselton, C. B., and Baker, J. W. (2013a). Conditional Spectrum-Based Ground Motion Selection. Part II: Intensity-Based Assessments and Evaluation of Alternative Target Spectra. *Earthq. Eng. Struct. Dyn.* 42, 1867–1884. doi:10.1002/eqe.2303

Lin, T., Haselton, C. B., and Baker, J. W. (2013b). Conditional Spectrum-Based Ground Motion Selection. Part I: Hazard Consistency for Risk-Based Assessments. *Earthq. Eng. Struct. Dyn.* 42 (12), 1847–1865. doi:10.1002/eqe.2301

Luco, N., and Cornell, C. A. (2007). Structure-Specific Scalar Intensity Measures for Near-Source and Ordinary Earthquake Ground Motions. *Earthq. Spectra* 23 (2), 357–392. doi:10.1193/1.2723158

Mackie, K. R., and Stojadinovi, B. (2005). "Comparison of Incremental Dynamic, Cloud, and Stripe Methods for Computing Probabilistic Seismic Demand Models," in Structures Congress 2005 (ASCE Library). doi:10.1061/40753(171)184

Martins, L., and Silva, V. (2020). Development of a Fragility and Vulnerability Model for Global Seismic Risk Analyses. *Bull. Earthq. Eng.* 19, 6719–6745. doi:10.1007/s10518-020-00885-1

Martins, L., Silva, V., Crowley, H., and Cavalieri, F. (2021). Vulnerability Modellers Toolkit, an Open-Source Platform for Vulnerability Analysis. *Bull. Earthq. Eng.* 19 (13), 5691–5709. doi:10.1007/s10518-021-01187-w

NIED (2022). NIED K-NET, KiK-Net. Available at: https://www.doi.org/10.17598/NIED.0004 (Accessed November 15, 2021).

Pagani, M., Monelli, D., Weatherill, G., Danciu, L., Crowley, H., Silva, V., et al. (2014). OpenQuake Engine: An Open Hazard (And Risk) Software for the Global Earthquake Model. *Seismol. Res. Lett.* 85 (3), 692–702. doi:10.1785/0220130087

SGC (2018). Modelo de Amenaza Sismica de Colombia. Available at: https://amenazasismica.sgc.gov.co/ (Accessed November 15, 2021).

SGC (2022). *Catálogo de Aceleraciones." Direccion de Geoamenazas*. Servicio Geologico Colombiano.

Silva, V., Crowley, H., Pagani, M., Monelli, D., and Pinho, R. (2014). Development of the OpenQuake Engine, the Global Earthquake Model's Open-Source Software for Seismic Risk Assessment. *Nat. Hazards* 72 (3), 1409–1427. doi:10.1007/s11069-013-0618-x

Sinisterra, H. (2017). *Determinación Del Desempeño Sísmico Para Edificios En Pórticos de Concreto Reforzado Diseñados Bajo La Norma de Diseño Sismo Resistente C.C.C.S.R-84*. Cali: Universidad Javeriana.

SSN-UNAM (2022). *Catalogo de Sismos*. IDG, Servicio Sismologico Nacional.

United Nations Office for Disaster Risk Reduction (2015). *Sendai Framework for Disaster Risk Reduction 2015-2030*. Geneva, Switzerland: UNDRR.

United Nations (2015). *Transforming Our World: The 2030 Agenda for Sustainable Development*. New York, United States: General Assembly September 25, 2015.

United Nations (2016). New Urban Agenda. Available at: http://uploads.habitat3.org/hb3/NUA-English.pdf (Accessed February 20, 2022).

United Nations (2019). *World Urbanization Prospects the 2018 Revision*. New York, United States: Department of Economic and Social Affairs.

Vamvatsikos, D., and Cornell, C. A. (2002). Incremental Dynamic Analysis. *Earthq. Eng. Struct. Dyn.* 31 (3), 491–514. doi:10.1002/eqe.141

Villar-Vega, M., Silva, V., Crowley, H., Yepes, C., Tarque, N., Acevedo, A. B., et al. (2017). Development of a Fragility Model for the Residential Building Stock in South America. *Earthq. Spectra* 33 (2), 581–604. doi:10.1193/010716EQS005M

Conflict of Interest: The authors declare that the research was conducted in the absence of any commercial or financial relationships that could be construed as a potential conflict of interest.

Publisher's Note: All claims expressed in this article are solely those of the authors and do not necessarily represent those of their affiliated organizations, or those of the publisher, the editors, and the reviewers. Any product that may be evaluated in this article, or claim that may be made by its manufacturer, is not guaranteed or endorsed by the publisher.

frontiers | Frontiers in Earth Science

TYPE Original Research
PUBLISHED 19 August 2022
DOI 10.3389/feart.2022.937848

OPEN ACCESS

EDITED BY
Simone Barani,
University of Genoa, Italy

REVIEWED BY
Paolo Boncio,
University of Studies G. d'Annunzio Chieti and Pescara, Italy
Snježana Markušić,
University of Zagreb, Croatia

*CORRESPONDENCE
Daniela Famiani,
daniela.famiani@ingv.it

SPECIALTY SECTION
This article was submitted to Geohazards and Georisks, a section of the journal Frontiers in Earth Science

RECEIVED 06 May 2022
ACCEPTED 15 July 2022
PUBLISHED 19 August 2022

CITATION
Famiani D, Cara F, Di Giulio G, Vassallo M and Milana G (2022), Detection of hidden faults within the Fucino basin from single-station ambient noise measurements: The case study of the Trasacco fault system.
Front. Earth Sci. 10:937848.
doi: 10.3389/feart.2022.937848

Detection of hidden faults within the Fucino basin from single-station ambient noise measurements: The case study of the Trasacco fault system

Daniela Famiani[1]*, Fabrizio Cara[1], Giuseppe Di Giulio[2], Maurizio Vassallo[2] and Giuliano Milana[1]

[1]Istituto Nazionale di Geofisica e Vulcanologia, Sezione di Sismologia e Tettonofisica, Roma, Italy, [2]Istituto Nazionale di Geofisica e Vulcanologia, Sezione di Sismologia e Tettonofisica, L'Aquila, Italy

The presence of normal fault systems in central Italy, outcropping or hidden below Quaternary covers in intra-mountain basins, is the expression of the Neogene–Quaternary evolution of the area, characterized by an extensional tectonic regime following the fold and thrust structuring of the Apennine orogen. Italian urban settlements of central Italy are developed on hills or mountains but also in lowland areas, which are often set up in sedimentary basins. In this framework, urban centers found close to fault lines are common, with strong implications on the seismic risk of the area. In this work, we performed a dense seismological passive survey (88 single-station ambient noise measurements) and used the horizontal-to-vertical spectral ratio (HVNSR) technique to investigate hidden faults in the Trasacco municipality located in the southern part of the Fucino Basin (central Italy), where microzonation studies pointed out hypothetical fault lines crossing the urban area with the Apennine orientation. These hidden structures were only suggested by previous studies based on commercial seismic lines and aerial photogrammetry; their presence in the basin area is confirmed by our measurements. This case study shows the potentiality of using the HVNSR technique in fault areas to have a preliminary indication of anomalous behaviors, to be investigated later with specific geophysical techniques. Our approach can support microzonation studies whenever fault zones are involved, especially in urban areas or in places designated for future developments.

KEYWORDS

microzonation, HVNSR, hidden faults, lateral heterogeneities, subsoil reconstruction

Introduction

Seismic microzonation studies are often carried out at a basic level, sometimes leaving open scientific points that require further *ad hoc* investigations to be solved. In this study, we face one of these cases regarding the Fucino Basin (hereinafter FB), a large intra-mountain continental basin in central Italy. The FB was the greatest lake of central Italy until its complete drainage at the end of the 19th century and has a tectonic origin related to the presence of important normal fault systems. Here, we focus on the southern part of the FB, specifically close to Trasacco village (red square in Figure 1). In 2013, the Trasacco municipality (about 6,000 inhabitants) has been the object of a seismic microzonation study, and one of the main objectives was to clarify the position of the Trasacco fault, an active and capable NW-SE oriented normal structure following the elongation of the Vallelonga valley (see zoom in Figure 1 for the location). In fact, the issue of characterizing and zoning active and capable faults is crucial for urban planning purposes and also for ensuring safe conditions to the pre-existing buildings. Despite the large amounts of data (geognostic, geophysical, and geotechnical) collected by professional geologists during the microzonation activities, no evidence of the fault was found in the urbanized area. The spatial continuation of this fault in the northern direction of the basin area is also uncertain.

Hence, we decided to perform a geophysical study devoted to identifying the extension of the Trasacco fault in the basin area and other possible tectonic structures in it. In particular, we performed a wide campaign of single-station ambient noise recordings, using the well-known horizontal-to-vertical spectral ratio (HVNSR) technique as the method of analysis (Nakamura, 1989). Some of these data, which were recorded simultaneously at different locations, have been also used to roughly estimate the shear-wave velocities of the sedimentary layers. The HVNSR results are discussed under two different perspectives: first, we adopt a classical interpretation scheme to get a first-order reconstruction of the subsoil of the study area through the identification of the fundamental resonance frequency (f0) of the investigated sites; and second, we perform a directional analysis on HVNSR, for e.g., by rotating the horizontal components of the ground motion for sites close to tectonic elements. The purpose of this latter study was to identify a sort of signature related to specific complexities of the investigated sites and possibly linked to the presence of the Trasacco fault and all the other tectonic structures. The correlation between these observations and the geology is supported by the availability of other relevant previous studies in the Fucino Basin.

Geological setting

The FB is an intra-mountain lacustrine basin with a tectonic origin. Some of the faults that originated in the basin are able to generate large seismic events, such as the 13 January 1915 M 7.0 Avezzano earthquake, which completely destroyed the town of Avezzano and caused about 30,000 casualties. The FB is infilled by Upper Pliocene–Holocene lacustrine and alluvial deposits (Bard and Bouchon, 1980a; Bard and Bouchon, 1980b; Giraudi, 1988; Bosi et al., 1995), which unconformably overlie Meso-Cenozoic carbonate and Neogene terrigenous successions (Cavinato et al., 2002). Quaternary deposits also include alluvial fans made by the dismantling of the surrounding reliefs. FB is the largest intra-mountain endoreic depression of the Apennines, filled by a well-preserved thick Quaternary continental succession (Mannella et al., 2019), representing an important record to reconstruct the geological evolution of central Italy (volcanic eruptions and climate changes). According to Galadini et al. (1995) and Cavinato et al. (2002), from a neo-tectonic point of view, the evolution of the FB has been mainly affected by the activity of two systems of faults that border the northern and eastern sectors of the area. These two can be described as the "active" sides of the basin, and they can be easily distinguished, for the evidence of structural elements and outcropping geological units, from the southern and western parts of the basin which, conversely, are supposed to have a passive role in the genesis of the plain.

The total subsidence of the area may be defined as the sum of the hanging-wall subsidence generated by the normal fault and sediment compaction, and the regional subsidence or uplift (Doglioni et al., 1998).

From the analysis of surface geological data and the interpretation of seismic lines, Cavinato et al. (2002) divided the sedimentary infilling of FB in two different groups of stratigraphic units: Lower and Upper Units. The Lower Units (Upper Pliocene) crop out in the northern and north-eastern margins of the basin and consist of breccia, fluvial, and marginal to open-lacustrine deposits. The Upper Units (Lower Pleistocene–Holocene) are represented by marginal lacustrine/fluvial deposits; thick coarse-grained fan-delta deposits are interfingered with fluvial–lacustrine deposits at the foot of the main relief. It is worth mentioning that some of the articles published for the area aimed at studying the characteristics of the recent units more in detail: general descriptions of continental deposits (Zarlenga, 1987), more specific analysis of morphotectonic (Bard and Bouchon, 1985; Blumetti et al., 1993) or geomorphological features, as alluvial fans (Frezzotti and Giraudi, 1992) or terraces (Accordi 1975; Messina 1996).

Focusing more on the structural elements present in FB, the main faults are (right side in Figure 1): the Tremonti–Celano–Aielli Fault (TCAF) (WSW–ENE) and S. Potito–Celano Faults (NW-SE) in the north; the Luco Fault (LF) in the west; and the Trasacco Fault (TF) and Villavallelonga Fault (VF), the Pescina–Celano Fault (PCF), and the Serrone Fault (NW–SE) in the southern and southeastern parts of the basin. Recently, Lanari et al. (2021) proposed a structural analysis of the FB making inferences on

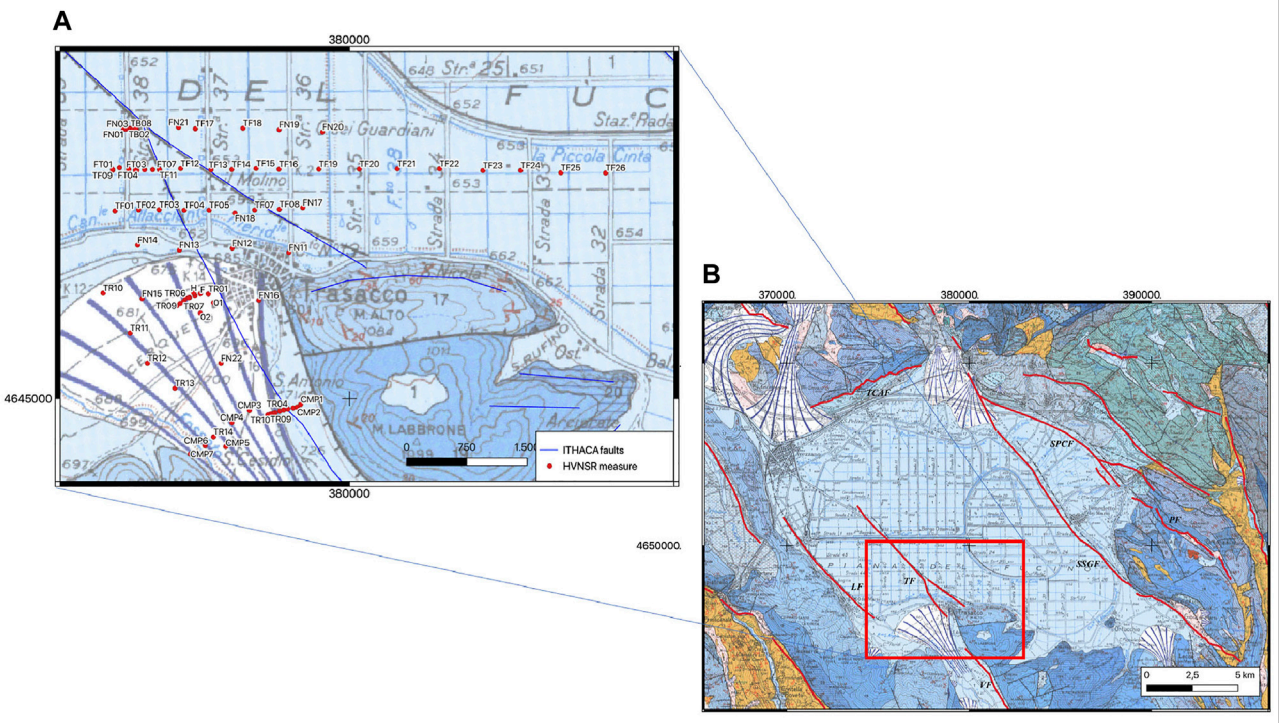

FIGURE 1
Geological map of the Fucino Basin (from Ghisetti and Vezzani, 1998) with the schema of the main fault lines in red **(B)**. Zoom of the study area with red dots representing the HVNSR investigations and fault lines in blue from the ITHACA database **(A)**.

how sediment loading/unloading influences the dynamics of fault systems, demonstrating positive feedback between sedimentation and faulting.

An important contribution for reconstructing the FB and understanding the role played by every structural element in its general evolution is given by the interpretation of industrial seismic reflection profiles [location by Patruno and Scisciani, (2021) displayed in Figure 2] which can identify the subsurface geometry of outcropping faults and also image the subsoil layers and their thickness.

For some authors, most of the thickness of the fluvio-lacustrine succession (more than 800 m) (Cavinato et al., 2002; Patacca et al., 2008; Cara et al., 2011) is generated by the San Benedetto–Serrone–Gioia dei Marsi fault (hereinafter SSGF) system, located in the eastern margin of the FB. Some others (Patruno and Scisciani 2021), conversely, acknowledged the maximum thickness of the Quaternary deposits (~1,750 m) in two depocentral areas, for the combined activity of the TCAF and San Benedetto–Serrone–Gioia dei Marsi Fault (SSGF).

In addition to the contribution of seismic lines, some authors (Cella et al., 2021; Mancinelli et al., 2021) recently performed studies on the magnetic anomalies of the FB. Cella et al. (2021) not only carried out a 3D gravity model for evaluating the depth of the Meso-Cenozoic carbonate bedrock but also provided additional constraints on the position of the known hidden faults. Both the aforementioned research works discuss the paleogeographic and paleotectonic evolutions of the FB confirming the presence of a major depocenter as the effect of the activity of the SSGF in the eastern part of the FB, and a second depocenter whose evolution is ascribable to the activity of the Trasacco fault, on its western side.

Mancinelli et al. (2021) reconstructed 2D gravity models along a grid of seven sections crossing the basin, in which is shown the influence of the Miocene flysch deposits in the observed residual general anomaly present in the FB. They also highlighted the thickness of Miocene deposits, as modeled in the sections. A higher thickness of flysch deposits (around 1,100 m) is found in the western part of the basin, consistent with a syn-orogenic emplacement of the deposits, and decreases toward the south and east.

Concerning the shallower part of the subsoil, paleo-seismological studies in FB started during the ‘80s (Giraudi 1986; Serva et al., 1986; Giraudi 1988; Galadini and Galli 1996; Michetti et al., 1996; Galadini et al., 1997; Galadini et al., 1997), and a collection of all the results is summarized in Galadini and Galli (1999). Amoroso et al. (2016) also presented a synoptic review of all the paleoseismic data collected for the FB, including information related to the slip

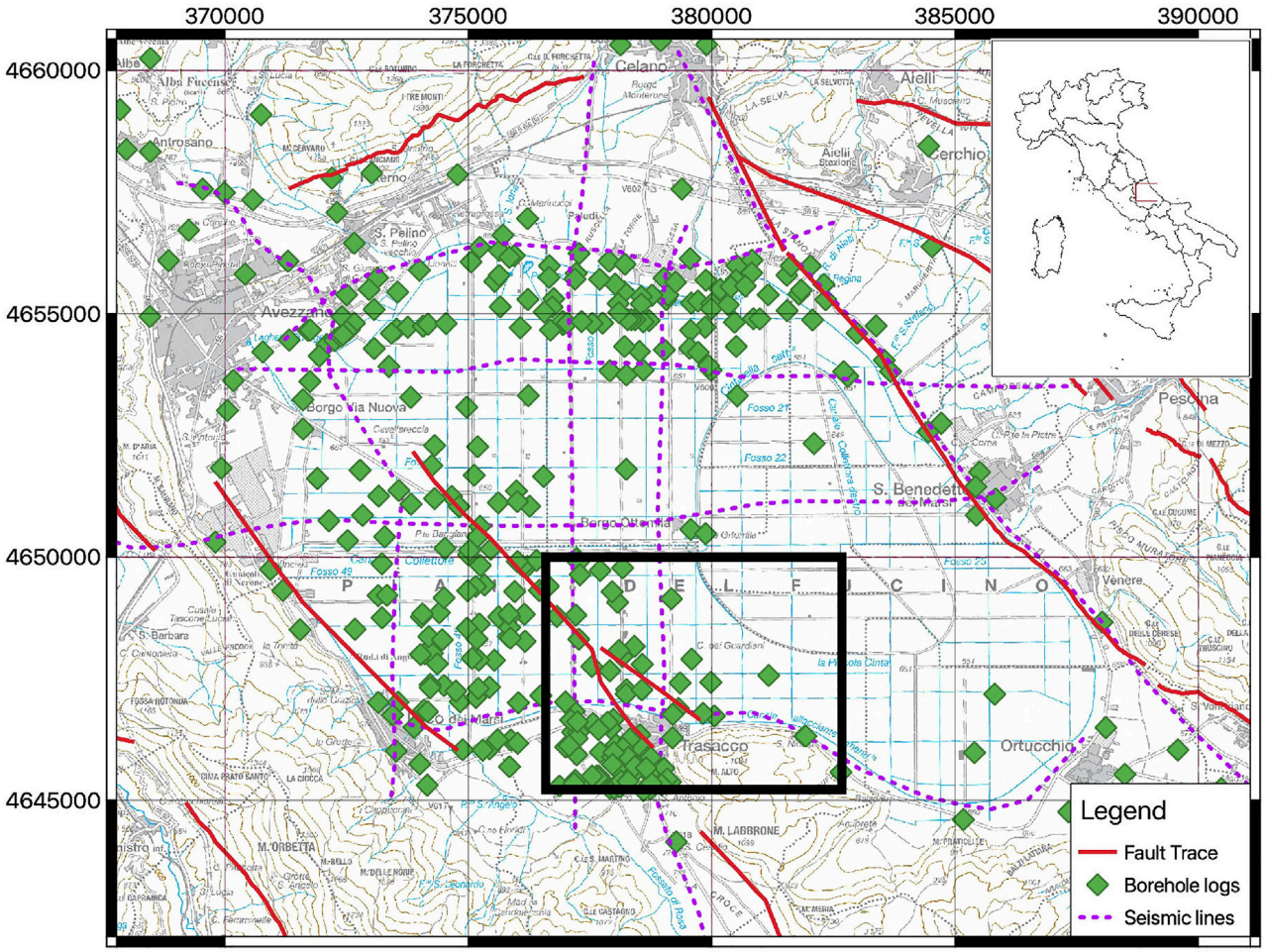

FIGURE 2
Map of previous investigations: the fault lines from the ITHACA database are in red, and boreholes from ISPRA and Ente Fucino are in green. The study area is delimited by a black box.

rates of all the tectonic structures, deriving a possible overall extension rate across the basin of about 3–3.5 mm/yr.

The study area of this work is located in the Trasacco municipality, going from the urban area toward the central part of the basin. The target area is interesting due to the presence of alluvial fans in the urbanized area and of buried faults in the most rural area. Although there is no evidence of fault scarps in this area, aerial photos show a straight NW-SE-oriented lineament (Oddone 1915; Galadini and Galli 1999) which represents the contact between soils with different lithologies. This feature addressed the excavation of a huge number of hand boreholes to precisely locate the fault in the field. Paleo-seismological trenches were performed in the area by Galli et al. (2012); Galadini and Galli, (1996), together with many boreholes and trenches, studied the Trasacco fault and reconstructed the vertical displacement along its length and associated them to specific historical seismic events. Results of their study highlighted the multiple activation of this fault during the Holocene: the most recent event is related to the 1915 Fucino earthquake and the previous one is dated to fifth–sixth A.D. The slip rate of the fault obtained from available data decreases toward its NW edge, reflecting the trend of its offsets toward the center of the basin.

Methods

Data

The single-station noise measurements were performed by using two different seismic stations: the Reftek-130 and Lennartz MarsLite digitizers modified by SARA electronic instruments connected to Lennartz 3D/5s velocimetric sensors and Terrabot (SARA electronic instruments) units, and all-in-one 24-bit

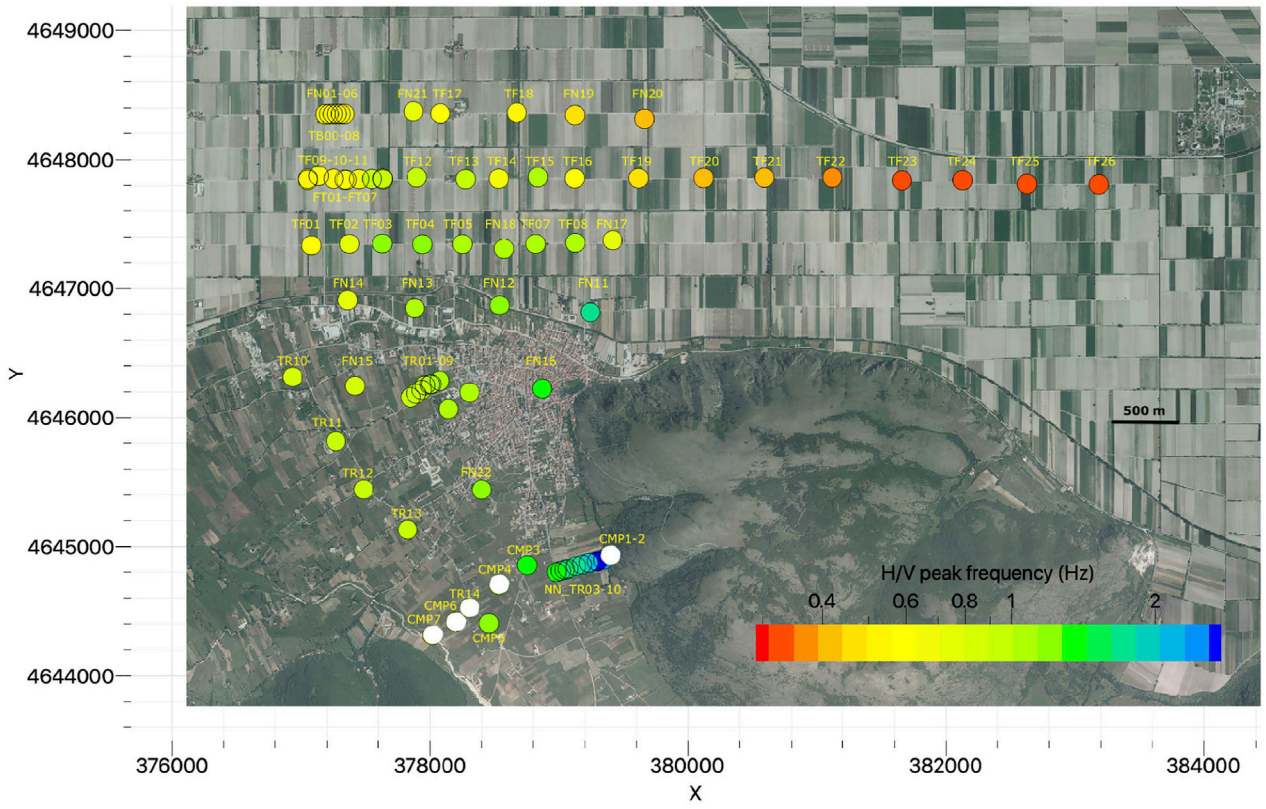

FIGURE 3
F0 map with the location of the HVNSR measurements (results in Supplementary Appendix S1). The color band represents the f0 value of each point of measure. White circles represent measures with no resonance peak or with bad quality data.

digitizers with internal 4.5 Hz sensors. For all the stations, time synchronization was ensured by GPS antennas.

Overall, the survey consisted of 88 noise measurements performed in different time periods (zoom in Figure 2), of which 12 have been visually inspected to evaluate the quality of data, by the analysis of the Fourier spectra. For some sites with bad quality data, we have repeated the measurement in different time periods (eg., TB** and FN** measures located along Section 1 in Figure 3, zoomed location in Figure 11). The minimum length of recording was fixed at 90 min, in order to allow a good statistic of the results in the frequency domain of interest. The sampling rate was set to 200 or 250 sps. Some sets of measurements were collected simultaneously.

The positions of the measurement points were chosen with the aim to obliquely cross the hypothetical surface projection of the Trasacco faults (Apennine trend of the tectonic structures), as evidenced from the seismic lines' interpretation.

Overall, the final geometry of the survey can be seen as a set of transects trying to cross orthogonally to the supposed fault line. Actually, the survey covered the entire study area but with an irregular density and with special attention to the basin area in the north of Trasacco where buried fault structures were suggested by previous studies. In fact, whenever a set of measurements ended, the following measurements were performed trying to refine the previous results. For this reason, the distance between stations of each transect was largely variable, ranging from 30 to 500 m.

One of the transects (corresponding to Section 2 in Figure 3) is 6 km long and largely exceeds the Trasacco area. The aim of this measurement line was to investigate and understand the general trend of the main impedance contrasts in the FB at a wider scale.

HVNSR analyses

Single-station noise data were analyzed using Geopsy software (Wathelet et al., 2020) in terms of HVNSR curves (Nakamura, 1989). The analysis was also computed by rotating the horizontal components from 0 to 180° in steps of 10. The complete steps of analysis, developed within the SESAME project (Site Effects Using Ambient Excitations, SESAME 2004), consist of:

1) Applying an anti-trigger algorithm that selects 40s-long windows into the whole three-component recordings, in order to avoid short or anomalous transients often of anthropic origins. The chosen length of the windows, 40s, guaranteed a good frequency sampling according to the targets of the study;
2) removing mean and linear trends from each time window;
3) tapering the edges of the time windows;
4) rotating the horizontal components of the desired angle;
5) computing the Fourier spectra of the three components;
6) smoothing the Fourier spectra using the logarithmic Konno–Ohmachi algorithm (Konno and Ohmachi, 1998), with the bandwidth coefficient b equal to 40;
7) by visual inspection, identifying regular trends on the Fourier spectra and discarding windows affected by possible anthropic disturbances;
8) dividing the rotated horizontal spectra by the vertical spectrum for the selected windows;
9) geometrically averaging the spectra or the HVNSR obtained for each 40s-long window.

The classical computation of HVNSR does not imply the directional analysis. In this case, the two horizontal components are NS (0°) and EW (90°), and after points e) and f), the two horizontal spectra are simply merged using an arithmetic mean, in order to have a unique horizontal spectrum for each 40s-long window.

Results of the directional analysis of HVNSR are often shown in an image map, with frequency as x-axis, angle of rotation as y-axis, and the color of the map that is representative of the amplitude of HVNSR for each frequency/angle pair. Nevertheless, the same results can also be shown by plotting the rotated HVNSR curves all together. This kind of representation is useful to prove any possible anisotropy of the wavefield. The classical post-processing of HVNSR (considering only the merged NS and EW components) consists of looking at the shape of each curve and retrieving the main peak, also called the fundamental or resonance frequency (f0) of the selected site. This step is not always trivial. Sometimes, the peak is unique, very narrow, and with an amplitude greater than 2. Therefore, the resonance peak can be recognized easily. On the contrary, there are several peaks very often, or the main peak is very broad and/or weak. In these cases, the user experience on the interpretation of the results is really crucial because it requires a general overview of both the geological setting and the HVNSR curves on the surrounding area of the selected measurement point. Hence, we were able to associate a resonance frequency value for all stations, except for some flat HVNSR curves (Supplementary Appendix S1). The frequency peaks are selected between 0.2 and 4 Hz, discarding higher frequency values because they were considered irrelevant for the scope of this work.

A way of representing the results obtained by the HVNSR technique is to plot the resonance frequencies in a map (Figure 3) and interpolate them (Figure 4) to produce a contour plot (ISPRA, 1881; ITHACA Working Group, 2019; Mascandola et al., 2019). An inverse distance weighting (IDW) method, for e.g., a deterministic spatial interpolation model, was applied to interpolate f0 data in the map. The general premise of this method is that the attribute values of any given pair of points are related to each other, but their similarity is inversely proportional to the distance between the two locations (Lu and Wong, 2008).

Another way of visualizing information from HVNSR results is to consider the entire curves, not the resonance frequency alone. For each transect, we produced an image map interpolating the HVNSR curves along the distance (Figures 5, 6). The linear regression method was applied to data to find the best fitting line to plot, and then spatial coordinates (in meters) were projected on it. This kind of plot is helpful to imagine subsoil heterogeneities (Joyner et al., 1981; Famiani et al., 2020): the amplitude of spectral ratio curves is represented in a colored scale, while the XY axis shows the distance of the single noise measurement with respect to the beginning of the transect and the frequency values of HVNSR, respectively.

Velocity profile estimation

Many of the noise measurements were collected in synchronous acquisition. Hence, the simultaneous recordings acted as a passive array of seismic stations, located in 1D (lines along transects) or 2D (when positioned in grids or irregular geometries) configurations. These kinds of data can then be used to retrieve the dispersion characteristics of the noise wavefield crossing the stations and finally estimating a velocity profile for the shallower layers of the area. Unfortunately, among all the possible simultaneous sets of stations, only the ones including stations from TB00 to TB08 (western part of Section 1 in Figure 11) gave reliable results.

To compute the dispersion curve from the noise data, we first calculated the cross-correlation (CC) functions between the vertical components of station pairs. The synchronized recordings of vertical components were first processed using the one-bit normalization and the spectral whitening (Bensen et al., 2007). Then, the CC functions were computed for each station pair. To compute the dispersion curve of the seismic signals emerging from the CC functions, we applied a velocity analysis to them. The method is similar to the constant velocity stack (CVS) analysis (Yilmaz, 1987; Yamanaka et al., 1994), which is very popular in active seismic reflection processing and has already been used on CC results for different Italian areas (Vassallo et al., 2019; Di Giulio et al., 2020). The CC functions were filtered in different frequency bands starting from 0.5 to 20 Hz. For each frequency band, the CC functions were shifted

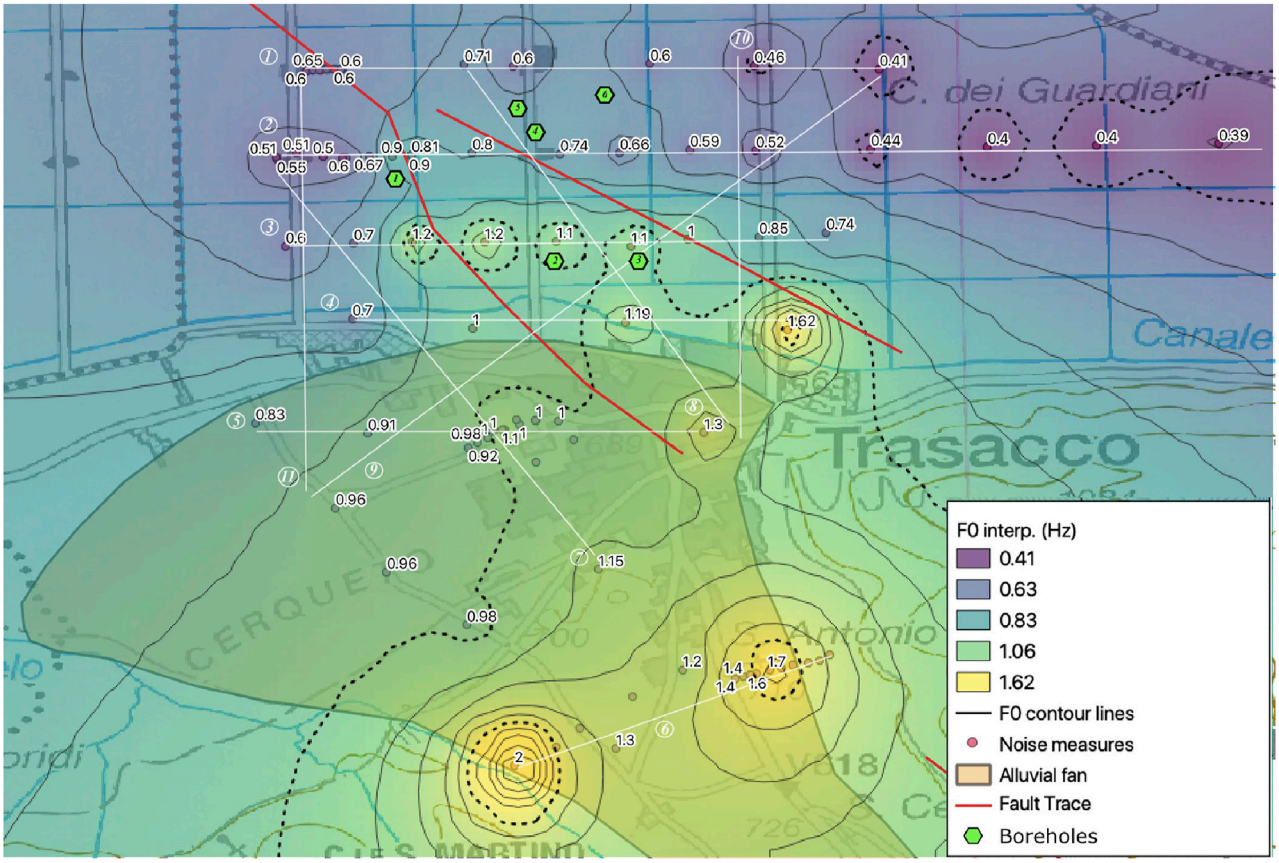

FIGURE 4
Map of f0 interpolation. Red dots represent the noise measurements with the f0 value reported. The fault lines in red come from the ITHACA database. Green diamonds represent the boreholes considered for 1D modeling (Figure 8).

back in time according to the theoretical surface travel times computed for different constant velocities starting from 50 m/s until 900 m/s using a velocity step of 10 m/s. Then, the phase-weighted Stack (PWS, Schimmel and Paulssen, 1997) was computed, and the absolute maximum of the PWS stack was used to estimate the presence of a horizontally aligned phase in the corrected seismic section. For each filter, the maximum stack function provides the velocity of the surface waves at the considered frequency.

The dispersion curves obtained through CC functions and the velocity analysis were finally inverted in order to obtain a preliminary 1D velocity profile of the subsoil. To improve the inversion process, the HVNSR results have also been used as constraints. In particular, the inversion process has been imposed to fit as best as possible to the part of the HVNSR curve around the resonance peak. The computation of the velocity models has been performed using Geopsy software, in particular, the dinver tool (Wathelet 2008): this code adopts a Monte Carlo-like approach, the so-called neighborhood algorithm, to search for subsoil velocity models that fit the data.

The initial parameterization of the subsoil consisted in a four-layered model over a half-space for all the tested sites, for which the shallower layer is assumed to have a linear increasing Vs. However, in order to avoid strict constraints to the process, a wide variability of the parameterization in terms of thickness and Vs of the layers was allowed.

Results

HVNSR results

The average spectral ratio curves of all the sites are plotted in Supplementary Appendix S1.

It is worth noting that most of the HVNSR curves showing a single peak, multiple peaks, or flat shapes (CMP2, CMP4, and CMP5) occur in the frequency range of interest (0.2—4 Hz). This observation suggests the presence of a unique strong impedance contrast in the subsoil, likely ascribable to the geological interface between the lacustrine filling and the bedrock of the area (Meso-

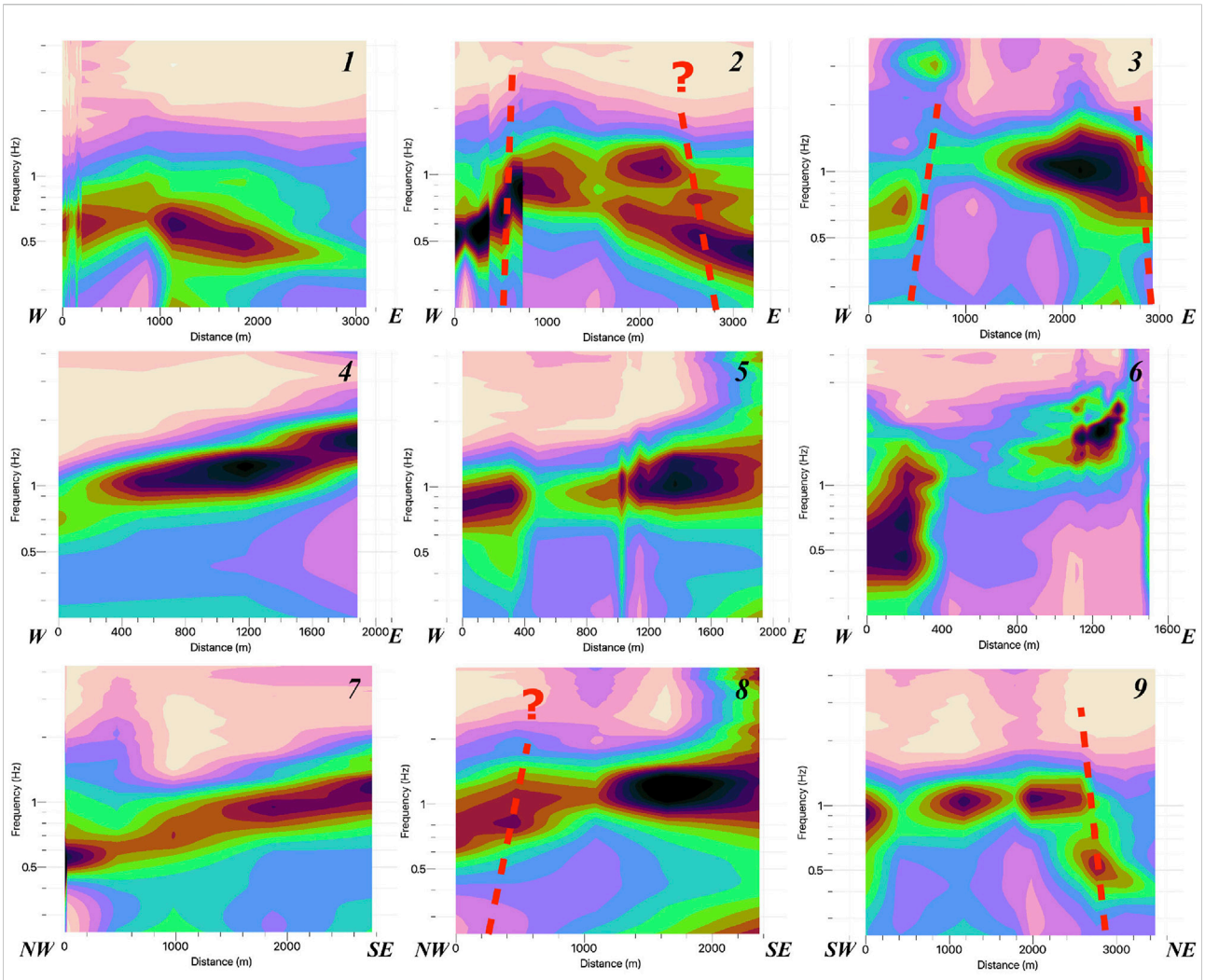

FIGURE 5
HVNSR contour plots of investigations organized along the transects. The plots correspond to sections 1–9 (see location in Figure 4).

Cenozoic carbonate and Neogene terrigenous successions). For the stations installed in correspondence to the deeper part of the basin (TF18, FN19, and FN20 in Section 1 and Figure 11 and from TF19 to TF26 in Section 2 and Figure 12), a second broad amplification peak after the fundamental one occurs.

Figures 3, 4 show the resonance frequency and the f0 value interpolation maps, respectively. The distribution of f0 follows a double trend: in the northern part of the maps (Sections 1, 2, and 3, location in Figure 4), there is a decrease of f0 moving toward north, whereas in the southern part (Sections 4, 5, and 6, location in Figure 4) the f0 values decrease toward NW. Contour plots of HVNSR curves along the sections are reported in Figure 5.

Sections from 1 to 6 are all W-E oriented and display HVNSR amplitude contouring from north to south of the study area. Assuming that the depth of the impedance contrast is linearly proportional to 1/f0, we can find a reasonable geologic interpretation of f0. Hence, we can state that sections 1, 2, and 3, representative of the basin part of the Trasacco municipal territory, show a regular decrease in f0, which means the deepening of the impedance contrast toward north and, at the same time, a trend that resembles a structural high feature in the central parts, especially in sections 2 and 3. Moving from the eastern part of Section 2, some HVNSR measurements were performed to follow the general E-W trend of the basin toward the eastern depocenter of the FB (Section 2b—Figure 7). A second broad resonance peak is displayed for the eastern part of this section, which could suggest the presence of a shallower impedance contrast unreachable by all the boreholes available in the area.

Section 4 represents a transition zone where there is a change in the f0 trend compared to sections 1, 2, and 3. In fact, it shows a

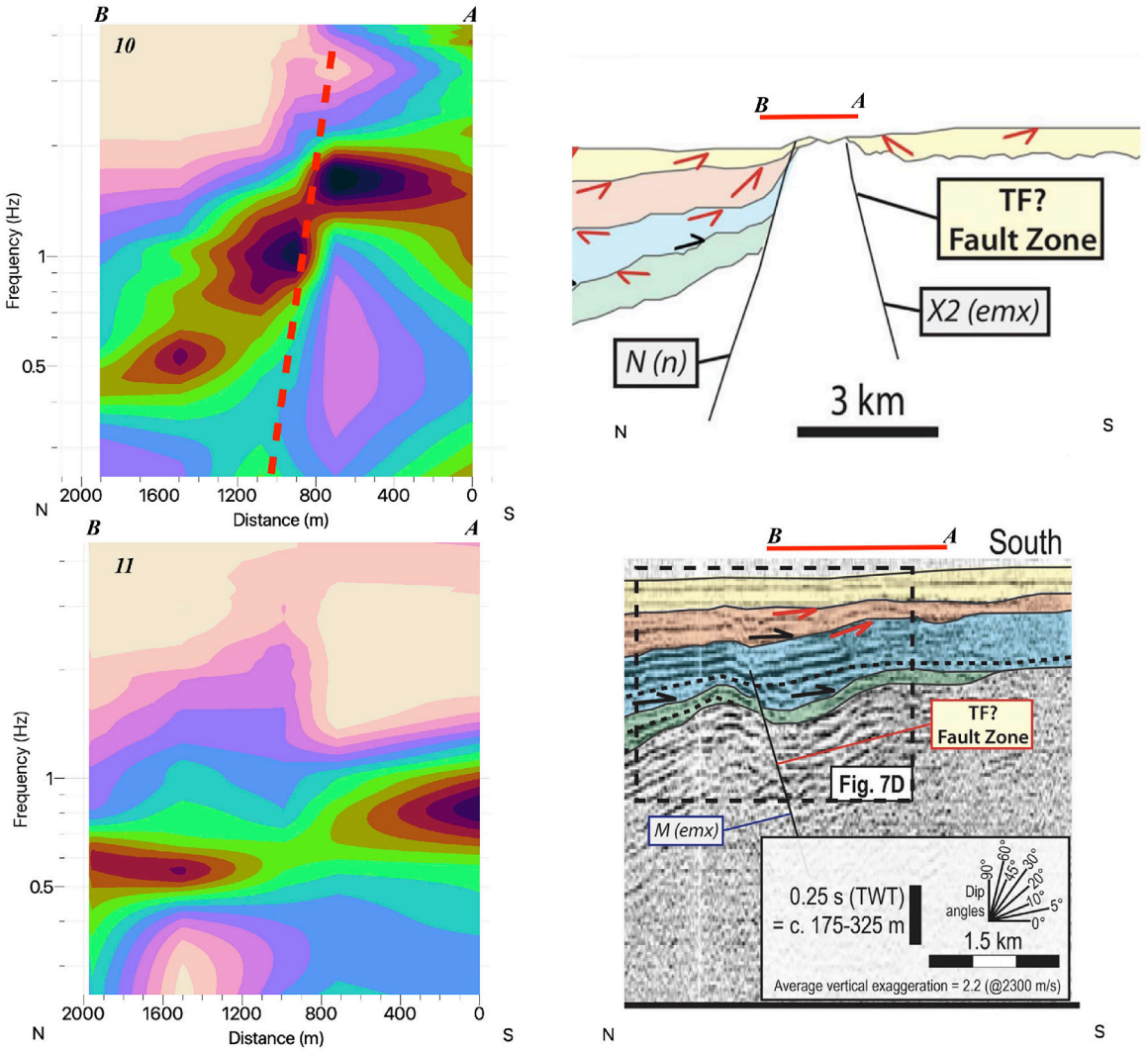

FIGURE 6
HVNSR contour plots of Section 10 and Section 11 located along seismic line 4 (top) and line 2 (bottom) interpreted in Patruno and Scisciani, (2021). The correspondence between the location of HVNSR contour-plot sections and the seismic line is reported with a red line and A and B extremes of the sections. A sketch of the hypothetical fault is also reported with a dotted red line.

more flat and continuous shape of the impedance contrast without any evidence of the structural high.

Sections 5–6 cross the alluvial fan, and the interpretation of the contouring of HVNSR is less straightforward because there is no information about the total thickness and shear-wave velocity of the alluvial fan deposits. When Section 5 shows, similar to Section 4, a continuous seismic interface, Section 6 reveals a typical valley shape, except for the low-frequency amplification for stations CMP6 and CMP7 located at the western border of the valley which might be due to 2D valley effects. Furthermore, in the eastern part of the section, the transect of ambient noise measurements (Figure 8) highlights a quick variation of f0 (from 2.5 to 1.5 Hz) in a very short distance (200 m) suggesting the presence of a quite abrupt interruption of the lateral continuity of the main impedance contrast. This behavior could be due to the presence of a normal fault which was reported by the ITHACA database (Figure 1A).

Taking into account that, from available geophysical investigations (multichannel analysis of surface waves) performed on the alluvial fan area (Palombelli, 2014), the average Vs for the shallow depths is around 500 m/s; we can say that the average depth of the Vallelonga valley is between 100 and 150 m. Another interesting observation is that the only three measurements which have a flat HVNSR shape (CMP2, CMP4, and CMP5) are in the central part of Section 6. They then have a similar response in terms of HVNSR as that of the rock

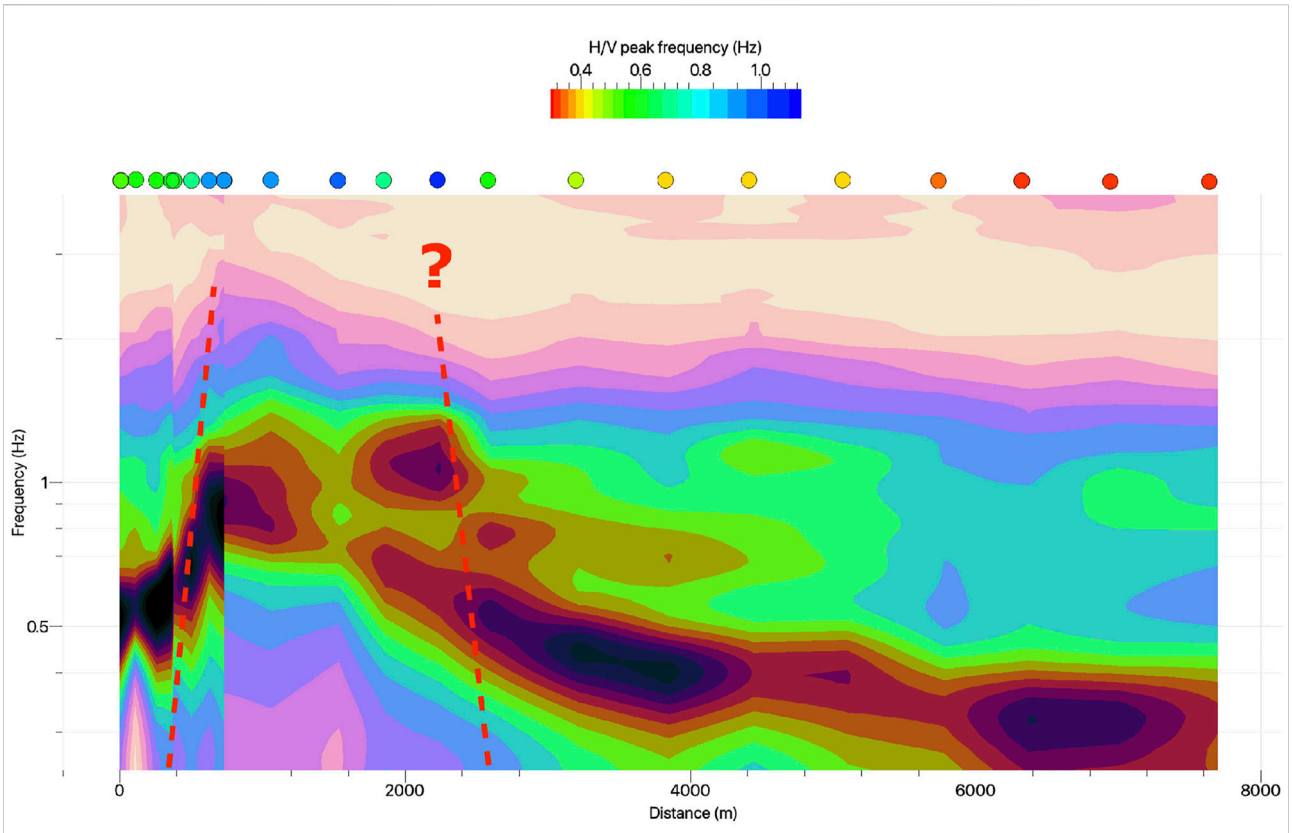

FIGURE 7
HVNSR section plot of Section 2b. The colored circles indicate the position of each ambient noise measurement along the section and their f0 value. A sketch of the hypothetical fault is reported with a dotted red line.

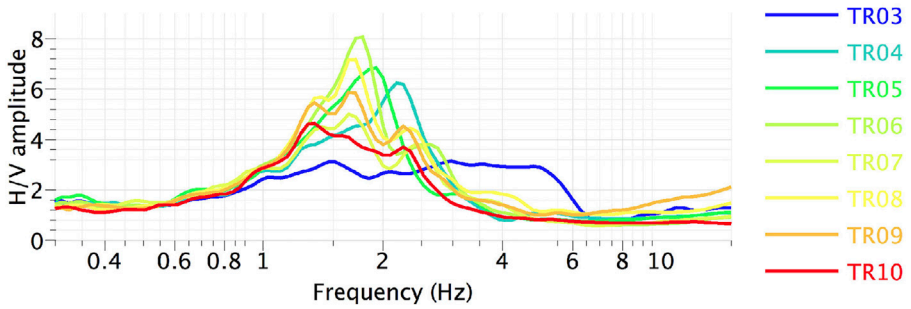

FIGURE 8
HVNSR curves of the eastern part of Section 6. The colors reported in the legend correspond to stations located from east (blue) to west (red) of the section, moving from the outcropping bedrock (almost a flat HVNSR average curve) toward the center of the valley (f0 from 2.5 to 1.5 Hz).

sites, suggesting that the presence of alluvial fans can result in deep layers with shear-wave velocities lower than the ones above them (e.g., velocity inversions). In these cases, the capability of the HVNSR technique to retrieve the real resonance frequency of the area is really poor, as also shown by Castellaro and Mulargia, (2009).

Sections 7–8 are both NW-SE oriented and located in the hanging-wall and foot-wall of the Trasacco fault, respectively. They show a similar trend of deepening toward the north but the presence of the structural high in Section 8 is reflected in higher f0 values in the north-western part of the section than Section 7. On the contrary, Section 9 is SW-NE oriented, crossing

perpendicularly the main fault structures as reported for the area in the ITHACA database. In this contour-plot is evident that there is a sudden deepening toward NE of the main seismic impedance contrast at around 2,800 m from the beginning of the section which corresponds to the noise measurement TF16 (see location in Figures 3, 4).

Sections 10 and 11 reported in Figure 6 (location in Figure 4) are drawn along two industrial seismic lines interpreted by Patruno and Scisciani, (2021); being particularly important, we postpone the comparison between the sections and the seismic lines afterward, in the Discussion section. However, both the sections are N-S oriented and focused on areas close to buried fault lines: in particular, Section 10 is N-S oriented, following toward the center of the basin in the eastern border of the Vallelonga valley (from FN16 to FN19 in Figure 3). A sudden decrease of the resonance frequency is reported between FN16 and FN11–FN12. Section 11 highlights a deeper seismic interface than Section 10, but ending, in its northern part, to similar frequency values.

1D subsoil models

In order to reconstruct some 1D subsoil velocity models and make inferences on the stratigraphic structure of the investigated area, we consulted public borehole log data, mostly drilled for hydrologic exploration, and few geognostic drillings made available by independent professionals. The basic level of seismic microzonation studies for the Trasacco municipality (www.webms.it) provided shallow geological and geotechnical data mainly located close to the urban area at the southern border of the FB. Other data consist of old stratigraphic logs coming from ISPRA (Italian Institute for Environmental Protection and Research) and "Ente Fucino", a local managing institution, for old wells drilled during the '50s, mainly consisting of stratigraphy of water wells.

We used them to fill the lack of geological information especially where no natural outcrops were available (e.g., in the urbanized area). Unfortunately, none of the available borehole logs reached the geologic bedrock in the Trasacco municipality and the only information that we took into account was the lithology and the thickness of the deposits, just to estimate qualitatively a reasonable average shear-wave velocity of the shallower fillings of the Vallelonga valley. The presence of a large alluvial fan inside the valley represents a big issue for the interpretation of our results. The noise measurements (TF17 and TF18 belonging to Section 1, FT06 and TF13 belonging to Section 2, and TF05 and FT18 on Section 3) that are close to boreholes (green diamonds in Figure 4) with stratigraphic information (Figure 9 left) were selected to make 1D preliminary models of the subsoil with the dinver tool of Geopsy. For the area where the points are located, the availability of the borehole logs, although the description of the stratigraphic log is not very detailed (some of them were old water wells), allowed us to conclude that the sedimentation conditions are relatively simple. In fact, the shallow layer consists in strata of fine-grained sediments sometimes inter-layered by a gravelly layer (see Figure 9 for details), finally overlying a gray-clay layer. None of these boreholes reaches the depth of the geologic bedrock.

The parameterization of the input subsoil starting model was designed according to the available stratigraphic logs.

The Vs models (Figure 9) obtained by joint-inverting the empirical HVNSR and the dispersion curve obtained through the cross-correlation technique (Figure 10) give an idea of the main impedance contrasts for the area. During the joint inversion, the HVNSR curve was assumed as the ellipticity of the fundamental mode of the Rayleigh wave. The inversion is able to reproduce the main features of the field curves even if in some cases the frequency trough present in the HVNSR curve is not found (e.g., for TF05 and FN18). Due to the simplified approximations of our inversion on the target curves, the 1D velocity results can be considered rough models with an increasing uncertainty at larger depths. However, we observe two main velocity contrasts in the profiles obtained from the inversion (Figure 9): the first one is found at a depth between 40 and 70 m and the second one at a depth between 200 and 520 m. From these preliminary models, we can summarize the results as follows:

1) TF05, FN18, and TF13 sites seem to be located on a structural high with a main impedance contrast located less than 250 m below the ground surface;
2) TF17 and TF18 are in an intermediate setting, with the depth of the main interface being between 280 and 300 m;
3) FT06 is outside the structural high, with a deep interface at 500 m.

Directional analysis of HVNSR

The directional analysis of HVNSR can highlight the possible 2D or 3D effects in the site response of some noise measurements. We explored specific features of these analyses trying to correlate them with other geological and geophysical information, retrieved from other studies. In particular, we focused on the points closer to the uncertain tectonic elements of the investigated area: the surface fault lines identified from the satellite imagery (ITHACA database) and the buried fault segments hypothesized by the interpretation of the seismic lines (Cavinato et al., 2002; Patacca et al., 2008; Patruno and Scisciani, 2021). The latter was useful to have an idea of the main seismic interfaces present in the area including fault lines and their mutual relations.

Directional HVNSR was computed for sites located along sections 1, 2, and 3 (Figure 4), and the results are plotted in Figures 11–13.

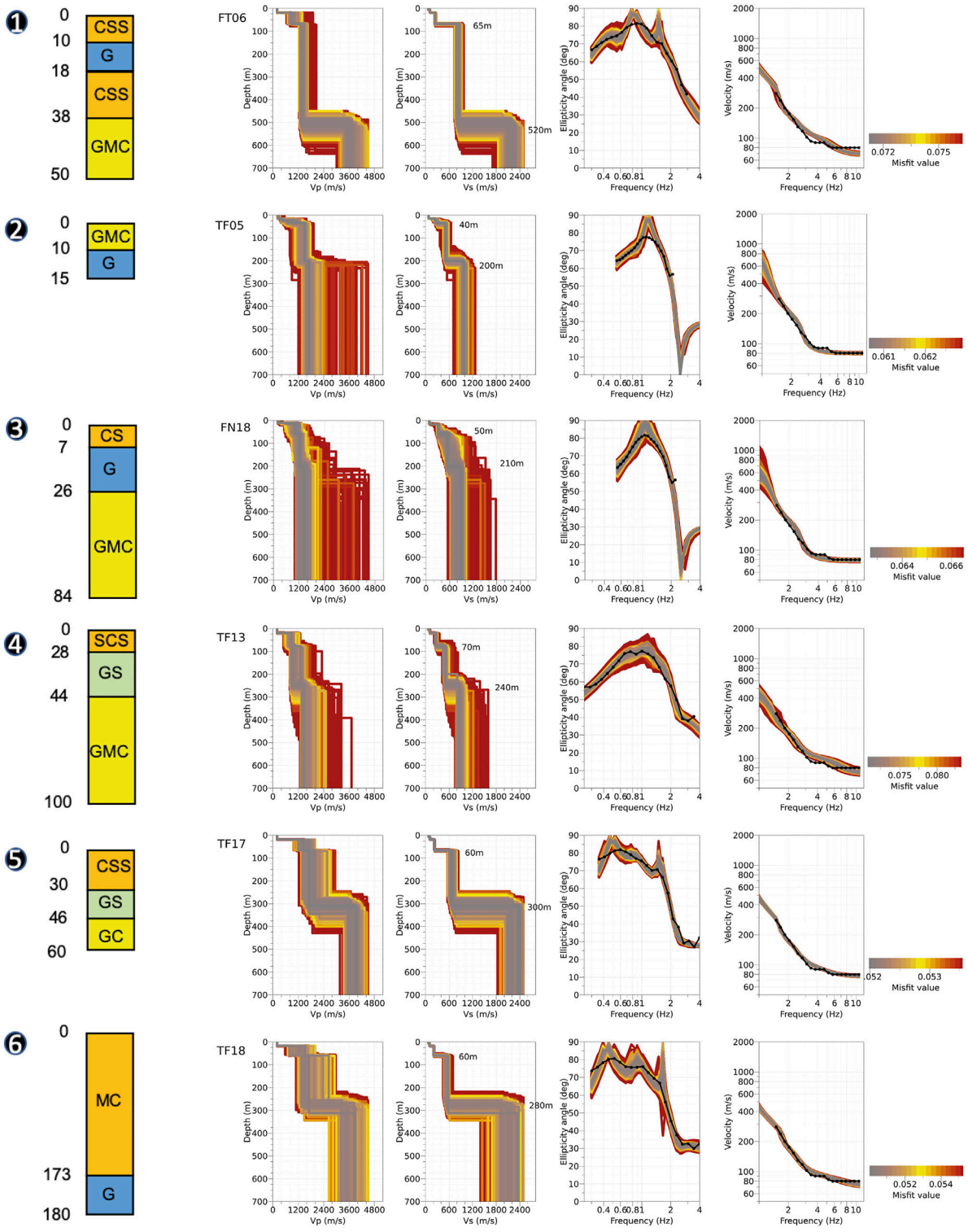

FIGURE 9
1D models (Vp and Vs on the left) for six representative sites selected in the study area (see location in Figure 4). The target curves of the joint inversion (HVNSR considered Rayleigh-wave ellipticity and dispersion curves) are shown in black. The color scale is proportional to the misfit between experimental and theoretical curves. On the left, the borehole logs available are used to set the shallow part of the initial subsoil structure for 1D models. Legend of borehole logs: C, MC, and GMC—clay deposits; CSS, SCS, and CS—sand deposits; GS and G—gravel deposits.

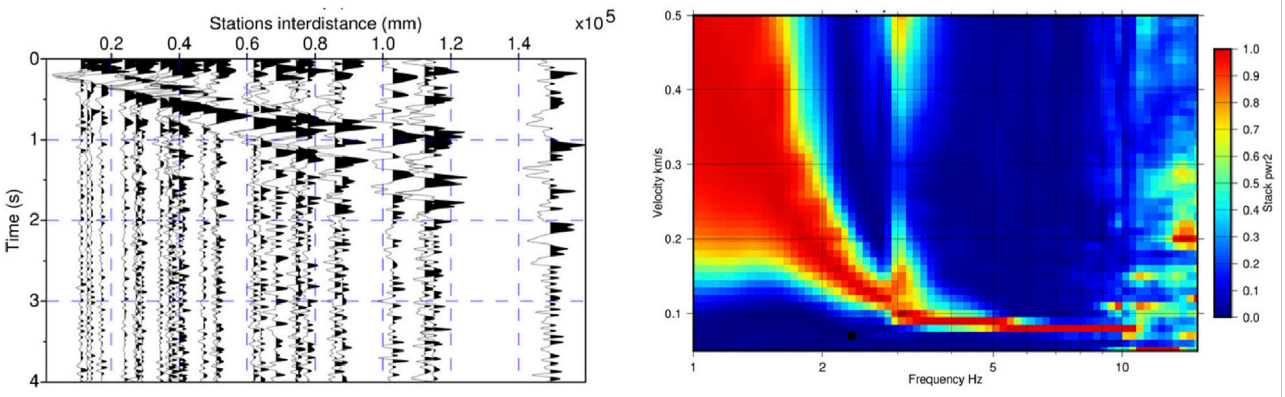

FIGURE 10
Cross-correlation of the ambient noise of synchronous HVNSR measurements in the northern part of the Trasacco area (Section 1).

For Section 3 (results in Figure 11 Figure 12 Figure 13), we observe a marked azimuthal dependence of the resonance frequency; moving from 80 to 170°, we notice a change in the f0 value from 0.85 to 1.2 Hz, respectively, for site TF08. A similar behavior is observed for stations FT06 and FT07 for Section 2 (results in Figure 12); moreover, in this case, the stations between TF12 and TF15 show a second peak close to the fundamental one not justifiable with abrupt changes of the stratigraphy.

For Section 1 (results in Figure 11 Figure 12 Figure 13), the directional analysis pointed out a clear azimuthal variation of HVNSR, for FN05 and TB04 stations, close to the Trasacco fault branch. In terms of HVNSR amplitudes, we observe at all the mentioned sites, minimum values around f0 for the azimuth parallel to the strike of the nearby fault. This is a feature also observed by Matsushima et al. (2014). Concerning the frequency of the HVNSR peaks, the results of Section 3 seem to be the clearer to interpret. In particular, the TF05 site, which is located on the structural high, shows a directional HVNSR revealed by the shift of the f0 peak from 1 Hz and the azimuth perpendicular to the strike of the fault (NW-SE direction), to the f0 peak of 1.3 Hz and the azimuth parallel to the strike of the fault. The TF08 results, conversely, highlight the opposite condition: the f0 peak value moving from values of 0.8 to 1 Hz for the azimuth parallel and perpendicular to the fault strike, respectively.

Discussion and conclusion

The detection of subsoil geological structures is a common goal for many geoscience disciplines. It is in general faced by integrating results coming from different geophysical techniques. The HVNSR technique is particularly effective for the estimations of the resonance frequencies of a given site and, by using independent information, for the estimations of the thickness or the average shear-wave velocity of the surface layers below the measurement point. It works well in simple geological settings, such as the sedimentary contexts, with horizontal and parallel low-velocity layers over a stiff seismic bedrock. The FB, of Quaternary age, only partially fulfills this geological simplicity, being interested by several faults, not all exactly known, that interrupt the homogeneity of the geological strata. Also, the presence of alluvial fans in large parts of the basin is a big issue for the right interpretation of HVNSR curves. In this work, we collected all the previous geological and geophysical information about the Trasacco area. This information not only drove the choice of the dense single-station noise survey but also helped in the interpretation of the HVNSR results. The starting motivation of this survey was to have an idea of the local structure of the continental basin but also to estimate the depth of the calcareous or siliciclastic bedrock. However, we were aware that the FB has a quite complex geologic setting: it has plenty of reverse and normal faults which, during their past activation, caused a relevant displacement of the geological layers and the interruption of their lateral continuity.

Nevertheless, we believe that the results of our noise survey added useful information for the subsoil reconstruction of the FB, shedding some lights on this complex topic, especially for the presence of buried structures in the basin area. The interpolation map of f0 allowed us to observe a double trend of the main impedance contrast of the subsoil. When the northern part of the study area shows a lowering of f0 values toward north (center of the basin), the f0 isolines (Figure 4) in the southern part show a slight change in the trend of the main impedance contrast which now dips toward NW; this variation can be explained by the co-presence of the Trasacco alluvial fan and the Vallelonga valley which could both locally influence the seismic response. Regarding the identity of the impedance contrast responsible for the fundamental resonance peak, we believe that it does not correspond to the top of calcareous rocks but to siliciclastic deposits, supported also by the high thickness values of flysch deposits reconstructed for the study area by Mancinelli et al. (2021).

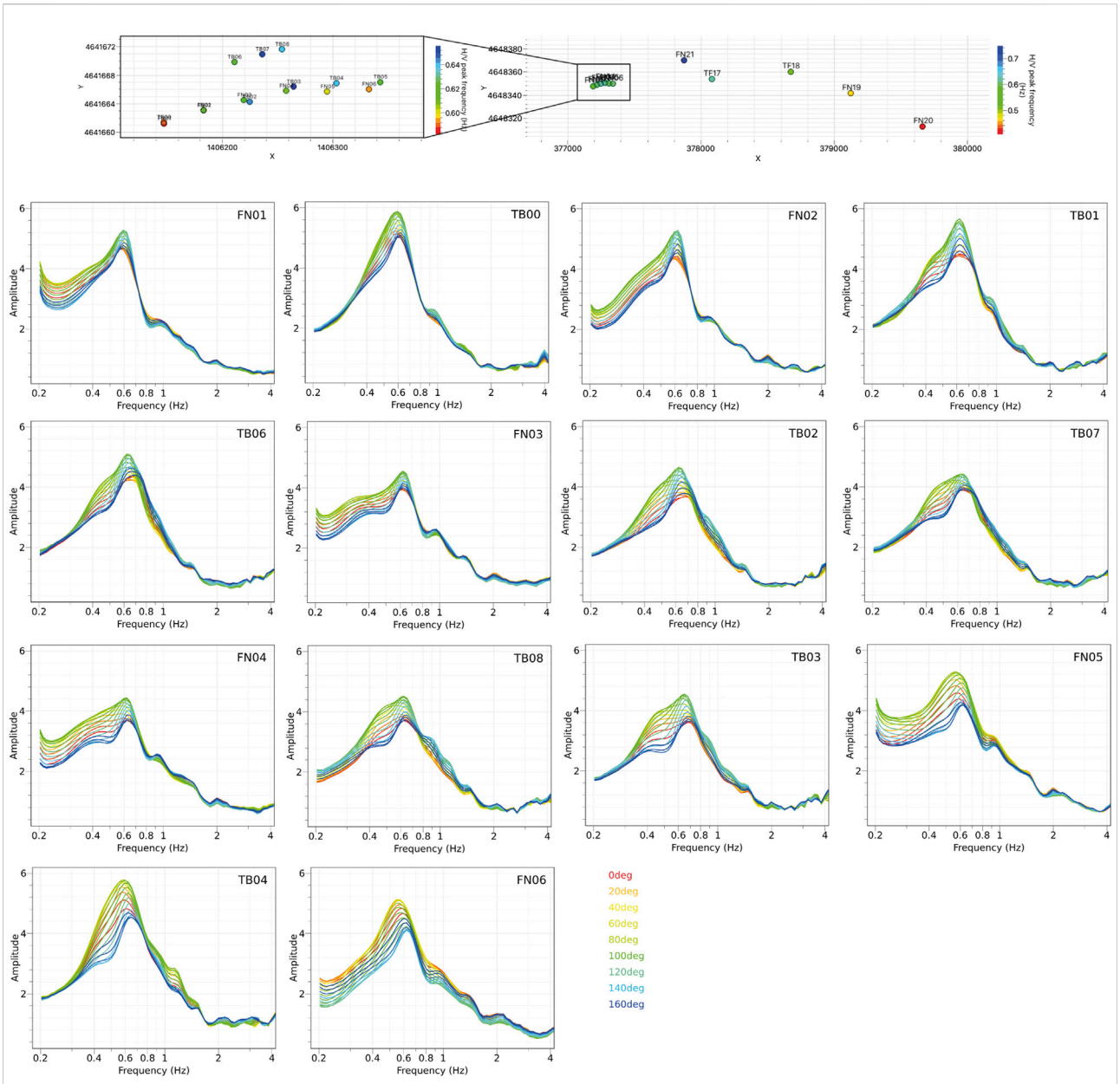

FIGURE 11
Directional HVNSR of Section 1.

Organizing the measurements in regular linear geometries has allowed the comparisons with the interpreted seismic lines already available in the FB. Despite a partial disagreement between the authors (Cavinato et al., 2002; Patacca et al., 2008; Patruno and Scisciani 2021) on the interpretation of some parts of the commercial seismic lines available in FB, the HVNSR curves interpolated along the sections (Figure 6) revealed similar results to what were provided by seismic reflection lines for depths compatible with the resonance frequency of the area.

The extension of the surveys to the scale of the municipality gave the chance to promptly reveal the presence of abrupt subsoil lateral heterogeneities as the presence of fault lines. This is easily proved following the f0 isolines from the map of f0 interpolation (Figure 4), and checking the trend of the HVNSR curves along the transects. Moreover, the strong azimuthal variation of HVNSR for the sites close to the tectonic elements supports their real presence where they are expected to be, as highlighted by Matsushima et al. (2014). A common feature for the HVNSR directional results is that, for sites close to tectonic structures, the

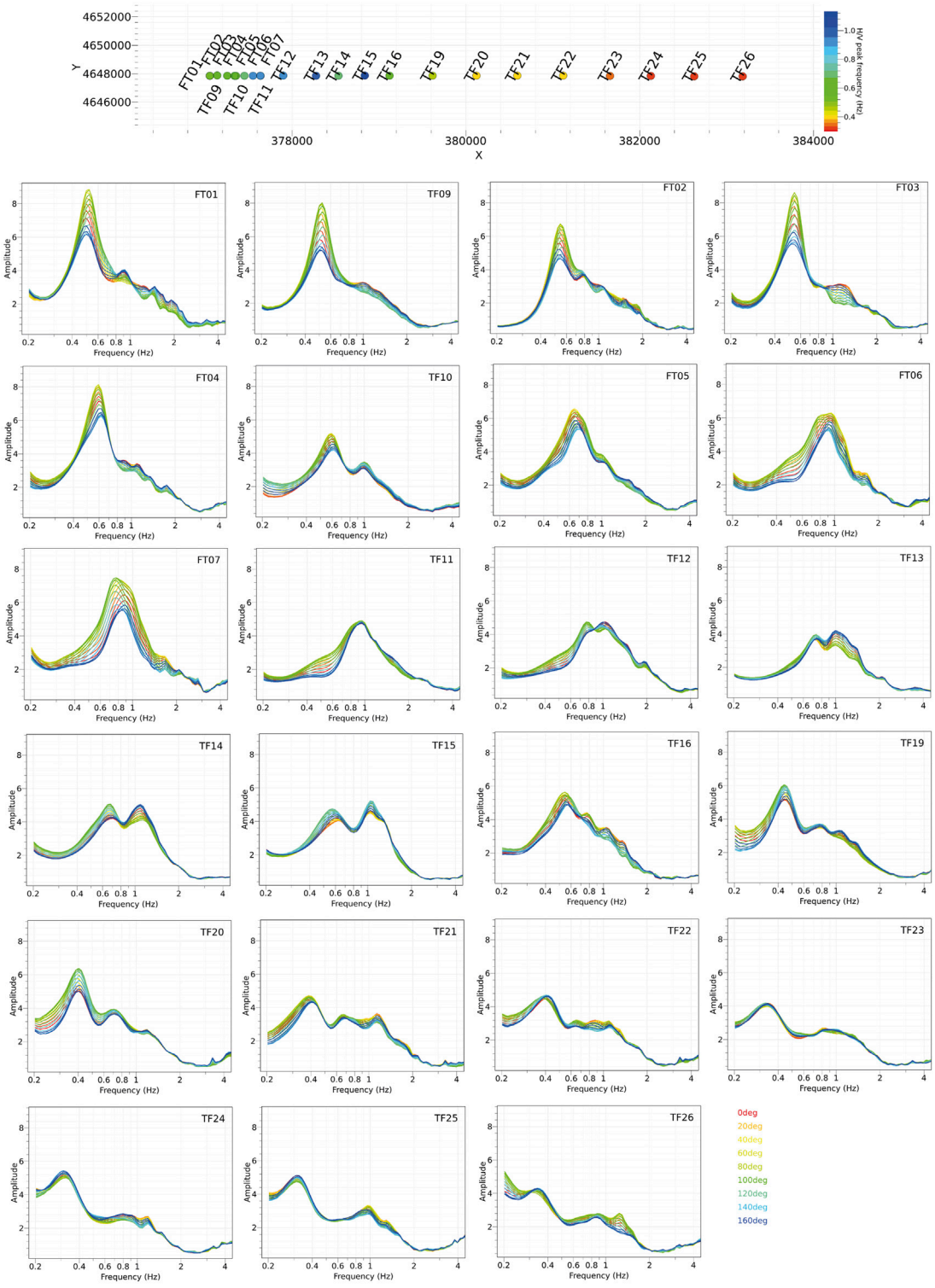

FIGURE 12
Directional HVNSR of Section 2.

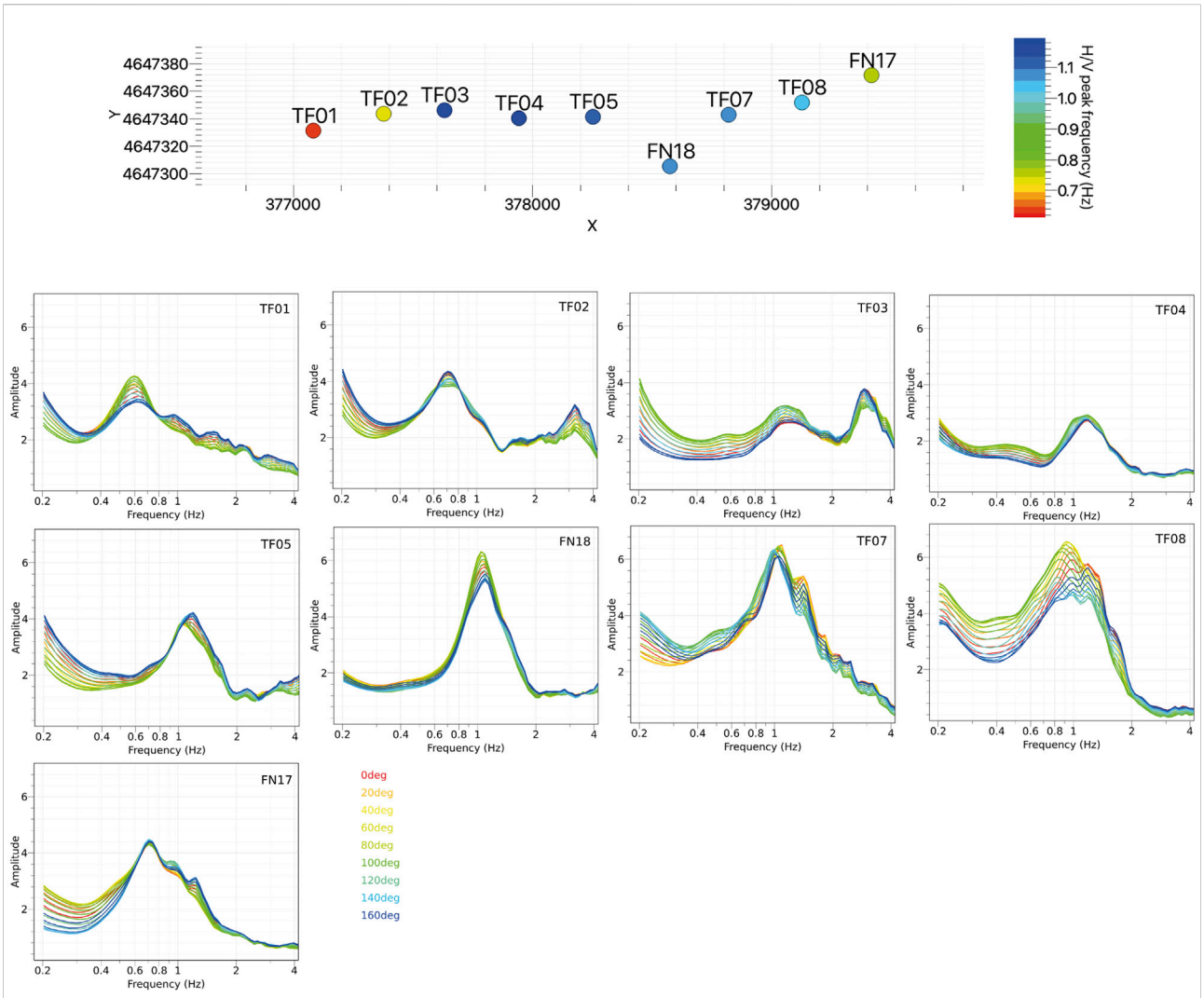

FIGURE 13
Directional HVNSR of Section 3.

spectral ratio curves display minimum amplitude around the f0 for the azimuth almost parallel to the strike of the fault. This seems to prove that the presence of lateral subsoil heterogeneities strongly influences the noise wavefield. This statement becomes more difficult to justify for TF12–TF13–TF14–TF15 sites (Section 2), where the amplitude values change for azimuth for the two HVNSR peaks which seem to be uncorrelated to the strike of the fault, maybe for a combined effect with other subsoil structures unknown so far. Concerning the azimuthal dependence of f0 peak values, while Section 1 does not show important f0 variations close to the Trasacco fault, and Section 2 is complex to interpret because of the disagreement in the structural reconstruction from commercial seismic lines which raise uncertainties in the existence and location of possible fault segments, Section 3 (HVNSR contour-plot in Figure 5 and directional HVNSR in Figure 13) leads itself to comment on that topic because its subsoil structure can be reasonably interpreted as a 2D structure. As discussed in the Results section, directional HVNSR curves for TF05 and TF08 sites (see location in Figure 3), among others, show a slight variation of the peak frequency related to the azimuth of computation. TF05, which we assume to be located on a structural high respect to the TF08 site (see Figure 9 for the numerical 1D simulation and comments in the related section), has an HVNSR curve with a lower f0 value (1 Hz) for the azimuth perpendicular to the fault strike and, conversely reaching a maximum of 1.3 Hz for the azimuth parallel to the fault. TF08 shows azimuthal dependence but with an opposite behavior in terms of f0 values changing from 0.8 to 1 Hz from azimuth parallel to perpendicular, respectively. We

propose the following: these sites can be affected by the proximity of a lateral variation in terms of frequency of the resonant layer; this means that the trend of subsoil geometries for the area drives the energy of the noise wavefield. To demonstrate directional effects on HVNSR measurements, Matsushima et al. (2014) showed that performing numerical modeling in these cases can help understand the contribution of 1D versus 2D and 3D structures on the wavefield and, therefore, on the HVNSR curves.

Many of the noise measurements were recorded simultaneously, and gave us the opportunity to use these data to estimate the dispersion characteristics of the noise wavefield in the 1.5–10 Hz frequency range. Finally, the dispersion curve obtained using both the cross-correlation and constant velocity stack (CVS) analyses was inverted to retrieve a reliable velocity profile for the shallower layers of the western edge of Section 1. Moreover, the dispersion curve (Figure 9, right) was used, together with the HVNSR curves, as a constraint for the calculation of 1D velocity models (Figure 9) for some test sites located close to boreholes where the stratigraphy was pretty well known. Of course, this inversion process assumed that the dispersion curve obtained for the western part of Section 1 is representative of the shallow velocities of the subsoil for the entire area. We believe that this assumption is fairly realistic because it is supported by the stratigraphic logs available for the area which reflect the general homogeneity of the lithologies representative of the subsoil. However, we assigned variable depth and thickness for all the layers included the inversion process as free parameters to avoid over-constraining of the initial model. The results of these inversions in terms of velocity profiles show a variability of the depth of the main geological interface.

Finally, taking into account all the limitations of the HVNSR technique, our study has demonstrated that if this method is used as a preliminary investigation tool to identify and locate the hypothetical hidden heterogeneity, it can give some important contributions for seismic risk assessment studies, with the advantage of being an easy application and cheap when compared with other geophysical techniques. Remarkably, the HVNSR technique can give significant advancements on the geometrical reconstruction and the geological evolution of an area similar to the FB, for which extensional quaternary tectonics played an important role for its general setting. The results of this study highlight the presence of a structural high hidden by Quaternary deposits in the northern part of the Trasacco territory within the basin area. Its shape was very well constrained by the dense mesh of HVNSR measures. Another important finding is that the directional analysis for the sites of Section 2 located over this structure (from TF12 to TF15), combined with the interpretation of seismic lines and a good stratigraphic knowledge for the area, suggests that the double peak in HVNSR curves is not related to a stratigraphic effect but probably connected to the lateral heterogeneity of the subsoil.

Nevertheless, the FB has been the object of several geophysical studies in the past, and apart from some uncertainties in the precise localization, most of the hidden structures are known.

The aim of our noise measurement survey was to verify if, even in a complex context as the FB, the HVNSR technique was able to give useful information.

Our study in the Trasacco area has demonstrated that most of the HVNSR curves show a unique frequency peak (as in the 1D conditions), but the more the measurement point is close to hidden tectonic elements, the more complex the HVNSR curves become. This major complexity also affects the azimuthal variation of the HVNSR frequency peaks. The loss of continuity of the resonance peak as well as the increase of azimuthal variations are directly related to the hidden faults. Therefore, the HVNSR technique can be used as a preliminary investigation tool to reveal the presence of these hidden tectonic elements.

Therefore, the HVNSR technique has a double potential: assessing the thickness and then the geometry of the sedimentary layers, and being an indicator of potential hidden structures.

Data availability statement

The original contributions presented in the study are included in the article/Supplementary Material; data presented in this study are available on request from the corresponding author. Further inquiries can be directed to the corresponding author.

Author contributions

DF: substantial contributions to the conception or design of the work, drafting the work or revising it critically for important intellectual content, acquisition, and analysis or interpretation of data for the work. FC: substantial contributions to the conception or design of the work, drafting the work or revising it critically for important intellectual content, acquisition, and analysis or interpretation of data for the work. GDG: drafting the work or revising it critically for important intellectual content, acquisition and analysis or interpretation of data for the work. MV: acquisition and analysis or interpretation of data for the work. GM: drafting the work or revising it critically for important intellectual content.

Funding

This work has been funded by MZS Avezzano livello 3 project. The authors DF, FC, GDG, and MV during part of

this research work held temporary positions at INGV supported by FIRB Abruzzo - UR07 (n. RBAP10ZC8K).

Acknowledgments

The authors thank the Laboratorio Effetti di Sito (https://www.ingv.it/it/monitoraggio-e-infrastrutture-per-la-ricerca/laboratori/laboratorio-effetti-di-sito) for providing seismic equipment used in the field measurements. The authors are grateful for the insightful comments and suggestions provided by Francesco Maesano about the study area and Alessia Mercuri for providing useful suggestions with Geopsy software tools and her comments in different stages of this research project. Useful contribution to improve the paper was given by the reviewers PB and SM.

Conflict of interest

The authors declare that the research was conducted in the absence of any commercial or financial relationships that could be construed as a potential conflict of interest.

Publisher's note

Supplementary material

The Supplementary Material for this article can be found online at: https://www.frontiersin.org/articles/10.3389/feart.2022.937848/full#supplementary-material

SUPPLEMENTARY MATERIAL S1
Average HVNSR for all the single station ambient noise measurements performed in the study area.

SUPPLEMENTARY TABLE S1
Main parameters of the HVNSR recordings: Site Name, Lat, Lon, f0n.

References

Accordi, G. (1975). Nuovi affioramenti di lacustre sollevato a terrazzi al bordo settentrionale del fucino (abruzzi). *Boll. Soc. Nat. Napoli* 84, 1

Amoroso, S., Bernardini, F., Blumetti, A. M., Civico, R., Doglioni, C., Galadini, F., et al. (2016). Quaternary geology and paleoseismology in the fucino and L'aquila basins. *Geol. Field T* 8 (1.2), 1–88. doi:10.3301/GFT.2016.02

Bard, P.-Y., and Bouchon, M. (1980a). The seismic response of sediment-filled valleys. Part 1. the case of incident *SH* waves. *Bull. Seismol. Soc. Am.* 70, 1263–1286. doi:10.1785/bssa0700041263

Bard, P.-Y., and Bouchon, M. (1980b). The seismic response of sediment-filled valleys. part 2. the case of incident P and SV waves. *Bull. Seismol. Soc. Am.* 70 (5), 1921–1941. doi:10.1785/bssa0700051921

Bard, P.-Y., and Bouchon, M. (1985). The two-dimensional resonance of sediment-filled valleys. *Bull. Seismol. Soc. Am.* 75, 519–541. doi:10.1785/bssa0750020519

Bensen, G. D., Ritzwoller, M. H., Barmin, M. P., Levshin, A. L., Lin, F., Moschetti, M. P., et al. (2007). Processing seismic ambient noise data to obtain reliable broad-band surface wave dispersion measurements. *Geophys. J. Int.* 169 (3), 1239–1260. doi:10.1111/j.1365-246x.2007.03374.x

Blumetti, A. M., Dramis, F., and Michetti, A. M. (1993). Fault-generated mountain fronts in the central apennines (Central Italy): geomorphological features and seismotectonic implications. *Earth Surf. Process. Landf.* 18, 203–223. doi:10.1002/esp.3290180304

Bosi, C., Galadini, F., and Messina, P. (1995). Stratigrafia Plio-Pleistocenica della conca del fucino. *Il Quat.* 8 (1), 83

Cara, F., Di Giulio, G., Cavinato, G. P., Famiani, D., and Milana, G. (2011). Seismic characterization and monitoring of fucino basin (central Italy). *Bull. Earthq. Eng.* 9, 1961–1985. doi:10.1007/s10518-011-9282-2

Castellaro, S., and Mulargia, F. (2009). The effect of velocity inversions on H/V. *Pure appl. Geophys.* 166, 567–592. doi:10.1007/s00024-009-0474-5

Cavinato, G. P., Carusi, C., Dall'Asta, M., Miccadei, E., and Piacentini, T. (2002). Sedimentary and tectonic evolution of plio–pleistocene alluvial and lacustrine deposits of Fucino Basin (central Italy). *Sediment. Geol.* 148, 29–59. doi:10.1016/s0037-0738(01)00209-3

Cella, F., Nappi, R., Paoletti, V., and Florio, G. (2021). Basement mapping of the fucino basin in central italy by ITRESC modeling of gravity data. *Geosci. (Basel).* 11, 398. doi:10.3390/geosciences11100398

Di Giulio, G., Ercoli, M., Vassallo, M., and Porreca, M. (2020). Investigation of the Norcia basin (Central Italy) through ambient vibration measurements and geological surveys. *Eng. Geol.* 267, 105501. doi:10.1016/j.enggeo.2020.105501

Doglioni, C., Mongelli, F., and Pialli, G. P. (1998). Boudinage of the alpine belt in the apenninic back-arc. *Mem. Soc. Geol. It.* 52, 457

Famiani, D., Brunori, C. A., Pizzimenti, L., Cara, F., Caciagli, M., Melelli, L., et al. (2020). Geophysical reconstruction of buried geological features and site effects estimation of the middle valle umbra basin (central Italy). *Eng. Geol.* 269, 105543. ISSN 0013-7952. doi:10.1016/j.enggeo.2020.105543

Frezzotti, M., and Giraudi, C. (1992). Evoluzione geologica tardo-pleistocenica ed olocenica del conoide complesso della Valle Majelama (Massiccio del Velino - Abruzzo). *Il Quat.* 5 (1), 33

Galadini, F., Galli, P., and Giraudi, C. (1997). Geological investigations of Italian earthquakes: new paleoseismological data from the fucino plain (central Italy). *J. Geodyn.* 24, 87–103. doi:10.1016/s0264-3707(96)00034-8

Galadini, F., Galli, P., Giraudi, C., and Molin, D. (1995). Il terremoto del 1915 e la sismicità della piana del Fucino (Italia Centrale). *Boll. Soc. Geol. It.* 114, 635–663. doi:10.12910/EAI2015-075

Galadini, F., and Galli, P. (1996). Paleoseismology related to deformed archaeological remains in the fucino plain. implications for subrecent seismicity in Central Italy. *Ann. Geofis.* 39, 925–940. doi:10.4401/ag-4025

Galadini, F., and Galli, P. (1999). The Holocene paleoearthquakes on the 1915 Avezzano earthquake faults (central Italy): implications for active tectonics in the central apennines. *Tectonophysics* 308, 143–170. doi:10.1016/s0040-1951(99)00091-8

Galli, P., Messina, P., Giaccio, B., Peronace, E., and Quadrio, B. (2012). Early Pleistocene to late Holocene activity of the magnola fault (fucino fault system, central Italy). *Boll. Di Geofis. Teor. Ed. Appl.* 53 (4), 435–458. doi:10.4430/bgta0054

Giraudi, C. (1988). Evoluzione geologica della Piana del Fucino (Abruzzo) negli ultimi 30.000 anni. *Il Quat.* 1 (2), 131.

Giraudi, C. (1986). Faglie ad attività olocenica nella piana del fucino. *Mem. Soc. Geol. It.* 35, 875

ISPRA (1881) Geological survey of Italy. Available at: http://sgi2.isprambiente.it/ithacaweb/Mappatura.aspx.

ITHACA Working Group (2019). *ITHACA (ITaly HAzard from CApable faulting), A database of active capable faults of the Italian territory*. Version December 2019. ISPRA Geological Survey of Italy. Available at: http://sgi2.isprambiente.it/ithacaweb/Mappatura.aspx.

Joyner, W. B., Warrick, R. E., and Fumal, T. E. (1981). The effect of Quaternary alluvium on strong ground motion in the coyote lake, california, earthquake of 1979. *Bull. Seismol. Soc. Am.* 71 (4), 1333–1349. doi:10.1785/bssa0710041333

Lanari, R., Faccenna, C., Benedetti, L., Sembroni, A., Bellier, O., Menichelli, I., et al. (2021). Formation and persistence of extensional internally drained basins: The case of the Fucino basin (central apennines, Italy). *Tectonics* 40, e2020TC006442. doi:10.1029/2020tc006442

Lu, G. Y., and Wong, D. W. (2008). An adaptive inverse-distance weighting spatial interpolation technique. *Comput. Geosciences* 34 (9), 1044–1055. ISSN 0098-3004. doi:10.1016/j.cageo.2007.07.010

Mancinelli, P., Scisciani, V., Patruno, S., and Minelli, G. (2021). Gravity modeling reveals a messinian foredeep depocenter beneath the intermontane fucino basin (central apennines). *Tectonophysics* 821, 229144. ISSN 0040-1951. doi:10.1016/j.tecto.2021.229144

Mannella, G., Giaccio, B., Zanchetta, G., Regattieri, E., Niespolo, E. M., Pereira, A., et al. (2019). Palaeoenvironmental and palaeohydrological variability of mountain areas in the central mediterranean region: a 190 ka-long chronicle from the independently dated fucino palaeolake record (central Italy). *Quat. Sci. Rev.* 210, 90–210. ISSN 0277-3791. doi:10.1016/j.quascirev.2019.02.032

Mascandola, C., Massa, M., Barani, S., Albarello, D., Lovati, S., Martelli, L., et al. (2019). Mapping the seismic bedrock of the po plain (Italy) through ambient-vibration monitoring. *Bull. Seismol. Soc. Am.* 109 (1), 164–177. doi:10.1785/0120180193

Matsushima, S., Hirokawa, T., De Martin, F., Kawase, H., and Sánchez-Sesma, F. J. (2014). The effect of lateral heterogeneity on horizontal-to-vertical spectral ratio of microtremors inferred from observation and synthetics. *Bull. Seismol. Soc. Am.* 104 (1), 381–393. doi:10.1785/0120120321

Messina, P. (1996). Tettonica meso pleistocenica dei terrazzi nord-orientali del Fucino (Italia centrale). *Il Quat.* 9 (1), 393

Michetti, A. M., Brunamonte, F., Serva, L., and Vittori, E. (1996). Trench investigations of the 1915 Fucino earthquake fault scarps (Abruzzo, Central Italy): geological evidence of large historical events. *J. Geophys. Res.* 101 (B3), 5921–5936. doi:10.1029/95JB02852

Nakamura, Y. (1989). A method for dynamic characteristics estimation of subsurface using microtremor on the ground surface. *Q. Rep. RTRI* 30 (1), 25

Oddone, E. (1915). Gli elementi fisici del grande terremoto marsicano-fucense del 13 gennaio 1915. *Boll. Soc. Sismol. Ital.* 19, 71

Palombelli, R. (2014). *Indagini geofisiche finalizzate allo studio della microzonazione sismica nel territorio del comune di Trasacco (AQ)*. Dissertation. Rome, Italy: Sapienza Università di Roma.

Patacca, E., Scandone, P., Di Luzio, E., Cavinato, G. P., and Parotto, M. (2008). Structural architecture of the central apennines: interpretation of the CROP 11 seismic profile from the adriatic coast to the orographic divide. *Tectonics* 27, 1–36. doi:10.1029/2005tc001917

Patruno, S., and Scisciani, V. (2021). Testing normal fault growth models by seismic stratigraphic architecture: The case of the pliocene-quaternary Fucino basin (central apennines, Italy). *Basin Res.* 33 (3), 2118–2156. doi:10.1111/bre.12551

Schimmel, M., and Paulssen, H. (1997). Noise reduction and detection of weak, coherent signals through phase-weighted stacks. *Geophys. J. Int.* 130 (2), 497–505. doi:10.1111/j.1365-246x.1997.tb05664.x

Serva, L., Blumetti, A., and Michetti, A. (1986). Gli effetti sul terreno del terremoto del Fucino (13 gennaio 1915); tentativo di interpretazione dell'evoluzione tettonica recente di alcune strutture. *Mem. Soc. Geol. It.* 35, 893–907.

Vassallo, M., De Matteis, R., Bobbio, A., Di Giulio, G., Adinolfi, G. M., Cantore, L., et al. (2019). Seismic noise cross-correlation in the urban area of Benevento city (Southern Italy). *Geophys. J. Int.* 217 (3), 1524–1542. doi:10.1093/gji/ggz101

Wathelet, M. (2008). An improved neighborhood algorithm: Parameter conditions and dynamic scaling. *Geophys. Res. Lett.* 35, L09301. doi:10.1029/2008GL033256

Wathelet, M., Chatelain, J.-L., Cornou, C., Di Giulio, G., Guillier, B., Ohrnberger, M., et al. (2020). Geopsy: a user-friendly open-source tool set for ambient vibration processing. *Seismol. Res. Lett.* 91 (3), 1878–1889. doi:10.1785/0220190360

Yamanaka, H., Takemura, M., Ishida, H., and Niwa, M. (1994). Characteristics of long-period microtremors and their applicability in exploration of deep sedimentary layers. *Bull. Seismol. Soc. Am.* 84, 1831–1841. doi:10.1785/bssa0840061831

Yilmaz, O. (1987). *Seismic data processing in investigations in geophysics, 2: Soc. Expl. Geophys, series*. Editors S. M. Doherty, and E. B. Neitzel, (Texas, United States: SEG).

Zarlenga, F. (1987). I depositi continentali del bacino del Fucino. *Geol. Rom.* 26, 25

frontiers | Frontiers in Earth Science

TYPE Original Research
PUBLISHED 24 August 2022
DOI 10.3389/feart.2022.951781

OPEN ACCESS

EDITED BY
Aybige Akinci,
Istituto Nazionale di Geofisica e Vulcanologia (INGV), Italy

REVIEWED BY
Alessandro Vuan,
Istituto Nazionale di Oceanografia e di Geofisica Sperimentale, Italy
Basil Margaris,
Institute of Engineering Seismology and Earthquake Engineering (ITSAK), Greece

*CORRESPONDENCE
J. Lin,
jiayue.lin@polimi.it

SPECIALTY SECTION
This article was submitted to Geohazards and Georisks, a section of the journal Frontiers in Earth Science

RECEIVED 24 May 2022
ACCEPTED 14 July 2022
PUBLISHED 24 August 2022

CITATION
Lin J and Smerzini C (2022), Variability of physics-based simulated ground motions in Thessaloniki urban area and its implications for seismic risk assessment.
Front. Earth Sci. 10:951781.
doi: 10.3389/feart.2022.951781

Variability of physics-based simulated ground motions in Thessaloniki urban area and its implications for seismic risk assessment

J. Lin* and C. Smerzini

Department of Civil and Environmental Engineering, Politecnico di Milano, Milan, Italy

An accurate characterization of earthquake ground motion and its variability is crucial for seismic hazard and risk analysis of spatially distributed portfolios in urban areas. In this work, a 3D physics-based numerical approach, based on the high-performance spectral element code SPEED (http://speed.mox.polimi.it/), is adopted to generate ground shaking scenarios for strong earthquakes (moment magnitude M_W=6.5–7) in the Thessaloniki area (Northern Greece). These simulations account for kinematic finite-fault rupture scenarios and a 3D seismic velocity including the two main geological structures present in the area (Thessaloniki and Mygdonia basins). The numerical model is successfully validated by comparing simulated motions, on the one hand, with the recordings of a real small-magnitude (M_W4.4) earthquake and, on the other, with empirical Ground Motion Models for the historical M_W6.5 1978 earthquake. The sensitivity of results to the velocity model, anelastic attenuation, and non-linear soil effects is evaluated. The variability of the ground motion intensity measures in Thessaloniki as a function of the finite-fault rupture realizations (causative fault, magnitude, hypocenter location) is explored to gain insight into its potential impact on seismic risk assessment in urban areas.

KEYWORDS

earthquake ground motion, 3D physics-based numerical simulation, finite-fault rupture scenarios, spatial correlation, seismic risk

1 Introduction

The characterization of earthquake ground motion and of its spatial variability is a key component of seismic risk modeling, especially for spatially distributed structures or infrastructure systems, such as bridge networks and building portfolios in large urban areas.

Empirical Ground Motion Models (GMMs) and ShakeMaps (Worden et al., 2020; Wald et al., 2021) represent the reference approach for earthquake ground motion prediction because of their consolidated utilization in the frame of probabilistic seismic hazard and risk analyses. Empirical GMMs are derived from the statistical processing of recordings of past earthquakes to provide the probability distribution of prescribed

ground motion Intensity Measures (IM) as a function of essential explanatory variables, such as earthquake magnitude, source-to-site distance, and soil conditions (Douglas and Edwards, 2016). Driven by the increasing availability of recordings, state-of-the-art GMMs are calibrated on comprehensive datasets by using robust mixed-effect regressions techniques (Stafford 2014) and by relaxing the assumption of ergodicity, i.e., the variability at a single site from a specific source is assumed identical to that derived from multiple sites over large regions (Villani and Abrahamson 2015; Kotha et al., 2020; Sgobba et al., 2021a; Caramenti et al., 2022). By providing region- and site-specific adjustments of the model parameters, non-ergodic models proved to offer significant improvements in terms of median shaking accuracy and reduction of GMM variability (i.e., standard deviation), especially in the far-field.

Despite these advancements, the main issue is that the paucity of ground motion recordings in the proximity of the earthquake source persists, implying that empirical GMMs are poorly constrained in the near-source region, and they are subject to high uncertainty. Recently, Paolucci et al. (2022) showed that the predictive performance of recent GMMs is still poor when assessed on the NEar-Source Strong-Motion recorded dataset NESS2.0 (Sgobba et al., 2021b), because of the still insufficient sampling of the GMM calibration datasets in the near-field. Furthermore, because of the limited within-event spatial sampling of the calibration datasets, in empirical GMMs the spatial correlation of ground motion is reproduced through simplified approaches based on the stochastic simulation of spatially correlated random fields under the hypotheses of ergodicity, isotropy, and stationarity (see review in Schiappapietra and Douglas 2020). However, such assumptions are hardly found in near-source conditions and may not be suitable to reproduce scenario- and region-specific features of ground motion spatial correlation and cross-correlation (see Chen and Baker 2019; Schiappapietra and Smerzini 2021). This may negatively impact on seismic risk assessments of regional-scale infrastructures or urban areas, where ground motion scenarios preserving a realistic spatial correlation structure are needed (Schiappapietra et al., 2022).

Due to the ever-growing increase of computational resources, physics-based numerical simulations (PBS) of source-to-site seismic wave propagation have been gradually playing a promising role in responding to the existing knowledge gaps in earthquake ground motion prediction (Bradley et al., 2017; McCallen et al., 2021a; 2021b; Paolucci et al., 2021; Touhami et al., 2022). Based on the numerical solution of the elastodynamics equation, PBS provides ground motion time histories reflecting the physics of the seismic wave propagation problem, from the fault rupture to the propagation path and complex site effects in shallow geology. PBS motions can be used: 1) to complement recordings, especially in those conditions where data are still sparse, such as in the near-source region of strong earthquakes, 2) to calibrate region-specific spatial correlation models, 3) to constrain site amplification studies in complex geological configurations (e.g. alluvial basins), 4) to gain insight into the physics of the complex interactions between the source process and the ground shaking, up to the coupling with the structural response, 5) to provide site-specific waveforms for structural analysis, also at spatially dense locations, as well as scenarios for region-specific hazard and risk assessments.

With this background, the goal of this work is to construct and validate a set of earthquake ground shaking scenarios from 3D PBS for the area of Thessaloniki (Northern Greece), given their future use in region-specific seismic risk assessments. The case study of Thessaloniki is considered because of the detailed knowledge on the geological and seismotectonic context, and vulnerability and exposure data (Crowley et al., 2020; Riga et al., 2021), which are critical ingredients for seismic risk evaluations. Starting from previous works (Smerzini et al., 2017; Smerzini and Pitilakis 2018), an updated version of the 3D numerical model of the broader Thessaloniki area is built in this work by bringing improvements to the geological and geophysical model.

PBS are carried out by the open-source computer code SPEED—Spectral Element in Elastodynamics with Discontinuous (Mazzieri et al., 2013, http://speed.mox.polimi.it/), developed at Politecnico di Milano. In the recent past, SPEED has been extensively used for the validation of PBS addressed to real earthquakes in Italy and worldwide (e.g. Paolucci et al., 2015; Evangelista et al., 2017; Infantino et al., 2020), for region-specific seismic hazard and risk evaluations (Smerzini and Pitilakis 2018; Stupazzini et al., 2021), and the construction of a dataset of broadband near-source simulated ground motions for earthquake engineering applications (Paolucci et al., 2021).

The paper is organized as follows. After providing in Section 2 an overview of the study area, the 3D numerical model is presented in Section 3, emphasizing the main changes introduced in this work with respect to the previously published version of the model for the same region. In Section 4 the numerical model is validated on the recordings of a real earthquake with moment magnitude M_W4.4, which occurred on 12th September 2005 in the Mygdonia graben. A set of sensitivity tests is shown for the calibration of model parameters. After the small magnitude event's validation, the M_W6.5 1978 earthquake simulation is addressed in Section 5 by comparing simulated ground motion intensity measures with empirical GMMs and by assessing the spatial correlation of spectral accelerations across different vibration periods. Finally, Section 6 illustrates the set of 60 physics-based earthquake scenarios rupturing two different active fault systems around Thessaloniki, namely the Gerakarou-Langadhas and the Anthemountas faults, with M_W in the range between 6.5 and 7.0.

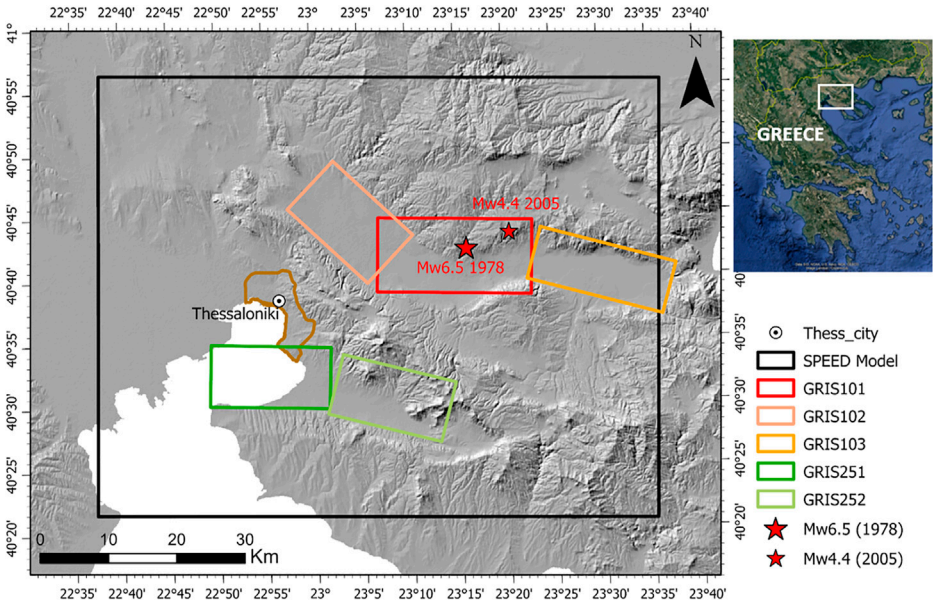

FIGURE 1
Overview of the study area with indication of the main seismogenic faults (according to the GreDaSS database) and the Thessaloniki urban area (superimposed brown contour). The extent of the SPEED model as well as the epicenters of the real M_W4.4 and M_W6.5 earthquakes considered in this work for validation purposes are shown.

2 Study area

The city of Thessaloniki is the second largest and the most relevant financial center in the territory of Greece, with more than one million inhabitants. Located in Central Macedonia and the inner part of the Thermaikos Gulf (see Figure 1), the city has an extensive industrial zone encompassing strategic infrastructures and a major international port functioning as a major gateway for the Balkan hinterland (Raucoules et al., 2008). The port of Thessaloniki is one of the most important harbors in Southeast Europe. It serves the needs of 15 million inhabitants of its international mainland and handles approximate trading of 16,000,000 tons of cargo annually.

The broader Thessaloniki area sits in Central Macedonia, a high-seismicity region characterized by an extensional tectonic regime associated with complex NW–SE, NE–SW, E–W, and NNE–SSW trending faults (Tranos et al., 2003; Paradisopoulou et al., 2006). The outcropping rocks forming the pre-alpine and alpine basement belong to the NNW–SSE-trending alpine Circum Rhodope Belt Thrust System (CRBTS), characterized by several NE-dipping asymmetric anticlinoria and synclinoria and repeated SW-directed thrust sheets (Tranos et al., 1999). Above this basement, NW–SE- and E–W-trending basins and grabens of tectonic origin, filled with Neogene and Quaternary sediments, are present. These basins were formed by an extensive extensional deformation associated with high-angle normal faults (Pavlides and Kilias, 1987; Tranos et al., 1999). Among these basins, the E–W-trending Mygdonia graben is within the study area, located around 25 km northeast of Thessaloniki.

The seismicity of the city of Thessaloniki is mainly associated with the activity of the Mygdonia and the Anthemountas fault systems (see Figure 1, according to the Greek Database of Seismogenic Sources-GreDaSS: http://gredass.unife.it/; Caputo et al., 2012), which were responsible for severe earthquakes with magnitudes up to M_W7.0 (Papazachos and Papazachou 1997). The Mygdonia source represents a large fault zone bordering the southern margin of the Mygdonia basin. It consists of three major fault segments: from west to east, 1) the NW-SE trending Langadhas Fault (GRIS102), 2) the EW trending Gerakarou Fault (GRIS101), which was reactivated during the Mw6.5 20 June 1978 earthquake, and 3) the Apollonia Fault (GRIS103), with a WNW-ESE strike and steeper dipping angles with respect to the previous fault segments. The Anthemountas source is a 40 km-long fault zone bounding the narrow E-W-striking Anthemountas basin to the south of Thessaloniki. It is separated into two segments: from west to east, 1) the Angelochori Fault (GRIS251) and 2) the Souroti Fault (GRIS252).

Destructive events, such as those occurring in the VIII century (677, M_W=6.4 and 700, M_W=6.5), the Assiros (5 July 1902, M_W=6.5) and Thessaloniki (20 June 1978, M_W=6.5) earthquakes, were generated by the seismic rupture of the Mygdonia seismogenic source. Instead, the Vasilika (1,677,

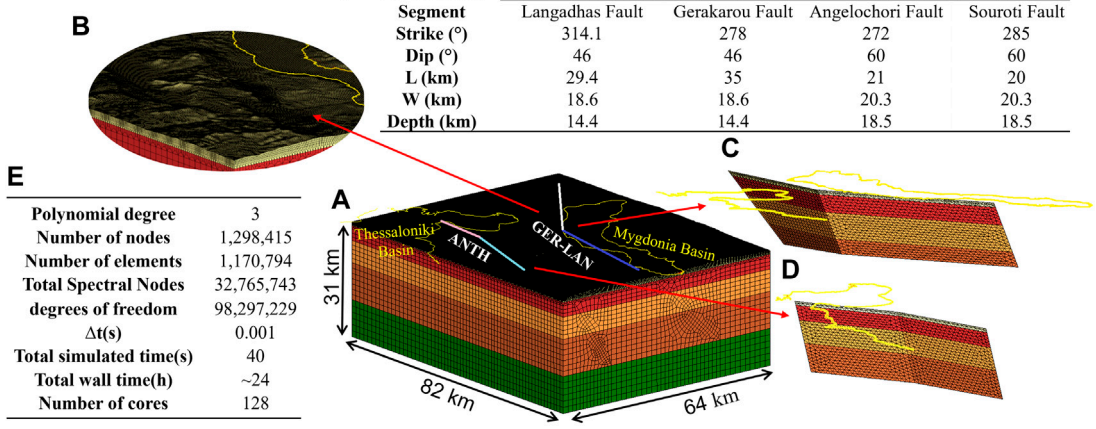

F

Fault System	Gerakarou-Langadhas (GER-LAN)		Anthemountas (ANTH)	
Segment	Langadhas Fault	Gerakarou Fault	Angelochori Fault	Souroti Fault
Strike (°)	314.1	278	272	285
Dip (°)	46	46	60	60
L (km)	29.4	35	21	20
W (km)	18.6	18.6	20.3	20.3
Depth (km)	14.4	14.4	18.5	18.5

E

Polynomial degree	3
Number of nodes	1,298,415
Number of elements	1,170,794
Total Spectral Nodes	32,765,743
degrees of freedom	98,297,229
Δt(s)	0.001
Total simulated time(s)	40
Total wall time(h)	~24
Number of cores	128

G

	Material	Thickness (m)	V_S (m/s)	V_P (m/s)	ρ (kg/m3)	Q_S	Q_P
Basin	Thessaloniki	0-800	Soft: $300+13.5\cdot z^{0.7}$ Stiff: $500+11.9\cdot z^{0.7}$	Soft: $1800+21.4\cdot z^{0.7}$ Stiff: $2000+19.8\cdot z^{0.7}$	$2000+0.4\cdot z$	[a]Note below	2Qs
	Mygdonia	0-450	$200+15\cdot z^{0.63}$	$1500+32.8\cdot z^{0.63}$	$2075+0.55\cdot z$	$0.1\cdot Vs$	2Qs
Crust 1		1000	See **Fig. 2A**	2.25*Vs	[b]See **Fig. 2A**	$0.1\cdot Vs$	2Qs
Crust 2		4000	3440	6060	2700	300	600
Crust 3		6000	3460	6070	2800	300	600
Crust 4		10000	3640	6370	2900	300	600
Crust 5		10000	3980	6960	3000	400	800

[a]*Note: $Q_s=20$; $z<=200$, $Q_s=50$; $z<=500$, $Q_s=100$; $z<=1000$, $Q_s=150$ (z=depth from ground surface)*
[b]*Note: The values of ρ are calculated according to the approach from Cotton et al. (2006).*

FIGURE 2
(A) Overview of the 3D numerical model and details on **(B)** mesh discretization in shallow layers and on the seismic faults, namely **(C)** GER-LAN fault and **(D)** ANTH fault. **(E)** Computational features. **(F)** Geometry of the seismic faults included in the numerical model. **(G)** 3D wave propagation model adopted for the sedimentary basins and for crustal rock layers (Shear-wave velocity: V_S; compressional wave velocity: V_P; soil density: ρ; quality factors: Q_S and Q_P).

M_W=6.2) and the Thessaloniki (22 June 1759, M_W=6.5) earthquakes are associated with the Anthemountas fault system.

In Figure 1, the superimposed black box indicates the size of the SPEED model, described in detail in the following Section.

3 An updated 3D numerical model of the Thessaloniki area

A 3D physics-based numerical approach, through the spectral element code SPEED (Mazzieri et al., 2013, http://speed.mox.polimi.it/), is used to simulate the seismic wave propagation during both real and scenario earthquakes occurring around the city of Thessaloniki. Smerzini et al. (2017) constructed the first 3D spectral-element model of the area and validated it on the available instrumental (one accelerometric recording in the city center) and macroseismic observations. In this work, an update of this 3D model is proposed concerning: 1) the inclusion of the Mygdonia basin in the 3D numerical model, which was neglected in Smerzini et al. (2017), 2) modification to the seismic velocity profile of the outcropping bedrock layer of the crustal model to provide more realistic velocities at shallow depths following Cotton et al. (2006); 3) new mesh of the model to provide adequate discretization of the low-velocity sediments of Mygdonia basin. Further details about model updates will be provided below.

The final 3D model extends over a volume of 82 × 64 × 31 km^3 and it is discretized using an unstructured hexahedral mesh capable of propagating frequencies up to 1.5 Hz, with a third-order spectral degree, leading to a total of 100 million degrees of freedom, see computational information from Figure 2E. Numerical simulations were carried out on the Galileo100 and Marconi100 Cluster at CINECA, the largest high-performance computing center in Italy (www.cineca.it).

As shown in Figure 2, the model includes:

- 3D geological model for both Thessaloniki and Mygdonia;
- crustal model for rock materials, as in Smerzini et al. (2017), apart from the modification of the velocity of the first layer, as explained below;
- the Gerakarou-Langhadas (GRIS101-GRIS102) Faults, referred to as GER-LAN hereafter, and the Anthemountas (GRIS251-GRIS252) Faults, referred to as

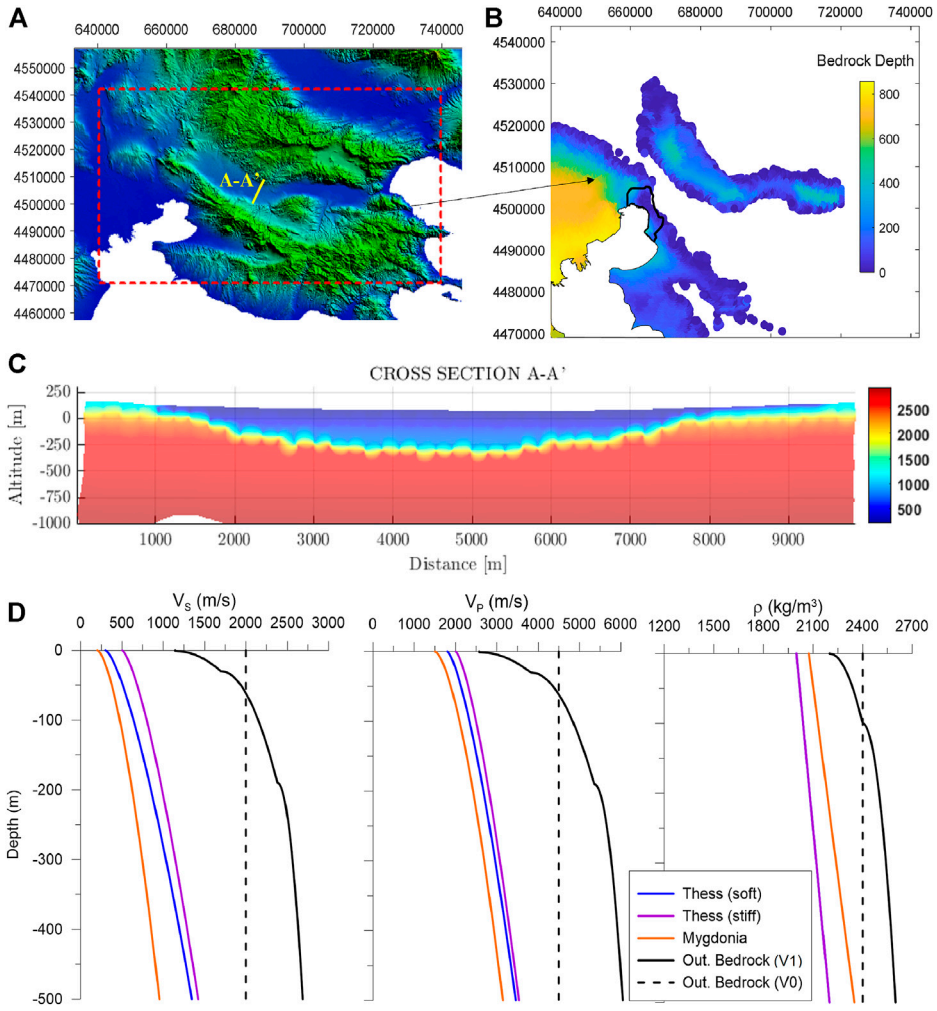

FIGURE 3
(A) Digital Elevation Model of the study area. **(B)** Depth of geologic bedrock in Thessaloniki and Mygdonia basins. **(C)** Velocity cross-section (A-A′) across the Mygdonia basin as indicated in Figure 3A. **(D)** V_S, V_P and ρ profiles within the Thessaloniki basin, Mygdonia basin and outcropping bedrock (V0 refers to the previous version in Smerzini et al., 2017; V1 refers to the model adopted in this work). Depth is measured with respect to the topographic surface.

ANTH. The location and geometry of these faults were retrieved and adapted from the GreDaSS database (http://gredass.unife.it/) and are summarized in Figure 2F;
- ground topography.

Efforts were devoted to constructing a large-scale 3D geological model including, in the same computational domain, both the Thessaloniki basin and the Mygdonia basin. While the Thessaloniki basin model (3D shape and geophysical model) was taken from Smerzini et al. (2017), the 3D shape of the Mygdonia basin is taken from Maufroy et al. (2016). The velocity model of the soft soil deposits inside the Mygdonia basin was calibrated based on previous studies (Maufroy et al., 2016) and available recorded profiles. Specifically, a parabolic profile was defined for both S and P wave velocity as a function of the depth from the topographic surface (z), while for soil density a linear profile was assumed, as follows:

For S wave velocity, $V_S = 200+15 \cdot z^{0.63}$

For P wave velocity, $V_P = 1500+32.8 \cdot z^{0.63}$

For soil density, $\rho = 2{,}075+0.55 \cdot z$

Besides, a frequency-proportional quality factor $Q_S = Q_0 \cdot f/f_0$ is assumed, with $f_0 = 1$ Hz (see sensitivity tests in Section 4) and $Q_0 = V_S/10$, which is a rule-of-thumb for estimating Q based on the V_S profile often used in the literature (see Laurendeau et al., 2018).

The 3D shape of both the Thessaloniki basin and the Mygdonia basin is shown in Figure 3B: the maximum sediment thickness reaches about 800 m and 500 m in the Thessaloniki and Mygdonia

TABLE 1 Numerical simulations performed in this study for validation and sensitivity purposes.

Model label	Source type	Thessaloniki basin		Mygdonia basin		Outcropping bedrock		f_0 (Hz)	
	Point source (Mw4.4)	Finite-fault (Mw6.5 1978)	LE[a]	NLE[b]	LE[a]	NLE[b]	Hard rock	Soft rock	
6.5-HR-T-E		√	√				√		0.67
6.5-SR-T-E		√	√					√	0.67
6.5-SR-TM-E		√	√		√			√	1
6.5-SR-TM-N		√		√		√		√	1
4.4-SR-TM-E0.67	√		√		√			√	0.67
4.4-SR-TM-E1	√		√		√			√	1

[a]LE, linear visco-elastic.
[b]NLE, non-linear visco-elastic.
[c]f0 = reference frequency for frequency-proportional damping: $Q(f)=Q_0.f/f_0$.

basin, respectively. Figure 3C shows a representative cross-section of the V_S model across the Mygdonia (A-A' in yellow line in Figure 3A).

Concerning the crustal model, the velocity of the uppermost layer was modified to provide a more realistic velocity profile of the outcropping bedrock in the area under study. Compared to Smerzini et al. (2017), where the outcropping bedrock layer consists of very hard rock with constant shear wave velocity V_S = 2,000 m/s, the updated crustal model features the first layer (see Crust 1 in Figure 2G) with a gradient of V_S from a minimum value of 1,150 m/s up to a value of 3,440 m/s at 1,000 m depth from the topographical surface, see continuous black line in Figure 3D. The gradient of this velocity profile was calibrated based on the studies conducted by Cotton et al. (2006) on rock velocity profiles. In Figure 3D, the V_S, V_P and ρ profiles for the sediments within both Thessaloniki and Mygdonia basins and the outcropping bedrock layer are shown.

4 Validation and sensitivity tests

This Section presents the validation and sensitivity tests performed on the 3D numerical model of the study area. Table 1 lists the PBS performed as propaedeutic analyses to check the performance of the numerical model especially in relation to the updates of the numerical model (see Section 3):

- *Type of source.* Two real earthquakes were considered for validation, the M_W4.4 12 September 2005 event and the M_W6.5 20 June 1978 earthquake. Provided the considerably different magnitude of the validation events, a point-source and a finite-fault kinematic source model is adopted for the medium and large magnitude earthquake, respectively. While Smerzini et al. (2017) focused on validating the model against the M_W6.5 1978 event, in this work emphasis is placed on the M_W4.4 event, which allows for a verification of the accuracy of the updated velocity model, neglecting the high uncertainties typically associated with the finite-fault modelling. For the 1978 event, the same kinematic source model (slip distribution and source time function) as in Smerzini et al. (2017) is adopted.
- *Basin models.* Numerical results with/without the Mygdonia basin and with the Thessaloniki basin are compared for the same source model, to check the influence of the added basin in the simulated ground motions in the city of Thessaloniki. While the influence of the basin is evident for the soft sites in the Mygdonia graben itself, the evaluation of the impact on sites at more considerable distances, such as in Thessaloniki at around 25 km from the basin, deserves some considerations.
- *Outcropping bedrock.* The effect of the new velocity profile for the outcropping bedrock is analyzed by comparing, for the same source model, results obtained with hard rock (V_S = 2,000 m/s) and with softer rock profile (see profiles in Figure 3) at shallow depths.
- *Linear* Vs. *non-linear elastic soil constitutive law.* While for the M_W4.4 event, a linear visco-elastic model is assumed as a reasonable assumption because of the low seismic excitation, for the M_W6.5 event, a non-linear elastic constitutive model is adopted using the shear modulus and damping curves adopted in Smerzini et al. (2017). For the non-linear elastic modelling approach, we refer to Stupazzini et al. (2009).
- *Anelastic attenuation model.* Sensitivity tests are performed for the anelastic attenuation properties. This work assumes a frequency-proportional quality factor for all soil layers, $Q_S = Q_0 \cdot f/f_0$, with Q_0 values given in Figure 2G and reference frequency f_0 varying between 0.67 and 1 Hz.

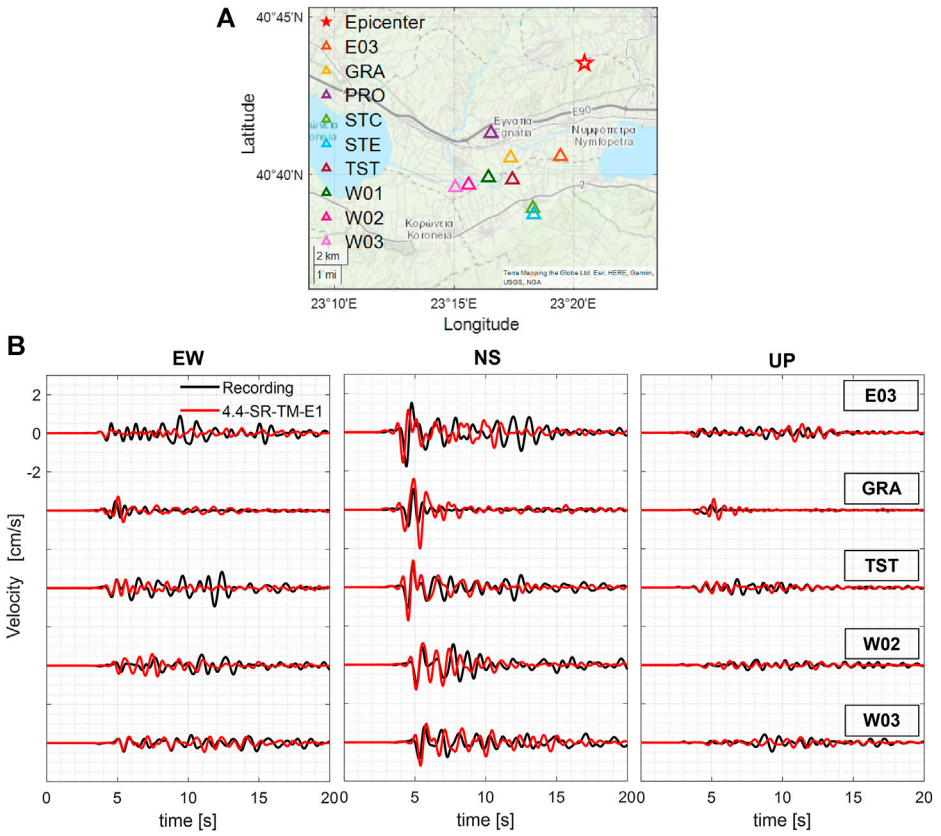

FIGURE 4
(A) Location of recording stations. **(B)** Comparison between recorded (black) and simulated (red, model: 4.4-SR-TM-E1) velocity time histories for EW, NS, UP components at the stations: E03 (R_{epi}=5.4 km), GRA (R_{epi}=6.9 km), TST (R_{epi}=7.9 km), W02 (R_{epi}=9.8 km) and W03 (R_{epi}=10.4 km).

4.1 Validation on the M_W4.4 12 september 2005 earthquake

The numerical model was applied to simulate a real M_W4.4 earthquake event (strike: 281°, dip: 52°, rake: −98°) which occurred on 12 September 2005 near the Mygdonia basin with hypocenter at (40.7255°N, 23.3408°E) with a focal depth of 10 km. Owing to the small magnitude, the finiteness of the fault rupture area is neglected, and a point-source model is considered. Because the accuracy of simulations is controlled by uncertainties in the source properties, propagation path, and shallow layer structure, selecting a point-like and relatively deep event (>8 km) allows one to focus on the validation of the propagation path and local site response.

The earthquake was recorded by a total of nine stations of the EUROSEISTEST strong motion network (http://euroseisdb.civil.auth.gr/) which are considered herein for comparison between simulated and recorded ground motions. The location of the stations is shown in the map of Figure 4A.

Figure 4B shows the comparison between the recorded (black) and simulated (red, model: 4.4-SR-TM-E1 of Table 1) velocity waveforms at five representative stations, namely E03, GRA, TST, W02, and W03. For the comparison, horizontal (EW and NS) and vertical (UD) components are considered and a low-pass filter at 1.5 Hz is applied. A comprehensive comparison in both time and frequency domain is available in Supplementary Image, where the recorded and simulated velocity time series and corresponding Fourier Amplitude Spectra (FAS) are shown for all nine stations which recorded the earthquake. In Supplementary Table S1, the complete list of station metadata is also provided.

The qualitative comparison of Figure 4 indicates that a satisfactory agreement is found between simulated and recorded waveforms, in terms of timing of first arrivals, amplitudes and duration. Horizontal components, especially on the NS, show a better agreement than the vertical ones. For the E03 station located at basin center, the direct arrivals on all components are well captured by the simulations but the numerical model lacks some complexity in late arrivals associated with reverberations in the basin. At GRA station, simulations overpredict the recorded peak velocity values, especially on NS and UD components, most likely because of the assumptions in the focal mechanism.

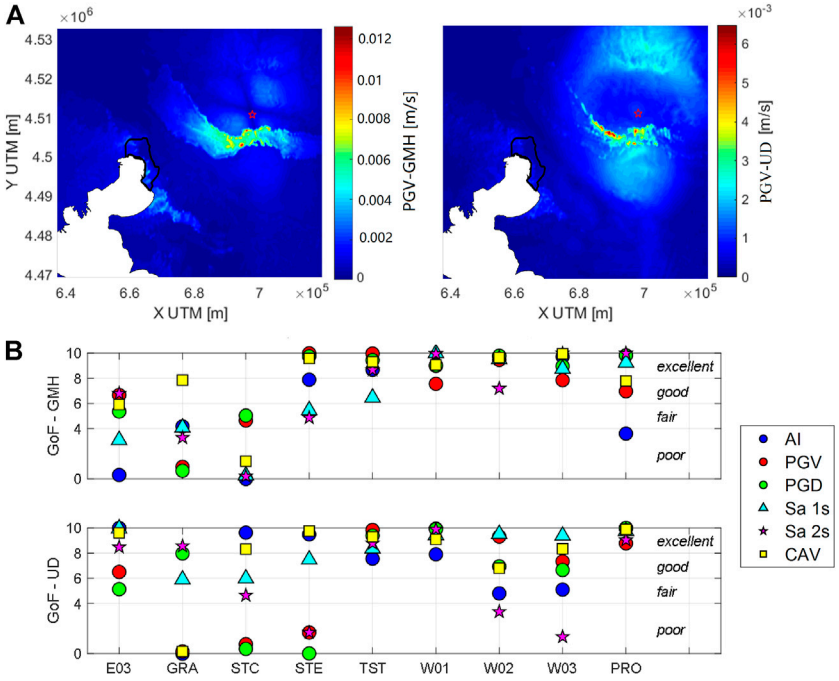

FIGURE 5
(A) Map of simulated peak ground velocity (PGV) for GMH and UD components. **(B)** Goodness-of-Fit according to Anderson (2004) evaluated on AI, PGV, PGD, SA (1s), SA (2s) and CAV for both GMH and UD components.

To provide a quantitative evaluation of the performance of the PBS, the Goodness-Of-Fit (GoF) criteria by Anderson (2004) were evaluated, considering six different ground motion intensity measures representative of both peak and integral parameters: Peak Ground Velocity (PGV), Peak Ground Displacement (PGD), Cumulative Absolute Velocity (CAV), Arias Intensity (AI), SA (1s), SA (2s). The scores, shown in Figure 5B, were computed on both the geometric mean of horizontal components (GMH) and the UD component. For all stations, except E03, GRA and STC, horizontal GoF scores are fair-to-excellent. In particular, on the same component, for stations TST, PRO, W01, W02, and W03, good-to-excellent scores are found for all ground motion intensity measures. UD scores are slightly worse than the ones for the horizontal components, but they remain in the fair-to-excellent range for a majority of stations and ground motion parameters. In the same figure (Figure 5A) the maps of PGV (GMH and UD components) are also shown, to appreciate the spatial distribution of the ground shaking, with clear evidence of site amplification effects, especially on horizontal ground motion, in the Mygdonia basin.

4.2 Sensitivity analyses

4.2.1 Sensitivity to the velocity model

In this section, with reference to the simulation of the Mw6.5 1978 earthquake, the impact of the 3D velocity model adopted in the simulation is investigated, by comparing the results obtained from models 6.5-HR-T-E (hard outcropping bedrock, with Thessaloniki basin only), 6.5-SR-T-E (softer outcropping bedrock, with Thessaloniki basin only) and 6.5-SR-TM-E (softer outcropping bedrock, with both Thessaloniki and Mygdonia basins). For all three simulations, a linear visco-elastic model is assumed.

Figure 6 shows the comparisons of NS velocity time histories and corresponding FAS (up to 1.5 Hz) obtained from the three PBS at two selected receivers close to the city of Thessaloniki, namely receiver A located on soft sediments in the vicinity of Thessaloniki shoreline and receiver B sited on outcropping bedrock, as indicated in Figure 6A. Results suggest that, at both receivers, softening of the mechanical rock properties produces a moderate-to-significant increase in the ground motions (peak velocities increase by a factor between 40% and 80% for rock and basin receivers, respectively). Enhancement of high frequency components is associated mainly with the site amplification features related to the softer rock layer, particularly evident at receiver B (Figure 6C). In contrast, the enrichment of lower frequencies is most likely related to the coupling of rupture propagation with softer layers. This effect is observable at both stations, confirming its correlation with the seismic source. Furthermore, the updated outcropping bedrock profile implies a more considerable impedance contrast between the sedimentary soil layers and the underlying bedrock at depths

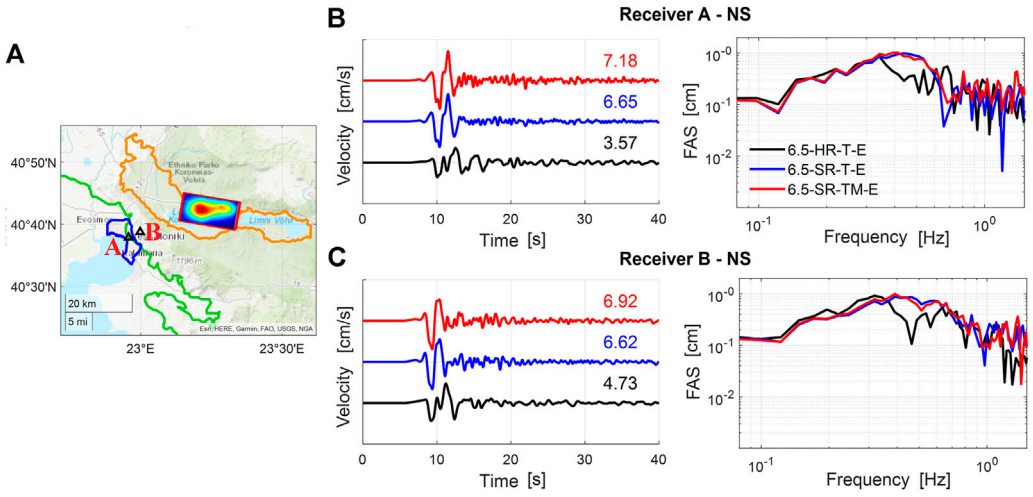

FIGURE 6
Sensitivity of results to the velocity models: 6.5-HR-T-E (black), 6.5-SR-T-E (blue) and 6.5-SR-TM-E (red). **(A)** Map indicating the location of receivers A and B and the slip distribution of the 1978 earthquake. **(B–C)** Comparison of velocity time histories and FAS computed at receiver A and B from the three models under consideration.

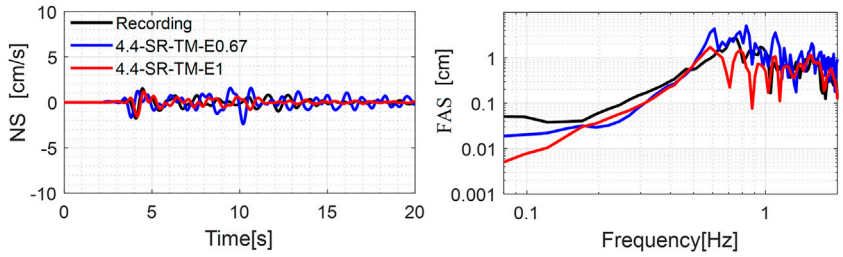

FIGURE 7
Comparison of velocity time histories and corresponding FAS (NS component) with respect to anelastic attenuation model (f_0) for M_W4.4 event.

larger than 100 m (see Figure 3D), yielding significant amplification effects at low frequency at about 0.4–0.6 Hz. As expected, the presence of the Mygdonia basin has a limited impact on the ground motions at the Thessaloniki sites because of the large distances involved. However, the signals are further enriched in the higher frequency range because of the higher complexity of the source-to-site propagation path traveling across the Mygdonia soft sediments.

4.2.2 Sensitivity to anelastic attenuation

As indicated previously, a frequency-proportional quality factor has been assumed in this work and different values of the reference frequency f_0 were tested. The target event is the M_W4.4 earthquake and the results of the simulations 4.4-SR-TM-E0.67 and 4.4-SR-TM-E1 at E03 station are analyzed and compared. Note that the simulations consider softer outcropping bedrock, with both Thessaloniki and Mygdonia basins, linear viscoelastic model, and differ only for the reference frequency f_0 which is changed from 0.67 to 1 Hz.

In Figure 7, the recorded NS velocity waveform and corresponding FAS are compared with those simulated using the two models with f_0=0.67 Hz (blue) and f_0=1 Hz (red, same as in Figure 4). The PBS with a lower reference frequency implies excessive reverberations in the coda of the signal because of lower damping values in the low-frequency range below around 1 Hz.

4.2.3 Effect of non-linear visco-elastic soil behavior

To simulate the seismic wave propagation more realistically for moderate-to-large magnitude events, the effect of non-linear visco-elastic soil behavior is investigated, referring to the

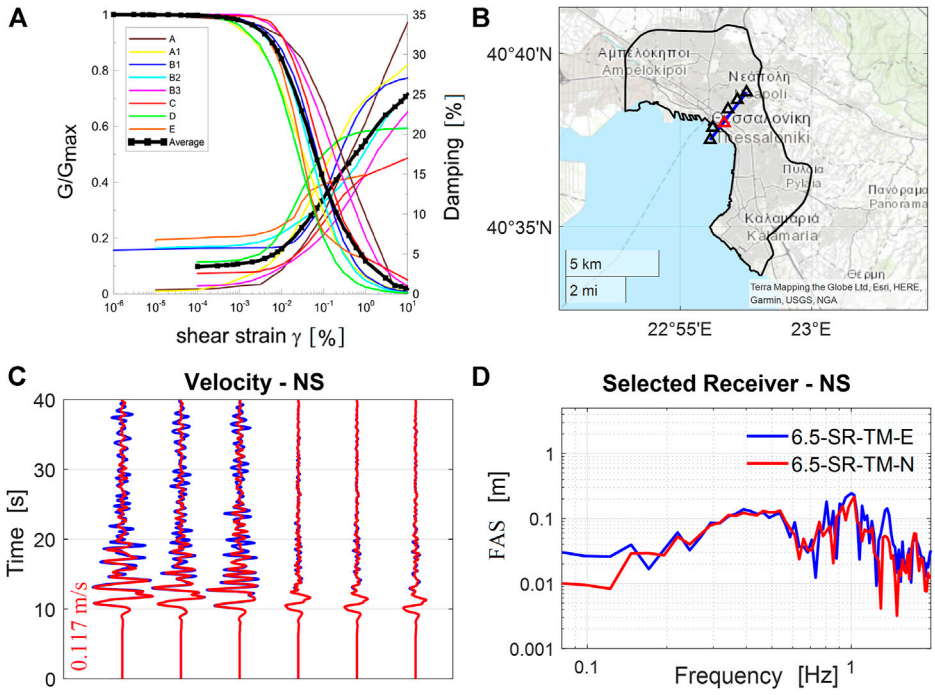

FIGURE 8
(A) G/G_{max}-γ and D-γ curves (from Smerzini et al., 2017). **(B)** A set of receivers (triangles) along a representative cross-section across Thessaloniki. **(C)** Comparison of velocity time histories (NS component) computed using a linear and non-linear elastic soil model for the set of receivers in **(B)**. **(D)** FAS of velocity waveform for a selected receiver (red triangle in Figure 8B).

1978 event. Non-linear soil behavior is implemented in SPEED by introducing and generalizing to the 3D case the shear modulus (G/G_{max}-γ) reduction and damping (D-γ) curves adopted routinely in 1D equivalent-linear approaches. Following Smerzini et al. (2017), a single set of G/G_{max}-γ and D-γ curves (see average curve in Figure 8A—black line) was employed for the shallowest 100 m thick soil deposits within both the Thessaloniki and Mygdonia basins.

In Figure 8C the horizontal (NS) velocity time histories computed under the assumption of linear (simulation 6.5-SR-TM-E, in blue) and non-linear (simulation 6.5-SR-TM-N, in red) soil behavior are shown for a set of receivers along a representative cross-section, passing through the city center (as indicated in Figure 8B). Note that not all receivers along the considered cross-section are on soft soils. Instead, the three receivers on the NE portion of the cross-section are located on outcropping bedrock.

Non-linearity features in ground shaking are found at the soft soil sites but such effects are limited and predominantly affect the coda of the signals due to the moderate level of ground shaking and the relatively narrow range of frequencies propagated by the model (<1.5 Hz). In Figure 8D, the FAS of the velocity motions simulated by the linear and non-linear model at a selected receiver (red triangle in the map of Figure 8B) is also shown. The analysis of the FAS of the two models confirms that, at this receiver and for this earthquake, non-linear effects slightly decrease the amplitude of frequencies above 0.7 Hz.

5 Earthquake ground motion for the M_W6.5 1978 earthquake

This section provides a general overview of the ground shaking simulated for the M_W6.5 1978 earthquake, emphasizing the comparison with empirical GMMs and the spatial correlation structure of ground motion. Note that the issues related to the validation of the PBS of this earthquake were already investigated by Smerzini et al. (2017), with particular reference to the finite-fault source model, which is recognized to play a major role in determining the ground motion in the epicentral area of a strong earthquake, as well as to the site response model in the Thessaloniki urban area. For the source model, a single rupture event was assumed as a reasonable simplification, although according to Papazachos et al. (1980) and Soufleris and Stewart (1981) it was a double event.

Low-frequency PBS are then enriched in the high-frequency range using the ANN2BB approach proposed by Paolucci et al. (2018; 2021). Essentially, broadband ground motions are

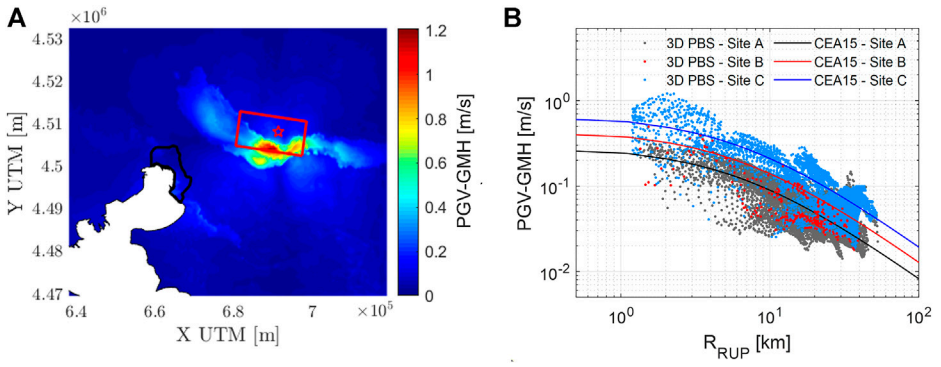

FIGURE 9
(A) Map of PGV (GMH), model 6.5-SR-TM-N. **(B)** Comparison of PGV (GMH) as a function of R_{rup} between 3D PBS and Cauzzi et al. (2015)-CEA15.

generated by combining the results of long-period PBSs with predictions of an Artificial Neural Network (ANN) trained on a set of strong motion records (in our case SIMBAD v6.0, Smerzini et al., 2014). Compared to standard hybrid approaches, one of the main advantages of the ANN2BB procedure is the capability to establish a correlation between short and long periods and, hence, to preserve a physically consistent spatial correlation structure also at high frequencies. Hereafter broadband ground motions will be considered.

5.1 Comparison with empirical ground motion models

Figure 9A shows the ground shaking map of PGV (GMH) obtained from the 3D PBS of the 1978 earthquake (model 6.5-SR-TM-N in Table 1). Maximum PGV-GMH values of 1.2 m/s are found inside the Mygdonia graben because of the coupling between the seismic source rupture with basin amplification effects. Within the urban area, PGV values between 0.025–0.25 m/s are found. Notably at the location corresponding to the station THE, a peak velocity amplitude of 6 cm/s is simulated, in fair agreement with the recorded one (equal to about 8 cm/s).

To check the overall consistency of the simulation, in Figure 9B the rate of attenuation of simulated PGV-GMH with the rupture distance (R_{rup}) is shown and compared with the one from the empirical GMM by Cauzzi et al. (2015), referred to as CEA15. Comparison is shown for three site categories (Site A, B, C) involved by the model according to EC8 (CEN-European Committee for Standardization, 2004) site classification. A satisfactory agreement is found between simulations and empirical predictions, especially in terms of site A (rock site) and site C (soft site), which are the predominant site classes in the model.

5.2 Spatial correlation of spectral accelerations

As indicated in the introduction, the 3D PBS presented in this work will represent the basis for conducting physics-based seismic risk evaluations in the Thessaloniki urban area. It is well-known that accounting for a realistic spatial correlation structure of ground motion intensity measures is relevant for risk assessment of spatially extended urban systems. To evaluate the spatial correlation, the procedure proposed by Infantino et al. (2021) is applied to the 3D PBS simulation of the 1978 Volvi earthquake. Specifically, under the hypotheses of stationarity and isotropy, the semivariogram γ is computed as a function of inter-station distance h on the within-event residuals of simulated spectral accelerations SA(T) with respect to the median trend using standard geostatistical tools. Referring the reader to Infantino et al. (2021) for the geostatistical approach, we limit herein to focus on the results of the semivariogram analysis for the 1978 earthquake. In Figure 10A, the sample semivariogram (grey dots) and the least-squares best-fitting exponential model (black line) are shown for PGA, SA (0.5 s), and SA (2.0 s), for the GMH component. In Figure 10B, the range, i.e., the distance above which the ground motion is assumed to be uncorrelated, and sill, i.e., the variance, are shown as a function of vibration period. As expected, range and sill are positively correlated. The range shows an increasing trend as a function of the period up to around 1 s. A maximum range of approximately 64 km is found, consistently with previous knowledge on this subject (e.g., Zerva and Zervas, 2002; Infantino et al., 2021), and, beyond this period, the range drops to values of about 20 km.

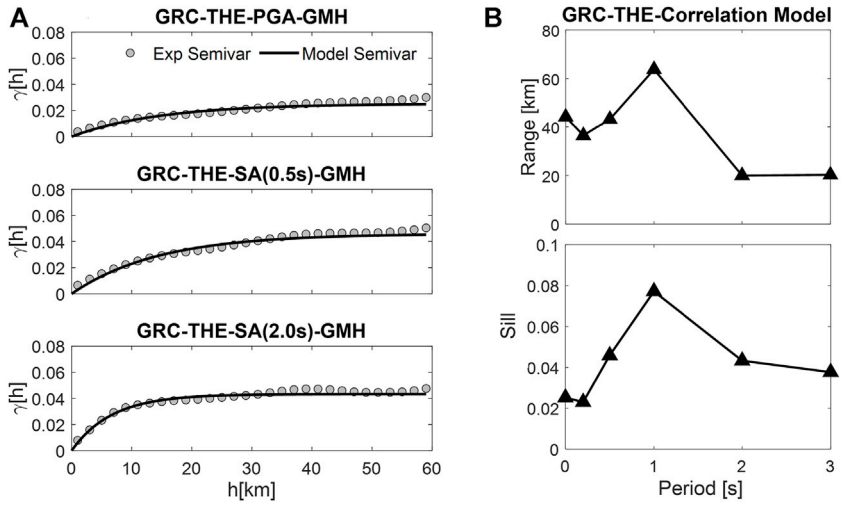

FIGURE 10
(A) Semivariogram for PGA, SA (0.5 s), and SA (2.0 s) for GMH component. **(B)** Range and sill of the best-fitting exponential model as a function of period.

A

	GER-LAN	ANTH
Mw=6.5	10	10
Mw=6.7	10	10
Mw=6.9		10
Mw=7.0	10	

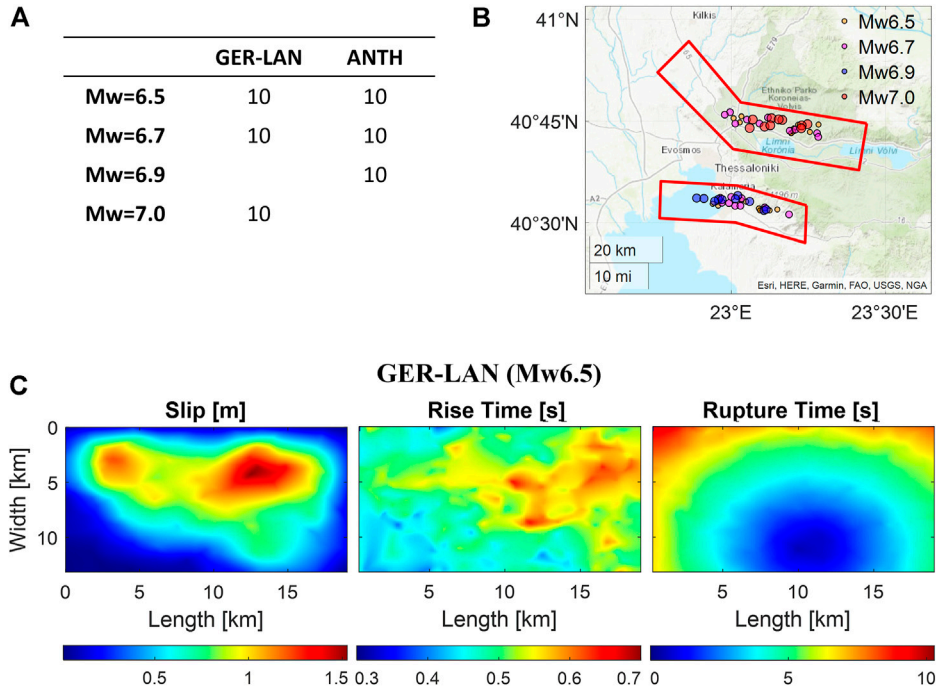

FIGURE 11
(A) List of earthquake scenarios rupturing from the GER-LAN and ANTH faults. **(B)** Epicenter distribution of the simulated earthquake scenarios. **(C)** Example of rupture realizations (M_W6.5 on GER-LAN fault) in terms of co-seismic slip, rise time and rupture time.

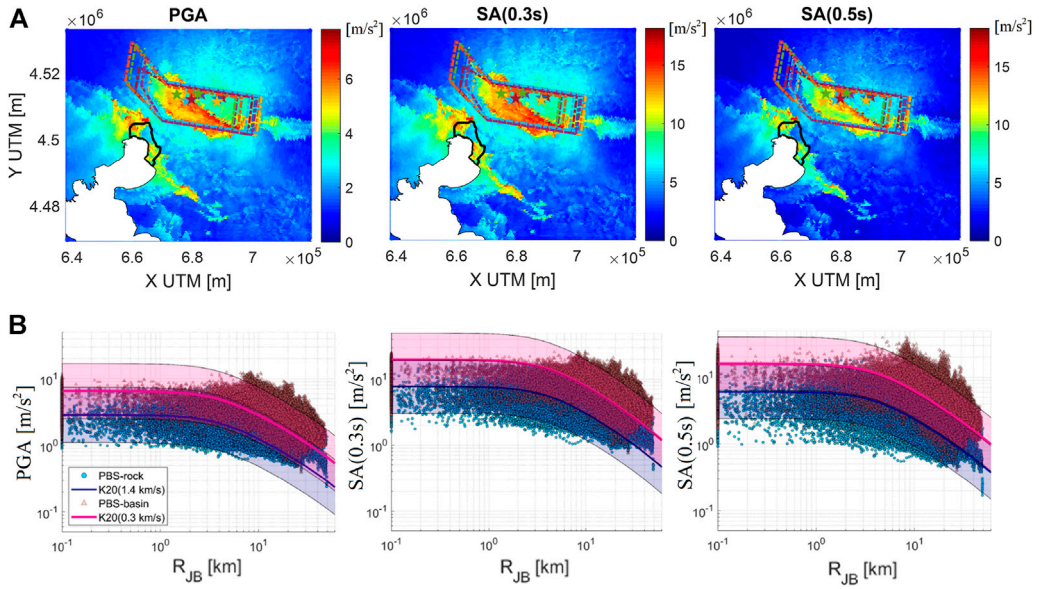

FIGURE 12
(A) Broadband simulated maps of median horizontal PGA, SA (0.3 s) and SA (0.5 s) for the 10 M_W7 GER-LAN scenarios. **(B)** Simulated spectral accelerations as a function of distance (R_{JB}) in comparison with the empirical GMM by Kotha et al., 2020 (K20) at both rock (blue) and basin (magenta) sites.

6 Variability of ground motions as a function of seismic rupture realizations

After the successful validations and sanity checks discussed in previous sections, PBS were carried out to simulate 60 different normal-type seismic rupture realizations with M_W in the range from 6.5 to 7.0 along the GER-LAN and ANTH fault systems. For all simulations, the reference model is "M"-SR-TM-N (see Table 1), where "M" (variable) is the magnitude of the scenario earthquake. As indicated in Figures 11A,B, for each fault, three magnitude levels (GER-LAN: M_W=6.5/6.7/6.9; ANTH: M_W=6.5/6.7/7.0) were simulated and, for each magnitude, a suite of 10 rupture realizations is generated. Globally, four magnitude levels from M_W=6.5 to 7.0 were considered. An example of rupture realization along the GER-LAN fault with M_W=6.5 is given in Figure 11C, in terms of the spatial distribution of co-seismic slip, rise time, and rupture time. Rupture realizations are generated within the SPEED engine assuming the kinematic source model proposed by Herrero and Bernard (1994) and applying some spatially correlated random perturbations to the rise time and rake angle following Smerzini and Villani (2012). Random perturbations of rupture times are disregarded to avoid potential super-shear issues.

Figure 12 shows an overview of the broadband simulated ground motions for the set of 10 M_W7.0 earthquake scenarios along the GER-LAN fault. Figure 12A shows the map of median horizontal (GMH) PGA, SA (0.3 s), and SA (0.5 s), assuming a lognormal statistical distribution of ground motion at each site [i.e., median = exp (μ_{ln}) where μ_{ln} is the average of natural logarithmic values]. Superimposed on the maps, the epicenters (colored stars) and corresponding effective fault areas (according to the definition by Mai and Beroza (2000) and Thingbaijam and Mai (2016)) of the 10 scenarios are displayed. In Figure 12B, for each intensity measure [PGA, SA (0.3 s), SA (0.5 s)], the entire set of 10 simulated spectral accelerations on both rock-stiff and soft sites (V_{S30}< 360 m/s) is shown as a function of Joyner-Boore distance (R_{JB}) in comparison with the GMM by Kotha et al. (2020), referred to as K20, for shallow crustal events (blue: rock, with V_{S30}=1,400 m/s; red: soft soil, with V_{S30} =300 m/s), in its ergodic formulation. V_{S30} values of empirical predictions are selected to match the average V_{S30} values implemented in the numerical model. For K20, median and corresponding dispersion bands (±σ) are shown. Short-period SA is selected herein because the Thessaloniki building stock is characterized by fundamental vibration periods approximately in this range (Riga et al., 2021). A satisfactory agreement is found between PBS and empirical predictions for all considered spectral accelerations both in terms of median values and variability.

In Figure 13, the comparison between PBS and K20 is extended to all simulated scenarios, for horizontal SA (1 s). Specifically, each graph of Figure 13 shows the decay with R_{JB} distance of horizontal SA (1 s) obtained from the entire set of 3D PBS, in comparison with K20 (median ±σ), for each target earthquake scenario. The latter is identified by the causative fault and magnitude. As commented previously, a general

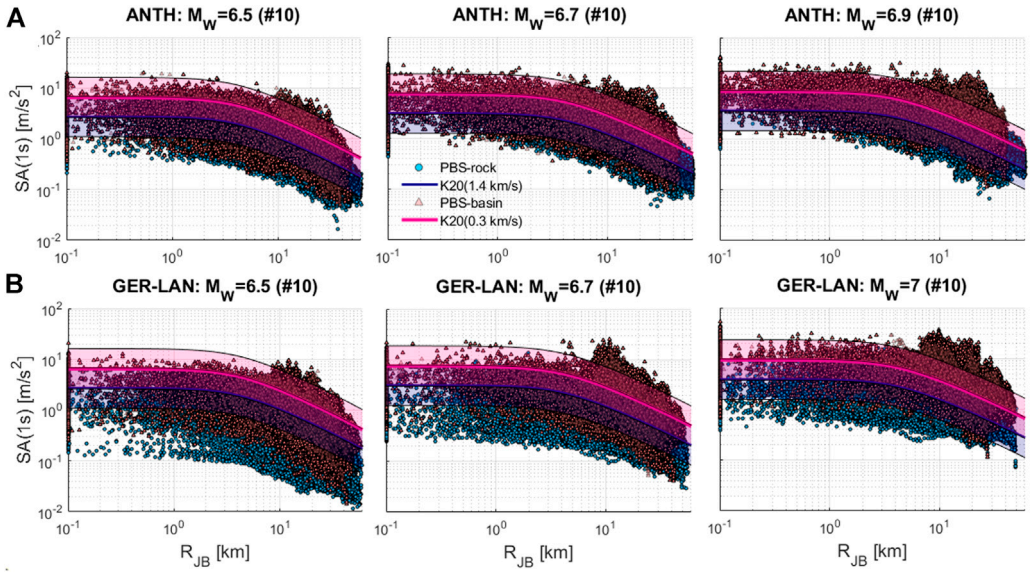

FIGURE 13
Comparison of simulated SA (1 s) as a function of distance (R_{JB}) with K20 at both rock (blue) and basin (magenta) sites for all earthquake scenarios considered in this work: **(A)** ANTH with M_W=6.5 (left), 6.7 (center), 6.9 (right) and **(B)** GER-LAN fault with M_W=6.5 (left), 6.7 (center), 7.0 (right).

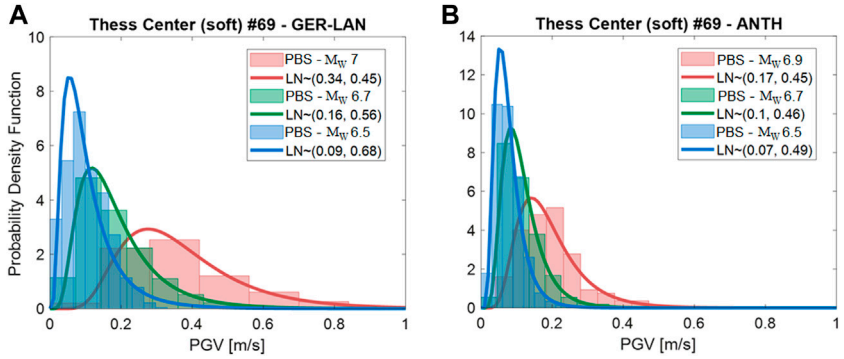

FIGURE 14
Frequency histograms and best-fitting lognormal distribution of PGV-GMH at Thessaloniki city center from the GER-LAN **(A,B)** ANTH earthquake scenarios with varying magnitude.

consistency is found between PBS and empirical predictions, although for lower magnitudes (M6.5) simulations tend to be lower, on average, than empirical GMM.

Finally, we analyzed the statistical distribution of simulated ground motions at selected sites within the urban area of Thessaloniki. To this end, Figure 14 shows the histograms of the frequency distribution of PGV-GMH values simulated at 69 soft sites within the Thessaloniki city center (at similar source-to-site distances and soil conditions), along with the best-fitting lognormal probability density function. The first statistical moments of the lognormal fit are reported in the figure legend. For a given target magnitude, the first statistical moments (median values and standard deviation) associated with GER-LAN (Figure 14A) scenarios tend to be systematically higher (or at least equal) than the ones for ANTH (Figure 14B) scenarios. This means that, for the city of Thessaloniki, earthquake scenarios from Mygdonia graben are more hazardous than those from the Anthemountas. This may be explained as a consequence of the relative location between the city of Thessaloniki and the causative faults, combined with the

radiation pattern features. The geometry and focal mechanism (normal) of both fault systems is such that directivity effects are mainly in the up-dip direction, i.e., along the path pointing to the South with respect to the hypocenter. For the ANTH case, significant ground motion amplification effects are found southward, in the opposite direction with respect to the city of Thessaloniki.

Standard deviation values (σ_{ln}) range between 0.45 and 0.7, with a central value of about 0.5, which is lower than the one associated with ergodic empirical GMMs. This is reasonable as the standard deviation from PBS simulations should be compared with non-ergodic σ_{ln} (e.g., according to Atik et al. (2010), it is about 0.4 for PGV).

7 Conclusions

In this research, a 3D spectral-element numerical model of the broader Thessaloniki region is constructed by including new features with respect to the previously published model. Specifically, the 3D seismic wave propagation model was updated by including, in addition to the Thessaloniki basin, the Mygdonia basin and by modifying the velocity of the outcropping bedrock of the crustal model. For model calibration, different sensitivity tests were performed to analyze the role played by the velocity model updates, the Q factors assumed in the simulation and the non-linear visco-elastic soil behavior. To validate the model, the PBS of two real earthquakes, a small M_W4.4 event and the destructive M_W6.5 1978 earthquake, both originating from the fault system bordering the Mygodnia basin, has been carried out. The validation is conducted at two levels, first by comparing the simulated velocity waveforms with the available recordings (for the Mw4.4 event) and with empirical GMMs (for the M6.5 event) and second, by computing the spatial correlation structure of spectral accelerations. These comparisons successfully validate the 3D model, making it suitable for calculating realistic ground motion scenarios in seismic risk studies.

After the validation of the numerical model, PBS were performed to simulate a broad set of earthquake scenarios with M_W from 6.5 to 7.0 rupturing the two fault systems (GER-LAN and ANTH), which are the most relevant for seismic hazard in the city of Thessaloniki. These scenarios will be used as input ground shaking scenarios for seismic risk analyses of the building portfolio in Thessaloniki in a future work. 10 different rupture realizations were considered to capture the aleatory variability associated with the source for each target magnitude level and causative fault. The variability of the simulated ground motions is analyzed with the twofold aim of 1) verifying that the median and scatter values of predicted response spectral accelerations are realistic, in comparison with the trends obtained from GMMs calibrated on recordings, and 2) quantifying the effect of source variability on the statistical distribution of ground motion parameters at the site. A satisfactory agreement is found between PBS and empirical GMMs for the different vibration periods, including the short periods predicted by the ANN-based technique, and for the different earthquake scenarios under consideration, both in terms of median values and standard deviation. The resulting ground motion variability at selected sites is comparable to the standard deviation values associated with non-ergodic GMMs. The analysis of the statistical distribution of PGV at sites located in the central area of Thessaloniki highlights the critical role played, for a given magnitude and similar source-to-site distances, by the relative position between the receiver and the causative fault as well as by the features of the fault rupture realization (source directivity, radiation pattern). It is found, in particular, that for the city of Thessaloniki, rupture scenarios originating from the GER-LAN fault tend to be more hazardous than those from the ANTH fault system because of the relative position with respect to the fault and the focal mechanism. The set of validated 3D PBS produced in this work may represent the basis for further studies focused on seismic risk assessment in Thessaloniki, such as 1) to develop non-ergodic hybrid (i.e., from recordings and simulations) GMMs for generating region- and site-specific seismic shaking scenarios; 2) to calibrate region-specific, anisotropic and non-stationary spatial correlation models; 3) to provide ground motion time series for constraining numerical seismic fragility studies especially at high levels of ground shaking intensity, for which recordings are still too sparse.

Data availability statement

The raw data supporting the conclusion of this article will be made available by the authors, without undue reservation.

Author contributions

JL: Modeling, Simulation, Formal Analysis, Investigation, Data curation, Writing—original draft, Writing—review and editing. CS: Conceptualization, Methodology, Supervision, Writing—Review and editing. All authors have read and agreed to the published version of the manuscript.

Funding

This work has been funded by the URBASIS Project “New challenges for Urban Engineering Seismology,” H2020-MSCA-ITN-2018, Grant Agreement No. 813137.

Acknowledgments

The authors wish to thank Manuela Vanini, Sri Sangaraju, Ilario Mazzieri and Chiara Amendola for their

support in the development and processing of the physics-based simulations. The authors thank also Fabrice Hollander for providing the 3D model of the Mygdonia basin. Authors are grateful to Alessandro Vuan and Basil Margaris for their constructive comments that helped improve the quality of the paper.

Conflict of interest

The authors declare that the research was conducted in the absence of any commercial or financial relationships that could be construed as a potential conflict of interest.

Publisher's note

Supplementary material

The Supplementary Material for this article can be found online at: https://www.frontiersin.org/articles/10.3389/feart.2022.951781/full#supplementary-material

References

Anderson, J. G. (2004). "Quantitative measure of the goodness-of-fit of synthetic seismograms," in Proceedings of the 13th World Conference on Earthquake Engineering, Vancouver, B.C., Canada, 1-6 August 2004 (Earthquake Engineering Research Institute). Paper 243.

Atik, L. A., Abrahamson, N., Bommer, J. J., Scherbaum, F., Cotton, F., Kuehn, N., et al. (2010). The variability of ground-motion prediction models and its Components. *Seismol. Res. Lett.* 81 (5), 794–801. doi:10.1785/gssrl.81.5.794

Bradley, B. A., Pettinga, D., Baker, J. W., and Fraser, J. (2017). Guidance on the utilization of earthquake-induced ground motion simulations in engineering practice. *Earthq. Spectra* 33 (3), 809–835. doi:10.1193/120216eqs219ep

Caputo, R., Chatzipetros, A., and Pavlides, S. (2012). The Greek database of seismogenic sources (GreDaSS): State-of-the-art for northern Greece. *Ann. Geophys.* 55 (5), 859–894. doi:10.4401/ag-5168

Caramenti, L., Menafoglio, A., Sgobba, S., and Lanzano, G. (2022). Multi-source geographically weighted regression for regionalized ground-motion models. *Spat. Stat.* 47, 100610. doi:10.1016/j.spasta.2022.100610

Cauzzi, C., Faccioli, E., Vanini, M., and Bianchini, A. (2015). Updated predictive equations for broadband (0.01–10s) horizontal response spectra and peak ground motions, based on a global dataset of digital acceleration records. *Bull. Earthq. Eng.* 13, 1587–1612. doi:10.1007/s10518-014-9685-y

CEN - European Committee for Standardization (2004). *Eurocode 8 Design of structures for earthquake resistance -Part 1: General rules, seismic actions and rules for buildings, EN 1998-1*. London: British Standards Institution.

Chen, Y., and Baker, J. W. (2019). Spatial correlations in CyberShake physics-based ground-motion simulations. *Bull. Seismol. Soc. Am.* 109 (6), 2447–2458. doi:10.1785/0120190065

Cotton, F., Scherbaum, F., Bommer, J., and Bungum, H. (2006). Criteria for selecting and adjusting ground-motion models for specific target regions: Application to central europe and rock sites. *J. Seismol.* 10, 137–156. doi:10.1007/s10950-005-9006-7

Crowley, H., Rodrigues, D., Silva, V., Toma-Danila, D., Despotaki, V., Riga, E., et al. (2020). Exposure model for European seismic risk assessment. *Earthq. Spectra* 36 (1), 252–273. doi:10.1177/8755293020919429

Douglas, J., and Edwards, B. (2016). Recent and future developments in earthquake ground motion estimation. *Earth-Science Rev.* 160, 203–219. doi:10.1016/j.earscirev.2016.07.005

Evangelista, L., Gaudio, S. D., Smerzini, C., D'Onofrio, A., Festa, G., Iervolino, I., et al. (2017). Physics-based seismic input for engineering applications: A case study in the aterno river valley, central Italy. *Bull. Earthq. Eng.* 15, 2645–2671. doi:10.1007/s10518-017-00897

Herrero, A., and Bernard, P. (1994). A kinematic self-similar rupture process for earthquakes. *Bull. Seismol. Soc. Am.* 84 (4), 1216–1228. doi:10.1785/BSSA0840041216

Infantino, M., Mazzieri, I., Özcebe, A. G., Paolucci, R., and Stupazzini, M. (2020). 3D physics-based numerical simulations of ground motion in istanbul from earthquakes along the marmara segment of the north anatolian fault. *Bull. Seismol. Soc. Am.* 110 (5), 2559–2576. doi:10.1785/0120190235

Infantino, M., Smeizini, C., and Lin, J. (2021). Spatial correlation of broadband ground motions from physics-based numerical simulations. *Earthq. Eng. Struct. Dyn.* 50 (10), 2575–2594. doi:10.1002/eqe.3461

Kotha, S. R., Weatherill, G., Bindi, D., and Cotton, F. (2020). A regionally-adaptable ground-motion model for shallow crustal earthquakes in Europe. *Bull. Earthq. Eng.* 18, 4091–4125. doi:10.1007/s10518-020-00869-1

Laurendeau, A., Bard, P. Y., Hollender, F., Perron, V., Foundotos, L., Ktenidou, O. J., et al. (2018). Derivation of consistent hard rock ($1000 < V_S < 3000$ m/s) GMPEs from surface and down-hole recordings: Analysis of KiK-net data. *Bull. Earthq. Eng.* 16, 2253–2284. doi:10.1007/s10518-017-0142-6

Mai, P., and Beroza, G. (2000). Source scaling properties from finite-fault-rupture models. *Bull. Seismol. Soc. Am.* 90 (3), 604–615. doi:10.1785/0119990126

Maufroy, E., Kristek, J., Moczo, P., Chaljub, E., Hollender, F., Bard, P., et al. (2016). 3D numerical simulation and ground motion prediction: Verification, validation and beyond – lessons from the E2VP project. *Soil Dyn. Earthq. Eng.* 91, 53–71. doi:10.1016/j.soildyn.2016.09.047

Mazzieri, I., Stupazzini, M., Guidotti, R., and Smerzini, C. (2013). Speed: Spectral elements in elastodynamics with discontinuous galerkin: A non-conforming approach for 3D multi-scale problems. *Int. J. Numer. Methods Eng.* 95 (12), 991–1010. doi:10.1002/nme.4532

McCallen, D., Petrone, F., Miah, M., Pitarka, A., Rodgers, A., Abrahamson, N., et al. (2021b). EQSIM - a multidisciplinary framework for fault-to-structure earthquake simulations on exascale computers, part II: Regional simulations of building response. *Earthq. Spectra* 37 (2), 736–761. doi:10.1177/8755293020970980

McCallen, D., Petersson, A., Rodgers, A., Pitarka, A., Miah, M., Petrone, F., et al. (2021a). EQSIM - a multidisciplinary framework for fault-to-structure earthquake simulations on exascale computers part I: Computational models and workflow. *Earthq. Spectra* 37 (2), 707–735. doi:10.1177/8755293020970982

Paolucci, R., Mazzieri, I., and Smerzini, C. (2015). Anatomy of strong ground motion: Near-source records and three-dimensional physics-based numerical simulations of the Mw 6.0 2012 may 29 Po plain earthquake, Italy. *Geophys. J. Int.* 203 (3), 2001–2020. doi:10.1093/gji/ggv405

Paolucci, R., Gatti, F., Infantino, M., Smerzini, C., Özcebe, A. G., Stupazzini, M., et al. (2018). Broadband ground motions from 3D physics-based numerical simulations using artificial neural networks. *Bull. Seismol. Soc. Am.* 108 (3), 1272–1286. doi:10.1785/0120170293

Paolucci, R., Aimar, M., Ciancimino, A., Dotti, M., Foti, S., Lanzano, G., et al. (2021). Checking the site categorization criteria and amplification factors of the 2021 draft of Eurocode 8 Part 1–1. *Bull. Earthq. Eng.* 19, 4199–4234. doi:10.1007/s10518-021-01118-9

Paolucci, R., Chiecchio, A., and Vanini, M. (2022). The older the better? The strange case of empirical ground motion models in the near-source of moderate-to-large magnitude earthquakes. *Bull. Earthq. Eng.* 20, 1325–1342. doi:10.1007/s10518-021-01304-9

Papazachos, B., and Papazachou, C. (1997). *The earthquakes of Greece*. France: Editions ZITI.

Papazachos, B., Mountrakis, D., Psilovikos, A., and Leventakis, G. (1980). Focal properties of the 1978 earthquakes in the Thessaloniki area. *Bulg. Geophys* 6 (1), 72–80.

Paradisopoulou, P. M., Karakostas, V. G., Papadimitriou, E. E., Tranos, M. D., Papazachos, C. B., Karakaisis, G. F., et al. (2006). Microearthquake study of the broader Thessaloniki area (Northern Greece). *Ann. Geophys.* 49 (4-5), 1081–1093. doi:10.4401/ag-3112

Pavlides, S., and Kilias, A. (1987). Neotectonic and active faults along the serbomacedonian zone (SE chalkidiki, northern Greece). *Ann. Tect.* 1 (2), 97–104.

Raucoules, D., Parcharidis, I., Feurer, D., Novalli, F., Ferretti, A., Carnec, C., et al. (2008). Ground deformation detection of the greater area of Thessaloniki (Northern Greece) using radar interferometry techniques. *Nat. Hazards Earth Syst. Sci.* 8 (4), 779–788. doi:10.5194/nhess-8-779-2008

Riga, E., Karatzetzou, A., Apostolaki, S., Crowley, H., and Pitilakis, K. (2021). Verification of seismic risk models using observed damages from past earthquake events. *Bull. Earthq. Eng.* 19, 1–32. doi:10.1007/s10518-020-01017-5

Schiappapietra, E., and Douglas, J. (2020). Modelling the spatial correlation of earthquake ground motion: Insights from the literature, data from the 2016–2017 central Italy earthquake sequence and ground-motion simulations. *Earth-Science Rev.* 203, 103139. doi:10.1016/j.earscirev.2020.103139

Schiappapietra, E., and Smerzini, C. (2021). Spatial correlation of broadband earthquake ground motion in Norcia (Central Italy) from physics-based simulations. *Bull. Earthq. Eng.* 19, 4693–4717. doi:10.1007/s10518-021-01160-7

Schiappapietra, E., Stripajová, S., Pažák, P., Douglas, J., and Trendafiloski, G. (2022). Exploring the impact of spatial correlations of earthquake ground motions in the catastrophe modelling process: A case study for Italy. *Bull. Earthq. Eng.* doi:10.1007/s10518-022-01413-z

Sgobba, S., Felicetta, C., Lanzano, G., Ramadan, F., D'Amico, M., Pacor, F., et al. (2021a). NESS2.0: An updated version of the worldwide dataset for calibrating and adjusting ground-motion models in near source. *Bull. Seismol. Soc. Am.* 111 (5), 2358–2378. doi:10.1785/0120210080

Sgobba, S., Lanzano, G., and Pacor, F. (2021b). Empirical nonergodic shaking scenarios based on spatial correlation models: An application to central Italy. *Earthq. Eng. Struct. Dyn.* 50, 60–80. doi:10.1002/eqe.3362

Smerzini, C., and Pitilakis, K. (2018). Seismic risk assessment at urban scale from 3D physics-based numerical modeling: The case of Thessaloniki. *Bull. Earthq. Eng.* 16 (7), 2609–2631. doi:10.1007/s10518-017-0287-3

Smerzini, C., and Villani, M. (2012). Broadband numerical simulations in complex near-field geological configurations: The case of the 2009 Mw 6.3 L'aquila earthquake. *Bull. Seismol. Soc. Am.* 102 (6), 2436–2451. doi:10.1785/0120120002

Smerzini, C., Galasso, C., Iervolino, I., and Paolucci, R. (2014). Ground motion record selection based on broadband spectral compatibility. *Earthq. Spectra* 30 (4), 1427. doi:10.1193/052312EQS197M

Smerzini, C., Pitilakis, K., and Hashemi, K. (2017). Evaluation of earthquake ground motion and site effects in the Thessaloniki urban area by 3D finite-fault numerical simulations. *Bull. Earthq. Eng.* 15, 787–812. doi:10.1007/s10518-016-9977-5

Soufleris, C., and Stewart, G. (1981). A source study of the Thessaloniki (northern Greece) 1978 earthquake sequence. *Geophys. J. Int.* 67 (2), 343–358. doi:10.1111/j.1365-246X.1981.tb02754.x

Stafford, P. J. (2014). Crossed and nested mixed-effects approaches for enhanced model development and removal of the ergodic assumption in empirical ground-motion models. *Bull. Seismol. Soc. Am.* 104 (2), 702–719. doi:10.1785/0120130145

Stupazzini, M., Paolucci, R., and Igel, H. (2009). Near-fault earthquake ground-motion simulation in the Grenoble valley by a high-performance spectral element code. *Bull. Seismol. Soc. Am.* 99 (1), 286–301. doi:10.1785/0120080274

Stupazzini, M., Infantino, M., Allmann, A., and Paolucci, R. (2021). Physics-based probabilistic seismic hazard and loss assessment in large urban areas: A simplified application to istanbul. *Earthq. Eng. Struct. Dyn.* 50, 99–115. doi:10.1002/eqe.3365

Thingbaijam, K., and Mai, P. (2016). Evidence for truncated exponential probability distribution of earthquake slip. *Bull. Seismol. Soc. Am.* 106 (4), 1802–1816. doi:10.1785/0120150291

Touhami, S., Gatti, F., Lopez-Caballero, F., Cottereau, R., Corrêa, L., Aubry, L., et al. (2022). SEM3D: A 3D high-fidelity numerical earthquake simulator for broadband (0–10 Hz) seismic response prediction at a regional scale. *Geosciences* 12 (3), 112. doi:10.3390/geosciences12030112

Tranos, M., Kilias, A., and Mountrakis, D. M. (1999). Geometry and kinematics of the tertiary post-metamorphic Circum Rhodope Belt thrust system (CRBTS), northern Greece. *Bull. Geol. Soc. Greece* 33, 5–16.

Tranos, M., Papadimitrioub, E., and Kiliasa, A. (2003). Thessaloniki–Gerakarou Fault zone (TGFZ): The Western extension of the 1978 Thessaloniki earthquake fault (northern Greece) and seismic hazard assessment. *J. Struct. Geol.* 25 (2003), 2109–2123. doi:10.1016/S0191-8141(03)00071-3

Villani, M., and Abrahamson, N. (2015). Repeatable site and path effects on the ground-motion sigma based on empirical data from southern California and simulated waveforms from the CyberShake platform. *Bull. Seismol. Soc. Am.* 105 (5), 2681–2695. doi:10.1785/0120140359

Wald, D. J., Worden, C. B., Thompson, E. M., and Hearne, M. (2021). ShakeMap operations, policies, and procedures. *Earthq. Spectra* 38 (1), 756–777. doi:10.1177/87552930211030298

Worden, C. B., Thompson, E. M., Hearne, M., and Wald, D. J. (2020). *ShakeMap manual online: Technical manual, user's guide, and software guide*. United States: U.S. Geological Survey. doi:10.5066/F7D21VPQ

Zerva, A., and Zervas, V. (2002). Spatial variation of seismic ground motions: An overview. *Appl. Mech. Rev.* 55 (3), 271–297. doi:10.1115/1.1458013

frontiers | Frontiers in Earth Science

TYPE Original Research
PUBLISHED 11 October 2022
DOI 10.3389/feart.2022.932110

OPEN ACCESS

EDITED BY
Matteo Picozzi,
University of Naples Federico II, Italy

REVIEWED BY
Stefania Tarantino,
Istituto Nazionale di Geofisica e Vulcanologia, Italy
Eugenio Chioccarelli,
Università Mediterranea di Reggio Calabria, Italy

*CORRESPONDENCE
Bojana Petrovic,
bpetrovic@ogs.it

SPECIALTY SECTION
This article was submitted to Geohazards and Georisks, a section of the journal Frontiers in Earth Science

RECEIVED 29 April 2022
ACCEPTED 01 August 2022
PUBLISHED 11 October 2022

CITATION
Petrovic B, Scaini C and Parolai S (2022), Applying the damage assessment for rapid response approach to the august 24 M6 event of the seismic sequence in central Italy (2016).
Front. Earth Sci. 10:932110.
doi: 10.3389/feart.2022.932110

Applying the damage assessment for rapid response approach to the august 24 M6 event of the seismic sequence in central Italy (2016)

Bojana Petrovic*, Chiara Scaini and Stefano Parolai

National Institute of Oceanography and Applied Geophysics - OGS, Italy

Seismic monitoring networks are increasingly being used in urban areas to record and locate earthquakes. Recordings in the proximity of buildings also allow assessing, as a first approximation, the expected building damage. The DARR (Damage Assessment for Rapid Response) method provides local-scale information on expected damage patterns. The potential of this approach is discussed here for the August 24 M6 event of the Central Italy seismic sequence (2016–2017). We focus only on the first event of the sequence because cumulative damage is outside the scope of this study. The earthquake recordings are available from two Italian monitoring networks: the Italian Accelerometric Archive (ITACA) and the OSS (Osservatorio Sismico delle Strutture), which collects data from monitored buildings and bridges in Italy. We selected four target areas (Amatrice, Norcia, Visso and Sulmona) characterized by different epicentral distances and building typologies, that suffered different levels of damage during the M6 event on 24 August 2016. Using recordings either in the free field or in the basement of buildings, the expected relative displacement of building typologies common in the studied areas is calculated with the DARR method. Using predefined damage thresholds from literature, the obtained results allow quantifying the expected damage for dominant building typologies in the surroundings of the recording sites. We investigate and discuss the potential use and applicability of the DARR method in different areas depending on the epicentral distance and building characteristics. The results indicate that the DARR approach is useful for supporting and improving rapid response activities after a seismic event.

KEYWORDS

seismic damage assessment, rapid response, DARR method, seismic building monitoring, Central Italy 2016 earthquake sequence, simplified building models, dynamic behavior of buildings, seismic retrofitting

Introduction

Most casualties caused directly by earthquakes are due to damage in residential buildings (So and Spence, 2013). For this reason, the rapid assessment of expected damage can support effective response actions and prioritize interventions, thereby reducing human losses. Assessing damage to buildings depends on multiple factors, such as the characteristics of the ground shaking, the building's vulnerability (and its response to shaking) and the occurrence of local amplification (site effects).

Ground motion recordings allow extracting the ground shaking characteristics and, in particular, the peak parameters (e.g., peak ground acceleration, PGA). The engineering community has devoted considerable effort to identifying the critical values of ground motion that lead to building damage and collapse. This was done based on both empirical (Rota et al., 2008; Masi et al., 2019) and analytical (Borzi et al., 2008; Donà et al., 2020) approaches. Fragility and vulnerability curves have been defined for different building types and are currently used to estimate expected damage in case of seismic events (e.g., Borzi et al., 2008; Poggi et al., 2020).

Measuring and analyzing the ground motion is therefore of paramount importance for estimating expected damage to buildings. However, using peak ground motion parameters to assess expected damage does not account for the frequency content of the recorded signal. For this reason, the coverage of seismic monitoring networks is increasing worldwide and includes seismic stations installed both in the field and in buildings or infrastructure (Mori et al., 1998; Trifunac et al., 2001; Okada et al., 2004; Espinosa-Aranda et al., 2009; Gorini et al., 2010; Satriano et al., 2011; Wu et al., 2013; Parolai et al., 2017; Bragato et al., 2021). In Italy, ground motion recordings are collected in the Italian Accelerometric Archive (ITACA, Russo et al., 2022). In addition, the Italian monitoring network, OSS (Osservatorio Sismico delle Strutture, Dolce et al., 2017) comprises more than 120 public buildings, and some bridges and dams continuously monitored by low-cost seismic sensors.

The recorded signal in buildings allows assessing their response to earthquakes and monitoring changes to their structural health (e.g., Rahmani et al., 2015; Rahmani and Todorovska, 2021). Past studies have demonstrated the relevance of assessing the building's fundamental period (Goel and Chopra, 1997), which is a key parameter for estimating the expected performance of buildings during earthquakes (Michel et al., 2010). Some authors (e.g., Crowley and Pinho, 2010; Michel et al., 2010) pointed out discrepancies between the simplified period-height relationships used in most building codes (e.g., Eurocode, CEN 2004) and the fundamental period estimated experimentally using ambient noise measurements (e.g., Gallipoli et al., 2009). Thus, several authors proposed period-height relationships based on experimentally estimated fundamental periods (e.g., Gallipoli et al., 2009; Michel et al., 2010; Gallipoli et al., 2022). It is also relevant to compare the fundamental frequency range of buildings and soils (e.g., Gallipoli et al., 2020) to assess the possible occurrence of soil-building resonance (e.g., Bard et al., 1996; Mucciarelli et al., 2004).

Since 2009, the OSS network has provided significant information on the dynamic response of single buildings during the main Italian earthquakes (Spina et al., 2010). The occurrence of damage is estimated by comparing the observed interstory drift values with thresholds defined in literature (e.g., Rossetto and Elnashai, 2003 for reinforced concrete, RC, buildings). However, the procedure requires at least two recordings (one at the top and another at the bottom of the building) in order to estimate the interstory drift ratio.

Based solely on recordings at the bottom of buildings (or in the free field nearby), it is possible to rapidly estimate the occurrence of damage by taking the simplified buildings linear dynamic response into account (Scaini et al., 2021; Petrovic et al., 2022). In fact, the DARR (Damage Assessment for Rapid Response) method uses the entire recording and simulates the maximum relative displacement (drift) for a specific building type (defined by fundamental frequency and damping ratio) based on simplified oscillators (single or multi-degree-of-freedom) using the Z transform (Lee, 1990; Jin et al., 2004; Parolai et al., 2015). The method has produced successful results for selected building types, including unreinforced masonry (URM) buildings (Petrovic et al., 2022), a common building typology in Italy and in particular in Central Italy (Sorrentino et al., 2019).

The DARR method can be extended to estimate expected damage to specific building typologies in the surrounding area of a recording (Scaini et al., 2021). In addition to interstory drift limits (e.g., Borzi et al., 2008; Rossetto et al., 2016), relative displacement limits (e.g., Lagomarsino and Giovinazzi, 2006) are available for different building types. These include both RC and URM typologies associated with different characteristics (height, age of construction, seismic design level). The occurrence of damage is assessed by comparing the estimated relative displacement or interstory drift (ratio) for each building type with the limits available in literature. However, DARR is based on a number of assumptions, in particular on an average building height (when considering building types instead of specific buildings) and the simplified dynamic behavior of building typologies (dominated by the fundamental mode/modes, obtained from period-height relationships from literature), the choice of thresholds for damage occurrence, and the homogeneous soil conditions in the target area.

In this work, we present an application of the DARR method to the first shock of the Central Italy seismic sequence, which occurred on 24 August 2016 (Rossi et al., 2018). Recordings are available at several locations (both in free field and in structures) and at different distances from the epicenter, from both the ITACA and OSS databases. We focus our study on four target areas (Amatrice, Norcia, Visso and Sulmona) with different epicentral distances for which different damage levels have

TABLE 1 Relative displacement limits (in centimeters) for selected building typologies according to Lagomarsino and Giovinazzi (2006).

Building typology	Seismic code	Relative displacement limits (cm) for selected damage levels		
		No damage (ND)	Extensive damage (ED)	Complete damage (CD)
Simple stone URM, low-rise (1–2 story)	n.a.	<0.19	>0.85	>1.40
Simple stone URM, mid-rise (3–5 story)	n.a.	<0.42	>1.35	>2.10
Regular URM, RC-floors, low-rise (1–2 story)	n.a.	<0.28	>1.38	>2.36
Regular URM, RC-floors, mid-rise (3–5 story)	n.a.	<0.62	>2.19	>3.50
RC frame, low-rise (1–3 story)	Low code	<1.67	>4.78	>7.16
RC frame, mid-rise (4–7 story)		<2.60	>7.42	>11.14
RC frame, low-rise (1–3 story)	Moderate code	<1.96	>6.48	>10.15
RC frame, mid-rise (4–7 story)		<2.79	>10.19	>16.39
RC frame, low-rise (1–3 story)	High code	<1.84	>7.47	>12.30
RC frame, mid-rise (4–7 story)		<2.23	>10.59	>17.99

Extensive and complete structural damage (ED, CD respectively) are associated with the exceedance of the respective limits. No damage (ND) is expected for displacement lower than the ND limit, while non-structural damage (NSD) is expected in all other cases. n.a. - not applicable.

been observed. The analysis of the available recordings of the event in the four locations shows that, based on the earthquake recordings and the building characteristics, it is possible to quickly estimate whether structural damage is expected for previously characterized building typologies dominant in the study area. Outcomes are compared with damage evidence collected during field surveys (visual inspection and subsequent damage assessment) performed in these areas after the 24 August 2016 event (e.g., Fiorentino et al., 2018; Sorrentino et al., 2019; D'Ayala et al., 2019).

DARR method and damage thresholds

For the damage assessment, we use DARR, a method proposed by Scaini et al. (2021) and Petrovic et al. (2022). The linear dynamic behavior of buildings is simulated as simple single-degree-of-freedom (SDOF) oscillators, describing the buildings in a first order approximation by their fundamental frequency and the damping ratio. The fundamental frequencies are estimated from building-soil specific period-height relationships from Gallipoli et al. (2022). An average story height of 3.5 m is assumed for the ground floor (e.g., Chieffo et al., 2019), for the upper storys 3 m are considered (e.g., Sorrentino et al., 2019). The latter is compatible with the minimum required height of 2.7 m in Italy and some other European countries (Appolloni and D'Alessandro, 2021) and accounts for the floor thickness. Additionally, 1.5 m are added for the roof. For the damping ratio, a standard value of 5% (e.g., Eurocode 8, CEN 2004) is used. The relative displacement between top and bottom (drift) is calculated with the Z transform (e.g., Lee, 1990; Jin et al., 2004; Parolai et al., 2015). The total displacement at the top can be obtained as the sum of the displacement at the bottom and the relative displacement. The interstory drift ratio is estimated by dividing the relative displacement (drift) by the building height.

The occurrence of damage can be estimated using either interstory drift (e.g., Rossetto et al., 2016) or relative displacement limits from literature (e.g., Lagomarsino and Giovinazzi, 2006), based on the characteristics (construction materials) and height of the studied buildings. In this study, we consider the relative displacement damage limits for low to mid-rise URM (simple stone and regular) and RC buildings, representative of the Italian building stock and dominant in the study area. The relative displacement thresholds for different damage states are adopted from Lagomarsino and Giovinazzi (2006, Table 1) for different building typologies. The limits for low, moderate and high-code RC frames are adopted for the zone of higher seismicity in the Italian official seismic zonation (Italian Seismic Hazard map, Meletti et al., 2006; Stucchi et al., 2011 and following modifications). The description of damage levels for both masonry and reinforced concrete buildings is based on the EMS-98 (Grünthal, 1998) macroseismic scale. The method focuses on the expected occurrence of structural damage (extensive or complete). Extensive damage corresponds to level-3 damage of EMS-98 (moderate structural damage, heavy non-structural damage). Complete damage includes

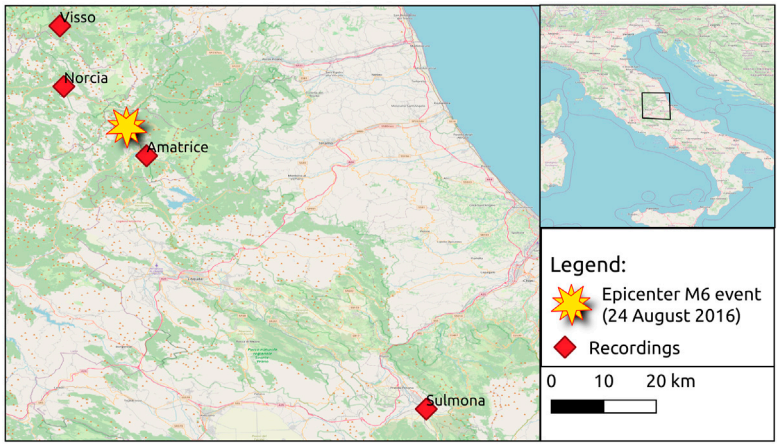

FIGURE 1
Map showing the locations of the four test sites Amatrice, Norcia, Visso and Sulmona (red rhombi) and the epicenter of the M6 event (yellow star).

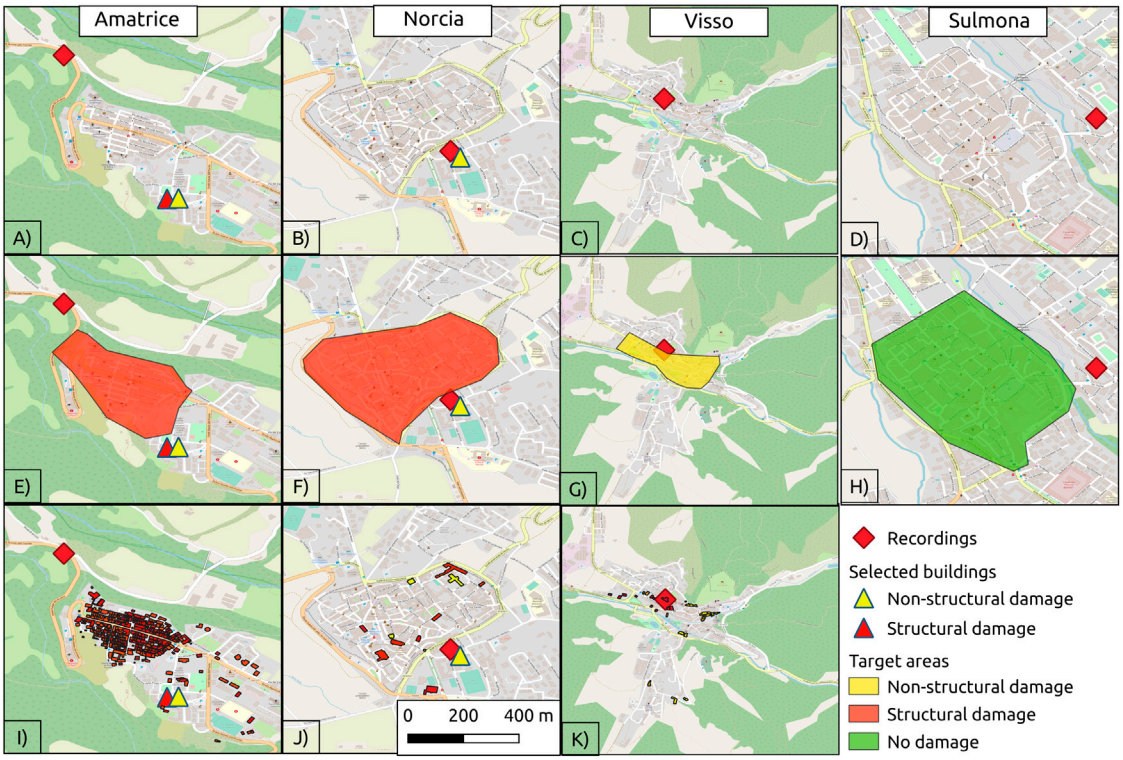

FIGURE 2
(A–D): Location of the earthquake recordings and the selected buildings for the four target areas (from left to right, Amatrice, Norcia, Visso and Sulmona). **(E–H)**: Results of DARR for 3-story simple stone URM buildings in the target areas of Amatrice, Norcia, Visso and Sulmona. **(I–K)**: Documented damage collected from post-event surveys after the 24 August 2016 event in Amatrice, Norcia and Visso. The damage patterns are extracted from OpenStreetMap (OpenStreetMap contributors, 2015) and are in good agreement with the documented post-event damage (e.g., Gaudiosi et al., 2016; Stewart and Lanzo, 2018; D'Ayala et al.,. 2019). In Sulmona no damage was observed in Sulmona.

both level 4 and 5 of the EMS-98 scale (heavy and very heavy structural damage and/or collapse). The absence of damage is associated with a relative displacement lower than 70% of the yielding displacement (Table 1), which corresponds to level-1 damage of the EMS-98 following Lagomarsino and Giovinazzi (2006). In all other cases, non-structural damage is assumed.

Damage assessment for building typologies in selected target areas

Our study makes use of the recordings collected by the OSS network (Osservatorio Sismico delle Strutture, Dolce et al., 2017) and the ITACA database (Russo et al., 2022), in order to estimate the expected damage for selected locations for the 24 August 2016 M6 event. We focus on the first event of the Central Italy 2016 sequence, since the applied DARR method (Scaini et al., 2021; Petrovic et al., 2022) does not account for cumulative damage.

Based on the analysis of the damage patterns after the first event of the Central Italy seismic sequence (24 August 2016, Figure 1), four areas (Figures 2A–D) are selected for the application of DARR: Amatrice, Norcia, Visso and Sulmona. Two of the selected areas were very close to the epicenter (Amatrice and Norcia, respectively 9 and 15 km away). Nonetheless, the observed damage patterns (Stewart and Lanzo, 2018; D'Ayala et al., 2019) are very different due to the characteristics of the buildings (e.g., presence or absence of retrofitting) and the occurrence of site effects. Moreover, the different damage patterns could be due to the near-source effect (Luzi et al., 2016; Tinti et al., 2016; Chiaraluce et al., 2017). The third area (Visso) is located at a medium distance of 28 km from the epicenter. Damage was mostly observed in the central-western part of the town and hardly in the historical center located in the southeastern part (Gaudiosi et al., 2016). The fourth area (Sulmona) is located at a greater distance from the epicenter (approximately 90 km): here, the shaking was perceived by inhabitants but did not cause significant damage to the buildings.

Since for Amatrice no recordings were available from the OSS network, a free field recording from the ITACA database located close to the historical center was used to estimate the expected damage for selected building typologies. For Norcia, Visso and Sulmona, recordings of sensors of the OSS, installed in the basement of a building located in the historical center (Norcia: 3 story RC school building, Visso: 2 story simple stone URM school building, Sulmona: 4 story RC hospital building) were used for the damage assessment in the target areas which correspond to the historical centers of the three towns. In the case of Visso, the target area also includes an urbanized area located in the central-western part of the town.

The building stock of the historical centers of the four considered towns is/was composed mainly of low- and mid-rise simple stone buildings mostly constructed before 1919 (Munari et al., 2010; Sorrentino et al., 2019). In addition, low- to mid-rise regular masonry and RC frame buildings were considered due to their presence in the studied areas. These buildings were constructed typically between 1950 and 1980.

Amatrice

The ground motion recordings in Amatrice are available from the ITACA database. The considered station AMT (Figure 2A, red square) is located on sandy-silty lithofacies (Todrani and Cultrera, 2021), which can be classified as soft soils. The minimum and maximum distances between the recording and the buildings in the old town are of 200 and 600 m, respectively (Figure 2A). Unfortunately, no recording in the historical center of Amatrice is available.

According to Vignaroli et al. (2019) and Milana et al. (2018), the old town of Amatrice was built on sands or conglomerates. Amplification effects affect the ground shaking on the Amatrice terrace (Milana et al., 2018). We assume that the recording from the AMT station can be used to assess the expected damage in the old town, but the ground acceleration on the Amatrice terrace might be larger than at the recording site due to amplification effects (Gaudiosi et al., 2021).

Following the DARR method, the relative displacement (drift) for different building typologies representative for the building stock of Amatrice (2 and 3 story URM buildings in the historical center and 3–6 story RC buildings in the town) are estimated (Table 2). The maximum absolute value of both components (aligned with the main perpendicular directions of the town) is reported in Table 2.

The studied building typologies were prevalent in the town of Amatrice. The building stock in the historical center was predominantly simple stone URM buildings (95%), most of them with 2 or 3 stories (Sorrentino et al., 2019). The fundamental periods T of the different building typologies are calculated using the period-height relationships proposed by Gallipoli et al. (2022) for URM and RC buildings on soft soils (URM: T = 0.0170H, RC-MRF: T = 0.0164H). The recordings of station AMT were first rotated to be aligned with the main perpendicular directions of the historical center, to take the orientation of the studied buildings (as a first order approximation, see Figure 2) into account. Based on the relative displacement limits in Table 1 (low-rise simple stone URM, extensive damage: 0.85 cm, complete damage: 1.40 cm; low-rise regular URM, extensive damage: 1.38 cm, complete damage: 2.36 cm), non-structural damage should be expected for 2 story simple stone and regular URM buildings (Table 2, relative displacement: 0.63 cm). Following the damage limits in Table 1, extensive damage should be expected for 3 story simple stone URM buildings (Table 2, relative displacement: 1.57 cm) and non-structural damage for 3 story regular URM buildings.

TABLE 2 Damage assessment for Amatrice for the most common building typologies (2-3 story URM and 3–6 story RC buildings).

Building typology	Average building height (m)	Period T* (s)	Frequency f (Hz)	Relative displacement (cm)	Expected damage
2 story URM	8	0.136	7.35	0.63	Simple stone and regular URM: NSD
3 story URM	11	0.187	5.35	1.57	Simple stone URM: ED, Regular URM: NSD
3 story RC	11	0.180	5.54	1.32	Low and moderate code RC frame: ND
4 story RC	14	0.230	4.36	2.92	Low and moderate code RC frame: NSD
5 story RC	17	0.279	3.59	3.31	Low and moderate code RC frame: NSD
6 story RC	20	0.328	3.05	4.88	Low and moderate code RC frame: NSD

*Calculated using T=cH from Gallipoli et al. (2022) for URM and RC buildings on soft soil.
ND, No structural damage; NSD, Non-structural damage; ED, Extensive damage; CD, Complete damage.

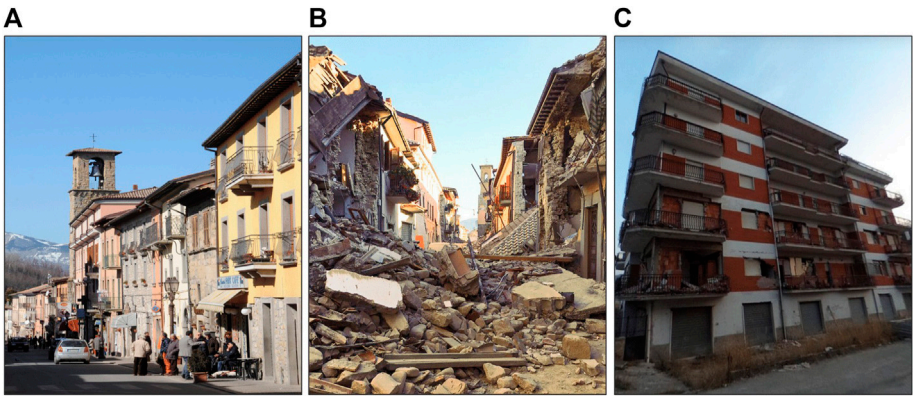

FIGURE 3
Photos of Amatrice. **(A)** View of the historical center of Amatrice on 26 February 2012 (Wikimedia Commons, Silvio Sorcini, licensed under CC-BY 4.0 and is available at: https://commons.wikimedia.org/wiki/File:2012-02-26_Corso_Amatrice.jpg); **(B)** Historical center on 29 August 2016, damaged by the M6 event of 24 August 2016 (Wikimedia Common, Diego Bianchi, licensed under CC-BY 2.0 and is available at: https://commons.wikimedia.org/wiki/File:Terremoto_centro_Italia_2016_-_Amatrice_-_corso_Umberto_I_(29242968591).jpg); **(C)** 5 story RC building, constructed following a low code, showing extensive damage photographed on August 31, 2017 (Mapillary, https://www.mapillary.com/, valentina_p, licensed under CC BY SA 4.0).

Our results for the expected extensive damage of 3 story simple stone URM buildings (Table 2; Figure 2E) are in accordance with the information on observed damage in the Amatrice historical center (e.g., Figure 2I; Stewart and Lanzo, 2018; D'Ayala et al., 2019). Following these reports, most of the low and mid-rise URM buildings were either highly damaged or totally destroyed during the 24 August 2016 event (see Figures 3A,B for a comparison of the main road before and after the considered M6 event). According to Sorrentino et al. (2019) most damage occurred to buildings with more than 2 stories. A video of the damage undergone by the historical center is available at: https://www.youtube.com/watch?v = 3-UDfhIH70M. Outside the historical center, in Amatrice a number of low (1–3 story) and mid-rise (4–7 story) RC buildings (of which 37 surveyed by Masi et al., 2019) were constructed in different time periods, based on different building codes (low and moderate). For these buildings, different damage levels were observed after the analyzed M6 event (Stewart and Lanzo, 2018; Masi et al., 2019; D'Ayala et al., 2019). In our study, we considered the damage thresholds for both low and moderate code RC frame buildings. Results are presented for 3–6 story RC buildings which are the most frequent RC buildings in the study area. Following both the low and moderate code thresholds, non-structural damage should be expected for 4–6 story RC frame buildings. Here, we present two examples of RC buildings for which information on the damage state is available from literature (D'Ayala et al., 2019). The first one is a 6 story RC building constructed in the late 1980s, following a moderate building code (Figure 2A, yellow triangle), only non-structural damage was inspected after the event. The second is a 5 story RC building constructed in the late 1970s or early 1980s following a low building code (Figures 3C, 2A, red triangle). This building was

TABLE 3 Damage assessment for different building typologies for Norcia (1-3 story URM and 3-5 story RC buildings).

Building typology	Average building height (m)	Period T* (s)	Frequency f (Hz)	Relative displacement (cm)	Expected damage
1 story URM	5	0.085	11.76	0.20	Simple stone and regular URM: NSD
2 story URM	8	0.136	7.35	0.98	Simple stone URM: ED, Regular URM: NSD
3 story URM	11	0.187	5.35	2.17	Simple stone URM: CD, Regular URM: NSD
3 story RC	11	0.180	5.54	2.26	Low and moderate code RC frame: NSD
4 story RC	14	0.230	4.36	2.20	Low and moderate code RC frame: ND
5 story RC	17	0.279	3.59	2.07	Low and moderate code RC frame: ND

*Calculated using T=cH from Gallipoli et al. (2022) for URM and RC buildings on soft soil.
ND, No structural damage; NSD, Non-strctural damage; ED, Extensive damage; CD, Complete damage.

extensively damaged during the M6 event (Figure 3C), suffering structural damage (partial collapse of the masonry infill panels and shear failure of some columns). Additional pictures of the damage (non-structural and structural) undergone by the two RC buildings are available in D'Ayala et al. (2019). Considering the damage thresholds for the two selected mid-rise RC frame buildings, from our results we expect non-structural damage for both buildings. This is in accordance with the observed damage for the moderate-code, but not for the low-code building.

Norcia

For Norcia, the M6 earthquake recordings of the sensors (OSS, Figure 2B) installed in the basement of the San Benedetto school building (e.g., Comodini et al., 2018; Falcone et al., 2021) were used to estimate the expected relative displacements (Table 3, maximum absolute values of the two horizontal components are reported) using the DARR method. The target area corresponds to the historical center, which according to Sorrentino et al. (2019) was mostly constituted by low-rise URM buildings (in total 95%): 74% of them had 2 stories, 15% 1 story and 11% 3 stories. Hence, the building typologies of 1–3 story URM buildings were analyzed in this study. Moreover, low and mid-rise RC buildings were studied.

The historical center is located in an intermountain sedimentary basin (e.g., Bindi et al., 2011; Luzi et al., 2019; Pagliaroli et al., 2020), i.e., on soft soils with potential occurrence of site effects. Thus, the fundamental periods T of the building typologies are calculated using the period-height relationships for URM and RC buildings on soft soil from Gallipoli et al. (2022). Since the school building was aligned the same way as most of the buildings in the historical center, the traces were not rotated.

Based on our results (Table 3, Figure 2F), non-structural, extensive and complete damage should be expected for 1, 2, and 3 story simple stone URM buildings, respectively. For 1–3 story regular URM buildings, non-structural damage should be expected. During the first event of the sequence, only a few buildings were damaged, most of them not structurally (Figure 2J and D'Ayala et al., 2019), but some of them also suffered structural damage. After the 1979 (Val Nerina) and 1997 (Umbria-Marche) events, most of the buildings in Norcia have been strengthened and retrofitted (Sisti et al., 2019; Sorrentino et al., 2019). Structural damage was only observed for a few masonry buildings with poor or no retrofitting. The URM buildings in the historical center of Norcia are assumed to behave as regular URM buildings to account for the retrofitting. In that case, only non-structural damage would be observed, in accordance with the few damage observed in the historical center of Norcia after the M6 event.

One example of the retrofitting of the buildings in Norcia is the 3 story RC school building, from which the recordings in the basement were used for the damage assessment. The building was designed in the 1960s and retrofitted in 2003 and 2011 (Comodini et al., 2018). The second retrofitting included the installation of dissipative braces on the 1st to 3rd floors. Figure 4 shows the simulated and observed relative displacements for this building for an M3.9 event occurring on 30 November 2013 at approximately 20 km distance and for the M6 event of 24 August 2016. The observed accelerations at the top and bottom of the building and the corresponding Fourier Spectra are presented in Supplementary Figure S1, S2. The building is simulated as an SDOF oscillator in both directions, with fundamental frequencies of 4.3 Hz (longitudinal direction X) and 4.6 Hz (transverse direction Y) and a damping ratio of 2% for small magnitude events. The values characterizing the SDOF oscillator (frequency and damping) have been estimated using a small magnitude event and tested for several small magnitude events, giving satisfactory results in all cases. As presented in Figure 4A, the simulated and observed maximum absolute relative displacements are similar for the M3.9 event for both directions. For the y direction, the relative displacement was almost precisely reconstructed. When considering the M6 event, probably due to the activation of the dissipators, the damping increases in the y direction. Therefore, a 10% damping ratio

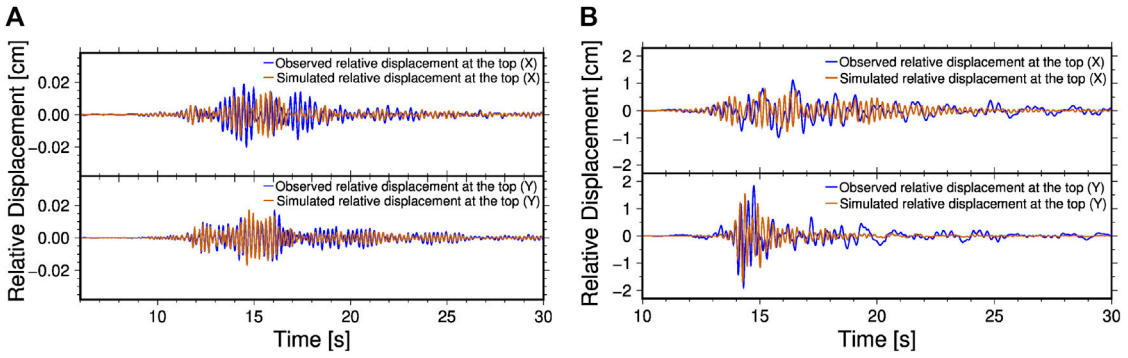

FIGURE 4
Observed (blue) and simulated relative displacements (orange) at the top of the building for an M3.9 event of 30-11-2013 **(A)** and the M6 event of 24-08-2016 **(B)** for the two main directions of the building (X and Y).

TABLE 4 Damage assessment for different building typologies for Visso (2-4 story URM buildings).

Building typology	Average building height (m)	Period T* (s)	Frequency f (Hz)	Relative displacement (cm)	Expected damage
2 story URM	8	0.136	7.35	0.23	Simple stone URM: NSD, Regular URM: ND
3 story URM	11	0.187	5.35	0.43	Simple stone URM: NSD, Regular URM: ND
4 story URM	14	0.238	4.20	1.14	Simple stone and regular URM: NSD

*Calculated using T=cH from Gallipoli et al. (2022) for URM and RC buildings soft soil.
ND, No damage; NSD, Non-structural damage; ED, Extensive damage; CD, Complete damage.

(Ferraioli and Lavino, 2019; Foti et al., 2020) is assumed for this direction. Although we do not precisely reconstruct the observed relative displacement at the top of the building, the simulated and observed maximum absolute relative displacements at the top of the building are similar. The simulated maximum absolute relative displacement was estimated as 1.7 cm. When considering the damage limits for a low-rise RC frame building constructed after a low or moderate code, non-structural or no damage should be expected, respectively. This is in accordance with the fact that only non-structural damage was observed.

Visso

For the Visso target area, the recordings in the basement of the Pietro Capuzi school building (OSS, Figure 2C) have been used to estimate the expected relative displacements (Table 4, maximum absolute values of the two horizontal components are reported) and the corresponding expected damage. The main axes of the school building were approximately oriented as the dominant building directions of the Visso town. The case study of the Visso school building has been studied in Petrovic et al. (2022) and, following the limits for 1–2 story simple stone URM buildings in Table 1, complete damage should be expected for the August 24 M6 event. After the event, moderate to severe damage has been observed (Brunelli et al., 2021). The Visso target area includes both the historical part (located in the southeast) and the central-western part of the town. The town of Visso is/was mainly composed of 2–4 story simple stone URM and 2–3 story regular URM buildings (Gaudiosi et al., 2016) constructed on soft soils (Brunelli et al., 2021). Thus, the T-h relationships for soft soils (Gallipoli et al., 2022) were used. Many buildings had been partially reconstructed or retrofitted after the 1997 Umbria-Marche sequence (Gaudiosi et al., 2016).

Following the considered damage limits (Table 1), non-structural damage should be expected for 2–4 story simple stone URM buildings (Table 4, Figure 2G). For 2–3 and 4 story regular URM buildings, no damage and non-structural damage should be expected, respectively. Our results are partially in accordance with the fact that damage has been observed only for a few buildings in the historical center (Gaudiosi et al., 2016).

However, the surveys performed after the 24 August event (Gaudiosi et al., 2016) show that both non-structural and structural damage occurred for many simple stone buildings outside the historical center (Figure 2K), including some partially reconstructed after the 1997 Umbria-Marche sequence (Gaudiosi et al., 2016). These differences might be due to a combination of factors including the variability of the dynamic behavior of

TABLE 5 Damage assessment for different building typologies for Sulmona (2-3 story URM and 3-5 story RC buildings).

Building typology	Average building height (m)	Period T* (s)	Frequency f (Hz)	Relative displacement (cm)	Expected damage
2 story URM	8	0.136	7.36	0.01	Simple stone and regular URM: ND
3 story URM	11	0.187	5.35	0.01	Simple stone and regular URM: ND
3 story RC	11	0.180	5.54	0.01	Low and moderate code RC frame: ND
4 story RC	14	0.230	4.36	0.02	Low and moderate code RC frame: ND
5 story RC	17	0.279	3.59	0.03	Low and moderate code RC frame: ND

*Calculated using T=cH from Gallipoli et al. (2022) for URM and RC buildings on soft soil.
ND, No structural damage; NSD, Non-structural damage; ED, Extensive damage; CD, Complete damage.

buildings within the same typology and the occurrence of site effects, also suggested by Gaudiosi et al. (2016).

Sulmona

The recordings in the basement of the Orthopedic Surgery Pavilion of the Sulmona hospital (part of OSS, Figure 2D) have been used to calculate the expected relative displacements (Table 5, maximum absolute values of the two horizontal components are reported) in the target area of Sulmona (epicentral distance: approximately 90 km). The buildings in the historical center are mostly URM (simple stone) buildings constructed before 1800 (Munari et al., 2010). Thus, we considered here 2 and 3 story URM buildings for the historical city center, as well as low and mid-rise RC buildings for the recently constructed buildings. Sulmona was constructed on terraced fluvial and alluvial deposits (Di Giulio et al., 2015), therefore, the T-h relationships for soft soils (Gallipoli et al., 2022) were considered. The hospital building's main directions are aligned with the dominant building directions in the town of Sulmona.

No damage should be expected Figure 2H based on the obtained relative displacement (Table 5, Figure 2H) using the limits for different damage states (Table 1) for all building typologies. Our results are in accordance with the fact that no damage was reported in Sulmona after the M6 event.

Discussion

In this study, we tested and verified the potential of the DARR method for providing local-scale information on structural damage for selected building typologies dominant in the studied areas. The estimation is based on a single recording in or close to be selected target area when the site conditions can be assumed homogeneous. Since only the recordings of one sensor are needed for each target area, it is a cost-effective and quick method for a rapid estimation of the expected damage both in single monitored buildings and target areas, and can support rapid response actions of the civil protection. If more than one recording is present for a considered target area, the choice should be made depending on the proximity of the recording and the similarity of geological conditions.

The DARR method relies on several assumptions discussed in Scaini et al. (2021) and Petrovic et al. (2022). There is a wide number of studies on the dynamic response of specific buildings to earthquakes (e.g., Rahmani and Todorovska, 2021) that allow identifying damage patterns in a precise way. The DARR method only accounts for the linear dynamic response of buildings, assuming that it can support the identification of structural damage. With this approximation, the precise reconstruction of the traces during the non-linear behavior is not possible, but the overstepping of the thresholds and the subsequent damage is successfully assessed (Scaini et al., 2021; Petrovic et al., 2022). For the purposes of rapid damage assessment, this approximation is satisfactory. DARR can be used for a large number of buildings with prior information (dominant building typologies, average building heights, period-height relationships, soil conditions) supporting rapid post-event damage assessment. Nonetheless, to correctly define the damage thresholds and to assess the expected damage, precise information on the building typologies (including construction age for building code identification) is needed. In particular, the use of period-height relationships requires information on the average building or story height, which might vary among the typologies, leading to different values of the fundamental frequency and thus, different relative displacement and expected damage. In case of scarce information on the building typologies, the identification of the damage thresholds and thus, the assessment of expected damage might be erroneous. In our study, we estimated the frequencies representative for the considered building typologies from period-height relationships from literature (Gallipoli et al., 2022). These relationships were developed from ambient vibration measurements in residential buildings in southern and northeastern Italy. There might be a variation in the frequencies of the building typologies of the studied area due to variations in the construction (e.g., materials, story

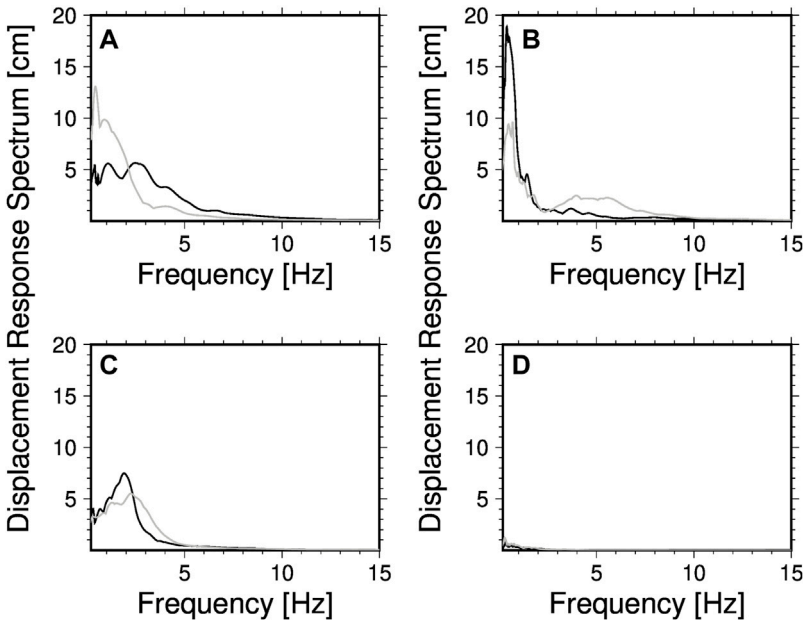

FIGURE 5
Displacement Response Spectra for **(A)** Amatrice **(B)** Norcia **(C)** Visso and **(D)** Sulmona for the two main directions of the buildings (gray and black lines) in the considered towns.

heights etc.). Peak relative displacements increase drastically for mid to high-rise buildings with frequencies lower than 2 Hz (Norcia) and 5 Hz (Amatrice), as shown by the response spectra in Figure 5. Following the damage limits (Table 1), these buildings would suffer extensive or complete damage according to DARR.

The DARR method relies heavily on the choice of the relative displacement or interstory drift limits used for the damage assessment. Currently, the literature provides both interstory drift (e.g., Borzi et al., 2008; Shahzada et al., 2011; Chourasia et al., 2016; Minas and Galasso, 2019) and relative displacement limits (e.g., Lagomarsino and Giovinazzi, 2006; Frankie et al., 2013; Lestuzzi et al., 2016). Each set of limit values is derived based on different assumptions and for specific building typologies and study areas, and their use and validity depends on the typology dynamic behavior. DARR assumes that the relative displacement and interstory drift limits derived with different methods (e.g., numerical methods) are comparable with those found with the Z-transform for the purpose of a simplified damage assessment. However, further work is needed to validate the usability of the relative displacement and interstory drift limits derived with numerical methods. This would be strongly supported by the availability of more recordings both at the bottom and at the top of damaged buildings in correspondence of structural damage.

In this study, we considered different building typologies that are representative for the studied areas. The selection of damage thresholds for the analyzed building typologies is critical and further work is needed in order to estimate the expected behavior of specific building types (e.g., retrofitted URM buildings) and the influence of different soil conditions (e.g., Gallipoli et al., 2020). In addition, different damage state definitions are available from literature, based either on empirical damage identification (e.g., EMS-98, Grunthal, 1998) or limit states identified by numerical modeling (e.g., Borzi et al., 2008). In order to compare the outcomes of different damage assessment, a strong uniformation effort is required, as discussed by e.g., Rossetto and Elnashai (2003), Faravelli et al. (2019).

Amatrice and Norcia had a similar epicentral distance (9 and 15 km, respectively) and the ground motion recordings of the August event in Norcia and Amatrice are comparable in terms of PGA and PGD. However, during the 24 August 2016 M6 event, masonry buildings in Norcia successfully resisted a ground motion that might have led to a structural damage state (D4-D5) as documented in Amatrice (Figure 2I). The different damage patterns might be due to several factors including site effects, building typologies (e.g., retrofitting) and orientation, and the main direction of seismic wave propagation. In particular, DARR assumes that the ground motion in the target areas is homogeneous and can be represented by the recording. However, Figure 5 shows the different response spectra in Amatrice and Norcia, with large amplitudes at lower frequency related to local site effects. All these factors should be pondered when interpreting the recording from a single station and concur to identify the target area for applying DARR. For the Amatrice test site, the location of the recordings was outside the historical center (target area). Due to site effects, the relative displacement and thus, the expected damage might be slightly underestimated.

Apart from a number of studies on specific buildings (e.g., Ferraioli and Lavino, 2019; Gandelli et al., 2019; Foti et al., 2020), to our knowledge there are no studies that estimate the expected increase in relative displacement or interstory drift capacity for specific retrofitted building typologies. Additional studies on relative displacement or interstory drift limits for retrofitted building typologies might improve the results on the expected damage from the DARR method. In addition, no specific period-height relationships exist for retrofitted buildings which modify the stiffness of the buildings (e.g., Michel et al., 2018). Finally, retrofitting can influence the building's damping and can be different in the two main building directions, as shown for the case of San Benedetto school in Norcia. Further research on the effect of retrofitting on the dynamic response of the considered building typologies would be desirable.

For the case study of Visso, non-structural damage should be expected for the August 24 event for 2–4 story simple stone URM buildings. The school building in Visso was a 2 story simple stone URM building and was damaged during this event. However, the school building has to be considered as a different building typology, with much higher floor heights and a more complex T shape. Following the T-h relationships from Gallipoli et al. (2022), for a 2 story building of 8 m height, we assume an average fundamental frequency of 7.35 Hz. In contrast, the school building was 13.5 m high and had a fundamental frequency of 3.18 Hz (Ferrero et al., 2020). For this reason, the expected relative displacement is much higher (3.5 cm) than the one estimated for a standard 2 story URM building, resulting in complete damage. The response spectra in Figure 5 shows that for Visso the expected relative displacement increases for fundamental frequencies below 4 Hz. In the study of the school building in Visso (Petrovic et al., 2022), the damping ratio has been estimated as 15%. In this study, the standard value of 5% (EC8, CEN 2004) was used, resulting in a slightly higher relative displacement.

DARR supports the combined use of both relative displacement and interstory drift limits which might be appropriate for different case-studies (e.g., high-rise flexible buildings). Further work is needed to explore how these limits work and their performance for different building types. The validation of DARR is, at the time, limited by the difficulties of having simultaneous availability of the required data which comprise earthquake recordings, buildings characteristics (type, material, age, height, fundamental frequencies and damping) and knowledge of the soil conditions. Future efforts will be devoted to testing the method in other areas where the information is available.

There are several studies on the effect of different ground motion parameters on the expected structural building damage (e.g., Ghimire et al., 2021 for RC buildings). The optimum criterion depends on the expected collapse mechanism (which varies between building typologies), and can be defined based on multiple indicators, including duration (Hancock and Bommer, 2006). This criterion would help the rapid identification of areas where structural damage is expected and prioritize interventions.

Conclusion

In this work, we present an application of the DARR method to the August 24 M6 event of the Central Italy seismic sequence (2016–2017). Expected damage is estimated in four selected towns in Central Italy (Amatrice, Norcia, Visso and Sulmona) where earthquake recordings were available. Results of the damage assessment, performed for dominant building typologies (URM and RC frames), were validated with post-event surveys. DARR successfully estimated expected damage for some building types as mid-rise URM (e.g. in the historical center of Amatrice) but failed to identify the damage occurred for low-rise URM buildings (e.g. in the town of Amatrice). The reasons for this are discussed in the article pointing out the aspects to be improved in future. Extensive and complete damage is obtained in accordance with the observed damage for 2 and 3 story simple stone URM buildings in Norcia and non-structural damage for regular URM buildings. It also correctly estimates the absence of structural damage in a target area located at a larger epicentral distance (Sulmona). Our results suggest that relative displacement limits are suitable for the damage assessment of low and mid rise building typologies considered in this work. DARR has the potential to provide a timely and cost-effective estimation of the expected damage, both for selected buildings and target areas, to support rapid response in the aftermath of a potentially destructive earthquake.

Data availability statement

The datasets presented in the study are publicly available. All datasets presented/accessed in this study are cited in the article/Supplementary Material. Earthquake recordings were extracted from ITACA (https://itaca.mi.ingv.it/) and OSS (https://oss.protezionecivile.it/osspublic/#/).

Author contributions

BP: Conceptualization, data analysis and interpretation, Writing-original draft preparation; CS: Conceptualization, data collection and interpretation, Writing-original draft preparation; SP: Conceptualization, Writing-reviewing and editing.

Funding

Bojana Petrovic is supported by a research fellowship from the German Research Foundation (Deutsche Forschungsgemeinschaft, DFG, PE 2891/1-1, Projektnummer 428372009). This research was partially funded by the Autonomous Region Friuli Venezia Giulia, Veneto Region and the ARMONIA project (real-time acceleration network for monitoring sites and buildings in Italy and Austria, 2014–2020 INTERREG V-A Italy–Austria).

Acknowledgments

The DARR method was developed for the Friuli Venezia-Giulia region within the research activities supported by the Autonomous Region Friuli Venezia Giulia, the Veneto Region and the ARMONIA project (real-time acceleration network for monitoring sites and buildings in Italy and Austria, 2014–2020 INTERREG V-A Italy–Austria).

Conflict of interest

The authors declare that the research was conducted in the absence of any commercial or financial relationships that could be construed as a potential conflict of interest.

Publisher's note

All claims expressed in this article are solely those of the authors and do not necessarily represent those of their affiliated organizations, or those of the publisher, the editors and the reviewers. Any product that may be evaluated in this article, or claim that may be made by its manufacturer, is not guaranteed or endorsed by the publisher.

Supplementary material

The Supplementary Material for this article can be found online at: https://www.frontiersin.org/articles/10.3389/feart.2022.932110/full#supplementary-material

References

Appolloni, L., and D'Alessandro, D. (2021). Housing spaces in nine European countries: A comparison of dimensional requirements. *Int. J. Environ. Res. Public Health* 18, 4278. doi:10.3390/Ijerph18084278

Bard, P. Y., Gueguen, G., and Wirgin, A. (1996). "A note on the seismic wavefield radiated from large building structures into soft soils," in Proceedings of 11th World Conference on Earthquake Engineering.

Bindi, D., Luzi, L., Parolai, S., Di Giacomo, D., and Monachesi, G. (2011). Site effects observed in alluvial basins: The case of Norcia (central Italy). *Bull. Earthq. Eng.* 9, 1941–1959. doi:10.1007/s10518-011-9273-3

Borzi, B., Crowley, H., and Pinho, R. (2008). Simplified pushover-based earthquake loss assessment (SP- BELA) method for masonry buildings. *Int. J. Archit. Herit.* 2, 353–376. doi:10.1080/15583050701828178

Bragato, P. L., Comelli, P., Saraò, A., Zuliani, D., Moratto, L., Poggi, V., et al. (2021). The OGS-Northeastern Italy seismic and deformation network: Current status and outlook. *Seismol. Res. Lett.* 92 (3), 1704–1716. doi:10.1785/0220200372

Brunelli, A., de Silva, F., Piro, A., Parisi, F., Sica, S., Silvestri, F., et al. (2021). Numerical simulation of the seismic response and soil–structure interaction for a monitored masonry school building damaged by the 2016 Central Italy earthquake. *Bull Earthquake Eng.* 19, 1181–1211. doi:10.1007/s10518-020-00980-3

CEN (2004). *European standard EN 1998-1: 2004—eurocode 8: Design of structures for earthquake resistance. Part 1: General rules, seismic action and rules for buildings*. Brussels, Belgium: European Committee for Standardization.

Chiaraluce, L., Di Stefano, R., Tinti, E., Scognamiglio, L., Michele, M., Casarotti, E., et al. (2017). The 2016 central Italy seismic sequence: A first look at the mainshocks, aftershocks, and source models. *Seismol. Res. Lett.* 88 (3), 757–771. doi:10.1785/0220160221

Chieffo, N., Formisano, A., and Ferreira, T. M. (2019). Damage scenario-based approach and retrofitting strategies for seismic risk mitigation: An application to the historical centre of Sant'Antimo (Italy). *Eur. J. Environ. Civ. Eng.* 25, 1929–1948. doi:10.1080/19648189.2019.1596164

Chourasia, A., Bhattacharyya, S. K., Bhandari, N. M., and Bhargava, P. (2016). Seismic performance of different masonry buildings: Full-scale experimental study. *J. Perform. Constr. Facil.* 30–5. doi:10.1061/(ASCE)CF.1943-5509.0000850

Comodini, F., Fulco, A., and Mezzi, M. (2018). *Performance of A building with dissipative bracing system under strong earthquakes*. Thessaloniki: 16th European conference on earthquake engineering, 18–21 June 2018.

Crowley, H., and Pinho, R. (2010). Revisiting Eurocode 8 formulae for periods of vibration and their employment in linear seismic analysis. *Earthq. Eng. Struct. Dyn.* 39 (2), 223–235. doi:10.1002/eqe.949

D'Ayala, D., Faure-Walker, J., Mildon, Z., Lombardi, D., Galasso, C., Pedicone, D., et al. (2019). *The M W 6.2 Amatrice*. Italy Earthquake Of 24th August 2016 - A Field Report By Eefit, ©EEFIT. London: EEFIT.

Di Giulio, G., De Nardis, R., Boncio, P., Milana, G., Rosatelli, G., Stoppa, F., et al. (2015). Seismic response of a deep continental basin including velocity inversion: The Sulmona intramontane basin (central apennines, Italy). *Geophys. J. Int.* 204, 418–439. doi:10.1093/gji/ggv444

Dolce, M., Nicoletti, M., De Sortis, A., Marchesini, S., Spina, D., and Talanas, F. (2017). Osservatorio sismico delle strutture: The Italian structural seismic monitoring network. *Bull. Earthq. Eng.* 15, 621–641. doi:10.1007/s10518-015-9738-x

Donà, M., Carpanese, P., Follador, V., Sbrogiò, L., and Da Porto, F. (2020). Mechanics-based fragility curves for Italian residential URM buildings. *Bull. Earthq. Eng.* 19, 3099–3127. doi:10.1007/s10518-020-00928-7

Espinosa-Aranda, J. M., Cuellar, A., Garcia, A., Ibarrola, G., Islas, R., Maldonado, S., et al. (2009). Evolution of the Mexican seismic alert system (SASMEX), seismol. *Res. Lett.* 80 (5), 694–706. doi:10.1785/gssrl.80.5.694

Falcone, G., Vacca, V., Mori, F., Naso, G., and Spina, D. (2021). Evaluation of building seismic retrofitting costs founded on experimental data. The case study of "San Benedetto" School (Norcia, Italy). *Italian J. Geosciences* 140 (3), 365–381. doi:10.3301/ijg.2021.09

Faravelli, M., Borzi, B., Polli, D., and Pagano, M. (2019). Calibration of a mechanics-based method for large-scale vulnerability assessment. *Bull. Earthq. Eng.* 17, 2485–2508. doi:10.1007/s10518-019-00560-0

Ferraioli, M., and Lavino, A. (2019). A displacement-based design method for seismic retrofit of RC buildings using dissipative braces. *Math. Probl. Eng.*, 1–28. doi:10.1155/2018/5364564

Ferrero, C., Lourenco, P. B., and Calderini, C. (2020). Nonlinear modeling of unreinforced masonry structures under seismic actions: Validation using a building hit by the 2016 central Italy earthquake. *Bull. Earthq. Eng.* 14 (51), 92–114. doi:10.3221/IGF-ESIS.51.08

Fiorentino, G., Forte, A., Pagano, E., Sabetta, F., Baggio, C., Lavorato, D., et al. (2018). Damage patterns in the town of Amatrice after August 24th 2016 central Italy earthquakes. *Bull. Earthq. Eng.* 16, 1399–1423. doi:10.1007/s10518-017-0254-z

Foti, D., Ruggiero, F., Sabbà, M. F., and Lerna, M. (2020). A dissipating frames for seismic retrofitting and building energy-efficiency. *Infrastructures* 5 (9), 74. doi:10.3390/infrastructures5090074

Frankie, T. M., Gencturk, B., and Elnashai, A. S. (2013). Simulation-based fragility relationships for unreinforced masonry buildings. *J. Struct. Eng. (U. S.)* 139, 400–410. doi:10.1061/(ASCE)ST.1943-541X.0000648

Gallipoli, M. R., Calamita, G., Tragni, N., Pisapia, D., Lupo, M., Mucciarelli, M., et al. (2020). Evaluation of soil-building resonance effect in the urban area of the city of Matera (Italy). *Eng. Geol.* 272, 105645. doi:10.1016/j.enggeo.2020.105645

Gallipoli, M. R., Mucciarelli, M., and Vona, M. (2009). Empirical estimate of fundamental frequencies and damping for Italian buildings. *Earthq. Eng. Struct. Dyn.* 38, 973–988. doi:10.1002/eqe.878

Gallipoli, M. R., Petrovic, B., Scaini, C., Calamita, G., Tragni, N., Barnaba, C., et al. (2022). *FRIBAS database for better characterization of RC and URM buildings: Towards specific T-H relationships*. (submitted to Bulletin of Earthquake Engineering, under review).

Gandelli, E., Taras, A., Distl, J., and Quaglini, V. (2019). Seismic retrofit of hospitals by means of hysteretic braces: Influence on acceleration-sensitive non-structural components. *Front. Built Environ.* 5 (100), 1–13. doi:10.3389/fbuil.2019.00100

Gaudiosi, I., Vignaroli, G., Sirianni, P., Giallini, S., Mori, F., Polpetta, F., et al. (2016). Local seismic response studies in the north-western portion of the August 24th, 2016 Mw 6.0 earthquake affected area. The case of Visso village (central Apennines). *Ann. Geophys.* 59. doi:10.4401/ag-7258

Gaudiosi, I., Simionato, M., Mancini, M., Cavinato, G. P., Coltella, M., Razzano, R., et al. (2021). Evaluation of site effects at Amatrice (central Italy) after the August 24th, 2016, mw 6.0 earthquake. *Soil Dyn. Earthq. Eng.* 144, 106699. doi:10.1016/j.soildyn.2021.106699

Ghimire, S., Guéguen, P., and Astorga, A. (2021). Analysis of the efficiency of intensity measures from real earthquake data recorded in buildings. *Soil Dyn. Earthq. Eng.* 147, 106751. doi:10.1016/j.soildyn.2021.106751

Goel, R. K., and Chopra, A. K. (1997). Period formulas for moment-resisting frame buildings. *J. Struct. Eng. (N. Y. N. Y).* 123, 1454–1461. doi:10.1061/(asce)0733-9445(1997)123:11(1454)

Gorini, A., Nicoletti, M., Marsan, P., Bianconi, R., De Nardis, R., Filippi, L., et al. (2010). The Italian strong motion network. *Bull. Earthq. Eng.* 8, 1075–1090. doi:10.1007/s10518-009-9141-6

Grünthal., G. (1998). "European macroseismic scale 1998 (EMS-98)," in *European seismological commission, subcommission on engineering seismology, working group macroseismic scales* (Luxembourg: Conseil de l'Europe, Cahiers du Centre Européen de Géodynamique et de Séismologie), 15.

Hancock, J., and Bommer, J. J. (2006). A state-of-knowledge review of the influence of strong-motion duration on structural damage. *Earthq. Spectra* 22 (3), 827–845. doi:10.1193/1.2220576

Jin, X., Ma, Q., and Li, S. (2004). *Comparison of four numerical methods for calculating seismic dynamic response of SDOF systems, 13th World Conf. on Earthquake Engineering*. Canada: Vancouver. 1–6 August 2004Paper Number 2889.

Lagomarsino, S., and Giovinazzi, S. (2006). Macroseismic and mechanical models for the vulnerability and damage assessment of current buildings. *Bull. Earthq. Eng.* 4, 415–443. doi:10.1007/s10518-006-9024-z

Lee, V. W. (1990). Efficient algorithm for computing displacement, velocity and acceleration responses of an oscillator to arbitrary ground motion. *Soil Dyn. Earthq. Eng.* l9 (6), 288–300. doi:10.1016/s0267-7261(05)80015-6

Lestuzzi, P., Podestà, S., Luchini, C., Garofano, A., Kazantzidou-Firtinidou, D., Bozzano, C., et al. (2016). Seismic vulnerability assessment at urban scale for two typical Swiss cities using Risk-UE methodology. *Nat. Hazards (Dordr).* 84, 249–269. doi:10.1007/s11069-016-2420-z

Luzi, L., D'Amico, M., Massa, M., and Puglia, R. (2019). Site effects observed in the Norcia intermountain basin (Central Italy) exploiting a 20-year monitoring. *Bull. Earthq. Eng.* 17, 97–118. doi:10.1007/s10518-018-0444-3

Luzi, L., Pacor, F., Puglia, R., Lanzano, G., Felicetta, C., D'Amico, M., et al. (2016). The central Italy seismic sequence between August and december 2016: Analysis of strong-motion observations. *Seismol. Res. Lett.* 88 (5), 1219–1231. doi:10.1785/0220170037

Masi, A., Chiauzzi, L., Santarsiero, G., Manfredi, V., Biondi, S., Spacone, E., et al. (2019). Seismic response of RC buildings during the Mw 6.0 August 24, 2016 Central Italy earthquake: The Amatrice case study. *Bull. Earthq. Eng.* 17, 5631–5654. doi:10.1007/s10518-017-0277-5

Meletti, C., Montaldo, V., Stucchi, M., and Martinelli, F. (2006). *Database della pericolosità sismica MPS04*. Rome: Istituto Nazionale di Geofisica e Vulcanologia (INGV). doi:10.13127/sh/mps04/db

Michel, C., Gueguen, P., Lestuzzi, P., and Bard, P.-Y. (2010). Comparison between seismic vulnerability models and experimental dynamic properties of existing buildings in France. *Bull. Earthq. Eng.* 8, 1295–1307. doi:10.1007/s10518-010-9185-7

Michel, C., Karbassi, A., and Lestuzzi, P. (2018). Evaluation of the seismic retrofitting of an unreinforced masonry building using numerical modeling and ambient vibration measurements. *Eng. Struct.* 158, 124–135. doi:10.1016/j.engstruct.2017.12.016

Milana, G., Cultrera, G., Bordoni, P., Bucci, A., Cara, F., Cogliano, R., et al. (2018). Local site effects estimation at Amatrice (Central Italy) through seismological methods. *Bull. Earthq. Eng.* 18, 5713–5739. doi:10.1007/s10518-019-00587-3

Minas, S., and Galasso, C. (2019). Accounting for spectral shape in simplified fragility analysis of case-study reinforced concrete frames. *Soil Dyn. Earthq. Eng.* 119, 91–103. doi:10.1016/j.soildyn.2018.12.025

Mori, J., Kanamori, H., Davis, J., Hauksson, E., Clayton, E., Heaton, T., et al. (1998). Major improvements in progress for Southern California earthquake monitoring. *Eos Trans. AGU.* 79, 217–221. doi:10.1029/98eo00157

Mucciarelli, M., Masi, A., Gallipoli, M. R., Harabaglia, P., Vona, M., Ponzo, F., et al. (2004). Analysis of RC building dynamic response and soil-building resonance based on data recorded during a damaging earthquake (Molise, Italy, 2002). *Bull. Seismol. Soc. Am.* 94, 1943–1953. doi:10.1785/012003186

Munari, M., Valluzzi, M. R., Cardani, G., Anzani, A., Binda, L., and Modena, C. (2010). "Seismic vulnerability analyses of masonry aggregate buildings in the historical centre of Sulmona (Italy)," in Proceeding 13th International Conference on Structural Faults and Repair (Edinburgh), 1–10.

Okada, Y., Kasahara, K., Hori, S., Obara, K., Sekiguchi, S., Fujiwara, H., et al. (2004). Recent progress of seismic observation networks in Japan hi-net, F-net, K-net and KiK-net. *Earth Planets Space* 56, xv. doi:10.1186/BF03353076

OpenStreetMap contributors (2015). OpenStreetMap contributors. Available at: https://planet.openstreetmap.org.

Pagliaroli, A., Pergalani, F., Ciancimino, A., Chiaradonna, A., Compagnoni, M., de Silva, F., et al. (2020). Site response analyses for complex geological and morphological conditions: Relevant case-histories from 3rd level seismic microzonation in central Italy. *Bull. Earthq. Eng.* 18, 5741–5777. doi:10.1007/s10518-019-00610-7

Parolai, S., Bindi, D., Boxberger, T., Milkereit, C., Fleming, K., and Pittore, M. (2015). On-site early warning and rapid damage forecasting using single stations: Outcomes from the REAKT project. *Seismol. Res. Lett.* 86 (5), 1393–1404. doi:10.1785/0220140205

Parolai, S., Boxberger, T., Pilz, M., Fleming, K., Haas, M., Pittore, M., et al. (2017). Assessing earthquake early warning using sparse networks in developing countries: Case study of the Kyrgyz Republic. *Front. Earth Sci.* 5. doi:10.3389/feart.2017.00074

Petrovic, B., Scaini, C., and Parolai, S. (2022). *Damage assessment for rapid response (DARR): Validation for different ground motion levels and building types*. (submitted to SRL, under review).

Poggi, V., Scaini, C., Moratto, L., Peressi, G., Comelli, P., Bragato, P. L., et al. (2020). Rapid damage scenario assessment for earthquake emergency management. *Seismol. Res. Lett.* 92, 2513–2530. doi:10.1785/0220200245

Rahmani, M., Ebrahimian, M., and Todorovska, M. I. (2015). Time-wave velocity analysis for early earthquake damage detection in buildings: Application to a damaged full-scale RC building. *Earthq. Eng. Struct. Dyn.* 44 (4), 619–636. doi:10.1002/eqe.2539

Rahmani, M., and Todorovska, M. I., (2021). Structural health monitoring of a 32-storey steel-frame building using 50 years of seismic monitoring data, *Earthq. Eng. Struct. Dyn.* 50, 1777–1800. doi:10.1002/eqe.3422

Rossetto, T., and Elnashai, A. (2003). Derivation of vulnerability functions for European-type RC structures based on observational data. *Eng. Struct.* 25, 1241–1263. doi:10.1016/s0141-0296(03)00060-9

Rossetto, T., Gehl, P., Minas, S., Galasso, C., Duffour, P., Douglas, J., et al. (2016). Fracas: A capacity spectrum approach for seismic fragility assessment including record-to-record variability. *Eng. Struct.* 125, 337–348. doi:10.1016/j.engstruct.2016.06.043

Rossi, A., Tertulliani, A., Azzaro, R., Graziani, L., Rovida, A., Maramai, A., et al. (2018). The 2016–2017 earthquake sequence in central Italy: Macroseismic survey and damage scenario through the EMS-98 intensity assessment. *Bull. Earthq. Eng.* 17, 2407–2431. doi:10.1007/s10518-019-00556-w

Rota, M., Penna, A., and Magenes, G. (2008). "A procedure for deriving analytical fragility curves for masonry buildings," in Proceeding 14th World Conference on Earthquake Engineering, Beijing, China, October 12–17, 2008.

Russo, E., Felicetta, C., D'Amico, M. C., Sgobba, S., Lanzano, G., Mascandola, C., et al. (2022). *Italian Accelerometric Archive v3.2 - Istituto Nazionale di Geofisica e Vulcanologia, Dipartimento della Protezione Civile Nazionale*, Roma. doi:10.13127/itaca.3.2

Satriano, C., Elia, L., Martino, C., Lancieri, M., Zollo, A., and Iannaccone, G. (2011). PRESTo, the earthquake early warning system for Southern Italy: Concepts, capabilities and future perspectives. *Soil Dyn. Earthq. Eng.* 31, 137–153. doi:10.1016/j.soildyn.2010.06.008

Scaini, C., Petrovic, B., Tamaro, A., Moratto, L., and Parolai, S. (2021). Near-real-time damage estimation for buildings based on strong-motion recordings: An application to target areas in northeastern Italy. *Seismol. Res. Lett.* 92 (6), 3785–3800. doi:10.1785/0220200430

Shahzada, K., Gencturk, B., Khan, A. N., Naseer, A., Javed, M., and Fahad, M. (2011). Vulnerability assessment of typical buildings in Pakistan. *Int. J. Earth Sciences Eng.* 4 (6), 208–211.

Sisti, R., Di Ludovico, M., Borri, A., and Prota, A. (2019). Damage assessment and the effectiveness of prevention: The response of ordinary unreinforced masonry buildings in Norcia during the central Italy 2016–2017 seismic sequence. *Bull. Earthq. Eng.* 17, 5609–5629. doi:10.1007/s10518-018-0448-z

So, E., and Spence, R. (2013). Estimating shaking-induced casualties and building damage for global earthquake events: A proposed modelling approach. *Bull. Earthq. Eng.* 11, 347–363. doi:10.1007/s10518-012-9373-8

Sorrentino, L., Cattari, S., Da Porto, F., Magenes, G., and Penna, A. (2019). Seismic behaviour of ordinary masonry buildings during the 2016 central Italy earthquakes. *Bull. Earthq. Eng.* 17, 5583–5607. doi:10.1007/s10518-018-0370-4

Spina, D., Acunzo, G., Fiorini, N., Mori, F., and Dolce, M. (2010). A probabilistic simplified seismic model of masonry buildings based on ambient vibrations. *Bull. Earthq. Eng.* 17, 985–1007. doi:10.1007/s10518-018-0481-y

Stewart, J. P., and Lanzo, G. (2018). "Engineering reconnaissance following the october 2016 central Italy earthquakes, GEER (geotechnical extreme events reconnaissance association), report No. GEER-0500,"Editors P. Zimmaro and J. P. Stewart. doi:10.18118/G6HS39

Stucchi, M., Meletti, C., and Montaldo, V. (2011). Seismic hazard assessment (2003-2009) for the Italian building code. *Bull. Seismol. Soc. Am.* 101 (4), 1885–1911. doi:10.1785/0120100130

Tinti, E., Scognamiglio, L., Michelini, A., and Cocco, M. (2016). Slip heterogeneity and directivity of theM_L6.0, 2016, Amatrice earthquake estimated with rapid finite-fault inversion. *Geophys. Res. Lett.* 43, 10745–10752. doi:10.1002/2016gl071263

Todrani, A., and Cultrera, G. (2021). Near-source simulation of strong ground motion in Amatrice downtown including site effects. *Geosciences* 11, 186. doi:10.3390/geosciences11050186

Trifunac, M. D., Hao, T. Y., and Todorovska, M. I. (2001). Response of A 14-story reinforced concrete structure to nine earthquakes: 61 Years of observation in the hollywood storage building. Available at: www.usc.edu/dept/civil_eng/Earthquake_eng/.

Vignaroli, G., Mancini, M., Bucci, F., Cardinali, M., Cavinato, G. P., Moscatelli, M., et al. (2019). Geology of the central part of the Amatrice basin (central apennines, Italy). *J. Maps* 15, 193–202. doi:10.1080/17445647.2019.1570877

Wu, W. M., Chen, D., Lin, T., Hsieh, C., Chin, T., Chang, W., et al. (2013). A high density seismic network for earthquake early warning in taiwan based on low cost sensors. *Seismol. Res. Lett.* 84 (6), 1048–1054. doi:10.1785/0220130085

Advantages of publishing in Frontiers

OPEN ACCESS
Articles are free to read for greatest visibility and readership

FAST PUBLICATION
Around 90 days from submission to decision

HIGH QUALITY PEER-REVIEW
Rigorous, collaborative, and constructive peer-review

TRANSPARENT PEER-REVIEW
Editors and reviewers acknowledged by name on published articles

Frontiers
Avenue du Tribunal-Fédéral 34
1005 Lausanne | Switzerland

Visit us: www.frontiersin.org
Contact us: frontiersin.org/about/contact

REPRODUCIBILITY OF RESEARCH
Support open data and methods to enhance research reproducibility

DIGITAL PUBLISHING
Articles designed for optimal readership across devices

FOLLOW US
@frontiersin

IMPACT METRICS
Advanced article metrics track visibility across digital media

EXTENSIVE PROMOTION
Marketing and promotion of impactful research

LOOP RESEARCH NETWORK
Our network increases your article's readership